2023-05-01

Thermal Behavior of Plain and Fiber-Reinforced Rigid Concrete Airfield Runways

Arash Karimi Pour
University of Texas at El Paso

THERMAL BEHAVIOR OF PLAIN AND FIBER-REINFORCED RIGID CONCRETE AIRFIELD RUNWAYS

ARASH KARIMI POUR

Doctoral Program in Civil Engineering

APPROVED:

Reza Salehi-Ashtiani, Ph.D., Chair

Vivek Tandon, Ph.D.

Lin Ma, Ph.D.

Yirong Lin, Ph.D.

Ruimin Ke, Ph.D.

Stephen Crites, Ph.D.
Dean of the Graduate School

DEDICATION

I would like to dedicate this thesis to my parents. Thank you so much for everything! Words can hardly describe my thanks and appreciation to you. You have been my source of inspiration, support, and guidance. You have taught me to be unique and determined, to believe in myself, and to always persevere. I am truly thankful and honored to have you as my parents.

THERMAL BEHAVIOR OF PLAIN AND FIBER-REINFORCED RIGID CONCRETE AIRFIELD RUNWAYS

by

ARASH KARIMI POUR

DISSERTATION

Presented to the Faculty of the Graduate School of

The University of Texas at El Paso

in partial fulfillment

of the requirements

for the degree of

DOCTOR OF PHILOSOPHY

Department of Civil Engineering

THE UNIVERSITY OF TEXAS AT EL PASO

MAY 2023

ACKNOWLEDGEMENTS

First of all, I would link to prompt my deepest gratitude to my Ph.D. supervisor, Dr. Reza Salehi-Ashtiani for his constant support and worth of insights on both an academic as well as personal level. My sincere appreciation and thanks go to Prof. Ferregut and Prof. Tandon for their guidance and support throughout the course of this research. I would also like to thank Prof. Lin Ma, Prof. Yirong Lin, and Dr. Ruimin Ke for serving on my committee and providing me with comments on my dissertation. I would like to extend my gratitude to the department faculty and staff, and CTIS for their assistance throughout the course of my study at UTEP.

Last but definitely not least; I would link to prompt my deepest gratitude to my mother and father for their love, patience, encouragement, and endless support throughout my Ph.D. journey.

ABSTRACT

Thermal Behavior of Plain and Fiber-Reinforced Rigid Concrete Airfield Runways

(April 2023)

Arash Karimi Pour

Cahir of Advisory Committee: Dr. Reza Salehi-Ashtiani

The environmental condition and temperature gradient are important factors resulting in concrete airfield runways cracking during the time. Rigid concrete airfield runways experience different thermal gradients during the day and night due to changes in air temperature. Curling and thermal expansion stresses are the main consequences resulting in various types of cracking over the surface and thickness of concrete airfield runways and increasing maintenance costs. The curvature of concrete slabs increases with an increase in the temperature gradient which is amplified when runways open to traffic. Additionally, the combination of the curling and shrinkage stresses, in rare circumstances, can be highly adequate that it cracks before the pavement is exposed to any traffic loading. In addition, the movement of vehicles and increasing stresses increase the depth of cracks and thus the separation of parts of the airfield runways. Therefore, the reconstruction requires the destruction of the previous concrete airfield runways which is very time-consuming and costly. Conversely, the size effect including the dimension of concrete segments and concrete material characteristics plays the main role in controlling the curling and thermal stresses in rigid concrete airfield runways which have not been comprehensively considered by previous investigations, up to now. Previous studies only examined the effect of a limited number of influential factors, and no solution has been provided to mitigate the thermal behavior of rigid concrete slabs, and needs a comprehensive study on the curling and thermal behaviors. Therefore,

there is a knowledge gap in mechanistic quantification of the damages imparted on rigid concrete airfield runways exposed to thermal stresses. Thus, this study was designed to bridge this gap by classifying the influence of various geometric characteristics, materials properties, environmental conditions, and boundary situations on the thermal and curling stresses of rigid concrete airfield runways and provide a solution to mitigate the negative influence of this type of environmental impact.

The primary goal of this study was to mechanistically quantify the damages and structural responses imparted on rigid concrete slabs due to thermal and curling stresses. To achieve the research objectives, initially, a comprehensive evaluation was carried out to measure the influence of various geometric characteristics and materials properties on the curling and thermal stresses of slabs exposed to various temperature gradients. For this aim, a total of 8213 numerical models have been carried out to consider the effect of slab dimensions, modulus of rupture, compressive strength, and thermal coefficient of concrete on the structural responses of rigid slabs. The secondary aim of this research was to provide a solution to mitigate the negative influence of thermal stress utilizing polypropylene fibers (PF) results to provide further insights on necessary improvements in rigid concrete slabs. For this aim, different PF fractions were incorporated in a combination of various geometric and concrete material properties to control the thermal behavior of rigid concrete slabs.

Then, the author utilized the ultrasonic imaging evaluation to simulate the non-destructive test using wave propagation over the thickness and surface of rigid concrete slabs. Ultrasonic imaging is a powerful nondestructive evaluation technology for examining the condition of concrete structures through focused images obtained with the Synthetic Aperture Focusing

Technique. Therefore, the results of this evaluation provide a comprehensive opportunity to measure the influence of material properties and geometric characteristics on the strength of rigid concrete slabs using wave propagation. The author then developed a theoretical concept named "advanced zero-stress assessment" to measure the depth of cracks through the slab's thickness. This impression provides a comprehensive overview of the cracking in rigid slabs due to the curvature under the influence of curling stress. For this purpose, the influence of wide-range variables on the depth of cracking and their propagation was assessed. Clearly, the results of this projected theory might be used by many businesses to create models, and DOTs could use them to construct robust concrete slabs that better account for improving the curling and thermal stresses. Then, a finite element method formulation was developed for measuring the curling stress in rigid concrete slabs considering all effective variables. The relevant information on curling and thermal stresses considering material properties and geometric characteristics was incorporated into a finite element modeling for developing a formulation to measure the curling-buckling behavior in rigid slabs under thermal stresses. The developed finite element method provides an inclusive evaluation to consider the effect of boundary conditions and fiber incorporation as well as the effect of base layer stiffness on the curvature, deformation, and buckling in rigid concrete slabs exposed to the temperature gradient.

Another noteworthy finding of this study was providing a highly accurate practical formula using a multi-layer genetic programming machine learning approach to predict the curling stress in rigid concrete airfield runways. Previously proposed equations showed a low accuracy and the lack of some main parameters' consideration. As a result, providing a new highly accurate formula including all effective geometric and material variables is necessary. This proposed theory's findings will undoubtedly be put to use by many firms to develop models, and DOTs and concrete

pavement designing standards may use them to build sturdy concrete slabs that better take into consideration the curling and thermal stresses. Additionally, a methodologically sound and robust protocol was developed using various artificial neural networks for the mechanistic characterization prediction of the curling and thermal stress impacts on transportation infrastructure. The devised multilevel prediction approach consists of the following analysis procedures: quantification of cracking, (2) pavement curling and thermal resistances, the potential of buckling resistance, and deformation. The multi-layer framework developed in this study gives engineers and agencies to have a comprehensive view of the thermal behavior of rigid concrete slabs for future construction.

Ultimately, findings were also employed in the risk analysis for pavement failure. The Rackwitz-Fiessler method introduces an analysis that takes into account the probability model of each variable. These reliability analysis methods will be used to verify how the structure would perform under loading and analyze the reliability index of determinate and indeterminate rigid concrete slabs and their failure probability under the effect of temperature variation considering a wide range of variables. As a result, the probabilistic study can give a broad view of the properties of the influence of various parameters on the curling and thermal behaviors of the rigid concrete slabs for engineers and DOTs.

The synthesized results of this research can provide insights to improve current protocols for the analysis and design of plain and fibers-reinforced rigid concrete airfield runways subjected to thermal and curling stresses.

Keywords: ABAQUS; advanced zero-stress assessment; artificial neural network; curling stress; finite element method; performance prediction; rigid concrete slabs; risk analysis; thermal behavior; temperature gradient.

TABLE OF CONTENTS

Content Page

DEDICATION i
ACKNOWLEDGEMENTS v
ABSTRACT vi
TABLE OF CONTENTS xi
LIST OF TABLES xvii
LIST OF FIGURES xviii
NOMENCLATURE xxxiii
CHAPTER I 1
INTRODUCTION 1
1.1. STATEMENT OF THE PROBLEM 1
1.2. RESEARCH OBJECTIVE AND SCOPE OF THE STUDY 4
1.2.1. Task 1: Review of the Literature 7
1.2.2. Task 2: Assessment of Size Effect and Variables on the Thermal and Curling Behavior of Rigid Concrete Slabs 7
1.2.3. Task 3: Advantages of Polypropylene Fibers Incorporation 9
1.2.4. Task 4: Ultrasonic Imaging Evaluation 10
1.2.5. Task 5: Advanced Zero-Stress Assessment 10
1.2.6. Task 6: Finite Element Method Formulation 11
1.2.7. Task 7: Presenting a Practical Formula 12
1.2.8. Task 8: Providing Prediction Algorithms 12
1.2.9. Task 9: Probabilistic Study on Rigid Concrete Slabs Failure 13
1.3. OUTLINE OF THE DISSERTATION 13
CHAPTER II 16
REVIEW OF THE LITERATURE 16
2.1. INTRODUCTION 16
2.1.1. Organization of the Chapter 16
2.2. THERMAL AND CURLING STRESSES 17

2.2.1. Curling stress due to temperature gradient 17
2.2.2. Built-in curling 23
2.2.3. Geometry of rigid concrete slabs 25
2.2.4. Concrete material characteristics 26
2.2.5. Base layer interaction 28
2.2.6. In Situ Weather Conditions 29
2.3. TECHNIQUES TO REDUCE RIGID CONCRETE SLAB CURLING STRESS 32
2.3.1. Material properties 32
2.3.2. Concrete mixture design 34
2.3.3. Rigid concrete slabs design 36
2.3.4. Construction applications 37
2.4. CASE STUDIES 38
2.5. NUMERICAL MODEL OF TEMPERATURE GRADIENT IN RIGID CONCRETE SLABS 51
2.6. SUMMARY OF THE PREVIOUS STUDIES AND CONCLUSIONS 57
CHAPTER III 60
ASSESSMENT OF SIZE EFFECT AND VARIABLES ON THE THERMAL AND CURLING BEHAVIORS OF RIGID CONCRETE SLABS 60
3.1. INTRODUCTION 60
3.1.1. Organization of the Chapter 60
3.2. FIELD MEASUREMENT 61
3.2.1. Mechanical properties of slabs 64
3.2.2. Temperature measurement in the field 65
3.3. ADVANCED MODELING OF THERMAL AND CURLING BEHAVIORS IN RIGID CONCRETE SLABS 67
3.4. ADVANCED NUMERICAL MODELING 67
3.4.1. Concrete slabs 69
3.4.2. Geometric characteristics and dimensions 72
3.4.3. Boundary Conditions 73
3.4.4. Interaction of Slabs with Base Layer 75
3.4.5. Temperature gradient 76

3.4.6. Meshing 78
3.5. VERIFICATION AND VALIDATION 78
3.6. NUMERICAL RESULTS AND DISCUSSIONS 82
3.7. MAJOR ADVANTAGES OF THE PROPOSED NUMERICAL MODELING APPROACH 83
3.8. SUMMARY & CONNECTION WITH THE SUBSEQUENT CHAPTER 124
CHAPTER IV 126
ADVANTAGES OF POLYPROPYLENE FIBERS INCORPORATION 126
4.1. INTRODUCTION 126
4.1.1. Organization of the Chapter 126
4.2. ADVANTAGES OF POLYPROPYLENE FIBERS INCORPORATION 127
4.3. MATERIALS CHARACTERISTICS FOR SIMULATION 133
4.4. NUMERICAL RESULTS AND DISCUSSIONS 137
4.5. SUMMARY & CONNECTION WITH THE SUBSEQUENT CHAPTER 153
CHAPTER V 155
ULTRASONIC IMAGING EVALUATION 155
5.1. INTRODUCTION 155
5.1.1. Organization of the Chapter 155
5.2. ULTRASONIC IMAGING APPLICATION 156
5.2.1. Apparatus and data 157
5.3. ADVANCED NUMERICAL SIMULATION 161
5.4. NUMERICAL RESULTS AND DISCUSSIONS 163
5.4.1. Frequency 163
5.4.2. Stress 168
5.1.1. Energy dissipation 173
5.1.2. New relationship to predict the compressive strength of concrete slabs 174
5.1.3. Influence of base layer stiffness 177
5.2. SUMMARY & CONNECTION WITH THE SUBSEQUENT CHAPTER 181
CHAPTER VI 183
ADVANCED ZERO-STRESS ASSESSMENT 183

6.1. INTRODUCTION 183
6.1.1. Organization of the Chapter 183
6.2. ZERO-STRESS EVALUATION THEORY 184
6.3. NOVEL ADVANCED ZERO STRESS ASSESSMENT 191
6.4. RESULTS AND DISCUSSIONS 193
6.5. SUMMARY & CONNECTION WITH THE SUBSEQUENT CHAPTER 216
CHAPTER VII 218
FINITE ELEMENT METHOD FORMULATION 218
7.1. INTRODUCTION 218
7.1.1. Organization of the Chapter 218
7.1.2. Basic concept about the thermal deformation of rigid concrete slabs 219
7.2. ASSUMPTION AND FORMULATION 222
7.3. RESULTS AND DISCUSSIONS 229
7.3.1. Buckling amplitude 229
7.3.2. Axial force 245
7.4. SUMMARY & CONNECTION WITH THE SUBSEQUENT CHAPTER 257
CHAPTER VIII 259
NOVEL PRACTICAL FORMULATION 259
8.1. INTRODUCTION 259
8.1.1. Organization of the Chapter 259
8.2. EXISTING MODELS TO MEASURE CURLING STRESS IN RIGID CONCRETE SLABS 260
8.3. GENETIC PROGRAMMING 264
8.4. MULTILAYER GENETIC PROGRAMMING MACHINE LEARNING TOOL 270
8.5. RESULTS AND DISCUSSIONS 276
8.5.1. Plain concrete slabs 276
8.5.2. Fiber-reinforced concrete 280
8.6. SUMMARY & CONNECTION WITH THE SUBSEQUENT CHAPTER 287
CHAPTER IX 289
CURLING AND THERMAL BEHAVIORS PREDICTION ALGORITHMS 289

9.1. INTRODUCTION 289
9.1.1. Organization of the Chapter 289
9.2. STATE OF ART 290
9.2.1. Pavement Management Stages 292
9.2.2. Deterministic Schemes 294
9.2.3. Expert techniques 296
9.2.4. Probabilistic Patterns 296
9.2.5. Artificial Neural Network (ANN) Models 297
9.3. DESCRIPTION OF THE NEURAL NETWORKS UTILIZED IN THE CURRENT RESEARCH 300
9.3.1. Multilayer perceptron (MLP) 301
9.3.2. Deep neural network (DNN) 304
9.3.3. Radial basis function (RBF) 306
9.1.1. Adaptive-network-based fuzzy inference system (ANFIS) 308
9.1.1. Support vector regression (SVR) 312
9.2. RESULTS AND DISCUSSIONS 315
9.2.1. Out-of-plane deformation 315
9.2.2. Tensile stress 320
9.2.3. Shear stress under the saw-cutting region 324
9.2.4. Bond resistance of dowel bars 328
9.3. SUMMARY & CONNECTION WITH THE SUBSEQUENT CHAPTER 335
CHAPTER X 338
PROBABILISTIC STUDY ON THE RIGID CONCRETE SLAB FAILURE AND RISK ANALYSIS 338
10.1. INTRODUCTION 338
10.1.1. Organization of the Chapter 338
10.2. RELIABILITY ANALYSIS FOR COMPLEX SYSTEMS 339
10.2.1. Complex system analysis 340
10.2.2. Implications for Reliability Analysis 341
10.3. RISK ANALYSIS AND UNCERTAINTY ASSESSMENT IN RIGID CONCRETE SLABS DESIGN 343

10.3.1. Terminology 343
10.3.2. Uncertainty Taxonomy 344
10.3.2.1. Reducible uncertainty of tests and construction 345
10.3.2.2. Reducible uncertainty of simplification and assumptions 345
10.3.2.3. Reducible uncertainty of materials 345
10.3.2.4. Reducible uncertainty of knowledge and experiences 346
10.3.3. Risk analysis 346
10.3.4. Risk identification 350
10.4. PROBABILISTIC STUDY ON RIGID CONCRETE SLABS FAILURE USING RACHQITZ-FIESSLER METHOD 356
10.5. RESULTS AND DISCUSSIONS 360
CHAPTER XI 371
CONCLUSIONS AND RECOMMENDATIONS 371
11.1. CONCLUSIONS 374
11.2. RECOMMENDATIONS FOR FUTURE WORK 386
REFERENCES 387
CURRICULUM VITA 410

LIST OF TABLES

Content Page

Table 2.1: International roughness index readings measured by the contractor daily on the westbound lane (Merritt et al. 2015) …….40

Table 2.2: Thermal characteristics of the pavement layers …….....53

Table 3.1: Geometric characteristics of rigid concrete slabs in EL Paso, Texas ……..62

Table 3.2: Obtained laboratory and field results for performed rigid concrete slabs ……...65

Table 3.3: Basic parameters of the slabs utilized for verification according to Mackiewicz and Szydło's study (2020) ……...81

Table 4.1: Mechanical properties of polypropylene fibers …….135

Table 8.1: Results of curling stress calculation for both plain and fiber-reinforced concrete slabs using the common effectiveness assessment techniques……..285

Table 9.1: Variations between PMS network and project stages (AASHTO, 2012) ……..292

Table 9.2: Results of curling behavior prediction for both plain and fiber-reinforced concrete slabs using the common effectiveness assessment techniques ……...…333

LIST OF FIGURES

Content Page

Figure 1.1: Example of cracks propagation over the rigid concrete slab thickness due to a) curling and b) expansion ……. 2

Figure 1.2: Main objectives of the current study …… …6

Figure 2.1: Tensile stresses at the top of the runway with an upward deformation and tensile stress at the bottom of the runway with a downward deformation are caused by curling…….18

Figure 2.2: Normal temperature distribution over the depth of a concrete slab (Choubane and Tia 1992) …….22

Figure 2.3: Elastic moduli of concrete with various types of aggregate ……..…..27

Figure 2.4: Representations of the support conditions under rigid concrete slabs: one with an idealized flat foundation (left) and the other with the impacts of settlement (right) (Yu et al. 2004)……..29

Figure 2.5: Seasonal influences on the amount of curling in restrained and unrestrained rigid concrete slabs (McCracken et al. 2008) …….31

Figure 2.6: Coefficient of thermal expansion of concrete with various kinds of aggregate …….32

Figure 2.7: Various aggregates' dry shrinkage over a year …….....33

Figure 2.8: Effect of water-to-cement ratio on the relative humidity in rigid concrete slabs ……35

Figure 2.9: Site of the US 34 curling study location …….39

Figure 2.10: Site of the I-70 close to the Kansas-Colorado border curling study location ……41

Figure 2.11: Measured curling in rigid concrete slabs in Colorado (Yu et al., 1998) ……41

Figure 2.12: Temperature gradients for the Colorado rigid concrete slabs (Yu et al., 1998) ……42

Figure 2.13: Site of the Kansas-Colorado border curling study location ……...…….43

Figure 2.14: Daily and seasonal temperature gradients through a 13-inch slab (Yu et al., 2001).43

Figure 2.15: Site of Interstates 70 and 135 curling study location …….47

Figure 2.16: LTPP SPS-2 Site in Arizona …….49

Figure 2.17: Diagram illustration for the heat transfer model ……..……..…52

Figure 2.18: A brief review of previous studies and their weakness …….59

Figure 3.1: Field assessment in El Paso, Texas, USA ……..……..62

Figure 3.2: Configuration of dowel bars over notches ……..…….63

Figure 3.3: Cracks over rigid concrete slabs due to temperature gradient ……63

Figure 3.4: Compressive strength measurement for performed rigid concrete slabs a) laboratory test and b) non-destructive test ……..64

Figure 3.5: Temperature measurement over slabs' surfaces at different hours during the day …..66

Figure 3.6: Temperature measurements for the top, middle, and bottom of the slabs ……66

Figure 3.7: Variables considered to determine the curling stress of rigid concrete airfield runways……..68

Figure 3.8: The behavior of concrete compressive resistance…….70

Figure 3.9: Defined concrete tensile behavior ……..…..71

Figure 3.10: Tensile behavior of concrete after cracking ……..71

Figure 3.11: Stress-strain relationship of concrete with various compressive strengths ……72

Figure 3.12: Simulated rigid concrete slabs in the 3D Finite Element Software ……74

Figure 3.13: Boundary condition considered in the current study …….75

Figure 3.14: Interaction condition between rigid concrete slabs and base layer ……76

Figure 3.15: Temperature gradient obtained from the field test at different times during a day in this study ……77

Figure 3.16: 3D Meshing employed in the current investigation ……..……79

Figure 3.17: Comparison between the tensile stress for slab thickness of 25 and 30 cm versus slab length for the current study and those reported by Mackiewicz and Szydło study (2020) ……82

Figure 3.18: Influence of compressive strength and thermal gradient on the maximum tensile strength of slabs with various lengths a) 25MPa, b) 30MPa, c) 35MPa, d) 40MPa and e) 45MPa 85

Figure 3.19: Influence of thermal on stress responses in 6m long slabs a) 10^{o}C, b)20^{o}C, and c)30^{o}C ……86

Figure 3.20: Influence of thickness and length on the maximum tensile stress of slabs with 25 MPa compressive strength under the effect of different thermal gradients a) 5^{o}C, b) 10^{o}C, c) 15^{o}C, d) 20^{o}C, e) 25^{o}C, f) 30^{o}C and g) 35^{o}C …….……88

Figure 3.21: Influence of thickness and length on the maximum tensile stress of slabs with 30 MPa compressive strength under the effect of different thermal gradients a) 5^{o}C, b) 10^{o}C, c) 15^{o}C, d) 20^{o}C, e) 25^{o}C, f) 30^{o}C and g) 35^{o}C ……89

Figure 3.22: Influence of thickness and length on the maximum tensile stress of slabs with 35 MPa compressive strength under the effect of different thermal gradients a) 5^{o}C, b) 10^{o}C, c) 15^{o}C, d) 20^{o}C, e) 25^{o}C, f) 30^{o}C and g) 35^{o}C …….91

Figure 3.23: Influence of thickness and length on the maximum tensile stress of slabs with 40 MPa compressive strength under the effect of different thermal gradients a) 5^{o}C, b) 10^{o}C, c) 15^{o}C, d) 20^{o}C, e) 25^{o}C, f) 30^{o}C and g) 35^{o}C ……93

Figure 3.24: Influence of thickness and length on the maximum tensile stress of slabs with 45 MPa compressive strength under the effect of different thermal gradients a) 5^{o}C, b) 10^{o}C, c) 15^{o}C, d) 20^{o}C, e) 25^{o}C, f) 30^{o}C and g) 35^{o}C ……94

Figure 3.25: Influence of thermal gradient on the out-of-plane deformation of 4.5m long slabs with 10cm thickness having various compressive strengths a) 25MPa, b) 35MPa, and c) 45MPa…….96

Figure 3.26: Influence of thermal gradient on the out-of-plane deformation of 4.5m long slabs with 20cm thickness having various compressive strengths a) 25MPa, b) 35MPa, and c) 45MPa…….97

Figure 3.27: Influence of thermal gradient on the out-of-plane deformation of 4.5m long slabs with 30cm thickness having various compressive strengths a) 25MPa, b) 35MPa, and c) 45MPa…….98

Figure 3.28: Influence of thermal gradient on the out-of-plane deformation of 6m long slabs with 10cm thickness having various compressive strengths a) 25MPa, b) 35MPa and c) 45MPa…...100

Figure 3.29: Influence of thermal gradient on the out-of-plane deformation of 6m long slabs with 20cm thickness having various compressive strengths a) 25MPa, b) 35MPa and c) 45MPa…...101

Figure 3.30: Influence of thermal gradient on the out-of-plane deformation of 6m long slabs with 30cm thickness having various compressive strengths a) 25MPa, b) 35MPa and c) 45MPa ……102

Figure 3.31. Influence of thermal gradient on the out-of-plane deformation of 7.5m long slabs with 10cm thickness having various compressive strengths a) 25MPa, b) 35MPa, and c) 45MPa…....104

Figure 3.32: Influence of thermal gradient on the out-of-plane deformation of 7.5m long slabs with 20cm thickness having various compressive strengths a) 25MPa, b) 35MPa, and c) 45MPa…....105

Figure 3.33: Influence of thermal gradient on the out-of-plane deformation of 7.5m long slabs with 30cm thickness having various compressive strengths a) 25MPa, b) 35MPa, and c) 45MPa……106

Figure 3.34: Influence of thermal on out-of-plan deformation response in 4.5m long slabs……107

Figure 3.35: Simultaneous influence of slabs width, thickness, and length on 25MPa concrete compressive strength exposed to various thermal gradients a) 5^{o}C, b) 15^{o}C, c) 25^{o}C and d) 35^{o}C……..…109

Figure 3.36: Simultaneous influence of slabs width, thickness, and length on 35MPa concrete compressive strength exposed to various thermal gradients a) 5^{o}C, b) 15^{o}C, c) 25^{o}C and d) 35^{o}C…….110

Figure 3.37: Simultaneous influence of slab width, thickness, and length on 45MPa concrete compressive strength exposed to various thermal gradients a) 5^{o}C, b) 15^{o}C, c) 25^{o}C and d) 35^{o}C…….112

Figure 3.38: Influence of friction ratio on the maximum tensile stress of slabs due to curling with various slab lengths a) 25MPa, b) 30MPa, c) 35MPa, d) 40MPa and e) 45MPa …….116

Figure 3.39: Influence of friction ratio on the maximum out-of-plane deformation of slabs due to curling with various slab lengths a) 25MPa, b) 35MPa, and c) 45MPa ……118

Figure 3.40: Influence of notch depth on the maximum tensile stress of slabs due to curling with various slab lengths a) 25MPa, b) 30MPa, c) 35MPa, d) 40MPa and e) 45MPa …….122

Figure 3.41: Influence of notch depth on the maximum out-of-plane deformation of slabs due to curling with various slab lengths a) 25MPa, b) 35MPa, and c) 45MPa ……123

Figure 3.42: Overview of the connection between Chapters III and IV……...…….125

Figure 4.1: Graphic Drawing of the beneficial effect of a) 0.5% and b) 1% PF on the compressive strength of concrete ……...129

Figure 4.2: Graphic Drawing of the beneficial effect of a) 0.5% and b) 1% PF on the flexural strength of concrete ……..…133

Figure 4.3: An example of polypropylene fibers ……..……134

Figure 4.4: Stress-strain relationship of concrete having various polypropylene fibers fractions with compressive strength of a) 25 MPa, b) 30 MPa, c) 35 MPa, d) 40 MPa, and e) 45 MPa ….136

Figure 4.5: Influence of fiber incorporation on the maximum tensile strength of slabs due to curling with various slab lengths a) 25MPa, b) 30MPa, c) 35MPa, d) 40MPa and e) 45MPa ……..140

Figure 4.6: Influence of fiber incorporation on the maximum tensile stress reduction of slabs due to curling with various geometric characteristics and thermal gradients …….141

Figure 4.7: Influence of fiber incorporation on the out-of-plane deformation of 4.5m long slabs with 10cm thickness having various compressive strengths a) 25MPa, b) 35MPa, and c) 45MPa ……..143

Figure 4.8: Influence of fiber incorporation on the out-of-plane deformation of 4.5m long slabs with 30cm thickness having various compressive strengths a) 25MPa, b) 35MPa and c) 45MPa.144

Figure 4.9: Influence of fiber incorporation on the out-of-plane deformation of 6m long slabs with 10cm thickness having various compressive strengths a) 25MPa, b) 35MPa and c) 45MPa…..146

Figure 4.10: Influence of fiber incorporation on the out-of-plane deformation of 6m long slabs with 30cm thickness having various compressive strengths a) 25MPa, b) 35MPa and c) 45MPa…..147

Figure 4.11: Influence of fiber incorporation on the out-of-plane deformation of 7.5m long slabs with 10cm thickness having various compressive strengths a) 25MPa, b) 35MPa and c) 45MPa.149

Figure 4.12: Influence of fiber incorporation on the out-of-plane deformation of 7.5m long slabs with 30cm thickness having various compressive strengths a) 25MPa, b) 35MPa and c) 45MPa.150

Figure 4.13: Influence of thermal on out-of-plane deformation response in 4.5m long slabs a) without fiber, b) with 0.5% fiber, and c) with 1.0% fiber …….151

Figure 4.14: Influence of fiber incorporation on the maximum out-of-plane deformation reduction of slabs due to curling with various geometric characteristics and thermal gradients for the length of a) 4.5m, b) 6m and c) 7.5m ……..153

Figure 4.15: Overview of the connection between previous Chapters and Chapter V ……154

Figure 5.1: An example of an ultrasonic imaging test ……..…158

Figure 5.2: Schematic of the synthetic aperture focusing technique …….…..159

Figure 5.3: Schematic of pulse-echo testing …….…...159

Figure 5.4: Location of sender and receiver sensors …….…..162

Figure 5.5: Applied wave spectrum for Synthetic Aperture Focusing Technique a) Amplitude-Time Diagram and b) Amplitude-Frequency Diagram ……163

Figure 5.6: Influence of concrete compressive strength of plain concrete on the received frequency with various thicknesses a) 10 cm, b) 20 cm, and c) 30 cm …….164

Figure 5.7: Influence of concrete compressive strength of 0.5% fiber-reinforced concrete on the received frequency with various thicknesses a) 10 cm, b) 20 cm, and c) 30 cm ……165

Figure 5.8: Influence of concrete compressive strength of 1.0% fiber-reinforced concrete on the received frequency with various thicknesses a) 10 cm, b) 20 cm, and c) 30 cm ……166

Figure 5.9: Effect of concrete compressive strength on the maximum received frequency considering various slab's thickness and fibers fractions ……167

Figure 5.10: Wave propagation over the surface of slabs ……168

Figure 5.11: Wave propagation over the thickness of slabs ……168

Figure 5.12: Influence of concrete compressive strength of plain concrete on the stress with various thicknesses a) 10 cm, b) 20 cm, and c) 30 cm ……...……170

Figure 5.13: Influence of concrete compressive strength of 0.5% fiber-reinforced concrete on the stress with various thicknesses a) 10 cm, b) 20 cm, and c) 30 cm ……171

Figure 5.14: Influence of concrete compressive strength of 1.0% fiber-reinforced concrete on the stress with various thicknesses a) 10 cm, b) 20 cm, and c) 30 cm ……171

Figure 5.15: Effect of concrete compressive strength on the maximum stress considering various slab's thickness and fibers fractions ……172

Figure 5.16: Effect of concrete compressive strength on the energy dissipation considering various slab's thickness and fibers fractions ……174

Figure 5.17: Relationship between the compressive strength of concrete and maximum stress for various types of slabs ……...175

Figure 5.18: Relationship between the maximum stress and received frequency for various types of slabs ……..……176

Figure 5.19: Influence of base layer modulus on the frequency history of a) plain concrete, b) 0.5% fibers-reinforced concrete, and c) 1.0% fiber-reinforced concrete with 25 MPa concrete compressive strength and 10 cm slab's thickness ……179

Figure 5.20: Influence of base layer modulus on the stress history of a) plain concrete, b) 0.5% fibers-reinforced concrete, and c) 1.0% fiber-reinforced concrete with 25 MPa concrete compressive strength and 30 cm slab's thickness ……181

Figure 5.21: Overview of the connection between previous Chapters and Chapter VI ……..…..182

Figure 6.1: CZST theoretical determination in case one ……..…185

Figure 6.2: CZST theoretical determination in case two ……..…187

Figure 6.3: Theoretical determination of Advanced Zero-Stress Assessment (AZSA) ……..193

Figure 6.4: Advanced Zero-Stress line for 10 cm thickness slab, 4.5m length and 25 MPa concrete compressive strength with various widths a) 3m, b) 4.5m and c) 6m …….194

Figure 6.5: Advanced Zero-Stress line for 30 cm thickness slab, 4.5m length and 25 MPa concrete compressive strength with various widths a) 3m, b) 4.5m and c) 6m …….195

Figure 6.6: Advanced Zero-Stress line for 10 cm thickness slab, 4.5m length and 35 MPa concrete compressive strength with various widths a) 3m, b) 4.5m and c) 6m …….197

Figure 6.7: Advanced Zero-Stress line for 30 cm thickness slab, 4.5m length, and 35 MPa concrete compressive strength with various widths a) 3m, b) 4.5m, and c) 6m ……..198

Figure 6.8: Advanced Zero-Stress line for 10 cm thickness slab, 4.5m length and 45 MPa concrete compressive strength with various widths a) 3m, b) 4.5m and c) 6m …….199

Figure 6.9: Advanced Zero-Stress line for 30 cm thickness slab, 4.5m length and 45 MPa concrete compressive strength with various widths a) 3m, b) 4.5m and c) 6m ……..200

Figure 6.10: Advanced Zero-Stress line for 10 cm thickness slab, 6m length and 25 MPa concrete compressive strength with various widths a) 3m, b) 4.5m and c) 6m …….202

Figure 6.11: Advanced Zero-Stress line for 30 cm thickness slab, 6m length and 25 MPa concrete compressive strength with various widths a) 3m, b) 4.5m and c) 6m …….203

Figure 6.12: Advanced Zero-Stress line for 10 cm thickness slab, 6m length and 35 MPa concrete compressive strength with various widths a) 3m, b) 4.5m and c) 6m ……..205

Figure 6.13: Advanced Zero-Stress line for 30 cm thickness slab, 6m length and 35 MPa concrete compressive strength with various widths a) 3m, b) 4.5m and c) 6m …….206

Figure 6.14: Advanced Zero-Stress line for 10 cm thickness slab, 6m length and 45 MPa concrete compressive strength with various widths a) 3m, b) 4.5m and c) 6m …….207

Figure 6.15: Advanced Zero-Stress line for 30 cm thickness slab, 6m length and 45 MPa concrete compressive strength with various widths a) 3m, b) 4.5m and c) 6m ……..208

Figure 6.16: Advanced Zero-Stress line for 10 cm thickness slab, 7.5m length and 25 MPa concrete compressive strength with various widths a) 3m, b) 4.5m and c) 6m ……...…210

Figure 6.17: Advanced Zero-Stress line for 30 cm thickness slab, 7.5m length and 25 MPa concrete compressive strength with various widths a) 3m, b) 4.5m and c) 6m …….……211

Figure 6.18: Advanced Zero-Stress line for 10 cm thickness slab, 7.5m length and 35 MPa concrete compressive strength with various widths a) 3m, b) 4.5m and c) 6m ……..……213

Figure 6.19: Advanced Zero-Stress line for 30 cm thickness slab, 7.5m length, and 35 MPa concrete compressive strength with various widths a) 3m, b) 4.5m, and c) 6m ……...…214

Figure 6.20: Advanced Zero-Stress line for 10 cm thickness slab, 7.5m length, and 45 MPa concrete compressive strength with various widths a) 3m, b) 4.5m, and c) 6m ……215

Figure 6.21: Advanced Zero-Stress line for 30 cm thickness slab, 7.5m length and 45 MPa concrete compressive strength with various widths a) 3m, b) 4.5m and c) 6m …….……216

Figure 6.22: Overview of the connection between previous Chapters and Chapter VII .……217

Figure 7.1: Buckling in rigid concrete slabs a) rigid base and b) weakened base ……..……..223

Figure 7.2: Effect of thermal gradient on the post-buckling of slabs with 10 cm thickness constrained by a weakened base with 3 m width and a) 4.5m, b) 6m and 7.5 m length……232

Figure 7.3: Effect of thermal gradient on the post-buckling of slabs with 10 cm thickness constrained by a rigid base with 3 m width and a) 4.5m, b) 6m and 7.5 m length ……..…233

Figure 7.4: Effect of thermal gradient on the post-buckling of slabs with 30 cm thickness constrained by a weakened base with 3 m width and a) 4.5m, b) 6m and 7.5 m length ……..…235

Figure 7.5: Effect of thermal gradient on the post-buckling of slabs width 30 cm thickness constrained by a rigid base with 3 m with and a) 4.5m, b) 6m and 7.5 m length ……..…235

Figure 7.6: Effect of thermal gradient on the post-buckling of slabs with 10 cm thickness constrained by a weakened base with 4.5 m width and a) 4.5m, b) 6m and 7.5 m length ……..…238

Figure 7.7: Effect of thermal gradient on the post-buckling of slabs with 10 cm thickness constrained by a rigid base with 4.5 m width and a) 4.5m, b) 6m and 7.5 m length …..……..…238

Figure 7.8: Effect of thermal gradient on the post-buckling of slabs with 30 cm thickness constrained by a weakened base with 4.5 m width and a) 4.5m, b) 6m and 7.5 m length …..……239

Figure 7.9: Effect of thermal gradient on the post-buckling of slabs with 30 cm thickness constrained by a rigid base with 4.5 m width and a) 4.5m, b) 6m and 7.5 m length ……..…240

Figure 7.10: Effect of thermal gradient on the post-buckling of slabs with 10 cm thickness constrained by a weakened base with 6 m width and a) 4.5m, b) 6m and 7.5 m length ……241

Figure 7.11: Effect of thermal gradient on the post-buckling of slabs with 10 cm thickness constrained by a rigid base with 6 m width and a) 4.5m, b) 6m and 7.5 m length ……242

Figure 7.12: Effect of thermal gradient on the post-buckling of slabs with 30 cm thickness constrained by a weakened base with 6 m width and a) 4.5m, b) 6m and 7.5 m length ……244

Figure 7.13: Effect of thermal gradient on the post-buckling of slabs with 30 cm thickness constrained by a rigid base with 6 m width and a) 4.5m, b) 6m and 7.5 m length ……244

Figure 7.14: Effect of thermal gradient on the axial force of slabs with 10 cm thickness constrained by a weakened base with 3 m width and a) 4.5m, b) 6m and 7.5 m length ……246

Figure 7.15: Effect of thermal gradient on the axial force of slabs with 10 cm thickness constrained by a rigid base with 3 m width and a) 4.5m, b) 6m and 7.5 m length ……..247

Figure 7.16: Effect of thermal gradient on the axial force of slabs with 30 cm thickness constrained by a weakened base with 3 m width and a) 4.5m, b) 6m and 7.5 m length ……248

Figure 7.17: Effect of thermal gradient on the axial force of slabs width 30 cm thickness constrained by a rigid base with 3 m width and a) 4.5m, b) 6m and 7.5 m length ……...…..249

Figure 7.18: Effect of thermal gradient on the axial force of slabs with 10 cm thickness constrained by a weakened base with 4.5 m width and a) 4.5m, b) 6m and 7.5 m length ……..251

Figure 7.19: Effect of thermal gradient on the axial force of slabs with 10 cm thickness constrained by a rigid base with 4.5 m width and a) 4.5m, b) 6m and 7.5 m length ……..251

Figure 7.20: Effect of thermal gradient on the axial force of slabs with 30 cm thickness constrained by a weakened base with 4.5 m width and a) 4.5m, b) 6m and 7.5 m length ……252

Figure 7.21: Effect of thermal gradient on the axial force of slabs with 30 cm thickness constrained by a rigid base with 4.5 m width and a) 4.5m, b) 6m and 7.5 m length ……253

Figure 7.22: Effect of thermal gradient on the axial force of slabs with 10 cm thickness constrained by a weakened base with 6 m width and a) 4.5m, b) 6m and 7.5 m length …….254

Figure 7.23: Effect of thermal gradient on the axial force of slabs with 10 cm thickness constrained by a rigid base with 6 m width and a) 4.5m, b) 6m and 7.5 m length ……..254

Figure 7.24: Effect of thermal gradient on the axial force of slabs with 30 cm thickness constrained by a weakened base with 6 m width and a) 4.5m, b) 6m and 7.5 m length …….256

Figure 7.25: Effect of thermal gradient on the axial force of slabs with 30 cm thickness constrained by a rigid base with 6 m width and a) 4.5m, b) 6m and 7.5 m length …….256

Figure 7.26: Overview of the connection between previous Chapters and Chapter VIII ……258

Figure 8.1: Simple GP flow diagram ……266

Figure 8.2: Tree to illustrate a mathematical equation …….270

Figure 8.3: Illustration of MLGPML tree 272

Figure 8.4: Crossover example based on MLGPML 272

Figure 8.5: Mutation example based on MLGPML 273

Figure 8.6: Mutation example based on MLGPML 274

Figure 8.7: Accuracy of curling stress calculation for plain concrete slabs using different models considering all geometric and mechanical characteristics of rigid concrete slabs a) Nishizawa et al (1990), b) Hernandez and Al-Qadi (2019), c) Salehi-Ashtiani (2011) and d) this study ……278

Figure 8.8: Error distribution and accuracy of different models for curling stress calculation in plain concrete slabs a) Nishizawa et al (1990), b) Hernandez and Al-Qadi (2019), c) Salehi-Ashtiani (2011) and d) this study ……280

Figure 8.9: Accuracy of curling stress calculation for fiber-reinforced concrete slabs using different models considering all geometric and mechanical characteristics of rigid concrete slabs a) Nishizawa et al (1990), b) Hernandez and Al-Qadi (2019), c) Salehi-Ashtiani (2011) and d) this study ……282

Figure 8.10: Error distribution and accuracy of different models for curling stress calculation in fiber-reinforced concrete slabs a) Nishizawa et al (1990), b) Hernandez and Al-Qadi (2019), c) Salehi-Ashtiani (2011) and d) this study ……284

Figure 8.11: Taylor illustration for the current and prior curling stress calculation models for a) plain concrete and b) fiber-reinforced concrete ……...286

Figure 8.12: Overview of the connection between previous Chapters and Chapter IX ……..288

Figure 9.1: Detailed flowchart of the actions taken through this chapter ……301

Figure 9.2: General design of the MLP algorithm ……...302

Figure 9.3: Structure of MLP algorithm with one neuron ……..303

Figure 9.4: Flowchart for MLP network to predict the thermal and curling responses ……303

Figure 9.5: DNN algorithm with three hidden layers ……..305

Figure 9.6: Flowchart for DNN algorithm to predict the thermal and curling responses ……306

Figure 9.7: Diagram of RBF structure ……..308

Figure 9.8: Flowchart for RBF algorithm to predict the thermal and curling responses …….309

Figure 9.9: Diagram of ANFIS structure ……..310

Figure 9.10: Flowchart for ANFIS algorithm to predict the thermal and curling responses …….311

Figure 9.11: Flowchart for SVR algorithm to predict the thermal and curling responses ……315

Figure 9.12: Out-of-plane deformation prediction for both plain and fiber-reinforced concrete slabs using various algorithms a) DNN, b) ANFIS, c) RBF, d) MLP and e) SVR …….317

Figure 9.13: Error distribution and accuracy of various algorithms in terms of out-of-plane prediction for a) DNN, b) ANFIS, c) RBF, d) MLP, and e) SVR ……320

Figure 9.14: Tensile stress prediction for both plain and fiber-reinforced concrete slabs using various algorithms a) DNN, b) ANFIS, c) RBF, d) MLP, and e) SVR …….321

Figure 9.15: Error distribution and accuracy of various algorithms in terms of tensile stress prediction for a) DNN, b) ANFIS, c) RBF, d) MLP, and e) SVR …….324

Figure 9.16: Shear stress prediction for both plain and fiber-reinforced concrete slabs using various algorithms a) DNN, b) ANFIS, c) RBF, d) MLP, and e) SVR ……...326

Figure 9.17: Error distribution and accuracy of various algorithms in terms of shear stress in the notch region prediction for a) DNN, b) ANFIS, c) RBF, d) MLP, and e) SVR …….328

Figure 9.18: Dowel bars bond resistance prediction for both plain and fiber-reinforced concrete slabs using various algorithms a) DNN, b) ANFIS, c) RBF, d) MLP, and e) SVR ……..330

Figure 9.19: Error distribution and accuracy of various algorithms in terms of dowel bars bond resistance prediction for a) DNN, b) ANFIS, c) RBF, d) MLP, and e) SVR …….332

Figure 9.20: out-of-plane deformation, b) tensile stress, c) shear stress in notch region, and d) dowel bars bond resistance …….…….335

Figure 9.21: Overview of the connection between previous Chapters and Chapter X …….337

Figure 10.1: Sample of a two-discipline complex system ……340

Figure 10.2: Statistical evaluation of systems using feedback ……342

Figure 10.3: Uncertainty in a slab's life-cycle …….343

Figure 10.4: Outlooks to examine rigid concrete runways……...352

Figure 10.5: Rigid concrete runways in view of various parts…….353

Figure 10.6: Rigid concrete runway design in Temporal view……354

Figure 10.7: Rigid concrete runway design in cost allocation view……..355

Figure 10.8: Rigid concrete pavement design as per MEPDG ……355

Figure 10.9: Rigid concrete pavement design as per ME methods ……..……356

Figure 10.10: Rackwitz-Fiessler procedure …….……358

Figure 10.11: Equivalent normal conditions of non-normal variable …….…….359

Figure 10.12: Influence of thermal gradient and geometric characteristics on the probability of failure in plain concrete slabs with 25 MPa compressive strength and various lengths a) 4.5m, b) 6m, and c) 7.5m ……...……361

Figure 10.13: Influence of thermal gradient and geometric characteristics on the probability of failure in 0.5% fiber-reinforced concrete slabs 25 MPa compressive strength and with various lengths a) 4.5m, b) 6m and c) 7.5m ……..362

Figure 10.14: Influence of thermal gradient and geometric characteristics on the probability of failure in 1.0% fiber-reinforced concrete slabs with 25 MPa compressive strength and with various lengths a) 4.5m, b) 6m and c) 7.5m …….363

Figure 10.15: Influence of thermal gradient and geometric characteristics on the probability of failure in plain concrete slabs with 35 MPa compressive strength and various lengths a) 4.5m, b) 6m, and c) 7.5m ……...……364

Figure 10.16: Influence of thermal gradient and geometric characteristics on the probability of failure in 0.5% fiber-reinforced concrete slabs 35 MPa compressive strength and with various lengths a) 4.5m, b) 6m and c) 7.5m ……..365

Figure 10.17: Influence of thermal gradient and geometric characteristics on the probability of failure in 1.0% fiber-reinforced concrete slabs with 35 MPa compressive strength and with various lengths a) 4.5m, b) 6m and c) 7.5m …….366

Figure 10.18: Influence of thermal gradient and geometric characteristics on the probability of failure in plain concrete slabs with 45 MPa compressive strength and various lengths a) 4.5m, b) 6m, and c) 7.5m ……...……367

Figure 10.19: Influence of thermal gradient and geometric characteristics on the probability of failure in 0.5% fiber-reinforced concrete slabs 45 MPa compressive strength and with various lengths a) 4.5m, b) 6m and c) 7.5m ……..368

Figure 10.20: Influence of thermal gradient and geometric characteristics on the probability of failure in 1.0% fiber-reinforced concrete slabs with 35 MPa compressive strength and with various lengths a) 4.5m, b) 6m and c) 7.5m ……..……369

Figure 10.21: Influence of fibers incorporation on reducing the probability of failure for slabs with various lengths a) 4.5m, b) 6m, and c) 7.5m ……..…..370

NOMENCLATURE

2D	Two-dimensional
3D	Three-dimensional
AASHTO	American Association of State Highway and Transportation Officials
AZSA	Advanced Zero Stress Assessment
ANNs	Artificial neural networks
ANFIS	Adaptive neuro-fuzzy inference system
A	Slab's cross-sectional area
a	Slab's length
b	Slab's width
CDOT	Colorado Department of Transportation
CZST	Conventional Zero-Stress Temperature
c	Relative heat capacities
c_w	Specific heats of water
c_a	Specific heats of cement
c_c	Specific heats of concrete
C_C	Cementitious material content
c_{ref}	Fictitious specific heat of hydrated concrete
d_c	Compression damage
d_t	Failure cracking factor in elasticity
DNN	Deep neural network
E_c	Modulus of elasticity
E	Activation energy
f	Axial resistance
f_0	Ultimate resistance
FIS	Fuzzy Inference System
FWD	Falling weight deflectometer
FHWA	Federal Highway Administration
GA	Genetic algorithm
GP	Genetic programming

GPR	Ground Penetrating Radar
G_1	Area under the curve
h	Thickness of rigid concrete slabs
h_c	Convection coefficient
H_u	Total heat of hydrated cementitious materials at 100% hydration
i	Duty cycle
I_f	Intensity factor
I	Pavement's second moment of cross-sectional area
JPCP	Jointed plain concrete pavements
k	Thermal conductivity of the mediums
k_∞	Thermal conductivity of hardened concrete
K_a	Thermal conductivity of the air
l	Lift-off length
L	Cholesky factor of the Pearson correlation matrix
MF	Membership functions
MLP	Multilayer perceptron
MSE	Mean squared error
MCC	Modified Cam-Clay
MAE	Mean absolute error
MAPE	Mean absolute percentage error
MLGPML	Multi-layer genetic programming machine learning
MEPDG	Mechanistic-Empirical Pavement Design Guide
M_y	Bending moment
NSI	Normalized sensitivity index
NMAE	Normalized mean absolute error
NMSE	Normalized mean squared error
NOAA	National Oceanic and Atmospheric Administration
NCHRP	National Cooperative Highway Research Program
OAT	One-factor-At-a-Time
OBF	Objective function

P	Conversion matrix probability
P_m	Probability of mutation
P_r	Probability of reproduction
P_o	Probability of crossover
P_i	Probability provision of i_{th} duty cycle
PF	Polypropylene fibers
PMS	Pavement management systems
P_r	Air's Prandtl number
QP	Quadratic Programming
q_{solar}	Maximum content of solar radiation throughout a day period
$q(t)$	Internal heat produced by cement hydration
q	Density
RBF	Radial basis function network
RMSE	Root mean squared error
r	Total travel distance
r_1	Incident travel distance
r_2	Reflection travel distance
R	Linear correlation coefficient
R^2	Coefficient of determination
SHAs	State highway agencies
SVR	Support vector regression
SVM	Support Vector Machine
$T_{effective}$	Combined effects of the daily temperature difference
$T_{top,\ daily}$	Inherent temperature difference leading to the effective temperature difference
$T_{bottom,\ daily}$	Diurnal variations in ambient temperature cause the top and bottom surface temperature
T_s	Temperature of the slab surface
T_a	Environmental temperature
T_k	Effective sky temperature
T_r	Reference temperature of concrete
T_{dp}	Dew point
t_{sr}	Sunrise time

t_{ss}	Sunset time
t_e	Equivalent age (hour)
t	Total journey duration
u_p	Axial displacement at the point of peeling
U_j	Center of neuron j in the hidden layer
V	Wave cover velocity
w	Local wind velocity
W_w	Weights of water
W_a	Weights of aggregate
W_c	Weights of cement
w_j	Associated weight
w/c	Water to cement ratio
x	Universal apodization weight
x_j	Input weight
$x_i^{(k)}$	ith component of the kth iteration point $x^{(k)}$
Z_i	Normal variable
ρ	Density of the medium
ξ	Stefan-Boltzmann coefficient
ε	Ground surface emissivity
ε_k	Sky emissivity
v	Air‘s kinematic viscosity
γ_{abs}	Surface absorptivity
θ	Hour angle
$\Delta\theta$	Angular beamwidth of the transducer array
$\bar{\varepsilon}_c^{in}$	Inelastic strains
ε_c^{el}	Elastic strain
ε_c	Concrete strain at different steps of loading
$\bar{\varepsilon}_c^{pl}$	Plastic strain
ε_m	Strain at the cross-centroid section
σ	Kernel factor of RBF

σ_c	Compression stress
σ_t	Ultimate curling stress
σ_j	Hidden layer's *j-th* neuron kernel parameter
α	Degree of hydration
α_u	Ultimate degree of hydration
τ	Hydration time parameter
β	Hydration shape parameter
p_{FA}	Weight ratios of fly ash in terms of the total cement contents
p_{SLAG}	Weight ratios of slag in terms of the total cement contents
p	Contact stress between the pavement and the base
μ	Parameter that outlines the curvature shape
κ	Pavement's bending curvature
Δt	Thermal gradient
$\mu_{Z_i}^{(k)}$	Mean of the equivalent normal variable
$\sigma_{Z_i}^{(k)}$	Standard deviation of the equivalent normal variable
$F_{X_i}(.)$	Distribution function and the density function of the original variable X_i
$\Phi(.)$	Standard Normal distribution function
$\phi(.)$	Density function

CHAPTER I

INTRODUCTION

1.1. STATEMENT OF THE PROBLEM

Environmental loadings occur over in-service concrete slabs even though the pavement isn't open to traffic. After opening the pavement for traffic, the simultaneous effect of stress due to external load and environmental conditions will intensify the stress and create permanent stresses in the pavement. Therefore, reducing the stresses caused by environmental conditions and controlling them can play a significant role in increasing the life of pavements and reducing maintenance costs. Curling stress is caused by thermal gradients and differences between the top and bottom surfaces of concrete slabs in terms of temperature. This type of stress is the main cause of stress in concrete slabs where there is a large temperature difference between day and night (Masad *et al.* 1996). Recent field test results in El Paso and Florida have indicated various cracking in concrete slabs: bottom-up transverse cracks, top-down transverse cracks, longitudinal cracks, corner breaks, and punchouts as presented in Figure 1.1. In addition to increasing the maintenance cost of the concrete airfield runways due to thermal cracking, pavement life reduction is another main reason associated with curling stress and thermal expansion. The curling of rigid concrete slabs is caused by a non-uniform temperature gradient over the slabs' thickness. Because the pavements are restrained by the shoulder or end-to-end lanes, the temperature gradient produces curling stress. The highlighted concerns are even more pronounced considering the dimension of concrete slabs, properties of concrete, notch location, elevated temperatures in summer seasons, and fiber contents as a solution to mitigate the negative influences of thermal stresses.

(a)

(b)

Figure 1.1: Example of cracks propagation over the rigid concrete slab's thickness due to a) curling and b) expansion

In very rare cases, the curling and shrinking strains combined can be so strong that the pavement base fractures even before any traffic loading is applied (Mackiewicz 2014). Additionally, cracking and curling strains are influenced by both diurnal and seasonal cycles. Temperature distributions in the pavement are mostly influenced by the heat flux at the top of the slab during the day and vice versa during the night because the slab's surface area receives greater heat flux than its depth. The surface of the slab warms up throughout the daytime while the interior remains quite cooler. Different deformations occur over the slabs as a result of this thermal gradient condition. As a result, the slabs' top and bottom surfaces experience compressive and tensile strains, respectively. In contrast, throughout the night, thermal radiation and heat convection deplete the solar energy that was received, resulting in a warmer deeper slab and a cooler near the surface. Summer curling stresses are therefore greater than winter curling stresses.

Additionally, due to the seasonal solar radiation pattern, heat is trapped beneath the slab during warmer seasons and released during cooler seasons. The nonlinearity of the slab-temperature profile over slab depth is influenced by this seasonally cyclic heat storage and heat dissipation, which affects the temperature at the bottom of a slab. As a result, there are daily and seasonal variations in the curling stress that is produced in rigid concrete airfield runways. This causes the fissures to widen through the slab's surface of the pavement and deepen beyond its thickness, especially during the summer. Because concrete is weak in tension, tensile loads in concrete slabs can induce deep cracks. As a result, as tensions rise and vehicles drive, the depth of these cracks deepens, leading to the separation of portions of the pavement. As a result, in the prior concrete airfield runways construction, the base layer must be destroyed before development can begin, which is both time-consuming and costly. Rigid concrete slabs are damaged by these curling and external traffic forces. In the early stages of pavement construction, shrinkage creates high pressures, which can induce hairline cracking at the top, exposing the slab to continuous cracking once it is open to traffic. The slab's bending tension is significantly raised by external loads. The underlying layers may be unable to sustain the slab if it is subjected to considerable bending loads, which could lead to slab cracking when heavy traffic passes over it.

In order to decrease crack growth and lengthen the service life of the rigid concrete airfield runways, it is important to increase the tensile strength of concrete. Mahboub et al. (2004) evaluated the joint impact of traffic and curling stresses in this regard. Their conclusions showed that airfield runway responses caused by temperature were more important than those caused by traffic load. Therefore, reducing curling stress, or at the very least controlling it, considerably enhances the structural performance of rigid concrete airfield runways. The expansion and longitudinal deformation of slabs are two additional heat-related impacts on the structural reactions

of rigid concrete slabs, in addition to curling stress. As a result, the occurrence of flexural and longitudinal stresses simultaneously with the traffic load intensifies the structural responses of the runways which controlling and reducing their effects can increase the service life of slabs and reduce maintenance costs.

Considering the highlighted issues and concerns, coupled with the absence of a practical procedure, analysis design protocols and practical models of the chilly need to be accordingly updated to account for the demanding loading conditions induced by the thermal and curling stresses which have not yet comprehensively addressed by previous studies, up to now. Essentially, the size effect of slabs and material characteristics including PF impacts the structural capacity, service life, and pavement stability and failure probability is the key step in designing concrete slabs. Therefore, there is an urgent need to properly assess the structural impacts of thermal and curling stresses to preserve the existing transportation network and properly plan for future rigid concrete airfield runways design in addition to providing a beneficial solution to control the negative impacts of these stresses and mitigate them significantly.

1.2. RESEARCH OBJECTIVE AND SCOPE OF THE STUDY

The primary goal of this research study is to develop frameworks to mechanistically measure the size effect on the curling stress of rigid concrete airfield runways and propose a new formula for determining the curling stress and their performance prediction. Therefore, the secondary goal of the research is to provide a comprehensive practical formulation for engineers to have an opportunity to easily calculate the curling stress of rigid concrete slabs including all important geometric and material characteristics. The final goal is to present a solution with the use of PF to reduce concrete slab damages and increase the service life of runway rigid concrete slabs.

Therefore, the main objectives of this investigation are illustrated in Figure 1.2, and summarized below:

- Review of all the current practices and developed approaches for the comprehensive assessment of the curling stress impacts in the rigid concrete airfield runways.
- Development of the database of size effect on the curling stress of rigid concrete slabs including the geometric characteristics, material properties, and environmental conditions. This information will be instrumental for a new practical formula.
- Introducing the PF as a solution to mitigate the negative influence of thermal and curling stresses.
- Measure the influence of mechanical properties and geometric characteristics on the strength of rigid concrete slabs using ultrasonic imaging evaluation.
- Development of a theoretical finite element method formulation to determine the accurate curling stress in rigid plain and fibers-reinforced concrete slabs.
- Development of a prediction algorithm to anticipate the performance of rigid concrete slabs subjected to thermal and curling stresses.
- Probabilistic study on slab failure considering the wide-range experimental and numerical results in addition to existing failure models' ability.

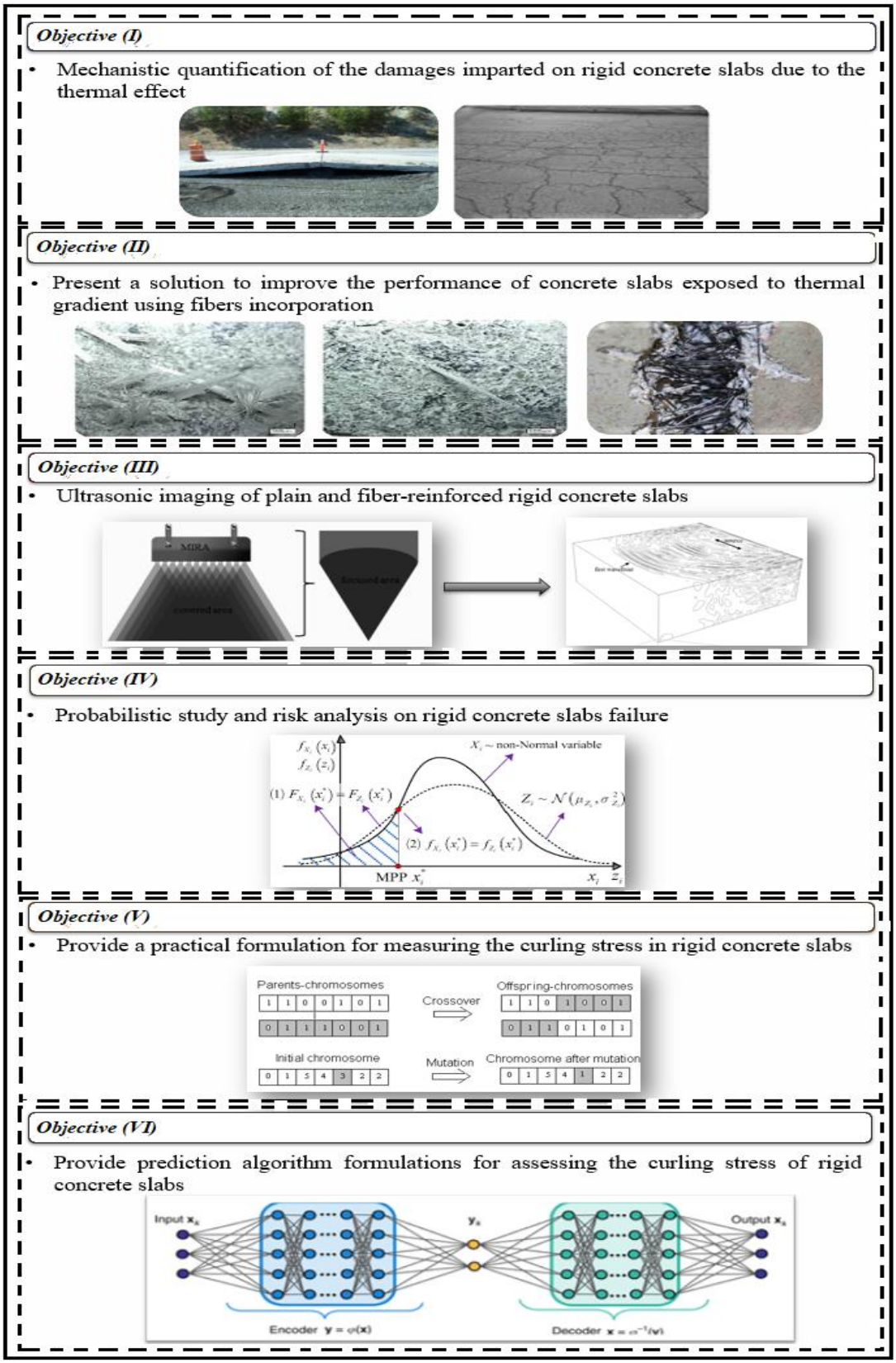

Figure 1.2: Main objectives of the current study

1.2.1. Task 1: Review of the Literature

In this task, a comprehensive literature review was conducted on the following topics:

- Influence of various parameters on the thermal and curling stress of rigid slabs.
- Associated problems with the curling stress and thermal behavior of rigid concrete airfield runways.
- Different proposed techniques and ideas to mitigate the negative influence of temperature on the structural responses of rigid concrete slabs.
- Theoretical and prediction models of rigid concrete slab behavior exposed to environmental conditions.
- Existing theoretical models for predicting the thermal and curling responses of rigid concrete slabs.

1.2.2. Task 2: Assessment of Size Effect and Variables on the Thermal and Curling Behavior of Rigid Concrete Slabs

Identifying factors affecting the behavior of rigid concrete airfield runways plays a key role in the design and optimal performance of concrete pavements. Also, considering the simultaneous effect of different parameters provides a comprehensive view of identifying the weak points of failures and cracking in rigid concrete airfield runways due to temperature gradient exposure. After reviewing previous studies, the weaknesses of the studies were identified and considered to cover the weaknesses and shortcomings of the studies and a comprehensive study in the field of thermal and curling behaviors in this task. Hence, the weaknesses and shortcomings of previous studies can be summarized as follows:

✓ Failure to check all geometric variables and material specifications.

- ✓ Failure to provide a practical technique to mitigate the negative effects of temperature gradient and environmental conditions.
- ✓ Lack of a complete practical formulation for measuring the curling stress of rigid concrete slabs involving all geometrical specifications and materials characteristics.

Therefore, the main objectives of this task include gathering information on the following subjects and performing an analysis using finite element method software. For this aim, a total of 8213 numerical models have been carried out to cover the geometric characteristics, material properties, and environmental conditions associated with the thermal and curling behaviors of rigid concrete airfield runways, as summarized below:

- ➢ Influence of geometric characteristics of concrete slabs on the curling stress.
- ➢ Effect of concrete mechanical properties on the performance of rigid concrete airfield runways subjected to thermal impacts.
- ➢ Influence of thermal gradient on the behavior of rigid concrete slabs.

This information will be instrumental in developing a new theoretical model for the subsequent tasks. To achieve this objective, various field testing was carried out using an infrared camera in El Paso as a case study to measure the temperature gradient over concrete airfield runways' thickness. For this aim, the temperature over the pavement's surface and through-thickness was recorded at different hours during days and nights. Then, these thermal results in addition to the mechanical characteristics of concrete were employed, and finite element modes software, ABAQUS, was utilized considering the critical responses of the previous task to capture the seasonal effect on the performance of rigid concrete airfield runways.

1.2.3. Task 3: Advantages of Polypropylene Fibers Incorporation

Up to now, no study has provided a comprehensive solution to mitigate the negative influence of thermal stresses and external load. Therefore, the primary objective of this task is to provide a methodology for improving the negative influence of thermal and curling stresses in the analysis of rigid concrete airfield runways. The developed approach aims to improve the critical airfield runways' responses under thermal stresses. Concrete slabs may be weak in tension and impact, but PF-reinforced concrete is a good material for cement concrete airfield runways because it has additional strength in flexural fatigue and impact as well as thermal stresses. Therefore, the advantages of PF incorporation in improving the performance of rigid concrete slabs, considered in this task, could be summarized below:

- Potholes in concrete pavements are commonly caused by waterlogging. However, because PF-reinforced concrete airfield runways are highly impermeable to water, they will not enable water logging or water to emerge from the subgrade on the surface.
- The use of PF for concrete will make it easier to install sensors in concrete slabs.
- The environmental load of PF-reinforced concrete airfield runways is much lower than that of conventional concrete airfield runways.
- Maintenance operations and costs associated with steel rebar corrosion will be reduced with the use of PF-reinforced concrete.
- PF in fresh concrete prevents aggregate particle settlement from the airfield runways surface, resulting in a more impermeable, durable, and skid resistance.
- Fibers help to decline plastic shrinking and splitting at an early age and after cracking.
- The usage of PF-reinforced concrete results in higher abrasion and impact resistance.
- Concrete's ductile and flexural toughness is also improved by PF-reinforced concrete.

1.2.4. Task 4: Ultrasonic Imaging Evaluation

As mentioned in the previous tasks, the thermal and curling behaviors of rigid concrete slabs are significantly associated with the strength of concrete and its geometric characteristics. It is very important to ensure that the strength of the cast concrete slabs is achieved in the field. Non-destructive tests are usually used to find the compressive strength and other mechanical characteristics of concrete from the existing rigid concrete airfield runways. The concrete structure's actual strength and qualities are revealed by this test, along with immediate results. Testing specimens cast concurrently for compressive, flexural, and tensile strengths are the norm for assessing the quality of concrete in buildings or other structures. Ultrasonic imaging is a beneficial nondestructive assessment technique for measuring the condition of concrete slabs through focused images achieved with the Synthetic Aperture Focusing Technique. Nevertheless, its application has been restricted to constant-velocity concrete structures; it has not been utilized with multi-layer concrete structures with various wave propagation velocities, such as pavement foundations. Theoretically, Synthetic Aperture Focusing Technique advancements have made it possible to image multi-layer concrete structures using ultrasound. In this chapter, Ultrasonic imaging has been performed in the finite element method, ABAQUS, to identify the influence of geometric characteristics and material properties on the strong performance of rigid concrete airfield runways.

1.2.5. Task 5: Advanced Zero-Stress Assessment

Identifying and controlling cracks along with providing a solution to reduce their depth and width will have a significant impact on reducing pavement maintenance costs. Therefore, providing a solution to determine the depth of cracks can play an important role. Therefore, the major objective of this task is to present a novel unique framework for measuring the influence of wide-range

variables on the possible depth of cracks. For this aim, the flexural behavior of rigid concrete slabs is taken into account considering the plate bending theory, and a new concept is proposed to identify the effect of different parameters on cracking in the rigid concrete airfield runways under the effect of curling stress and bending deformation. To propose this technique, the following assumptions have been established:

1) Cracking occurs due to tensile stress over the thickness of rigid concrete slabs.
2) Cracking will not occur where there is no stress.
3) Between the tensile and compressive stresses, there is the zero-stress line where there is no cracking because of $\sum Strength / \sum tensile\ stress \geq 1.0$.

1.2.6. Task 6: Finite Element Method Formulation

The main objective of this task is to present a finite element method formulation to determine the behavior of plain and fibers-reinforced concrete airfield runways considering the stiffness of the base layer and boundary conditions based on post-buckling behavior. The proposed formulation can serve as a design check for the pavement engineer in the mechanistic design of plain and fibers-reinforced concrete airfield runways. The importance of curling control of rigid concrete pavements becomes more pronounced when both thermal stress and external traffic loads are applied over pavements while the control of thermal and curling stresses has a significant effect in reducing the structural responses of rigid concrete slabs under the effect of traffic. Therefore, the protocol developed in this task will also provide information on the critical responses in the rigid concrete airfield runways for which the stability of the rigid concrete pavements needs to be checked under a thermal gradient.

1.2.7. Task 7: Presenting a Practical Formula

This task aims to provide a comprehensive practical formula for the use of researchers, engineers, and agencies, taking into account the impact of various parameters for designing rigid concrete airfield runways. For this aim, a multi-layer genetic programming machine learning approach (MLGPML) is employed. As a result, the relationship presented in this task is not only highly accurate in predicting the curling stress in rigid concrete slabs but also has a simple form for all engineers and designers. To show the ability of the method, the error was measured using various statistical techniques.

1.2.8. Task 8: Providing Prediction Algorithms

The objective of this task is to develop a tool based on nontraditional mathematical techniques such as artificial neural networks (ANNs) for predicting the inputs of finite element software as a function of geometric characteristics, the material properties of concrete slabs, and environmental conditions. Sensitivity analysis was performed on the model to extract physically meaningful relations between the size effect and curling stress. Additionally, five high accurate ANNs were utilized to assess the performance of different neural networks: Multilayer perceptron (MLP), Radial basis function (RBF), Support vector regression (SVR), Adaptive-network-based fuzzy inference system (ANFIS), and Deep neural network (DNN).

In addition, the results achieved in the training and testing classes from MLP, RBF, SVR, ANFIS, and DNN models for curling and thermal responses have been evaluated using the most popular error and efficiency assessment metrics. These parameters include mean squared error (MSE), normalized mean squared error (NMSE), root mean squared error (RMSE), mean absolute error (MAE), normalized mean absolute error (NMAE), mean absolute percentage error (MAPE),

Nash–Sutcliffe model efficiency coefficient (NSE) and linear correlation coefficient (R) and coefficient of determination (R^2) which shows the accuracy of the proposed prediction results. Therefore, the results of this task will cover pattern recognition and dimensionality reduction techniques such as principal component analysis.

1.2.9. Task 9: Probabilistic Study on Rigid Concrete Slabs Failure

The objective of this task is to analyze the probability ratio of failure among various determinate and indeterminate rigid concrete slabs under the influence of temperature gradient using the Rackwitz-Fiessler technique. The curling equations developed by previous studies and the current evaluation as well as finite element method results will be analyzed to verify the probability of failure. The Rackwitz-Fiessler method introduces an analysis that takes into account the probability model of each variable. These reliability analysis methods will be used to verify how the structure would perform under loading and analyze the probability of failure of determinate and indeterminate rigid concrete slabs and their failure probability under the effect of temperature considering a wide range of variables discussed in Task 2.

1.3. OUTLINE OF THE DISSERTATION

Generally, the contents of this dissertation can be logically divided into eight sections. The first section deals with the behavior of rigid concrete slabs under the influence of thermal and curling stresses using the finite element method strategies. To accomplish the research goals, a thorough analysis was first conducted to determine the impact of different geometric features and material parameters on the curling and thermal stresses of slabs subjected to various temperature gradients. The second section aims to provide a new solution using PF for reducing thermal stress's harmful effects, it is possible to gain more knowledge about the rigid concrete airfield runways that need

to be improved. The third section provides a comprehensive evaluation of the effect of material properties and geometric characteristics on the strength of rigid concrete slabs. For this aim, the non-destructive test was performed numerically using an ultrasonic imaging evaluation. In the fourth section of this study, a new theoretical concept named “advanced zero-stress assessment” was developed to measure the depth of cracks through the slab’s thickness. This impression provides a comprehensive overview of the cracking in rigid slabs due to the curvature deformation under the influence of curling stress. The fifth section deals with the development of a brand-new finite element technique formulation to measure the curling-buckling behavior in rigid slabs under thermal loads considering material properties and geometric characteristics. With regard to the curvature, deformation, and buckling of rigid concrete slabs subjected to the temperature gradient, the developed finite element approach offers a thorough assessment to take boundary conditions, fiber inclusion, as well as base layer stiffness into consideration. In the sixth section, novel highly accurate practical formula using a multi-layer genetic programming machine learning approach to determine the curling stress in rigid concrete slabs. This proposed theory's findings will undoubtedly be put to use by many firms to develop models, and DOTs and concrete pavement designing standards may use them to build rigid concrete slabs that better take into consideration the thermal stresses of rigid concrete airfield runways. The seventh section deals with the analysis of the comprehensive rigid concrete slab system database developed in this study using various artificial neural networks. The devised multilevel prediction approach consists of the following analysis procedures: quantification of cracking, pavement curling and thermal resistances, the potential of buckling resistance, and deformation. The multi-layer framework developed in this study gives engineers and agencies to have a comprehensive view of the thermal behavior of rigid concrete slabs for future construction. For this aim, Multilayer perceptron (MLP), Radial basis

function (RBF), Support vector regression (SVR), Adaptive-network-based fuzzy inference system (ANFIS), and Deep neural network (DNN) were utilized. In addition, the models' robustness of all used algorithms was measured to predict the critical responses of curling stress of rigid concrete slabs. Ultimately in the last section, findings were employed for risk analysis of rigid concrete airfield runways failure. The Rackwitz-Fiessler method introduces an analysis that considers the probability model of each variable. These reliability analysis methods will be used to verify how the structure would perform under thermal stresses and analyze the failure probability of determinate and indeterminate rigid concrete slabs under the effect of temperature considering a wide range of variables. As a result, the probabilistic study can give a broad view of the properties of the influence of various parameters on the curling and thermal behaviors of the rigid concrete airfield runways for engineers and DOTs.

CHAPTER II

REVIEW OF THE LITERATURE

2.1. INTRODUCTION

This chapter's main goal is to provide a review summary for evaluating the effects of thermal and curling stresses on the structural behavior of rigid concrete airfield runways. The preceding section of this chapter is followed by a brief summary of earlier research studies on the assessment of structural impacts and damages imparted on rigid concrete airfield runways as a result of thermal and curling stresses.

2.1.1. Organization of the Chapter

This chapter consists of five main sections. Subsequent to the introductory section, Section 2 provides information associated with the reasons for curling stress occurrence in rigid concrete slabs. Section 3 discusses the recent methodologies to decrease the thermal and curling stresses proposed by prior investigations. Section 4 provides a large number of case studies and field problems of rigid concrete highways in different states in the U.S. This section highlights the importance of the study on the curling and thermal stresses in rigid concrete airfield runways. Section 5 provides discussions on the previous numerical methodologies in order to measure the thermal distribution over the surface and thickness of rigid concrete slabs. Finally, the key findings from the analysis of the prior material are also given in this section.

2.2. THERMAL AND CURLING STRESSES

2.2.1. Curling stress due to temperature gradient

Upward or downward deflection of rigid concrete slabs can happen from the curling caused by changes in environmental circumstances. The two most important environmental variables that might affect volumetric variations in rigid concrete slabs are temperature and moisture. Curling stress is caused by non-uniform temperature gradients. The top of a rigid concrete slab will often expand more than the bottom portion when the top has a higher temperature gradient than the bottom. This upward slab curling is known as a positive gradient. In contrast, if the bottom of a slab has a greater temperature than the top, there will be a negative gradient and the bottom portion of the slab will expand more than the top, causing the slab to curl upward. Additionally, a temperature gradient that is positive generally happens during the day and a temperature gradient that is negative usually happens at night. Additionally, the diurnal temperature effect is most noticeable at night and in the morning the next day (Masad et al. 1996). It should be noted, nevertheless, that seasonal ambient temperature fluctuations can impact the temperature profile of a slab's whole depth, as opposed to diurnal ambient temperature variations, which only affect the temperature profile of a slab's upper half. Due to diurnal factors, the temperature gradient between a slab's mid-point and the bottom is essentially negligible (Nantung 2011). On one occasion the curling-induced concrete slab curvature has started, the slab restraints will usually apply tensile stresses to the slab to withstand the varying strain reaction across the slab depth. Typically, abrupt and significant fluctuations in ambient temperature are what define the magnitudes of the crucial tensile stress (Nantung 2011). The tensile stresses in the slab caused by non-uniform temperature gradient and slab restrictions are shown in Figure 2.1.

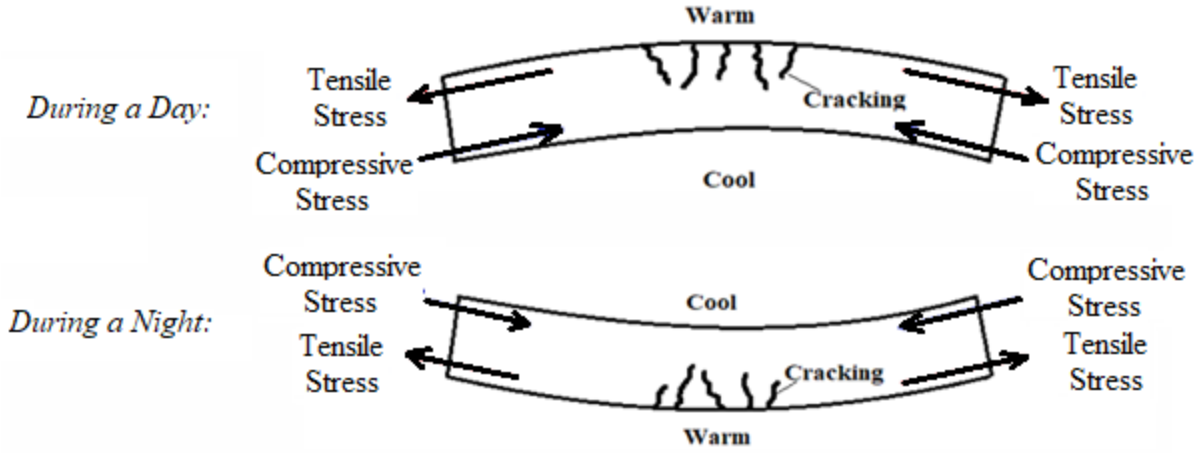

Figure 2.1: Tensile stresses at the top of the runway with an upward deformation and tensile stress at the bottom of the runway with a downward deformation are caused by curling

The most common concrete runway limitations are the slabs' self-weight, dowel bars, aggregate interlock, and friction among the slab and base layer (Kim et al. 2007, Wells 2005). It should be emphasized as well that a rigid concrete slab's deflection in the field is often asymmetric as a result of varying constraints along the slab. Therefore, the strains brought on by curling might cause cracking (Hansen and Wei 2008, Lim and Tayabji 2005). According to some studies, the effect of curling on the occurrence of early cracking may be even more significant than the effect of traffic volumes (Mahboub et al. 2004, Nantung 2011, Zhang et al. 2003). In the beginning, Hveem (1949) looked into fractures brought on by twisted rigid concrete slabs. He described the tendency of concrete airfield runways to bend, typically generating high joints, as the curling-related deflection of the slab. The research was conducted by Hudson and Flanagan (1987) to examine the damage caused by traffic loads and environmental influences. In order to determine how Indiana's pavements are affected by climate change, Nantung (2011) carried out the research. Before the freshly manufactures plain concrete airfield runways were opened to traffic, the investigation found that a few areas of slabs had mid-slab cracking. So, curling stress can have a significant impact on rigid concrete airfield runways, particularly at an early age.

Additionally, the impact can be multiplied by the simultaneous traffic loads and curling stress occurrence, even if the tensile stress caused by curling may not be important or sufficient to start fatigue cracking (Yoder and Witczak 1975). For instance, bottom-up cracking may arise from the slab's top temperature differences that cause downward curling when paired with heavy traffic load. On the other hand, upward curling and traffic loads can combine to cause top-down cracking. Besides, the contact between the slab and the base layer might likewise be lost due to curling. When the slab curls downward or upward, there is a loss of contact between the slab and the base layer at the slab's center and corners, respectively. Increased strains brought on by a loss of contact between the slab and the base layer might worsen pavement degradation from cyclic loads (Rao and Roesler 2005). Additionally, the rigid concrete slab has a tendency to curl upward under negative temperature gradients, leading to the joint opening between nearby slabs which is the main reason for cracks propagation over the notch’s region.

Furthermore, the rate of cracks opening can be affected by drying shrinking and slab length. (Bissonnette et al. 2007). By examining the impact of temperature gradient on rigid concrete slabs with no traffic loads, Westergaard (1926) was one of the first scientists to explore slab curling. An infinite or semi-infinite rigid concrete slab anchored on a Winkler base was thought to offer potential answers for loading conditions at the slab's corners, sides, and interior (Westergaard 1926). For this aim, the linear distribution of temperature throughout the slab depth was another assumption made by Westergaard (1927). By taking into consideration the positive and negative temperature gradients, he developed a numerical approach for determining curling stress. Westergaard's research was developed by Teller and Sutherland (1935) and found that temperature is in fact distributed nonlinearly surrounded by rigid concrete slabs. The nonlinear distribution may be caused by material and spatial nonlinearities. Additionally, the scientists discovered that

the recorded curling stress can equal those produced by the heaviest allowed wheel loads (Teller and Sutherland 1935). Bradbury (1938) devised a formulation to determine the ultimate stress in a finite concrete slab with all free boundaries, thus expanding Westergaard's investigation. He applied the slab length/radius of relative stiffness fraction to create a simpler chart to calculate curling stress. Curling stress was discovered to be influenced by slab length and the level of support beneath the slab (Bradbury 1938). While curling stress did not receive much consideration until later researchers discovered evidence of the importance of curling stress from field tests and numerical analysis (Choubane and Tia 1992). Although both Westergaard's and Bradbury's work indicated that the stresses induced by temperature gradient alone may be comparable to the stresses induced by traffic loading under extreme climatic conditions (Choubane and Tia 1992). The common numerical analysis schemes, counting the guess of a linear temperature variation, still rely on Westergaard's and Bradbury's examination, even though it has already been established that the real temperature profile is highly nonlinear under realistic conditions (Liang and Niu 1998).

Two-dimensional (2D) finite element approaches, which could only account for linear temperature gradients, were utilized for curling stress evaluation by the end of the 20th century (Harik et al. 1994). Traditional 2D shell element analyses required less input and execution time than subsequent three-dimensional (3D) finite element approaches, but these schemes had drawbacks in terms of vision and predicted precision (Harik et al. 1994). The first researcher to assess the curling stress in rigid concrete slabs under the premise of a nonlinear temperature gradient in the slab was to be expected Thomlinson (1940a, 1940b). According to Choubane and Tia (1992, 1995), the temperature gradient in the rigid concrete slab was largely nonlinear and could be reasonably described by a quadratic trend to define the temperature as a function of

thickness. The corresponding thermal gradient components were then described using the given formulation. The authors also came to the conclusion that the nonlinear stresses that would have resulted if the additive influences of moisture difference at night had been taken into account; thus, the critical stress test may be affected by an irregular temperature variation (Choubane and Tia 1992, 1995). Harik et al. (1994) have suggested a technique for treating a nonlinear temperature gradient through the depth of rigid concrete slabs using a 2D finite element method analysis.

Despite being a 2D model, it may nonetheless superimpose the nonlinear temperature distribution's influence on the finite element method answers. Findings of previous studies showed that it is not prudent to ignore temperature stresses in rigid concrete slabs design (Harik et al. 1994). Nonlinear 3D finite element method simulation of rigid concrete slabs gained popularity in terms of curling stresses during the 1990s (Channakeshava et al. 1993, Kuo et al. 1996, Zaghloul et al. 1994). Kuo (1998) came to the conclusion that support from the underlying layers, concrete's self-weight, and temperature gradient were the main influences on curling stress. Liang and Niu (1998) used a closed-form analytical technique to measure the effect of temperature gradient on the structural responses of rigid concrete slabs. The predicted temperature gradient over the slab depth is more affected by the frequency of temperature differences than by their magnitude. The level of temperature change was found not to significantly alter the form of temperature distribution (Liang and Niu 1998). However, the real characteristic of the temperature profile across the thickness of rigid concrete slabs, as illustrated in Figure 2.2., is a nonlinear distribution decomposed into three parts: (i) a uniform segment that experiences uniform temperature variation-induced longitudinal elongation or contraction, (ii) a straight element responsible for the slab's twisting, and (iii) a self-equilibrating tension is caused by a zero-moment nonlinear element (Yu et al. 2004).

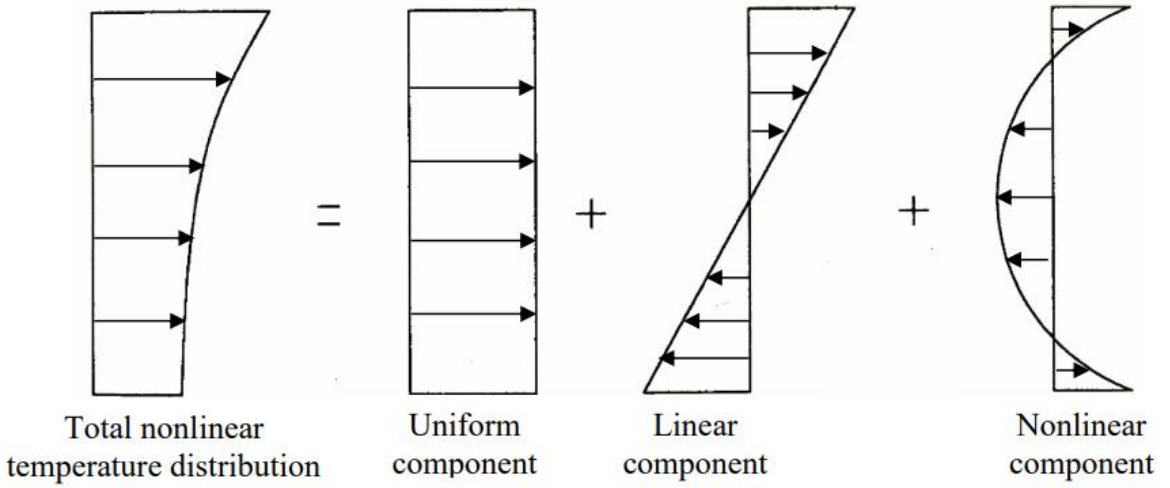

Figure 2.2: Normal temperature distribution over the depth of a concrete slab (Choubane and Tia, 1992).

As was previously mentioned, compared to the findings of a nonlinear temperature gradient, a linear temperature distribution will produce overstated ultimate tensile stress during the day and underestimated ultimate tensile stress during the night (Choubane and Tia 1995, Masad et al. 1996). Despite the fact that it has long been understood that the slab temperature distribution over the thickness is actually nonlinearly distributed, many investigations studies conducted in the 20th century assumed a linear temperature profile in order to make calculations simpler and to provide clearer results. In order to measure the slab's temperature gradient over the thickness, Janssen and Snyder (2000) presented the idea of "temperature moment" and showed how to calculate it in order to determine the temperature gradient for additional stress evaluation. Additionally, some studies declared that rigid concrete slab deflection may be substantially more affected by temperature differential than moisture gradient which highlights the importance of measuring the curling stress in rigid concrete slabs (McCracken 2008). Because temperature-related curling stress can be amplified when the combination of traffic load can start fatigue cracking, even while the curling stress does not exceed the permissible stresses, the influence of

temperature gradient has been given increased consideration in rigid concrete slab design methods (Choubane and Tia 1995, Harik et al. 1994, Yoder and Witczak 1975). The Mechanistic-Empirical Pavement Design Guide (MEPDG) created by National Cooperative Highway Research Program (NCHRP) Project 1-37A more closely considers the impact of climate on concrete runways design. Furthermore, the thermal characteristics of materials are used as direct input variables by the MEPDG to forecast rigid concrete slab performance (ARA, Inc. 2004, Chung 2012, Nantung 2011). To measure the impacts of temperature gradients, all environmental variables that affect rigid concrete slab performance are translated to equivalent temperature differences in the design guide (Yu et al. 2004).

2.2.2. Built-in curling

In the summer, it is customary to build new rigid concrete slabs during the day, which makes the slab surface warmer while the setting takes place. With a positive temperature gradient, the rigid concrete slabs will therefore start to harden and maintain their flatness. As the atmospheric temperature starts to decline, the temperature gradient tends to become zero or negative, which causes upward curling to occur. In other terms, a negative temperature gradient develops inside the concrete when the rigid slabs have a colder exterior (Hansen and Wei 2008, Rao and Roesler 2005a, Yu and Khazanovich 2001). Additionally, this upward curling brought on by the negative temperature gradient might cause the negative temperature gradient to rise at night and the positive temperature gradient to fall during the day. In addition, the slab may only return to its original flat form if a strong enough positive gradient emerges to counteract the negative gradient created by concrete hardening (Lederle et al. 2011). Because of the low atmospheric temperature at night, the first night after concrete paving is important for built-in curling because

the sidewalk surface needs to be colder. When the power acquired is still minimal, substantial stresses frequently arise (Lim and Tayabji 2005). Therefore, before the runway is opened to traffic, this built-in curling may result in cracks, and after the pavement is exposed to traffic, top-down cracks may start to propagate from the top of the slab. The ambient temperature, concrete setting, and pavement design elements such as joint spacing, dowel bars, sublayer type, and the thermal coefficients of the materials employed all have an impact on built-in curling (Rao and Roesler 2005a, Yu and Khazanovich 2001). The circumstances of base contact over the service life of the rigid concrete slabs can also be greatly affected by the temperature gradient during the final set (Hansen and Wei 2008). Hansen and Wei (2008) proposed the concept of an operative temperature gradient in response to the influence of the built-in curling on the daily temperature variation. Equation (2.1) may be used to compute the effective temperature difference as follows:

$$T_{effective} = \left(T_{top,daily} - T_{bottom,daily}\right) - \left(T_{top,finalset} - T_{bottom,finalset}\right) \quad (2.1)$$

In which, $T_{effective}$, $T_{top,daily}$ and $T_{bottom,daily}$ denote the combined effects of the daily temperature difference and the inherent temperature difference leading to the effective temperature difference, diurnal variations in ambient temperature cause the top and bottom surface temperature, respectively. In addition, $T_{top,finalset}$ and $T_{bottom,finalset}$ designate the top and bottom exterior temperature at the final set, individually. The built-in curling has also been quantified in terms of temperature differential or gradient by a number of studies using formulae or models. The terms effective built-in temperature gradient, built-in equivalent temperature gradient, and permanent curling effective temperature gradient are used to describe these equations or models (Rao and Roesler 2005a; ARA Inc. 2004; Vandenbossche et al. 2010). Although built-in curling has long been identified and researched, it is still challenging to quantify it accurately

due to the numerous influencing factors, such as temperature variation during the casting, differential shrinkage, creep, breeze, and moisture ratio (Merritt et al. 2015, Rao et al. 2001). The MEPDG/AASHTOWare Pavement ME includes the built-in curling during the concrete casting and the daily curling during the service life of the airfield runways (Yu and Khazanovich 2001).

2.2.3. Geometry of rigid concrete slabs

In rigid concrete slabs, thermal and curling stresses are significantly influenced by slab geometry, including, width, length, and thickness. Generally, a thicker slab might result in less curling stress (Rao and Roesler 2005a, Siddique and Hossain 2005). Thinner concrete slabs are more likely to curl because of their decreased self-weight and greater curing shrinkage. However, prior to MEPDG, none of the rigid concrete slab design methods took the impacts of temperature gradient-induced curling into account (Chung 2012). In this area, Childs and Kapernick (1958) found that increasing the slab thickness from 6 inches to 8 inches caused a 50% reduction in curling deflection. Based on field measurements obtained from data gathering tools, Nantung (2011) evaluated rigid concrete slab stresses. It was found that thinner slabs frequently had greater stresses than larger slabs under the same saw-cutting separation. Thinner concrete slabs are more prone to bending because they have a smaller moment of inertia than broader slabs. A shortened slab might also result in less curling tension (Cement Concrete & Aggregates Australia 2006, Rao and Roesler 2005a). However, based on the outcomes of Westergaard's equations and Bradury's chart, it was previously believed that slab length had a minimal bearing on curling stresses. The length of the slab may not affect the curling responses without dowels because dowels in transverse joints can curve to withstand concrete runways shrinkage.

Furthermore, the consistent temperature factor could cause axial enlargement or shrinkage, and due to the constraints imposed by the underpinning support, curling stresses could start. The ratio of notch spacing to the radius of relative stiffness can change the restrictions resulting from the level of support. Thus, a lengthier slab's length and/or a sturdier underlying layer may cause greater pressures (Jeong and Zollinger 2005). Upward bending increases when the length increases from 15 to 20ft, according to Ytterberg (1987). Eisenmann and Leykauf (1990) discovered similar results, namely that upward curling deteriorates as slab length increases. Furthermore, Nantung (2011) found that rigid concrete slab curling stresses, particularly those in the longitudinal direction, are reduced when notch spacing is reduced.

2.2.4. Concrete material characteristics

The ratio of the stresses to the corresponding strain is the simplest way to determine the concrete elastic moduli, abbreviated as E. The concrete elastic moduli can influence the temperature and curling stress because it is connected to the characteristics of creep and stress release. Higher elastic moduli may exhibit more curling due to greater self-desiccation, less creep, and less downward relaxation of the curled slabs during the time. (Lederle et al. 2011, Rao and Roesler 2005a). Additionally, the stiffness of the coarse aggregate has a significant impact on the elastic moduli of concrete. Aggregates with higher toughness values frequently lead to concretes with higher E values. Figure 2.3 provides the E values of concretes made with various kinds of aggregate that were studied by Aitcin and Mehta (1990). This graph demonstrates that concrete produced with limestone has a slightly greater E value than concrete produced with other kinds of aggregates.

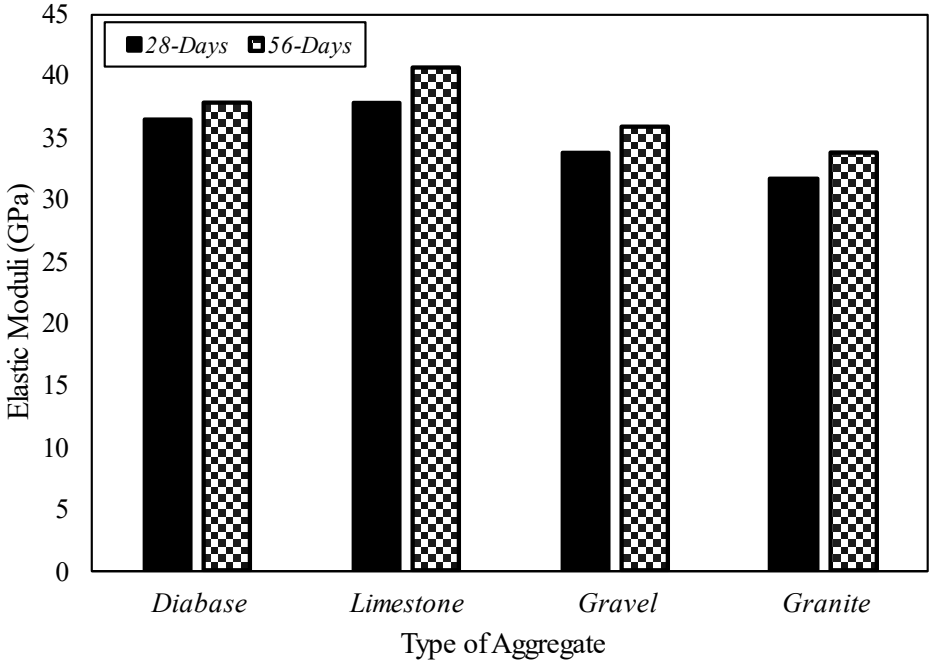

Figure 2.3: Elastic moduli of concrete with various types of aggregate

Usually, rigid concrete slabs with a higher coefficient of thermal expansion values undergo higher volume changes when exposed to the same thermal gradients. As a result, there is greater curling deflection. Additionally, there are large curling strains because of the drastic contrast in the coefficient of thermal expansion values between the rigid concrete slabs and the underlying layer. This occurs as a result of the two adjacent layers' different strain responses, which lead to significant frictional stresses and ultimately significant curling stresses (Asbahan 2009, Wells 2005). Concrete's coefficient of thermal expansion is mostly influenced by the kind of aggregate and saturation level. In comparison to concrete made with other types of aggregates, concrete made with limestone often has a lower coefficient of thermal expansion value. The thermal characteristics of aggregates or concrete, such as coefficient of thermal expansion, thermal conductivity, and heat capacity have drawn attention recently as crucial material characteristics for preventing rigid concrete slab curling. They have been recognized as important factors in

mechanistic-based thickness design methods, such as the MEPDG/AASHTOWare Pavement ME Design approaches, for predicting runways characteristics (ARA Inc. 2004, Chung 2012).

2.2.5. Base layer interaction

As was already mentioned, the bottom layer's restrictions produce stresses that induce curling stress. Increased curling stress is often caused by higher friction from constraint. According to Rivero-Vallejo and McCullough (1976), the primary element impacting crack propagation was significant friction between the top rigid concrete slab layer and the base layer. In this regard, a 3D finite element method simulation and interface components were used by Masad et al. (1996) to simulate the interaction between a rigid concrete slab and its supporting layer. Shorter slabs were found to have a greater frictional coefficient than longer slabs, and the greatest strains were found to be generated close to the center (Masad et al. 1996). This result supported Huang's (2004) assertion that friction is inversely related to slab length but independent of slab thickness. Additionally, the weight of the concrete has an impact on friction. As demonstrated in Figure 2.4 by Yu et al. (2004), the underlying layer is not always flat, therefore the rigid concrete slab may not accurately represent the state of its underneath supporting layer.

When the slab deforms, extra stresses are created by a stiff underlayer. A rigid underlying layer prevents the slab from settling into the underlying layer when curling occurs (Ytterberg 1987). A soft underlying layer can generate less curling tension due to the "bedding" effect, which reduces the impact of the restriction from the base layer. (Eisenmann and Leykauf 1990). Traffic loads, however, can cause greater deflections and the underlying layer provides less resistance than deformation brought on by temperature alone, so serious tensile stresses may be advanced in runways with a soft base when taken into consideration. (Dere et al. 2006). Therefore, the loss of

subgrade support brought on by curling may result in voids under the rigid concrete slabs, which can quickly lead to pumping and structural degradation (Nantung 2011).

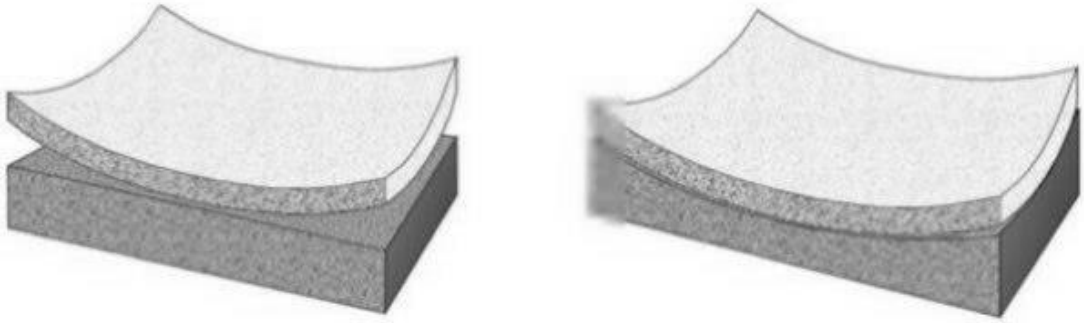

Figure 2.4: Representations of the support conditions under rigid concrete slabs: one with an idealized flat foundation (left) and the other with the impacts of settlement (right) (Yu et al. 2004)

2.2.6. In Situ Weather Conditions

Weather conditions affecting curling stress are also influenced by local climatic factors including sun radiation and wind speed. The distribution of rigid concrete slab temperature is directly influenced by solar radiation. In addition, cracks widths, periods of freezing and thawing, and joint load transfer may all be impacted by sun radiation. (Chung and Shin 2015). Depending on the concrete's absorptivity, absorbed heat may be partly retained and transferred to the concrete beneath the upper layer. The short-wave surface absorptivity of the rigid concrete slab and solar radiation both affect how much heat is absorbed. The surface absorptivity often fluctuates inside concrete depending on the texture and color of the runways. Depending on the season, the overall heat gain or loss caused by the sun's radiation impact might change. While the high solar energy causes a net heat gain during the summer, the extremely low ambient temperature frequently causes a net heat loss during the winter. In this regard, using a one-dimensional heat transfer model, Yinghong (2011) examined the impact of solar radiation on the distribution of temperature and

thermal stresses in rigid concrete slabs. The distribution of temperature and thermal stresses was shown to be primarily influenced by solar radiation at the concrete slab surface, and greater solar radiation values can lead to higher maximum tensile stresses.

Additionally, the effect of the heat record is minimal at the top of the slab but significant at the bottom of the slab (Yinghong 2011). By altering heat transfer and temperature distribution, wind speed significantly affects heat convection at the rigid concrete slab surface (Chung and Shin 2015). Furthermore, it is common knowledge that wind may hasten water evaporation and thus cause significant drying shrinkage during the installation of concrete. The correlation between wind speed, water evaporation, and shrinkage was mapped out by Holt and Leivo in 2004. They demonstrated how high winds cause more water to evaporate and drying shrinkage. The effect of wind speed on temperature, the spread of thermal stress, and the heat convection rate in concrete runways were also studied by Yinghong (2011). It was found that the direction of the sidewalk and the season had an impact on how the spread of stress was affected by wind speed. For example, if the pavement is constructed in a hot climate or at a lower latitude, the wind will extract more heat from the pavement surface to lessen the temperature differential, resulting in reduced thermal and curling stresses (Yinghong 2011). Other environmental factors, including ambient temperature and relative humidity, can have an impact on curling and thermal stresses in addition to solar radiation and wind. High ambient temperatures might cause substantial built-in curling during pavement construction. To reduce curling stress, the recommended methods for rigid concrete slabs are presented in the following section. Seasonal variations may also have an impact on how much curling occurs. McCracken et al. (2008) published the data displayed in Figure 2.5 for both restrained and unrestrained slabs in Pennsylvania using strain measurements, along with the following observations:

- The development of total strain in the concrete slabs was mostly influenced by temperature-induced strain measurements
- Wintertime temperature changes resulted in increased slab contraction, which led to higher temperature-induced strain readings.
- In both the restrained and unrestrained slabs, the strain readings brought on by moisture and other variables were higher in the fall than in other seasons.

In contrast to the findings from the strain capacities, McCracken et al. (2008) used surface profile measurements as well. The measurement results showed that the total degree of curling stress can be higher in the summer. However, the winter had the least amount of diurnal curling fluctuations in both sets of test findings. This is due to the existing seasonal temperature arrangements and the length of daylight cycles (Wells 2005).

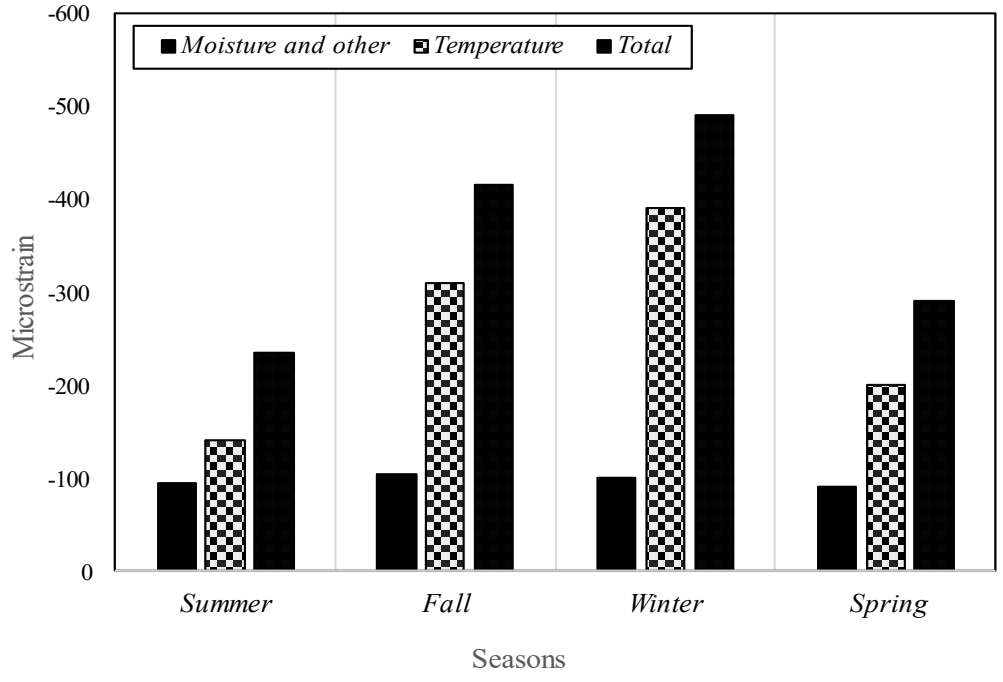

Figure 2.5: Seasonal influences on the amount of curling in restrained and unrestrained rigid concrete slabs (McCracken et al. 2008)

2.3. TECHNIQUES TO REDUCE RIGID CONCRETE SLAB CURLING STRESS

Although rigid concrete slab curling stress cannot be totally eliminated under practical circumstances, the effect should still be as little as feasible during material properties, mixture design, slab design, and construction. The general strategies for lessening the effects of rigid concrete slabs' curling stress are summarized below:

2.3.1. Material properties

The heat gradient within the concrete is connected to a thermal characteristic of concrete called the coefficient of thermal expansion. The coarse particles used in concrete are a major factor in the concrete coefficient of thermal expansion. A low coefficient of thermal expansion coarse aggregates is used in the production of concrete, which lowers the possibility of curling. The lowest coefficient of thermal expansion values is shown in Figure 2.6 for concrete containing andesite, basalt, and limestone.

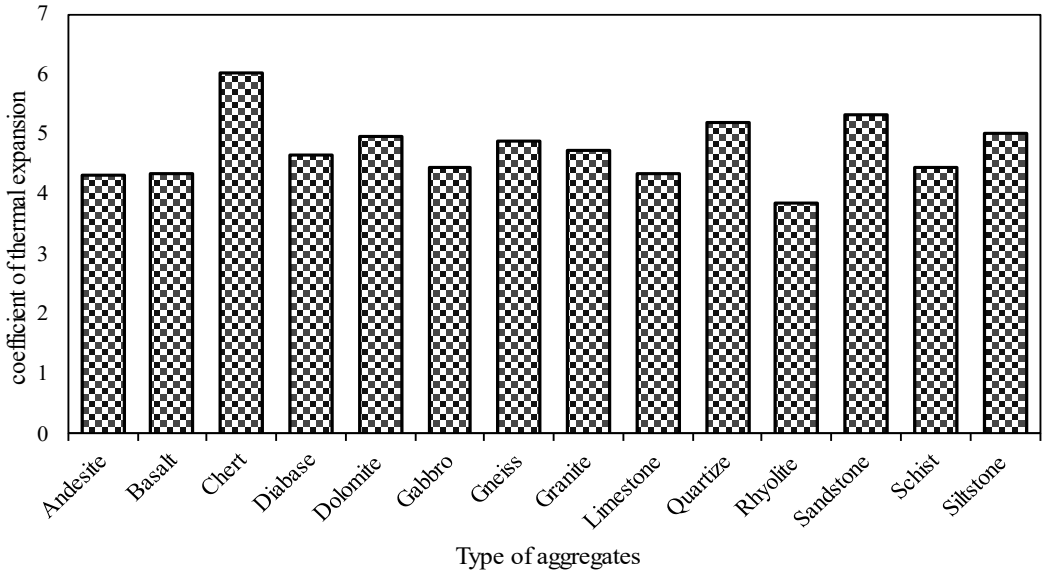

Figure 2.6: Coefficient of thermal expansion of concrete with various kinds of aggregate

Taylor and Wang (2014) provided a summary of the variables affecting the thermal behavior of rigid concrete slabs. Utilizing aggregates with lower water absorption often results in less thermal and curling behavior. Therefore, it is preferable to use coarse aggregates with low water absorption values (0.5%) (Babaei and Purvis 1995). Therefore, Quartz has a greater chance of curling because of its comparatively higher coefficient of thermal expansion, as illustrated in Figure 2.7.

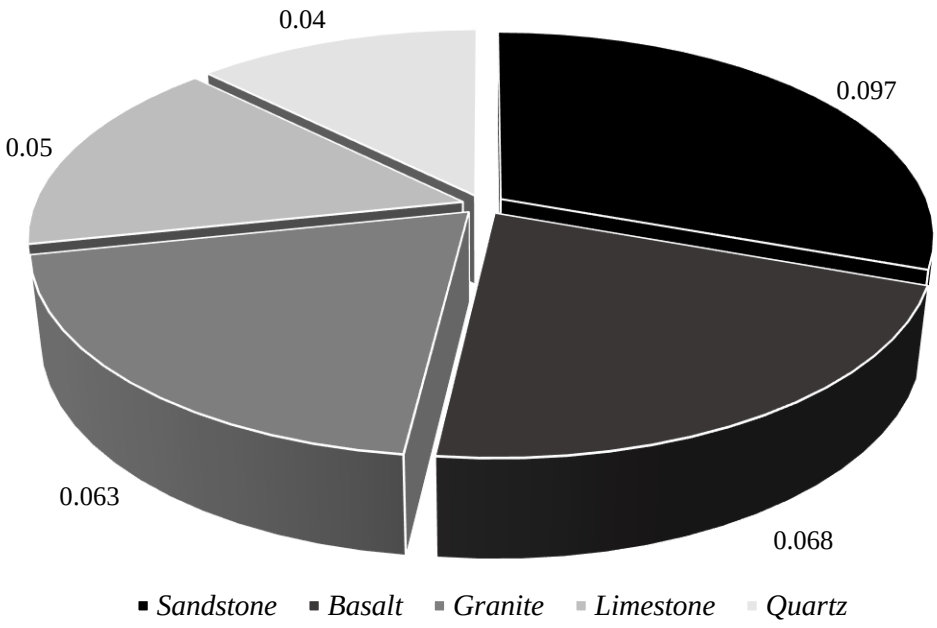

Figure 2.7: Various aggregates' dry shrinkage over a year

According to findings from the calculation and finite element method simulation provided by Leonards and Harr (1959) and Al-Nasra and Wang (1994), concrete with a high elastic modulus may cause lower curling deflection. In conclusion, using coarse aggregates with a lower coefficient of thermal expansion and water absorption values is preferable for reducing rigid concrete slab curling and thermal stresses (Cement Concrete & Aggregates Australia 2002). To avoid shrinkage and to avert fractures from spreading the coarse aggregate must also be strong, rigid, long-lasting,

and moisture-resistant. It must also be free of clay or other fine particles (Rao and Roesler 2005a, Smiley and Hansen 2007, Wilson and Kosmatka 2011). Limestone is preferable because it has a lower coefficient of thermal expansion and less chance of shrinking, according to Figures 2.6 and 2.7. Additionally, coarse particles with high specific gravity values can improve concrete self-weight and hence reduce vertical deflection in order to prevent curling deflection. However, because of the higher constraint in these situations, the tensions that cause curling may also rise.

2.3.2. Concrete mixture design

In order to reduce thermal and curling stresses, the proportions of the concrete mix should be created to reduce shrinkage and heat emitted during the cement hydration procedure. A high cement hydration rate may be the source of a high concrete mixture temperature, which is readily produced during summer construction. Then, at night, when the surface temperature drops but the bottom temperature stays high, negative built-in temperature differences or gradients can be generated. Consequently, it must be assured that the temperature of the concrete mixture never rises over the maximum temperature permitted as stipulated during construction (Rao and Roesler 2005a, Smiley and Hansen 2007). Therefore, for concrete airfield runways mix design, additional cementitious materials including fly ash and ground granulated blast furnace slag are advised (Nantung 2011). Moreover, large maximum coarse aggregate size and volume are preferred in rigid concrete slabs to reduce curling. Typically, more cement paste in the concrete mix might result in more shrinkage. By using a larger coarse material dimension in the construction of the concrete mixture, less cement paste is left in the combination. Also, a rather low water-to-cement fraction is recommended since it might aid in preventing quick moisture evaporation from the rigid concrete slab's surface. According to research performed by Yinghong (2011), variations in

relative humidity along a rigid concrete slab are not proportional to changes in water-to-cement fraction. A lower water-to-cement fraction may lead to reduced moisture loss throughout the course of the runway surface's life and make the concrete slabs more resistant to wetting and drying cycles, as shown in Figure 2.8.

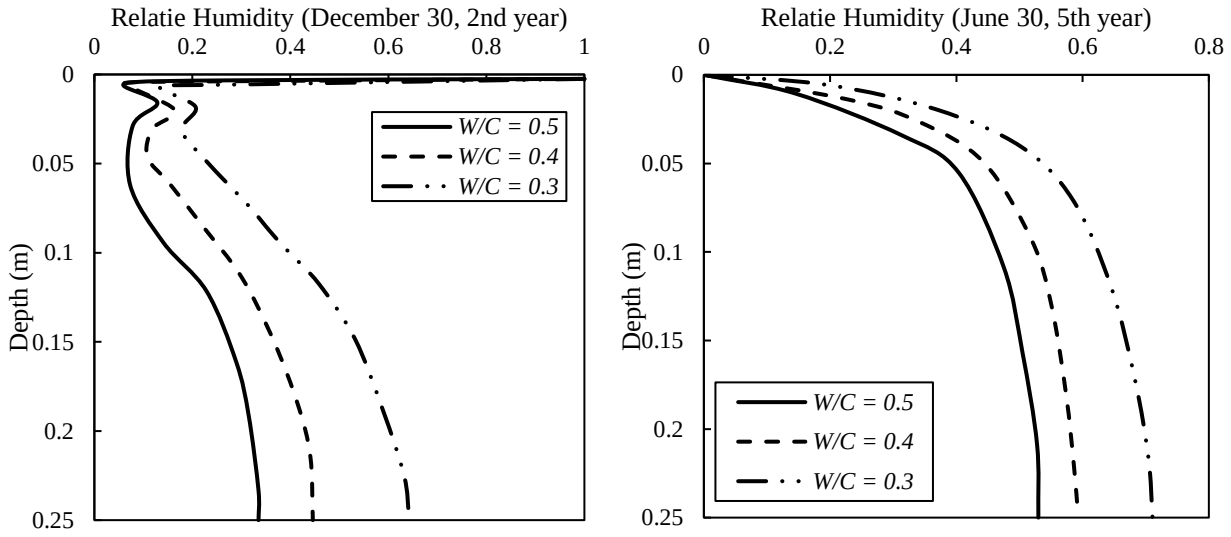

Figure 2.8: Effect of water-to-cement ratio on the relative humidity in rigid concrete slabs Yinghong (2011)

Furthermore, because surface moisture is mostly controlled by boundary conditions, changes in the water-to-cement fraction seldom affect the moisture at the top of slabs but can have a significant influence on moisture towards the bottom of the slab. The controlling water-to-cement fraction in the mix design should be in the middle. As previously mentioned, a high water-to-cement fraction can promote moisture loss, and worsen drying shrinkage, whereas a very low water-to-cement fraction may enhance the concrete slab's autogenous thermal and curling stresses. Therefore, it is suggested to use a modest water-to-cement fraction to cause less thermal and curling deformations (Yinghong 2011, Rao and Roesler 2005a). The total volume proportion of cement and water shouldn't be greater than 27% of the total volume of the concrete, it is also

recommended (Schmitt and Darwin 1999). Moreover, chemical admixtures that might lessen shrinkage can assist diminish curling. Admixtures with shrinkage-reducing properties can lower early-age deformation by around 30% to 40%. (Altoubat 2010).

2.3.3. Rigid concrete slabs design

Dowel bars, the kind of underlying layer, and concrete slab geometry should all be taken into consideration while designing a rigid concrete slab to minimize thermal and curling stresses. As previously mentioned, shorter slab lengths and thicker slabs can be used to reduce curling stresses. Most rigid concrete slab design guidelines typically advise that slab length should be proportionate to slab thickness. Shorter slabs appear to be more prone to mid-slab or mid-panel cracking if loss of support occurs, therefore enough attention should be made to the support from the underlying layers if loss of support arises (Smiley and Hansen 2007). Dowel bars are crucial in the design of rigid concrete airfield runways because they prevent deflection, particularly near joints. Dowel-bar reinforced rigid concrete pavements often show less curling deflection (Nassiri 2011, Wells 2005). However, restrictions brought on by the presence of dowel bars may also result in increased curling forces. Aggregate interlock is also necessary for load transmission in concrete runways without dowel bars. Dowel bars can increase the effectiveness of load transmission and reduce rigid concrete slab curling deflection (Lederle et al. 2011). Davids (2001) used a 3D finite element method simulation to examine the effectiveness of load transmission in dowel-curled rigid concrete pavements. Dowel bars can also reduce the influence of slab length on curling behavior (Nassiri 2011, Vandenbossche 2003). Moreover, as the underlying layers directly affect stress generation, and degree of support, and so that, appropriate selection of the underlying layers of concrete airfield runways is crucial for reducing curling stress (Rao and Roesler 2005a). A stronger

foundation often causes a bigger area of the concrete slab to remain unsupported during curling because it prevents the slab from moving downward (Smiley and Hansen 2007). When considering traffic loads, a soft base layer may produce a "bedding" effect to offset the slab's downward motions, but it may also result in greater deflection. Therefore, while choosing the underlying layers, the trade-off between the effects of curling and traffic loads on the performance of rigid concrete airfield runways should be taken into account.

2.3.4. Construction applications

Built-in curling during a concrete setting is greatly influenced by the surrounding temperature. To minimize the temperature effects on built-in curling, great care must be taken while choosing the time of paving. The season for paving, timing, and weather during construction are all factors to take into account. Although totally eradicating built-in curling is challenging, it should be minimized as much as feasible by taking into account the aforementioned factors and associated tactics. Therefore, in order to maximize the durability of rigid concrete slabs, the appropriate paving season should take the local climatic pattern into account. Rigid concrete slab construction often takes place throughout the summer and during the day. The atmospheric temperature is high during summer or when the weather is sweltering and arid, which can rapidly result in upward built-in curling in slabs. As per Hansen et al. (2006), Michigan runways constructed in the late fall have less built-in curling. Summer daytime construction should be avoided as built-in curling is common when placing concrete in the morning (Lederle et al. 2011, Smiley and Hansen 2007). If rigid concrete slabs are constructed in the morning, the afternoon is when the concrete will set and harden. The strongest possible negative built-in temperature gradient is anticipated to form in this situation. Consequently, nighttime paving is recommended by Kim et al. (2008), Lederle et al.

(2011), and Merritt et al. 2015. Pavements created during the day versus those built at night were studied by Rao et al. (2001), who assessed that nighttime construction could suggestively lessen built-in curling (Rao et al. 2001). Due to the high probability of actual negative temperature variations, construction should be evaded during hot and arid environmental circumstances. In fact, many jurisdictions have rules governing the highest ambient temperature that can be reached during a building project in hot weather. States often don't let the ambient temperature get over 90 to 95°F while placing concrete (Merritt et al. 2015). During the laying of the concrete, the temperature differential between the top and bottom of the slab layer should be kept to a maximum of 10°F.

Additionally, it's best to stay away from high winds and sun radiation while building pavement since they might cause the base course to become hot before paving and make the temperature differential worse (Smiley and Hansen 2007). Additionally, rigid concrete slab construction needs to be postponed on days that can experience abrupt or significant changes. For instance, abrupt shifts from warm to cold conditions in the early winter might cause significant maximum curling stress (Nantung 2011). To reduce curling stress, it is preferable to keep the temperature throughout the thickness of the concrete relatively constant (Hansen and Wei 2008). Curling can be reduced by maintaining ideal conditions for the subsurface layers for slab construction. Therefore, in order to prevent curling, the maximum and lowest temperatures of the foundation during paving should be kept near the temperature of the concrete (Merritt et al. 2015).

2.4. CASE STUDIES

Figure 2.9 depicts the reconstruction of a section of US Highway 34 near Greeley, Colorado, between about mileposts 113.4 and 115.3 in 2012. A new 9-inch-thick jointed plain concrete slab

was manufactured to substitute the previous concrete surface. When the eastbound lanes were built in September 2012, they had a ride quality that was noticeably different from the westbound lanes, which had been built in July 2012. Colorado Department of Transportation (CDOT) was trying to figure out why there was such a difference in ride quality for the pavement with the same design and materials. This investigation was started to see if the major reason for the variation in ride quality was indeed slab curling, which was believed to be the case. To address this problem in future projects, CDOT is also looking for suggestions for modifications to the current jointed concrete pavement construction and profile data-gathering processes.

Figure 2.9: Site of the US 34 curling study location

After ride quality values for profile data acquired by the contractor and values collected by CDOT on the same length of pavement were noticeably different, first concerns regarding the impacts of slab curling on ride quality were raised. Both profilers were tested simultaneously at a calibration location to ensure that they were measuring the same data and operating properly. The CDOT readings were gathered early on two consecutive days, and the outcomes were the same. In the afternoon, the contractor tests were conducted. Keep in mind that contractor data are presented as mean roughness index and CDOT results are published as half-car roughness index. Given that

the half-car roughness index for jointed concrete pavements is generally 90–95% of the international roughness index, the discrepancy between the contractor's and CDOT's values becomes even more substantial (Karamihas, 2012).

The contractor then measured a segment of the wheel path lane at three separate times on the same day because they suspected that the time of day of profiling would be the reason for the discrepancy between CDOT and contractor measurements. The results of this testing are shown in Table 2.1, which confirms that the collecting of profile data at different times of the day had a substantial impact on international roughness index values. The CDOT measurements from the final acceptance testing on the same patch of pavement are also included. These measurements were taken on a separate day in the early afternoon.

Table 2.1: International roughness index readings measured by the contractor daily on the westbound lane (Merritt et al. 2015)

Station		**8:00 am**			**1:00 pm**			**5:00 pm**			**CDOT**
Start	**End**	**RWP**	**LWP**	**MRI**	**RWP**	**LWP**	**MRI**	**RWP**	**LWP**	**MRI**	**acceptance roughness index**
554+99	547+91	109.5	99.2	104.4	80.9	71.0	75.9	78.6	71.1	74.9	60.5
547+71	544+43	98.4	95.8	97.1	66.7	66.8	66.7	65.7	67.8	66.8	59
544+43	539+15	89.9	88.5	89.2	61.0	61.2	61.1	59.4	62.7	61.0	64.8
539+15	533+87	92.8	88.7	90.7	63.8	59.1	61.5	63.6	59.4	61.5	65.4

* RWP: right wheel path
* LWP: left wheel path
*MRI: mean roughness index

Based on the suggestions made from this research on the US 34 project, the final outcome of this study will be enhanced concrete pavement performance in Colorado, both structurally and functionally. In a different study, Yu et al. (1998) evaluated the structural characteristics of concrete runways to temperature and vehicle loads from instrumented slabs. The results of research

carried out in Colorado to confirm the real field response of jointed concrete pavements are presented (Yu et al. 1998). The summer of 1994 saw observations of temperature and curling along test portions built on I-70 close to the Kansas-Colorado border, as illustrated in Figure 2.10. A jointed plain concrete overlay over an existing asphalt pavement included the test portions. The temperature gradient measurements are shown in Figures 2.11 and 2.12, correspondingly.

Figure 2.10: Site of the I-70 close to the Kansas-Colorado border curling study location

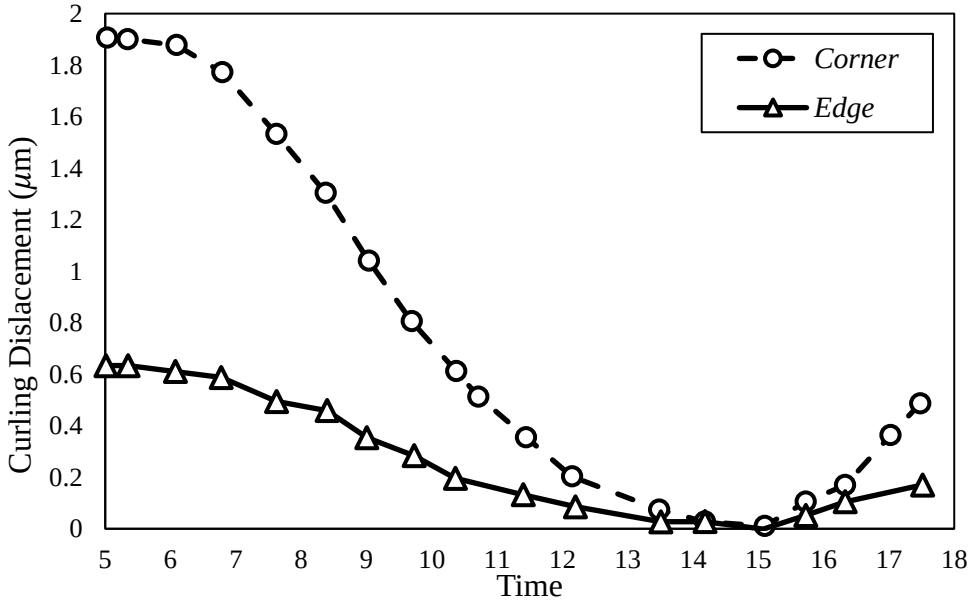

Figure 2.11: Measured curling in rigid concrete slabs in Colorado (Yu et al., 1998).

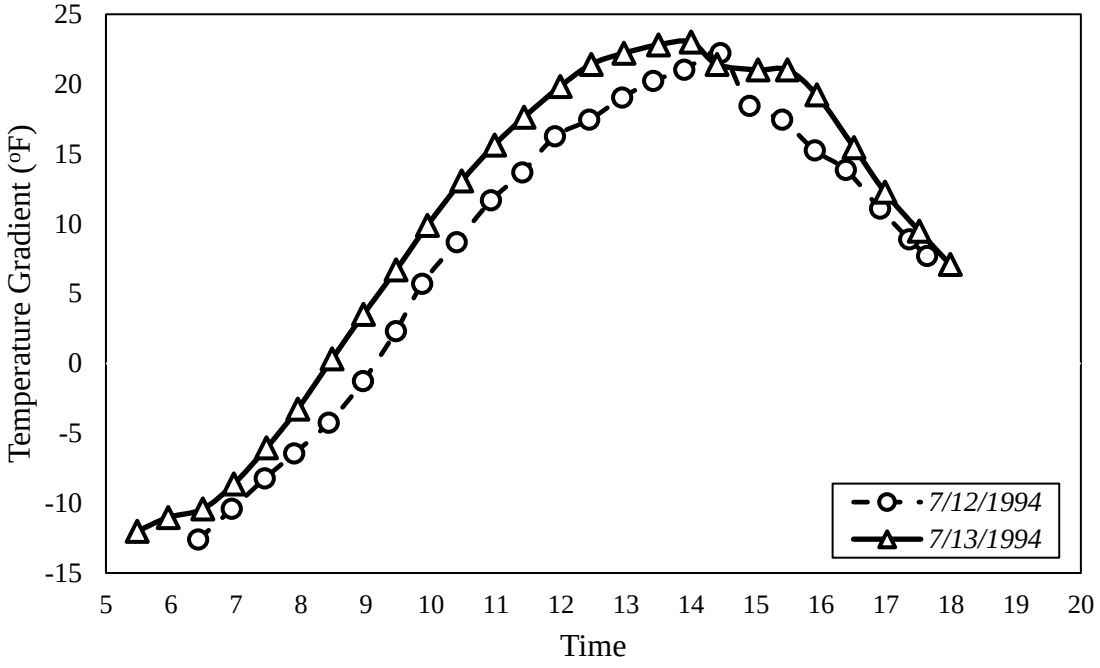

Figure 2.12: Temperature gradients for the Colorado rigid concrete slabs (Yu et al., 1998).

The examination of these observations revealed that to match the estimated and actual curling values, a large built-in negative temperature differential close to -20°F was required. Also, the impact of temperature gradients on critical edge stresses may not be as significant as previously believed, and corner loading may occasionally result in more dangerous slab cracking circumstances, according to further study findings. A physical link between pavement layers is not necessary to get a bonded reaction from concrete pavements, according to other results reported by Yu et al. (2001). Additionally, Yu et al. (2001) worked on the construction and curling behavior and developed a method for determining the extent of construction curling using the field data from Pennsylvania's I-80, as demonstrated in Figure 2.13. According to reported results, if the magnitude of built-in curling is sufficiently great, multi-axle loading during nighttime temperature circumstances becomes more significant, and the slabs can break from the top-down, instead of the bottom-up. The author noted that built-in curling is challenging to measure and that it also fluctuates during the course of a project depending on the paving temperatures, as seen in Figure

2.14. According to the results, it is not possible to quantify the impact of built-in curling just based on the pavement surface profile; and the deflection data must also be included. Using field data from I-80 in Pennsylvania, a method to calculate built-in curling based on pavement deflections and slab temperatures was described.

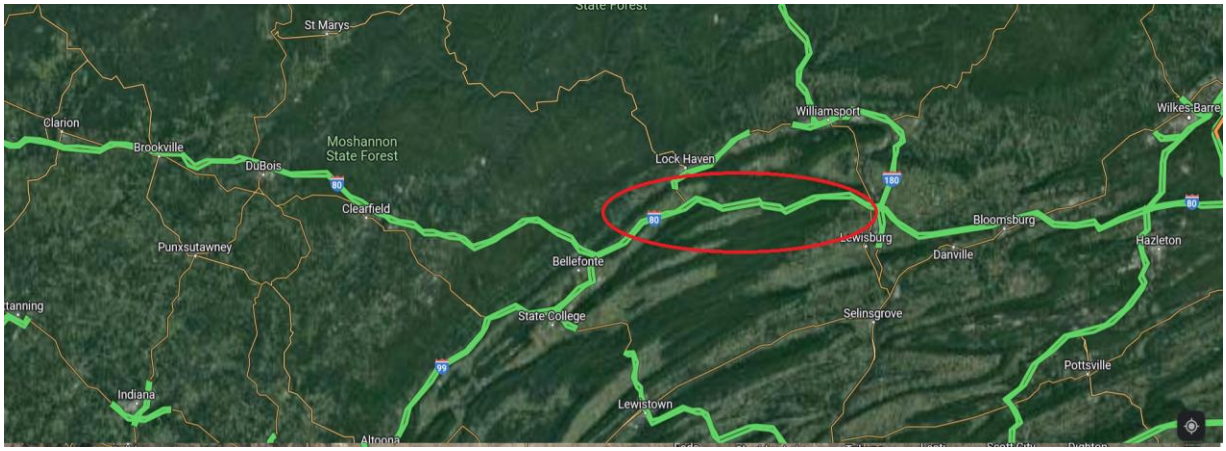

Figure 2.13: Site of the Kansas-Colorado border curling study location

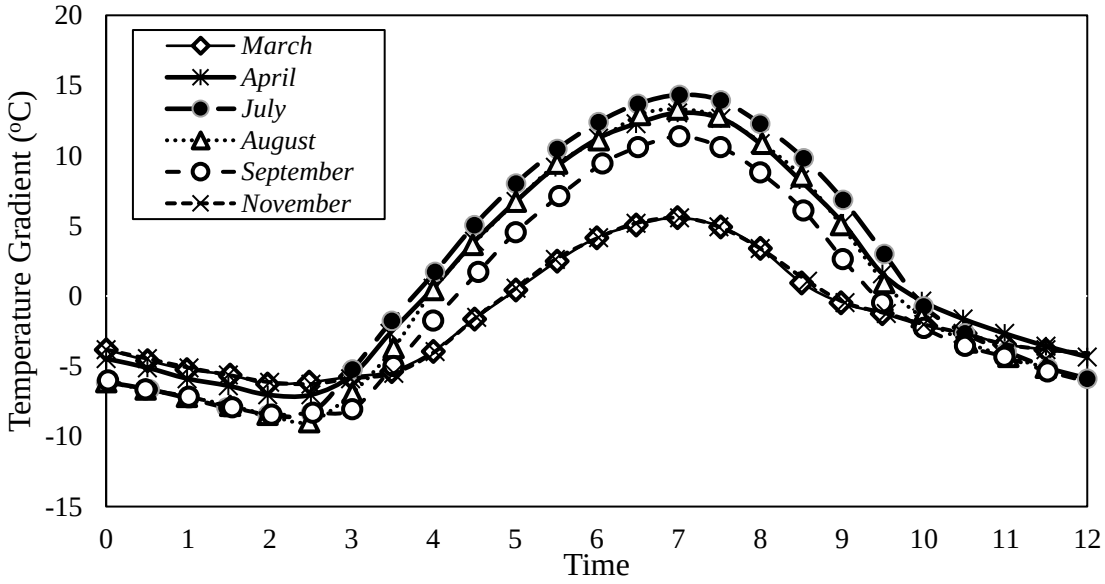

Figure 2.14: Daily and seasonal temperature gradients through a 13-inch slab (Yu et al., 2001).

In another field study, Ceylan et al. (2007) demonstrated how additional environmental factors, including moisture fluctuation, drying shrinkage, and temperature conditions during

pavement construction, also have an impact on curling behavior at early ages. Within the parameters of this experiment, it may be deduced that, in terms of smoothness criteria, observable changes in early-age pavement smoothness do occur over time. The main conclusions of Ceylan's study are as follows:

- The measured smoothness index values between morning and afternoon times showed some variations.
- Based on the limited field data, it appears that morning paving produces smoother rigid concrete slabs than afternoon paving.
- Within the scope of this project, it can be concluded that measurable changes in early-age pavement smoothness do occur over time from the standpoint of smoothness specifications because the measured smoothness index values were different at different measurement locations within a pavement test section.
- Other environmental factors, including moisture fluctuation, drying shrinkage, and wind conditions during pavement construction, have an impact on altering slab curvature at an early age.
- A linear relationship between the real temperature difference that was measured and the corresponding temperature difference related to the actual deformation of the slab under pure environmental stress was found.
- The temperature variations on rigid concrete slabs are typically positive during the day and early at night and negative late at night and early in the morning
- The temperature of the slabs is often higher than the surrounding air's and follows a pattern like that of the air's temperature with a one- to two-hour period.

According to this study, the permanent curling effective temperature difference varied roughly between -8^{o}F and -12^{o}F depending on the location, measuring technique, and finite element method programs. (Take note that in the recently disclosed MEPDG via national calibration data, -10^{o}F is specified as a permanent curling effective temperature difference). In an additional investigation, Hansen et al. (2008) performed an experimental evaluation to measure the importance of built-in curling for Michigan environments and also to expand acknowledgment criteria to quantify built-in curling during and after construction. Temperature data were taken from instrumented slabs on I-94 in June 2005 and US 23 in late October 2005 to achieve the first goal. According to the study, the building may take place in Michigan at temperatures as high as -20°F in the summer and +3°F in the late fall. The recommendations of the study include:

- Temperature monitoring of the rigid concrete slabs during hot weather paving to ascertain its temperature gradient at the time of set to ascertain the degree and severity of built-in curling that may have taken place.
- To determine the typical daily temperature variations across the slab, temperature monitoring should continue after construction.

In 2011, Lederle et al. performed various field tests to measure the curling levels built-in into rigid concrete slabs. The purpose of their examination was to investigate the elements that contribute to built-in curling and to evaluate the techniques for identifying built-in curling in existing slabs.

During this study's exhaustive literature analysis, it was discovered that factors such as material, geometry, constraint, curing, and local ambient relative humidity have a significant impact on both construction curling and drying shrinkage, which causes built-in curling in rigid concrete slabs. This study includes a part that focuses on construction procedures that are known

to directly impact the size of the built-in temperature gradient, including paving season, time of day, curing processes, and mix design. This portion is pertinent to this literature search for CDOT. They mentioned the following findings from earlier research:

- Paving Season: In general, large negative built-in temperature gradients will occur from the construction of concrete pavements in a hot, dry climate or during the summer season. On the other hand, there won't be much to no built-in curl if pavements are laid throughout the spring and fall or in a cool and wet region.
- Paving duration: The highest built-in temperature gradient will be produced by paving in the morning on a hot and sunny day since the slab will harden in the afternoon during the period of greatest heat and solar radiation (Hansen, 2006).
- Curing methods: The sorts of curing methods that are utilized have a significant impact on the effective temperature gradient that is created in the slab. It has also been demonstrated that the use of wet curing has a number of advantageous advantages concerning built-in curling.

In another evaluation, Siddique et al. (2004) conducted a comparison between the back-calculated curling and the evaluated slab curvature with various surface profiling techniques. This report aimed to examine and quantify the impact of slab curling on initial and short-term smoothness as well as to pinpoint the variables influencing both curling and roughness. On six recently constructed parts of Interstates 70 and 135 (see Figure 2.15), smoothness and construction history data were gathered for twelve test sections. The findings of the study include suggestions for modifying design and/or building methods.

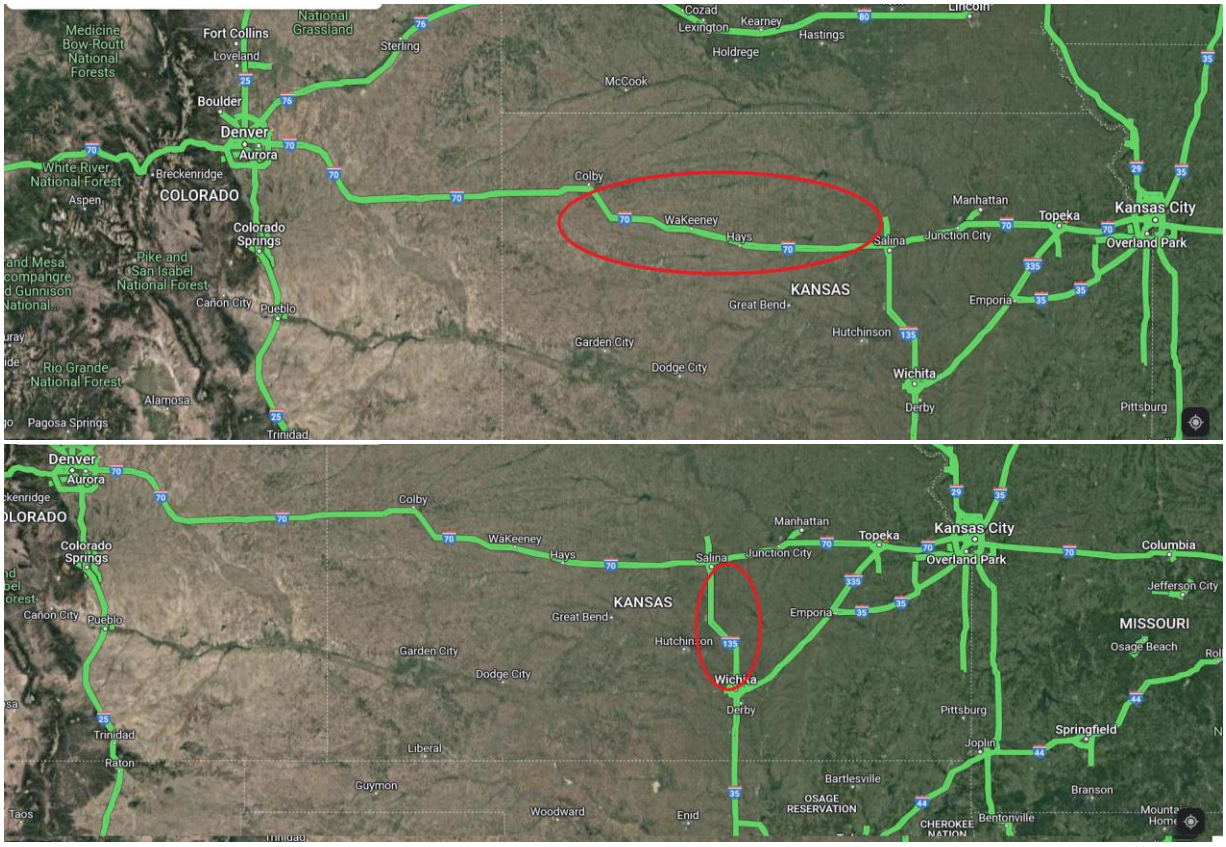

Figure 2.15: Site of Interstates 70 and 135 curling study location

Their finding could be summarized as:

- There can be a significant temperature gradient between the top and bottom of a rigid concrete slab in Kansas (up to 30°F).
- Applying two curing compounds to freshly laid concrete slabs tends to reduce the temperature difference between the top and bottom of the slab. Comparing the slabs with a single application of curing chemical to the slabs without one, the temperature gradients were 2°F to 10°F lower.

In another study, Johnson, (2010) carried out a comprehensive evaluation of the effect of rigid concrete slab curling on the international roughness index for the South Carolina region. In order to gather enough information to properly define slab curvatures, profile measurements were taken

in accordance with quality assurance procedures created as part of the project in all climatic zones, diurnal times, and seasons throughout the U.S. Also, in order to associate pavement performance with curling and warping, both functional and structural pavement performance was measured. So, a new method for measuring curling stress in rigid concrete slabs as well as a methodology for determining how diurnal and seasonal variations affect curvature and slab structural performance are among the study's outputs. Therefore, based on their study, the following conclusions could be drawn for South Carolina region rigid concrete slabs:

- Slab curling can have diurnal effects on the Half-car Roughness Index as high as 0.63 m/km, with an average of around 0.16 m/km.
- Particularly for agencies working under incentive-disincentive requirements, it may be advisable to focus more emphasis on the timeliness of roughness measurements within specifications. The fact that diurnal and seasonal impacts differ greatly between sites necessitates addressing this problem site-by-site.
- The change in International Roughness Index caused by the daily temperature change in South Carolina is anticipated to be less than 10 inches/mile based on the data gathered for this study project. Less than 5 inches/mile is anticipated to be the change in International Roughness Index brought on by seasonal fluctuations in slab curvature. These modifications are rather minor, especially when you take into account the variation in single-point laser profiler readings brought on by a diamond-ground concrete pavement's surface roughness.
- In general, the roughness of the slabs increased as the temperature rose in the middle of the day and decreased in the evening as the pavement's temperature gradient decreased.

- The terrestrial laser scanner revealed the capacity to measure minor changes in the slab's surface, but this is a generalization since there are other elements contributing to the slab's curvature, most notably the built-in curling from the conditions when the slab was cast.

In a further project, Karamihas et al. (2012) investigated the thermal and curling stresses in rigid concrete slabs for the LTPP SPS-2 Site in Arizona, as presented in Figure 2.16.

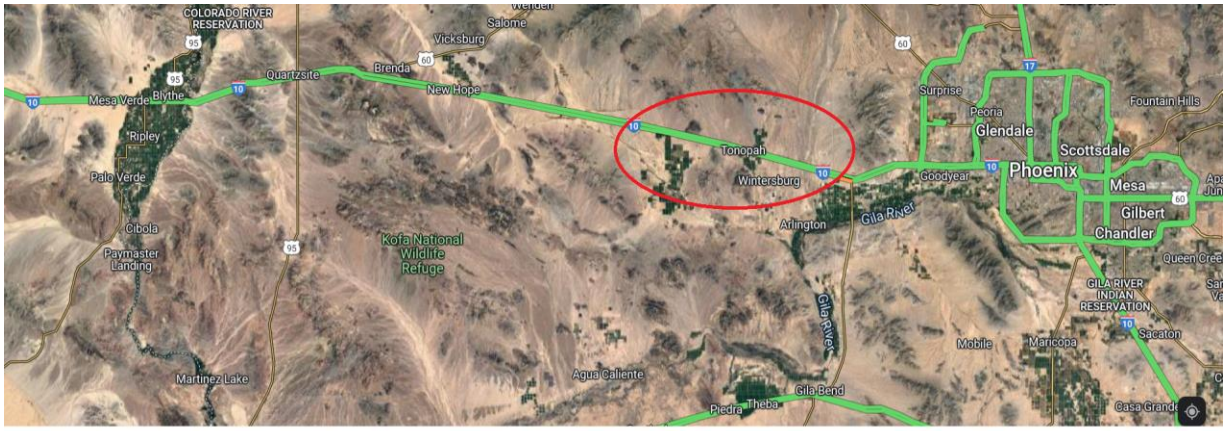

Figure 2.16: LTPP SPS-2 Site in Arizona

The examination of the development of roughness at a long-term rigid concrete slab performance in Arizona over the first 16 years following construction is described in their report. The thickness, lane width, flexural strength, and foundation type of the 21 portions under evaluation varied. Using profile data gathered over 16 years, the amount of curling was calculated and expressed as a pseudo strain gradient value for each individual slab. In order to find any links, the pseudo strain gradient and its variations over time were compared to changes in roughness. The relation between the pseudo strain gradient and International Roughness Index was used in the study to show the possibility of separating the impacts of concrete slab curling from other causes of roughness (faulting, cracking, etc.). The following conclusions give a summary of additional measures to reduce curling stress during design and construction:

- Change the concrete mix properties to minimize the ultimate drying shrinkage. Because aggregates offer internal resistance to shrinkage in addition to reducing the amount of water in the concrete, reducing the cementitious materials content by increasing aggregate volume would minimize the final shrinkage of the concrete. Concrete drying shrinkage may now be greatly reduced because of the development of shrinkage-reducing admixtures. However, because of their expensive cost and lack of long-term efficiency in pavement applications, shrinkage-reducing admixtures have not been widely used in pavements.
- Implement improved curing procedures to reduce moisture loss at early ages.
- Employ design strategies for concrete pavement that reduce the negative effects of long-term curvature on ride quality.

Therefore, design features that can assist alleviate the severity of long-term upward curvature due to curling in jointed concrete pavements and lessen its influence on the International Roughness Index include the use of shorter slabs, dowelled joints, and bonding of the concrete slab to an underpinning stabilized foundation. In addition to the conventional bottom-up mid-slab transverse cracking, Hiller and Roesler (2006) discussed the creation of an alternative software program (RadiCAL) that takes into consideration longitudinal and corner cracking due to curling. In their work, an overview of the equivalent built-in temperature difference developed by Rao and Roesler (2000) was also studied. The authors explain this value can be back-calculated in a variety of ways including falling weight deflectometer testing, joint deflection measuring devices, multi-depth reflectometers, or surface profiling. This value, as defined by Rao and Roesler (2000), takes into consideration the built-in temperature difference from construction, permanent differential shrinkage, and reversible thermal gradients, as well as the creep of the concrete, which could negate some of this permanent curling.

2.5. NUMERICAL MODEL OF TEMPERATURE GRADIENT IN RIGID CONCRETE SLABS

The estimation of the maximum pavement surface temperature and the calculation of the thermally induced tension created via a slab are both related to the prediction of pavement temperature. To forecast the temperature distribution through in-service concrete pavement slabs, significant numerical modeling has been done. The computation of the heat convection coefficient and the handling of the lower boundary condition both need to be improved for these models. In order to replicate pavement temperature across the depth of the structure, a review of heat transfer models is assessed in this section. The heat convection coefficient at the rigid concrete slab's surface is calculated using the widely established theory of heat transfer. Long-term and short-term field temperature readings are both utilized to assess the model's dependability. Because a slab's width and length are much greater than its thickness, the heat flux at the top primarily regulates pavement temperatures. Therefore, a slab's and its underlying layers' temperature distribution may be predicted using a one-dimensional heat transfer model. The following presumptions are made in order to simplify the heat transfer models be previous investigations:

i. In the pavement structure and beneath layers, heat conduction predominates the heat transmission mechanism.

ii. The occurrence of moisture transport under the slab has no effect on the thermal characteristics of the underlying layer. So, the thermal conductivities, heat capacities, and densities of the pavement and the underlying layers are not affected by temperature fluctuation. The solar radiation, convection, irradiation, and emissivity happening at the slab surface make up the

heat flow at the top border, as illustrated in Figure 2.17. The heat flow from the interior of the earth has the most impact on the temperature at the deep ground which exhibits less variation.

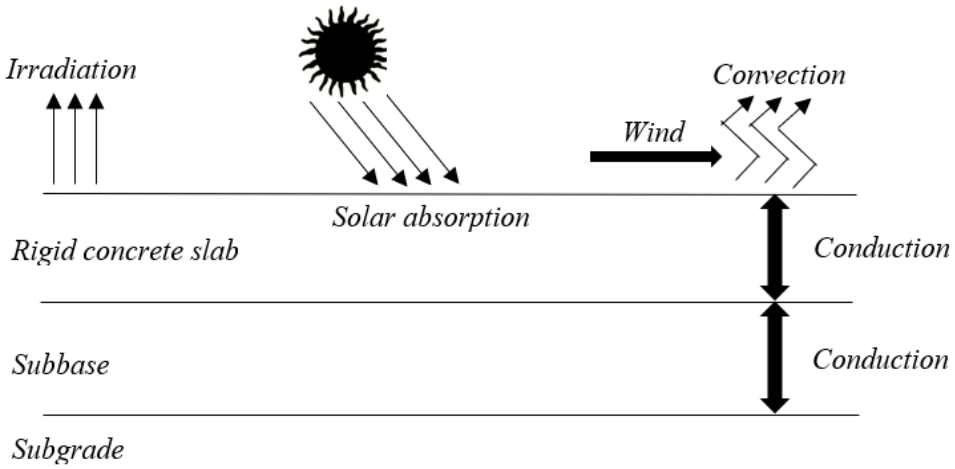

Figure 2.17: Diagram illustration for the heat transfer model

According to site-specific conditions, the depth of zero yearly temperature amplitude varies between 10 and 20 m below the surface of the ground (Andersland and Ladanyi 1994). To prevent this depth lower than the bottom of the computational domain, the lower boundary for this investigation is set at 20 m below the base layer of the pavement. For heat transfer simulation over rigid concrete slab thickness, the Fourier equation has been widely utilized to consider the temperature T (the pavement slab and the underlying layers):

$$\rho c = div(k.grad(T)) + q_{hydra} \tag{2.1}$$

Where k (W/m^oC^{-1}) is the thermal conductivity of the mediums, ρ (kg/m^3) is the density of the mediums, and c ($J/kg/^oC$) is their relative heat capacities. For cured concrete, the internal heat production rate is zero q_{hydra} (W/m^{-2}). Previous scholars have provided extensive documentation on the thermal conductivity, density, and thermal capacity of concrete (Khan 2002; Kim et al.

2003; Chung and Shin 2008). These parameters, such as the w/c fraction, aggregate form, aggregate size, and concrete porosity, rely on the concrete mixture. Site-specific parameters with reasonable controllability make up the detailed values. The values of the presumptive parameters and their usual ranges are shown in Table 2.2.

Table 2.2: Thermal characteristics of the pavement layers

Layer	k (W/m^oC^{-1})	c ($J/kg/^oC$)	ρ (kg/m^3)
Rigid concrete slab	1.5-3.5	0.84-1.17	2200-2400
Base	1.5-2.0	0.9-1.3	2297-2425
Subbase	1.5-1.8	0.7-0.9	1972-2405
Subgrade	0.5-2.0	0.8-0.9	1380-1600

The temperature of the surrounding air, the dew point, the wind speed, and other elements all have an impact on the heat flow at the rigid concrete slab surface. The National Oceanic and Atmospheric Administration (NOAA) database has information on these elements. Long-wave heat fluxes between the earth's surface and the sky are known as thermal irradiation. According to the Stefan-Boltzmann equation, the total irradiation emitted is often stated as:

$$q_i = \xi \times \varepsilon \times T_k^4 - T_s^4 \tag{2.2}$$

In which T_s indicates the temperature of the slab surface, ξ is the Stefan-Boltzmann coefficient, T_k denotes the effective sky temperature and ε is the ground surface emissivity (Kapila et al. 1997; Rohsenow et al. 1998). Also, T_k could be determined as per Kapila et al. (1997) using the next formula:

$$T_k = \varepsilon_k^{0.25} \times T_a \tag{2.3}$$

In which, T_a is environmental temperature and ε_k is the sky emissivity provided by Tang et al. (2004) as below:

$$\varepsilon_k = 0.754 + 0.0044T_{dp} \quad (2.4)$$

where T_{dp} is the dew point. Besides, the local dew point could be determined using the following equation:

$$T_d = b\gamma(T, RH)/[a - \gamma(T, RH)] \quad (2.5)$$

In which a is 17.3, b is 237.7°C and $\gamma(T, RH)$ is $aT/(b + T) + \ln(RH/100)$. Moreover, heat convection at the pavement surface is given by:

$$q_c = h_c(T_a - T_s) \quad (2.6)$$

In which h_c is convection coefficient and is determined by the local Reynolds number, K_a is the thermal conductivity of the air and *Pr* is the air's Prandtl number. According to conventional heat transfer theory, consists of two components: free and forced convection (Rohsenow et al. 1998; Jiji 2009). On a flat surface, the heat convection coefficient of free air convection is roughly 5.6 W/m°C^{-1} (Jiji 2009). Therefore, the heat convection models could be considered as below:

$$h_c = 5.6 + 0.332Re^{0.5}Pr^{1/3}K_a/L \quad (2.7)$$

Also, the Reynolds number could be defined as:

$$Re = wL/v \quad (2.8)$$

In which w indicates the local wind velocity and v is the air‘s kinematic viscosity. Furthermore, energy from solar radiation moves in a brief wave that reaches the ground's surface. The following formula was suggested by McCullough and Rasmussen (1999) for the short-wave absorption of solar radiation q_{abs}.

$$q_{abs} = \gamma_{abs} \times I_f \times q_{solar} \quad (2.9)$$

In which γ_{abs} is the surface absorptivity, and I_f is the intensity factor taking into account the sun's angle throughout a 24-hour day; and q_{solar} denotes the maximum content of solar radiation throughout a day period. The color of the slab's surface, the components of the concrete, how much the slab has been scratched, etc. all affect solar absorptivity (Levinson and Akbari 2002). For new and older concrete, the ranges for pavements made of concrete are 0.5 and 0.9, respectively. The meteorological conditions, time of day, and incidence angle of the sun's rays on the earth's surface all have a significant impact on the solar radiation intensity factor and so the curling behavior of rigid concrete slabs. The amount of solar radiation is quite little at night. is presumed to follow a sinusoidal function during the day (Bentz 2000; Ge 2005). It fluctuates throughout the day, from zero at sunrise and sunset to a maximum value at midday. The sunrise time (t_{sr}) and sunset time (t_{ss}) can be determined using the next formulas:

$$t_{sr} = 13 - 1/15 \times \arccos\theta \tag{2.10}$$

$$t_{sr} = 13 + 1/15 \times \arccos\theta \tag{2.11}$$

In which θ is the hour angle. The numbers "13" in equations (2.10) and (2.11) are used during standard time (the fall and winter seasons), but during daylight saving time, they would be "12", however, the exact value could be calculated using the next formula:

$$w_0 = (\sin(-0.83^o) - \sin\varphi \sin\delta)/\cos\varphi\cos\delta) \tag{2.12}$$

In which $\varphi(^o)$ is the pavement site's latitude (positive in the northern hemisphere, negative in the southern hemisphere), and $\delta(^o)$ is the sun declination determined using the following formula:

$$\delta = 23.45\sin\left(\frac{2\pi(284+D)}{365}\right) \tag{2.13}$$

In where D is the day of the year (January 1 is the first day, or D = 1).

The latitude of the pavement and the sky's characteristics, such as cloud cover, both affect solar radiation's maximum value. Weather stations typically offer monthly maximum, mean, and lowest sun radiations (rather than daily comprehensive solar radiation measurements. A flat-plate collector normally keeps track of all of them. Usually, there is some ambiguity in the observed data. In this instance, feeding the heat transfer model's mean value ignores the effects of the pavement slab's highest temperature and heat history. Thus, a mix of the deterministic and probabilistic radiations must be included with $\pm 9\%$ uncertainty when adding solar radiations to a slab-temperature forecast model. The deterministic component considers the q_{max} . The probabilistic part oscillates between q_{max} and q_{min} according to a random normal distribution whose standard deviation is influenced by the degree of observational uncertainty. As a result, the q_{solar} of the heat transport model is as follows:

$$q_{solar} = 12\pi \times 41.67 \frac{q_{mean} + 0.5(q_{max} - q_{min}) \times random(0,1)/1.38}{t_{sr} - t_{ss}} \tag{2.14}$$

In which random (0,1) generates a number using the ordinary normal distribution; the denotation of the number 1.38 reflects the measurement uncertainty (9%); and the number 41.67 is the conversion component. Consequently, the total heat flux q_{total} at the rigid concrete slab's surface could be determined by:

$$q_{total} = q_c + q_i + q_{abs} \tag{2.15}$$

Also, the temperature at the base of the slab is changeable rather than constant. It depends on the physical characteristics of the underlying layers as well as the boundary conditions at the pavement surface. At a particular point in deep ground, there is a depth where the annual temperature gradient is zero. It is challenging to establish this depth since both its temperature and

location depend on one another. The geothermal gradient at the deep ground, however, is constant for a particular site (Andersland and Ladanyi 1994). As a result, the lower boundary condition of the computational domain depicted in Figure 2.17 is signified by a geothermal gradient (Goering and Kumar 1996). This geothermal gradient maintains the deep subterranean thermal gradient, not the temperature magnitude, by adding additional heat.

2.6. SUMMARY OF THE PREVIOUS STUDIES AND CONCLUSIONS

Figure 2.18 presents a summary of the major previous research studies conducted to evaluate the impacts of temperature gradient on rigid concrete slabs as well as methodology and the major findings of the conducted research. The effects of climate and the resulting harm on rigid concrete runways were explored in earlier studies, as this chapter explains. However, the majority of the proposed analysis approaches typically rely on general observations and measurements made in the field without mechanistic characterization of the associated damages and also considering the limited number of variables affecting the thermal and curling stresses. Essentially, several researchers in the prior studies either conducted pavement condition surveys in the field or deployed nondestructive testing equipment to preliminarily evaluate the imparted damages or the changes in structural capacity of the rigid concrete runways subjected to the temperature. Additionally, the majority of the mechanistic-based damage quantification studies either rely on the issued permit data as the primary source to characterize the air temperature or are based on limited sections and data points. Simplifying assumptions such as the use of permit records instead of field data collection, as well as the lack of high-precision modeling that takes into account all important variables, ignoring the influence of weather, as well as the characteristics of the rigid concrete runways and their contact with the underlying layers and the unique characteristics of

individual pavement structures at any location can potentially compromise the accuracy and reliability of damage quantification and residual life analysis of pavement facilities. Another limitation in the literature is the lack of a high-precision relationship to predict the thermal behavior of rigid concrete airfield runways. Relying on such simplifying assumptions can be detrimental to the accuracy of the analysis of the impacts of temperature gradient on the performance of rigid concrete slabs. Hence, there is a lack of a well-accepted and verified finite element method analysis protocol for quantification of the imparted damages and the loss of service life of the pavements imparted by a temperature gradient, considering the concrete properties, geometric characteristics of slabs and their contact with a base layer, as well. Evidently, this is a persistent problem at the national level that has never been fully handled by the preceding analysis techniques suggested by earlier research works. Consequently, it deems necessary to develop an all-encompassing protocol for accurate quantification of the imparted damage, and various structural impacts of the temperature gradient on rigid concrete slabs, considering all effective variables and conditions.

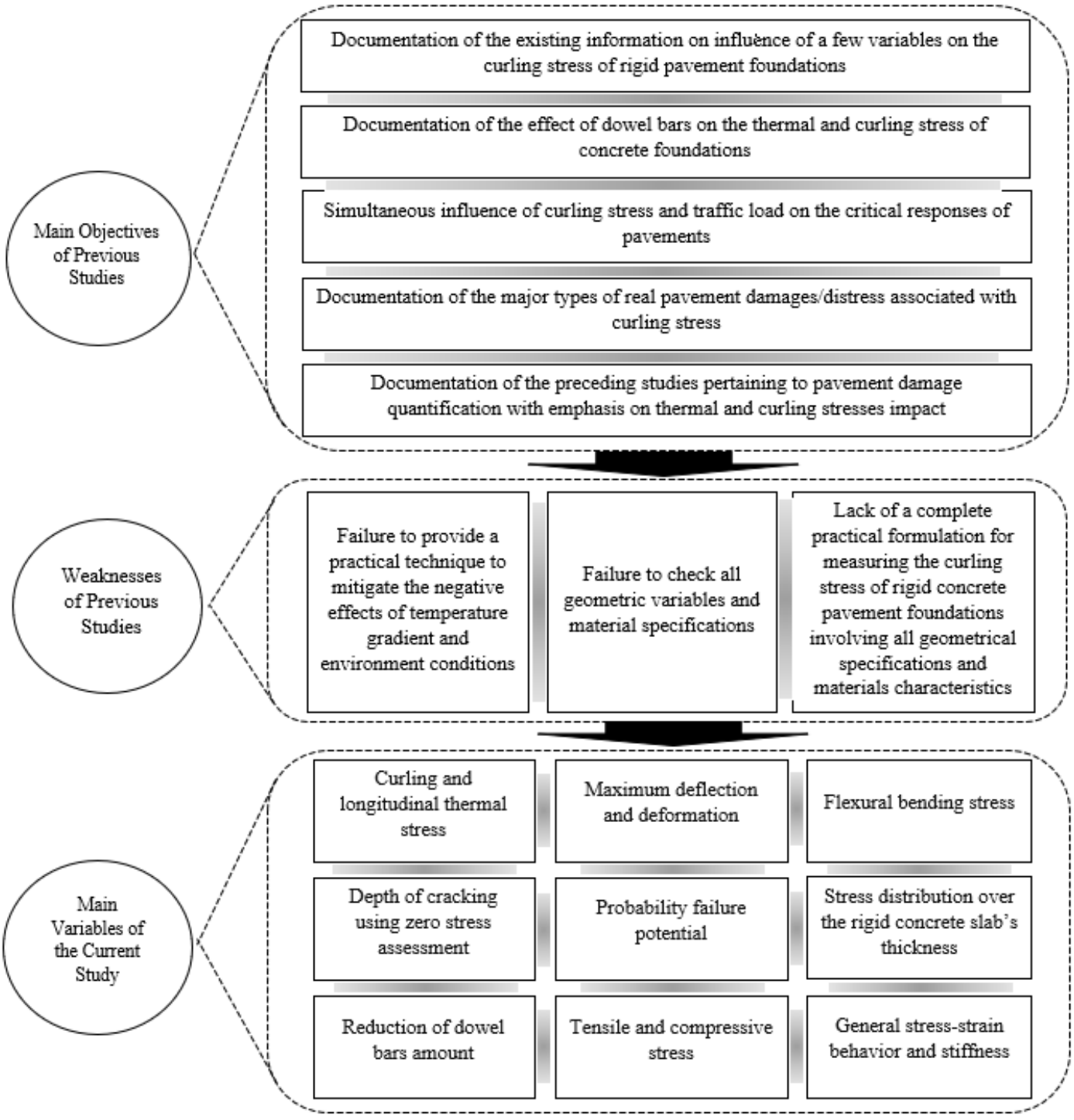

Figure 2.18: A brief review of previous studies and their weakness

CHAPTER III

ASSESSMENT OF SIZE EFFECT AND VARIABLES ON THE THERMAL AND CURLING BEHAVIORS OF RIGID CONCRETE SLABS

3.1. INTRODUCTION

This chapter's main goal is to provide a comprehensive evaluation of the effect of various variables: materials properties, geometric characteristics, contact behavior, and environmental conditions on the thermal and curling behaviors of rigid concrete airfield runways. The preceding section of this chapter is followed by finite element method parameters, boundary conditions, and verification of the assessment of structural impacts and damages imparted on rigid concrete slabs as a result of the temperature gradient.

3.1.1. Organization of the Chapter

This chapter consists of seven main sections. Subsequent to the introductory section, Section 2 provides information associated with the field measurement results in terms of temperature distribution and concrete slab resistance using non-destructive tests. Section 3 discusses the obtained laboratory test results and those reported by previous investigations about the mechanical characteristics of concrete materials. Section 4 provides the advanced finite element simulation steps and different parts associated with the simulation of the structural responses of rigid concrete airfield runways. In this section, the variables considered in this study are also discussed. Section 5 provides discussions on the verification and validation of models assessed in this study considering the results of previous researchers as a benchmark. Then, the main results of this study

are presented and discussed to show the effect of various variables on the thermal and curling behaviors of rigid concrete slabs. Finally, a summary of this section will be presented so that its relationship with the next section and also the importance of the next section can be clearly stated.

3.2. FIELD MEASUREMENT

In this study, the field results in terms of temperature distribution, mechanical characteristics, and failure in rigid concrete slabs constructed in El Paso, Texas, USA, as shown in Figure 3.1., were collected to identify the main reason associated with curling performance. In this field, the vertical over the slabs' thickness and lateral cracks were observed after the construction. This is the main problem associated with an increase in the maintenance cost of airfield runways. To identify the main reason for this type of cracking, the temperature on various days was measured as well as the mechanical properties of produced concrete slabs. To measure the mechanical properties of concrete slabs, the non-destructive test using a Schmidt hammer and compressive strength apparatus in the lab was utilized. Besides, the temperature on various days was measured using an Infrared camera. Table 3.1. summarized the geometric characteristics of manufactured rigid concrete slabs in El Paso, Texas, USA.

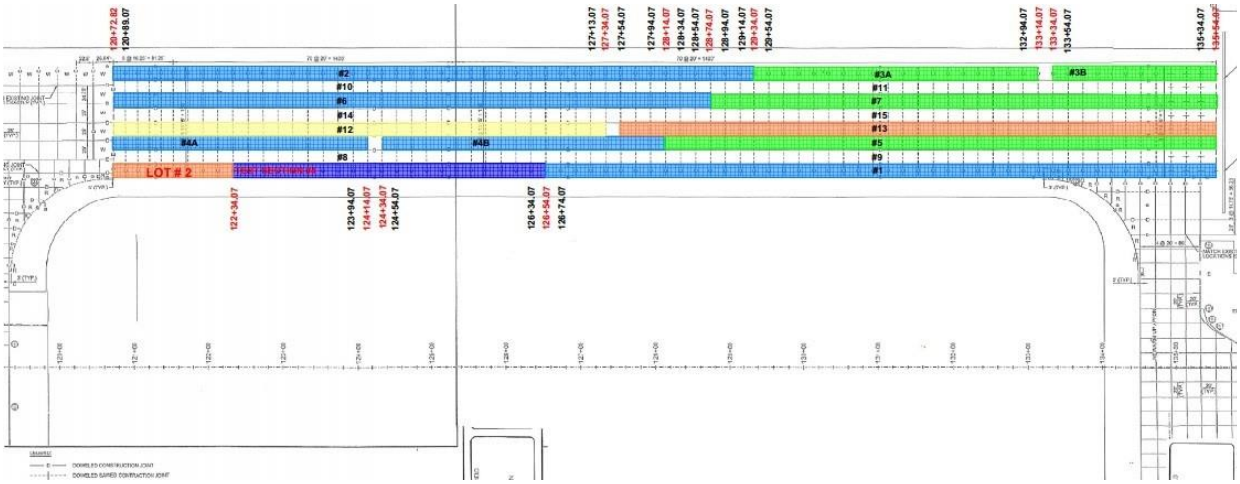

Figure 3.1: Field location in El Paso, Texas, USA

The cast rigid concrete slabs in the field had different geometric characteristics: width, length, thickness, and notch dimensions. The geometric characteristics of different manufactured rigid concrete airfield runways are provided in Table 3.1. Additionally, slabs were reinforced with epoxy dowel bars from the notch regions to control the deflection in two adjacent slabs under the influence of temperature and traffic loads, as demonstrated in Figure 3.2. After the implementation of concrete slabs, due to temperature changes during the day as well as concrete shrinkage, longitudinal and transverse cracks were observed on the slabs' surface as shown in Figure 3.3.

Table 3.1: Geometric characteristics of rigid concrete slabs in EL Paso, Texas

Section	Slab width (ft)	Slab length (ft)	Slab thickness (in)	Depth of notch (in)	Width of the notch (in)	Number of slabs	Diameter of dowel bar (in)	Dowel spacing (in)	Dowel length (in)
1	37.5	960	20	3.5	½-$^5/_8$	Every 20 ft	$1^1/_4$	18	20
2	37.5	808	20	3.5	½-$^5/_8$	Every 20 ft	$1^1/_4$	18	20
3	37.5	808	20	3.5	½-$^5/_8$	Every 20 ft	$1^1/_4$	18	20
4	20.75	900	20	3.5	½-$^5/_8$	Every 20 ft	$1^1/_4$	18	20
5	18.75	801.5	20	4.37	½-$^5/_8$	Every 20 ft	$1^1/_4$	18	20
6	18.75	680	20	4.37	½-$^5/_8$	Every 20 ft	$1^1/_4$	18	20
7	18.75	741	20	4.37	½-$^5/_8$	Every 20 ft	$1^1/_4$	18	20
8	18.75	741	20	4.37	½-$^5/_8$	Every 20 ft	$1^1/_4$	18	20

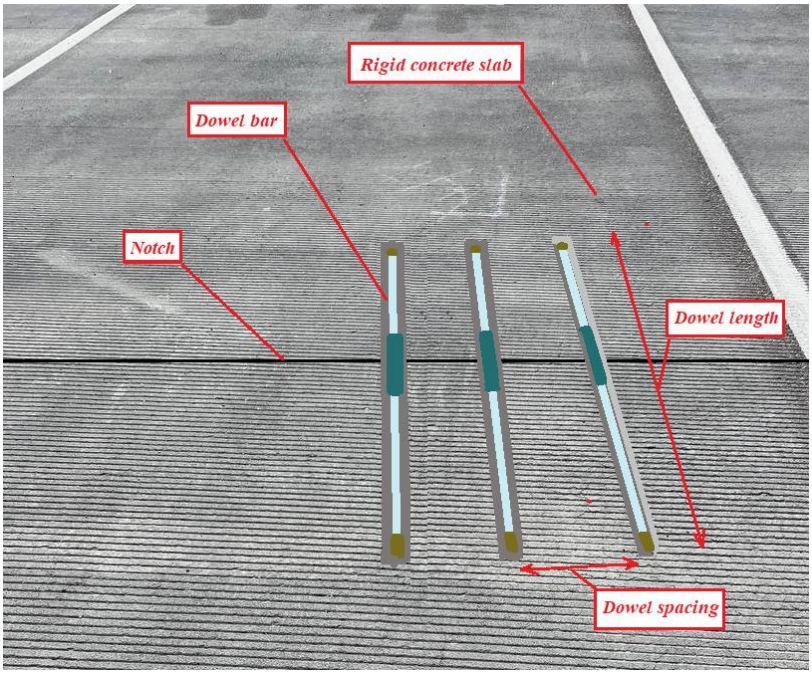

Figure 3.2: Configuration of dowel bars over notches

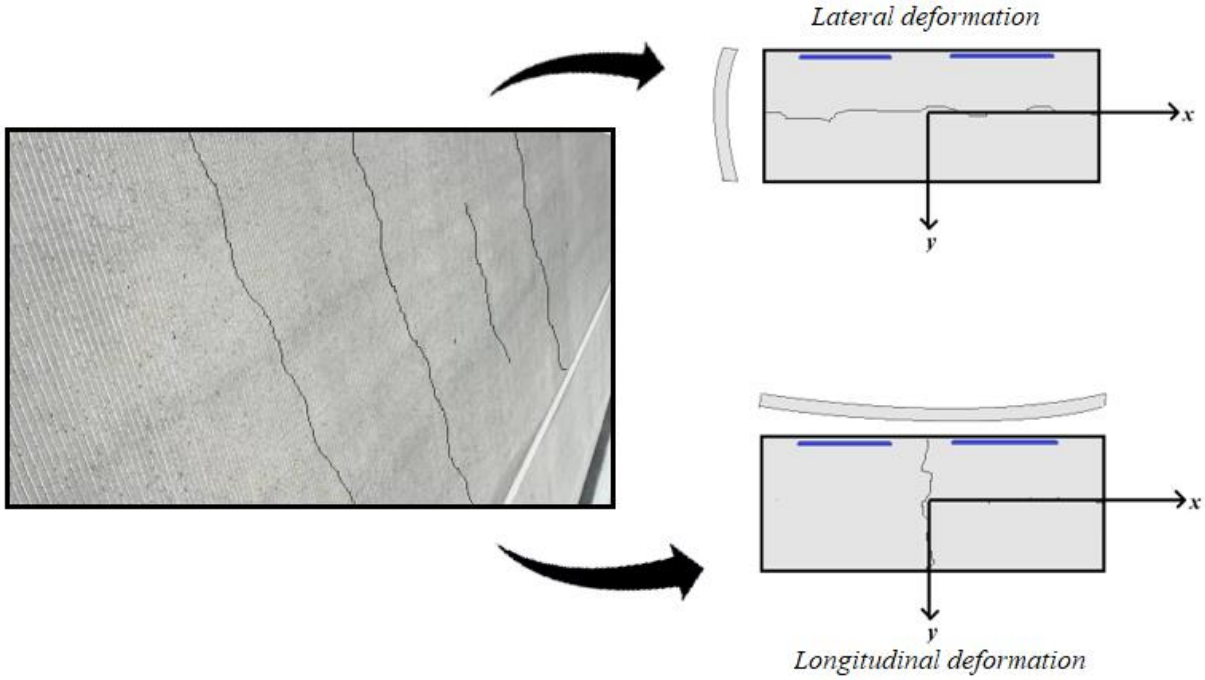

Figure 3.3: Cracks over rigid concrete slabs due to temperature gradient

According to Figure 3.3, the lateral and longitudinal cracks occurred over the thickness and surface of rigid concrete slabs due to longitudinal and lateral out-of-plane deflection, respectively.

This problem gained our research group's attention to find the main problem and propose a solution.

3.2.1. Mechanical properties of slabs

The mechanical properties of preformed concrete slabs are the main variable affecting the thermal and curling stresses of rigid concrete slabs. The most important properties of concrete are compressive strength, modulus of rupture, and elastic modulus. To ensure that the necessary specifications for the implemented pavements are reached, the compressive strength was investigated by sampling and conducting laboratory tests, as well as by non-destructive test Schmidt hammer) in the field, as shown in Figure 3.4. Table 3.2 summarized the obtained results from the field measurements and laboratory tests.

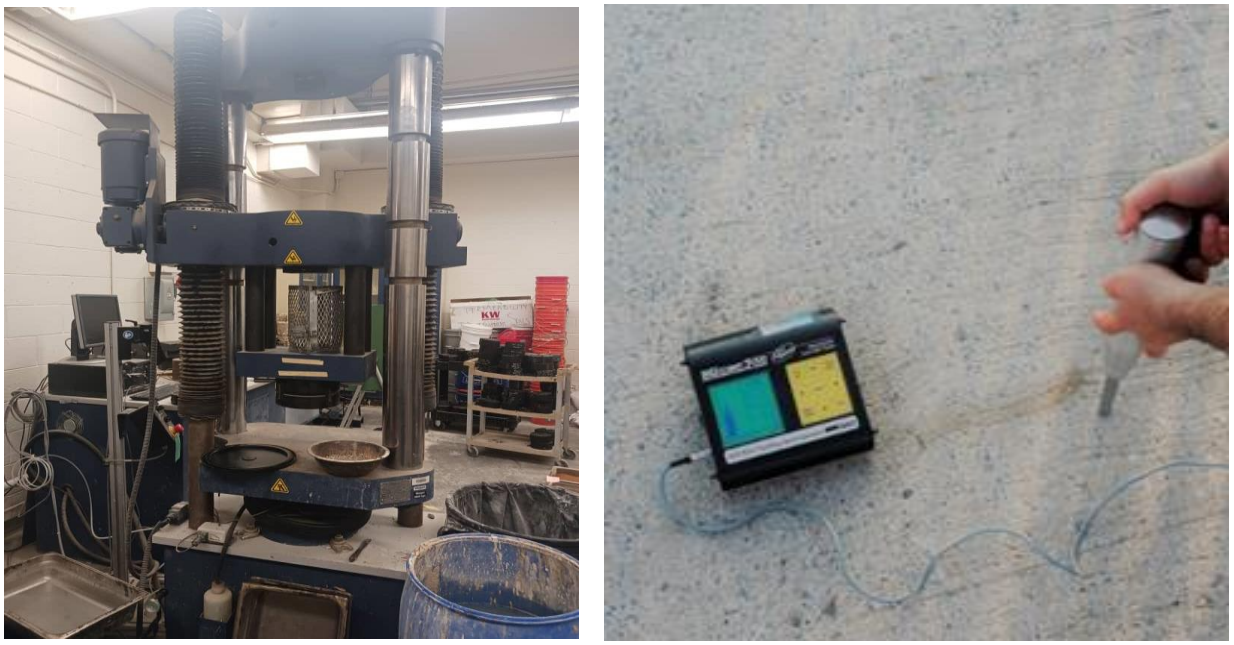

(a) (b)

Figure 3.4: Compressive strength measurement for performed rigid concrete slabs a) laboratory test and b) non-destructive test

Table 3.2: Laboratory and field results for performed rigid concrete slabs

Section No.	Compressive strength (psi)			Tensile strength (psi)			Modulus of rupture (psi)			Modulus of elasticity (psi)			Slump (in)	Density (ft^3)
	7 Days	14 Days	28 Days	7 Days	14 Days	28 Days	7 Days	14 Days	28 Days	7 Days	14 Days	28 Days		
1	2560	2770	3650	25.3	26.3	30.2	425	500	495	2883997	2999955	3443668	1.0	0.496
2	2620	3000	3530	25.6	27.4	29.7	410	545	500	2917598	3122019	3386587	0.75	0.496
3	2710	2970	3660	26	27.2	30.2	460	525	505	2967287	3106369	3448382	0.75	0.496
4	2520	3080	3730	25.1	27.7	30.5	435	500	550	2861377	3163372	3481202	1.25	0.496
5	2990	3390	4290	27.3	29.1	32.7	460	480	555	3116811	3318751	3733391	1.25	0.496
6	2830	3580	4320	26.6	29.9	32.9	475	510	535	3032271	3410487	3746422	0.75	0.496
7	2550	2690	3540	25.2	25.9	29.7	520	560	620	2878359	2956317	3391380	1.0	0.496
8	2530	2690	3500	25.1	25.9	29.6	490	545	610	2867049	2956317	3372165	1.0	0.496

3.2.2. Temperature measurement in the field

In addition to the mechanical characteristics of the material and geometric properties of the slabs, the air temperature over the surface and thickness of the slabs were measured using the Infrared camera, as demonstrated in Figure 3.5. According to this figure, the maximum surface temperature of 147 ^{o}F was observed at 3:00 p.m. which could result in a high longitudinal and out-of-plan deformation in cast rigid concrete slabs. But since one of the main aims of this study is to assess the influence of temperature gradient on the curling stress of the slab, the temperature was measured at three main locations through the thickness: top, middle, and bottom. The obtained results are presented in Figure 3.6. According to this figure, the difference between the top and bottom of slabs is significant which could result in considerable curling stress and out-of-plan deformation as the main reason for cracking in slabs. Using these obtained results and the importance of increasing the lifetime of rigid concrete slabs, an advanced finite element method simulation has been developed to assess the effect of a wide range of variables as discussed in subsequence sections.

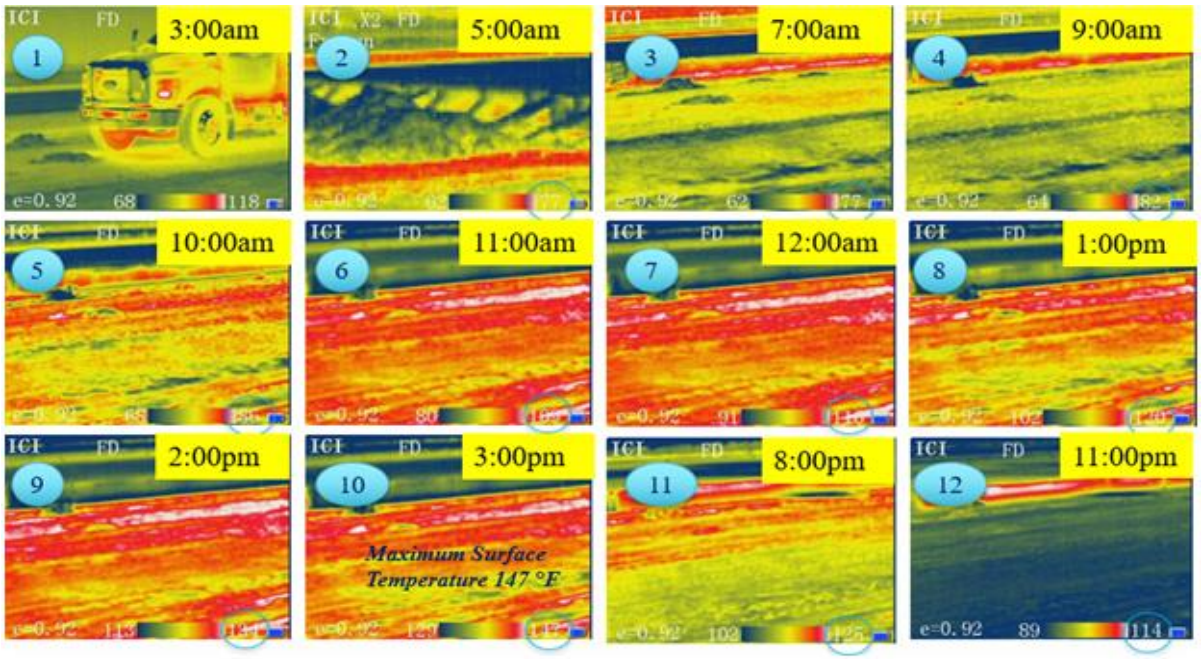

Figure 3.5: Temperature measurement over slabs' surfaces at different hours during a day

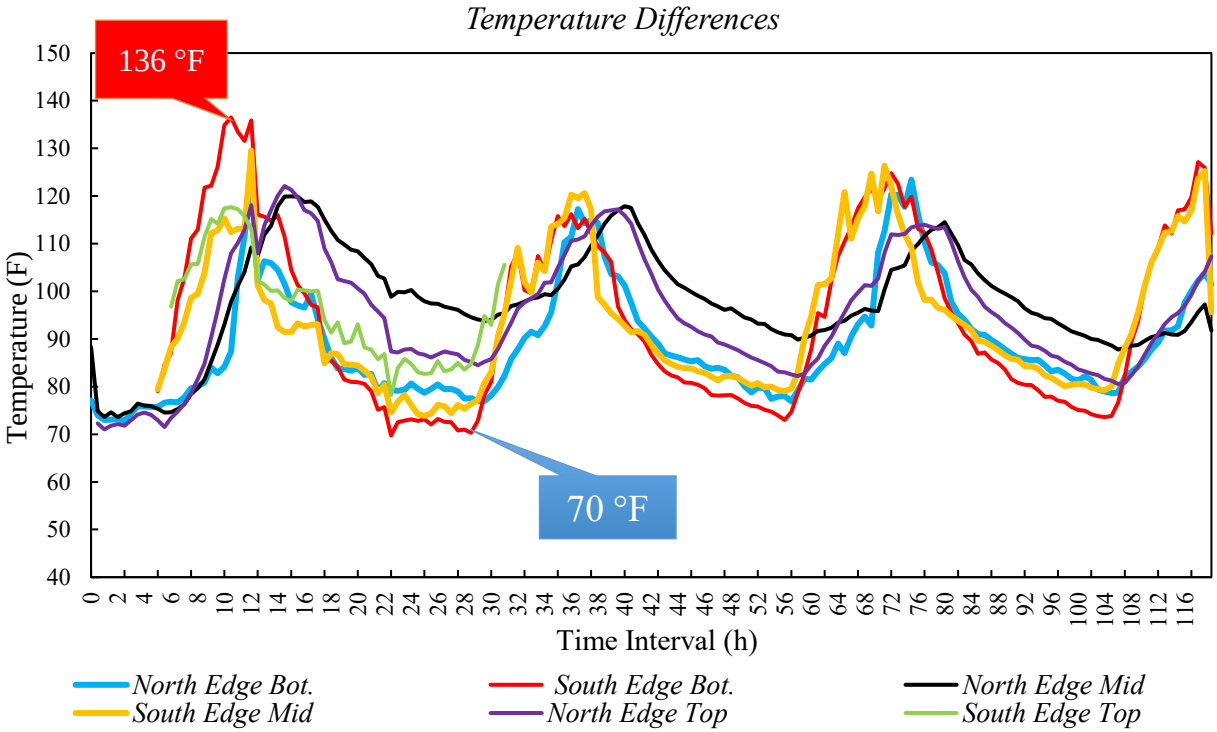

Figure 3.6: Temperature measurements for the top, middle, and bottom of the slabs

3.3. ADVANCED MODELING OF THERMAL AND CURLING BEHAVIORS IN RIGID CONCRETE SLABS

Damage quantification and service life prediction algorithms, using numerical modeling approaches, should properly account for the realistic simulation of the pavement structural properties and the induced external loading conditions. Such necessity is even more pronounced for the analysis of rigid concrete airfield runways exposed to thermal conditions that impose curling and thermal stresses. The primary objective of this chapter is to offer a finite element simulation that makes satisfactory provisions for advanced modeling of curling and thermal stresses to precisely measure the induced rigid concrete slab performance. The finite element program will be utilized for the determination of the crucial rigid concrete slab responses considering a wide range of variables including geometric characteristics, material properties, and environmental and boundary conditions.

3.4. ADVANCED NUMERICAL MODELING

Realistic simulation of the curling and thermal stresses greatly influences the accuracy of the assessment of the rigid concrete slab responses imposed by demanding environmental conditions as well as material properties. To realistically model the curling and thermal stresses in this subtask of the project, the research team developed a FE code that incorporates adequate provisions for advanced modeling of the thermal gradient. For this simulation, lab testing results were utilized to define the exact performance of concrete materials in the software. The site-specific information was relevant to the geometric characteristics of the slab, materials properties, contact and boundary conditions, as well as temperature, and was incorporated into the developed FE code to simulate the structural characteristics of the representative rigid concrete slabs. Figure 3.7 provides an

overall view of the considered variables and parameters in the simulation. For this aim, a total of 8213 models have been assessed.

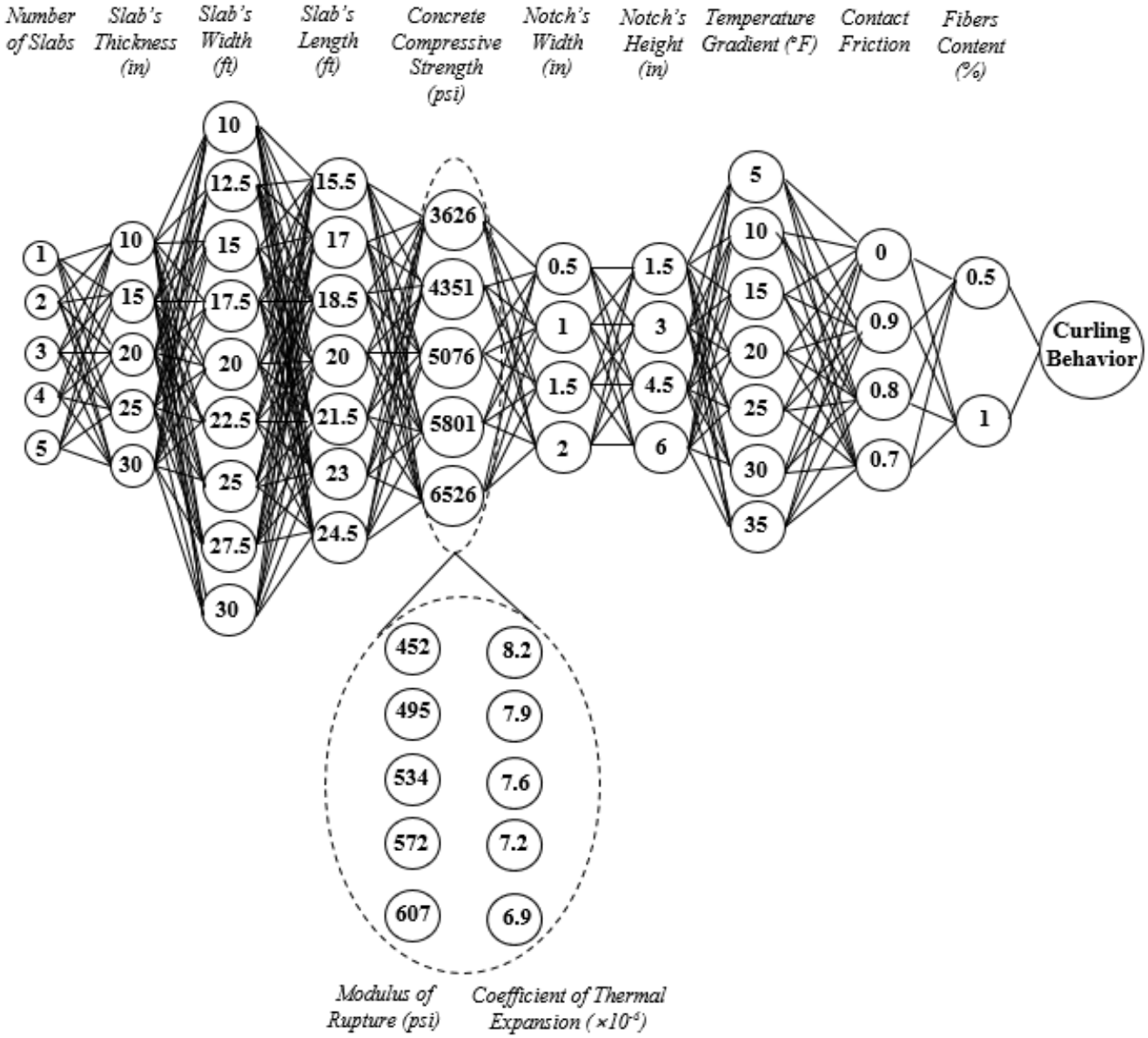

Figure 3.7: Variables considered to determine the curling stress of rigid concrete airfield runways in this study

3.4.1. Concrete slabs

The actual concrete behavior simulation needs accurate laboratory testing results. In this study, we have two types of concrete: plain and fibers-reinforced concrete with various mechanical characteristics: compressive strength, modulus of rupture, etc. This is primarily attributed to the exact simulation fibers reinforced rigid concrete slabs. The mechanical properties of concrete were sorted from the previous experimental results and incorporated into the current finite element method simulation. So, the thermos-plastic model was utilized for concrete considering conductivity, expansion, yield strain-inelastic strain, damages parameter-inelastic strain, etc. So, to define linear and nonlinear structural properties, the behavior of concrete is considered as shown in Figure 3.8. For analyzing the rigid concrete slabs, the isotropic SOLID C3D8R element of the ABAQUS software was employed. Nonlinear behavior characteristics are applied to determine the concrete damage model. It should be reminded that this criterion is the generalized state of the Drucker-Prager collapse criterion, which considers a cone defect level to define the failure of concrete. To determine the stress-strain relationship of concrete, compressive strength, nonlinear strain, and compression damage (d_c) and corresponding strain should be considered. According to Eq. (3.1), the real strain values are converted to a nonlinear strain, as follows (Kaw, 2006):

$$\bar{\varepsilon}_c^{in} = \varepsilon_c - \varepsilon_c^{el} \tag{3.1}$$

Where, $\bar{\varepsilon}_c^{in}$ is inelastic strains, ε_c^{el} is elastic strain and ε_c is the concrete strain at different steps of loading. Furthermore, using Eq. (3.2), the plastic strain calculated corresponds to the instantaneous compressive strength of the concrete, in which, $\bar{\varepsilon}_c^{pl}$, σ_c and E_c denote the plastic strain, compression stress, and elastic moduli, respectively (Kaw, 2006).

$$\bar{\varepsilon}_c^{pl} = \bar{\varepsilon}_c^{in} - \frac{d_c}{(1-d_c)}\frac{\sigma_c}{E_c} \tag{3.2}$$

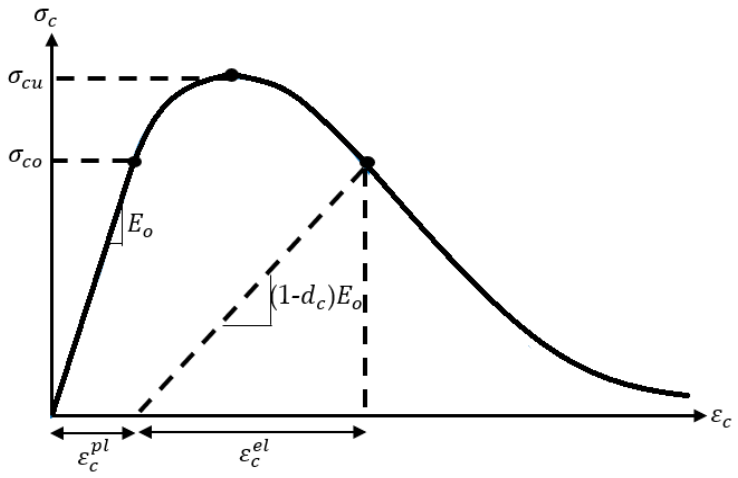

Figure 3.8: The behavior of concrete compressive resistance

Additionally, the next formula for compression damage is used (Kaw, 2006):

$$d_c = 1 - \left[\frac{\frac{\sigma_c}{E_0}}{0.2\varepsilon_c^{in} + \frac{\sigma_c}{E_0}}\right] \tag{3.3}$$

The compressive and tensile strengths of the concrete are also modeled. To determine the stress-strain relationship of concrete tensile behavior concerning tensile strength, nonlinear strain, and tensile damage, the actual strain is changed to a nonlinear strain according to Eq. (3.3). In Figure 3.9, concrete tensile behavior is shown. In this study, the values of the plastic strain, corresponding to the tensile strength at any given moment, are calculated by the subsequent relation:

$$\bar{\varepsilon}_c^{pl} = \bar{\varepsilon}_c^{in} - \frac{d_c}{(1-d_t)}\frac{\sigma_t}{E_c} \tag{3.4}$$

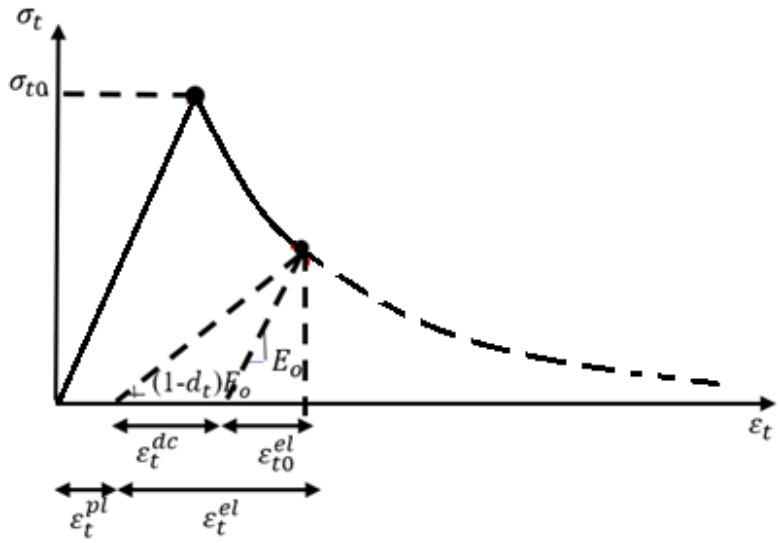

Figure 3.9: Defined concrete tensile behavior

According to Figure 3.10, the tensile behavior of concrete after cracking has been defined using the next formula:

$$u_{1o} = 2G_1/\sigma_{10} \tag{3.5}$$

Here, G_1 is the area under the curve. Also, d_t is failure cracking factor in elasticity. The latter one is calculated from the below relationship:

$$d_t = 1 - \frac{\sigma}{f_t} \tag{3.6}$$

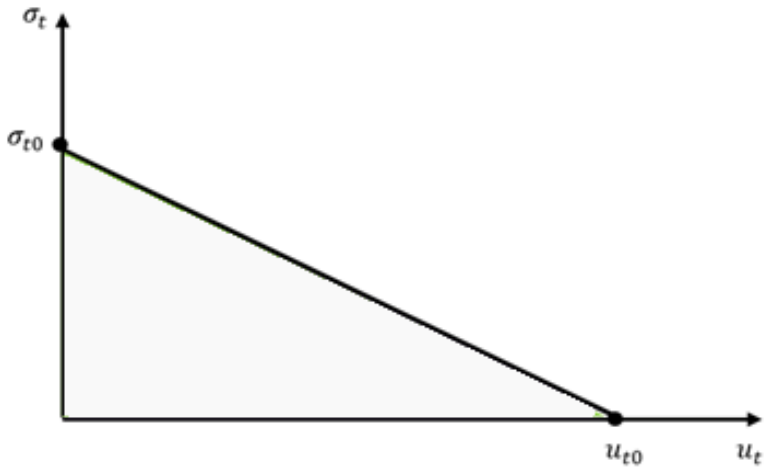

Figure 3.10: Tensile behavior of concrete after cracking

To define the variables discussed above, a laboratory stress-strain curve of concrete with different compressive strengths should be used. For this aim, the experimental results provided by previous studies have been utilized (Huang et al. 2020, Al-Rousan, 2018, Xu et al. 2018), Additionally, Xu et al. (2018) provided a model to develop the stress-strain curve for concrete to simulate rigid concrete slabs properties in the finite element method, ABAQUS, software. Figure 3.11 presents these outcomes.

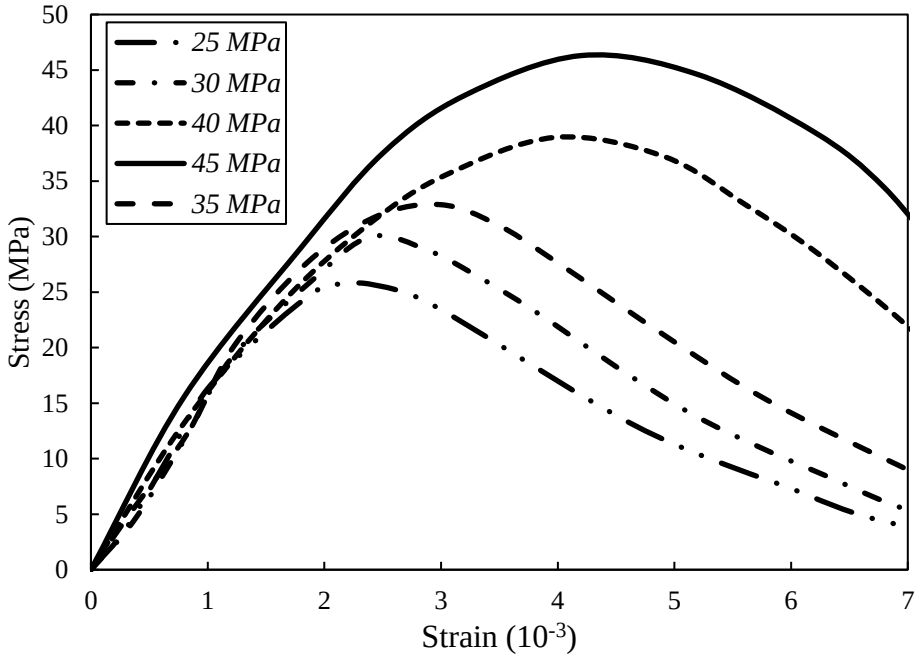

Figure 3.11: Stress-strain relationship of concrete with various compressive strengths

3.4.2. Geometric characteristics and dimensions

The geometric and dimensional characteristics of slabs are the main variables considered in this investigation to measure the size effect on the thermal and curling performance of rigid concrete slabs. For this aim, the research team carried out a comprehensive sensitivity analysis to determine the adequate geometric characteristics to decline the negative influence of temperature on rigid concrete slab performance. To achieve this objective, the number of slabs, the notch's width and

height, and the slabs' width, length, and thickness were taken into account and the effect of these geometric variables on the thermal and curling behaviors of rigid concrete airfield runways was studied, as summarized below and also demonstrated in Figure 3.12. Therefore, a 3D block of rigid concrete pavement structure was modeled using 3D continuum elements:

- *Number of slabs:* 1, 2, 3, 4, 5 and 6
- *The thickness of the slabs:* 10 in, 15 in, 20 in, 25 in, and 30 in
- *Width of slabs:* 10 in, 12.5 in, 15 in, 17.5 in, 20 in, 22.5 in, 25 in, 27.5 in, and 30 in
- *Length of slabs:* 15.5 ft, 17 ft, 18.5 ft, 20 ft, 21.5 ft, 23 ft, and 24.5 ft
- *Width of notches:* 0.5 in, 1.0 in, 1.5 in, and 2.0 in
- *Height of notches:* 1.5 in, 3.0 in, 4.5 in, and 6.0 in

It should be noted that some of the values considered for variables are not commonly used in real construction but to have a comprehensive view of the influence of variables and also for developing new formulas in the subsequent chapter, a wide range of values were taken into account.

3.4.3. Boundary Conditions

Boundary conditions are principally described as the displacement or rotation constraints to avoid the movement of the selected degrees of freedom, or to impose the displacement or rotation for each selected degree of freedom (ABAQUS Manual, 2015). Given the importance of boundary circumstances in FE modeling, care should be taken to define suitable boundary conditions to ensure an accurate simulation. Figure 3.13 indicates various types of boundary conditions specified in the simulation of the rigid concrete slabs in this study model. ENCASTRE boundary condition was employed at the bottom of the subgrade layer to simulate

the bedrock. ENCASTRE is a specific type of boundary condition that restricts displacement and rotation in all directions. Furthermore, two other boundary conditions were specified in the FE models to constrain the displacement in the orthogonal directions to the surfaces.

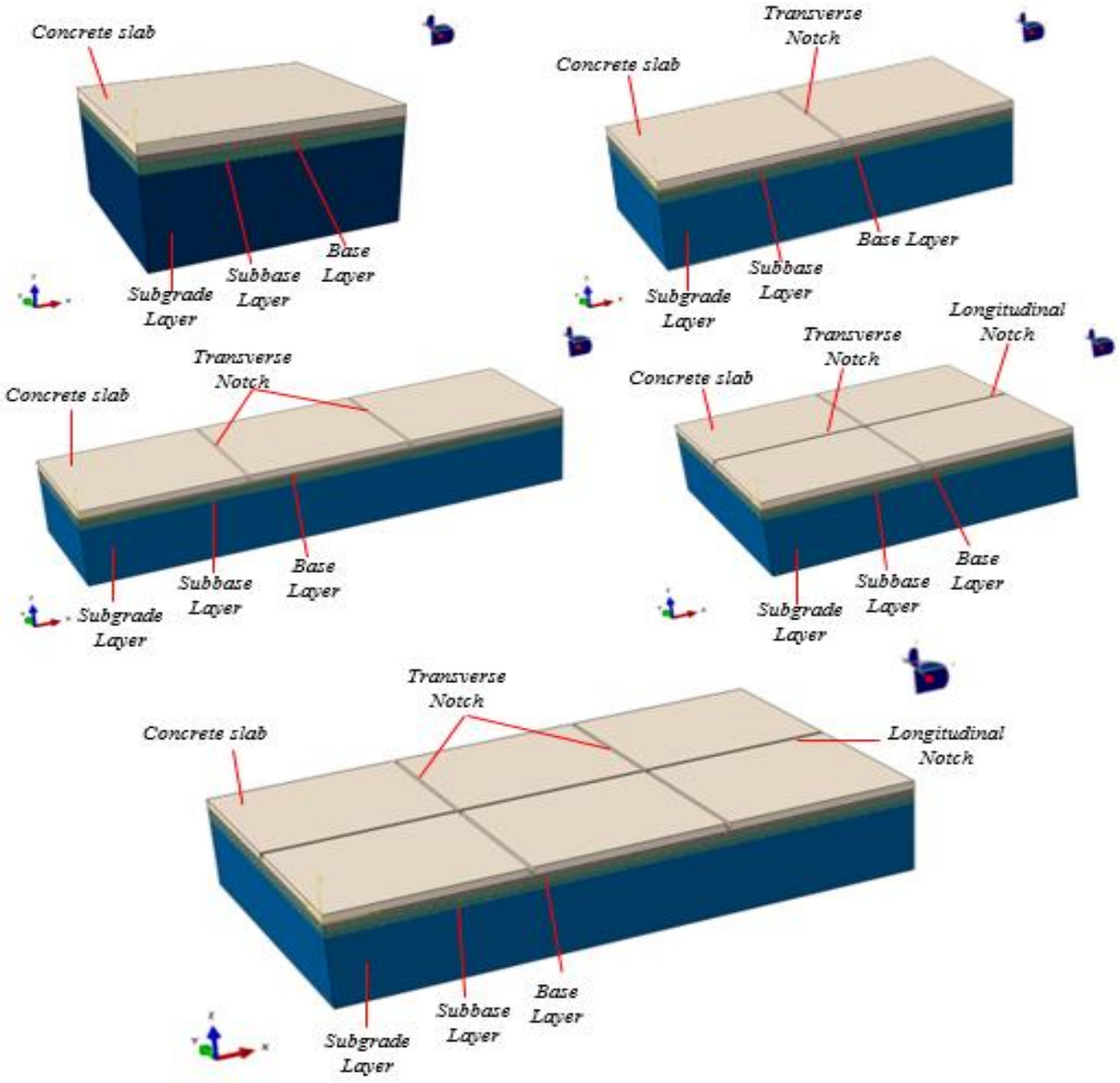

Figure 3.12: Simulated rigid concrete runways in the 3D Finite Element Software

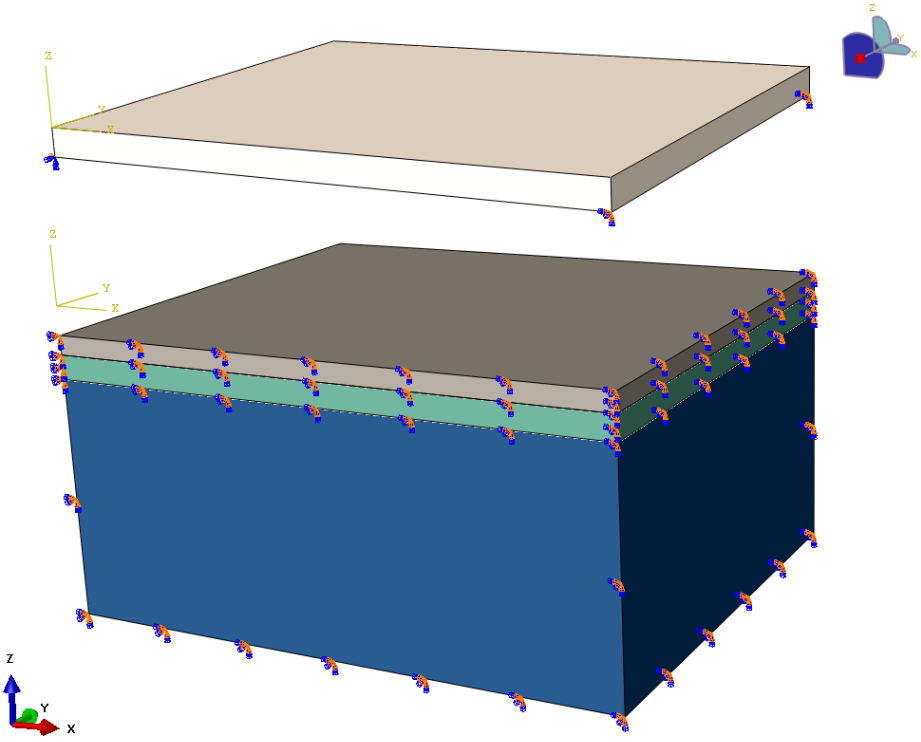

Figure 3.13: Boundary condition considered in the current study

3.4.4. Interaction of Slabs with Base Layer

The constraints in the bottom layer create strains that play a crucial role in curling stress, as was already described. Increasing friction from limitation is a common source of increasing curling stresses. According to Rivero-Vallejo and McCullough (1976), there was a lot of friction between the top stiff concrete slab layer and the base layer, which had a major influence on crack propagation and out-of-plane deformation. In this context, Masad et al. (1996) simulated the interaction between a stiff concrete slab and its supporting layer using a 3D finite element technique simulation and interface components. According to their findings, friction is inversely linked to slab length but independent of slab thickness, which was made by Huang (2004). Friction is also influenced by the weight of the concrete. When curling occurs, a hard underlying layer prevents the slab from settling into the underlying layer (Ytterberg 1987). A soft underlying layer

might result in lower curling stresses due to the "bedding" influence, which reduces the impact of the constraint from the underlying layer (Eisenmann and Leykauf 1990). So, in this study, to assess the influence of interaction between rigid concrete slabs and base-layer was measured by considering four values for friction fractions: 0, 0.9, 0.8, and 0.7. the friction consideration conditions are shown in Figure 3.14.

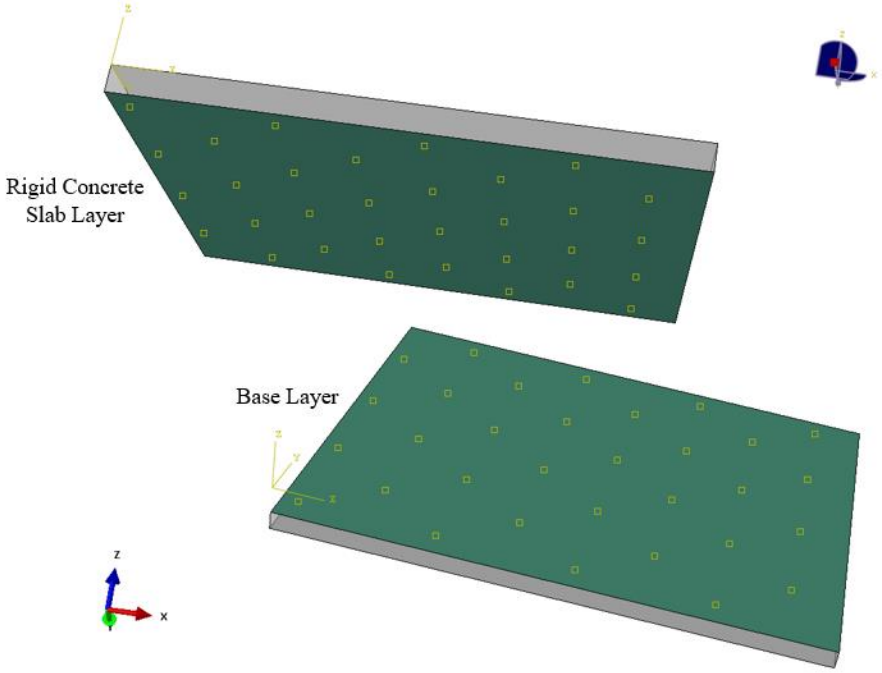

Figure 3.14: Interaction condition between rigid concrete slabs and base layer

3.4.5. Temperature gradient

The curling behavior of rigid concrete slabs is mainly associated with thermal gradient through the thickness. Nonlinear 3D finite element method simulation of rigid concrete slabs gained popularity in terms of curling stress during the 1990s (Zaghloul et al. 1994). As was already noted, a linear temperature variation will result in overestimated highest tensile stresses throughout the day and understated highest tensile stresses at night when compared to the results of a nonlinear temperature variation (Masad et al. 1996). Despite the fact that it has long been understood that

the slab temperature distribution over the thickness is actually nonlinearly distributed, many investigations studies conducted in the 20th century assumed a linear temperature profile in order to make calculations simpler and to provide clearer results. The National Cooperative Highway Research Program's Mechanistic-Empirical Pavement Design Guide (MEPDG) more closely considers the impact of climate when designing concrete runways (NCHRP). Furthermore, the thermal characteristics of materials are used as direct input variables by the MEPDG to forecast rigid concrete slab performance (Chung 2012, Nantung 2011). In the current study, the authors measured the temperature gradient over the thickness, as shown in Figure 3.15. Regarding this figure, the nonlinearity in temperature gradient could be observed. Therefore, to highly accurate model of the thermal and curling behaviors in rigid concrete slabs, the nonlinear distribution for temperature gradient was taken into account in this study.

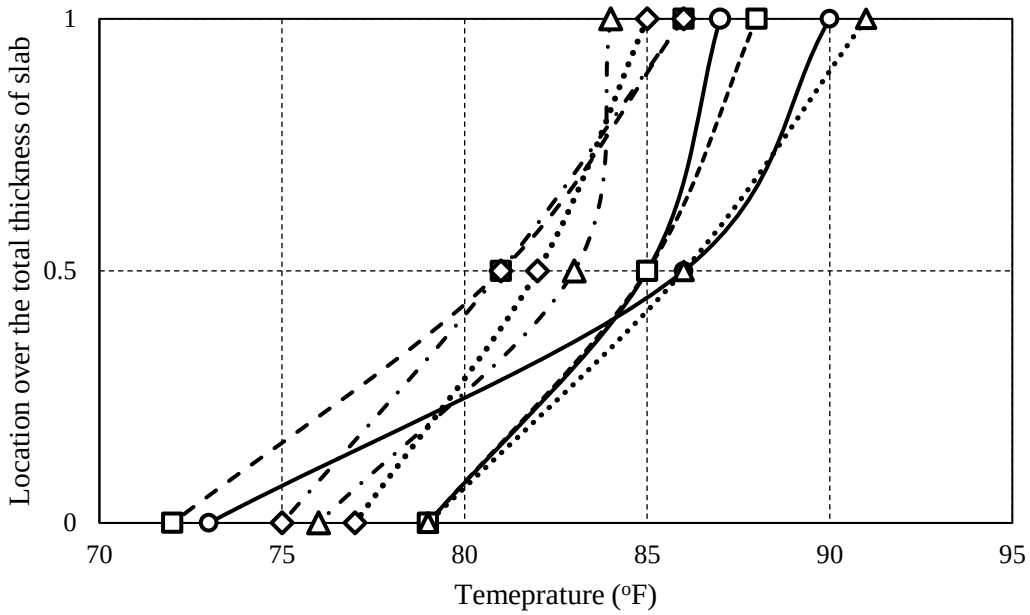

Figure 3.15: Temperature gradient obtained from the field test at different times during the day in this study

3.4.6. Meshing

The study team defined a finer mesh in this area for more accurate results since the most crucial reaction locations in the rigid concrete slab measurement technique are situated under the influence of temperature gradient. But in the regions of dowel bars from the loading zones, a finer mesh was utilized to have more accurate results through notches due to smaller dimensions in comparison with the whole slabs dimensions. As a result, the model's three-dimensional continuum components C3D10 (ten-node quadratic tetrahedron) were utilized, as presented in Figure 3.16. To assure increased accuracy, a transition zone was also established between the fine and coarse mesh sections.

3.5. VERIFICATION AND VALIDATION

In numerical studies, verification plays the main role to show the accuracy and validity of the simulation. In this study, the results presented by Mackiewicz and Szydło (2020) were utilized for the verification and measuring of the accuracy of the results. The finite-element technique was used to generate a concrete pavement model in the three-dimensional (*XYZ*) Cartesian coordinate system. The model was generated using data from temperature investigations and load-bearing capacity estimations on a particular concrete pavement in central Poland. There is a significant daily temperature range for the area under study.

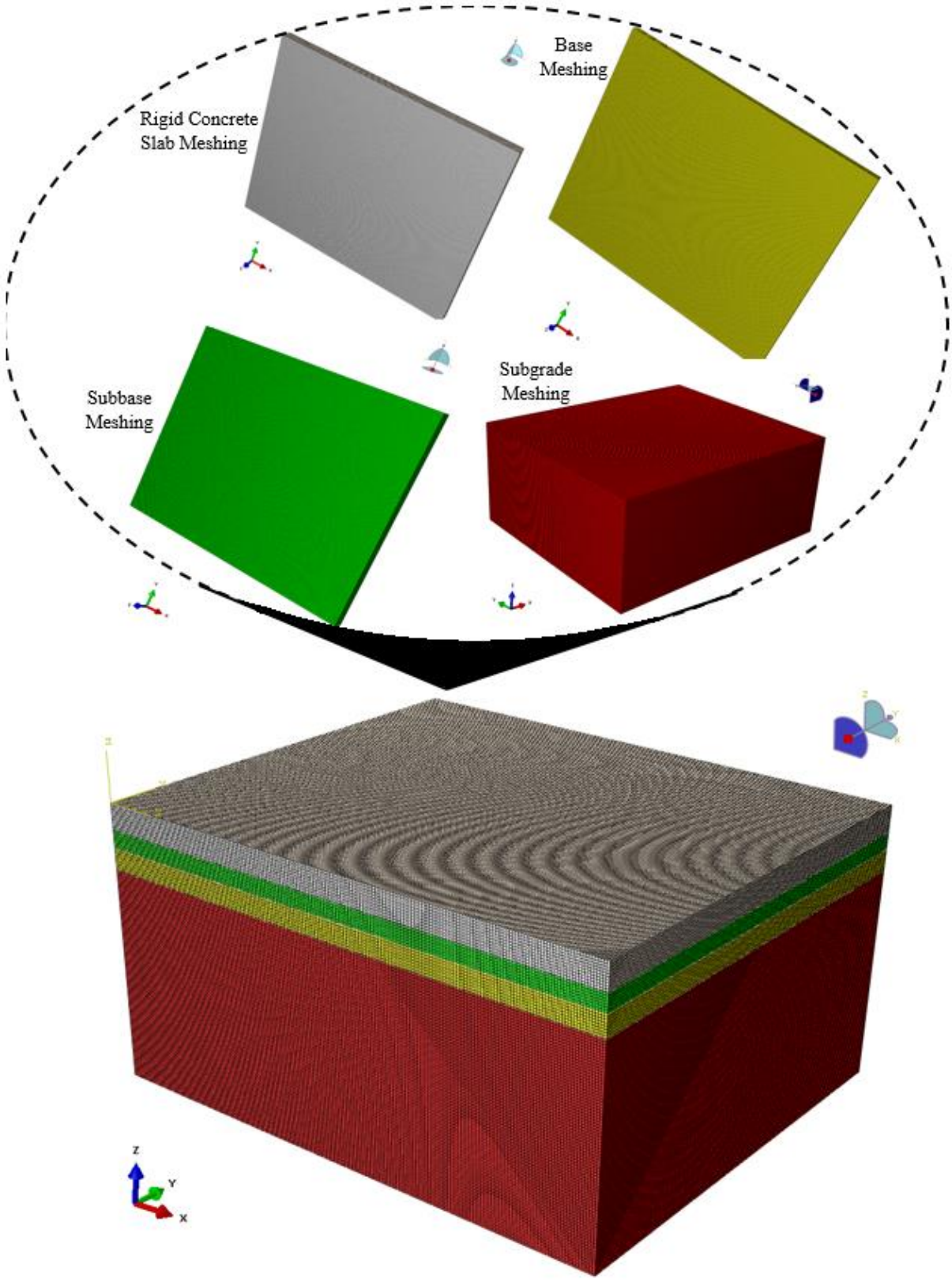

Figure 3.16: 3D Meshing employed in the current investigation

In the verification and validation step, the slab was between 5.0 and 7.0 m long and 3.5 m wide. Dowels of a 0.03 m diameter, 0.5 m length, and 0.21 m spacing were employed. Based on deflection measurements and back-calculation of layer moduli, falling weight deflectometer (FWD) tests were used to confirm the pavement layers' approved characteristics (Szydlo 1995). Materials that are thermo-linear-elastic were used in the analyses. Additional characteristics were assumed for the concrete slab, including thermal conductivity of 2.5 W/m°C, specific heat of 700 J/kg°C, the thermal expansion coefficient of 0.00001 m/m°C, and mass density of 2,400 kg/m^3, to do accurate calculations with temperature taken into consideration. The model also took into account the interaction between the concrete slab and subbase as well as adequate boundary conditions. For this, appropriate GAP-contact components were employed. In 2D and 3D contact situations where elements are in touch as a result of external pressures, two-node GAP elements are frequently employed. A sliding interface was established between each dowel bar and the surrounding concrete material, where the coefficient of sliding friction was considered to be 0.05, and the concrete slab and subbase partially cooperated during computation. Despite using the well-established 3D FEM approach, they applied the full-dimensional model to the whole slab without making any assumptions about axial symmetry.

Additionally, they took into account the friction between the concrete dowels and the slab as well as the subbase. Besides, they covered dense division on finite components, which is crucial for researching stresses around dowel bars. They also took into account the expansion joint and the proper contact between slabs with excess values of permitted displacements and gravity, which have a large impact on the stress and form of bent slabs. Moreover, they accounted for the slab's heat flow, which is dependent on the range of daily average air temperatures. In chosen nodes of the slab, suitable temperature values that were consistent with experimental results were used to

account for thermal interactions, resulting in the proper values of both positive and negative thermal gradients. Table 3.3 provides the information for the used model for verification as per Mackiewicz's and Szydło's study (2020). Then, the tensile stress over the slab's length was assessed for verification, and the obtained results are presented in Figure 3.17. Regarding this figure, the performed modeling in this study has a high accuracy performance. Also, lower stress values than those for the 25-cm-thick slab were observed for the short 30-cm-thick slabs. Lower stresses developed in the thinner slab for slabs longer than 4.5 m (at a positive gradient) and 5 m (at a negative gradient). The temperature difference was less in the case of the 25-cm-thick slab, measuring 7.5°C (at a negative gradient of 0.3°C/m) and 16.75°C (with a positive gradient of 0.67°C), correspondingly. The thicker slab displayed bigger thermal variations between its top and bottom surfaces and at longer lengths due to the greater nonuniformity with which the whole volume of the slab heated up. Additionally, it was more vulnerable to thermal shocks.

Table 3.3: Basic parameters of the slabs utilized for verification according to Mackiewicz and Szydło's study (2020)

Number	Layer	Modulus of layer (MPa)	Poisson's ratio	Thermal conductivity (W/m°C)	Coeff. of thermal expansion [m/(m°C)]	Mass density (kg/m^3)	Thickness (m)
1	Concrete slab	30000	0.20	2.5	1.00×10^{-5}	2400	0.30
2	Subbase	10000	0.30	0.05	7.00×10^{-6}	2200	0.20
3	Protection layer	200	0.35	0.05	7.00×10^{-6}	2200	0.25
4	Subgrade	120	0.35	0.05	7.00×10^{-6}	2050	2.50

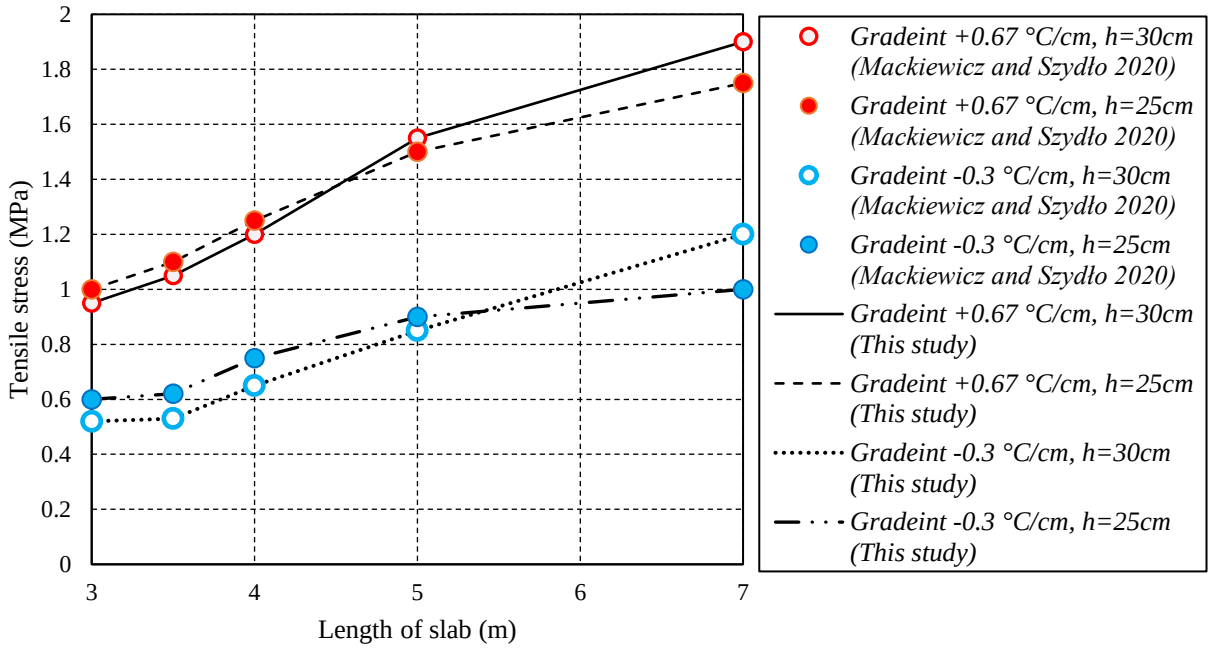

Figure 3.17: Comparison between the tensile stress for slab thickness of 25 and 30 cm versus slab length for the current study and those reported by Mackiewicz and Szydło study (2020)

3.6. NUMERICAL RESULTS AND DISCUSSIONS

After the verification of this project, the research team incorporated various geometric characteristics and mechanical properties as well as the temperature gradient in a comprehensive sensitivity analysis to account for measuring the curling and thermal behaviors of rigid concrete slabs. To consider the influence of contact and boundary conditions, various friction values were taken into account between the slabs and the base layer. Ultimately, the corresponding responses induced within the airfield runway structure were calculated for further comparisons.

3.7. MAJOR ADVANTAGES OF THE PROPOSED NUMERICAL MODELING APPROACH

The FE numerical modeling code developed in this study makes adequate provisions for advanced modeling of curling and thermal behaviors to accurately calculate the induced rigid concrete slab responses under complex thermal loading conditions. The proposed numerical modeling approach considers the nonlinear thermal gradient, size effect etc. In addition to the elaborated advantages, the developed FE code is instrumental in simulating several prominent features associated with the rigid concrete slab geometric characteristics such as slabs width, length, thickness, notch's location, the contact state between slabs and base layer, boundary condition, and environmental conditions. In this section, firstly, the influence of compressive strength and slabs' length on the maximum tensile stress due to various thermal gradients is measured. The obtained results are presented in Figure 3.18. Generally, with an increase in thermal gradient, flexural moment and as result the maximum tensile stress increased. Also, the increase in temperature increases the incidence of nonlinear behavior in materials and the nonlinear distribution of heat gradients along the thickness. This issue shows the importance of bearing in mind the non-linear and plastic behavior for concrete considering cracking as well as the non-linear distribution of thermal gradient. In low compressive strength concrete, up to 30MPa, with an increase in the length of slabs, the maximum tensile strength was increased and then declined when the length of the slab was greater than 6m. This could be associated with the lateral deformation performance of slabs. Since, the performance of long-length slabs with a length greater than 6m is membrane shell performance while for the shorter-length slabs, the behavior is plate-bending element behavior. However, when the compressive strength of the slabs was higher

than 35MPa, the maximum tensile stress increases with a rise in the slabs' length. This behavior could be contributed to a switch in the behavior of long-length slabs from the membrane shell behavior to plate-bending performance which led to increasing the tensile and curling stresses in rigid concrete slabs. Additionally, in slabs up to 6m in length, the maximum tensile stress declined by swelling the compressive strength of concrete while for 7.5m length slabs, the maximum tensile stress slightly rose and then decreased by increasing the compressive strength. So, the maximum tensile stress in slabs with 7.5m length was observed when the compressive strength was 35MPa and the thermal gradient was considered 35ºC (Figure 3.18c).

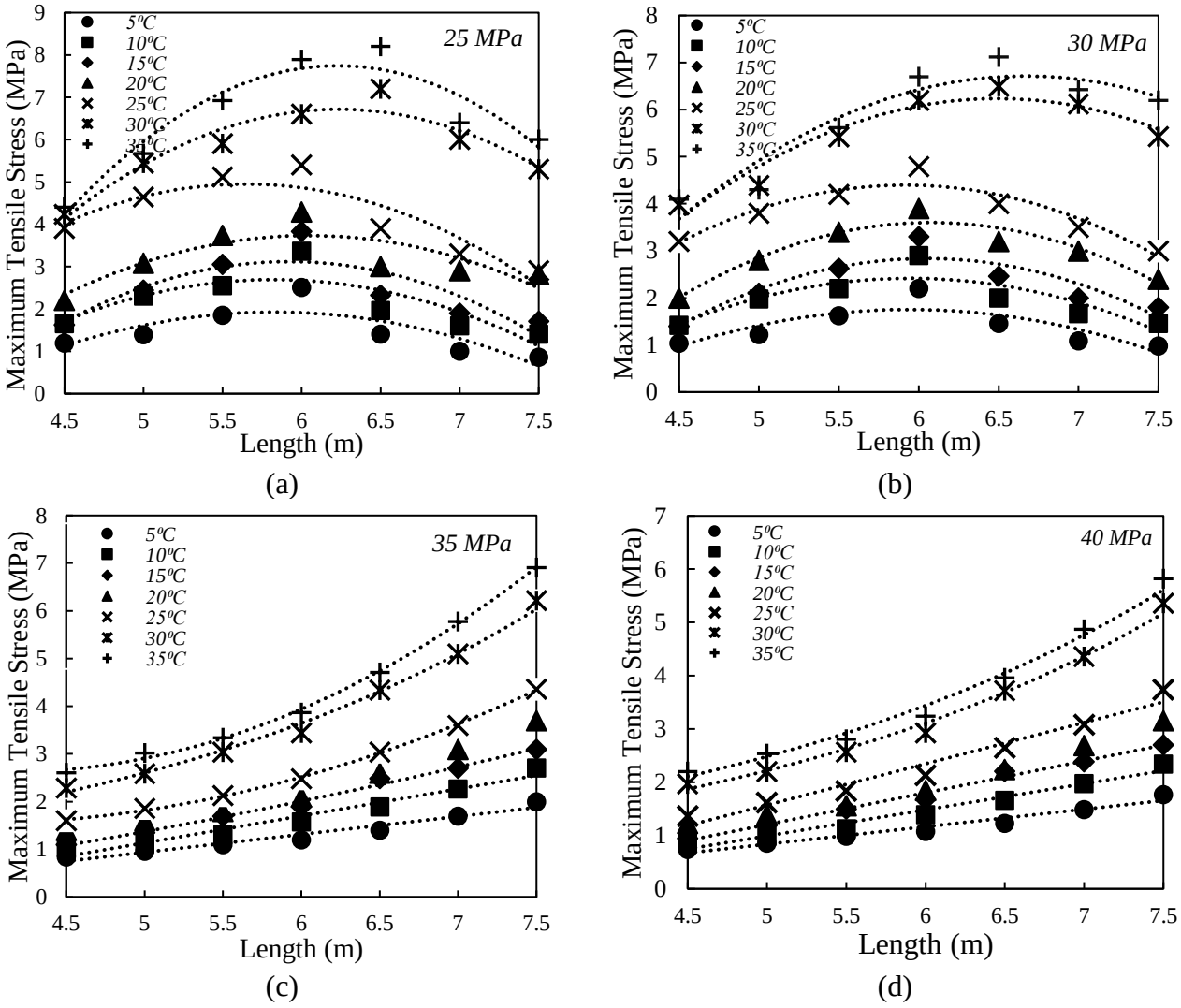

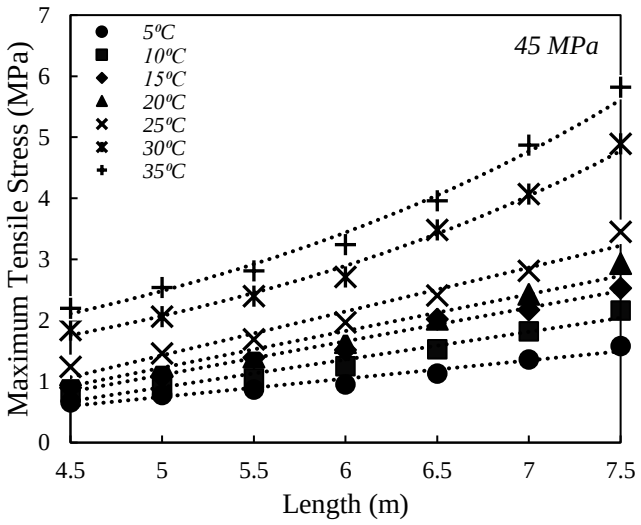

(e)

Figure 3.18: Influence of compressive strength and thermal gradient on the maximum tensile stress of slabs with various lengths a) 25MPa, b) 30MPa, c) 35MPa, d) 40MPa, and e) 45MPa

Figure 3.19 shows the typical influence of thermal gradient on the stress distribution of a 4.5m long slab with different properties, obtained by advanced finite element method simulation. According to this figure, the maximum tensile stress increased with an increase in a temperature gradient.

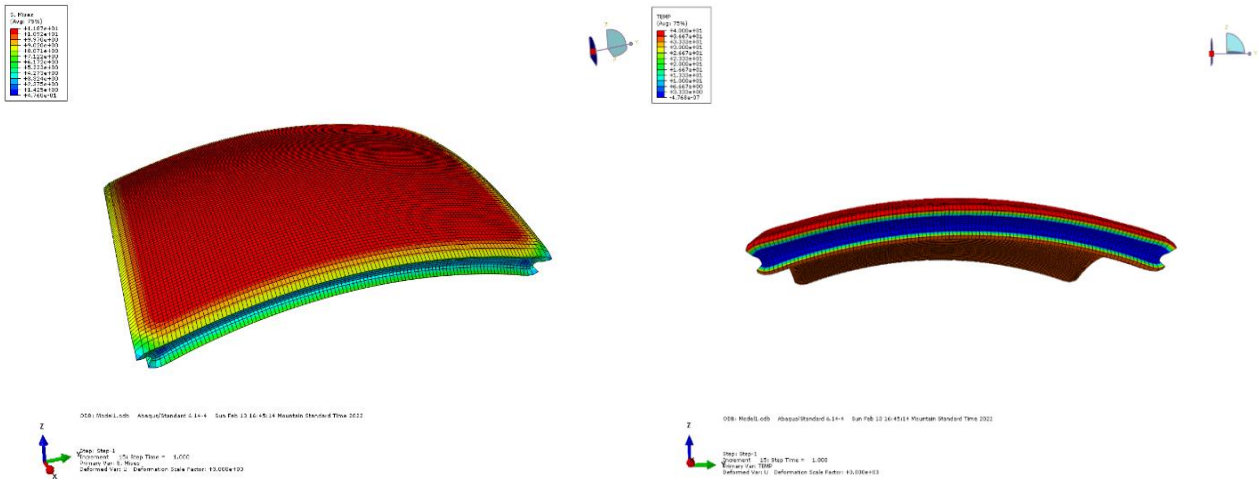

(a)

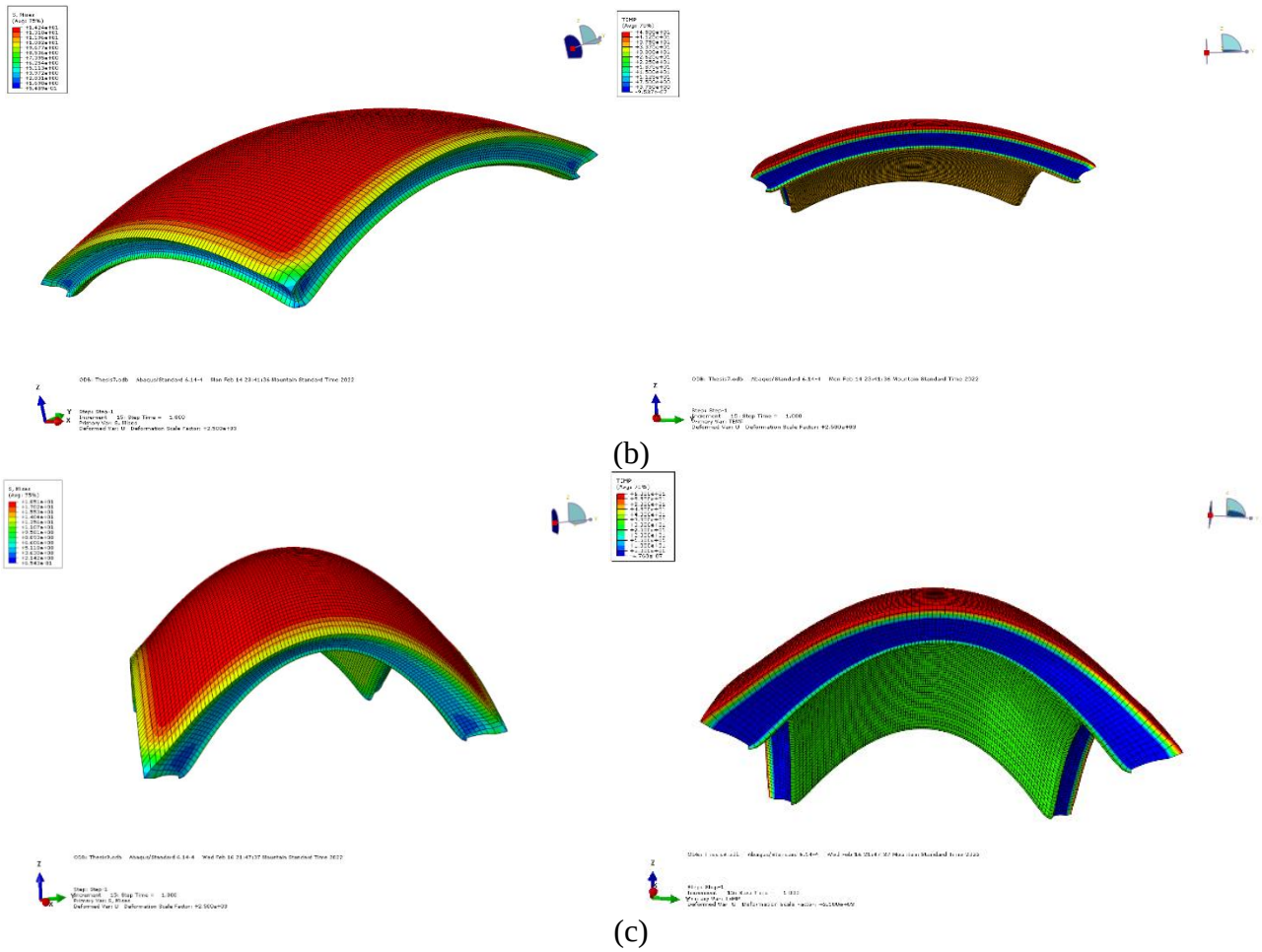

Figure 3.19: Influence of thermal on stress responses in 6m long slabs a) 10ºC, b)20ºC, and c)30ºC

Furthermore, the simultaneous effect of slab length and thickness has been taken into account considering various compressive strengths and thermal gradients. The results are provided in Figures 3.20 to 3.24. According to Figure 3.20, the maximum tensile increase in slabs with 25MPa compressive strength increased and then declined by increasing the length of slabs, and the maximum tensile strength was observed in slabs with 6m length. Additionally, in slabs up to 6m in length, increasing the thickness of slabs played a positive role in reducing the maximum tensile strength, however, the opposite behavior was observed in 7.5m length slabs, and with growing the thickness, the maximum tensile strength was marginally amplified. This could be associated with the membrane shell behavior of long-length slabs. Conversely, increasing the temperature led to increasing the tensile stress, particularly in slabs with 7.5m length. The compressive strength of

concrete is another important feature affecting the thermal responses of rigid concrete airfield runways. According to Figure 3.21, increasing the compressive strength resulted in the maximum tensile stress reduction in slabs with up to 6m in length. However, in 7.5m long concrete slabs, the maximum tensile stress slightly increased with an increase in the compressive strength from 25MPa to 30MPa. This could be associated with the out-of-plane deformation and modes of failure in long-length rigid concrete slabs. Therefore, the highest tensile stress was observed in 7.5m length slabs with 30cm thickness exposed to 35ºC by around 8MPa stress.

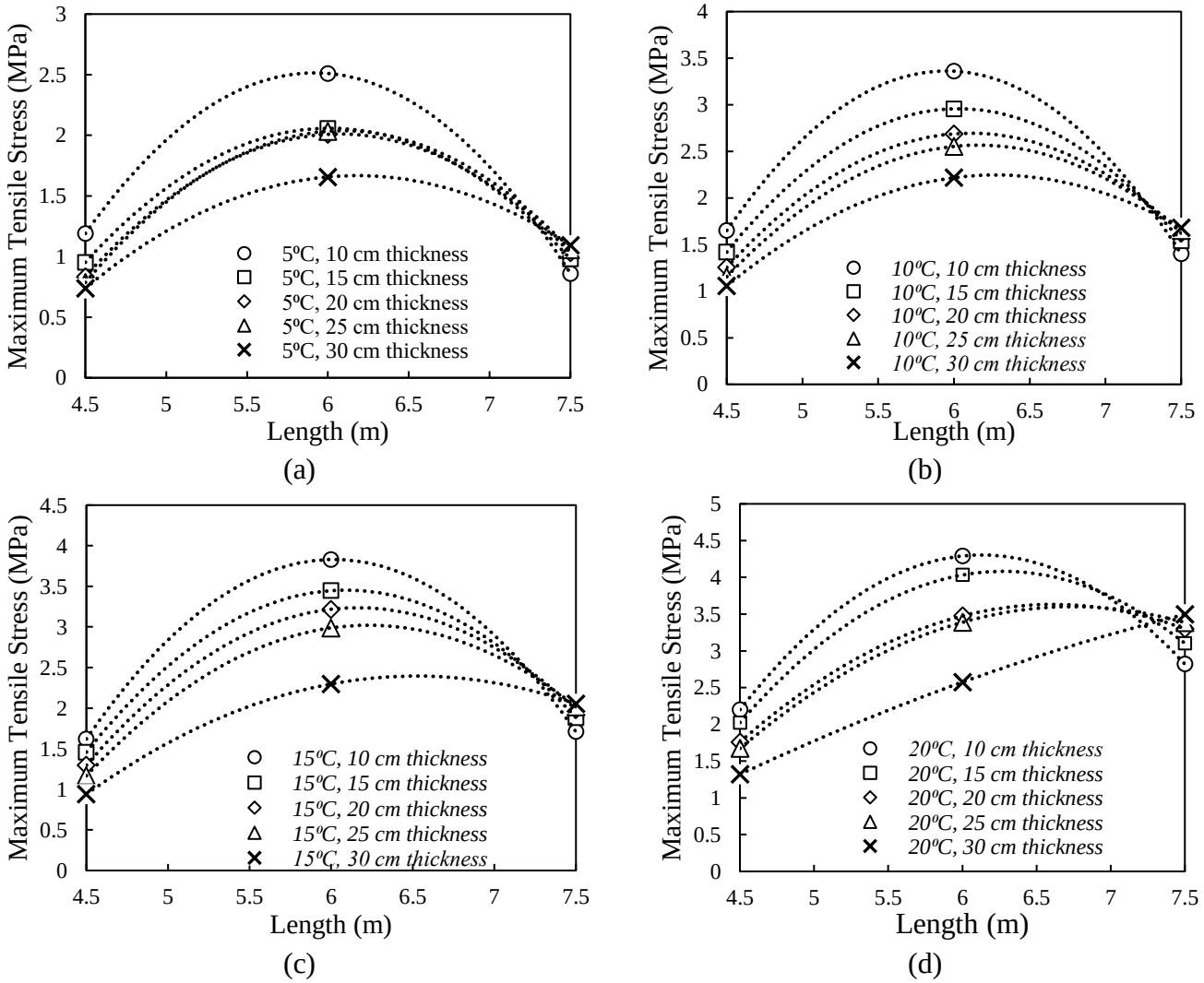

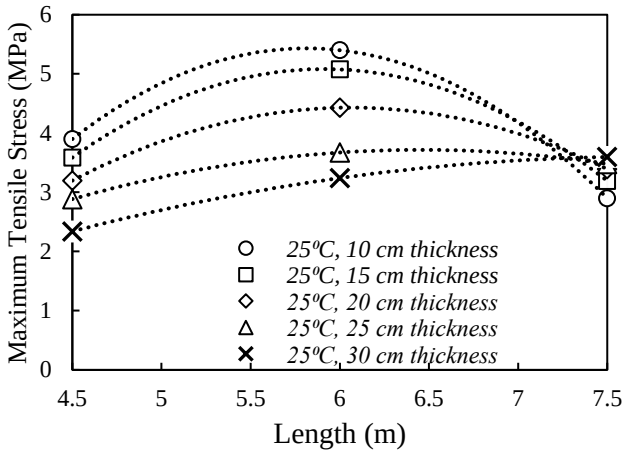

(e)

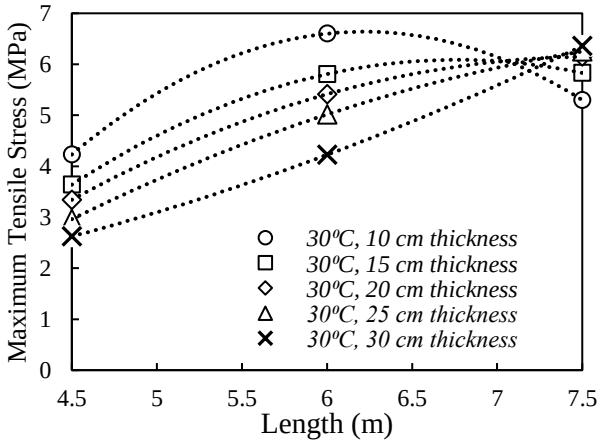

(f)

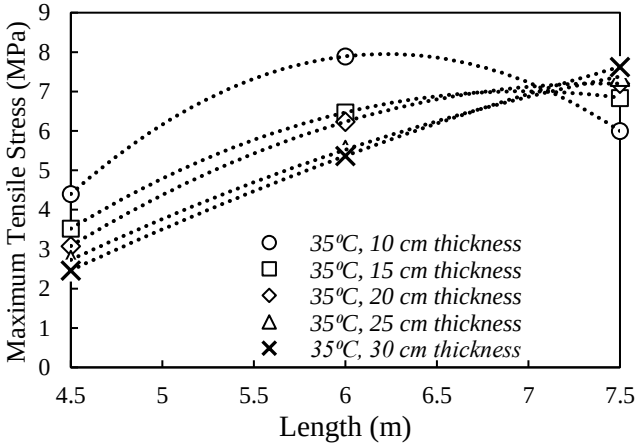

(g)

Figure 3.20: Influence of thickness and length on the maximum tensile stress of slabs with 25 MPa compressive strength under the effect of different thermal gradients a) 5ºC, b) 10ºC, c) 15ºC, d) 20ºC, e) 25ºC, f) 30ºC and g) 35ºC

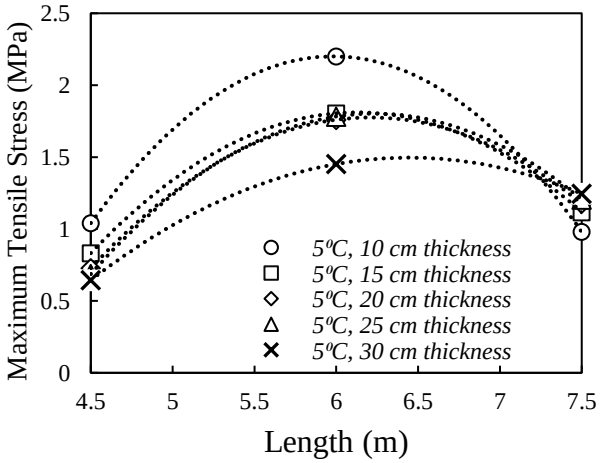

(a)

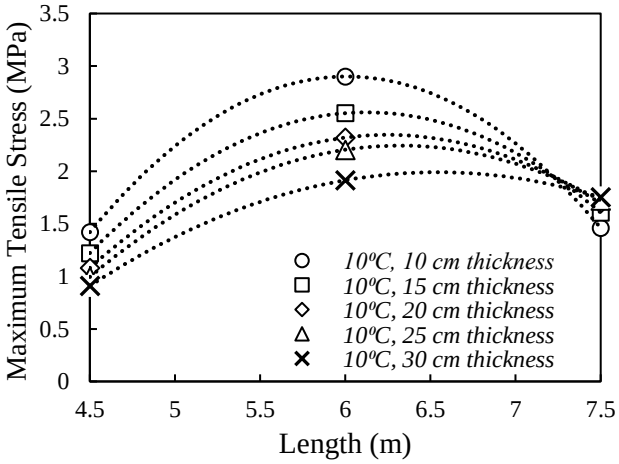

(b)

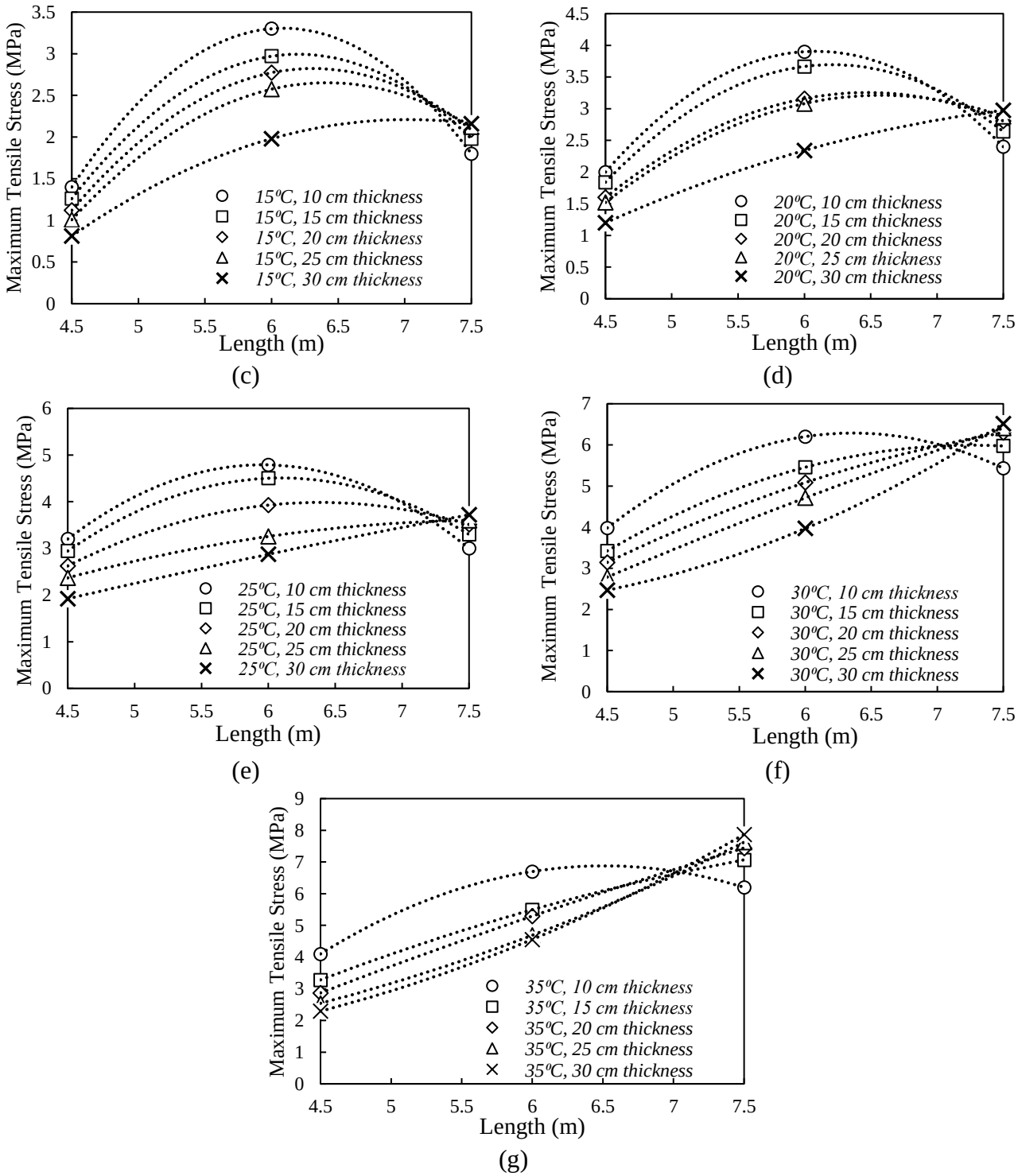

Figure 3.21: Influence of thickness and length on the maximum tensile stress of slabs with 30 MPa compressive strength under the effect of different thermal gradients a) 5ºC, b) 10ºC, c) 15ºC, d) 20ºC, e) 25ºC, f) 30ºC and g) 35ºC

Regarding Figure 3.22, by further increasing the compressive strength of concrete up to 35 MPa, the behavior of the slabs has significantly changed in terms of maximum tensile stress. Therefore, with an increase in the length of slabs, the maximum tensile stress increased and the nonlinearity behavior was considerably amplified when the length of slabs was greater than 6m, particularly under the influence of a high thermal gradient. Therefore, it is necessary to consider the nonlinear mechanical behavior of concrete materials as well as nonlinear thermal gradient distribution over the thickness of the slab when the temperature variation is high and long-length slabs are constructed. This could be concluded that in long-length slabs (greater than 6m in this study), the maximum tensile stress due to curling stress increased with a simultaneous rise in thickness and compressive strength up to 35MPa, particularly under the influence of a 35ºC thermal gradient.

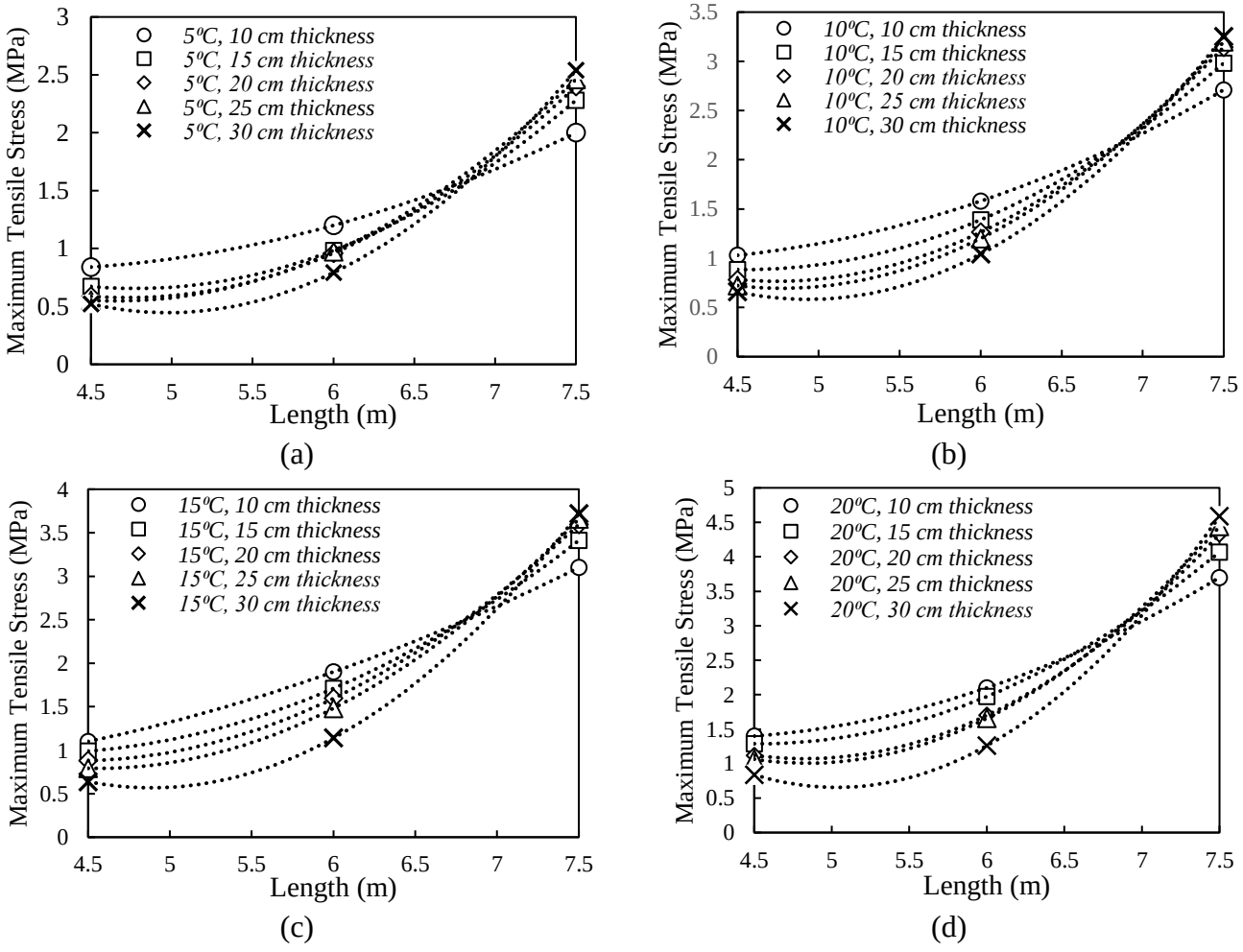

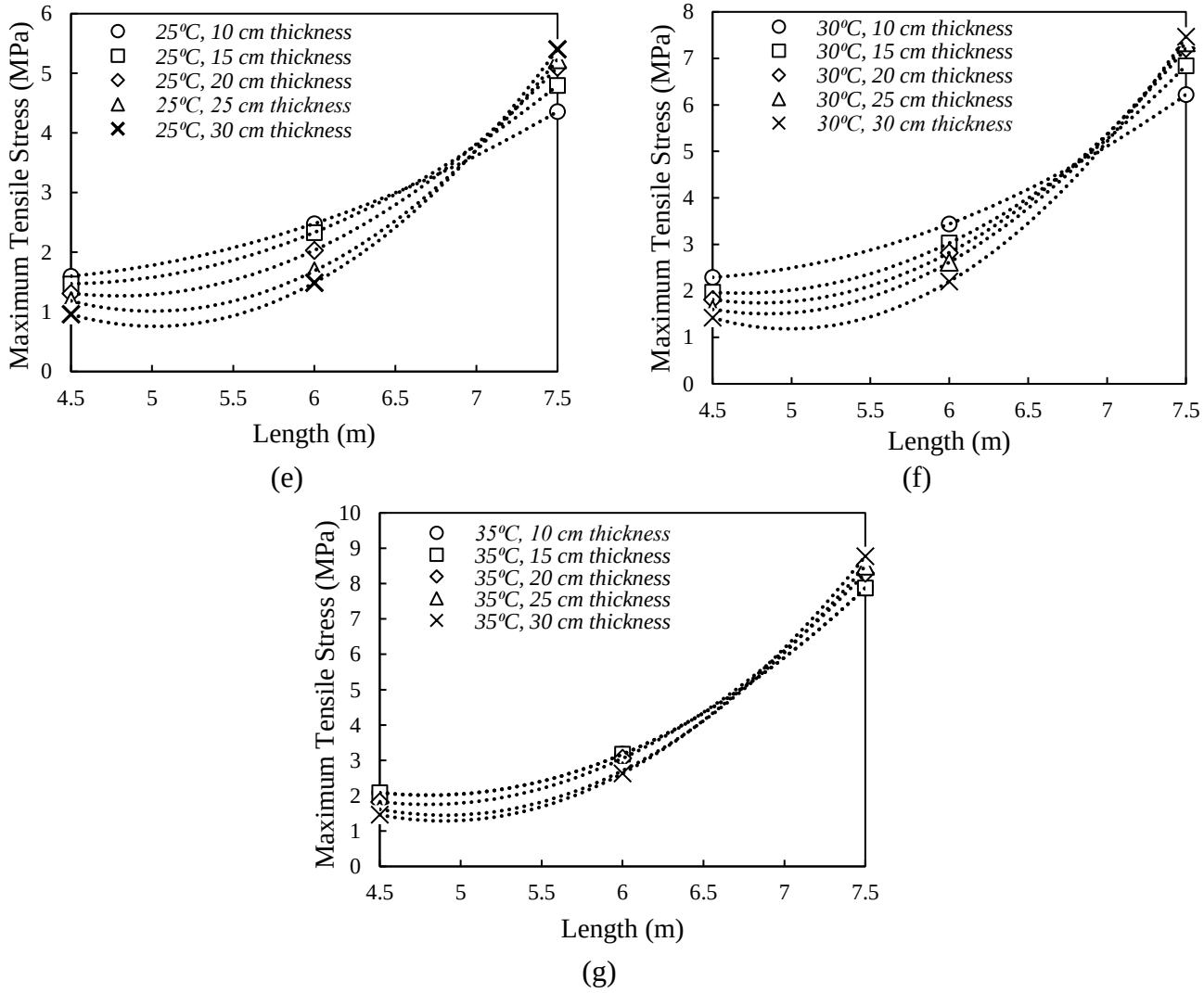

Figure 3.22: Influence of thickness and length on the maximum tensile stress of slabs with 35 MPa compressive strength under the effect of different thermal gradients a) 5ºC, b) 10ºC, c) 15ºC, d) 20ºC, e) 25ºC, f) 30ºC and g) 35ºC

Figures 3.23 and 3.24 provide the influence of thickness and length on the maximum tensile stress of slabs with 40MPa and 45 MPa compressive strength under the effect of the different thermal gradients. According to these results, the maximum tensile stress in all slabs with various lengths and thicknesses was decreased when the compressive strength of concrete was greater than 35MPa. Additionally, in high-strength concrete slabs, the plate element behavior was observed in slabs

with various lengths and thicknesses. Additionally, with a raise in thermal gradient, higher maximum tensile stress due to curling and a higher flexural moment happened. However, increasing the thickness of slabs led to a considerable reduction in tensile stress as a result of improving the lateral and out-of-plane deformation, predominantly in slabs with shorter lengths, up to 6m.

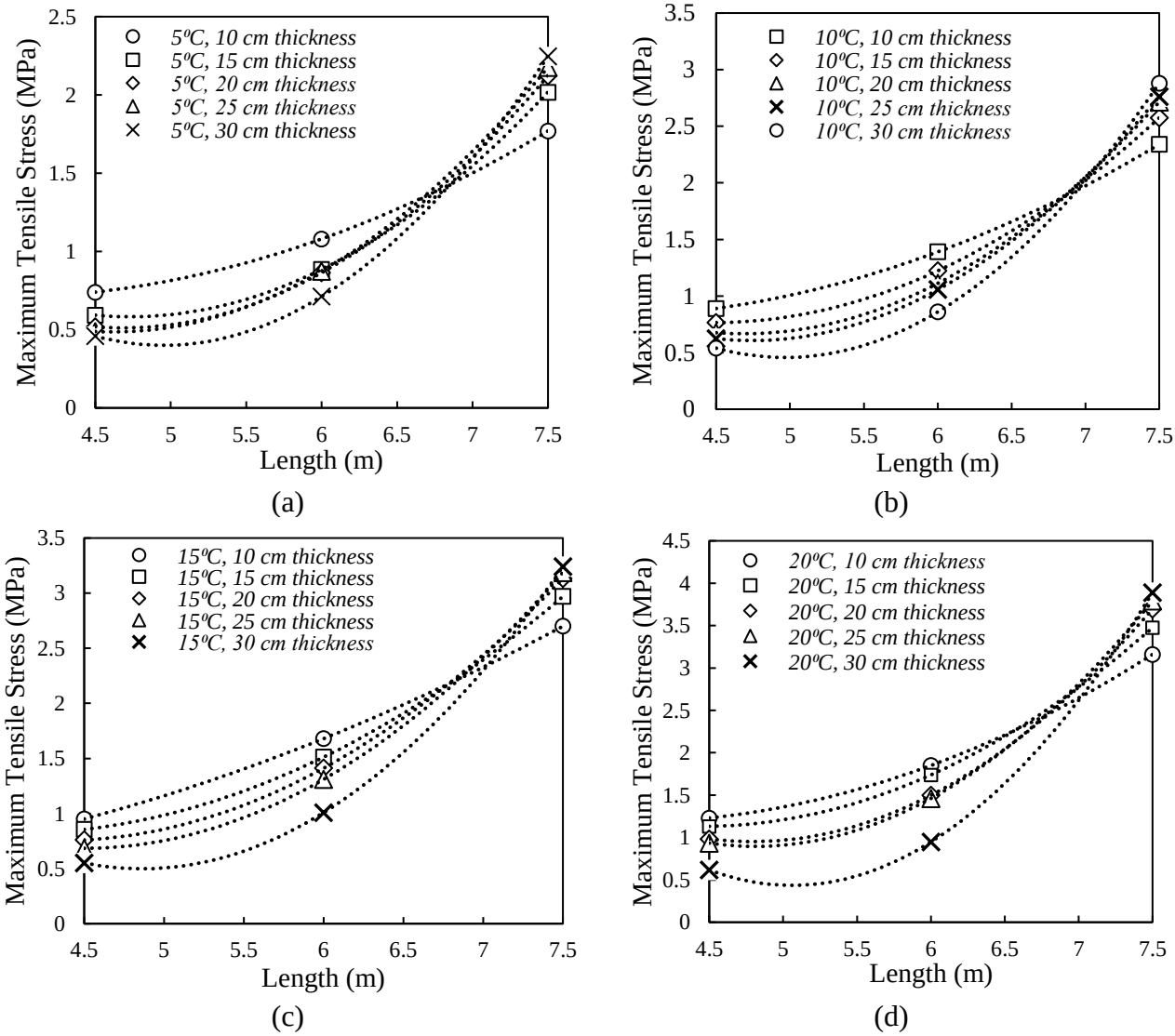

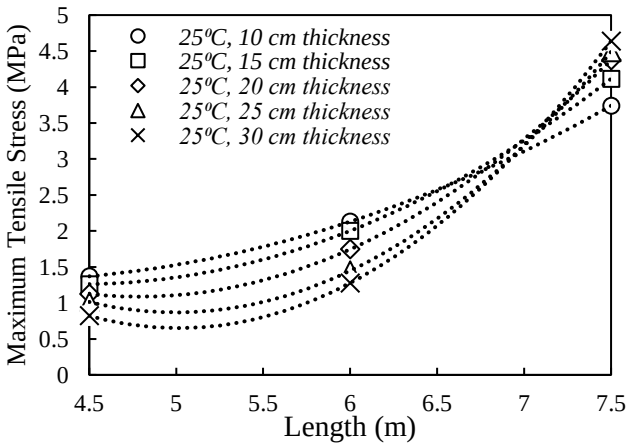

(e)

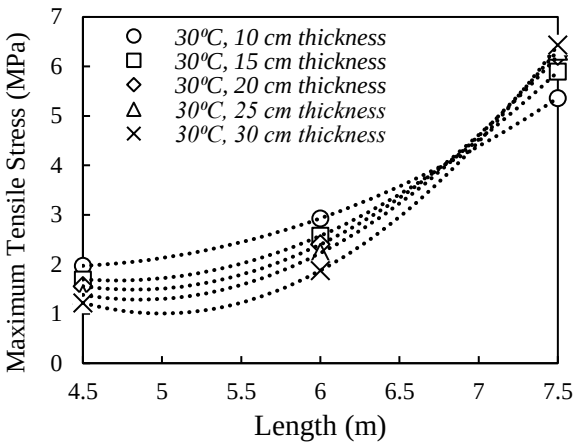

(f)

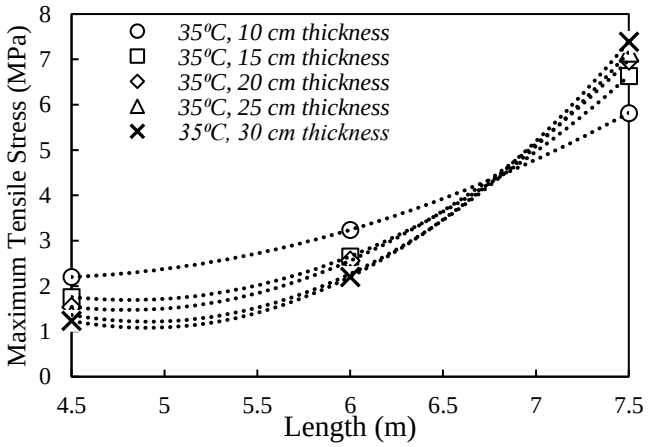

(g)

Figure 3.23: Influence of thickness and length on the maximum tensile stress of slabs with 40 MPa compressive strength under the effect of different thermal gradients a) 5ºC, b) 10ºC, c) 15ºC, d) 20ºC, e) 25ºC, f) 30ºC and g) 35ºC

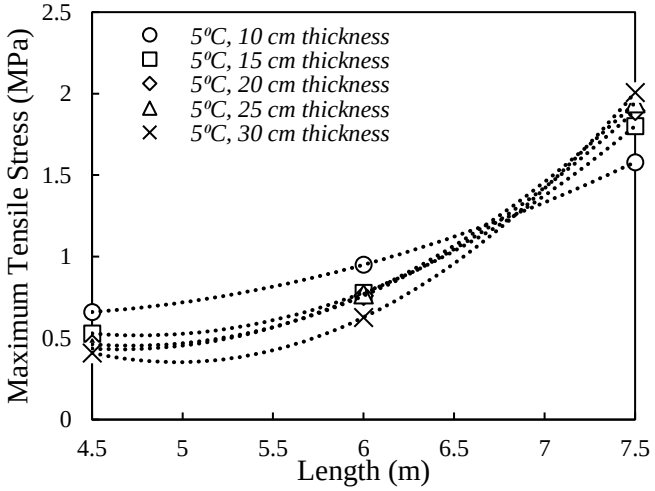

(a)

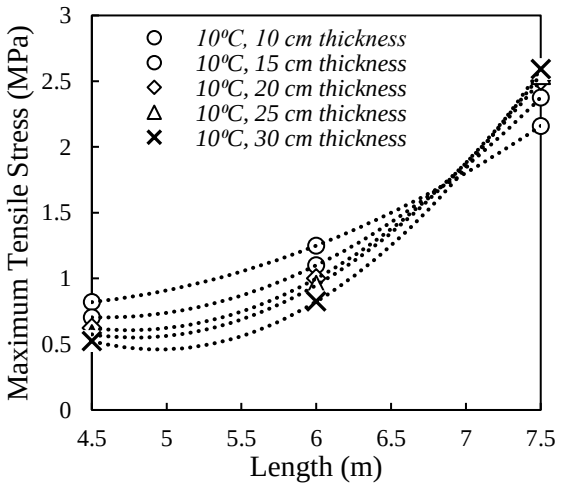

(b)

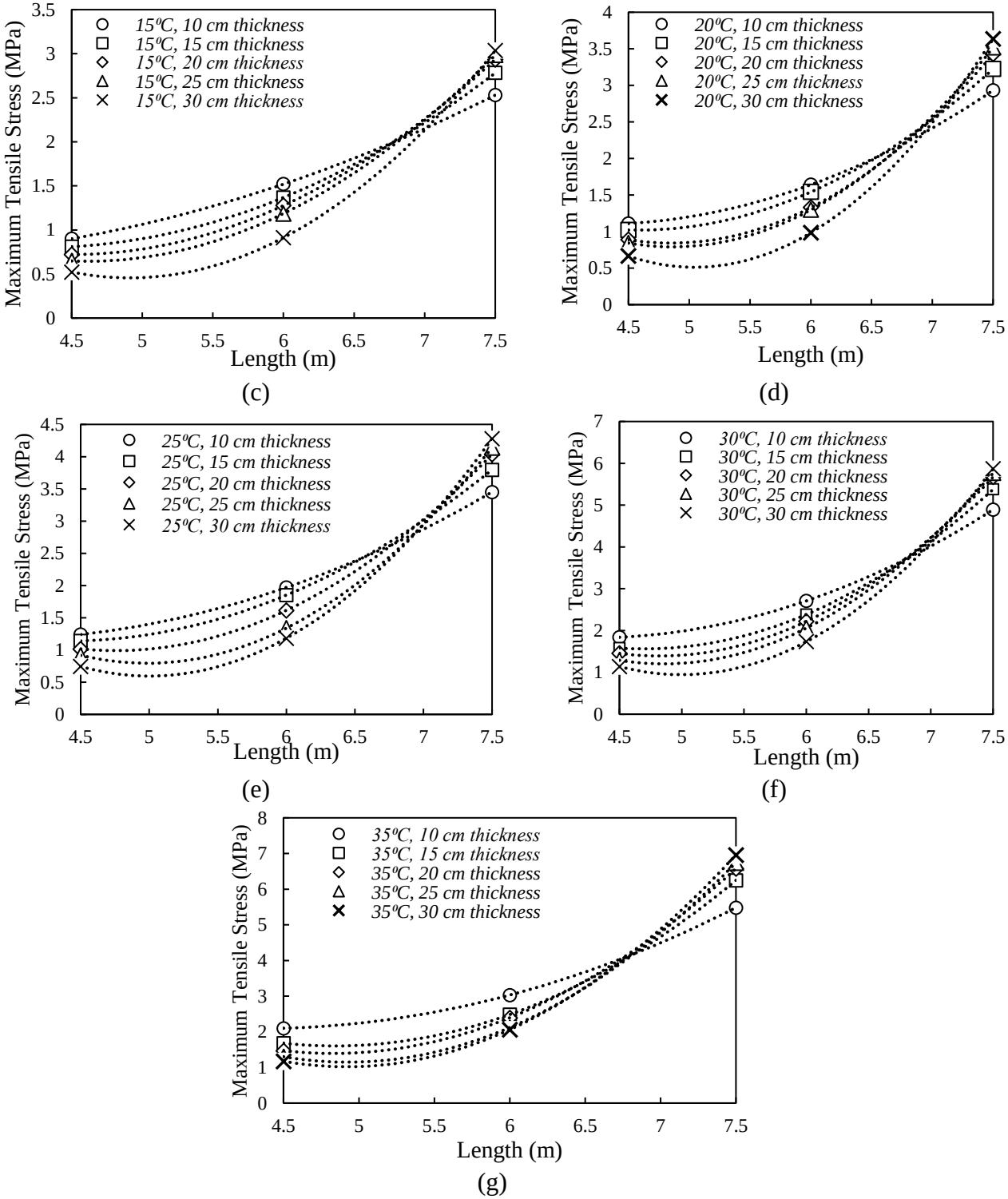

Figure 3.24: Influence of thickness and length on the maximum tensile stress of slabs with 45 MPa compressive strength under the effect of different thermal gradients a) 5^{o}C, b) 10^{o}C, c) 15^{o}C, d) 20^{o}C, e) 25^{o}C, f) 30^{o}C and g) 35^{o}C

Out-of-plane and lateral deformation is another important response of rigid concrete airfield runways resulting in cracking over the surface and thickness of slabs. In this regard, Figure 3.25 shows the influence of thermal gradient and compressive strength on the out-of-plane deformation of 4.5m long slabs with 10cm thickness. According to this figure, the maximum lateral deformation declined with an increase in the compressive strength of concrete which could be associated with increasing the lateral resistance. It should be noted that the general lateral behavior of 4.5m long slabs could be considered as a bending plate element. Conversely, the thermal gradient has a negative influence on out-of-plane deformation in rigid concrete airfield runways. Therefore, by reducing the lateral deformation, the crack length throughout the thickness of slabs might be decreased resulting in improving the structural and thermal behaviors of rigid concrete airfield runways.

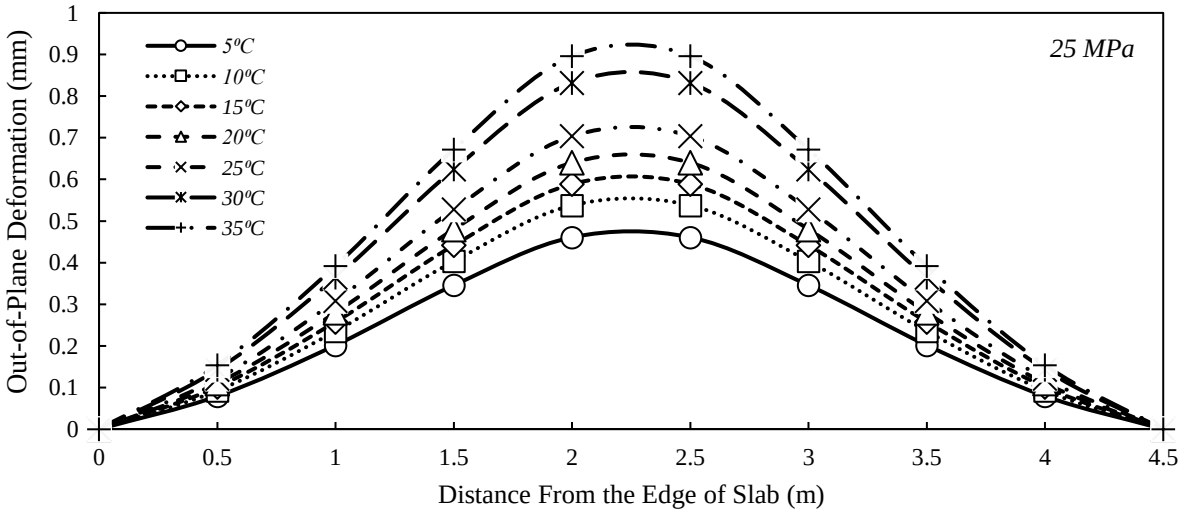

(a)

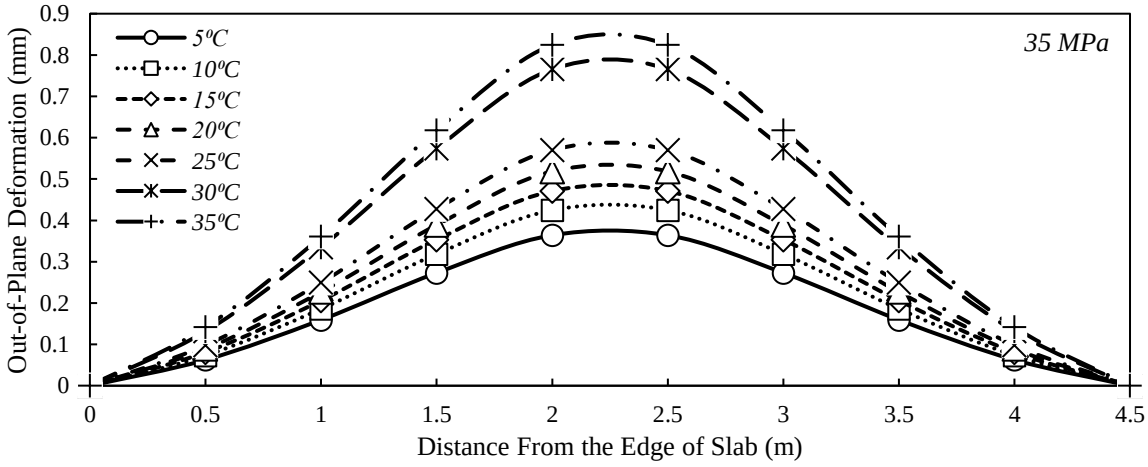

(b)

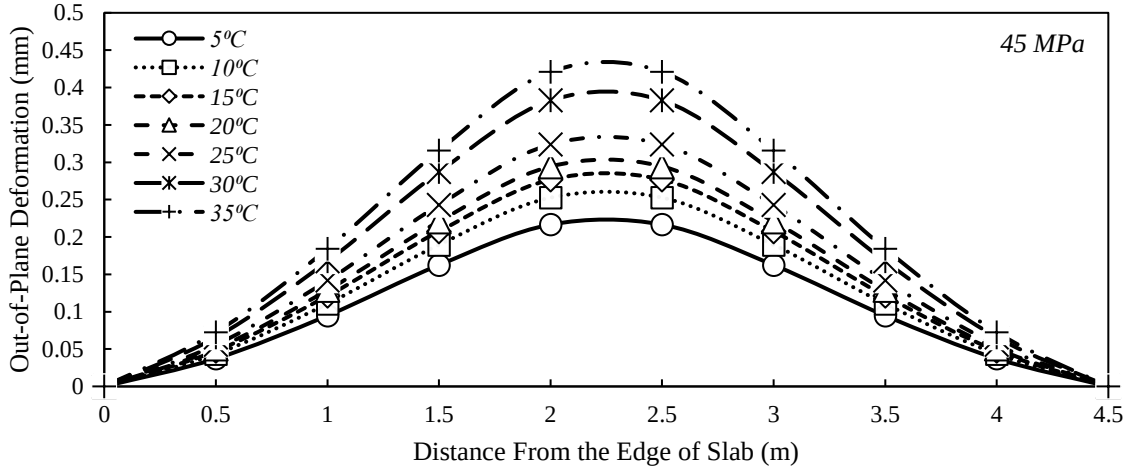

(c)

Figure 3.25: Influence of thermal gradient on the out-of-plane deformation of 4.5m long slabs with 10cm thickness having various compressive strengths a) 25MPa, b) 35MPa and c) 45MPa

The same improvement behavior could be observed in Figures 3.26 and 3.27 when the thickness of slabs was increased by 10cm and 20cm, respectively. So, this could be concluded that in short-length slabs, the simultaneous increase in compressive strength of concrete and thickness of slabs could be considered for a substantial improvement in lateral out-of-plane deformation and generally the thermal and curling behaviors of rigid concrete airfield runways. The curve-shaped lateral deformation could be observed in slabs with 6m length.

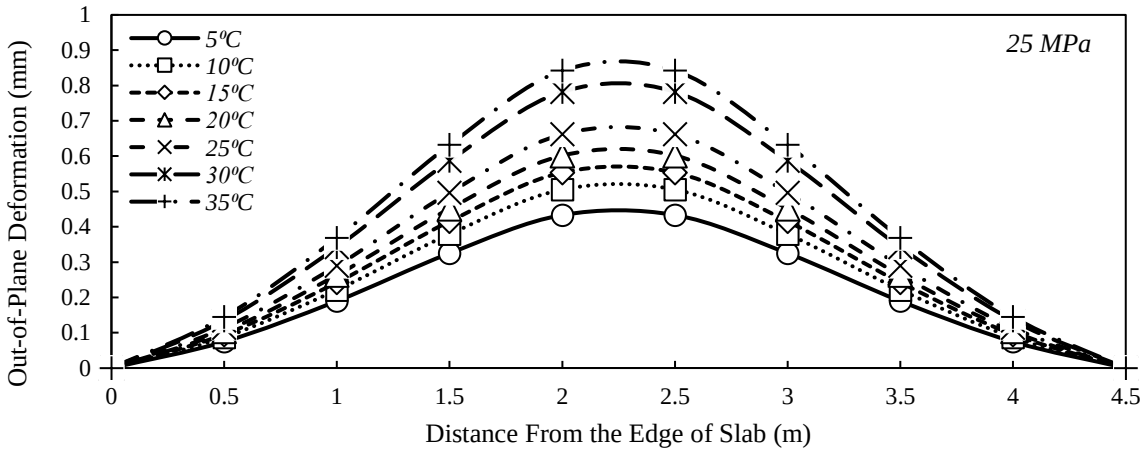

(a)

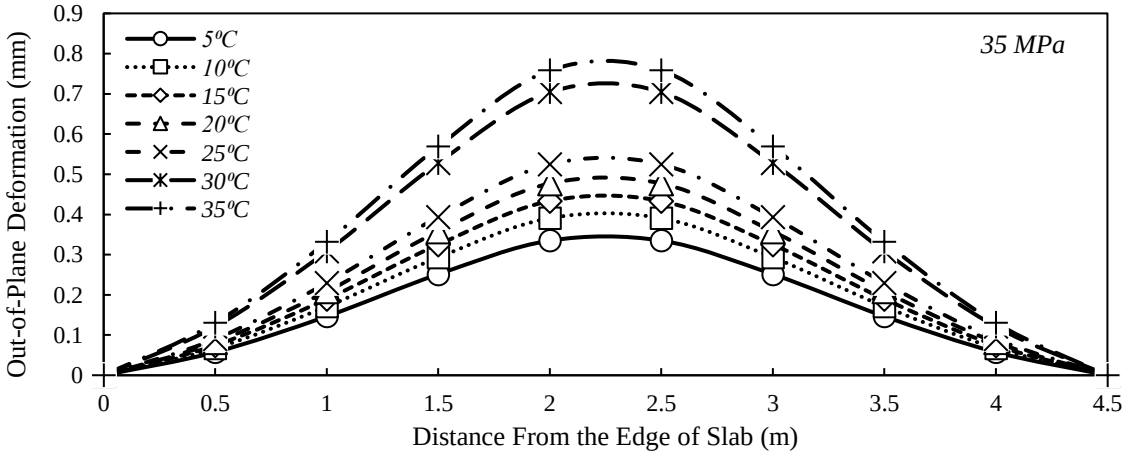

(b)

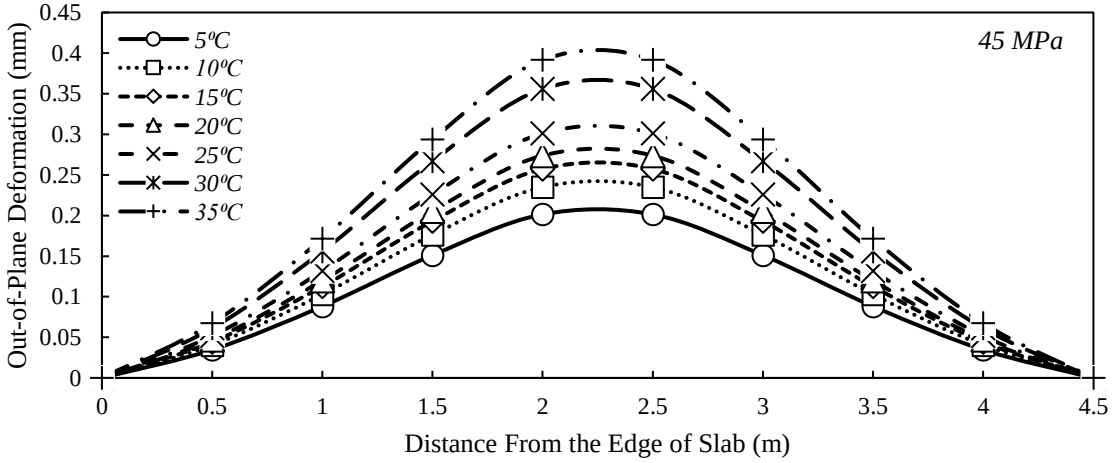

(c)

Figure 3.26: Influence of thermal gradient on the out-of-plane deformation of 4.5m long slabs with 20cm thickness having various compressive strengths a) 25MPa, b) 35MPa and c) 45MPa

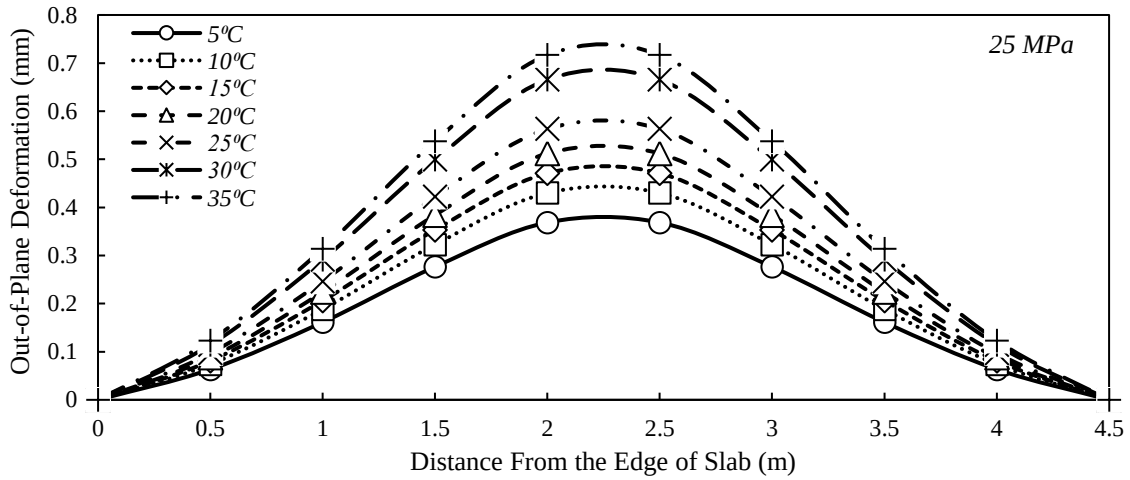

(a)

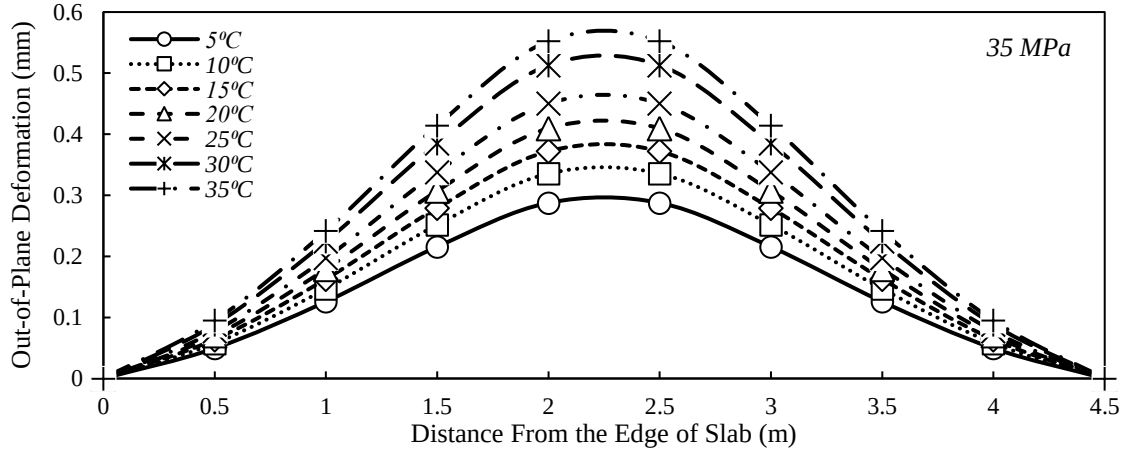

(b)

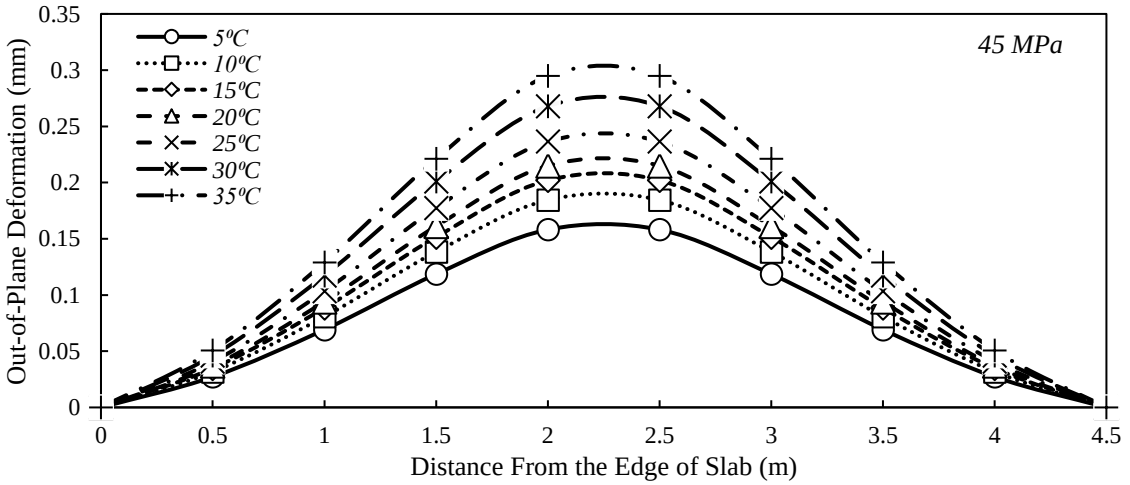

(c)

Figure 3.27: Influence of thermal gradient on the out-of-plane deformation of 4.5m long slabs with 30cm thickness having various compressive strengths a) 25MPa, b) 35MPa and c) 45MPa

In addition to considering the effect of compressive strength, thermal gradient, and thickness of slabs on the out-of-plane deformation, the effect of length as another important parameter has been taken into consideration and analyzed. Therefore, the out-of-plane deformation in 6m long rigid concrete slabs is presented in Figures 3.28 to 3.30. The same results could be observed in slabs with 6m length in comparison with 4.5m long slabs. However, with an increase in slab length, the lateral deformation value was slightly increased due to increasing the bending moment and reduction in lateral stiffness of slabs. With a rise in concrete's compressive strength, which may be related to raising the lateral resistance, the greatest lateral deformation was reduced. It should be mentioned that the 6m long slabs' overall lateral motion could be regarded as a bending plate element similar to 4.5m long rigid concrete slabs. In contrast, rigid concrete runways' out-of-plane deformation is negatively impacted by the thermal gradient. Therefore, by decreasing the lateral deformation, the crack length through the width of slabs might be reduced resulting in enhancing the structural and thermal characteristics of airport runways. Additionally, to consider the influence of thickness in longer length slabs, 6m in this study, the influence of thermal gradient on the out-of-plane deformation of 6m long slabs with 20cm and 30cm thicknesses having various compressive strengths are provided in Figures 3.29 and 3.30.

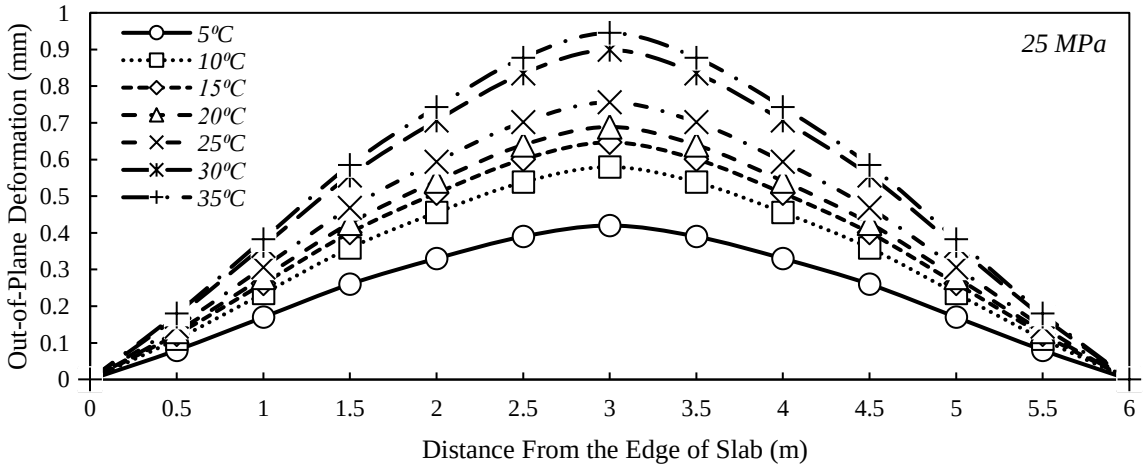

(a)

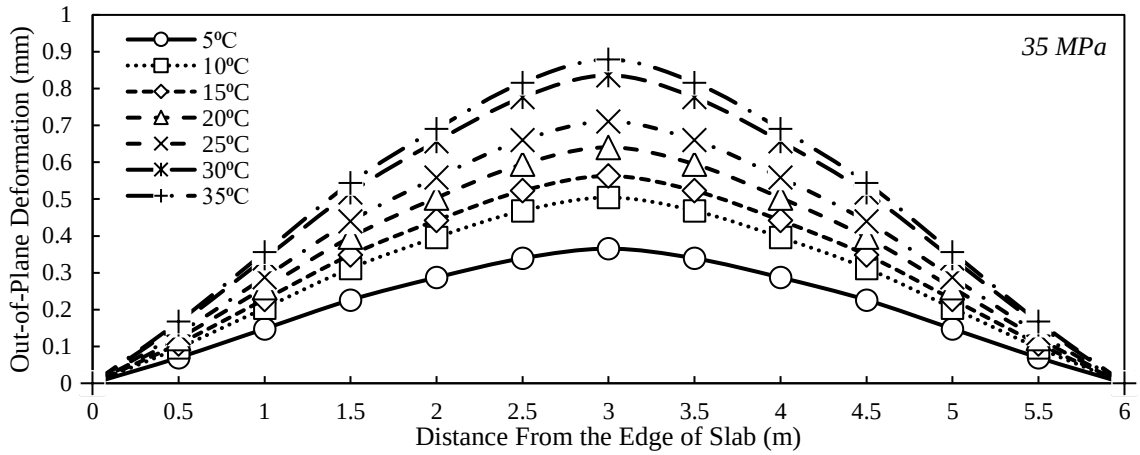

(b)

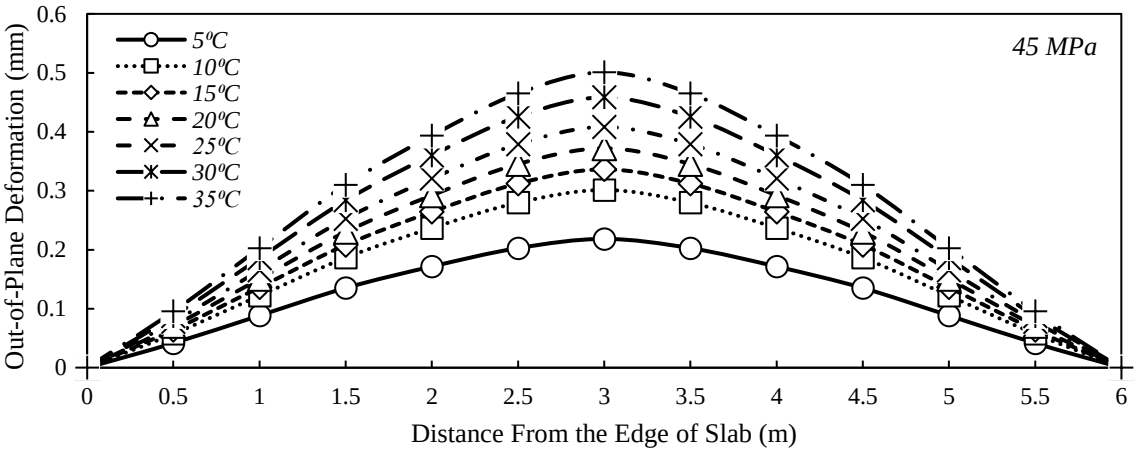

(c)

Figure 3.28: Influence of thermal gradient on the out-of-plane deformation of 6m long slabs with 10cm thickness having various compressive strengths a) 25MPa, b) 35MPa and c) 45MPa

Figures 3.29 and 3.30 show the same pattern of progress when the slab width was raised by 10 cm and 20 cm, respectively. The lateral out-of-plane deformation and generally the thermal and curling behaviors of rigid concrete airfield runways could thus be improved in short-length slabs due to the simultaneous increase in concrete's compressive strength and slab thickness. In slabs with a 6 m length, the vertical deformation could be seen as a curve. Although the bending deformation of the slab with increasing length is significant. This issue shows the change of the mode of failure of the slab from the bending plate element to the membrane shell element, in which in this case, the in-plane responses and behaviors are more prominent. As a result, the failure shape of the slabs has been changed from the curved state obtained in slabs with a length of 4.5 meters.

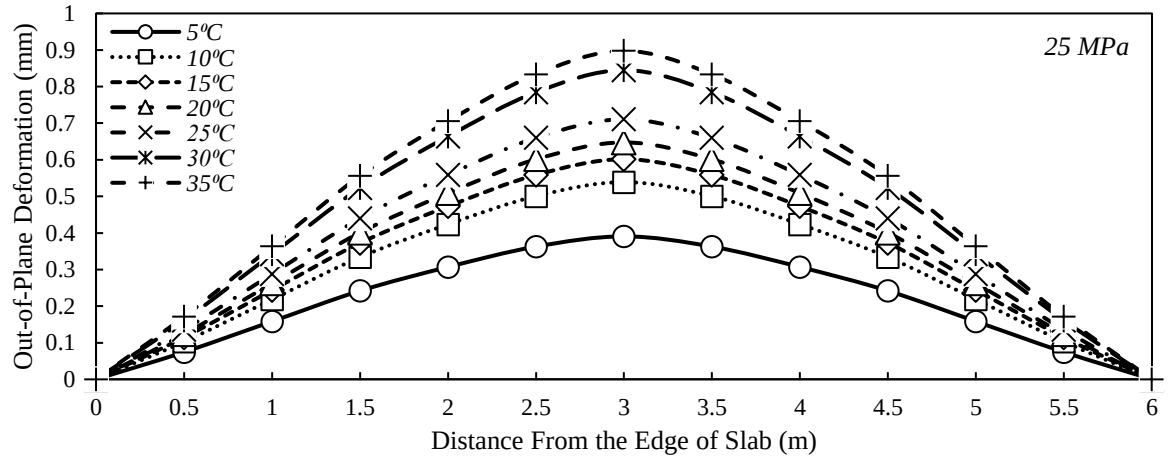

(a)

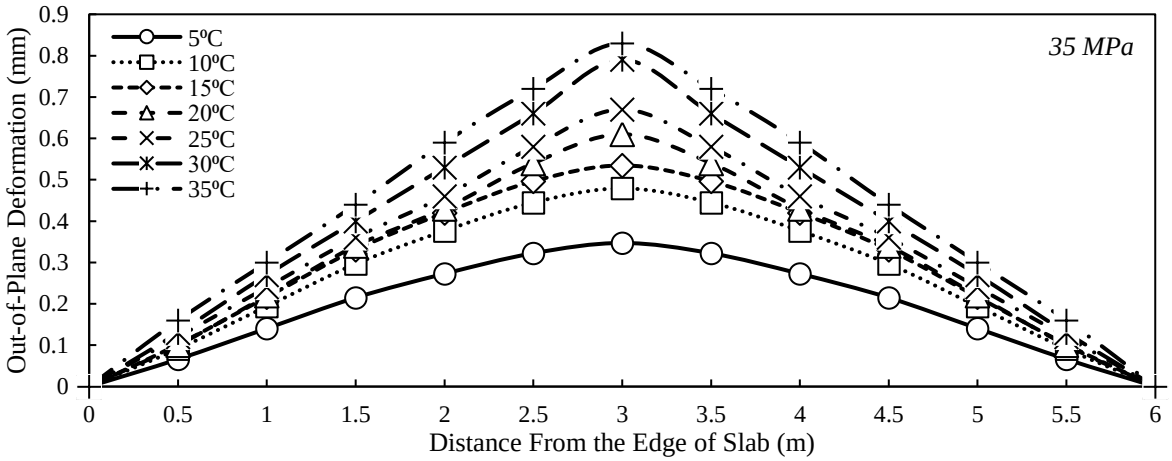

(b)

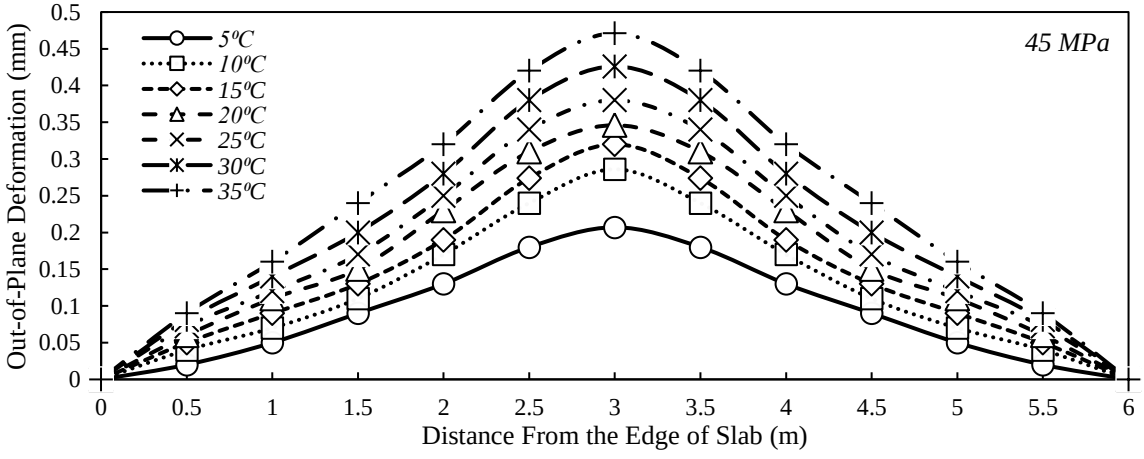

(c)

Figure 3.29: Influence of thermal gradient on the out-of-plane deformation of 6m long slabs with 20cm thickness having various compressive strengths a) 25MPa, b) 35MPa and c) 45MPa

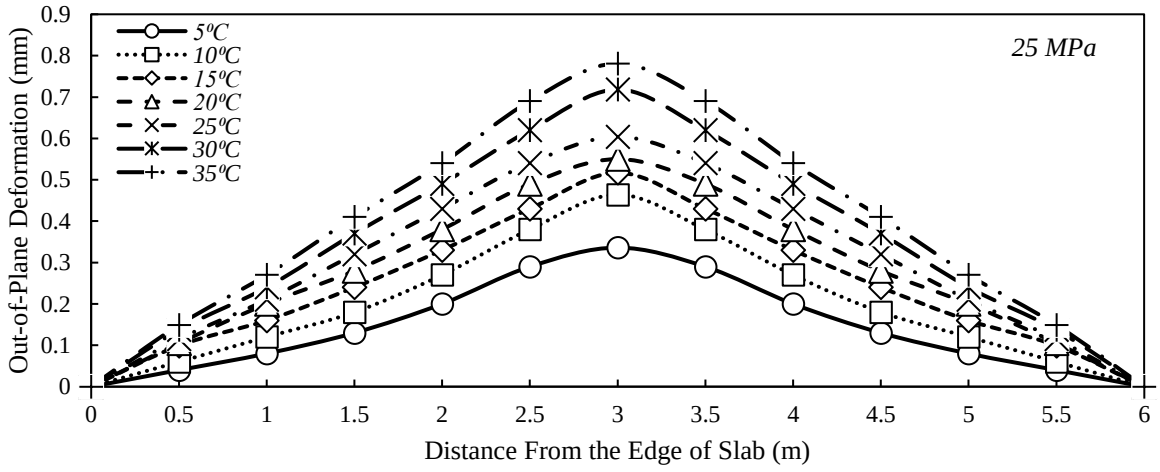

(a)

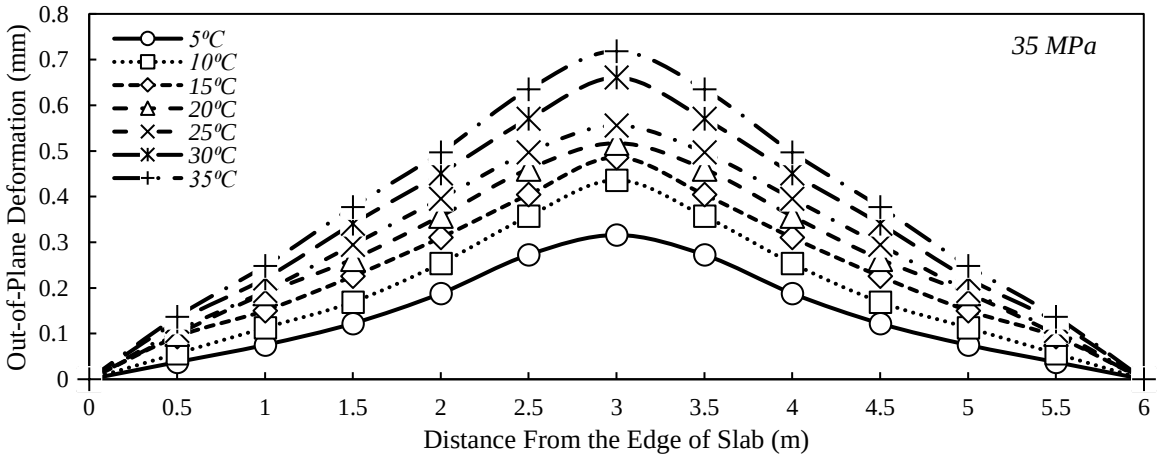

(b)

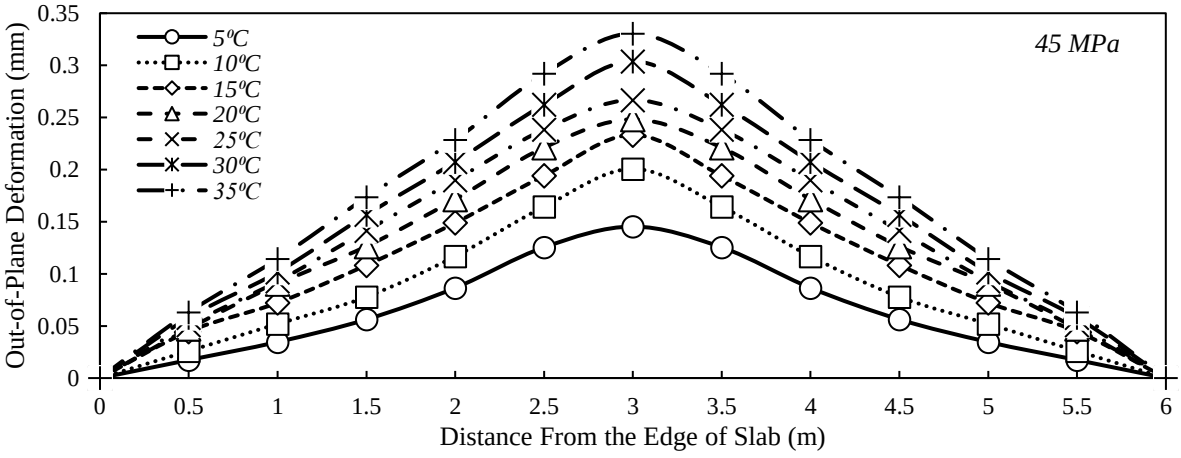

(c)

Figure 3.30: Influence of thermal gradient on the out-of-plane deformation of 6m long slabs with 30cm thickness having various compressive strengths a) 25MPa, b) 35MPa and c) 45MPa

Moreover, the lateral out-of-plane deformation in long-length rigid concrete slabs was assessed for 7.5m long slabs, and the obtained results are provided in Figures 3.31 to 3.33 for slabs with various thicknesses and compressive strengths. According to the obtained results, the out-of-plane behavior of long slabs is different from short slabs. Therefore, the behavior of short slabs should be considered as bending plates and long slabs as membrane shells. As it is clear from Figure 3.31, with the increase in the length of the slab from 6m to 7.5m, the lateral deformation of the slab and the overall shape of its failure have changed, and the shape of the curve has changed to the deformation of our peak point. Also, increasing the compressive strength of concrete in a slab with a thickness of 10cm causes an increase in lateral deformation and, as a result, intensification of thermal stresses and an increase in cracks along the thickness of the slab. This change of state in the lateral behavior of the slabs can be considered as a transition state from the plate bending behavior to the membrane shell state. Also, the increase in thermal gradient has increased the lateral deformation in slabs with a length of 7.5m, although the amount of changes in long slabs is less than in slabs with a shorter length.

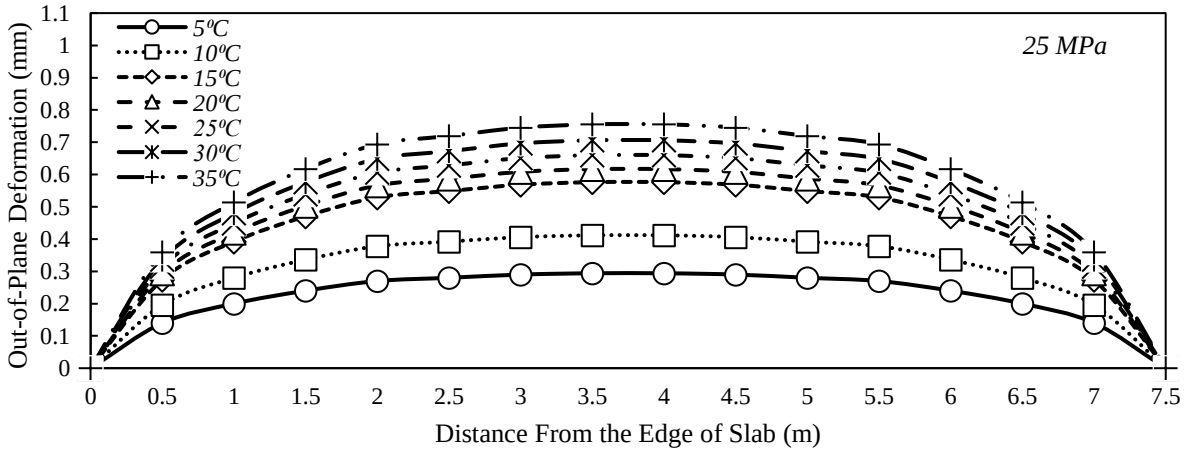

(a)

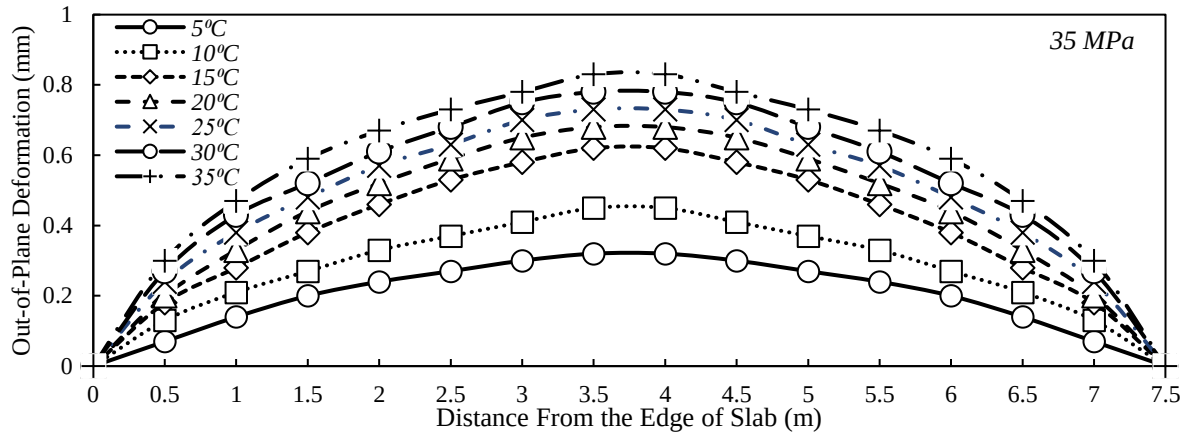

(b)

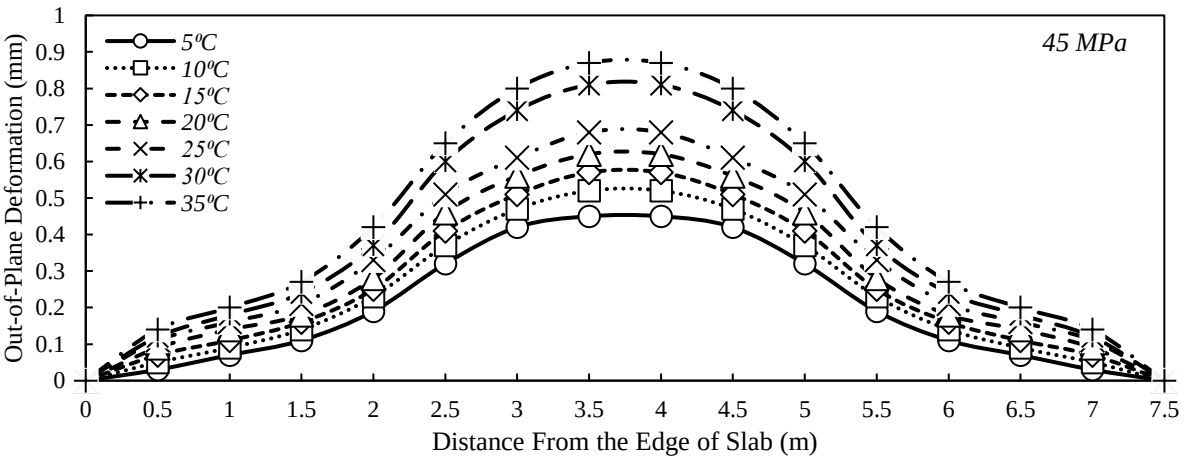

(c)

Figure 3.31: Influence of thermal gradient on the out-of-plane deformation of 7.5m long slabs with 10cm thickness having various compressive strengths a) 25MPa, b) 35MPa and c) 45MPa

With an increase in the thickness of slabs to 20cm, the bending plate behavior was observed in 7.5m long slabs ad so that the maximum tensile stress increased. However, this response slightly declined when the thickness of the slabs was increased to 30cm. So, it is highly recommended to use thick rigid concrete airfield runways when long slabs are going to be constructed. Furthermore, due to the simultaneous rise in concrete's compressive strength and slab thickness, the vertical out-of-plane deformation and usually the thermal and curling characteristics of thick concrete airfield runways could thus be enhanced in long-length slabs. This issue demonstrates the shift in the slab's mode of failure from the membrane shell to the bending plate element for thick-long-length slabs, where the in-plane reactions and behaviors are more pronounced in this instance.

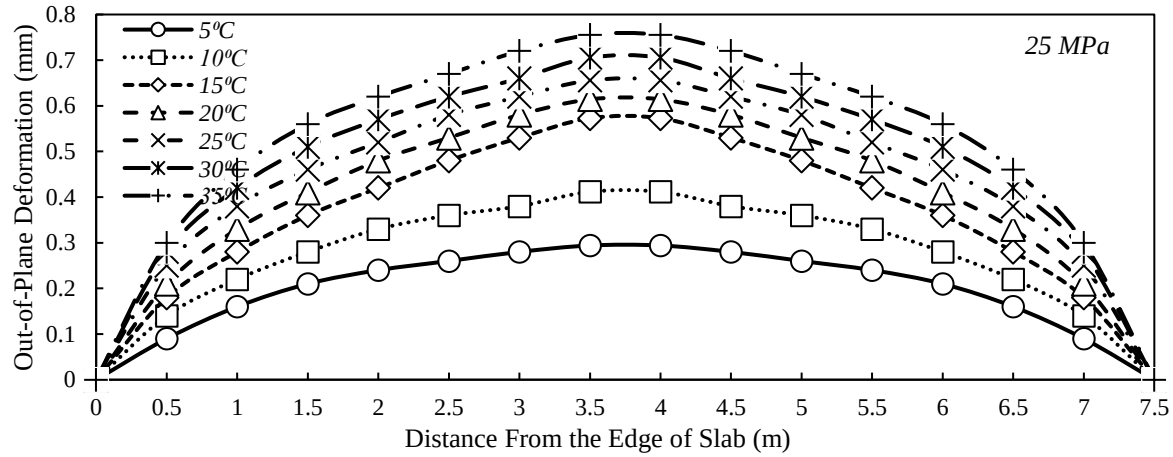

(a)

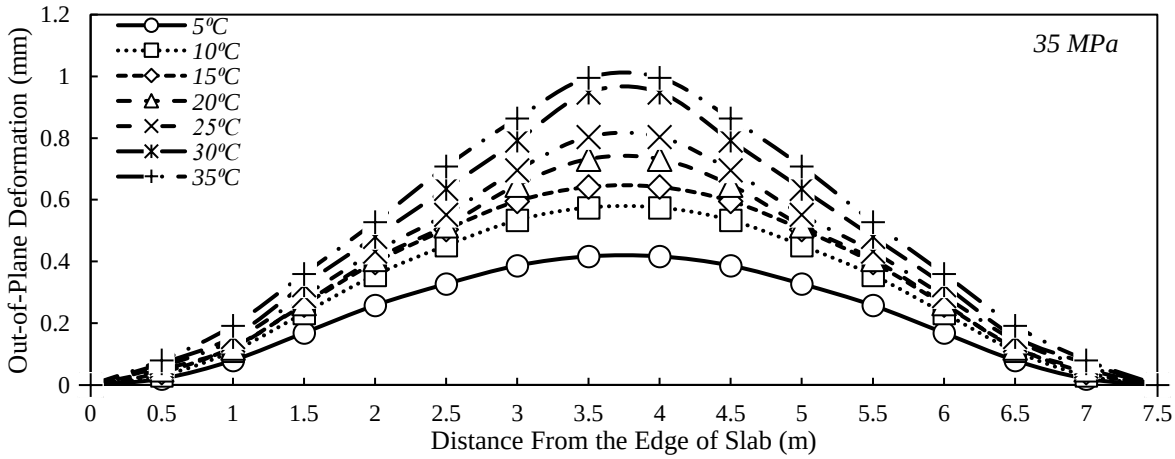

(b)

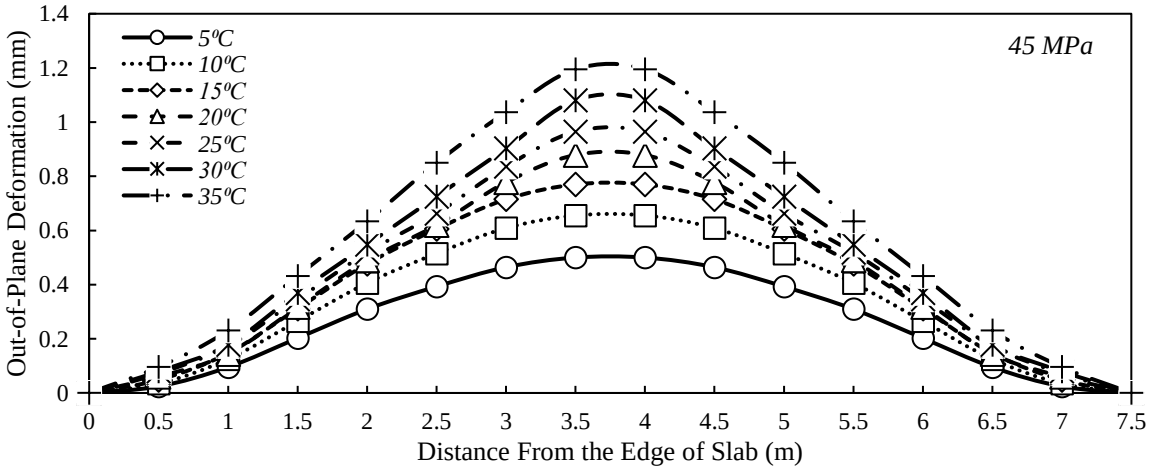

(c)

Figure 3.32: Influence of thermal gradient on the out-of-plane deformation of 7.5m long slabs with 20cm thickness having various compressive strengths a) 25MPa, b) 35MPa and c) 45MPa

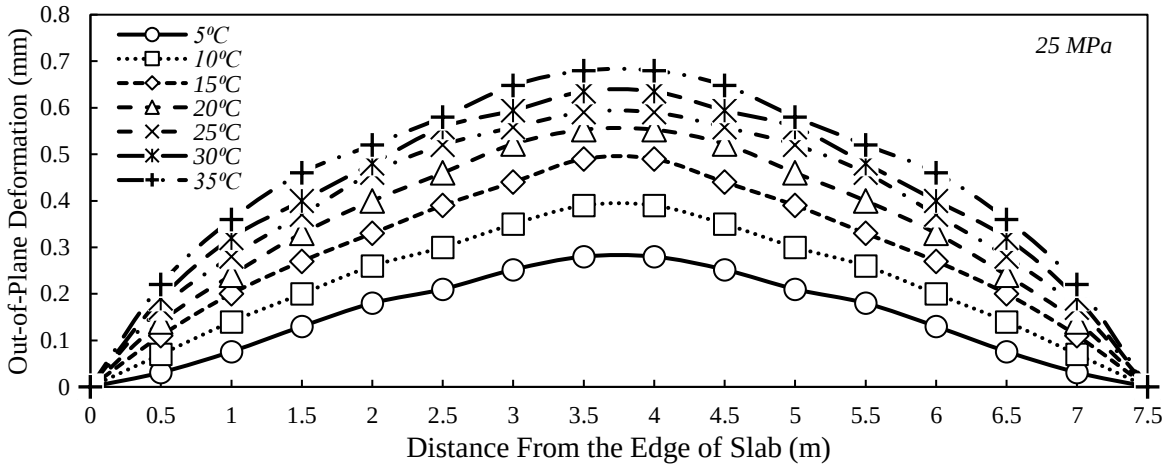

(a)

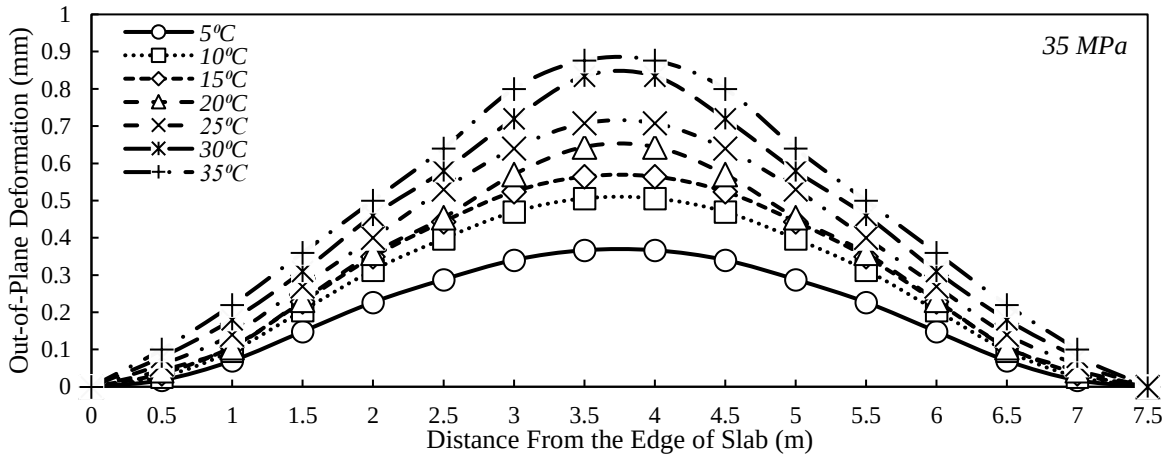

(b)

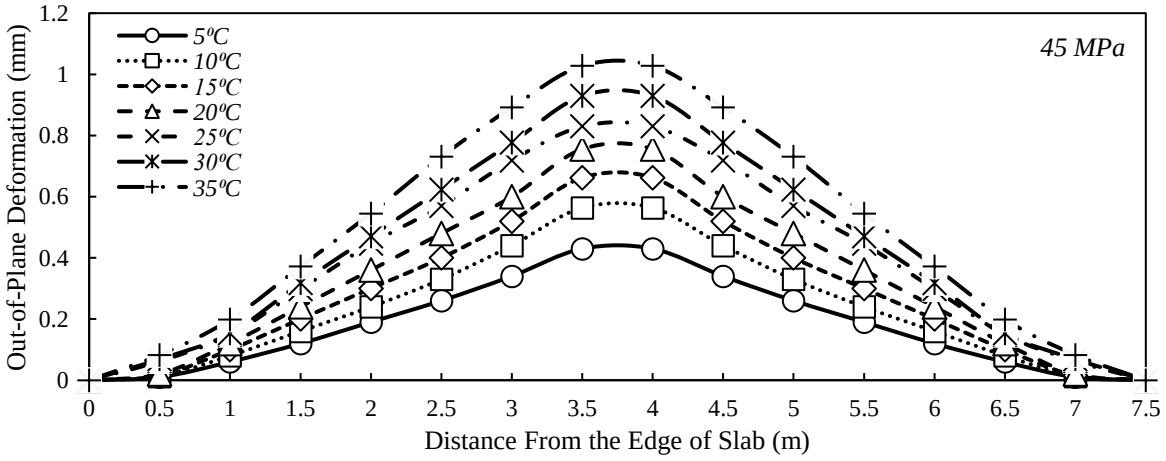

(c)

Figure 3.33: Influence of thermal gradient on the out-of-plane deformation of 7.5m long slabs with 30cm thickness having various compressive strengths a) 25MPa, b) 35MPa and c) 45MPa

Figure 3.34 shows the typical influence of thermal gradient on the deformation of a 4.5m long slab with different properties, obtained by advanced finite element method simulation.

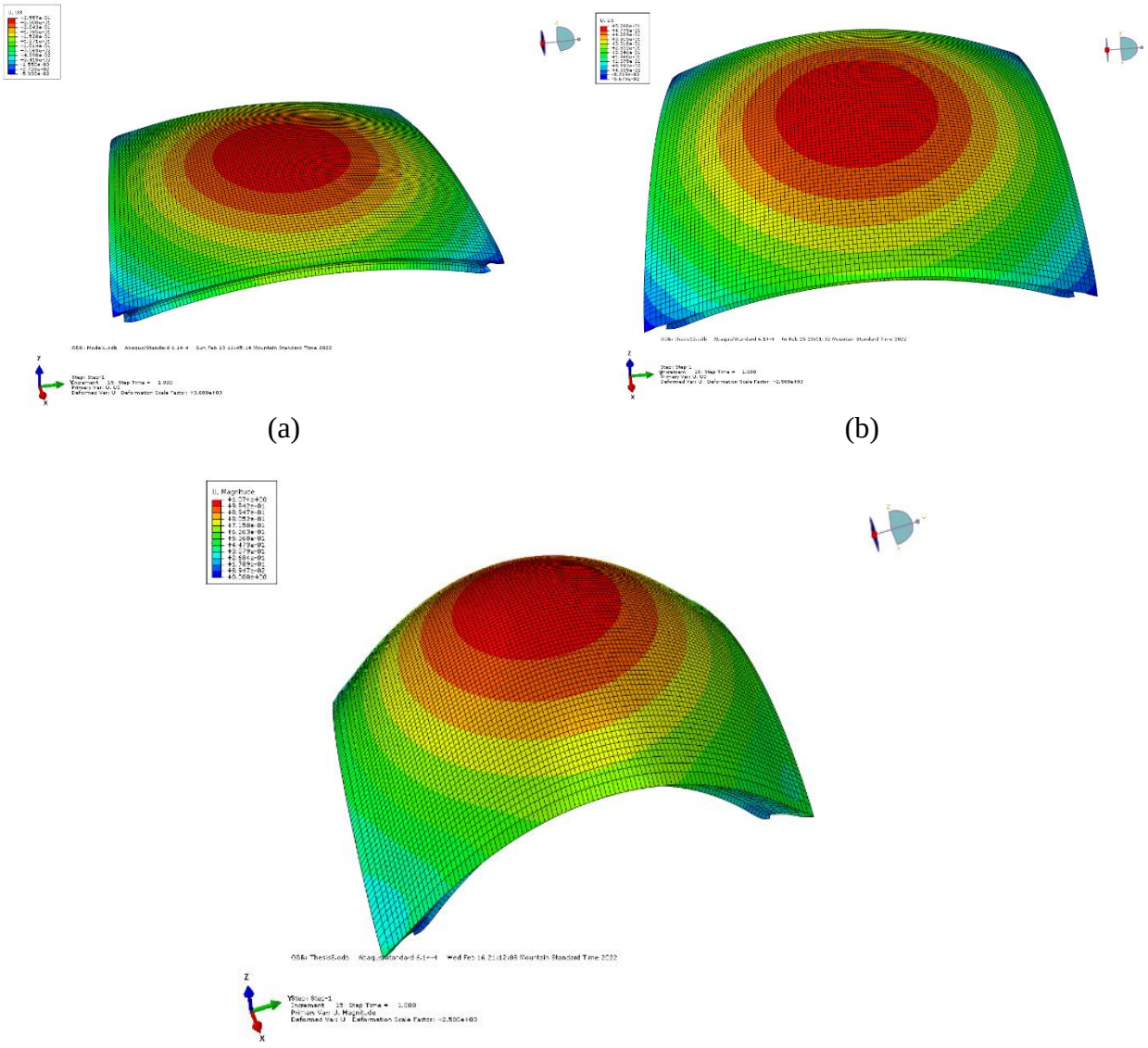

(a) (b)

(c)

Figure 3.34: Influence of thermal on out-of-plan deformation response in 4.5m long slabs

Since the simultaneous effect of different parameters can have a different effect than the effect of one parameter, in this section, the simultaneous effect of all variables including thickness, width, and length is assessed in this section. Figure 3.35 shows the effect of geometric characteristics and

environmental conditions on the maximum tensile strength of concrete slabs with 25MPa compressive strength. Generally, increasing the thermal gradient led to increasing the maximum tensile stress. In 25MPa concrete compressive strength, with an increase in thickness of slabs with 7.5m length, the tensile stress increased while in shorter slabs, this response declined. Additionally, in 4.5m long slabs exposed to up to 15ºC thermal gradient, increasing the slab width increased the tensile stress while for 6m and 7.5m long slabs, the maximum tensile stress declined. Conversely, by increasing the thermal gradient to more than 15ºC, the maximum stress increased with a temperature rise (Figures 3.35c and d). it could be also observed that by increasing the length of slabs, higher tensile stress occurred with various thicknesses and widths.

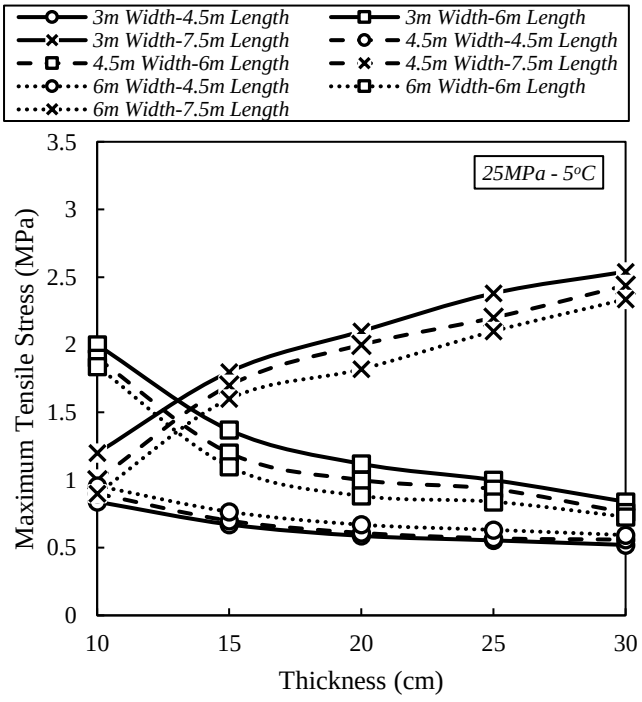

(a)

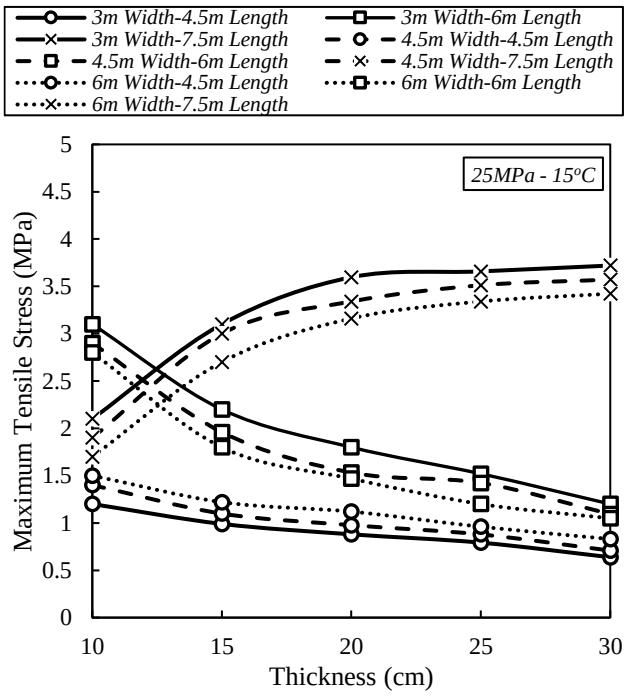

(b)

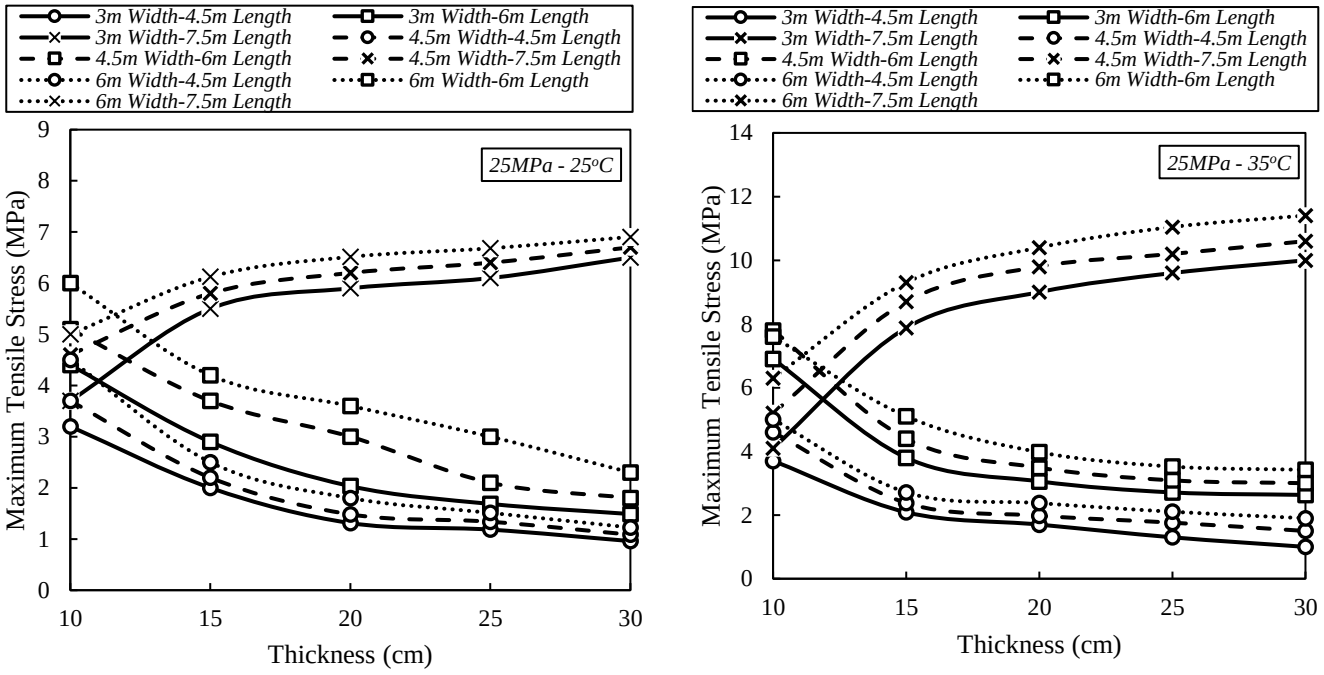

(c) (d)

Figure 3.35: Simultaneous influence of slabs width, thickness, and length on 25MPa concrete compressive strength exposed to various thermal gradients a) 5ºC, b) 15ºC, c) 25ºC and d) 35ºC

Increasing the compressive strength has significantly affected the thermal behavior of slabs. In this regard, Figure 3.36 shows the effect of geometric characteristics and environmental conditions on the maximum tensile strength of concrete slabs with 35MPa compressive strength. With a jump to 35MPa compressive strength from 25MPa, the maximum tensile stress declined. The tensile stress rose as the width of slabs with 7.5m length grew, but this reaction decreased for shorter slabs. Additionally, raising the slab width raised the tensile stress in slabs and for a high thermal gradient, more than 15ºC, the maximum tensile stress was obtained in 6m long slabs. On the other hand, the maximal stress increased as the temperature rose when the thermal gradient was raised by more than 15ºC. It may also be assumed that as slab length increased, tensile stress increased at different densities and lengths.

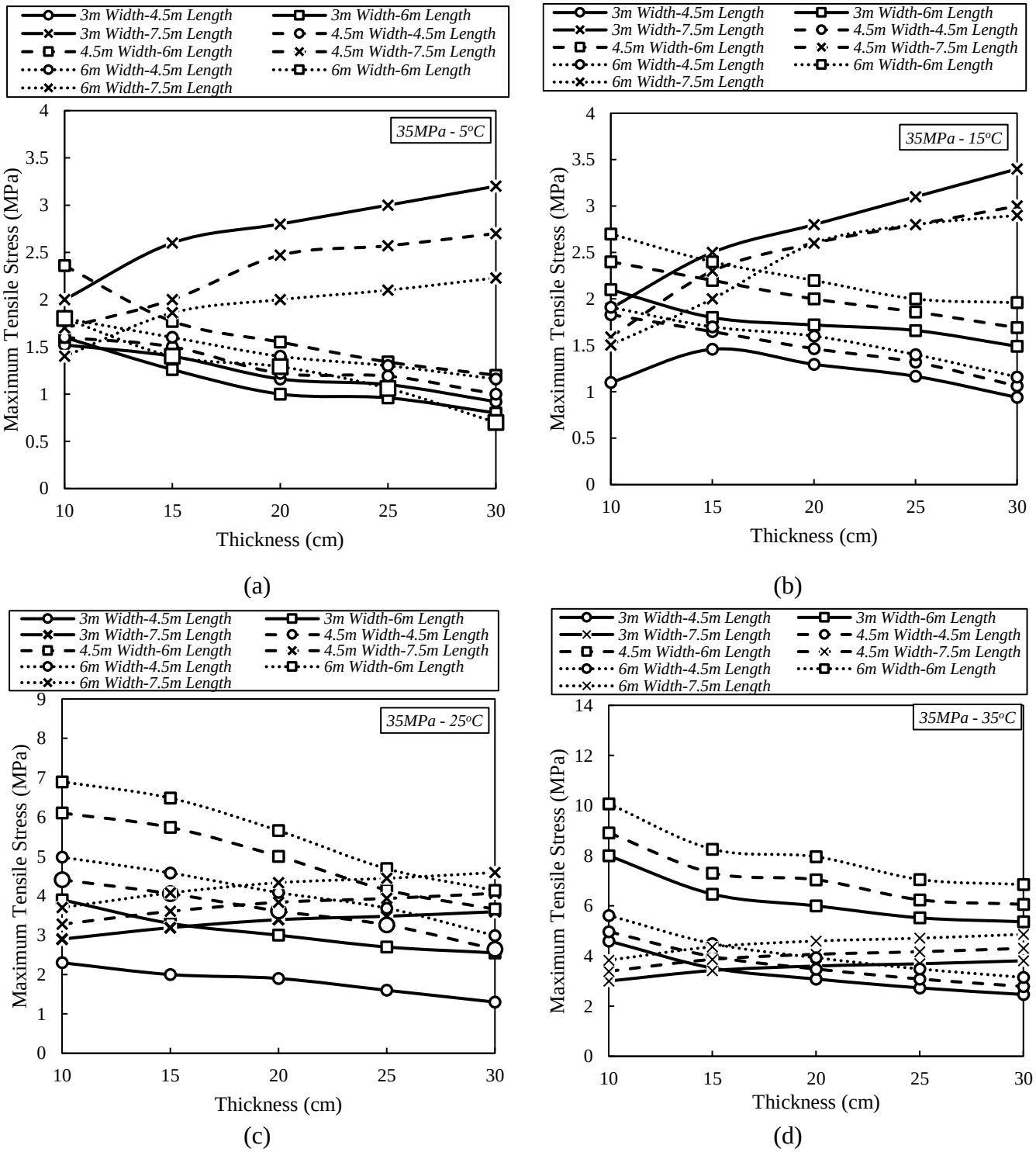

Figure 3.36: Simultaneous influence of slabs width, thickness, and length on 35MPa concrete compressive strength exposed to various thermal gradients a) 5ºC, b) 15ºC, c) 25ºC, and d) 35ºC

Conversely, a difference was obtained in slabs with 45MPa concrete compressive strength. There, the influence of geometric characteristics and external factors on the highest tensile strength of concrete slabs with a compressive strength of 45MPa is depicted in Figure 3.37. According to this figure, an increase in the thickness of slabs with various widths and lengths demonstrated a downward trend in terms of maximum tensile stress. However, with a rise in slab width, the tensile stress increased. This could be associated with the curved-shape deformation and out-of-plane behavior of slabs. Additionally, the nonlinear behavior was observed with an increase in a thermal gradient. Also, the maximum tensile stress was achieved in 7.5m long slabs, particularly when the width of the slabs was also increased, as illustrated in Figure 3.37d.

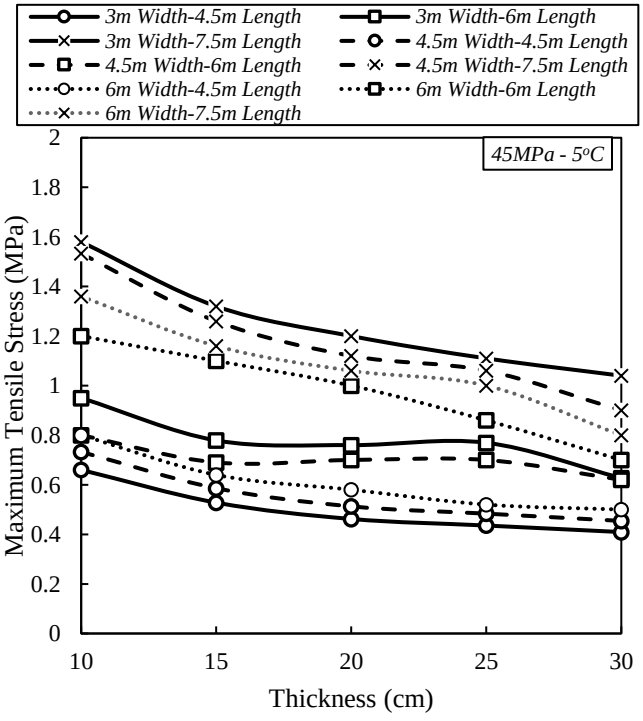

(a)

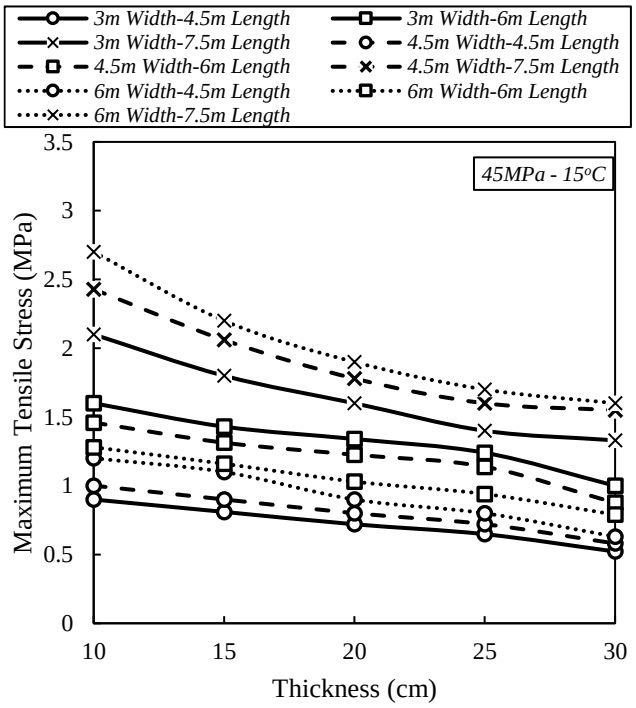

(b)

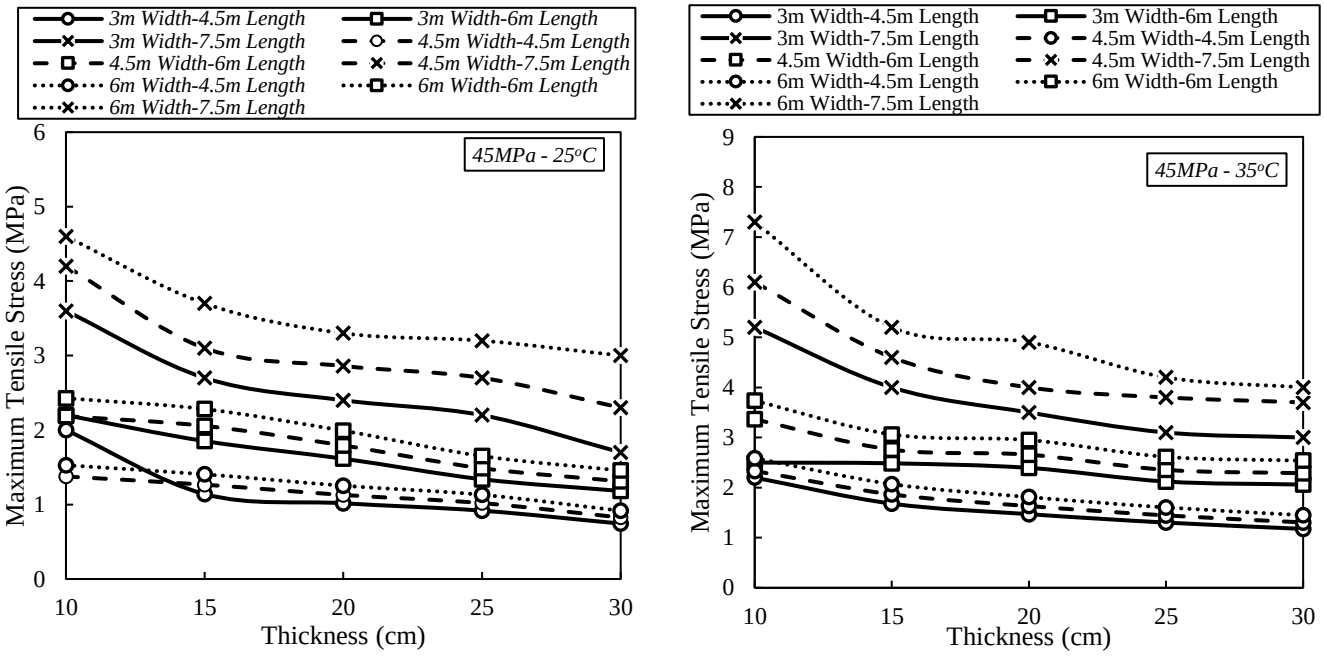

Figure 3.37: Simultaneous influence of slabs width, thickness, and length on 45MPa concrete compressive strength exposed to various thermal gradients a) 5ºC, b) 15ºC, c) 25ºC and d) 35ºC

Friction between the concrete slab and the underneath layer plays an important role in controling the thermal performance of rigid concrete airfield runways. Therefore, the influence of various contact friction including 1, 0.9, and 0.8 on the thermal performance of rigid concrete slabs is evaluated. There, Figure 3.38 shows the influence of friction on the maximum curling stress. Regarding these results. The maximal tensile stress generally increased as the heat gradient increased, as did the flexural moment. Additionally, nonlinear behavior in materials and the nonlinear performance of heat gradients throughout the length are increasingly frequent as the temperature rises. This issue highlights the need of considering the non-linear and plastic behavior of concrete when cracking and non-linear temperature gradient distribution is being taken into account. Low compressive strength concrete's peak tensile strength, up to 30 MPa, increased as slab length grew before decreasing as slab length grew over 6m. This may be related to how

effectively slabs accommodate vertical movement. The highest tensile strength of low compressive strength concrete, up to 30MPa, rose as slab length increased before declining as slab length increased past 6m. This might be connected to how well slabs handle horizontal displacement. Since the performance of long slabs longer than 6 m is that of a membrane shell, the behavior of shorter slabs is that of a plate-bending element. The highest tensile tension rises with an increase in slab length, though, when the slabs' compressive strength is greater than 35MPa. The change in long-length slab behavior from membrane shell behavior to plate-bending performance, which increased the tensile and curling loads in stiff concrete slabs, may be responsible for this behavior. Additionally, for slabs up to 6m in length, the maximum tensile stress was reduced by raising the concrete's compressive strength, while for slabs longer than 7.5m, the maximum tensile stress first marginally increased before being reduced by raising the concrete's compressive strength. Therefore, when the compressive strength was 35 MPa and the temperature gradient was taken into account as 35^{o}C, the maximum tensile stress in slabs of 7.5 m in length was found. On the other hand, increasing the amount of friction between the concrete layer and the underlying layer increases the tensile stress. This issue can be due to the creation of secondary stresses caused by limiting the movement of the slab due to thermal gradient and increasing tensile stress. Also, the effect of increasing friction on the increase of tensile stresses at high temperatures is more significant and this causes a significant increase of tensile stress at higher temperatures.

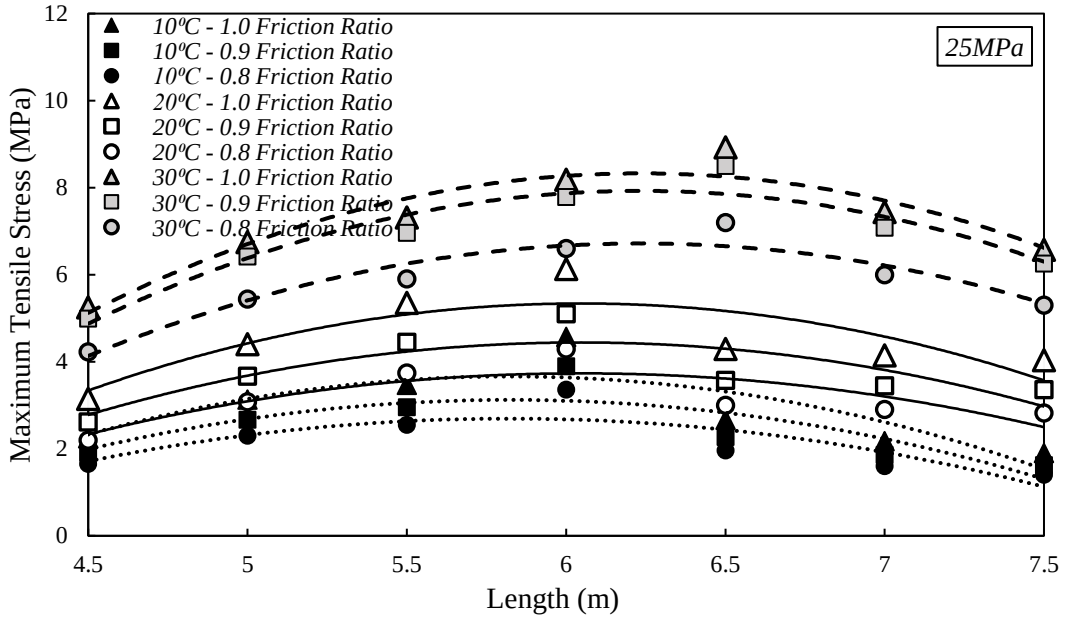
10ºC - 1.0 Friction Ratio
10ºC - 0.9 Friction Ratio
10ºC - 0.8 Friction Ratio
20ºC - 1.0 Friction Ratio
20ºC - 0.9 Friction Ratio
20ºC - 0.8 Friction Ratio
30ºC - 1.0 Friction Ratio
30ºC - 0.9 Friction Ratio
30ºC - 0.8 Friction Ratio
25MPa
Maximum Tensile Stress (MPa)
Length (m)
0
2
4
6
8
10
12
4.5
5
5.5
6
6.5
7
7.5

(a)

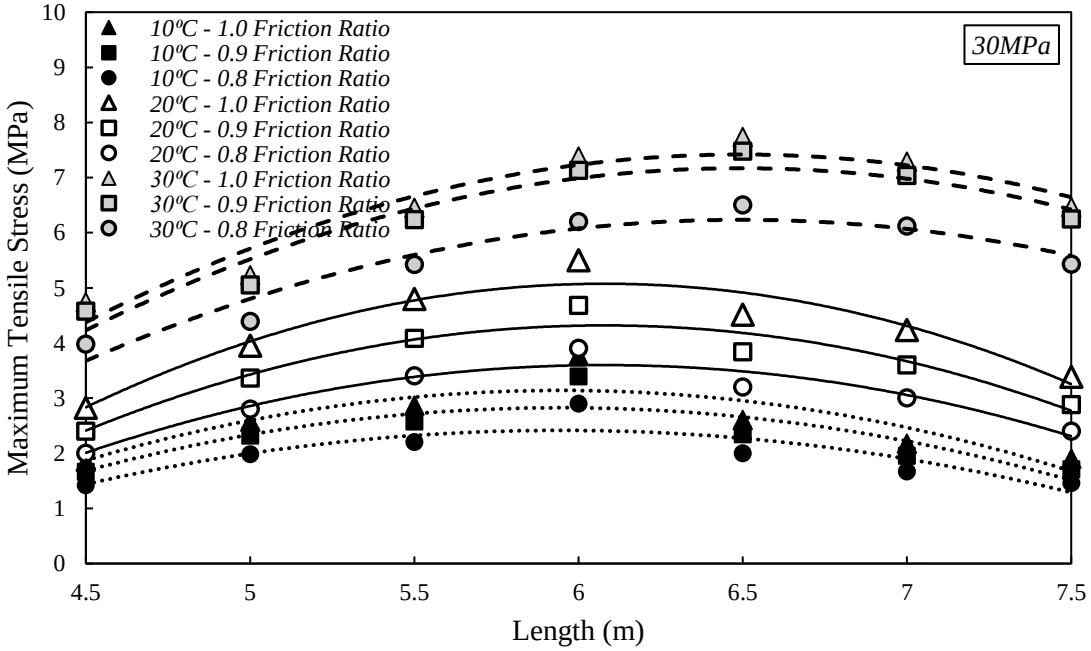
10ºC - 1.0 Friction Ratio
10ºC - 0.9 Friction Ratio
10ºC - 0.8 Friction Ratio
20ºC - 1.0 Friction Ratio
20ºC - 0.9 Friction Ratio
20ºC - 0.8 Friction Ratio
30ºC - 1.0 Friction Ratio
30ºC - 0.9 Friction Ratio
30ºC - 0.8 Friction Ratio
30MPa
Maximum Tensile Stress (MPa)
Length (m)
0
1
2
3
4
5
6
7
8
9
10
4.5
5
5.5
6
6.5
7
7.5

(b)

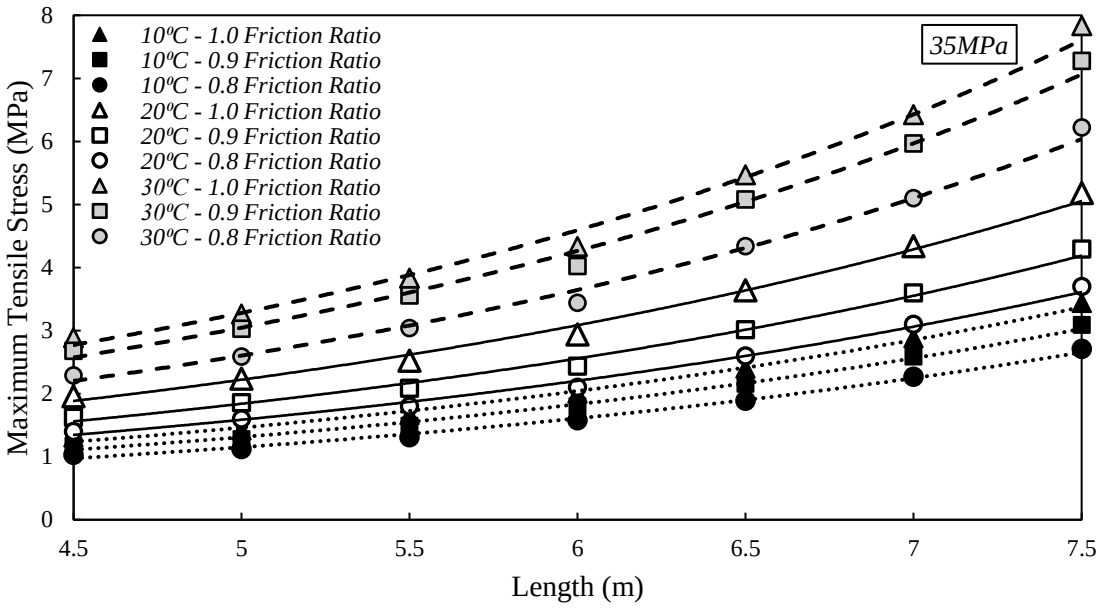
35MPa
10ºC - 1.0 Friction Ratio
10ºC - 0.9 Friction Ratio
10ºC - 0.8 Friction Ratio
20ºC - 1.0 Friction Ratio
20ºC - 0.9 Friction Ratio
20ºC - 0.8 Friction Ratio
30ºC - 1.0 Friction Ratio
30ºC - 0.9 Friction Ratio
30ºC - 0.8 Friction Ratio
Maximum Tensile Stress (MPa)
Length (m)
0
1
2
3
4
5
6
7
8
4.5
5
5.5
6
6.5
7
7.5

(c)

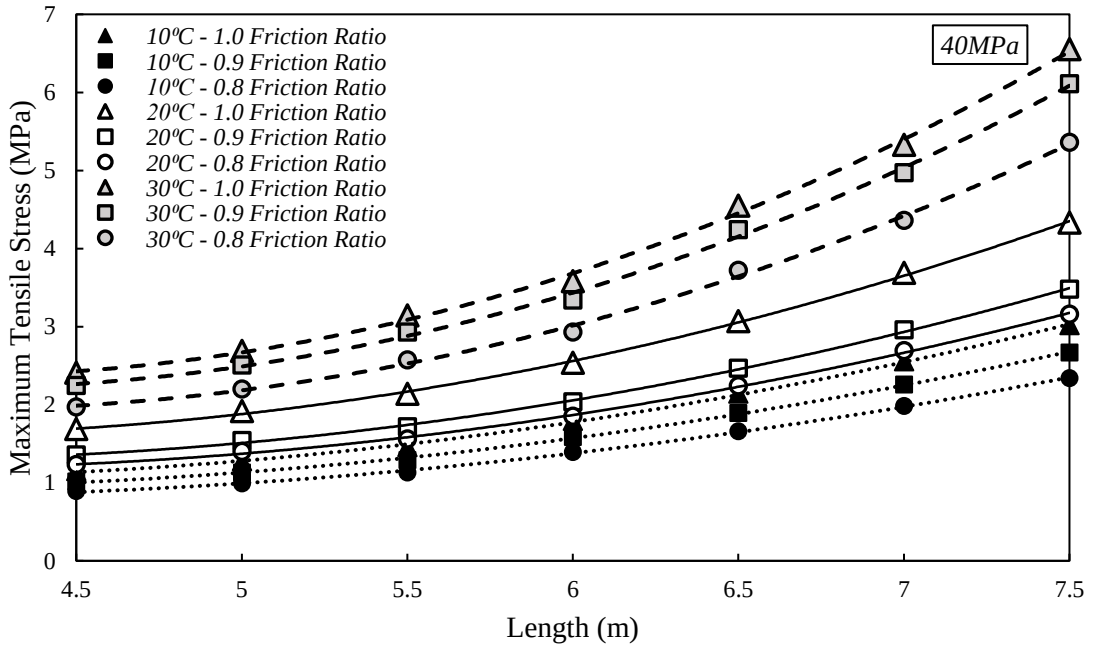
40MPa
10ºC - 1.0 Friction Ratio
10ºC - 0.9 Friction Ratio
10ºC - 0.8 Friction Ratio
20ºC - 1.0 Friction Ratio
20ºC - 0.9 Friction Ratio
20ºC - 0.8 Friction Ratio
30ºC - 1.0 Friction Ratio
30ºC - 0.9 Friction Ratio
30ºC - 0.8 Friction Ratio
Maximum Tensile Stress (MPa)
Length (m)
0
1
2
3
4
5
6
7
4.5
5
5.5
6
6.5
7
7.5

(d)

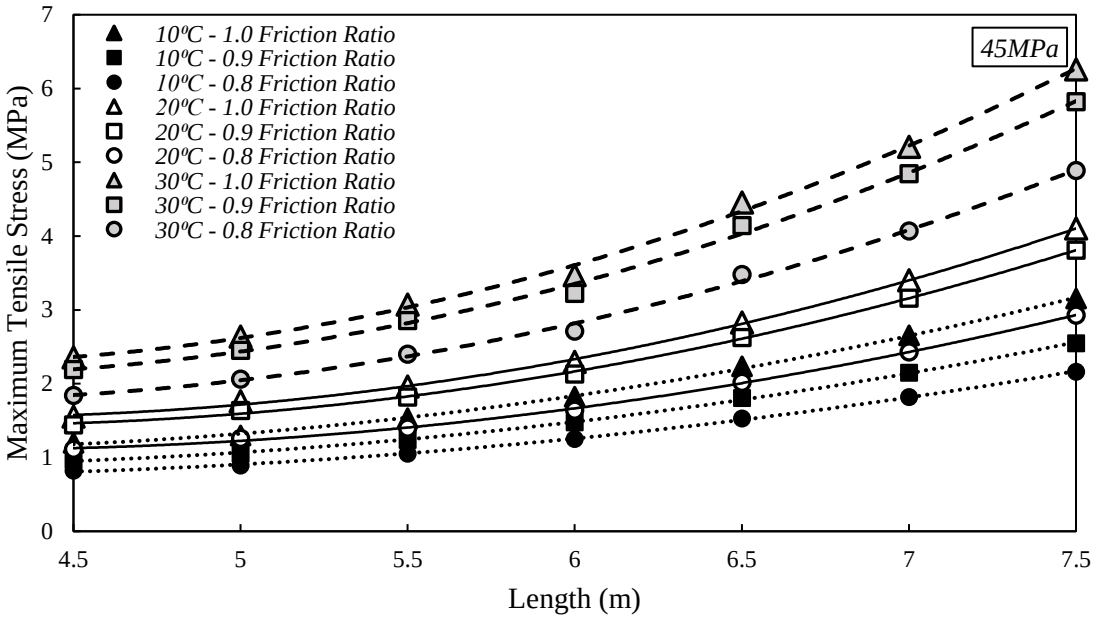

(e)

Figure 3.38: Influence of friction ratio on the maximum tensile stress of slabs due to curling with various slab lengths a) 25MPa, b) 30MPa, c) 35MPa, d) 40MPa and e) 45MPa

Furthermore, Figure 3.39 provides the influence of friction ratio on the maximum out-of-plane deformation versus slabs' length considering the thermal gradient and compressive strength of rigid concrete slabs. According to this figure, With the increase of the thermal gradient, the out-of-plane deformation of the slabs increases, and this issue is more evident in slabs with a length of 6m. Also, the increase in the friction ratio between the concrete slab layer and its underlying layer has caused a decrease in the change of the lateral stress of the slab. This issue can be due to the reduction of the in-plane changes of the slabs and also the connection between the two layers.

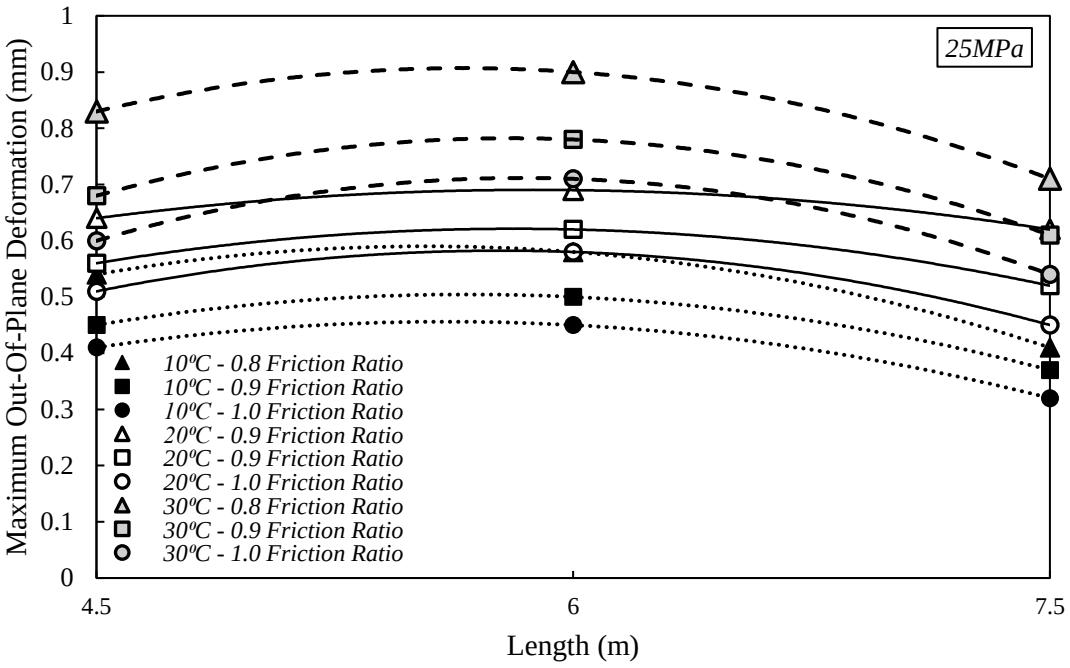
25MPa
Maximum Out-Of-Plane Deformation (mm)
Length (m)
10ºC - 0.8 Friction Ratio
10ºC - 0.9 Friction Ratio
10ºC - 1.0 Friction Ratio
20ºC - 0.9 Friction Ratio
20ºC - 0.9 Friction Ratio
20ºC - 1.0 Friction Ratio
30ºC - 0.8 Friction Ratio
30ºC - 0.9 Friction Ratio
30ºC - 1.0 Friction Ratio

(a)

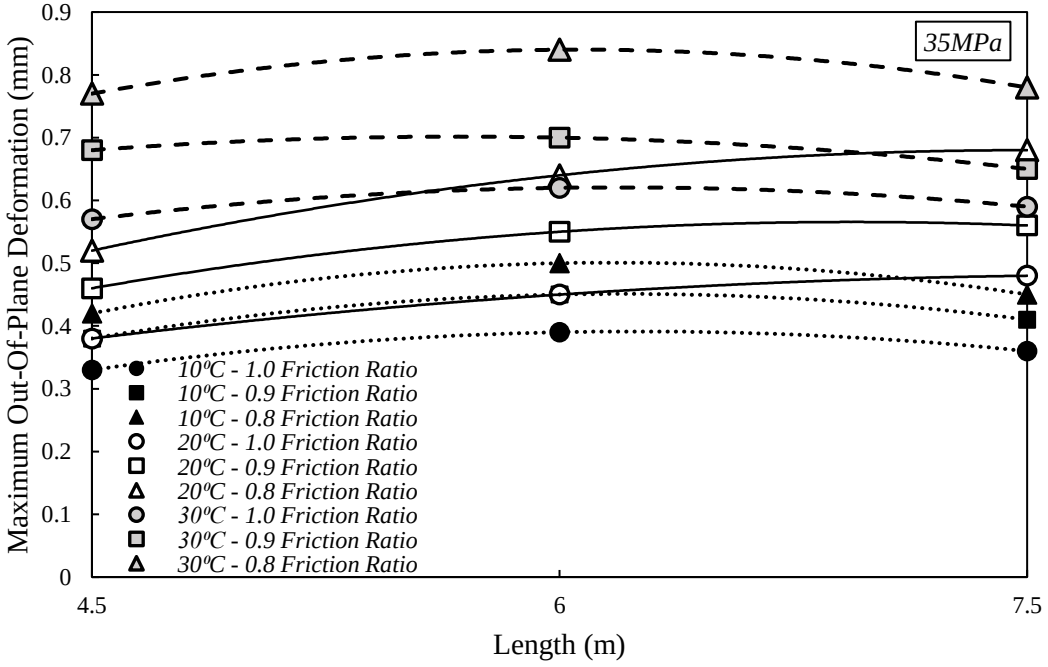
35MPa
Maximum Out-Of-Plane Deformation (mm)
Length (m)
10ºC - 1.0 Friction Ratio
10ºC - 0.9 Friction Ratio
10ºC - 0.8 Friction Ratio
20ºC - 1.0 Friction Ratio
20ºC - 0.9 Friction Ratio
20ºC - 0.8 Friction Ratio
30ºC - 1.0 Friction Ratio
30ºC - 0.9 Friction Ratio
30ºC - 0.8 Friction Ratio

(b)

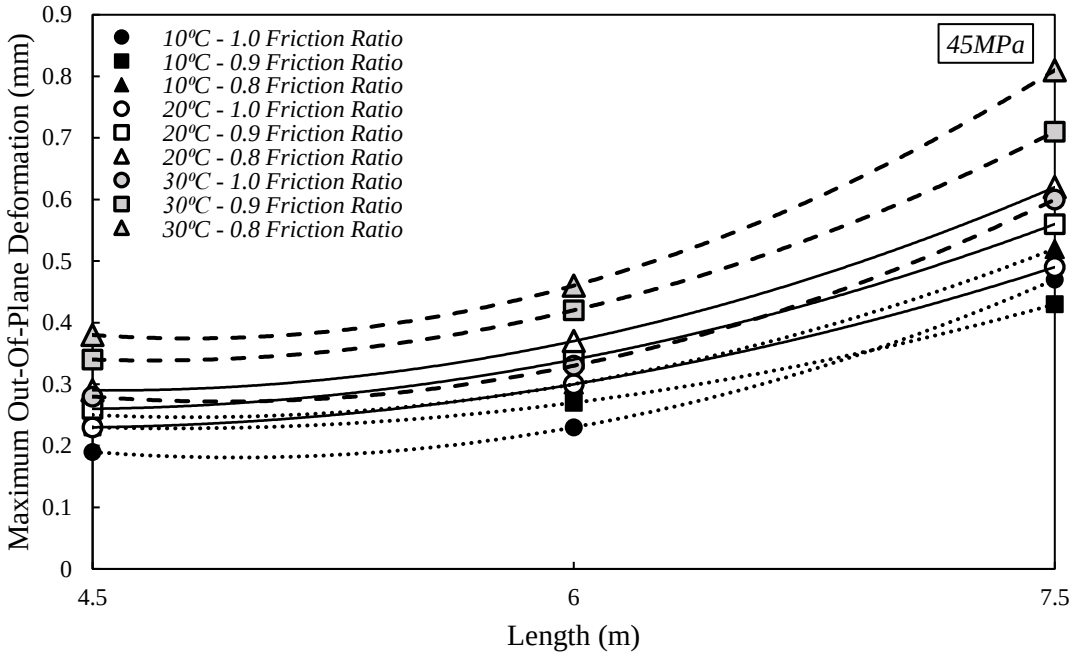

(c)

Figure 3.39: Influence of friction ratio on the maximum out-of-plane deformation of slabs due to curling with various slab lengths a) 25MPa, b) 35MPa, and c) 45MPa

As presented above, geometric characteristics play an important role in controling the thermal performance of rigid concrete airfield runways. For this aim, the influence of saw-cutting depth is measured as an important feature. The obtained results are illustrated in Figure 3.40 for notch depth of 4cm, 8cm, and 12cm slab with 25cm thickness. As the heat gradient grew, so did the flexural moment and the peak tensile stress in general. Additionally, as the temperature rises, nonlinear behavior in materials and the nonlinear performance of heat gradients throughout the length become more common. This problem serves as a reminder of the need of taking concrete's non-linear and plastic behavior into consideration when addressing non-linear temperature gradient distribution and cracking. Compressive strength is the low peak tensile strength of concrete, which may reach 30 MPa, which rose as slab length climbed before declining as slab length increased above 6m. This could have something to do with how well slabs can handle vertical movement.

Low compressive strength concrete's peak tensile strength, up to 30 MPa, increased as slab length grew before decreasing as slab length grew over 6 m. However, when the slabs' compressive strength is greater than 35MPa, the greatest tensile tension increases with slab length. This behavior may be related to the long-length slab's transition from membrane shell behavior to plate-bending performance, which raised the tensile and curling loads in stiff concrete slabs. Additionally, the maximum tensile stress was first somewhat raised before being decreased by increasing the concrete's compressive strength for slabs up to 6m in length. However, for slabs longer than 7.5m, the maximum tensile stress was first slightly increased before being lowered by increasing the concrete's compressive strength. Conversely, increasing the notch depth increases the tensile stress caused by the thermal gradient. This effect is more evident in higher temperature changes (30^{o}C in this study). Therefore, in locations where temperature changes during the day and night are more, it is recommended to use saw-cutting with a lower depth. This issue can be due to the reduction of the influence of the adjacent slabs due to the increase in the depth of the notch, which causes out-of-plane deformation and, as a result, more tensile stress in the slabs. Also, in concretes with a strength higher than 30 MPa, the effect of increasing the crack depth on the tensile stress of slabs is more significant with increasing slab length. As a result, it is always recommended to use a slab with a shorter length and higher concrete strength, as well as a lower crack depth. Additionally, It follows that a significant improvement in lateral out-of-plane deformation and generally the thermal and curling behaviors of rigid concrete airfield runways could be expected in short-length slabs with concurrent increases in concrete compressive strength.

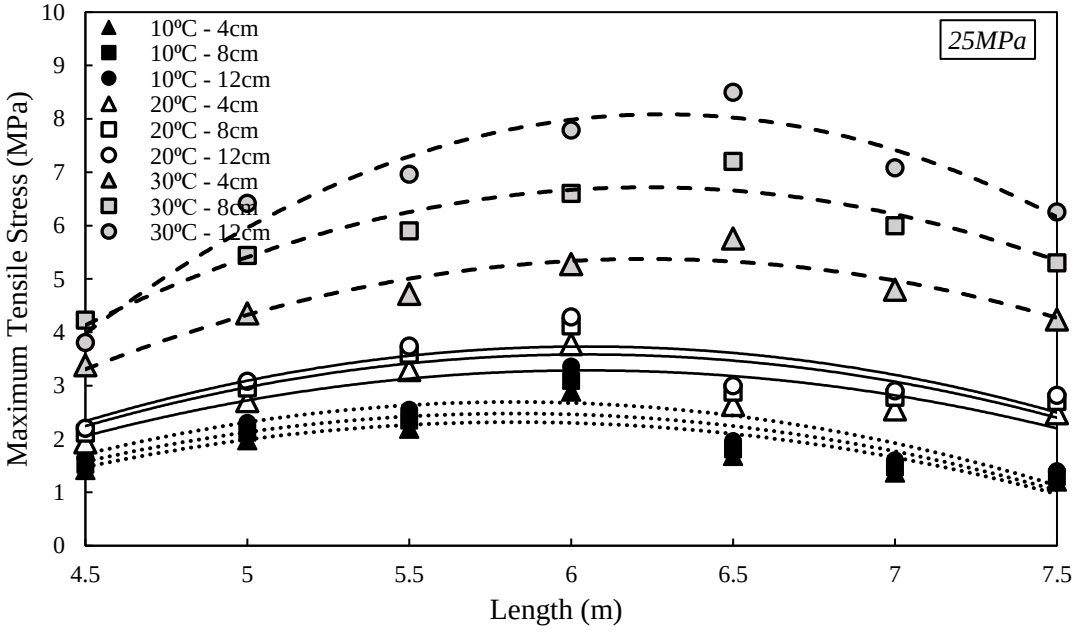
10ºC - 4cm
10ºC - 8cm
10ºC - 12cm
20ºC - 4cm
20ºC - 8cm
20ºC - 12cm
30ºC - 4cm
30ºC - 8cm
30ºC - 12cm
25MPa
Maximum Tensile Stress (MPa)
Length (m)
0
1
2
3
4
5
6
7
8
9
10
4.5
5
5.5
6
6.5
7
7.5

(a)

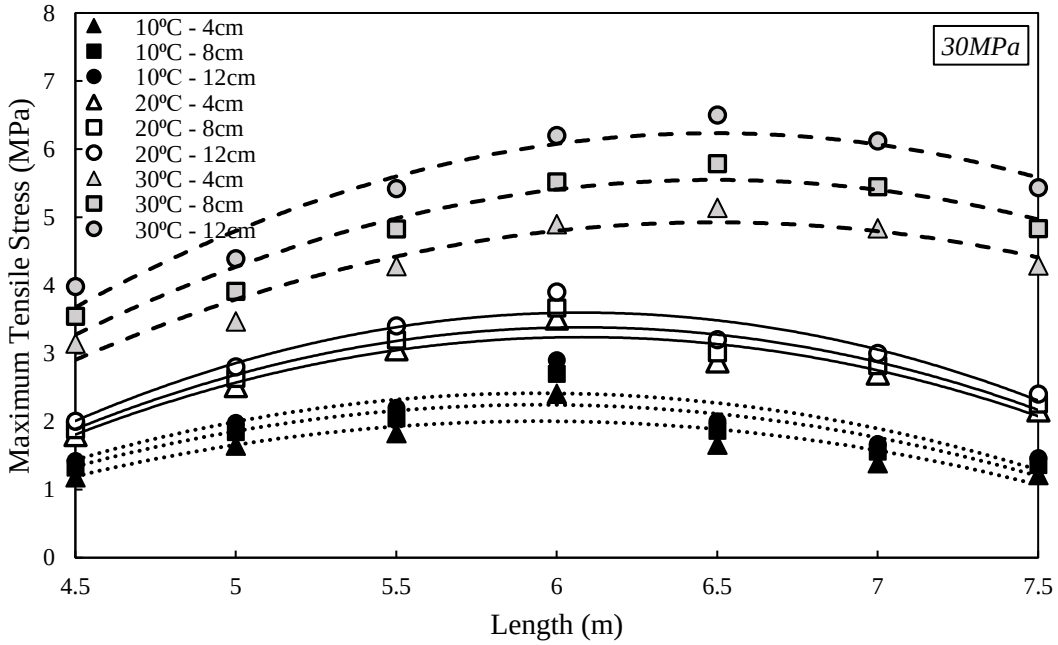
10ºC - 4cm
10ºC - 8cm
10ºC - 12cm
20ºC - 4cm
20ºC - 8cm
20ºC - 12cm
30ºC - 4cm
30ºC - 8cm
30ºC - 12cm
30MPa
Maximum Tensile Stress (MPa)
Length (m)
0
1
2
3
4
5
6
7
8
4.5
5
5.5
6
6.5
7
7.5

(b)

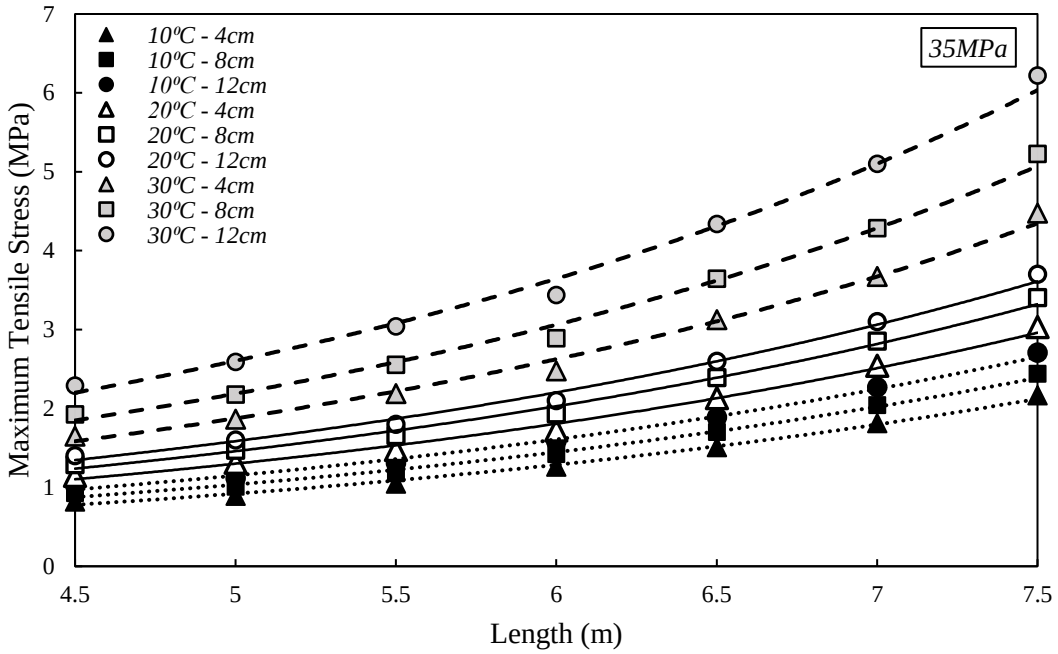
10ºC - 4cm
10ºC - 8cm
10ºC - 12cm
20ºC - 4cm
20ºC - 8cm
20ºC - 12cm
30ºC - 4cm
30ºC - 8cm
30ºC - 12cm
35MPa
Maximum Tensile Stress (MPa)
Length (m)
0
1
2
3
4
5
6
7
4.5
5
5.5
6
6.5
7
7.5

(c)

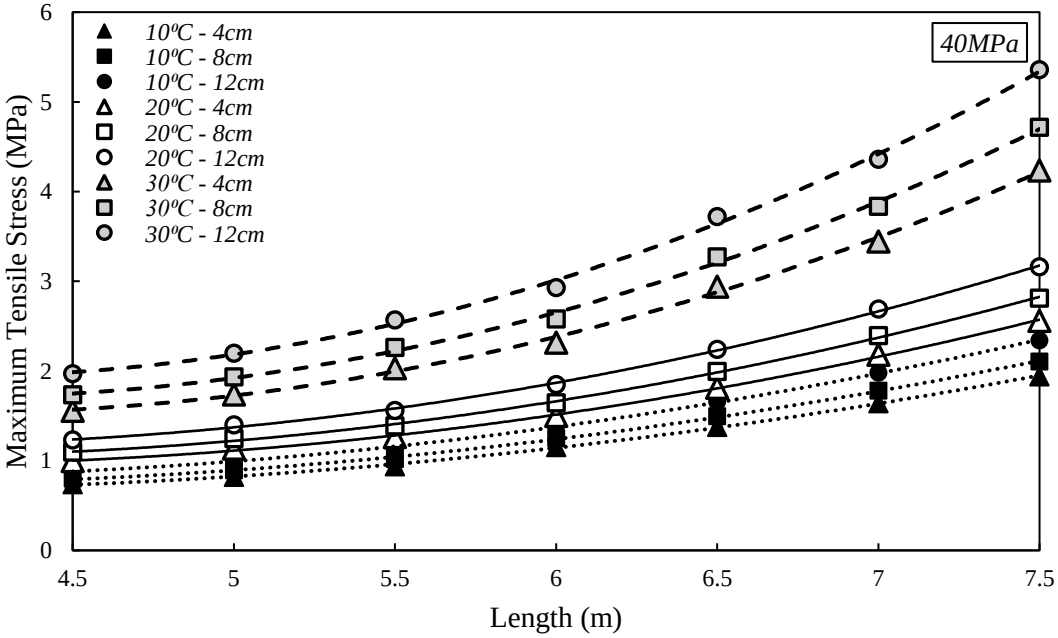
10ºC - 4cm
10ºC - 8cm
10ºC - 12cm
20ºC - 4cm
20ºC - 8cm
20ºC - 12cm
30ºC - 4cm
30ºC - 8cm
30ºC - 12cm
40MPa
Maximum Tensile Stress (MPa)
Length (m)
0
1
2
3
4
5
6
4.5
5
5.5
6
6.5
7
7.5

(d)

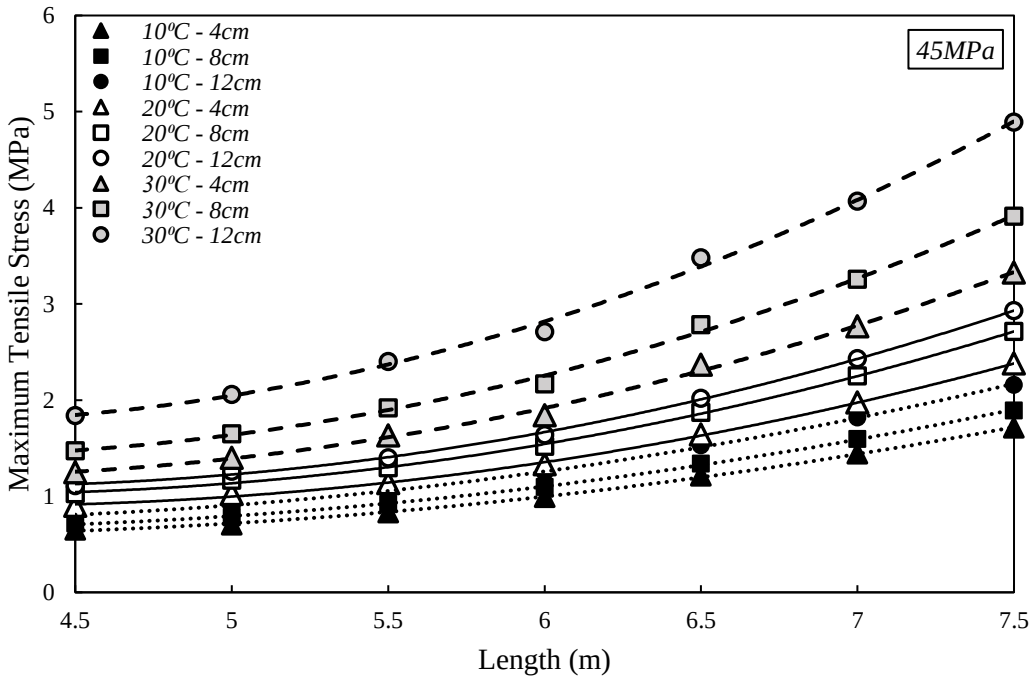

(e)

Figure 3.40: Influence of notch depth on the maximum tensile stress of slabs due to curling with various slab lengths a) 25MPa, b) 30MPa, c) 35MPa, d) 40MPa and e) 45MPa

Furthermore, Figure 3.39 provides the effect of saw-cutting depth on the maximum out-of-plane deformation versus slabs' length considering the thermal gradient and compressive strength of rigid concrete slabs. Regarding these results, with the increase of the thermal gradient, the out-of-plane deformation of the slabs increases, and this issue is more evident in slabs with a length of 6m. Also, The increase in the depth of the gap due to the reduction of the influence of the adjacent slabs on each other and also the increase of tensile stresses caused by the thermal gradient increases the out-of-plane deformation in the slabs. The highest deformation, however, rises with slab length when the slabs' compressive strength is larger than 35MPa. The change of the long-length slab from membrane shell behavior to plate-bending performance, which increased the tensile and curling stresses in slabs, may be the cause of this behavior. Additionally, for slabs up to 6m in length, the maximum lateral deformation was first slightly increased before being reduced by

boosting the concrete's compressive strength. The maximum out-of-plane deformation was, however, first slightly raised for slabs longer than 7.5m before being reduced by raising the concrete's compressive strength.

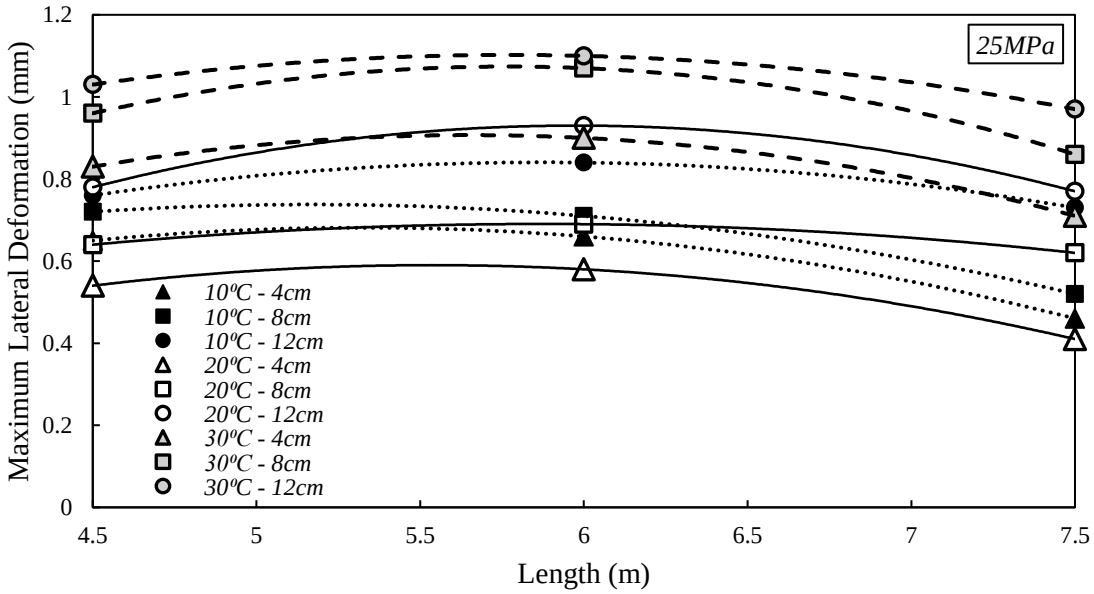

(a)

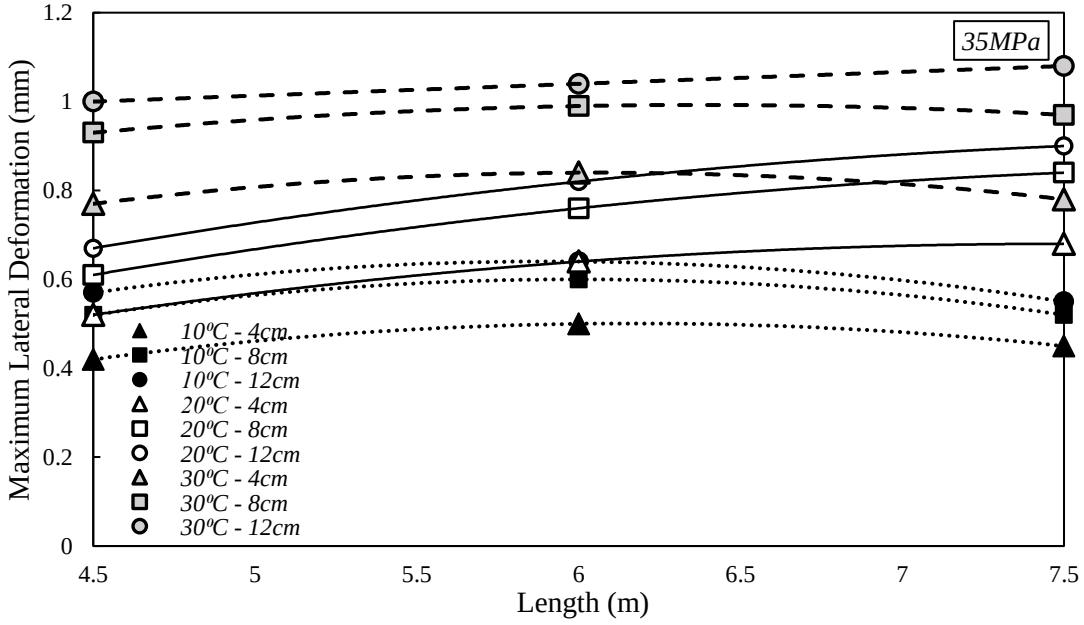

(b)

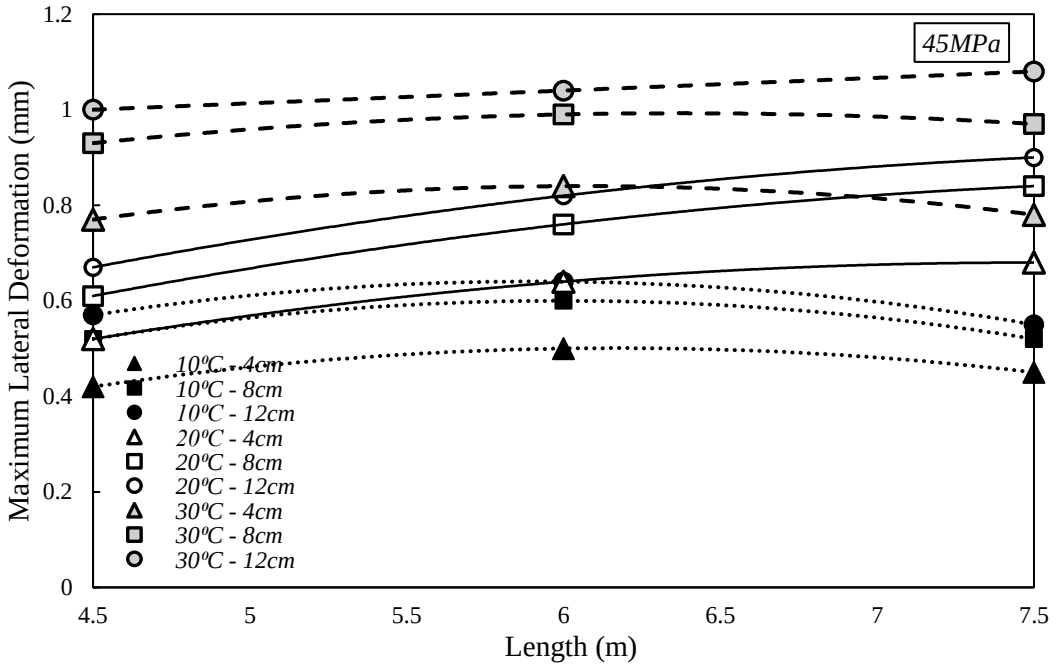

(c)

Figure 3.41: Influence of notch depth on the maximum out-of-plane deformation of slabs due to curling with various slab lengths a) 25MPa, b) 35MPa, and c) 45MPa

3.8. SUMMARY & CONNECTION WITH THE SUBSEQUENT CHAPTER

This chapter provided a comprehensive evaluation of the influence of various variables including material properties, geometric characteristics, environmental circumstances, and boundary conditions, on the thermal and curling stresses of rigid concrete slabs. The results of this chapter provide a comprehensive decision-making strategy for in-field construction and rigid concrete airfield runways design. But geometrical and material characteristics controling is not an affordable way to control the project and construction budget. So, additional techniques should be taken into consideration to increase the strength of rigid concrete airfield runways accounting for the lower construction cost. For this aim, the next chapter will provide a solution to reduce the material consumption and geometric dimensions with no reduction in slab strength and curling and

thermal performance which leads to a significant reduction in the project cost. For this aim, polypropylene fibers (PF) will introduce as a solution considering the effect of various important material and geometric characteristics. As a result, Figure 3.42 provides a connection with the subsequent chapter overview.

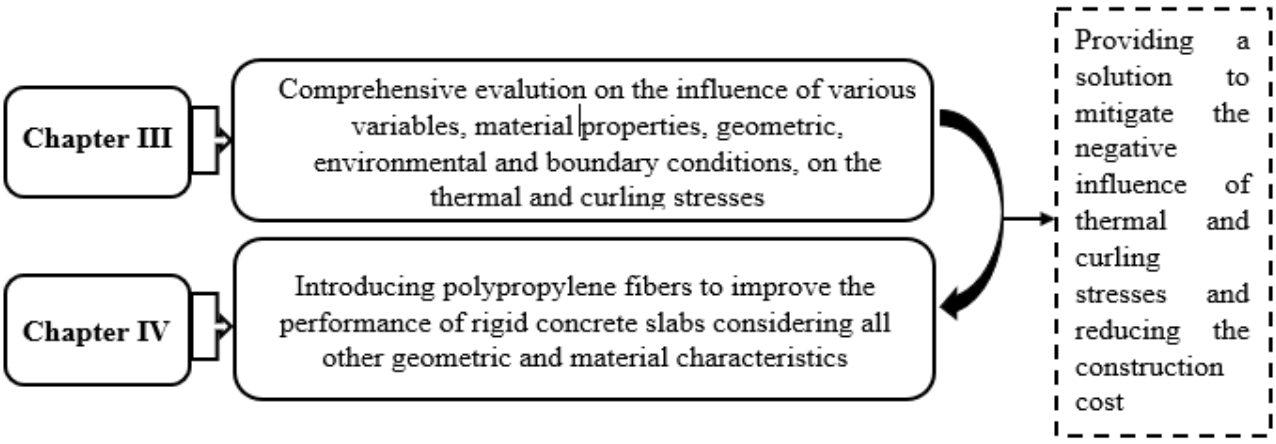

Figure 3.42: Overview of the connection between Chapters III and IV

CHAPTER IV

ADVANTAGES OF POLYPROPYLENE FIBERS INCORPORATION

4.1. INTRODUCTION

This chapter's main goal is to provide a comprehensive evaluation of the effect of PF to mitigate the negative influence of thermal gradient on the structural responses of rigid concrete airfield runways. Also, this chapter provides a novel simulation for fibers-reinforced concrete considering the mechanical properties obtained using the laboratory tests. The preceding section of this chapter is followed by finite element method parameters, boundary conditions, and verification of the assessment of structural impacts and damages imparted on rigid concrete slabs reinforced by PF as a result of the temperature gradient.

4.1.1. Organization of the Chapter

This chapter consists of five main sections. Subsequent to the introductory section, Section 2 provides information associated with the positive influence of PF on improving the mechanical characteristics of concrete and reducing the negative influence of thermal gradient in controlling the curling stress. Section 3 discusses the methodologies to simulate fibers-reinforced rigid concrete slabs in finite element method software and used experimental results to reach this goal. Then, the main results of this study are presented and discussed to show the effect of PF as well as geometric parameters on the thermal and curling behaviors of rigid concrete slabs. Finally, A summary of this section will be provided so that its connection with the subsequent section and also the importance of the subsequent section can be clearly identified.

4.2. ADVANTAGES OF POLYPROPYLENE FIBERS INCORPORATION

PF is produced from monomeric C3H6 which is resistant to chemicals. Their hydrophobic surface is not wetted by the cement paste, and it also aids to avoid crushing the PF during mixing. PF have a bridging role in the concrete by retaining distinct particles near to one another, which enhances the material's mechanical qualities like compressive and tensile strengths. This sort of fiber is produced either by extruding plastic film through a rectangular negative or by drawing wire with a circular cross-section (Sastry et al. 2011; Joshaghani et al. 2020; Chen et al. 2012). Additionally, PF can be applied to concrete elements to give them various characteristics. As a result, several investigations on the impact of PF on the physical and mechanical characteristics of concrete members have been conducted. The fibers improve cement and aggregate continuity, which enhances some mechanical characteristics of concrete and also reduces shrinkage cracks (Duan et al. 2016). Therefore, PF can increase the concrete's tensile and compressive strengths as well as impact resistance, toughness, ductility, and deformability. To create concrete members such as pavement slabs, piles, restricted concrete members, and shotcrete in tunnels, channels, and reservoirs, which can be added to the mix composition (Naskar and Kumar, 2016). In recent decades, different types of fibers have widely been utilized by researchers Sanchez and Sobolev, 2010; Rashidian-Dezfouli et al., 2018; Duan et al. 2016; Naskar and Chakraborty, 2016; Rattanasak et al. 2010; Yang et al. 2015). In this regard, Ganesh and Muthukannan (2020) studied the characteristics of fiber-reinforced concrete and showed that energy absorption was enhanced, and brittleness was considerably reduced when fibers were added to concrete mixes.

Both fresh- and hardened-state characteristics of PF-reinforced concrete were assessed by Moradikhou et al. (2020). Findings showed that the incorporation of PF considerably increased

the compressive and tensile strengths as well as the concrete resistance to a high thermal gradient. According to Liu et al analysis, the mechanical characteristics and impact resistance of concrete reinforced with fibers (Yoo et al. 2020; Karimi Pour et al. 2023a; Karimi Pour et al. 2023b) were significantly enhanced by the addition of ceramic ball aggregates and fibers. They demonstrated that increasing the volume and length of the fibers allowed con concrete to achieve its maximum compressive and cracking tensile strengths. However, the addition of fibers made the concrete less workable. This is due to the fact that a lateral expansion takes place in the center of the specimen's height when it is subjected to compressive stress. The bridging function of PF improved the compressive performance of PF-reinforced concrete by increasing the tensile strength and increasing the cohesion between concrete paste and aggregates. In a previous study, a similar statement regarding the bridging mechanism of fiber incorporation in enhancing the compressive strength of concrete was made (Karimi Pour et al. 2022a). Besides, Wu et al. (2016) and Yoo et al. (2020) claimed that the main factor improving the compressive strength of concrete when fibers were added was the higher modulus of elasticity of PF compared to concrete paste because increasing their contents led to a reduction in the space between them, which constrained the crack propagation in the specimens. Therefore, as seen in Figure 4.1, increased stress transfers along the cracks result in an increase in concrete compressive strength capacity. Evaluations of the plastic shrinkage and permeability of PF-reinforced concrete were conducted by Islam and Gupta (2016). The PF (aspect ratio 300) was employed in that investigation in several ratios, including 0.10, 0.15, 0.2, 0.25, and 0.3% by volume. While the tensile strength improved by 39% with the same fiber content as compared to the plain concrete, the addition of 0.1% PF resulted in a modest (2%) decrease in compressive strength. According to the experimental results, plastic shrinkage cracks in concrete were decreased by 50–99% compared to ordinary concrete when 0.1-0.3% of PF was added.

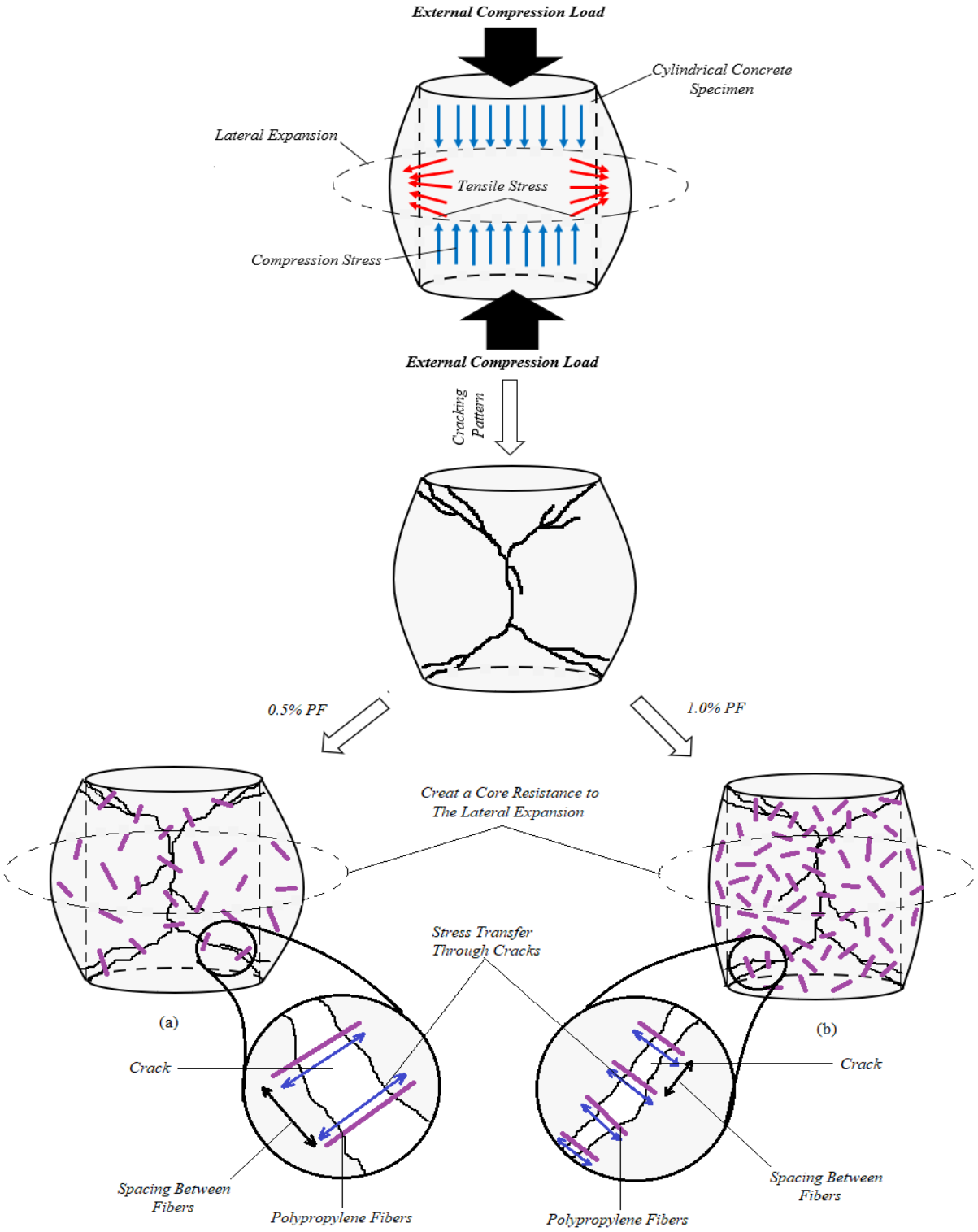

Figure 4.1: Graphic Drawing of the beneficial effect of a) 0.5% and b) 1% PF on the compressive strength of concrete

Furthermore, Eidan et al. (2019) examined the mechanical characteristics of PF-reinforced concrete that remained after heating in different research. In that study, experimental findings on the residual mechanical characteristics of PF-reinforced specimens subjected to high temperatures are presented, including compressive and tensile strengths, elastic modulus, and cracking modes. After being exposed to various heating temperatures and being cooled down, seven series of concrete mixtures, comprising six series of PF-reinforced concrete and one plain concrete specimen, were examined. The results showed that PF-reinforced concrete performs better when exposed to high temperatures than normal concrete behaves (Karimi Pour 2022b). Müller et al. (2019) evaluated the failure behavior of PF-reinforced concrete exposed to high temperatures in a different experiment to ascertain the impact of temperature on the functionality of concrete containing PF. The experimental study's major goals were to examine the material's actual strength in a fire scenario and the validity of Schmidt's rebound hammer test when used to test concrete at high temperatures. It specifically refers to 800°C temperature-tested PF-reinforced and plain concrete. Experiments showed that the incorporation of PF significantly improved the non-destructive strength of concrete exposed to high temperatures.

One of the most important characteristics to consider when evaluating concrete's performance under fast loading is impact resistance which could be associated with the effect of traffic loads. The weight drop test is typically used for this purpose to evaluate the impact resistance of concrete (Badr et al. 2006). The findings of experiments on high-strength PF-reinforced concrete demonstrated that the number of permitted impacts varies significantly. According to earlier research, adding 1% by volume of PF to concrete resulted in the best energy absorption (Badr et al. 2006; Marar and Eren, 2001, Karimi Pour 2022). Conversely, concrete loses strength as the temperature rises. The major cause of decreased concrete strength at high temperatures is an increase in internal pressure (Qadi et al. 2011).

The surfaces of the aggregates are scaling and separating from the concrete, and water vapor cannot escape the concrete, which results in increasing internal pressure. The effects of high temperatures on the behavior of PF-reinforced concrete have been the subject of several investigations since the 1980s. These investigations demonstrated that concrete's scaling potential rises with temperature (Metin 2006; Castillo and Durrani, 1990; Karimi Pour et al. 2022c). The characteristics of concrete dramatically alter after being exposed to fire, according to studies on the load-displacement curves of high-strength concrete specimens under direct fire (Felicetti et al. 1996). Therefore, it is crucial to improve concrete's performance in high-temperature environments. The United States Standard and Technology Association, therefore, looked at how temperatures affected concrete's mechanical characteristics. They came to the conclusion that concrete's mechanical characteristics significantly decreased as the temperature rose.

The mechanical characteristics and physical properties of concrete under the influence of temperature, including impact, compressive, and tensile stresses have been the subject of a wide variety of studies. According to the JSCE's second-class rating standard, the workability of PF-reinforced concrete has been evaluated using three classes: fresh concrete flowability, filling ability, and segregation resistance. The following parameters were determined after the sample had been cured for 28 days in terms of MP of SCC: compressive and tensile strengths, elastic moduli, and flexural resistance. A method to reduce spalling caused by high temperatures in concrete was presented by Lura et al. This method involved adding PF while the concrete was being mixed. According to the findings, adding PF to concrete mixtures that have been pre-stressed can aid to decrease spalling. Besides, the impact of specimen shape and fiber content on the remaining strength of concrete subjected to evaluated temperatures ranging from 200^{o}C to 600^{o}C was examined by Al-Qadi et al. (2011). According to the aforementioned study, due to the larger losses in compressive strength in cubes, the

thermal shock caused by air cooling cycles caused more severe damage to concrete. The residual strength and fracture energy of concrete exposed to the thermal shock brought on by air cooling from high temperatures of up to 600^{o}C to room temperature can also be improved by PF. In this regard, Yahaghi et al. (2016) measured the impact resistance of concrete reinforced by PPF. The reproduction of a low-velocity projectile effect on slab samples was obtained by considering two types of steel balls (weighing 0.38 and 1.25 kg), with a drop height of 360 mm, using a self-fabricated drop-weight impact test rig. Twelve cube samples (100 mm) were used in total. The result is from cutting three cube specimens per each mix into 4, 3, and 2 cm thicknesses. The PF volume fraction, impact resistance, and fracture resistance ratio all showed a clear linear connection (Karimi Pour et al. 2021a; Gencel et al. 2021; Sutcu et al. 2022). Also, the impact resistance was significantly improved by increasing the thickness, however, the impact was more pronounced for ultimate failure crack resistance than for initial crack resistance.

Additionally, employing PF improved the ultimate flexural strength of concrete, and this characteristic was further improved with an increase in the PF concentration which could play an effective role to mitigate the negative influence of curling stress. PF's bridging function reduces the spacing of cracks and maintains particles together in the matrix (Karimi Pour et al. 2021b; Ghalehnovi et al. 2021). Because the top and bottom cross-sectional portions of concrete slabs undergo compressive and tensile stresses when it is exposed to a flexural load, the flexural strength was enhanced by enhancing the compressive and splitting tensile strengths of concrete, as shown in Figure 4.2. Concerning the flexural behavior of PF-reinforced concrete, similar findings were published by Sastry et al. (2021). They found that the 28-day flexural strength of concrete could be improved by roughly 32% with the addition of 5% PF.

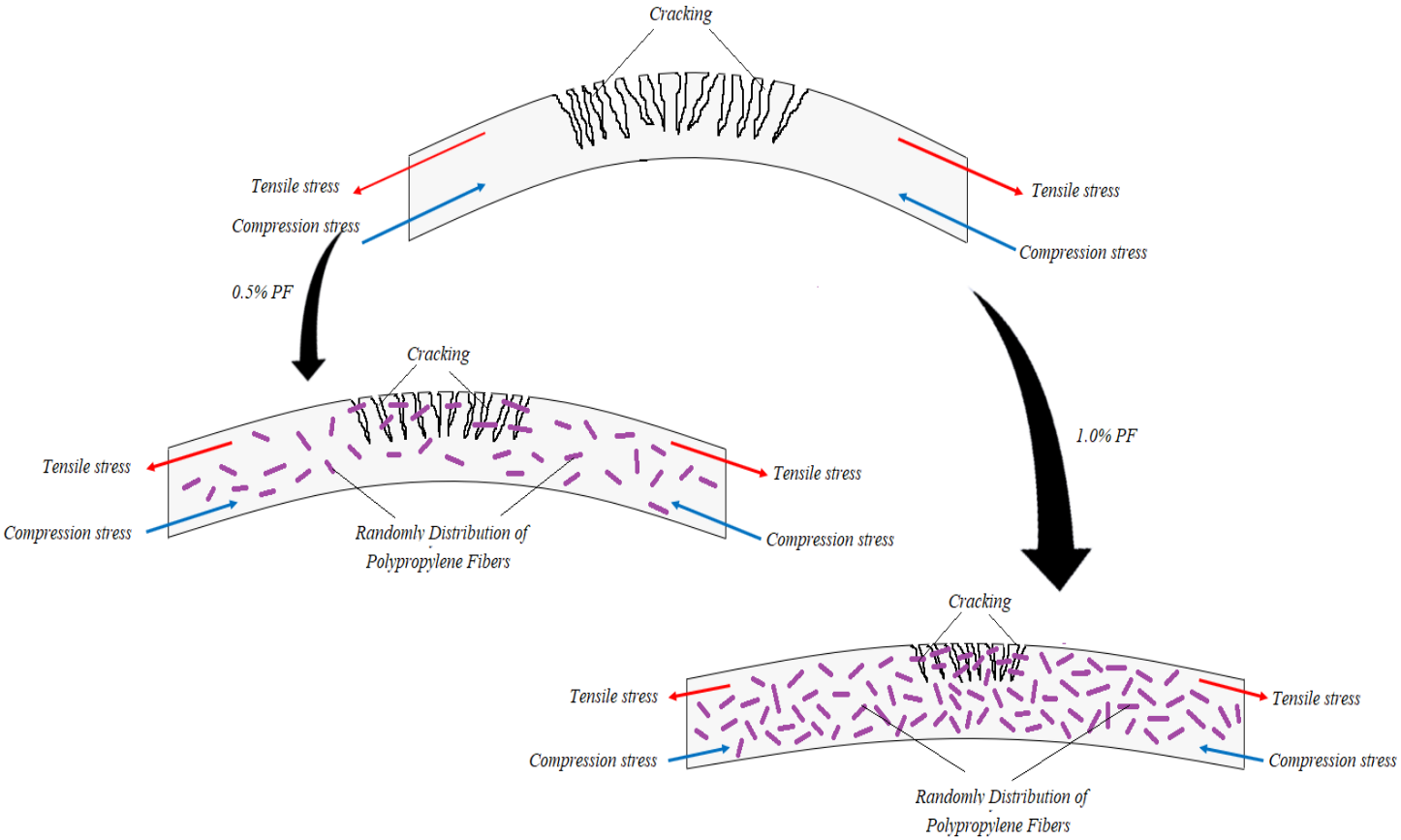

Figure 4.2: Graphic Drawing of the beneficial effect of a) 0.5% and b) 1% PF on the flexural strength of concrete

According to the literature review, PF incorporation has played a significant role in improving the mechanical and thermal characteristics of concrete. Therefore, adding PF could be beneficial in improving the curling and thermal behaviors of rigid concrete slabs. As a result, in this chapter, the effect of PF, in addition to other variables discussed in the previous chapter, is studied.

4.3. MATERIALS CHARACTERISTICS FOR SIMULATION

In this study, two different types of concrete were used and their influence on the thermal and curling stresses of rigid concrete slabs was measured: plain and fibers reinforced concrete. to

mitigate the negative effects of the temperature gradient, polypropylene fibers were incorporated into the numerical simulations. Fibers are randomly distributed in a concrete matrix. To model the influence of fibers, two different strategies could be followed: 1) simulation of the exact random distribution of fibers considering their mechanical characteristics and 2) simulation of the mechanical characteristics of concrete reinforced by fibers. For the first simulation methodology, the simulation of the exact random distribution of fibers considering their mechanical characteristics, Fang and Zhang (2013) performed a comprehensive finite element simulation. However, the accuracy of their simulation for polypropylene fibers was highly accurate but the exact simulation is so complex and needs a high space for computer calculation. Therefore, in this study, the influence of polypropylene fibers was performed considering the mechanical characteristics of concrete reinforced by fibers (second technique).

To reinforce concrete, polypropylene fibers were considered in this study for two fractions values in terms of weight of 0.5% and 1%, as shown in Figure 4.3. Also, the mechanical properties of polypropylene fibers are provided in Table 4.1.

Figure 4.3: An example of polypropylene fibers

Table 4.1: Mechanical properties of polypropylene fibers

Property	Value
Fiber type	White polypropylene fibers
Length (mm)	12
Diameter (mm)	0.034
Unit weight (kN/m^3)	9.1
Tensile strength (MPa)	500-700
Modulus of elasticity (MPa)	2800
Melting point (^oC)	160
Burning point (^oC)	590
Elongation at breakage (%)	25

To define the variables in software as discussed in the previous chapter, a laboratory stress-strain curve of fibers-reinforced concrete with different compressive strengths should be used. For this aim, the experimental results provided by previous studies have been utilized (Huang et al. 2020, Al-Rousan, 2018, Xu et al. 2018), Additionally, Xu et al. (2018) provided a model to develop the stress-strain curve for plain and polypropylene fibers reinforced concrete with various compressive strength and fibers fractions which were employed in this study to simulate rigid concrete slabs properties in the finite element method ABAQUS software. The stress-strain results for concrete with different compressive strengths and various polypropylene fiber fractions are presented in Figure 4.4. Regarding this figure, the stress of samples (compressive strength) improved with the use of polypropylene fibers which could result in improving the thermal and curling behaviors of rigid concrete slabs.

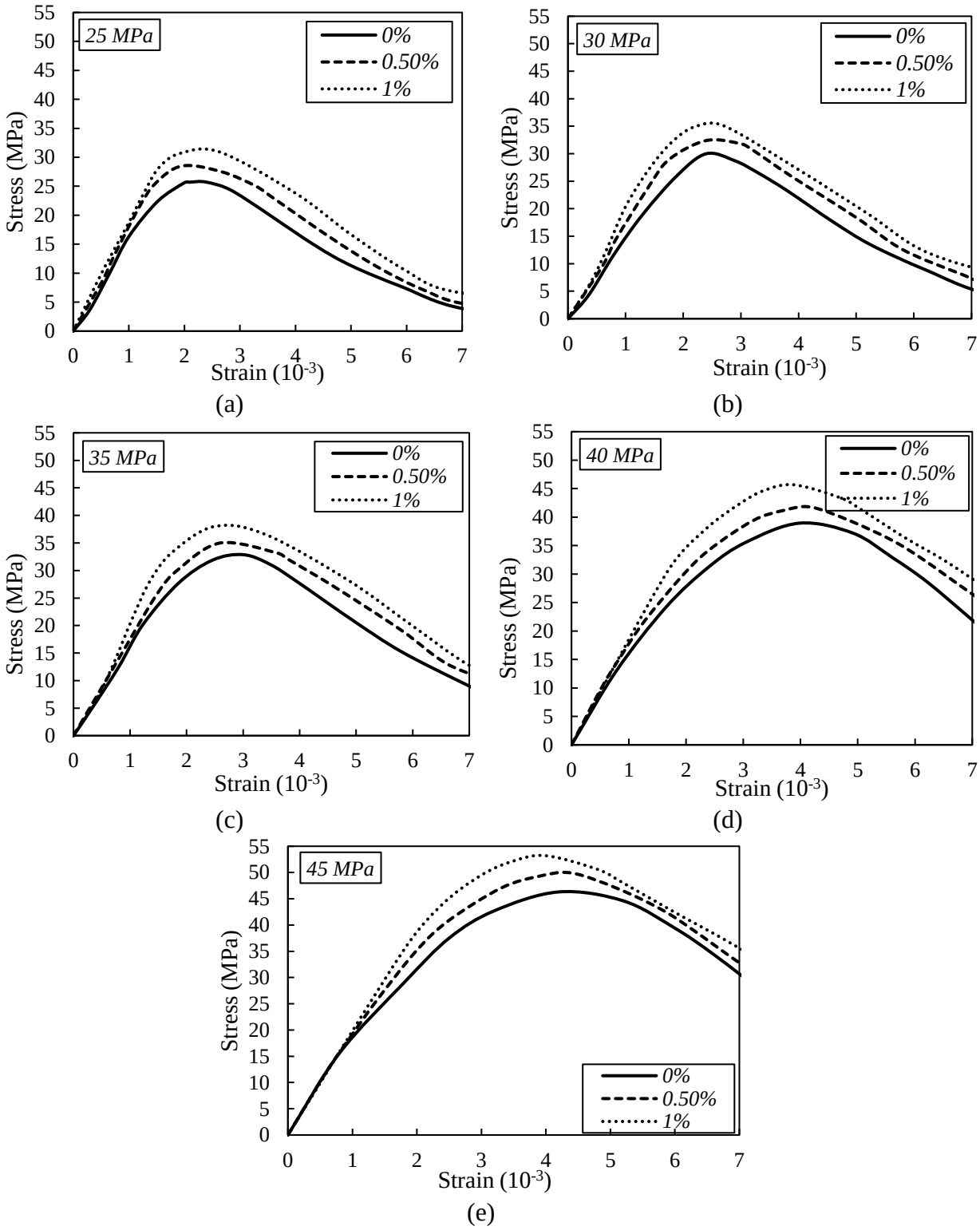

Figure 4.4: Stress-strain relationship of concrete having various polypropylene fibers fractions with compressive strength of a) 25 MPa, b) 30 MPa, c) 35 MPa, d) 40 MPa, and e) 45 MPa

4.4. NUMERICAL RESULTS AND DISCUSSIONS

The advanced modeling of curling and thermal behaviors of fiber-incorporated rigid concrete slabs is adequately supported by the FE numerical modeling algorithm created in this Chapter, allowing for accurate calculation of the generated fiber-incorporated rigid concrete slab responses under challenging thermal loading circumstances. The nonlinear thermal gradient, size impact, fiber incorporation effects, etc. are taken into account by the suggested numerical modeling method in this section. Along with the above-mentioned benefits, the developed FE code is helpful in simulating a number of prominent features related to the geometric characteristics of plain and fiber-reinforced rigid concrete slabs, such as slabs' length. In this part, the maximum tensile tension caused by different thermal gradients is first evaluated, along with the impact of compressive strength and slab length for fiber-reinforced concrete slabs. Figure 4.5 presents the findings that were obtained. In general, flexural moment and, as a consequence, maximal tensile stress rose with a rise in a thermal gradient. Additionally, as the temperature rises, nonlinear behavior in materials and the nonlinear dispersion of heat gradients along the length become more common. This problem demonstrates how crucial it is to take into account concrete's non-linear and plastic behavior when cracking and non-linear temperature gradient dispersion are being considered. The highest tensile strength of low compressive strength concrete, up to 30MPa, rose as slab length increased before declining as slab length increased past 6m. This might be connected to how well slabs handle vertical displacement. Also, the final flexural strength of concrete was increased by using PF, and this feature was further enhanced by increasing the PF content, which could effectively counteract the detrimental effects of curling stress. The bridging function of PF keeps particles together in the matrix and decreases the distance between cracks. The flexural strength

was improved by increasing the compressive and splitting tensile strengths of concrete because the top and bottom cross-sectional sections of concrete slabs experience compressive and tensile strains when they are subjected to a flexural load. Therefore, the curling behavior of rigid concrete slabs is enhanced and the fiber incorporation could be considered as an operative tool. Moreover, the nonlinearity in the structural performance of fiber-reinforced concrete slab behavior declined. So, almost the linear behavior could be taken into consideration for the modeling and analysis of fiber-reinforced rigid concrete airfield runways. Conversely, in plain concrete slabs with compressive strength up to 30MPa, the maximum tensile stress was observed in slabs with 6m length, however, in fiber-reinforced samples particularly those reinforced by 1% PF, the maximum tensile stress as a result of thermal gradient was observed in slabs with 7.5m length. This could be associated with changing the structural behavior of long slabs from membrane shell to bending plate due to a significant improvement in the mechanical characteristics of concrete as a result of fiber incorporation.

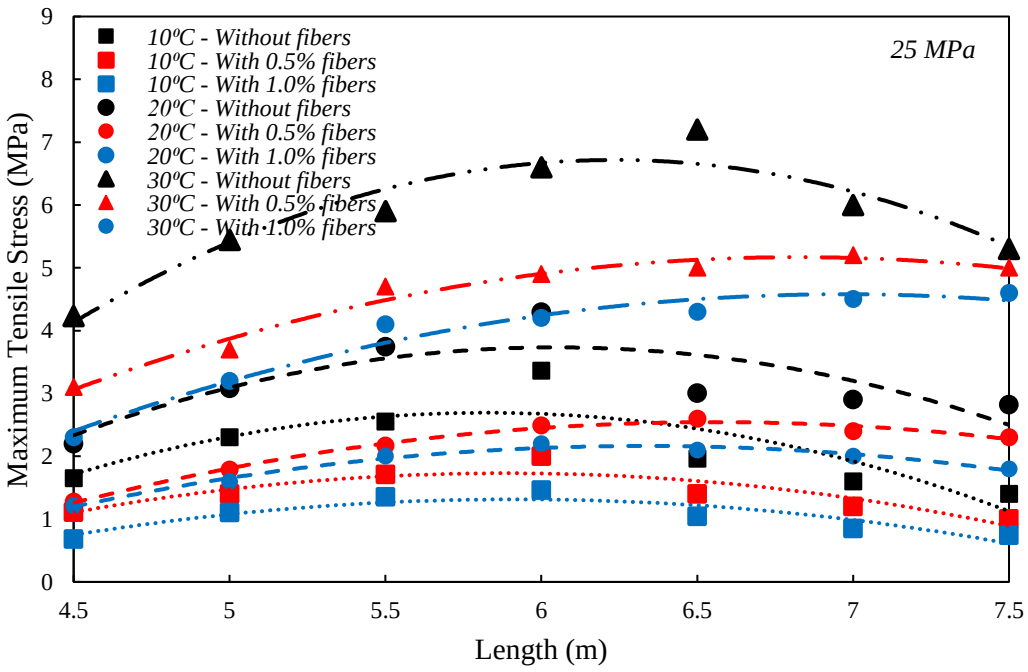

(a)

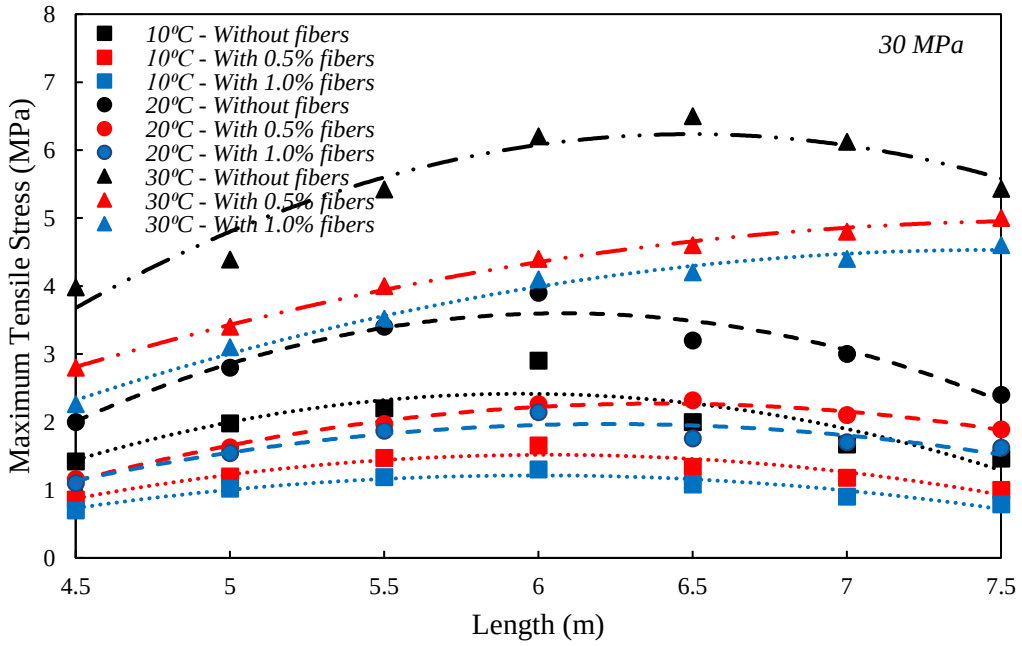
10ºC - Without fibers
10ºC - With 0.5% fibers
10ºC - With 1.0% fibers
20ºC - Without fibers
20ºC - With 0.5% fibers
20ºC - With 1.0% fibers
30ºC - Without fibers
30ºC - With 0.5% fibers
30ºC - With 1.0% fibers
30 MPa
Maximum Tensile Stress (MPa)
Length (m)
0
1
2
3
4
5
6
7
8
4.5
5
5.5
6
6.5
7
7.5

(b)

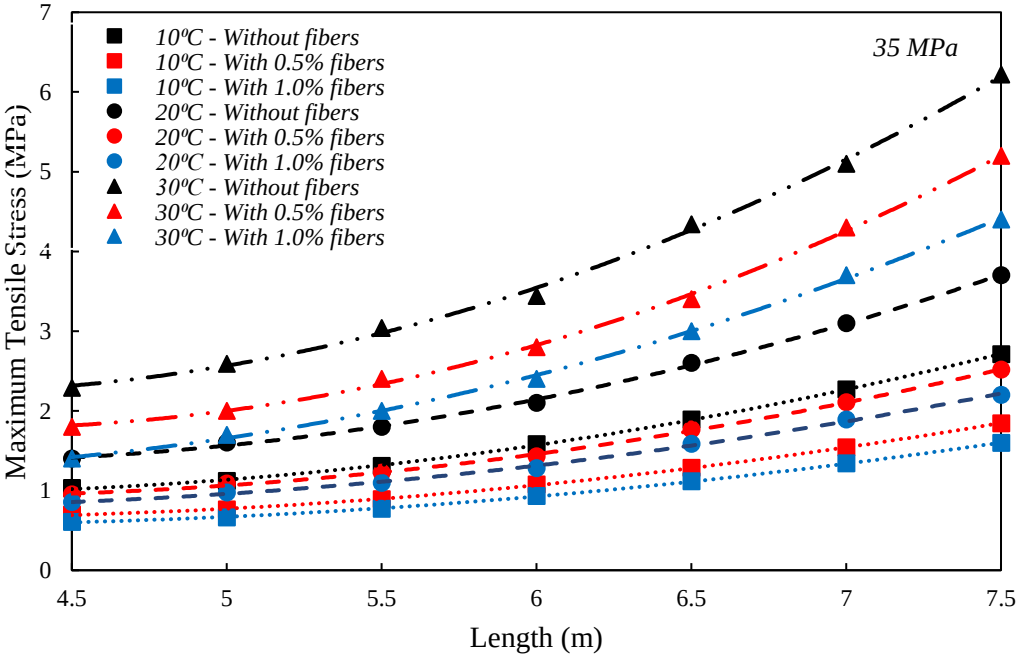
10ºC - Without fibers
10ºC - With 0.5% fibers
10ºC - With 1.0% fibers
20ºC - Without fibers
20ºC - With 0.5% fibers
20ºC - With 1.0% fibers
30ºC - Without fibers
30ºC - With 0.5% fibers
30ºC - With 1.0% fibers
35 MPa
Maximum Tensile Stress (MPa)
Length (m)
0
1
2
3
4
5
6
7
4.5
5
5.5
6
6.5
7
7.5

(c)

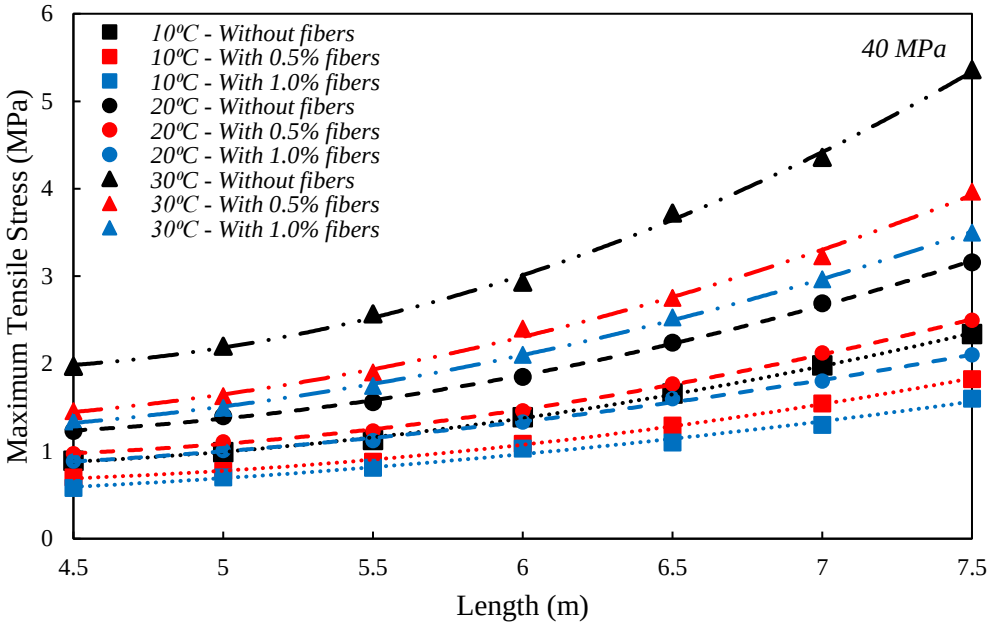

(d)

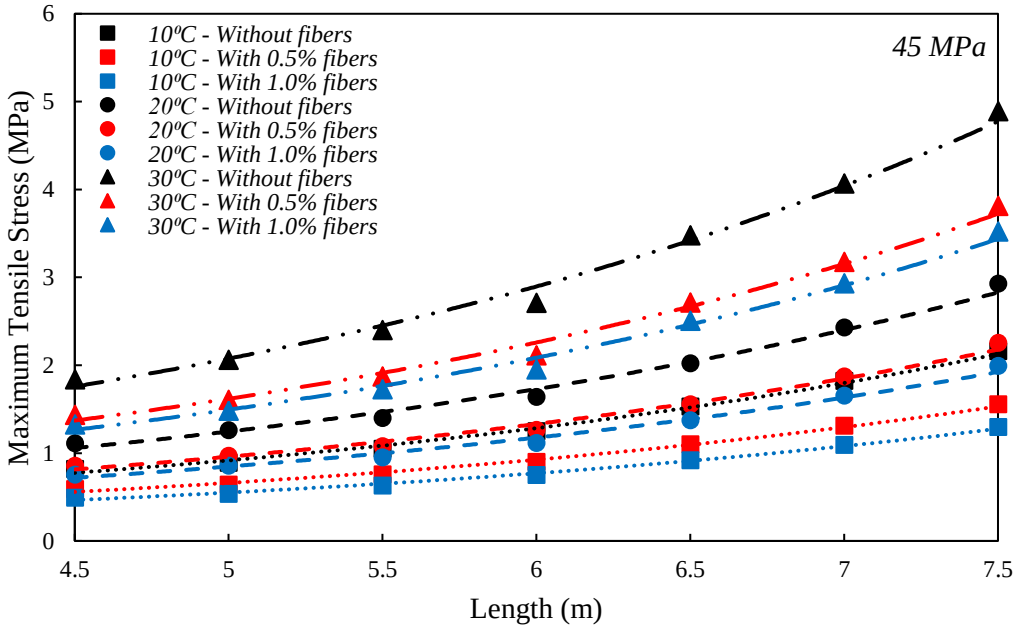

(e)

Figure 4.5: Influence of fiber incorporation on the maximum tensile stress of slabs due to curling with various slab lengths a) 25MPa, b) 30MPa, c) 35MPa, d) 40MPa and e) 45MPa

Furthermore, Figure 4.6 provides the positive effect of fiber incorporation on reducing the maximum curling stress in rigid concrete slabs with various geometric characteristics and thermal

variations. Regarding this figure, incorporating 0.5% PF led to reducing the stress due to thermal gradine and this response was a further decline with a surge in fiber fraction. Also, with the increase in the compressive strength of concrete, the effect of fibers has decreased, which can be due to the decrease in the contribution of fibers due to the high tensile strength of concrete on its own. Therefore, adding 0.5% PF decreased the average reduction of maximum tensile stress by 28.5%, 31.5%, 27.9%, 22.6%, and 24.3% for slabs with compressive strength of 25, 30, 35, 40, and 45 MPa, respectively. Additionally, almost the same reduction of 41.6%, 40.9%, 37.5%, 30.9%, and 33.3% was observed for samples with compressive strength of 25, 30, 35, 40, and 45 MPa, respectively, when 1.0% PF were utilized.

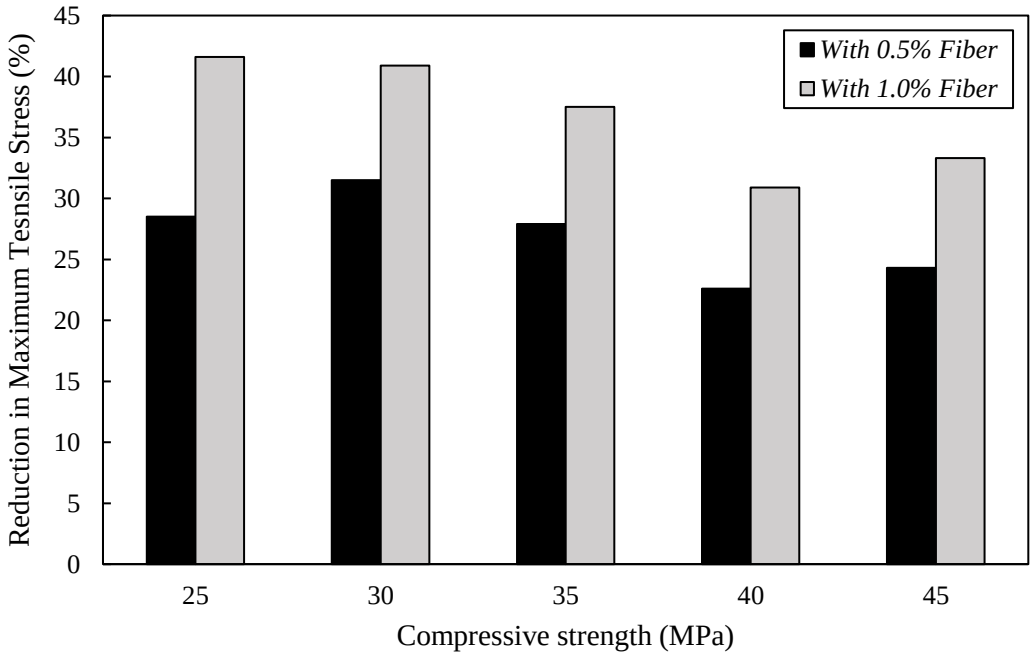

Figure 4.6: Influence of fiber incorporation on the maximum tensile stress reduction of slabs due to curling with various geometric characteristics and thermal gradients

Another significant reaction of rigid concrete airfield runways that causes cracking over the surface and width of slabs is out-of-plane and vertical deformation. In this respect, Figure 4.7 illustrates the impact of compressive strength and fiber fraction on the out-of-plane deformation of slabs

exposed to a thermal gradient with 4.5m in length and 10cm in thickness. This graph shows that the greatest lateral displacement decreased as concrete's compressive strength increased, which may be related to a rise in lateral resistance. Additionally, fiber incorporation improved the thermal behavior of slabs and the out-of-plane deformation decreased when fiber was utilized in concrete. The bridging function of PF keeps particles together in the matrix and decreases the distance between cracks. The flexural strength was improved by increasing the compressive and splitting tensile strengths of concrete because the top and bottom cross-sectional sections of concrete slabs experience compressive and tensile strains when they are subjected to a flexural load. Therefore, the curling behavior of rigid concrete slabs is enhanced and the fiber incorporation could be considered as an operative way to enhance the curling performance of rigid concrete airfield runways. It should be mentioned that 4.5m long slabs' overall lateral behavior could be considered as a bending plate element. In contrast, rigid concrete airfield slabs' out-of-plane deformation is negatively impacted by the thermal gradient. Therefore, decreasing lateral deformation may result in a reduction in the length of runways across the width of slabs, which would improve the structural and thermal characteristics of rigid concrete airfield runways.

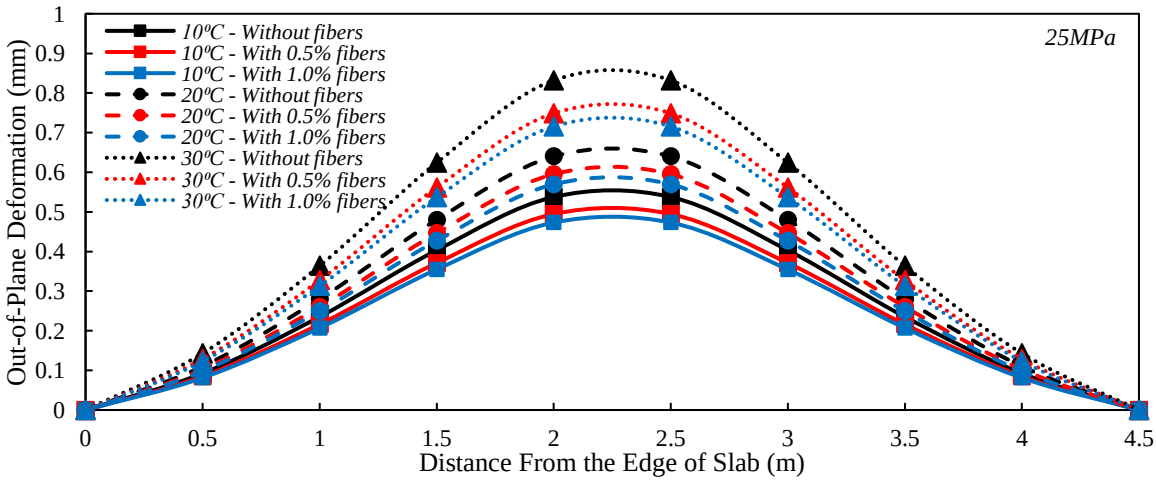

(a)

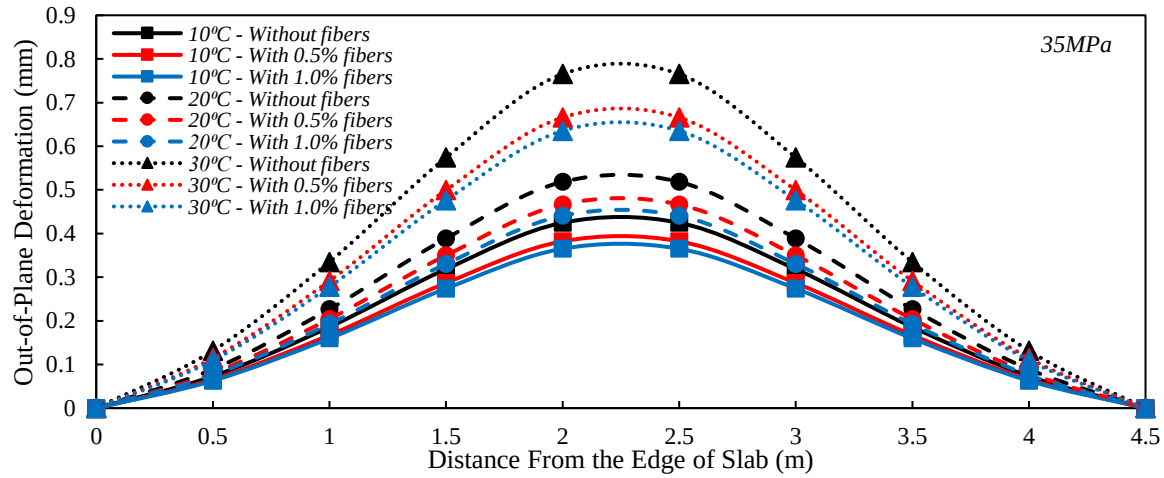

(b)

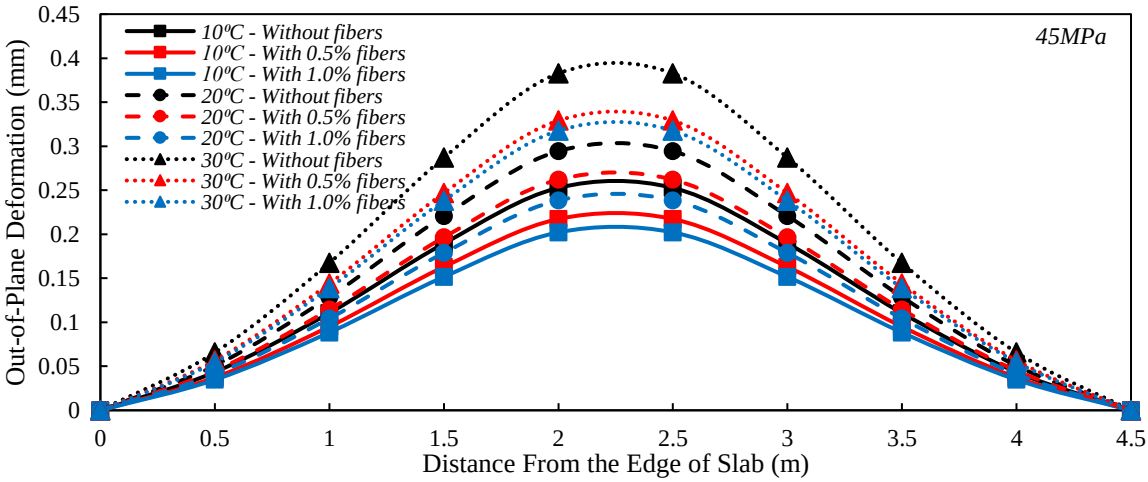

(c)

Figure 4.7: Influence of fiber incorporation on the out-of-plane deformation of 4.5m long slabs with 10cm thickness having various compressive strengths a) 25MPa, b) 35MPa and c) 45MPa

When the slab thickness was raised to 30cm, Figure 4.8 showed the same enhancement behavior. It follows that a significant improvement in lateral out-of-plane deformation and generally the thermal and curling behaviors of rigid concrete airfield runways could be expected in short-length slabs with concurrent increases in concrete compressive strength and slab thickness. Additionally, the improvement influence of fiber on reducing the lateral deformation of slabs is more prominent when the thickness was increased. This could be associated with the higher incorporation volume of fiber when the thickness increased and generally, the volume of used concrete increased.

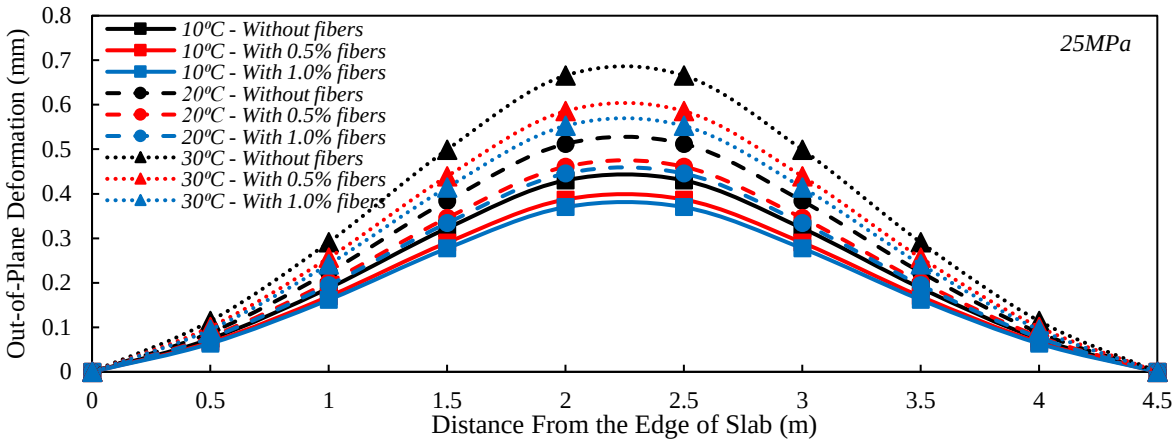

(a)

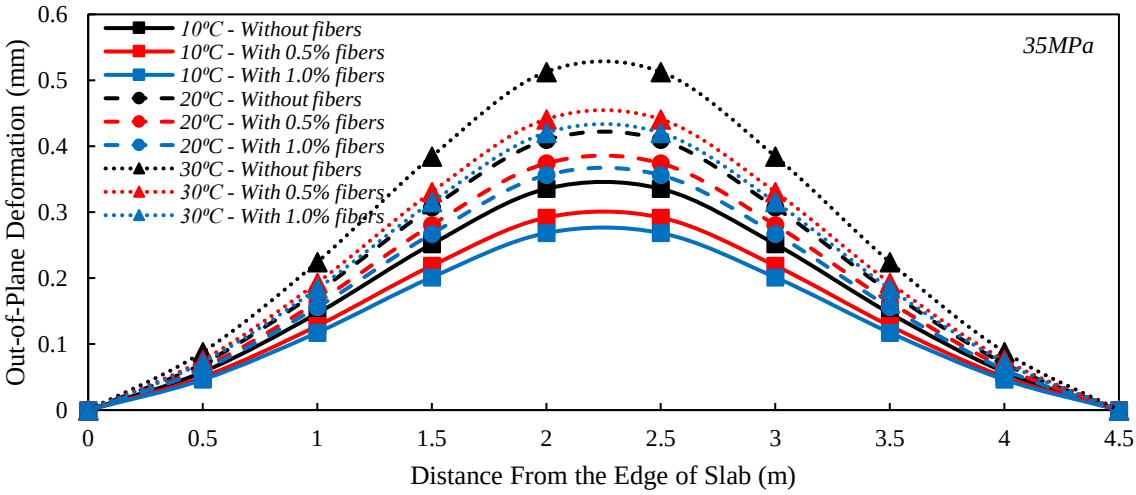

(b)

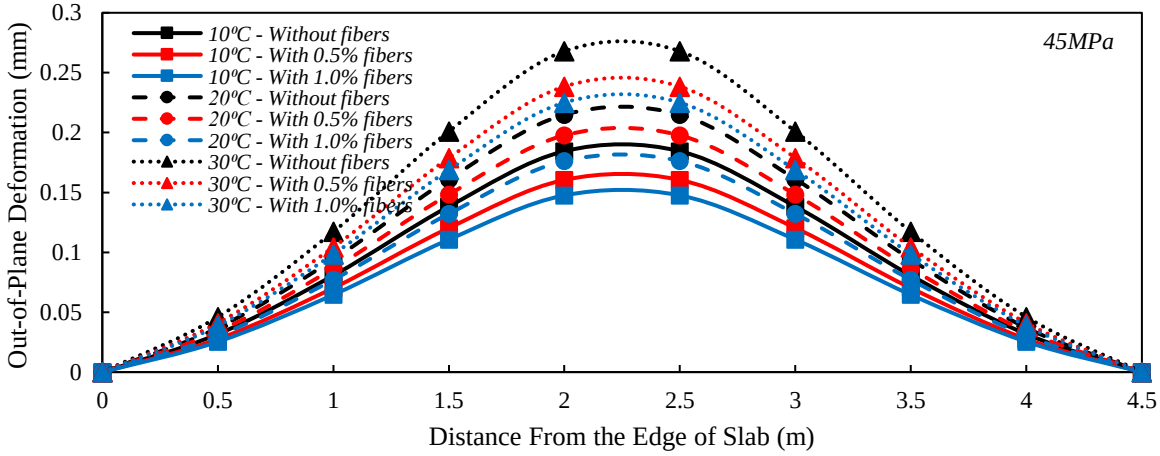

(c)

Figure 4.8: Influence of fiber incorporation on the out-of-plane deformation of 4.5m long slabs with 30cm thickness having various compressive strengths a) 25MPa, b) 35MPa and c) 45MPa

The impact of length, another significant measure, has been taken into account and studied in addition to the effects of compressive strength, temperature gradient, slab thickness, and fiber fraction on out-of-plane deformation. As a result, Figure 4.9 shows the out-of-plane displacement in 6m long rigid concrete slabs. In contrast to slabs that were 4.5m long, the almost same findings could be seen in slabs that were 6m long. However, as slab length grew, the lateral deformation value also rose marginally as a result of the increased bending moment and decreased lateral stiffness of the slabs. The largest lateral deformation was decreased as the concrete's compressive strength increased, which may be associated with an increase in the lateral resistance. Additionally, when fiber was added to concrete, out-of-plane deformation was reduced and the thermal behavior of the slab was enhanced. Since the top and bottom cross-sectional portions of concrete slabs encounter compressive and tensile strains when they are exposed to a flexural load, the flexural strength was enhanced by raising the compressive and splitting tensile strengths of concrete as a result of fiber usage. It should be noted that the total vertical motion of the 6m long slabs could be compared to that of 4.5m long rigid concrete slabs when considered as a bending plate element. The thermal difference, however, adversely affects the out-of-plane deformation of rigid concrete runways.

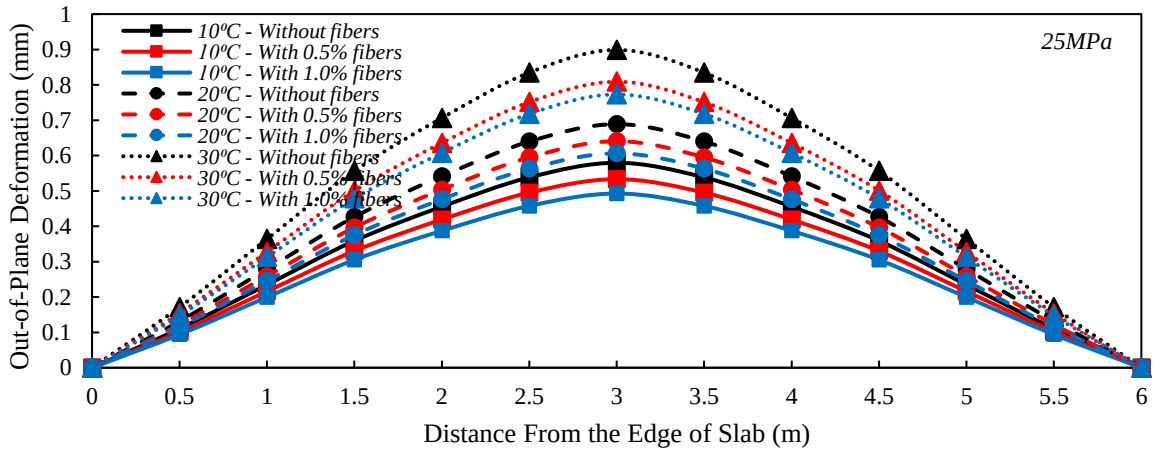

(a)

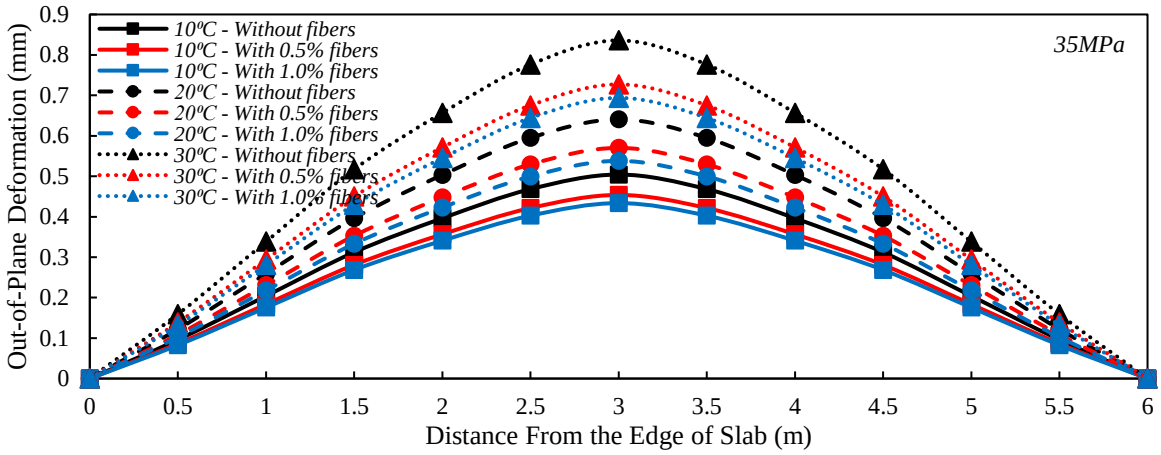

(b)

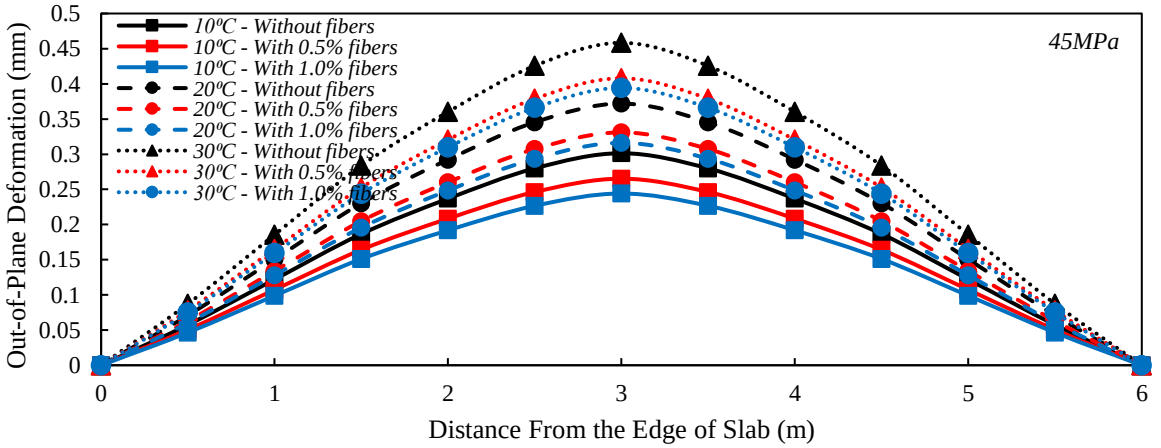

(c)

Figure 4.9: Influence of fiber incorporation on the out-of-plane deformation of 6m long slabs with 10cm thickness having various compressive strengths a) 25MPa, b) 35MPa and c) 45MPa

The same pattern of development is shown in Figure 4.10 when the slab thickness is increased to 30cm. Due to the combined rise in concrete's compressive strength and fiber incorporation, the lateral out-of-plane deformation and usually the thermal and curling characteristics of strigid concrete airfield runways could thus be enhanced in short-length slabs. The vertical deformation in slabs with a 6m length could be seen as a curve. Although the slab's bending response to lengthening is substantial. This problem demonstrates the shift in the slab's mode of failure from the bending plate element to the membrane shell element, where the in-plane reactions and behaviors are more pronounced in this instance. As a consequence, instead of the curved condition

found in slabs with a length of 6m, the failure structure of the slabs has altered, however, fiber incorporation improved the out-of-plane deformation as well as the curling strength.

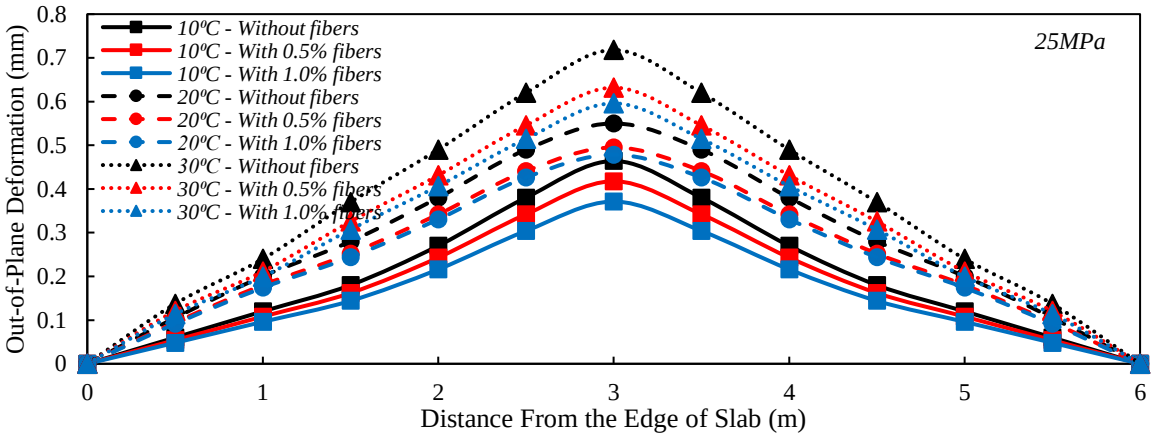

(a)

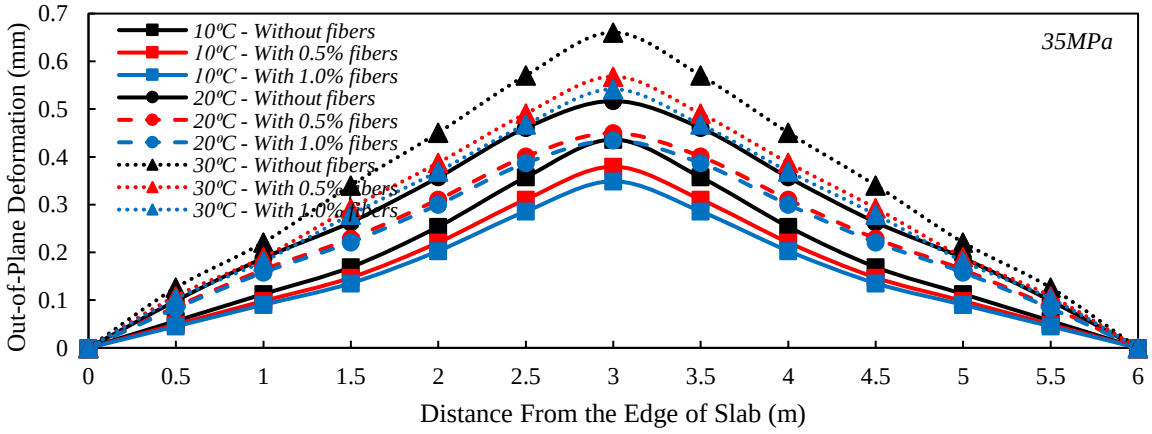

(b)

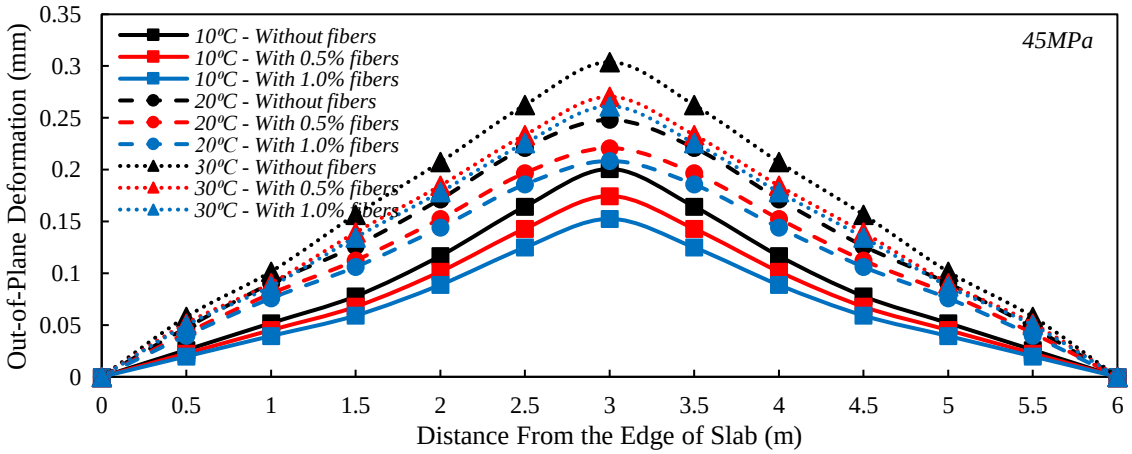

(c)

Figure 4.10: Influence of fiber incorporation on the out-of-plane deformation of 6m long slabs with 30cm thickness having various compressive strengths a) 25MPa, b) 35MPa and c) 45MPa

In addition, the vertical out-of-plane deformation in 7.5m long rigid concrete slabs was evaluated, and the resulting figures are shown for slabs with different thicknesses, compressive strengths, and fiber fractions. The findings show that long slabs behave differently from short slabs when they are out-of-plane; however, fiber incorporation showed the same influence in terms of deformation enhancement. Short slab behavior should therefore be considered as that of bending plate element, and long slab behavior as that of membrane shell. As shown in Figure 4.11, the slab's lateral deformation and general failure structure changed as its length increased from 6 to 7.5m. Additionally, raising the simultaneous use of higher compressive strength and fiber in a slab with a thickness of 10cm leads to a significant improvement in terms of out-of-plane deformation, which could be associated with the bridging character of fibers which leads to improving the mechanical characteristics of concrete. Additionally, although the quantity of changes in long slabs is less than in short slabs, the rise in thermal gradient has raised the vertical deformation in slabs with a length of 7.5m.

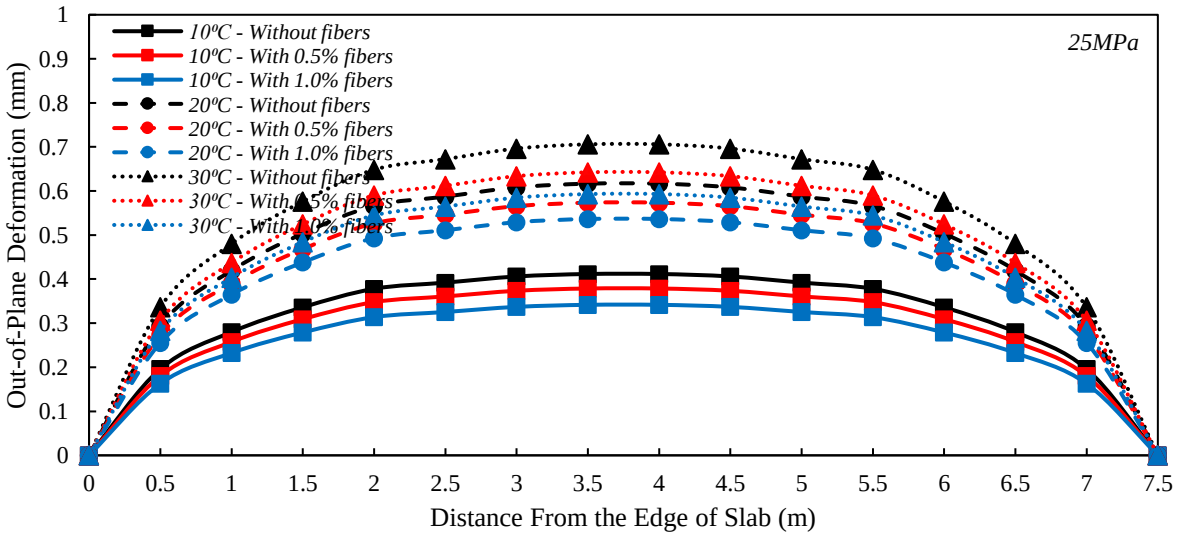

(a)

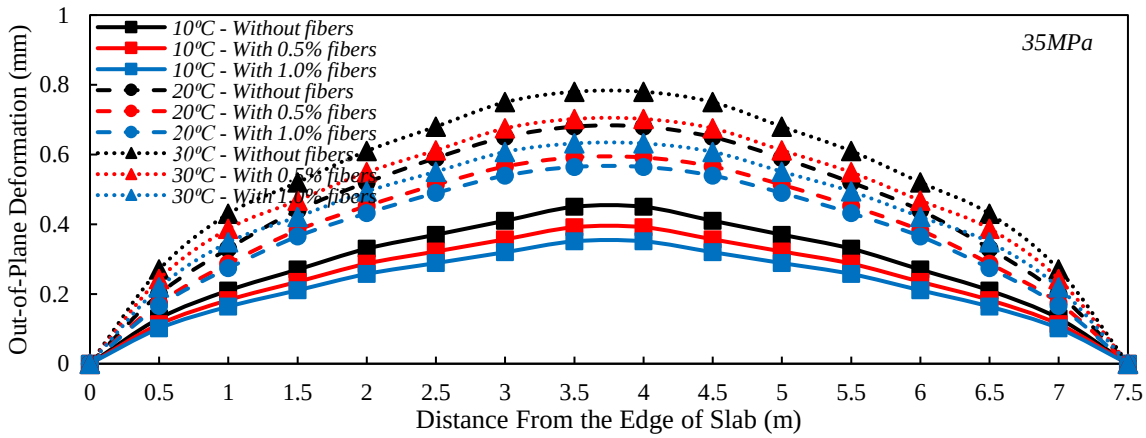

(b)

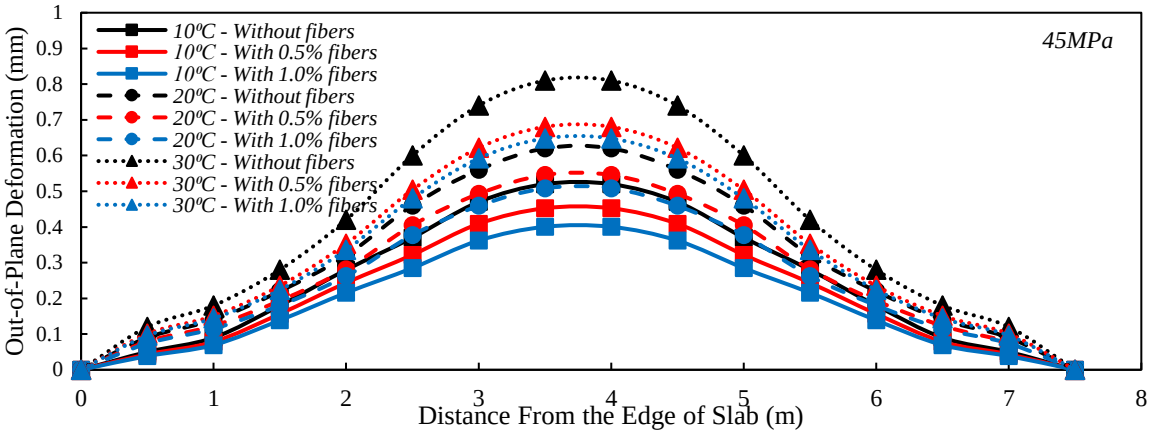

(c)

Figure 4.11: Influence of fiber incorporation on the out-of-plane deformation of 7.5m long slabs with 10cm thickness having various compressive strengths a) 25MPa, b) 35MPa and c) 45MPa

Furthermore, the maximum tensile stress improved as fiber-reinforced slab thickness increased to 30cm and the bending plate behavior was seen in slabs that were 7.5m long. When the slabs were made 30cm thick, this reaction did, however, marginally diminish. Therefore, it is strongly advised to use thick and fiber-reinforce rigid concrete airfield runways when it is required to manufacture lengthy slabs. Additionally, the vertical out-of-plane distortion and typically the thermal and curling properties of thick concrete airport approaches could be improved in long-length slabs due to the concurrent increase in concrete's compressive strength and fiber incorporation. This problem illustrates the change in the slab's mode of failure for thick-long-length slabs from the membrane

shell to the bending plate element, where the in-plane responses and behaviors are more obvious in this case, as shown in Figure 4.12.

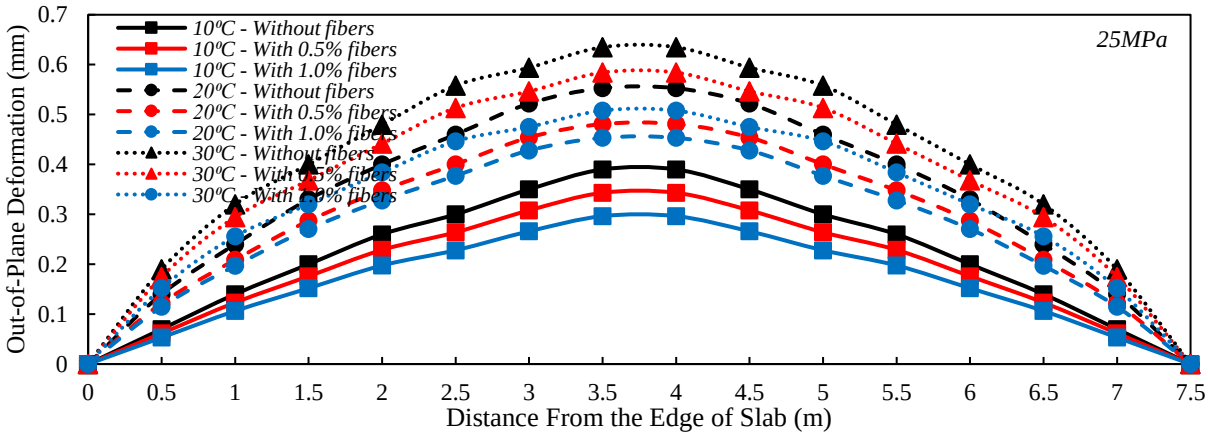

(a)

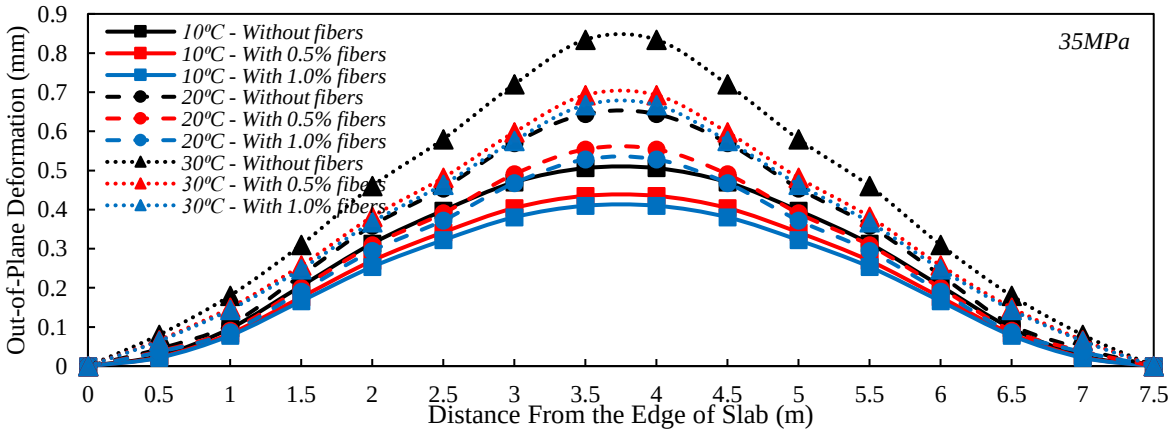

(b)

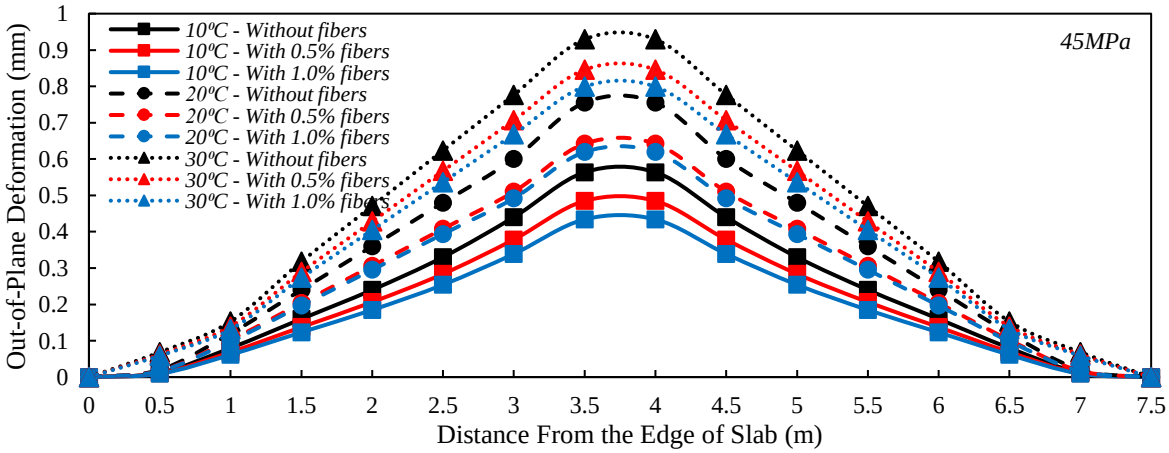

(c)

Figure 4.12: Influence of fiber incorporation on the out-of-plane deformation of 7.5m long slabs with 30cm thickness having various compressive strengths a) 25MPa, b) 35MPa and c) 45MPa

Figure 4.13, acquired through advanced finite element method modeling, illustrates the impact of fiber incorporation and thermal gradient on the deformation of 6m long slabs. Regarding this figure, fiber integration could be taken into consideration to enhance the curling behavior of rigid concrete slabs since the out-of-plane deformation was decreased and this behavior was further enhanced with a surge in fiber fraction.

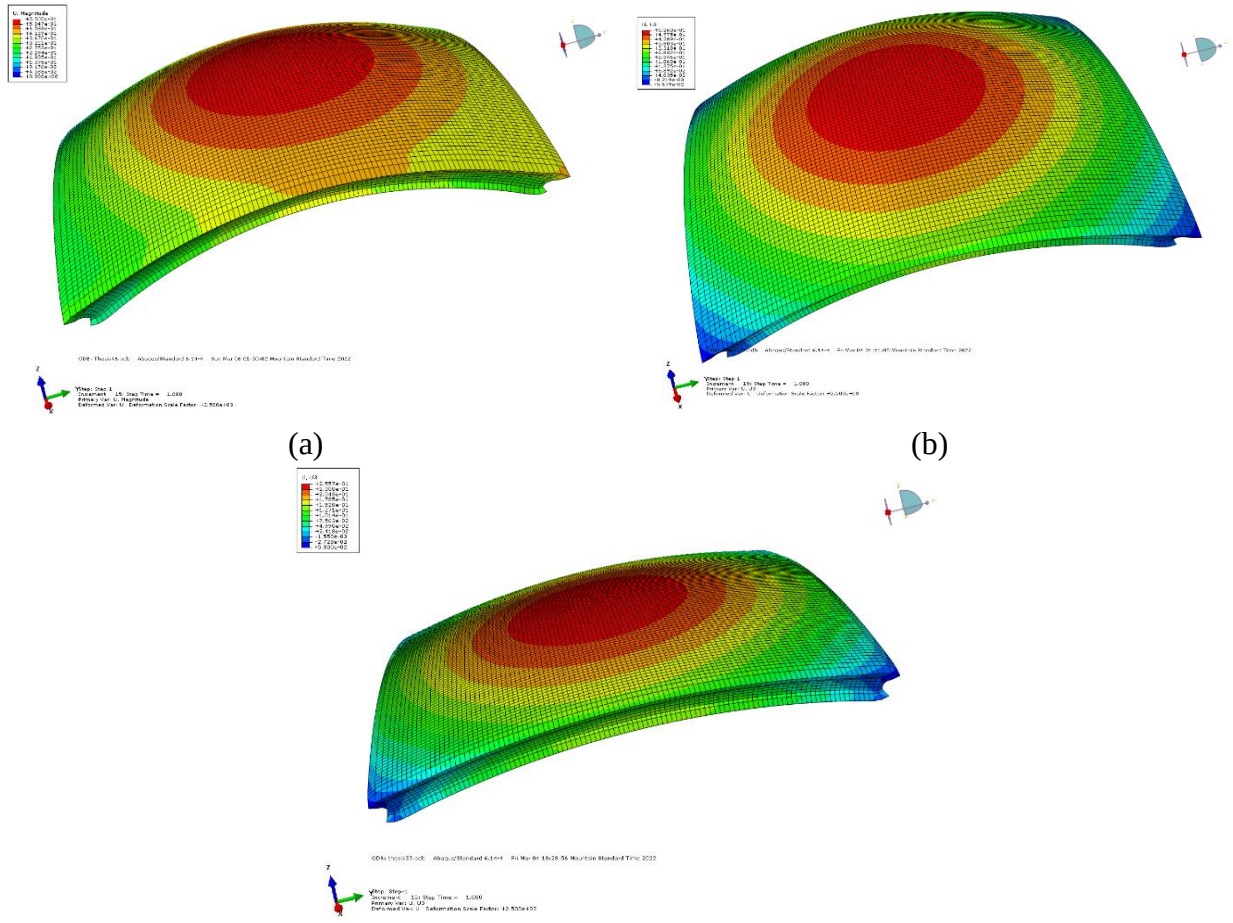

(a) (b)

(c)

Figure 4.13: Influence of thermal on out-of-plane deformation response in 4.5m long slabs a) without fiber, b) with 0.5% fiber, and c) with 1.0% fiber

To identify the improvement influence of fiber fraction on reducing the maximum out-of-plane deformation, the reduction percentage was measured for slabs with various geometric

characteristics, thermal gradients, and materials properties, as presented in Figure 4.14. As shown in this figure, the maximum out-of-plane deformation declined with an increase in fiber fraction. This could be associated with the bridging character of fiber in increasing the mechanical characteristics of concrete slabs. Therefore, in slabs with 4.5m length, the addition of 1% PF led to reducing the maximum deformation by 18%, 14%, and 24% in slabs with 25, 35, and 45 MPa compressive strength, respectively (see Figure 4.14a). Additionally, in slabs with 7.5m length, using 1% PF led to reducing the maximum deformation by 17%, 21%, and 23% in slabs with 25, 35, and 45 MPa compressive strength, correspondingly (see Figure 4.14c)

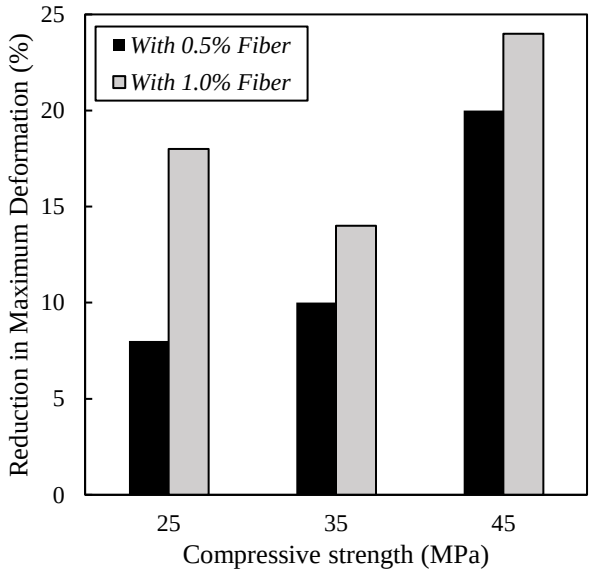

(a)

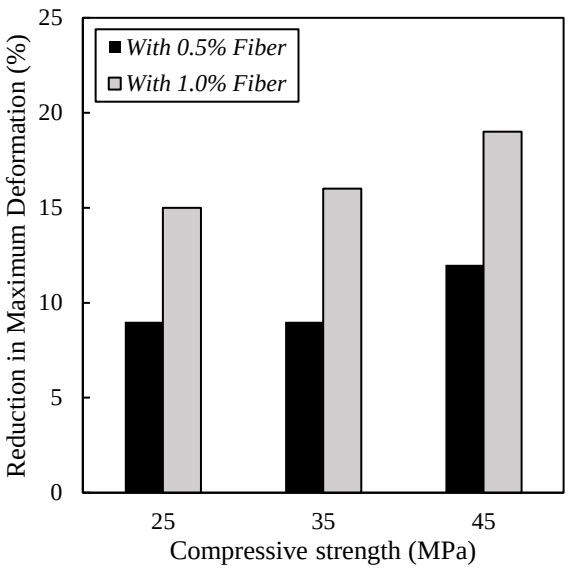

(b)

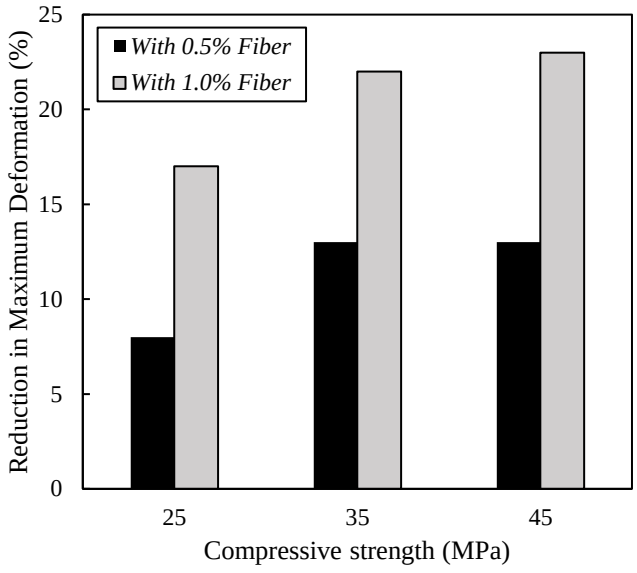

(c)

Figure 4.14: Influence of fiber incorporation on the maximum out-of-plane deformation reduction of slabs due to curling with various geometric characteristics and thermal gradients for the length of a) 4.5m, b) 6m, and c) 7.5m

4.5. SUMMARY & CONNECTION WITH THE SUBSEQUENT CHAPTER

This chapter provided a solution by PF incorporation to lessen the negative influence of thermal and curling stresses. For this aim, a finite element method software, ABAQUS, was utilized. In addition, the simultaneous effect of PF and other geometric characteristics and material properties were assessed to provide a comprehensive overview of the positive role of fibers in improving the structural responses of rigid concrete airfield runways. Conversely. in-field construction needs to perform a non-destructive test evaluation to make sure about the performance of rigid concrete slabs. To reduce the in-field test cost, an advanced numerical analysis could also play a crucial role. So, to measure the effect of various variables and PF incorporation on the strength of the in-field performed concrete slab, a numerical non-destructive test is developed in the next chapter

based on wave propagation and penetration through slab thickness. Therefore, the next Chapter will significantly help engineers to identify the influence of various parameters on the structural performance and strength of rigid concrete slabs, particularly in terms of flexural deformation and stress. As a result, Figure 4.15 provides a connection with the subsequent chapter overview.

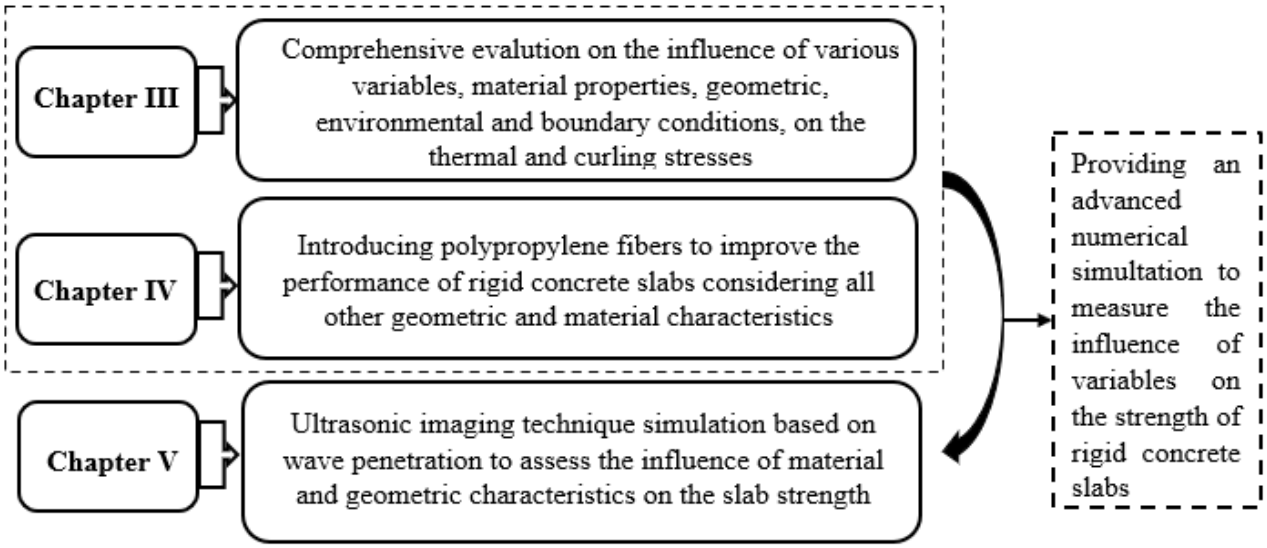

Figure 4.15: Overview of the connection between previous Chapters and Chapter V

CHAPTER V

ULTRASONIC IMAGING EVALUATION

5.1. INTRODUCTION

This chapter's main goal is to provide an advanced numerical simulation to measure the influence of material properties and geometric characteristics on the strength of rigid concrete slabs using a wave propagation technique. For this aim, this chapter provides an ultrasonic imaging technique simulation for fibers-reinforced concrete considering the mechanical properties obtained using the laboratory tests. The preceding section of this chapter is followed by finite element method parameters, boundary conditions, and wave propagation over the surface and thickness of slabs on the assessment of structural impacts imparted on rigid concrete slabs reinforced by PF.

5.1.1. Organization of the Chapter

This chapter consists of five main sections. Subsequent to the introductory section, Section 2 provides information associated with the ultrasonic imaging technique and wave propagation about the influence of material properties and geometric characteristics on the structural performance of rigid concrete slabs which are significantly associated with the thermal and curling behaviors of rigid airfield runways. Section 3 discusses the methodologies to simulate the ultrasonic imaging technique and wave propagation in finite element method software to reach this goal. Then, the main results of this study are presented and discussed to show the benefit of ultrasonic imaging technique simulation to identify the effect of material properties and geometric characteristics on the structural performance of plain and PF-reinforced rigid concrete slabs. Finally, A summary of

this section will be provided so that its connection with the subsequent section and also the importance of the subsequent section can be clearly identified.

5.2. ULTRASONIC IMAGING APPLICATION

Overdriven images acquired using the Synthetic Aperture Focusing Technique, ultrasonic imaging is a potent nondestructive assessment knowledge for measuring the structural performance of concrete. Its use has been restricted to constant-velocity concrete structures; multi-layer concrete structures with varying wave propagation velocities, including bridge decks with overlays, have not been included. Theoretically, Synthetic Aperture Focusing Technique advancements have made it possible to image multi-layer concrete slabs using ultrasound. Concrete construction problems have been extensively found using ultrasonic imaging (Schickert et al. 2003; Popovics et al. 2017; Krause et al. 2001; Freeseman et al. 2016; Khazanovich and Hoegh, 2016; Hoegh et al. 2012; White et al. 2014). To study the structural performance of concrete slabs, the Synthetic Aperture Focusing Technique has been used in modern ultrasonic equipment such as MIRA (De La Haza et al. 2013), EyeCon (De La Haza et al. 2013), and Pundit (2017). This method assumes that concrete is a homogeneous medium with a distinct, constant shear-wave velocity. The adoption of modern technology has been restricted to single-layer concrete constructions because of this presumption. Theoretically, several latest developments in Synthetic Aperture Focusing Technique methodology such as Wu et al. (2016), Skjelvareid et al. (2011), and Yang et al. (2006) have made it possible to image multi-layer concrete structures with ultrasound. This technique more precisely locates objects of interest by using the shear-wave velocity of each layer (e.g., defect depth for rigid concrete slabs with overlays). In this study, finite element simulation data of

MIRA tests on a representative concrete specimen with various material properties and geometric characteristics are evaluated.

5.2.1. Apparatus and data

The MIRA-A1040 was considered for the ultrasonic apparatus in this investigation. 48 Forty-eight point-contact transmitting and receiving transducers are used in the MIRA-A1040, which features a matrix antenna array with 12 channels spaced 30 mm apart and four transducers per channel spaced 25 mm apart. When one channel functions as a transmitter, emitting shear-horizontal waves, and one of the other channels act as a receiver, successively taking up direct and reflected waves, a data array is obtained. Thus, there are 132 transmitting and receiving pairs for 12 channels and each channel can be either a transmitter or a receiver. Due to the reciprocity theory, just 66 pairs of the 132 pairs are necessary. This is because half of them are equivalent to the other half, as illustrated in Figure 5.1. The first channel is the receiver, while the other channels are demonstrated as transmitters. The transmitter's nominal center frequency in this investigation is 50 kHz, while the receiver's frequency is 1 MHz. Each ultrasound test results in a unique longitudinal direction and continuous ultrasound scanning in the longitudinal direction of the apparatus result in a comprehensive longitudinal direction. The ultrasonic apparatus can be shifted in both longitudinal and transverse directions to cover the entire surface of the test material to obtain all longitudinal direction data for a concrete slab. The slice in the equipment transverse direction produces a panoramic transverse direction after all longitudinal directions data have been fused, and the slice at each depth produces a panoramic depth direction

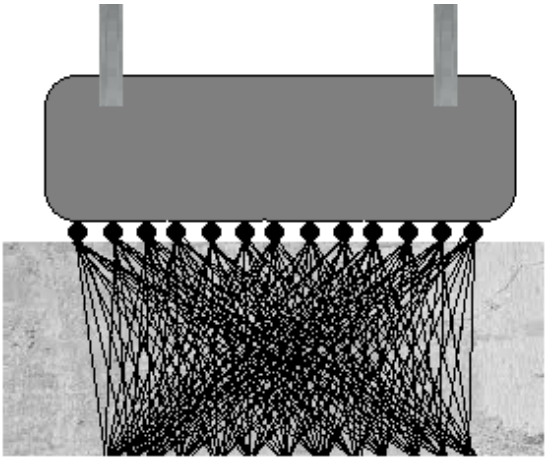

Figure 5.1: An example of an ultrasonic imaging test

Active imaging systems such as radar (Cumming and Wong, 2004) and sonar (Hansen, 2017) frequently employ the Synthetic Aperture Focusing Technique, which uses measurements taken from many points to create a synthetic aperture (Figure 5.2). Each point in the reconstruction region can be determined using Synthetic Aperture Focusing Technique. Figure 5.2 depicts the dedicated region and the covered area. The Synthetic Aperture Focusing Technique was first utilized to evaluate metal components (Muller et al. 1991) in the field of nondestructive assessment before being adopted to test concrete elements (Schickert et al. 2003; Popovics et al. 2017; Krause et al. 2001; Freeseman et al. 2016; Khazanovich and Hoegh, 2016; Hoegh et al. 2012; White et al. 2014; De La Haza et al. 2013). One channel provides a pulse for the measurements in this investigation, and a different channel catches the echoes at a different location. Figure 5.3 depicts a schematic of such pulse-echo assessment.

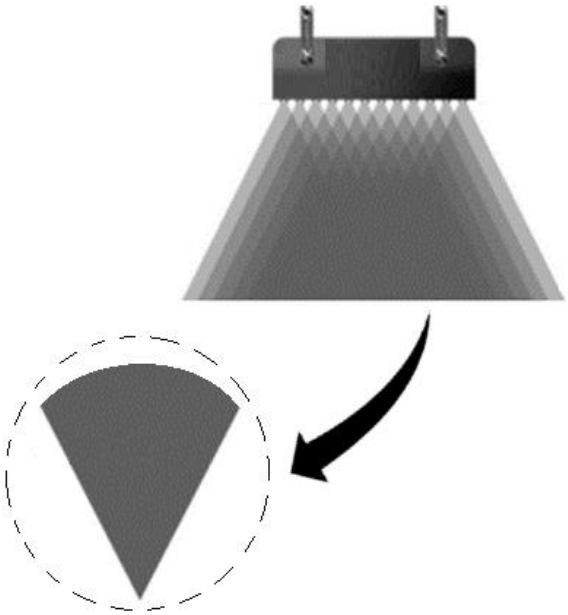

Figure 5.2: Schematic of the synthetic aperture focusing technique

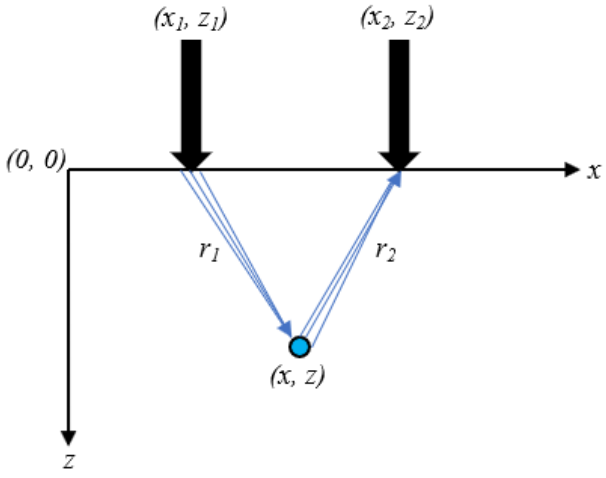

Figure 5.3: Schematic of a pulse-echo testing

All echoes from a point scatter can be represented using a hyperbolic curve:

$$t = \frac{r}{V} = \frac{r_1 + r_2}{V} \tag{5.1}$$

In which, *V*, *t*, and *r* denote the wave cover velocity, the total journey duration, and the total travel distance (the sum of r_1: the incident travel distance and r_2: the reflection travel distance, respectively. All echoes from a point scatter can be represented by a hyperbolic curve. Therefore, it can be computed that the one-way journey distance could be determined using the next formula:

$$r_i = \sqrt{(x_i - x)^2 + (z_i - z)^2} \tag{5.2}$$

The echo signal recorded at (x_2, z_2) can be expressed as the equation in Equation (5.3) by scaling and delaying per the attenuation throughout the travel distance *r* if a pulse is produced by the point source at (x_1, z_1) at $t = 0$ ($s_0(t)$) (Kinsler et al. 1999):

$$s(x_2, z_2) = \frac{s_0(x_1, z_1)}{f(r)} \tag{5.3}$$

In which *f(r)* accounts for the attenuation of the signal across the travel distance *r*. Since signal attenuation has no impact on the position information in the imaging findings, Synthetic Aperture Focusing Technique algorithms can be not taken into account. So, all the echo signals can be stacked to determine the reflection concentration from the point scatter (*x*, *z*).

$$p(x, z) = \int s(x_i, z_i) dx_i \tag{5.4}$$

To lessen the side-lobe artifacts in the B-scan, Equation (5.4) is given a universal apodization weight, *x*. Additionally, Equation (5.5) provides the pixel value of the focused picture at (*x*, *z*) (Langenberg et al. 1986).

$$P(x,z) = \int a(x).s(x_i,z_i)dx_i \tag{5.5}$$

A single pixel is created by this integration along the hyperbola, $t = r/V$. A single concentrated B-scan is produced by replicating this data managing each pixel and overlaying the outcomes. In this work, apodization is accomplished using the Hann weight scheme (Martinez et al. 1999):

$$a(\hat{x}) = \begin{cases} (1+\cos(2\pi\hat{x}))/2, & |\hat{x}| < 1/2 \\ 0 & other\ points \end{cases} \tag{5.6}$$

In which $\hat{x} = (x - x')/\Delta x(z)$, *x'* indicates the receiver point on the *x* axis (*z* = 0), $\Delta x(z) = 2z\ tan\ (\Delta\theta/2)$, and $\Delta\theta$ denotes the angular beamwidth of the transducer array.

5.3. ADVANCED NUMERICAL SIMULATION

In this study, the non-destructive test has been modeled according to MIRA test apparatus characteristics. Figure 5.4 provides information on this test setup. In this study, the Synthetic Aperture Focusing Technique has been utilized to do shear wave simulation using a finite element method software, ABAQUS. For this aim, both plain and fiber-reinforced rigid concrete slabs have been modeled as described in Chapter III. Then, the shear wave penetration has been applied to the slab's surface. Therefore, two sender and receiver sensors have been modeled with 2cm distance, as illustrated in Figure 5.4. It is worth mentioning that this distance was considered based on the MIRA test setup. To apply the load, there are two ways: load control and displacement control conditions. The disadvantage of the load control condition is stress concentration which leads to the response's divergence. Therefore, in this study, the displacement control condition was taken into account and a harmonic unit load was applied based on the location of the sensor,

presented below in Figure 5.5. In addition, the applied load history is also shown below in Figure 5.5.

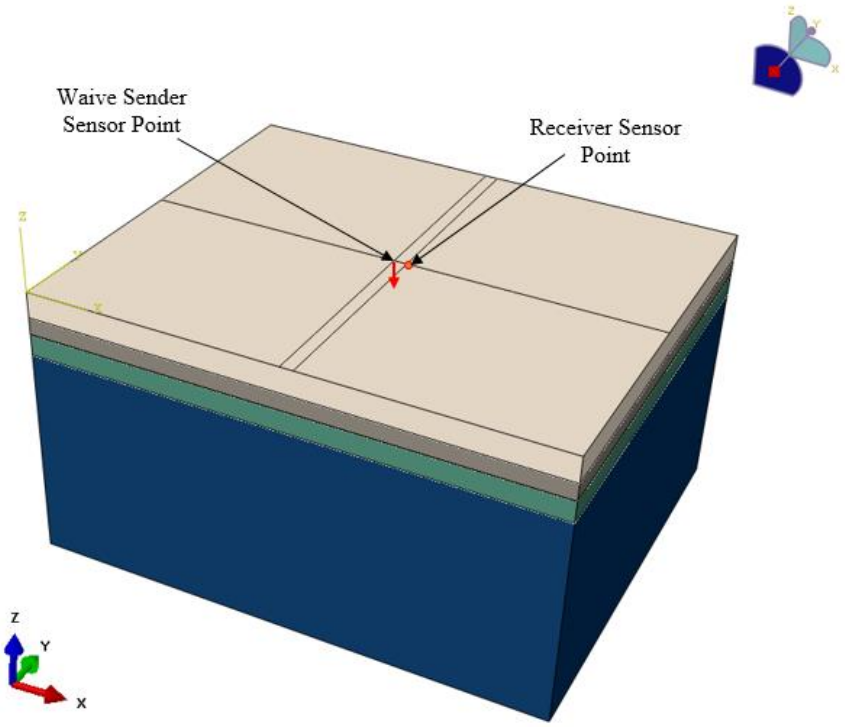

Figure 5.4: Location of sender and receiver sensors

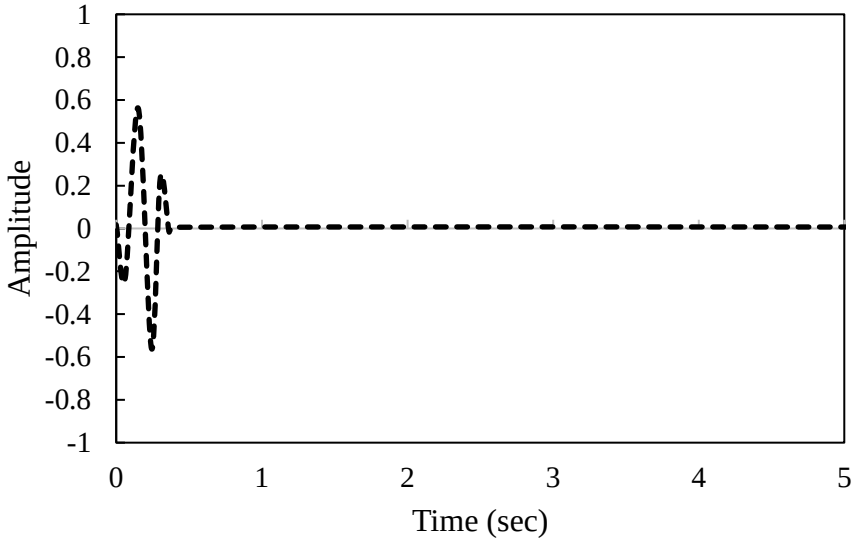

(a)

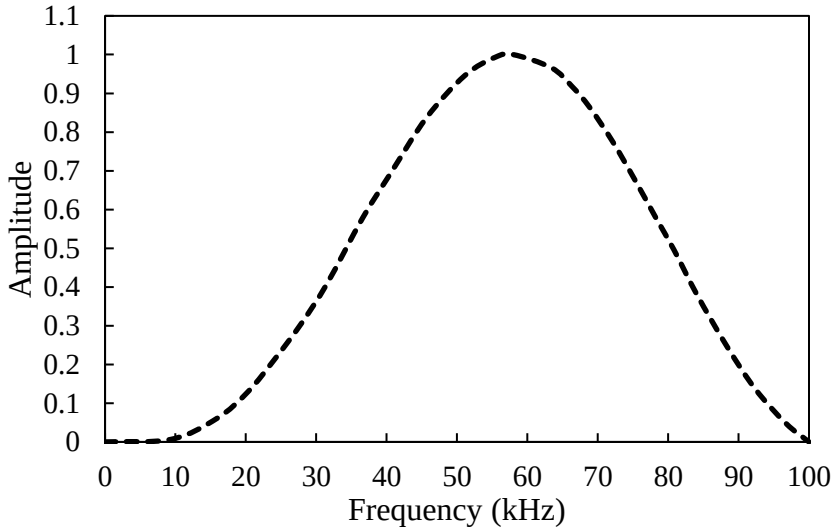

(b)

Figure 5.5: Applied wave spectrum for Synthetic Aperture Focusing Technique a) Amplitude-Time Diagram and b) Amplitude-Frequency Diagram

5.4. NUMERICAL RESULTS AND DISCUSSIONS

5.4.1. Frequency

In this section, the frequency distribution of the received wave from the receiver sensor versus time is measured to identify the influence of material properties and geometric characteristics of rigid concrete slabs on the strength parameters. The results are measured for 200μs. Figure 5.6 shows the influence of slabs' thickness and compressive strength for plain concrete slabs on the frequency-time performance. Regarding this figure, the maximum received frequency was increased when the compressive strength of concrete increased. So, it could be concluded that by increasing the compressive strength more energy dissipated and the maximum amplitude of frequency amplified. Also, the frequency amplitude shifted to the right by reducing the compressive strength. Additionally, increasing the thickness of slabs led to increasing the peak frequency which indicates the improvement in the strength and structural responses of rigid

concrete slabs. It is worth to be mentioned that by increasing the thickness of slabs, the fluctuation in received frequency was smoother which indicated higher continuity and uniformity in the real airfield runways constructions.

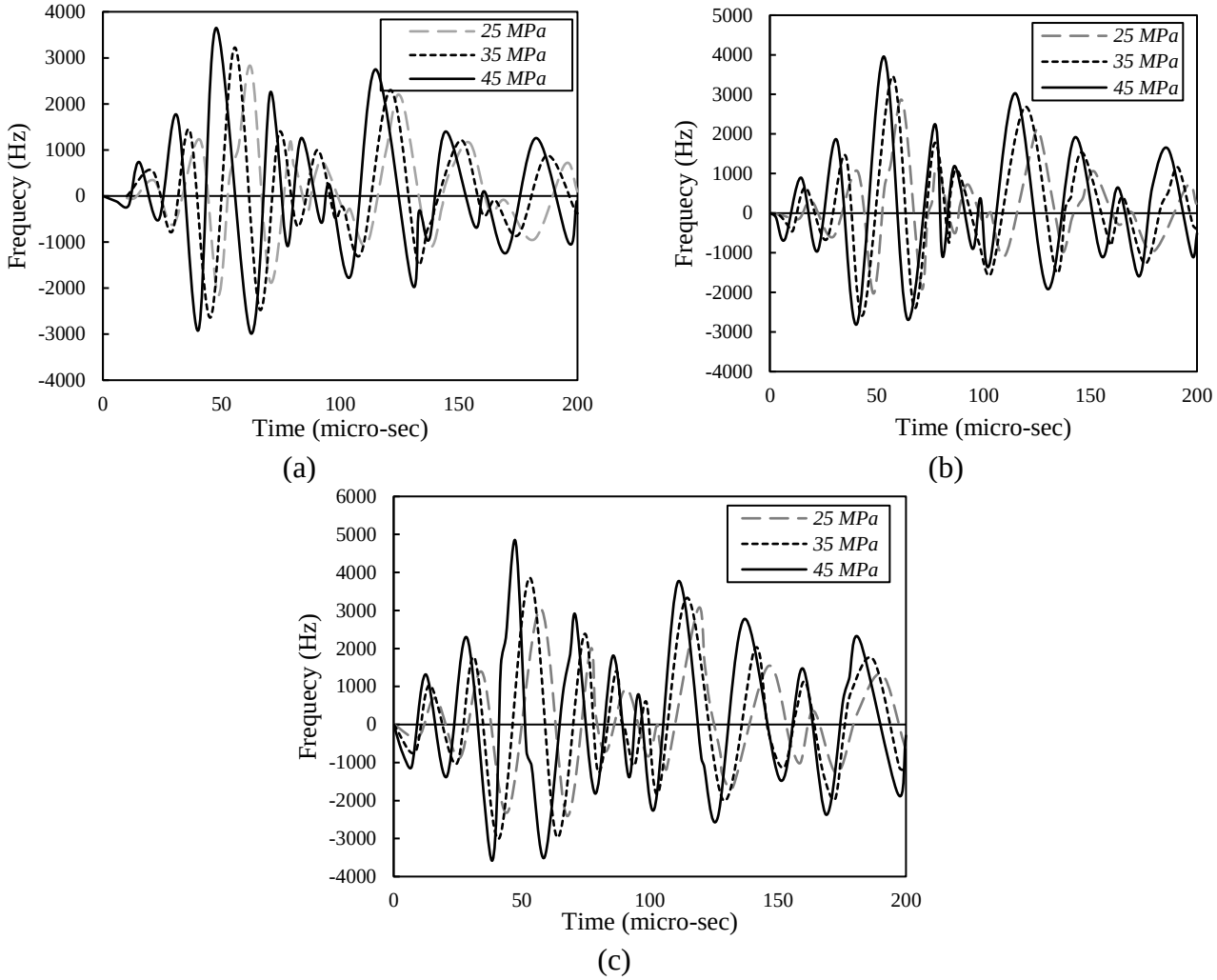

Figure 5.6: Influence of concrete compressive strength of plain concrete on the received frequency with various thicknesses a) 10 cm, b) 20 cm, and c) 30 cm

In addition, the influence of fiber incorporation on improving the strength and structural responses of rigid concrete slabs is measured, and the obtained results are presented in Figures 5.7 and 5.8 for 0.5% and 1.0% fibers incorporation fraction, respectively. Almost the same observation as same as plain concrete slabs were achieved for fiber-reinforced airfield runways. However, fiber

incorporation led to a sharper fluctuation in frequency-time responses of slabs. Additionally, the peak of received frequency was increased when fiber was incorporated and the value was further amplified by increasing the fiber incorporation fraction which indicates more energy dissipation as a result of increasing the strength of slabs. Moreover, increasing the compressive strength and using fiber simultaneously led to a shift in maximum frequency value to the left side of responses, and the maximum value was obtained in a shorter time.

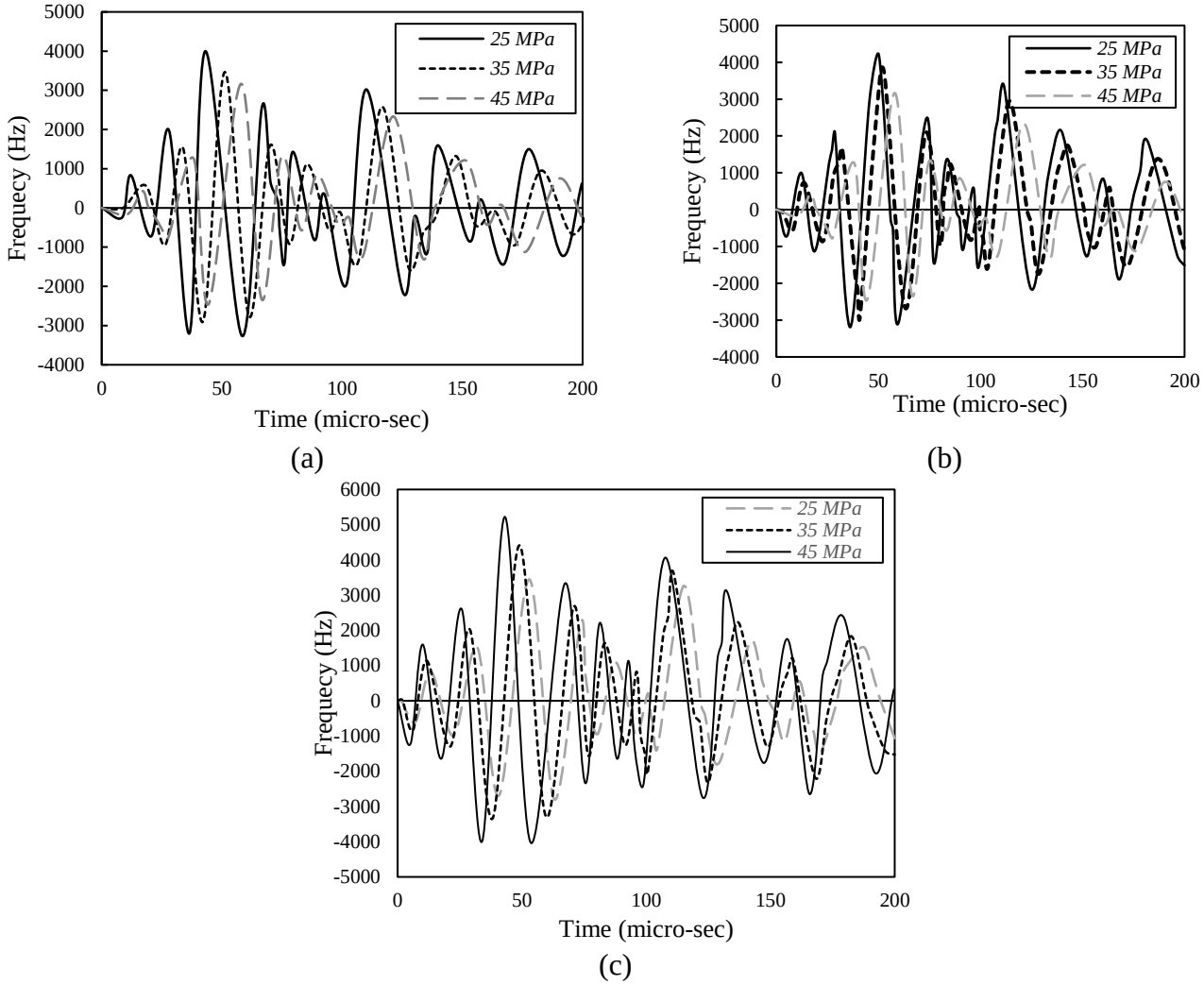

Figure 5.7: Influence of concrete compressive strength of 0.5% fiber-reinforced concrete on the received frequency with various thicknesses a) 10 cm, b) 20 cm, and c) 30 cm

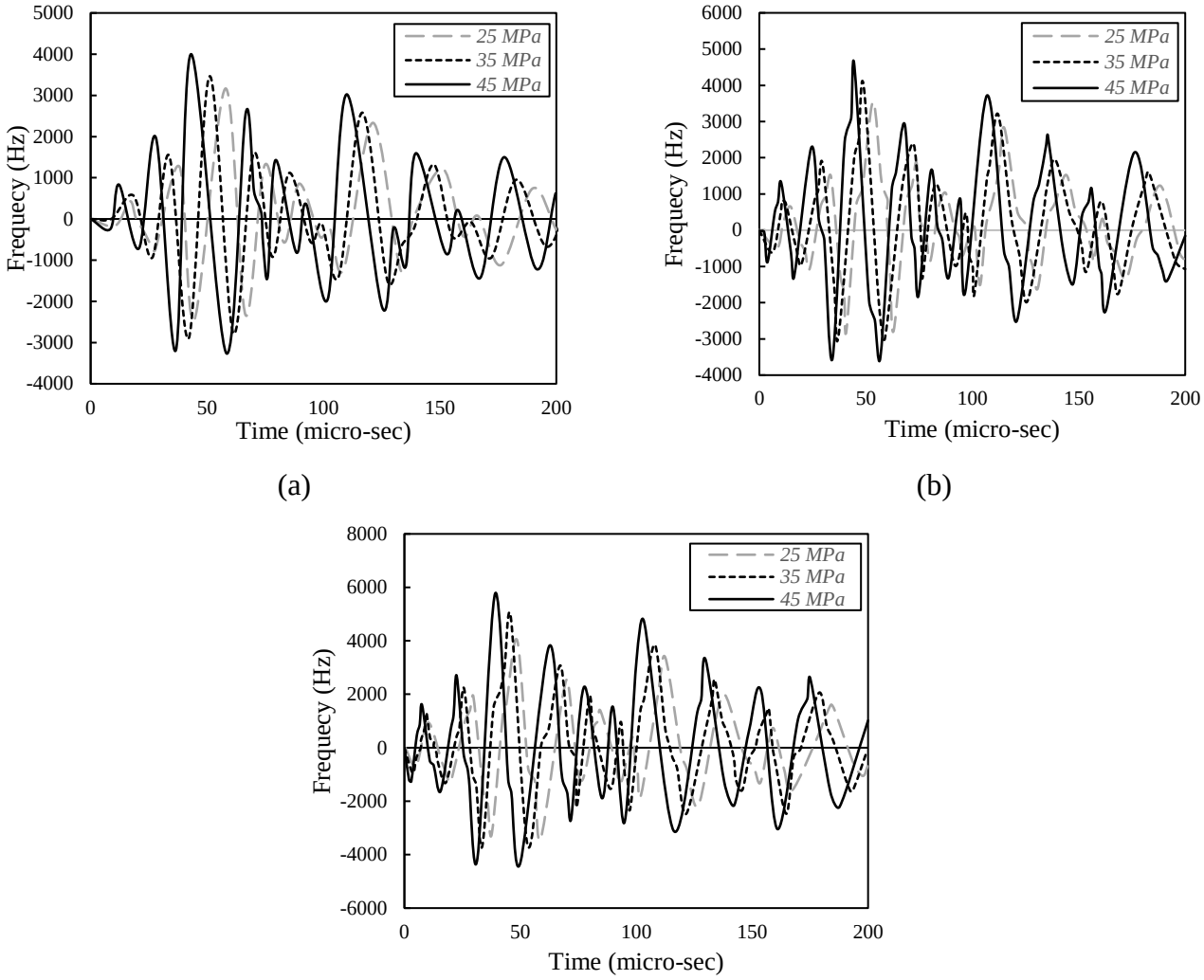

Figure 5.8: Influence of concrete compressive strength of 1.0% fiber-reinforced concrete on the received frequency with various thicknesses a) 10 cm, b) 20 cm, and c) 30 cm

Furthermore, the thickness of the slabs was an important factor in increasing their strength of slabs. Therefore, more energy was dissipated and consequently, the peak frequency was increased when the thickness of the slabs increased. To have a better understanding of the influence of various variables on the resistance and structural responses of rigid concrete airfield runways, the maximum values of received frequency by the receiver sensor were measured and provided in Figure 5.9. The fiber incorporation led to increasing the peak of wave frequency. Therefore, in

slabs with 30 cm thickness, adding 0.5% and 1.0% PF led to increasing the maximum frequency by 40% and 47% when the compressive strength of concrete was also increased from 25MPa to 45MPa. Also, when the thickness was increased to 30 cm and compressive strength increased from 25MPa to 45MPa, incorporating 0.5% and 1.0% PF resulted in swelling the peak of frequency by 51% and 53%, respectively, which indicates an improvement in terms of concrete slabs strength and higher energy dissipation. Furthermore, Figures 5.10 and 5.11 shows the wave propagation over the surface and thickness of slabs

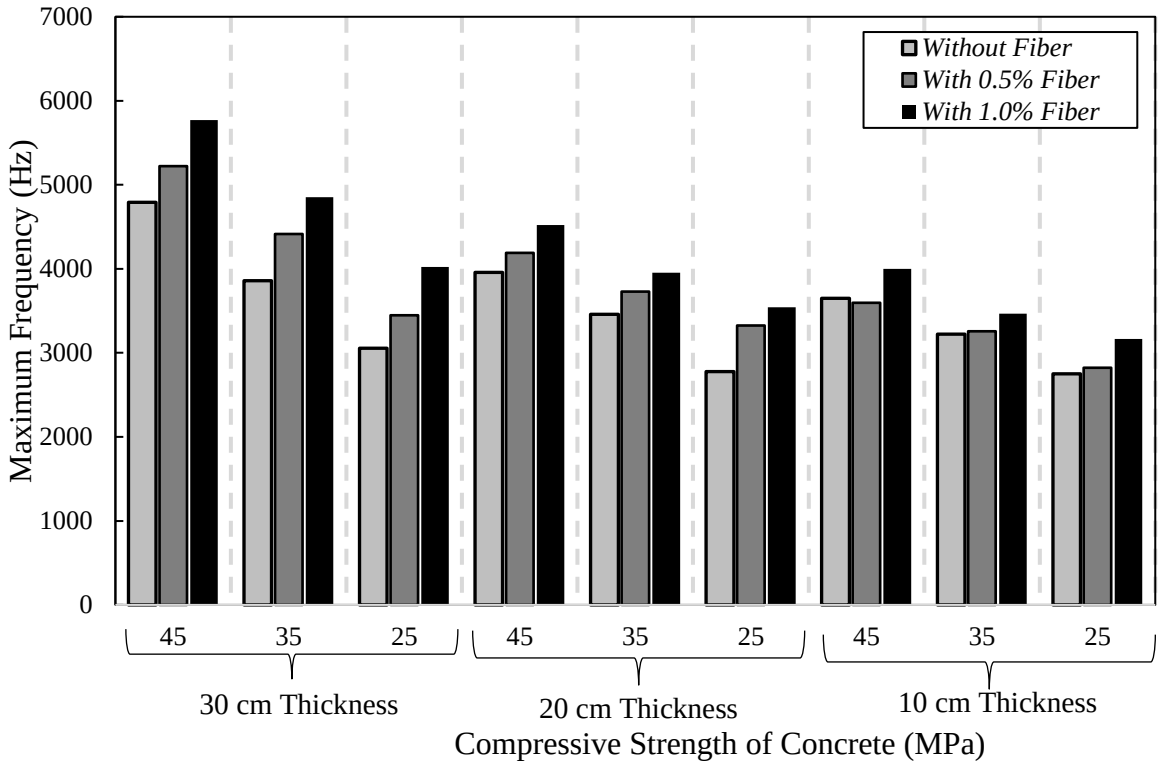

Figure 5.9: Effect of concrete compressive strength on the maximum received frequency considering various slab's thickness and fibers fractions

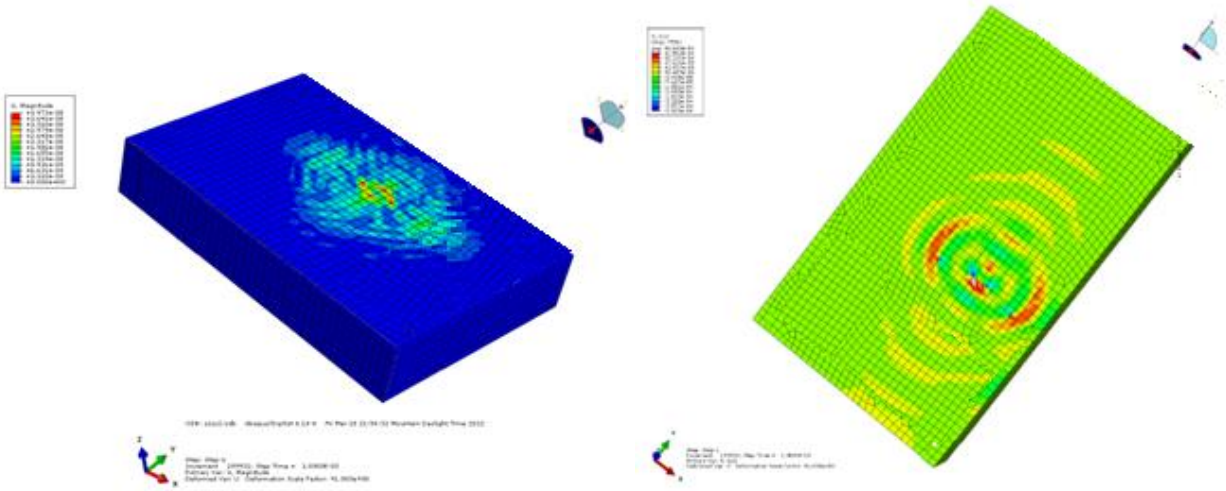

Figure 5.10: Wave propagation over the surface of slabs

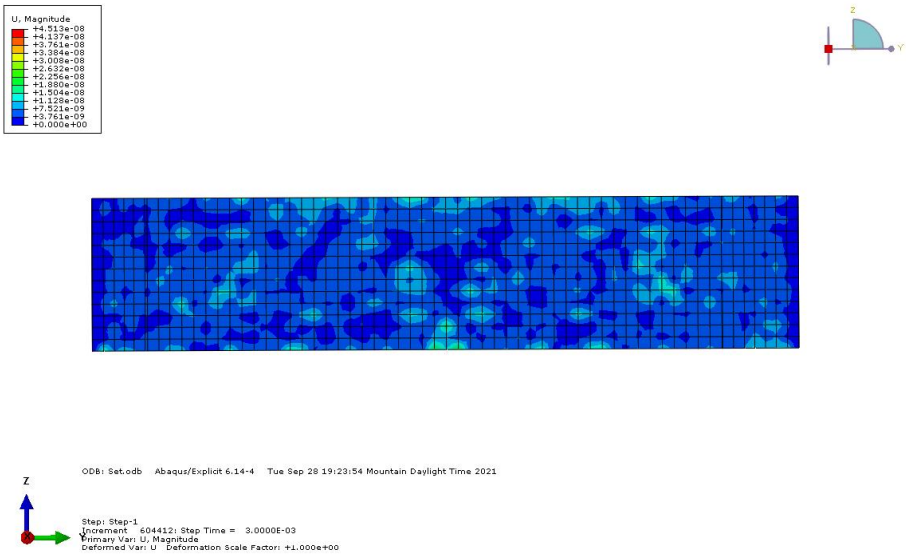

Figure 5.11: Wave propagation over the thickness of slabs

5.4.2. Stress

One of the main factors associated with the strength of concrete slabs is the stress resulting from the wave propagation over the slabs. Therefore, in this section, the stress-time responses of received frequency are measured considering the geometric characteristics, material properties, and fiber incorporation effect. The results are presented in Figures 5.12 to 5.14. The results are measured for 200μs. According to Figure 5.12, the maximum received stress increased as the

concrete's compressive strength rose. Therefore, it could be inferred that as compressive strength increased, more energy was lost and the highest stress amplitude was amplified. Increasing the compressive strength also resulted in a leftward change in the stress-time responses. Additionally, raising slab thickness increased to stress's peak, indicating that rigid concrete slabs' strength and structural responses have improved. It is important to note that by raising slab thickness, the received stress fluctuation became smoother, indicating greater continuity and regularity in the actual airfield runway constructions. Additionally, the number of maximum peaks over time was amplified when the thickness increased. Additionally, it is determined how much fiber inclusion improves the strength and structural responses of rigid concrete airfield runways. The resulting data are shown in Figures 5.7 and 5.8 for corresponding fiber incorporation fractions of 0.5% and 1.0%. For fiber-reinforced airfield runways, nearly the same results were obtained as with conventional concrete slabs. However, fiber integration caused slabs' stress-time reactions to fluctuating more sharply. Additionally, the apex of the received stress rose when fiber was incorporated, and the value of increasing even more when the fiber incorporation percentage was raised, indicating greater energy loss as a result of raising slab strength. Furthermore, shifting the maximum stress value to the left side of answers and utilizing fiber at the same time resulted in a shorter time needed to reach the maximum value.

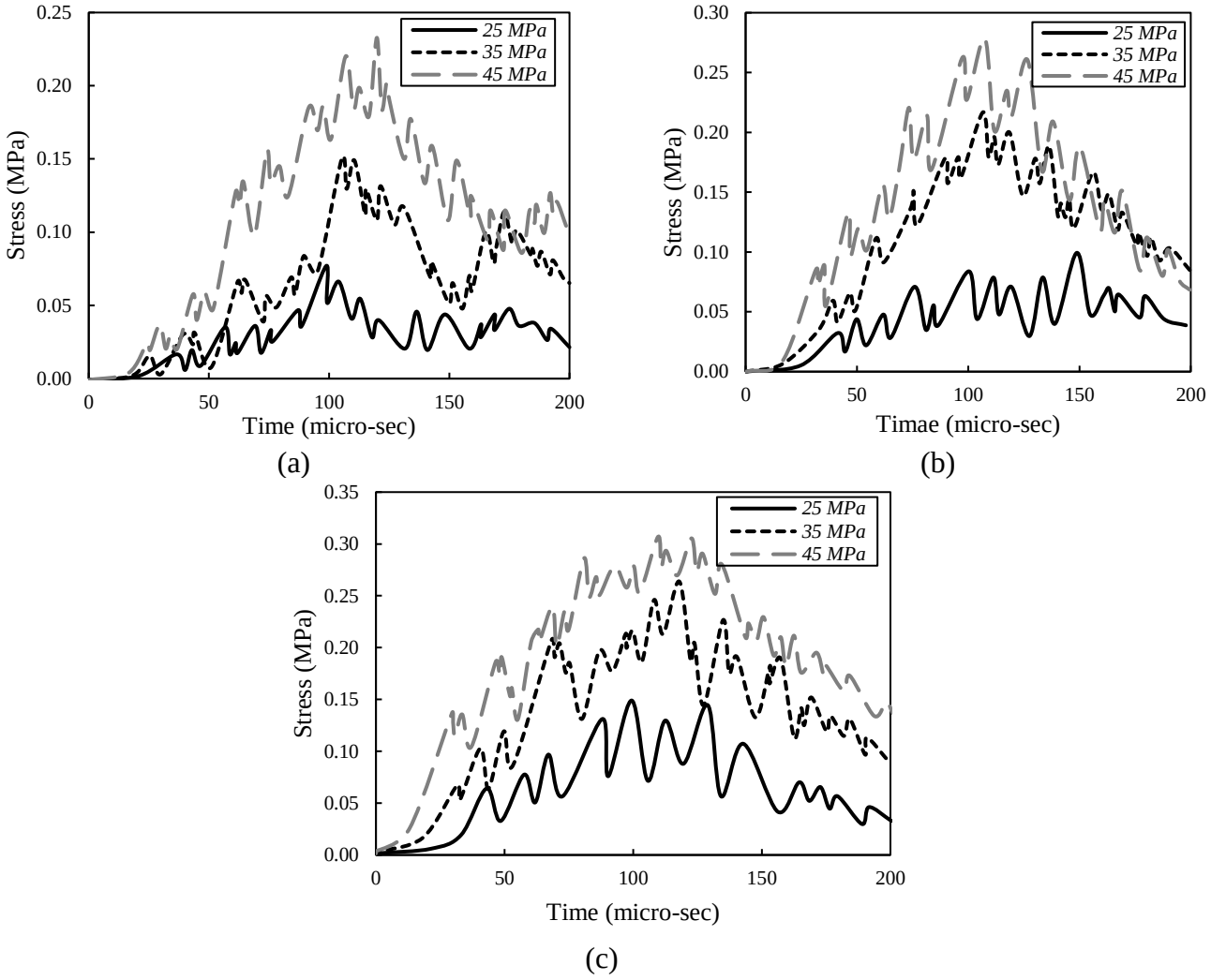

Figure 5.12: Influence of concrete compressive strength of plain concrete on the stress with various thicknesses a) 10 cm, b) 20 cm, and c) 30 cm

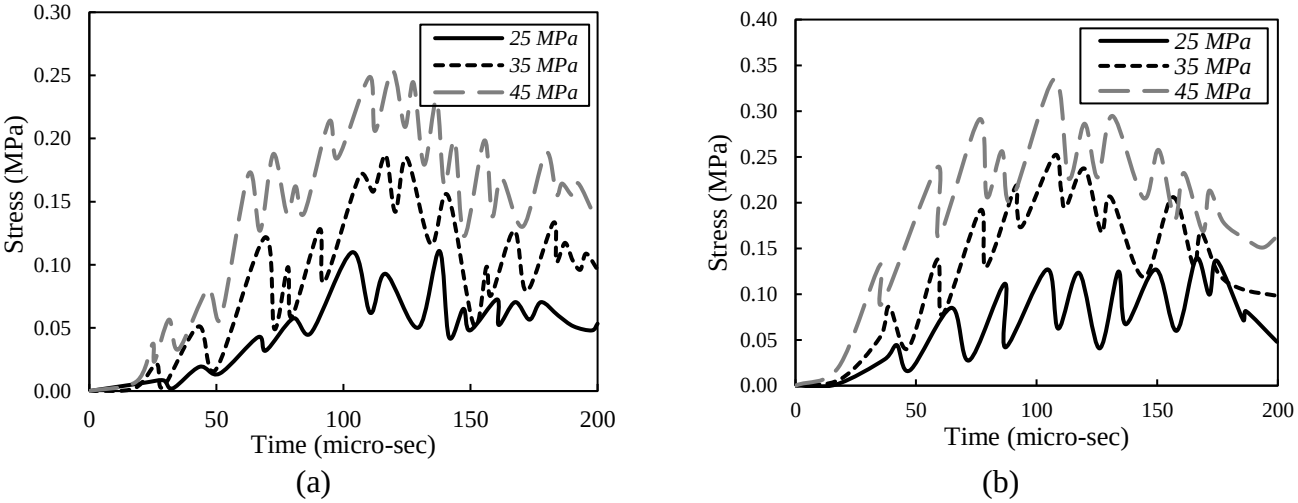

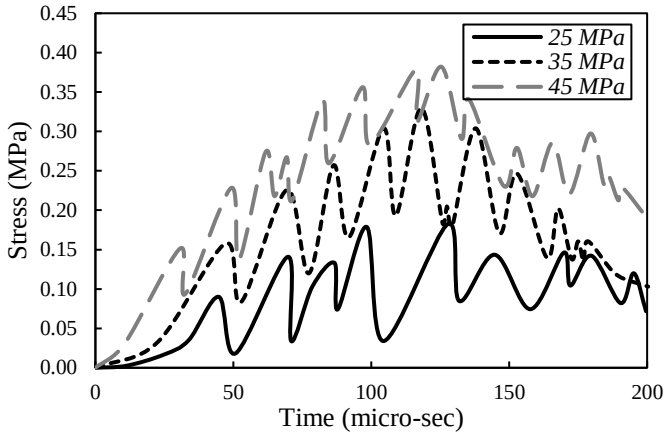

(c)

Figure 5.13: Influence of concrete compressive strength of 0.5% fiber-reinforced concrete on the stress with various thicknesses a) 10 cm, b) 20 cm, and c) 30 cm

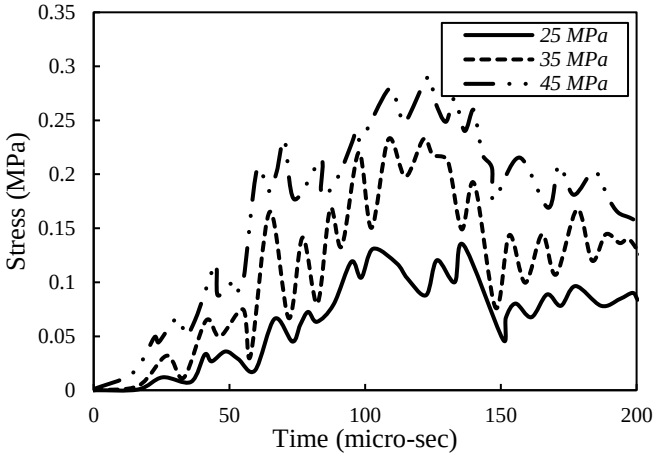

(a)

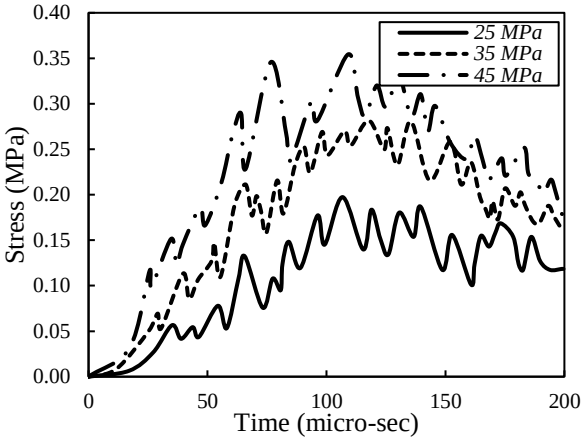

(b)

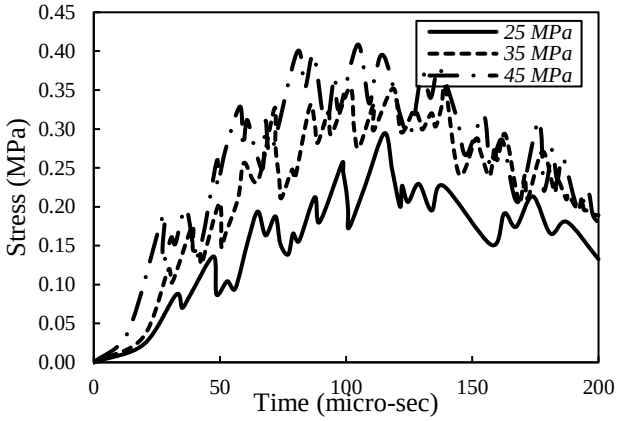

(c)

Figure 5.14: Influence of concrete compressive strength of 1.0% fiber-reinforced concrete on the stress with various thicknesses a) 10 cm, b) 20 cm, and c) 30 cm

Additionally, a significant element in raising the resistance of rigid concrete slabs was their thickness. As a result, as slab thickness grew, more energy was lost, which led to an increase in stress peak. The highest values of received stress by the receiver sensor were recorded and are shown in Figure 5.15 in order to better understand the effects of different factors on the resistance and structural responses of rigid concrete airfield runways as a non-destructive test. The highest wave stress was increased as a result of fiber integration. Therefore, when the compressive strength of concrete was also raised from 25 MPa to 45 MPa in a slab with a 30 cm thickness, adding 0.5% and 1.0% PF resulted in an increase in the highest stress of 55.3% and 63.5%, respectively. Additionally, adding 0.5% and 1.0% PF caused the peak stress to increase by 72.8% and 81.2%, respectively, when the thickness was raised to 30 cm and the compressive strength was raised from 25 MPa to 45 MPa, indicating an improvement in the strength of the concrete slabs and greater energy dissipation.

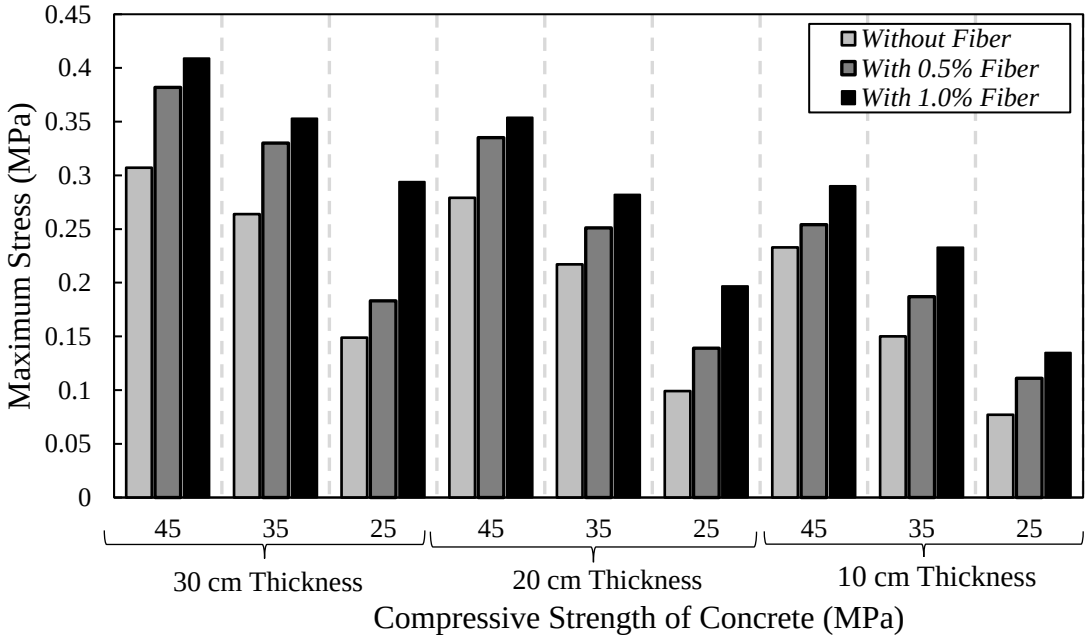

Figure 5.15: Effect of concrete compressive strength on the maximum stress considering various slab's thickness and fibers fractions

5.1.1. Energy dissipation

According to the presented results in previous sections, the main reason for the influence of material properties and geometric characteristics on the received frequency and stress is energy dissipation. Therefore, in this section, the effect of various considered variables on energy dissipation is measured. For this aim, the enclosed area by stress-time responses of slabs is investigated as energy dissipation, and the achieved consequences are presented in Figure 5.16. As a consequence, as the width of the slab increased, more energy was dissipated, which caused an improve the structural performance of rigid concrete slabs. For the purpose of a non-destructive test to better understand the effects of various variables on the resistance and structural responses of rigid concrete airport runways, the maximum dissipated values were measured. The fiber integration led to a rise in the greatest energy dissipation. The dissipated energy increased by 169% and 207%, respectively, when the compressive strength of concrete was increased from 25 MPa to 45 MPa in a slab with a 30 cm thickness by adding 0.5% and 1.0% PF. Additionally, when the thickness was increased to 30 cm and the compressive strength was increased from 25 MPa to 45 MPa, adding 0.5% and 1.0% PF caused the dissipated energy to rise by 215% and 253%, respectively, indicating an improvement in the strength of the concrete slabs and greater energy degeneracy.

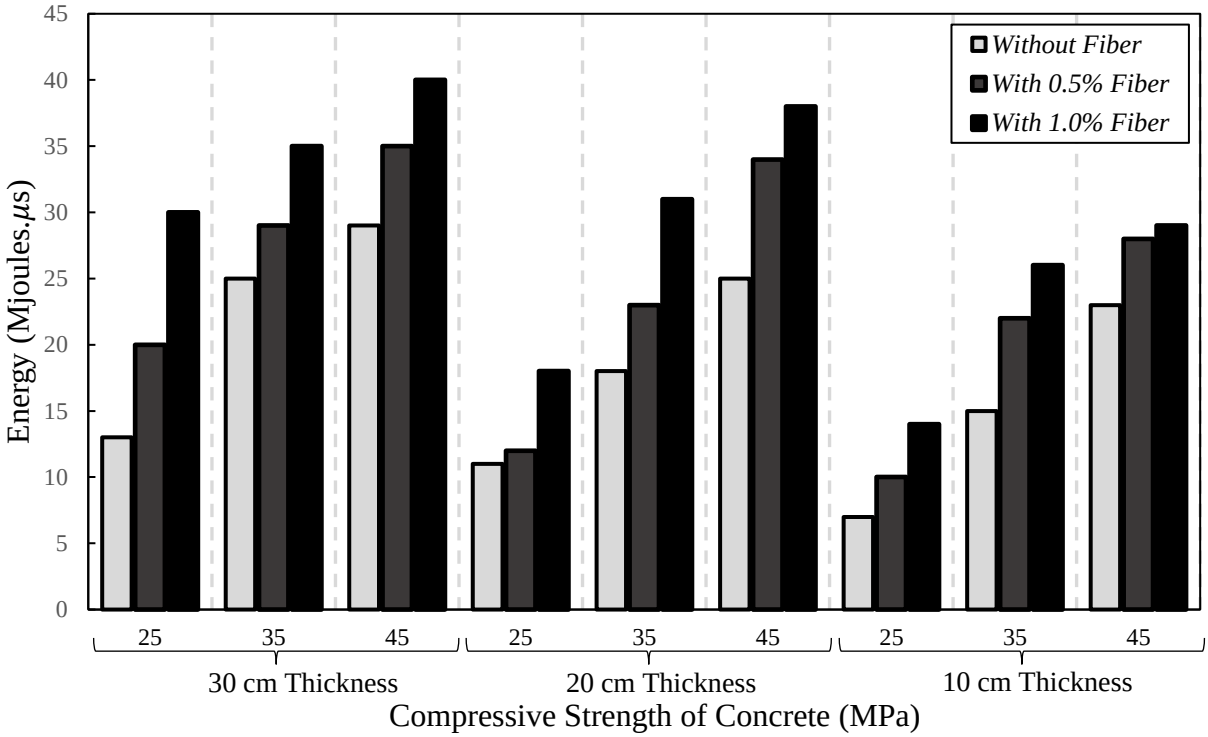

Figure 5.16: Effect of concrete compressive strength on the energy dissipation considering various slab's thickness and fibers fractions

5.1.2. New relationship to predict the compressive strength of concrete slabs

According to the obtained results, increasing the thickness and compressive strength of slabs as well as fiber incorporation plays a crucial role in improving the strength of rigid concrete airfield runways. In the field, the Synthetic Aperture Focusing Technique based on ultrasonic imaging only provides engineers with the frequency performance and received responses by the receiver sensor. However, the obtained frequency results give a prediction about the possible micro-cracks and the inside structure of rigid concrete airfield runways. The disadvantage of using this apparatus is the lack of slab resistance and strength prediction. So, in this section of the current research, the relationship between the stress and maximum peak of frequency was identified and the obtained results are presented in Figure 5.17. According to this figure, increasing the compressive strength

of concrete slabs resulted in increasing the stress values which indicates the improvement in the strength and structural performance of concrete slabs. Additionally, the relationship between the compressive strength of concrete slabs and the maximum peak of stress was identified, as shown in Figure 5.18. According to this figure, by increasing the compressive strength of concrete slabs considering various thicknesses of slabs, the stress value rose with almost the same slope and relationship. So, it helped us to generate a relationship between the peak of received frequency value by the receiver sensor and the compressive strength of concrete slabs which was the disadvantage of using the Synthetic Aperture Focusing Technique. The obtained results are provided in Eqs. 5.7 to 5.9.

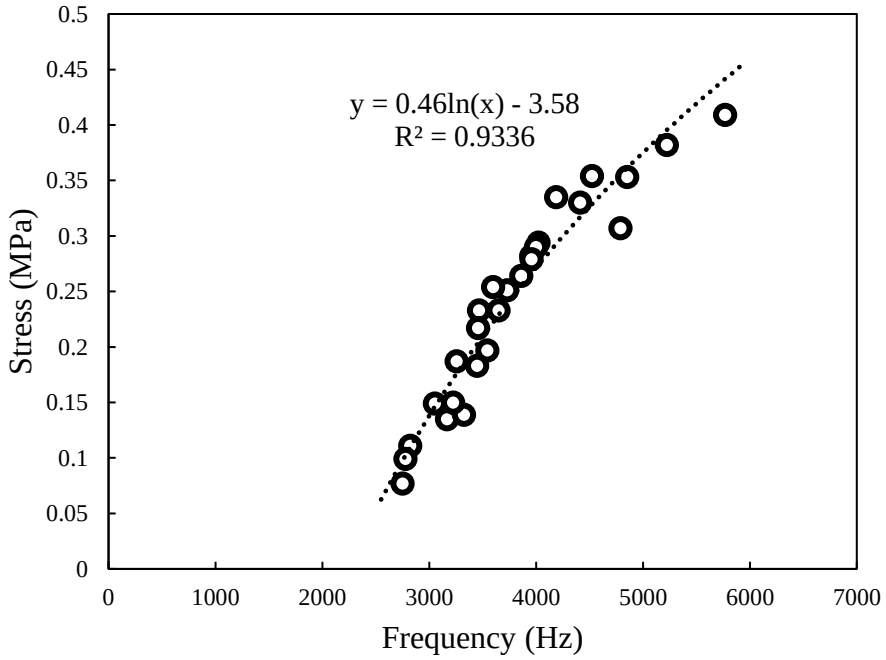

Figure 5.17: Relationship between the maximum stress and received frequency for various types of slabs

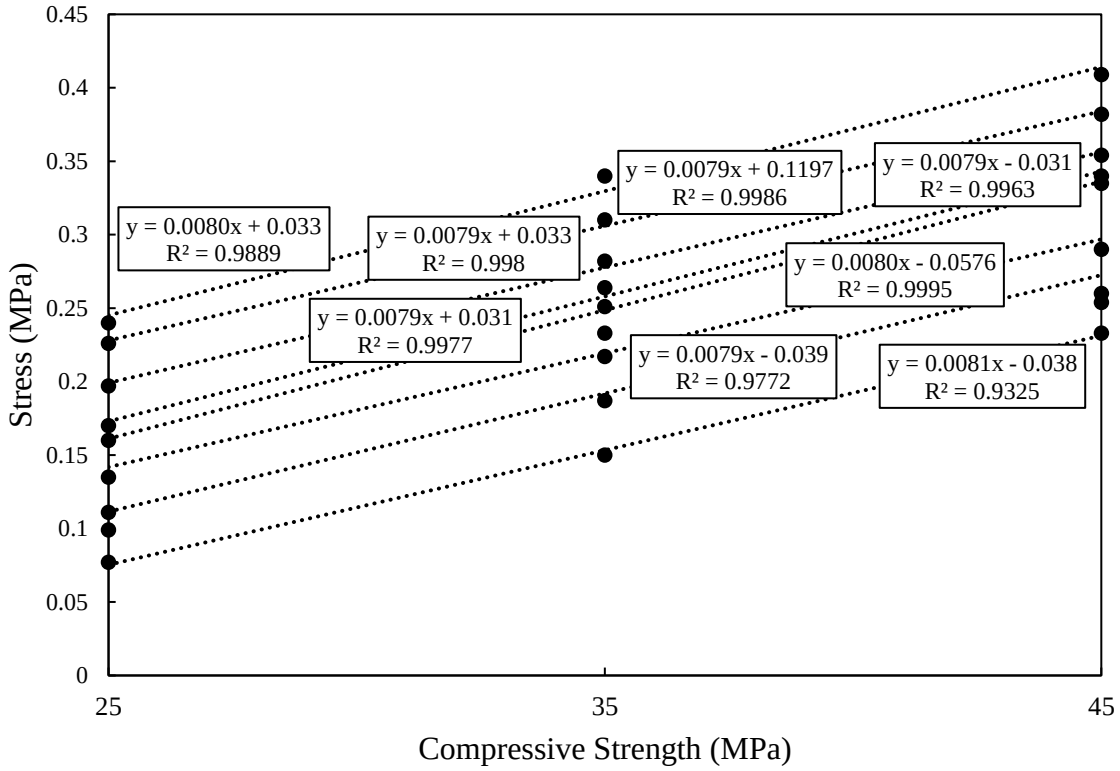

Figure 5.18: Relationship between the compressive strength of concrete and maximum stress for various types of slabs

Eqs. 5.7 and 5.8 present the stress-compressive strength and stress-maximum frequency relationships, respectively. According to Figures 5.17 and 5.18, the proposed relationships with high accuracy (R^2>0.95) could be utilized as beneficial tools.

$$\sigma_U = -0.008 f_c' + 0.035 \tag{5.7}$$

$$\sigma_U = 0.46 \ln f - 3.58 \tag{5.8}$$

Where, σ_U, f_c' and f indicates the maximum stress, compressive strength of concrete, and peak of received frequency by the receiver sensor, respectively. Therefore, my inserting Eq. 5.7 to 5.8, the relationship between the maximum received frequency and compressive strength of concrete could be established as shown in Eq. 5.9.

$$f_c' = -57.5 \ln f + 452 \quad (5.9)$$

5.1.3. Influence of base layer stiffness

An ultrasonic imaging test is a useful technique to identify the possible problems inside the slabs like microcracks and also the influence of underneath layers on the structural performance of rigid concrete airfield runways. Therefore, in this section, the effect of the stiffness of the base layer on the frequency and stress received by the receiver sensor is measured. It should be noted that the reflected responses from the surface of the base layer with various stiffnesses are measured and the penetration of waves inside the base layer is not the aim of this study. Figure 5.19 shows frequency-time responses of rigid concrete slabs with various base layer stiffnesses considering the effect of fiber incorporation in concrete slabs. Regarding these results, the frequency of slabs before reaching the base layer is the same. However, the reflected frequency from the harder base layer was superior to those samples with lower base layer stiffness which indicates better performance of the pavement. Also, by incorporating the fiber, the maximum received frequency increased. So, using the fiber and harder base layer simultaneously played a crucial role in improving the structural performance of rigid concrete airfield runways, particularly when the runways open to traffic.

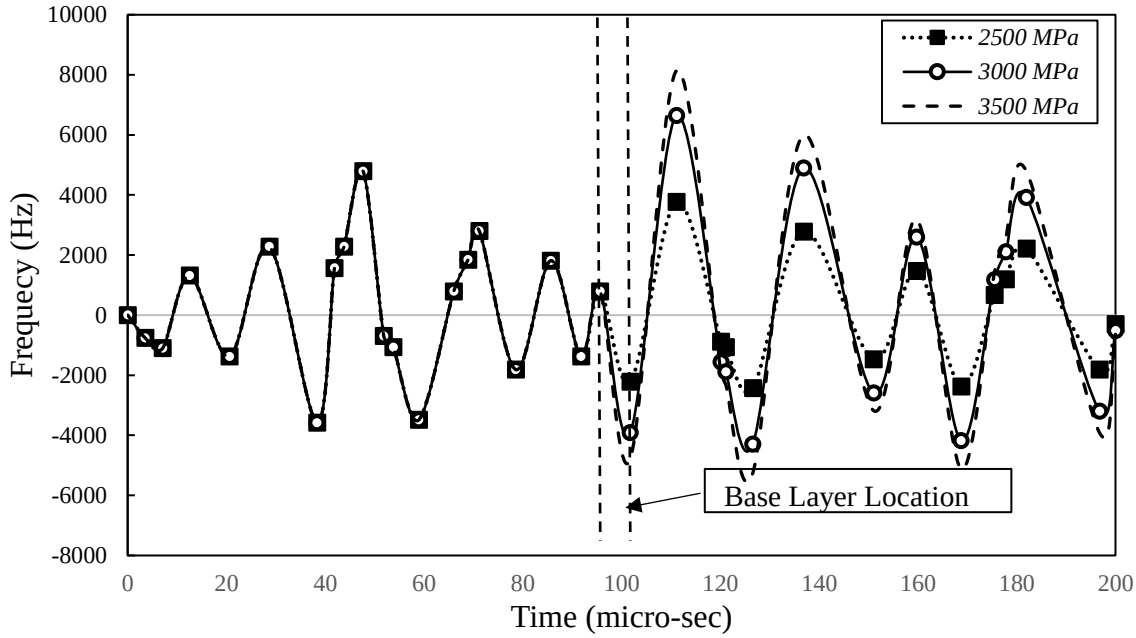
10000
8000
6000
4000
2000
0
-2000
-4000
-6000
-8000
Frequecy (Hz)
0
20
40
60
80
100
120
140
160
180
200
Time (micro-sec)
2500 MPa
3000 MPa
3500 MPa
Base Layer Location

(a)

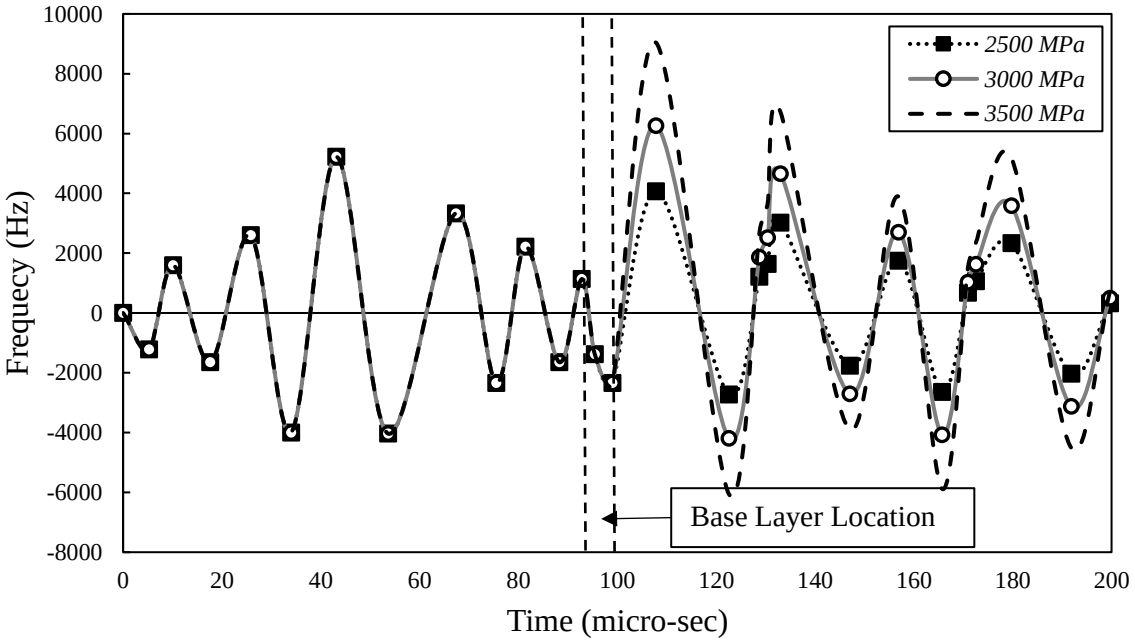
10000
8000
6000
4000
2000
0
-2000
-4000
-6000
-8000
Frequecy (Hz)
0
20
40
60
80
100
120
140
160
180
200
Time (micro-sec)
2500 MPa
3000 MPa
3500 MPa
Base Layer Location

(b)

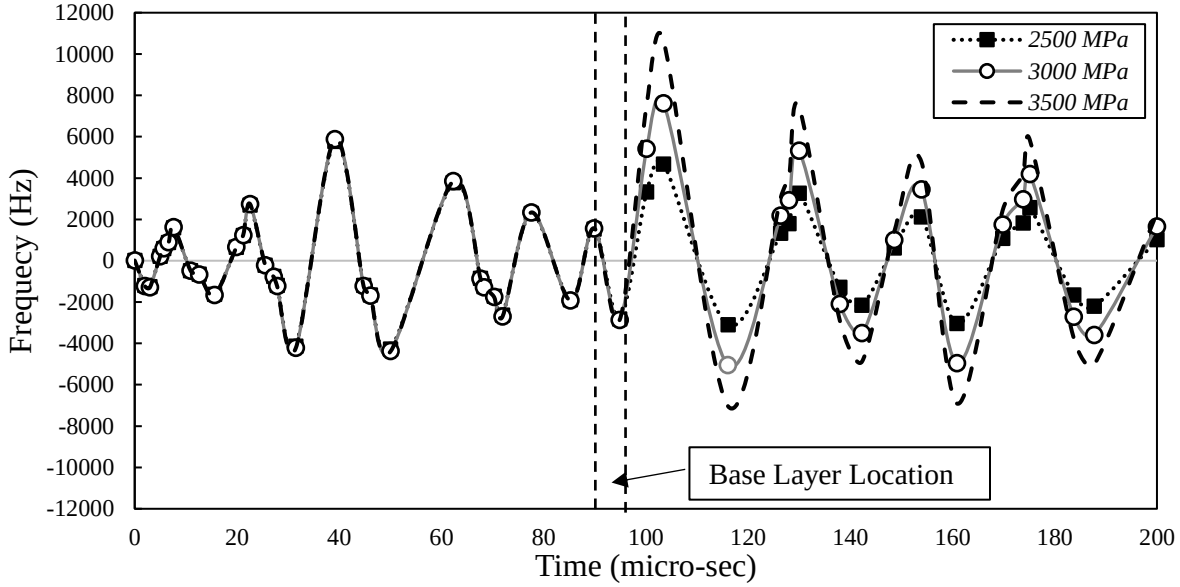

(c)

Figure 5.19: Influence of base layer modulus on the frequency history of a) plain concrete, b) 0.5% fibers-reinforced concrete, and c) 1.0% fiber-reinforced concrete with 25 MPa concrete compressive strength and 10 cm slab's thickness

Figure 5.19 depicts the stress-time reactions of rigid concrete slabs with different base layer stiffnesses while taking into account the impact of fiber inclusion. According to these findings, the stress of slabs before the base layer is constant. The better performance of the paving, however, is indicated by the reflected stress from the harder base layer, which was preferable to those specimens with reduced base layer stiffness. Additionally, the highest received stress rose with the addition of fiber. In order to improve the structural performance of stiff concrete airfield runways, especially when the runways are open to traffic, fiber, and a harder base layer were used simultaneously.

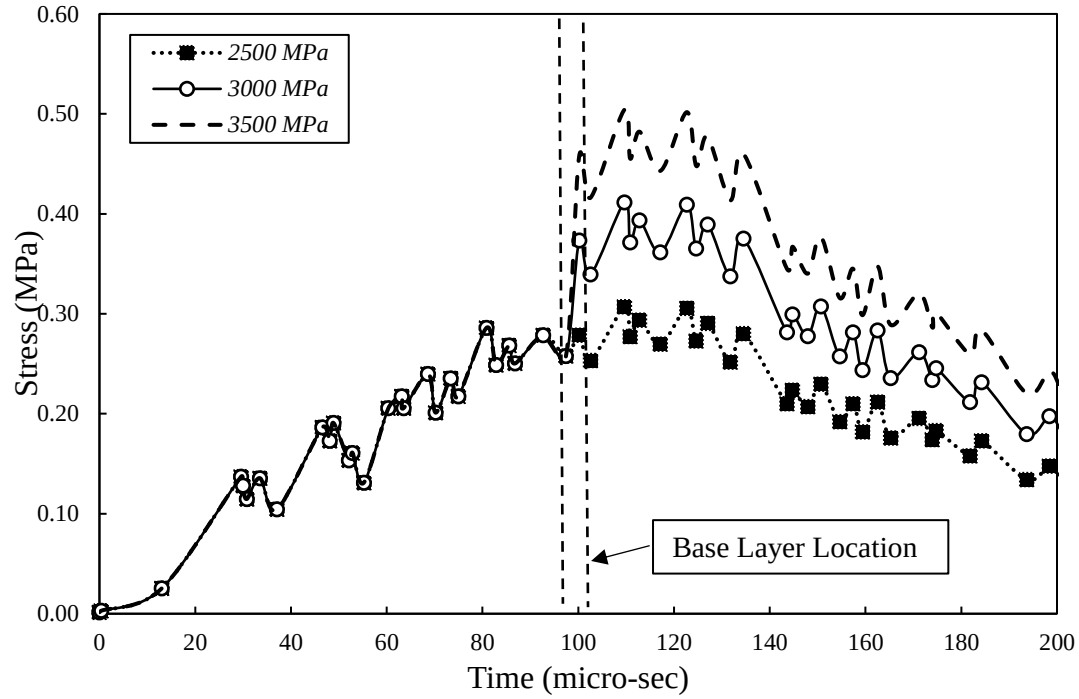
2500 MPa
3000 MPa
3500 MPa
Base Layer Location
Stress (MPa)
Time (micro-sec)
0.00
0.10
0.20
0.30
0.40
0.50
0.60
0
20
40
60
80
100
120
140
160
180
200

(a)

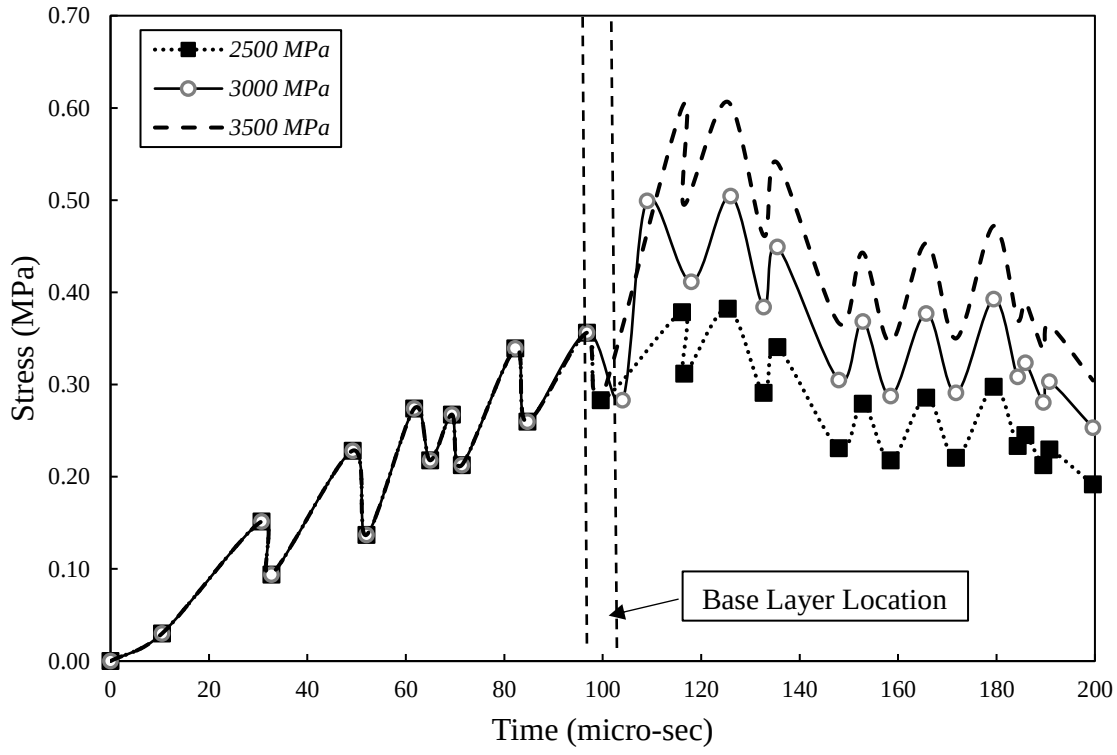
2500 MPa
3000 MPa
3500 MPa
Base Layer Location
Stress (MPa)
Time (micro-sec)
0.00
0.10
0.20
0.30
0.40
0.50
0.60
0.70
0
20
40
60
80
100
120
140
160
180
200

(b)

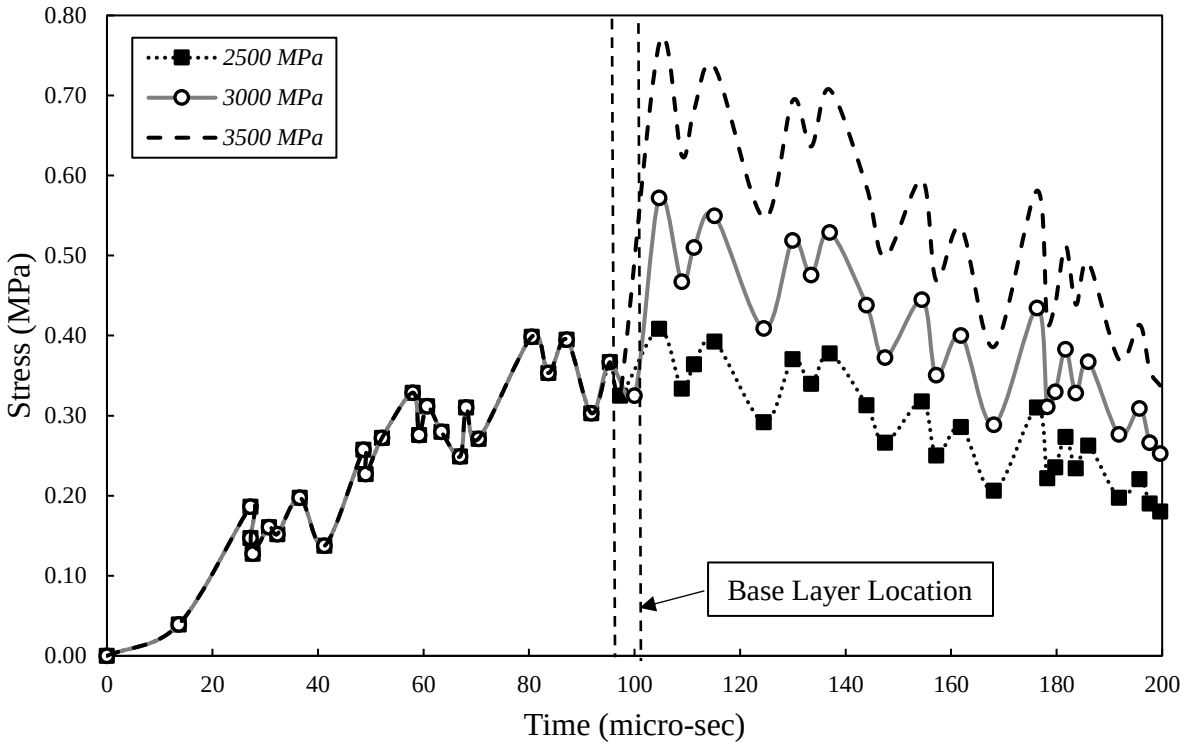

(c)

Figure 5.20: Influence of base layer modulus on the stress history of a) plain concrete, b) 0.5% fibers-reinforced concrete, and c) 1.0% fiber-reinforced concrete with 25 MPa concrete compressive strength and 30 cm slab's thickness

5.2. SUMMARY & CONNECTION WITH THE SUBSEQUENT CHAPTER

This chapter provided an advanced numerical simulation to measure the effect of various variables on the strength of rigid concrete slabs as a non-destructive test assessment. The technique was established based on wave propagation and penetration using Synthetic Aperture Focusing Procedure. The result helps to make sure about the strength of performed rigid concrete airfield runway construction. These results help to predict cracks algorithm and propagation which are significantly associated with service life and maintenance period. Therefore, using the obtained results from previous and current chapters about the influence of various variables on the thermal

performance and strength of rigid concrete slabs, a new method is developed in the next chapter named “Advanced Zero Stress Assessment”. Therefore, the crack depth over the slab thickness could be prophesied in addition to predicting the strength of rigid concrete slabs considering all geometric characteristics and material properties. Accordingly, Figure 5.21 provides a connection with the subsequent chapter overview.

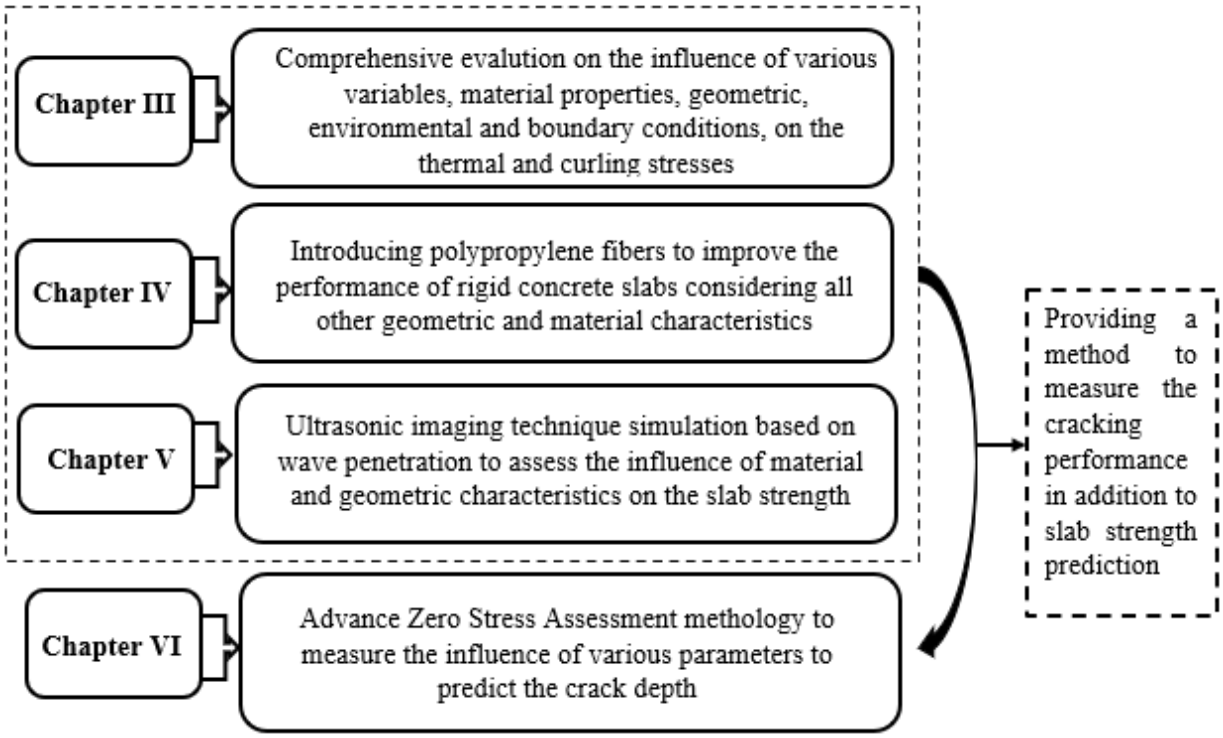

Figure 5.21: Overview of the connection between previous Chapters and Chapter VI

CHAPTER VI

ADVANCED ZERO-STRESS ASSESSMENT

6.1. INTRODUCTION

This chapter's main goal is to present a novel unique framework for measuring the influence of wide-range variables on the possible depth of cracks. The preceding section of this chapter is followed by finite element method results collected from previous chapters to identify the stress distribution over the slab's thickness to assess damages and crack depth imparted on rigid concrete slabs reinforced by PF as a result of the temperature gradient. The results of this task might be used by many businesses to create models, and DOTs could use them to construct robust concrete slabs that better account for improving the curling and thermal stresses of rigid concrete slabs.

6.1.1. Organization of the Chapter

This chapter consists of five main sections. Subsequent to the introductory section, Section 2 provides information associated with cracking in rigid concrete slabs over time due to shrinkage and stress distributions. Section 3 discusses a new advanced zero stress assessment over the thickness of slabs associated with stress distribution. This technique has been developed based on the conventional zero-stress evaluation methodology to measure the influence of various variables on the crack depth all over the slab's thickness. Next, the main results of this study are presented and discussed to show the effect of PF, geometric characteristics, and material properties on in-depth crack propagation and penetration. In the end, a summary of this section will be supplied so that its connection with the subsequent section and also the significance of the subsequent section can be clearly found.

6.2. ZERO-STRESS EVALUATION THEORY

Thermal and moisture variations cause concrete slabs to vary in volume. Early on, the heat of cement hydration dominates the thermal fluctuations in concrete's volume change. The composition of the cementing ingredient, the environment, and the structural integrity of the concrete all affect how much volume changes occur. Because the frictional base layer and their own weight severely restrict the concrete slabs' ability to move, strains develop in the slabs after the concrete has had time to set. Depending on whether the concrete temperature increases or lowers after the concrete setting time, the tension in the concrete slab now shows as tensile or compressive. The typical temperature and stress developments of concrete slabs at an early stage are shown in Figure 6.1. As can be observed, when the concrete has had time to cure, the temperature rises, which causes the slab to experience compressive stress. This problem typically arises when concrete is laid during hot weather. The temperature of the concrete then drops as the maximum temperature is reached, relieving the compressive stress. The stress in the concrete slab is zero when this compressive stress is fully released. The Conventional Zero-Stress Temperature (CZST) is the term used to describe this point's temperature, which is not zero (Sok et al. 2020; Breitenbücher, 1990; MEPDG, 2002; Schindler et al. 2002; Yeon et al. 2013; Hansen et al. 2006).

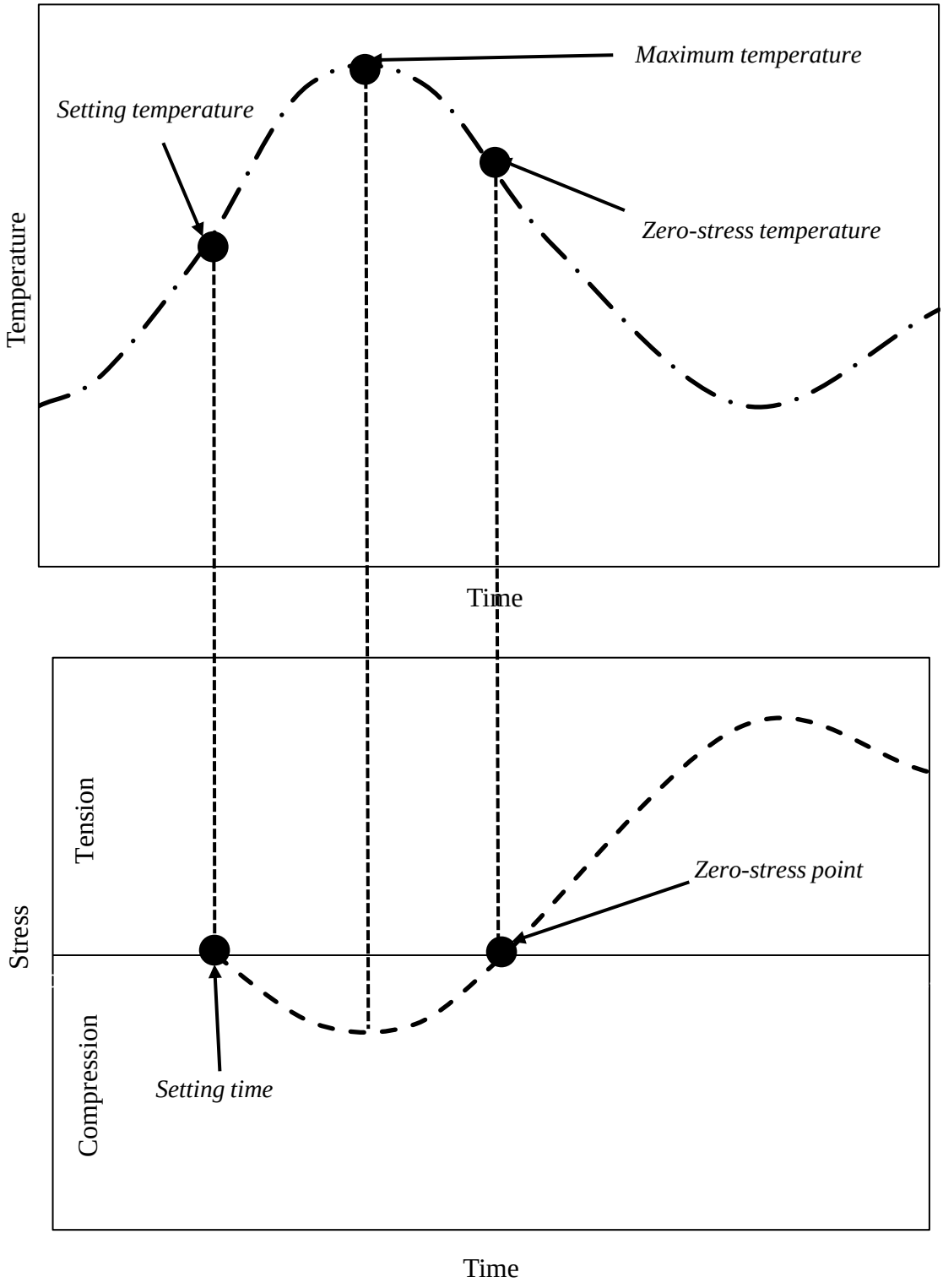

Figure 6.1: CZST theoretical determination in case one

Due to the creep and relaxation influences of the early-age concrete stress, the CZST was observed to be higher than the concrete setting temperature for hot environmental conditions (Breitenbücher, 1990; MEPDG, 2002; Schindler et al. 2002; Yeon et al. 2013; Hansen et al. 2006). Conversely, if the concrete is put during the cold weather season, the CZST may be somewhat comparable and lower than the concrete setting temperature (Hansen et al. 2006). An example of the early-age development of temperature and stress in the concrete pavement slab for cold weather construction could be seen in Figure 6.2. Tensile stress in the slab is caused when the temperature of the concrete drops after the concrete has had time to set. The tensile stress is entirely released and turns zero as the temperature rises after reaching the least temperature. CZST stands for the temperature that corresponds to this zero-stress point. The CZST in the concrete placement slab that was built during the colder season (fall season), as opposed to the hot season, was up to 2^{o}C lower than the concrete setting temperature, according to Hansen et al. (2006). CZST is one of the crucial variables influencing the behavior and performance of concrete slabs, claims MEPDG[1] (2002). Additionally, a great deal of earlier research has shown that CZST substantially influences the concrete slab characteristics at both an early and advanced age (MEPDG, 2002; Hansen et al. 2006; Nam, 2005). In terms of joint or crack width, punchout for continuously reinforced concrete pavements (CRCP), and faulting for jointed plain concrete pavements (JPCP), the MEPDG reported that CZST had substantial impacts (MEPDG, 2002). Low CZST, following Nam (2005), would result in narrower crack widths and raise the slab stiffness of CRCP. Low CZST would lead to substantially smaller later-age joint openings than those with high CZST, according to Hansen et al. (2006).

[1] Mechanistic-Empirical Pavement Design Guide

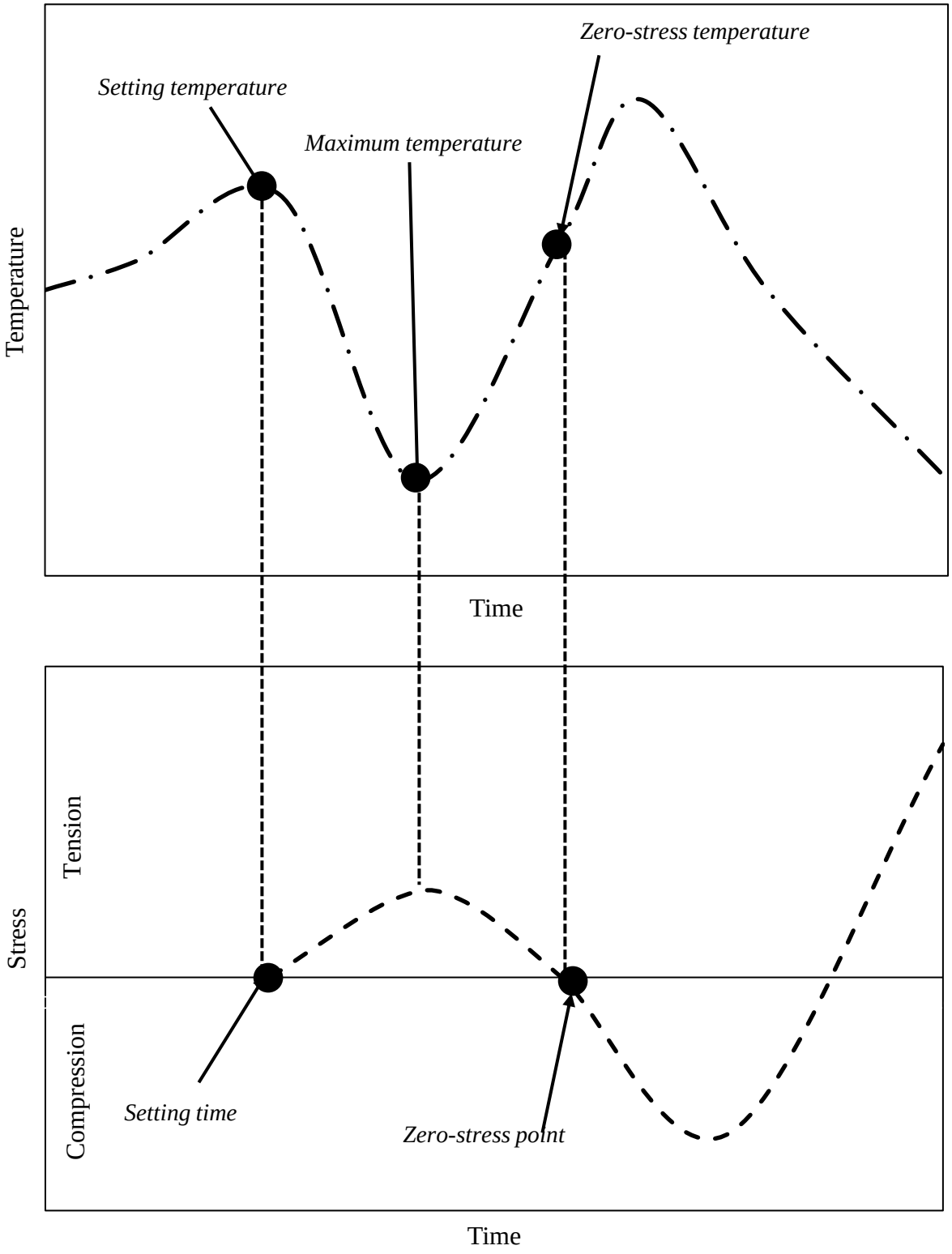

Figure 6.2: CZST theoretical determination in case two

According to Schindler et al. (2002), CZST has an impact on how much steel is used in the CRCP's design. To keep the transverse cracks closed when the CZST is high-level, more steel must be used to design rigid concrete slabs. Although CZST has been identified as a crucial variable influencing the performance of rigid concrete slabs, there are currently very few reliable methods or guidelines for predicting the CZST of Portland cement concrete slabs. To estimate the CZST, the MEPDG has offered a simple empirical equation that only depends on two variables: cement content and the mean monthly temperature during construction (MEPDG, 2002). The construction season, the amount of time it takes to place the concrete in a day, the method utilized for curing, the percentage of the concrete mixes, and the thickness of the slab can all have an impact on how much CZST occurs. Numerous researchers have suggested ways to measure the CZST in concrete slabs as a result of these restrictions (Schindler et al. 2002; Yeon et al. 2013; Hansen et al. 2006; Yeon, 2011). By measuring the early-age concrete temperature and stress of fully restrained concrete slabs in the lab, Hansen et al. (2006) were able to quantify the CZST. They discovered that when the concrete was laid during the hot season, CZST was up to 10^{o}C higher than the final set temperature, whereas it was up to 2 ^{o}C lower than the final set temperature during the cold season. In order to construct CZST in the concrete slab, Schindler et al. (2002) established the numerical analysis to forecast concrete temperature and stress.

It was discovered that the CZST can be calculated from the highest concrete temperature at an early age, 92-94% of that temperature. Although there is a nonlinear temperature distribution in rigid concrete slabs, this model can only be used provided the temperature loading is uniform across the specimen's cross-section (Schindler et al. 2002). By measuring and analyzing the early-age stress development in concrete slabs in conjunction with measurements of the concrete temperature profile, Yeon et al. (2013) estimated the CZST. They discovered that CZST ranged

from 88.9 to 99.9% of the maximum concrete temperature for the early age. However, their model did not explore the impacts of other cement types or the replacement ratio of supplemental cementitious material on CZST and was largely focused on CRCP with class P concrete, which is frequently used in Texas (Yeon, 2011). The CZST in a rigid concrete slab has been evaluated using a number of proposed methods, although they are still rather limited. Therefore, additional research on CZST and the elements that affect it in Portland cement concrete pavement is still needed. The development of concrete mechanical properties (such as concrete strength and elastic modulus, and creep and relaxation coefficient), as well as the development of early-age stress in concrete pavement slabs, were then calculated using the findings of the temperature forecast. The field measurement was used to verify the CZST results from the created numerical model.

In concrete slabs, the longitudinal and transverse dimensions are disproportionately large to the thickness (vertical direction). As a result, it is reasonable to infer that the concrete pavement slab's temperature distribution varies exclusively across its depth. The following equation (6.1) represents Fourier's law for the heat transfer equation, where k is thermal conductivity (W/m/C), T is the temperature (C), x is pavement depth (m), $q(t)$ is internal heat produced by cement hydration (W/m3/m3), q is density (kg/m3/m3), c is specific heat (J/kg/C), and t is time (s). Following the cement hydration product, the specific heat c and the thermal conductivity significantly vary when the concrete hardens.

$$\frac{\partial}{\partial x}\left(k\frac{\partial T}{\partial x}\right) + q(t) = \rho.c.\frac{\partial T}{\partial t} \tag{6.1}$$

In their equation for calculating thermal conductivity as a function of the degree of hydration and the thermal conductivity of hardened concrete k_∞, Ruiz et al. (2001) provided the following formula:

$$k = k_{\infty}(1.33 - 0.33\alpha) \tag{6.2}$$

Where k_{∞} is in (W/m/C) and α represents the degree of hydration. The equation developed by Van Breguel (1991) is utilized to represent the time-dependent change in the concrete specific heat and is written as follows:

$$c = \frac{1}{\rho}\left(W_c \alpha c_{rep} + W_c(1-\alpha)c_c + W_a c_a + W_w c_w\right) \tag{6.3}$$

In which W_w, W_a and W_c are the weights of water, aggregate, and cement (kg/m^3), respectively; c_w, c_a and $c_c$are the specific heats of water, aggregate, and cement (J/kg/C); and c_{ref} is a fictitious specific heat of hydrated concrete (J/kg/C). Because they can account for both the effects of time and temperature for the very young-age concrete, the equations for determining thermal conductivity (k) and specific heat of concrete (c) as stated in Equations (6.2) and (6.3) are used. The heat of hydration is the term for the heat generated by the heat-releasing interaction between water and cement. It is controlled by a variety of variables, such as the ratio of water to cement, the composition and fineness of the cement, the curing temperature, and supplementary cementitious material. The Schindler and Folliard (2005) heat of hydration model is used because it can account for all these influencing factors, particularly the effects of using supplementary cementitious material like fly ash and slag on heat generation and degree of hydration. The next formula represents it:

$$q(t) = H_u . C_c . \left(\frac{\tau}{t_e}\right)^{\beta} . \left(\frac{\beta}{t_e}\right) . \alpha(t_e) . \exp\left[\frac{E}{R}\left(\frac{1}{273+T_r} - \frac{1}{273+T}\right)\right] \tag{6.4}$$

With

$$\alpha(t_e) = \alpha_u . \exp\left(-\left[\frac{\tau}{t_e}\right]^{\beta}\right) \tag{6.5}$$

$$\alpha_u = \frac{1.031 \times w/c}{0.194 + w/c} + 0.5p_{FA} + 0.3p_{SLAG} \leq 1.0 \tag{6.6}$$

In which H_u and C_C stand for total heat of hydrated cementitious materials at 100% hydration (J/kg) and cementitious material content (kg/m3); w/c stands for water to cement ratio; α_u, τ, and β stand for the ultimate degree of hydration, hydration time parameter, and hydration shape parameter; t_e stands for equivalent age (hour), and T_r stands for reference temperature of concrete (21.1 ^{o}C); R is the universal gas constant (8.3144 J/mol/K); E is the activation energy (J/mol); and p_{FA} and p_{SLAG} are the weight ratios of fly ash and slag in terms of the total cement contents.

6.3. NOVEL ADVANCED ZERO STRESS ASSESSMENT

Az described above about CZST; the conventional techniques could be utilized as a good tool to predict the thermal performance of rigid concrete slabs in terms of longitudinal cracking after curing. So, the conventional method is unable to participate in cracking prediction associated with the curling and bending performance of rigid concrete slabs. Therefore, in the current research, a novel Advanced Zero Stress Assessment (AZSA) has been developed considering the general definition of CZST. Additionally, considering the results of Chapters III and IV, various variables could significantly affect the curling and lateral deformation as well as buckling in rigid concrete slabs which could be associated with crack propagation through slabs' thickness. Therefore, considering the Zero-Stress Temperature theory and its development, a new concept will be presented to identify the effect of different parameters on possible cracks in the rigid concrete slabs

under the effect of curling stress and bending deformation. To propose this technique, the following assumptions have been established:

1) Cracking occurs due to tensile stress over the rigid concrete slabs' thickness.
2) Plane sections remain plane after the deformation and that deformed slab angles (slopes) are small.
3) Cracking will not occur where there is no stress.
4) Between the tensile and compressive stresses, there is the zero-stress line here there is no cracking as a result of $\sum Strength/\sum tensile\ stress \geq 1.0$
5) Cracks propagate over the thickness of slabs up to the zero-stress line.
6) The location of the zero-stress line considering the effect of various variables could be considered as a depth of cracks

According to the above hypotheses, the zero-stress line can be considered as illustrated in Figure 6.3. Regarding this figure, cracks can increase up to this line along with the slab thickness. As a result, by reducing the distance of this line from the slab surface in the tensile section, the depth of cracks will decrease and as a result, their width will decrease. In this study, with the help of the advanced zero-stress concept, the effect of various parameters on the spread of possible cracks will be investigated, as discussed in the next section.

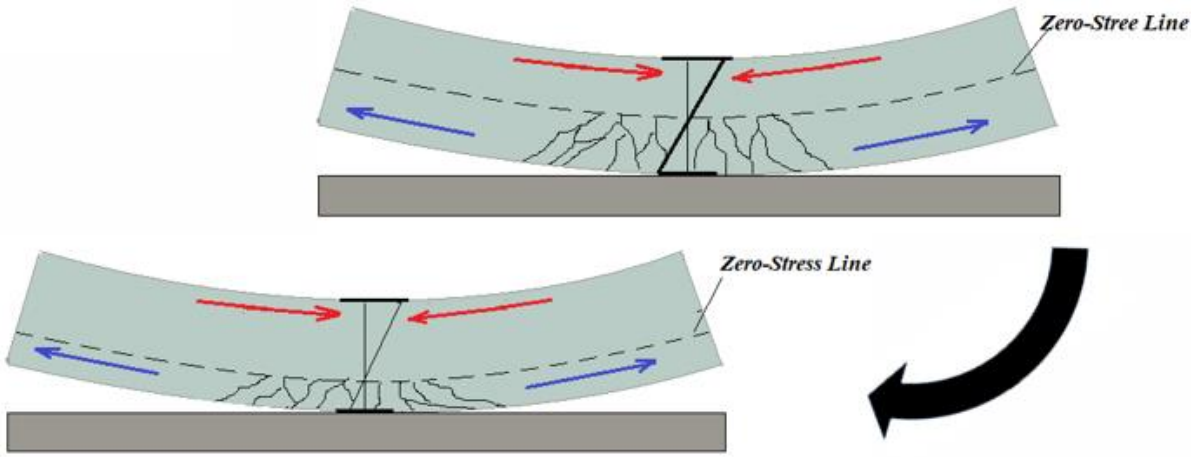

Figure 6.3: Theoretical determination of Advanced Zero-Stress Assessment (AZSA)

6.4. RESULTS AND DISCUSSIONS

In this section, the possible cracks propagation from the bottom of slabs is assessed using the proposed AZSA. For this aim, the zero-stress line was taken into account as the ratio of tensile stress to the tensile strength of rigid concrete slabs. Figures 6.4 and 6.5 show the zero-stress line for 25MPa concrete slabs with 4.5m length and various widths,3m, 4.5m, and 6m, and 10 cm and 30 cm thickness. Generally, fiber incorporation significantly decreased the depth of the zero-stress line which indicates fewer cracks in depth. This could be attributed to the bridging character of fibers in reducing the cracks width (Ghalehnovi et al. 2020). Therefore, the width of cracks declined and more cracks propagated through the thickness. Additionally, with an increase in thermal gradient, the zero-stress line depth increased with indicates to increase in the dept of propagated cracks. Also, in 4.5m length slabs, a rise in slabs' width led to increasing the depth of cracks as well as their width due to increasing the curvature in rigid concrete airfield runways under the effect of the thermal gradient. Additionally, increasing the thickness of slabs could be

considered an effective factor in reducing the depth of cracks as the ratio of bending-tensile stress over the bending-tensile resistance of concrete declined.

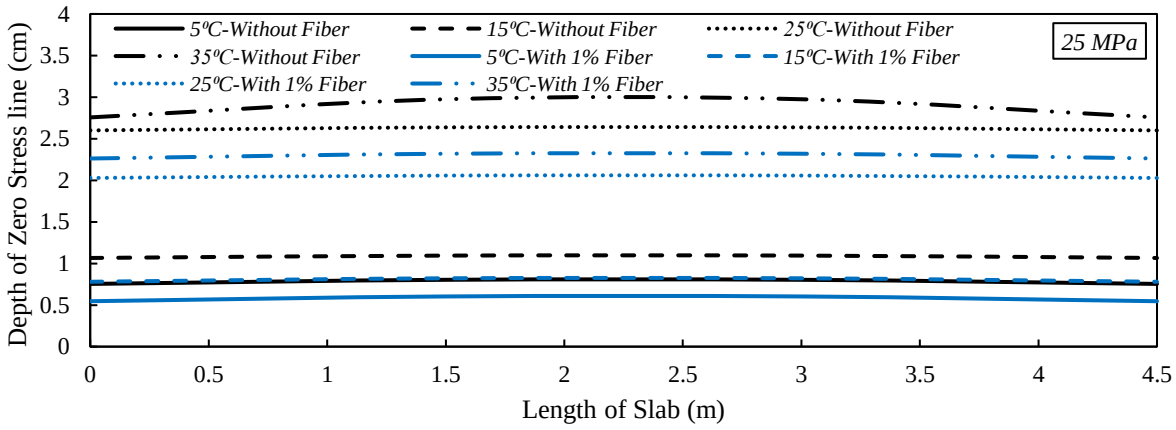

(a)

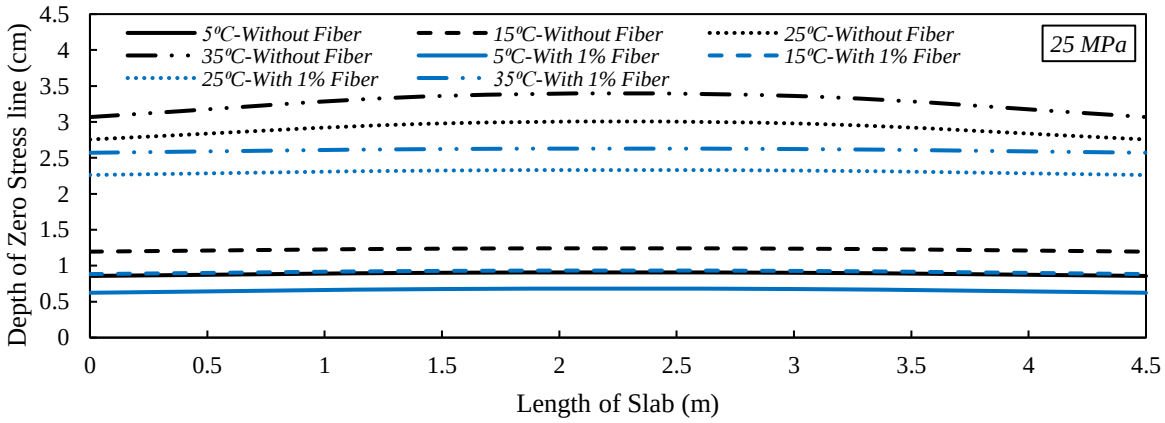

(b)

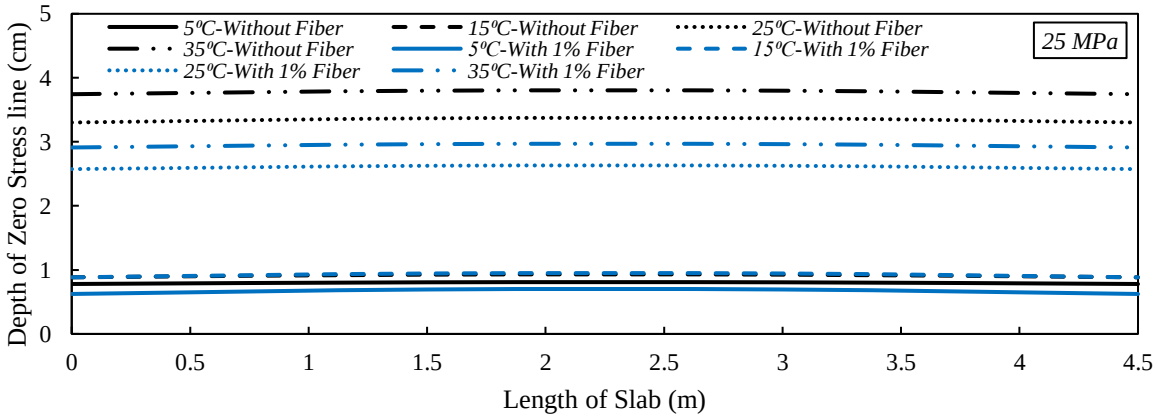

(c)

Figure 6.4: Advanced Zero-Stress line for 10 cm thickness slab, 4.5m length, and 25 MPa concrete compressive strength with various widths a) 3m, b) 4.5m, and c) 6m

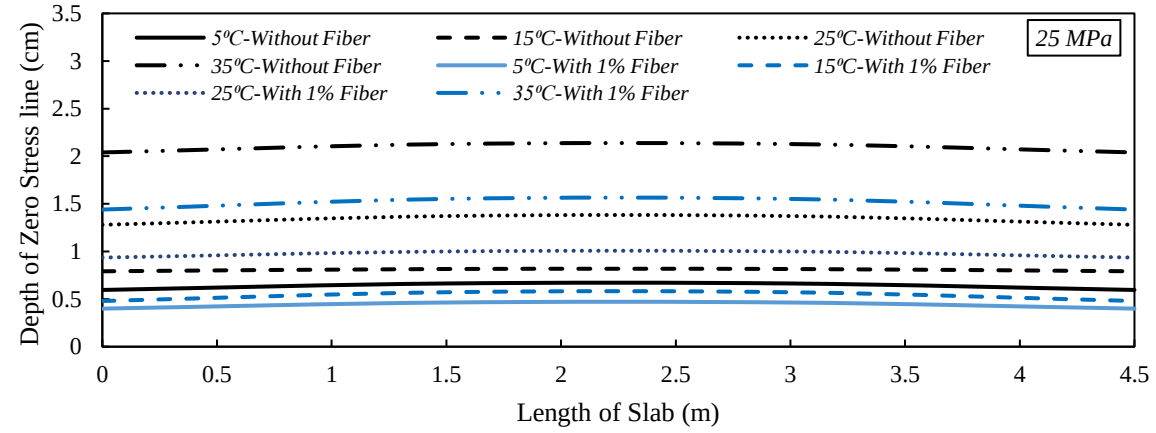

(a)

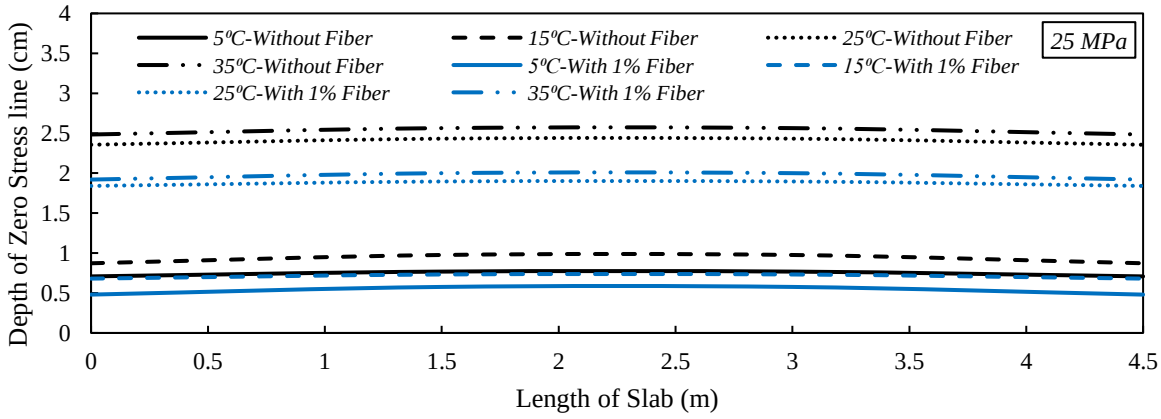

(b)

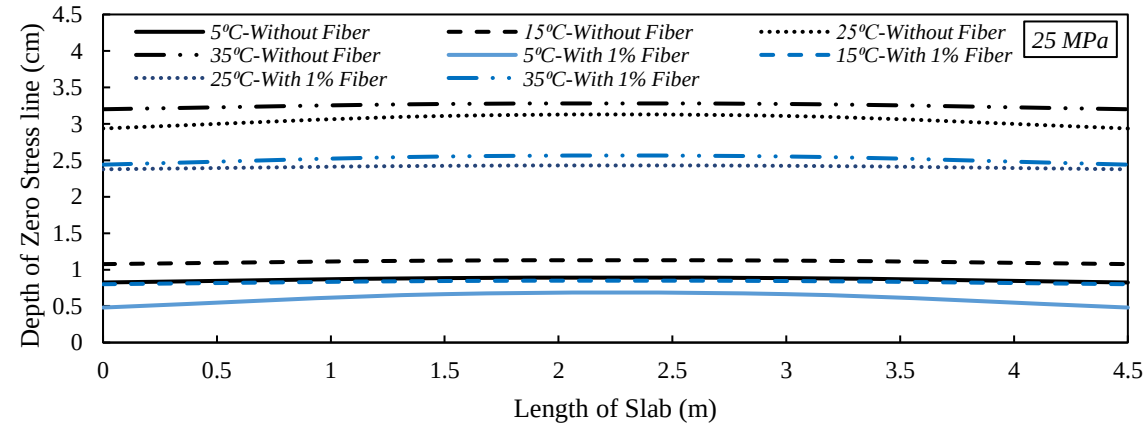

(c)

Figure 6.5: Advanced Zero-Stress line for 30 cm thickness slab, 4.5m length, and 25 MPa concrete compressive strength with various widths a) 3m, b) 4.5m, and c) 6m

Furthermore, the effect of compressive strength for concrete slabs on AZSA was also measured. The results for 35MPa concrete slabs with 4.5m length and various widths, 3m, 4.5m, and 6m, and

10 cm and 30 cm thickness, are presented in Figures 6.6 and 6.7, respectively. According to Figures 6.6a and 6.6b, increasing the compressive strength in slabs with 4.5m length led to reducing the depth of possible cracks, and by raising the compressive strength to 35MPa, the crack depth was further decreased. Also, increasing the thickness played an effective role in reducing the cracks depth, however, by increasing the width of the slabs, and cracks' depth was significantly increased. As it could be observed from the presented results, the negative influence of thermal gradient on slabs with 6m width was more obvious than those slabs with shorter width which could be associated with the difference in out-of-plane and post-buckling performance of shorter width rigid concrete slabs.

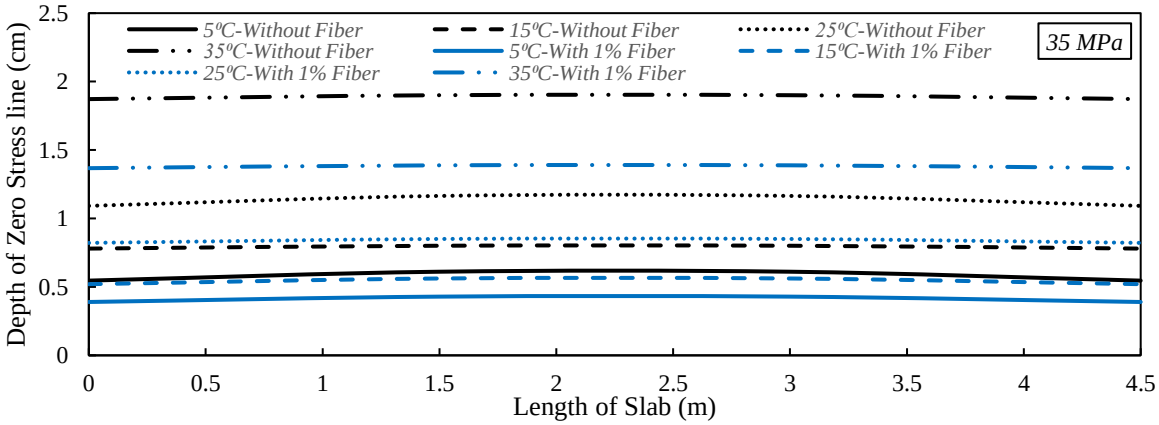

(a)

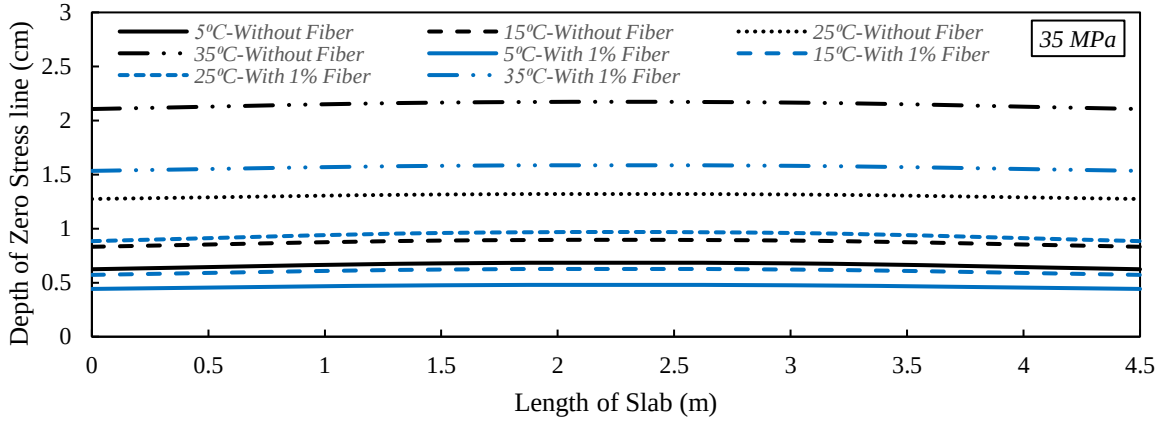

(b)

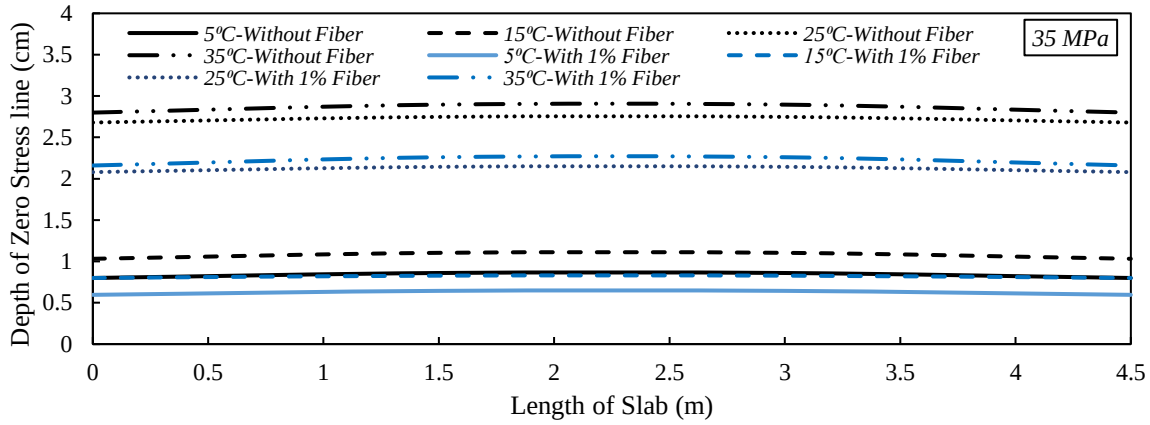

(c)

Figure 6.6: Advanced Zero-Stress line for 10 cm thickness slab, 4.5m length, and 35 MPa concrete compressive strength with various widths a) 3m, b) 4.5m, and c) 6m

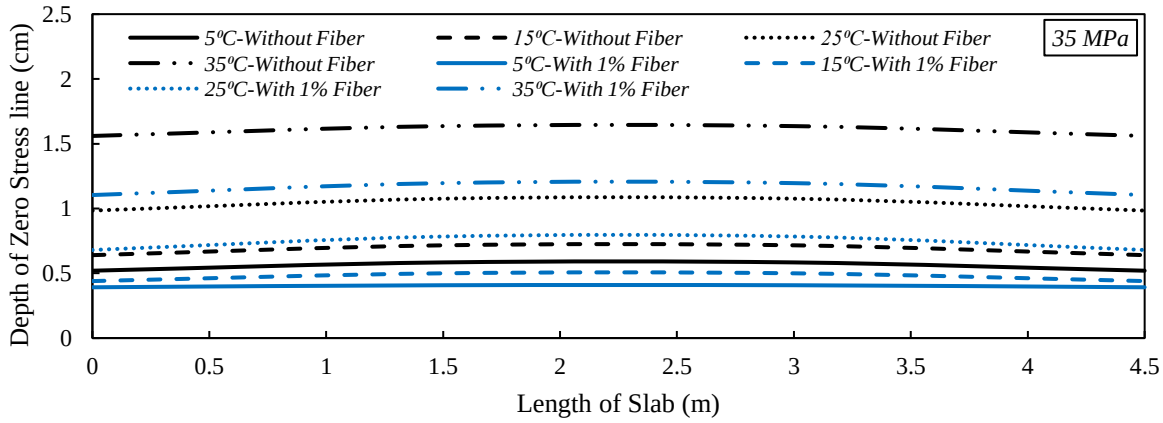

(a)

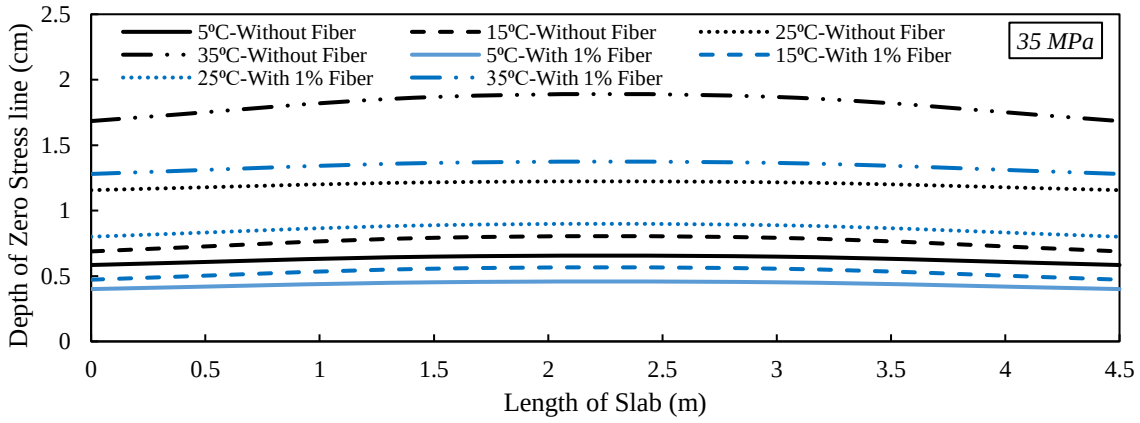

(b)

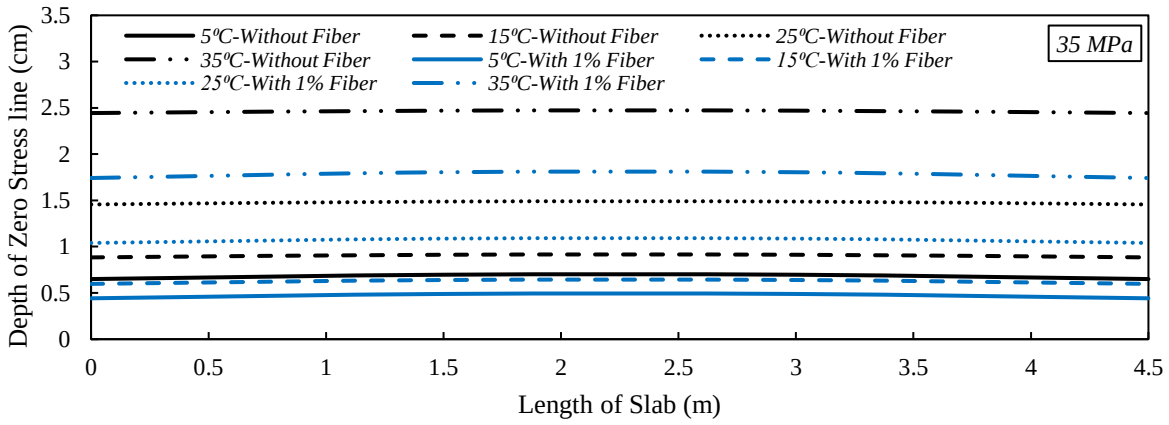

(c)

Figure 6.7: Advanced Zero-Stress line for 30 cm thickness slab, 4.5m length, and 35 MPa concrete compressive strength with various widths a) 3m, b) 4.5m, and c) 6m

As a result, slabs with a longer width are more sensitive to temperature changes and it is recommended to use shorter width slabs in the airfield runways construction. Finally, the compressive strength of slabs increased to 45MPa and the results for 45MPa concrete slabs with 4.5m length and various widths, 3m, 4.5m and 6m, and 10 cm and 30 cm thickness, are provided in Figures 6.8 and 6.9, respectively. There, the simultaneous use of high concrete compressive strength and fiber incorporation significantly enhanced the cracking behavior of rigid concrete slabs with 4.5m length, and fewer cracks developed through the thickness, particularly for shorter-width slabs. Additionally, raising the thickness had a significant impact on decreasing the depth of cracks; however, as slab width grew, so did the depth of the cracks. The findings showed that the negative impact of thermal gradient on slabs wider than 4.5m was more pronounced than on slabs narrower than that, which may be related to the different out-of-plane and post-buckling capabilities of stiff concrete slabs of various widths.

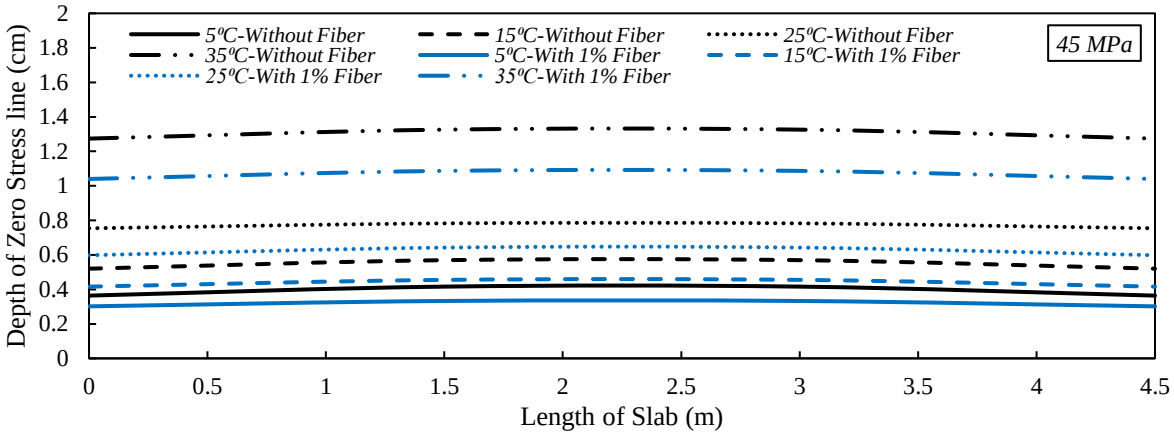

(a)

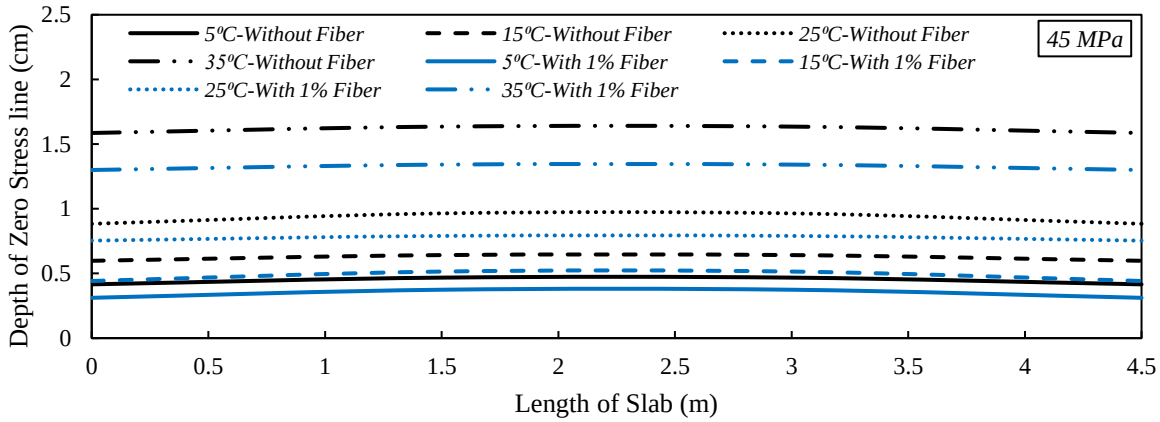

(b)

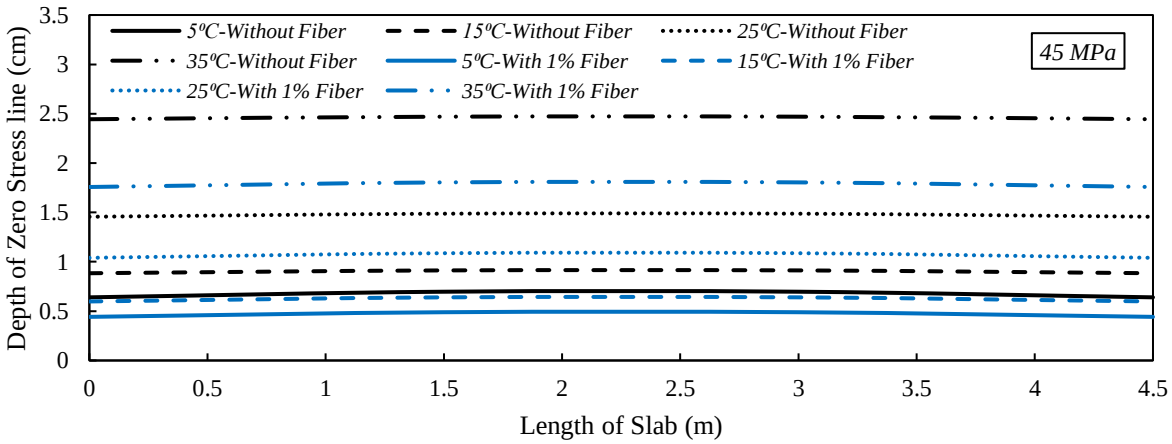

(c)

Figure 6.8: Advanced Zero-Stress line for 10 cm thickness slab, 4.5m length, and 45 MPa concrete compressive strength with various widths a) 3m, b) 4.5m, and c) 6m

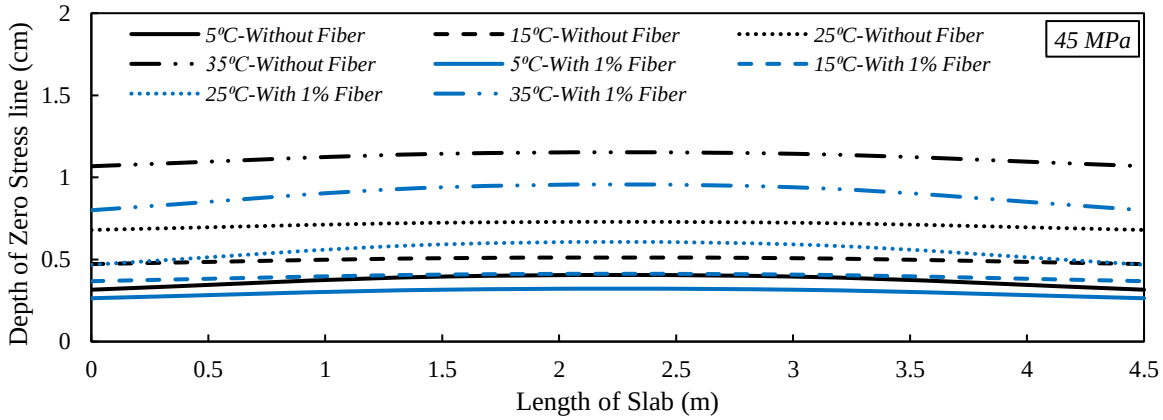

(a)

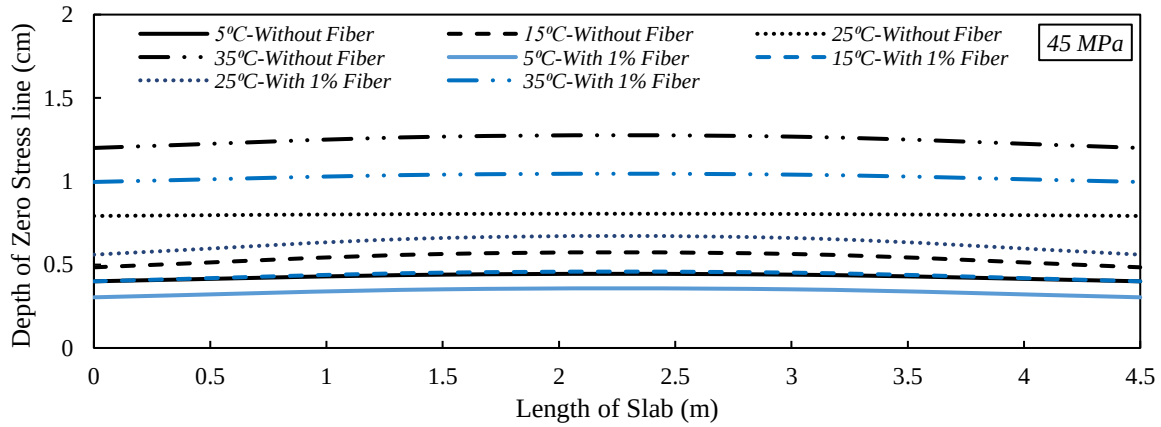

(b)

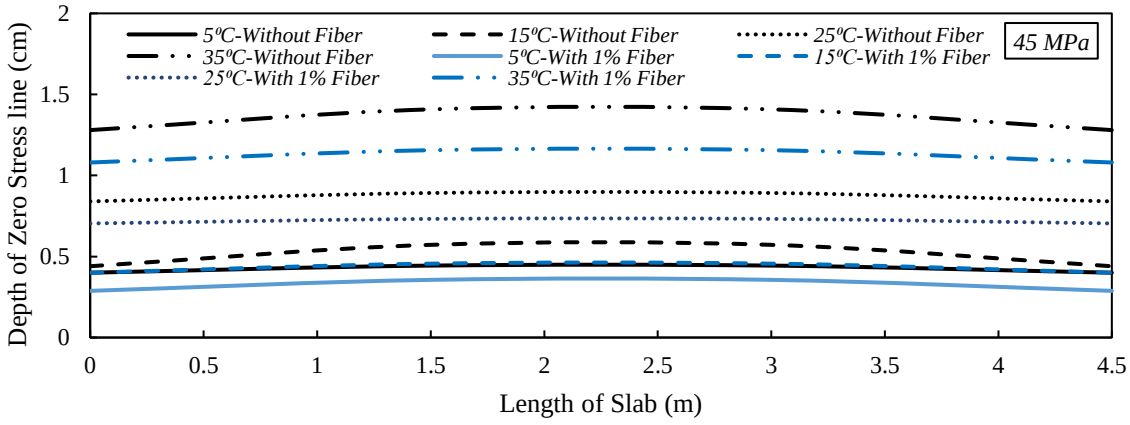

(c)

Figure 6.9: Advanced Zero-Stress line for 30 cm thickness slab, 4.5m length, and 45 MPa concrete compressive strength with various widths a) 3m, b) 4.5m, and c) 6m

Another factor playing an effective role in the thermal characteristics of rigid concrete airfield runways is the length of the slabs. The depth of the zero-stress line for slabs width 6m in length with various compressive strengths and widths are illustrated in Figures 6.10 to 6.15. The same trend was observed for slabs with 6m slabs as slabs with 4.5m length. Regarding Figure 6.10, increasing the length of slabs to 6m led to increasing the depth of the zero-stress line and more cracks depth in comparison with 4.5m length slabs. According to Figures 6.10 and 6.11, the depth of the zero-stress line considerably dropped with the inclusion of fibers, indicating less cracking. This may be ascribed to the fibers' ability to bridge gaps, narrowing cracks. As a result, the crack width decreased and more cracks spread throughout the thickness. Additionally, as the temperature gradient rose, so did the depth of the zero-stress line, which pointed to deeper propagated cracks. Additionally, in 4.5 m long slabs, an increase in slab width caused cracks to widen and deepen as a result of the impact of thermal gradient on rigid concrete airport runways. Additionally, as the ratio of bending-tensile stress over the bending-tensile resistance of concrete decreased, raising the thickness of slabs could be thought of as a useful component in decreasing the depth of cracks.

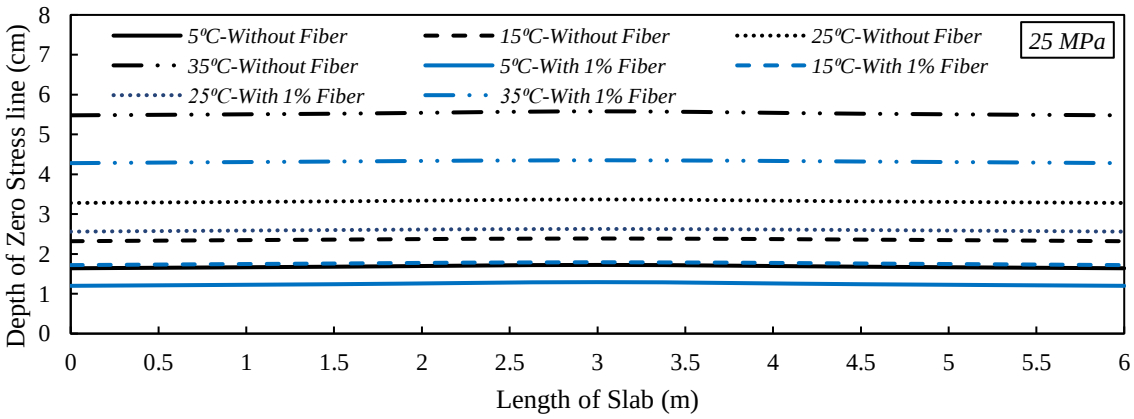

(a)

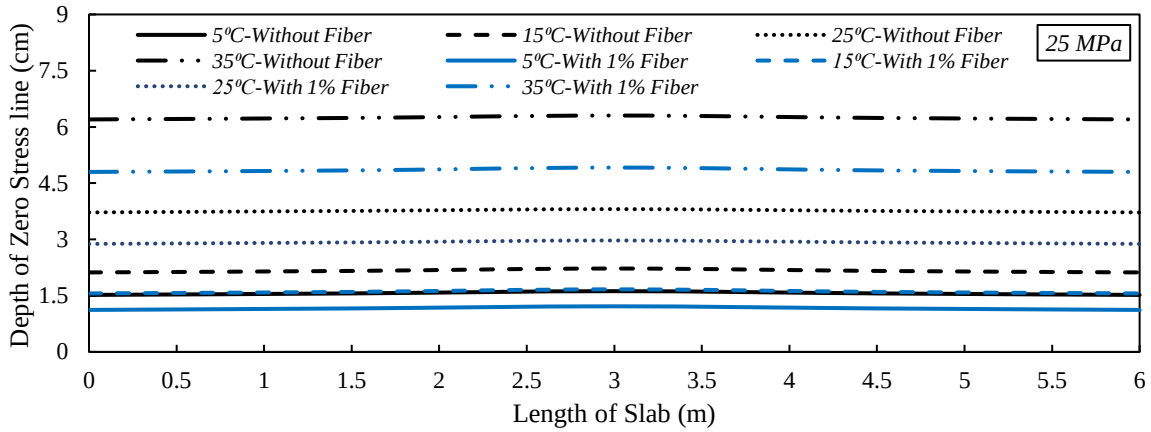

(b)

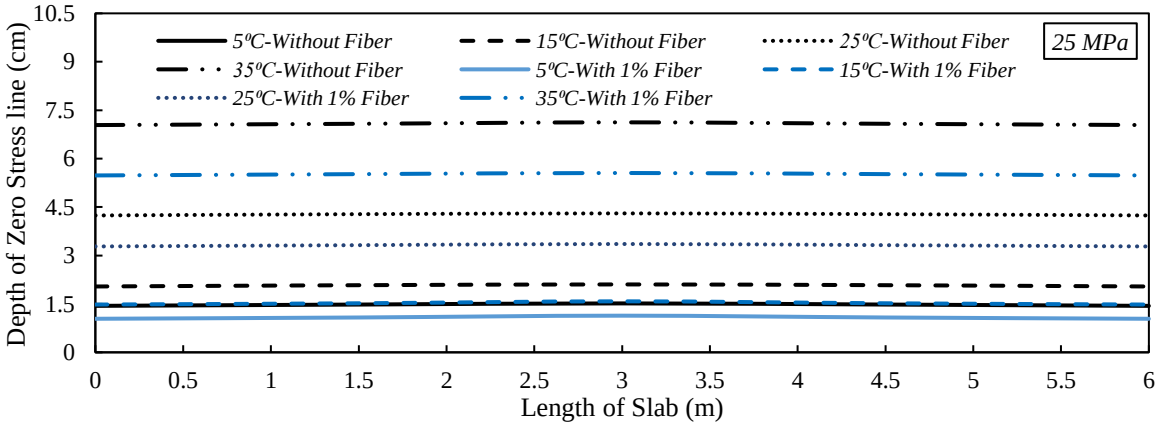

(c)

Figure 6.10: Advanced Zero-Stress line for 10 cm thickness slab, 6m length, and 25 MPa concrete compressive strength with various widths a) 3m, b) 4.5m, and c) 6m

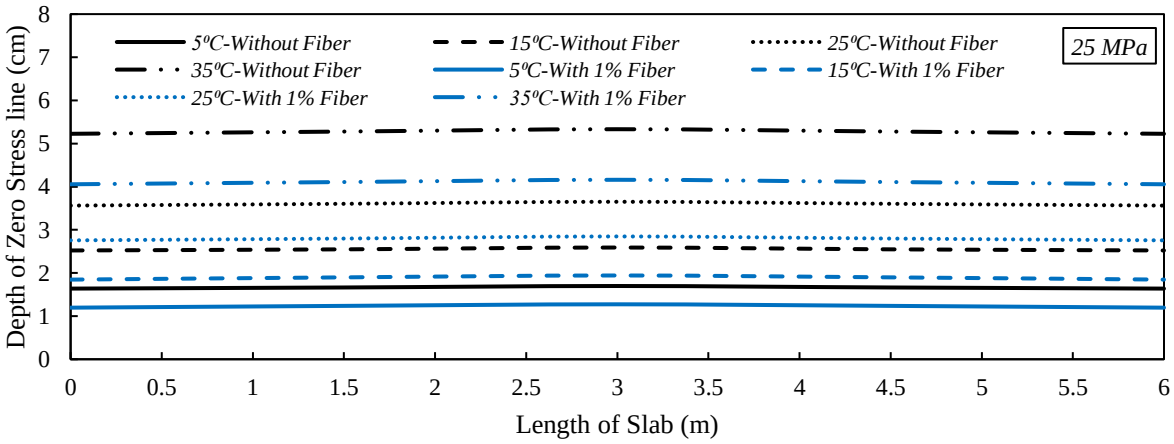

(a)

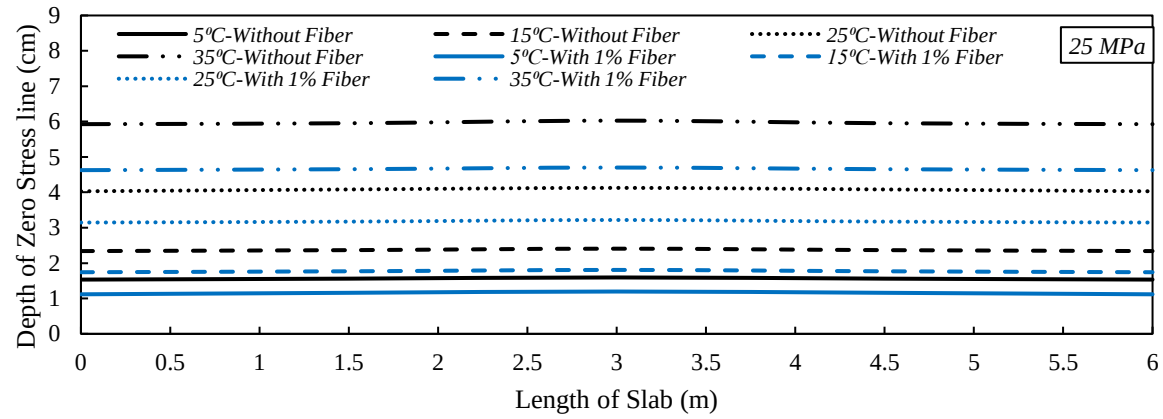

(b)

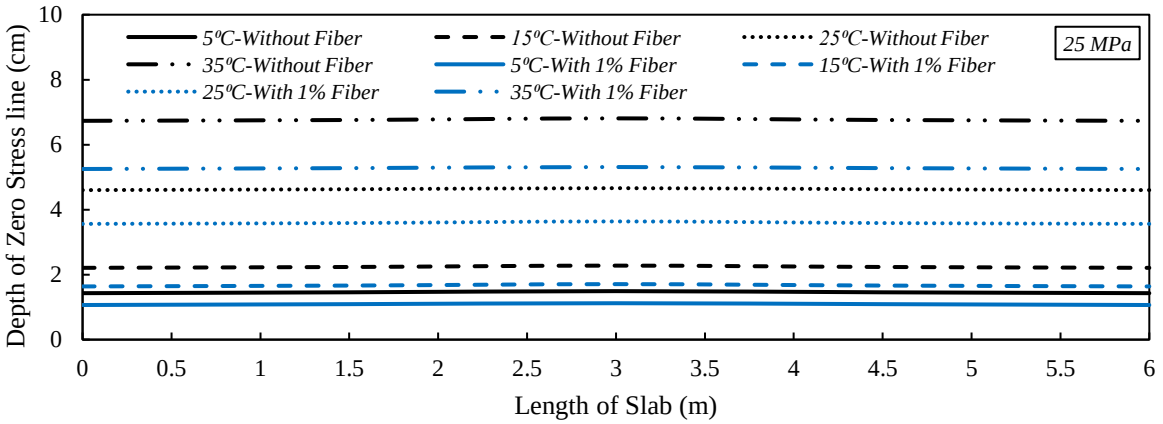

(c)

Figure 6.11: Advanced Zero-Stress line for 30 cm thickness slab, 6m length, and 25 MPa concrete compressive strength with various widths a) 3m, b) 4.5m, and c) 6m

Additionally, measurements were made of how concrete slab tensile strength affected AZSA. Figures 6.14 and 6.15, respectively, show the findings for 35MPa concrete slabs with 6m length, different widths of 3m, 4.5m, and 6m, and thicknesses of 10 cm and 30 cm. Figures 6.6a and 6.6b shows that in slabs with 4.5m length, increasing compressive strength reduced the potential depth of cracks, and increasing compressive strength to 35MPa further reduced crack depth. Additionally, raising the thickness had a significant impact on decreasing the depth of cracks; however, as slab width grew, so did the depth of the cracks. As it could be observed from the presented results, the negative influence of thermal gradient on slabs with 6m width was more

obvious than those slabs with shorter width which could be associated with the difference in out-of-plane and post-buckling performance of shorter width rigid concrete slabs. The findings showed that the negative impact of thermal gradient on slabs wider than 6m was more pronounced than on slabs narrower than that, which may be related to the different out-of-plane and post-buckling capabilities of stiff concrete slabs of various widths.

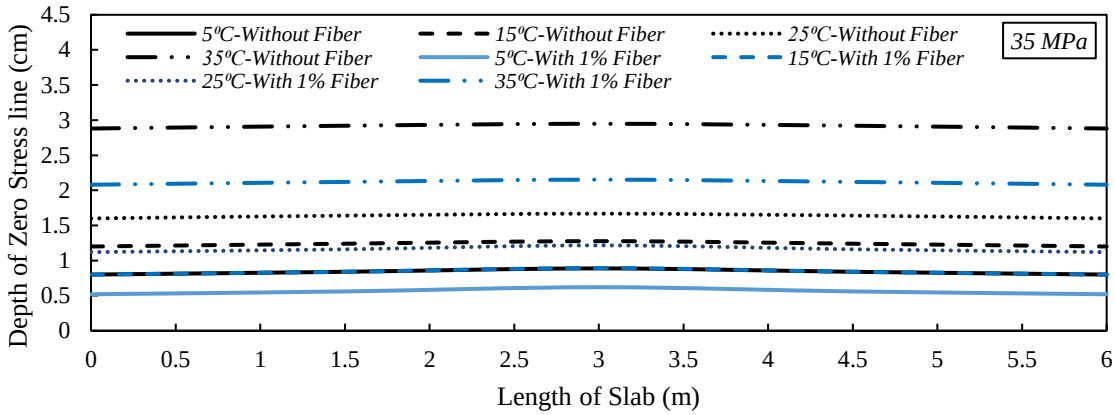

(a)

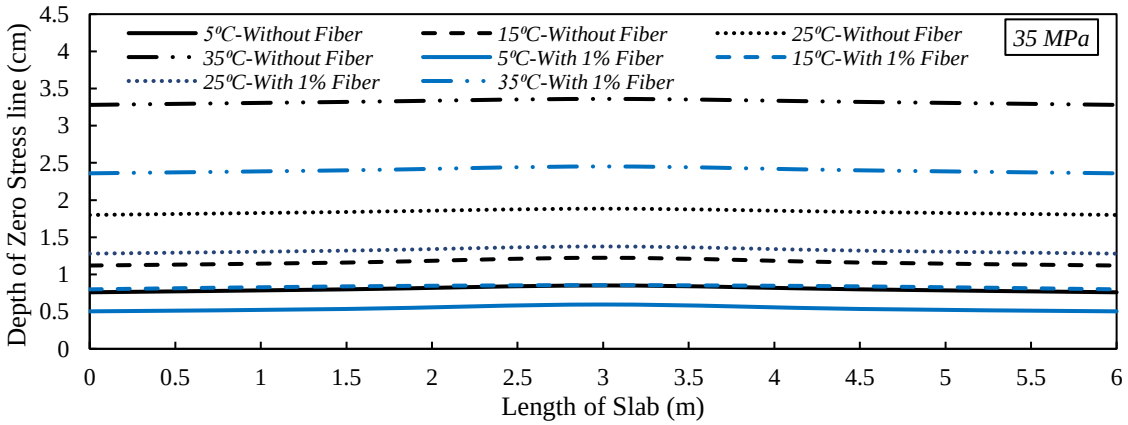

(b)

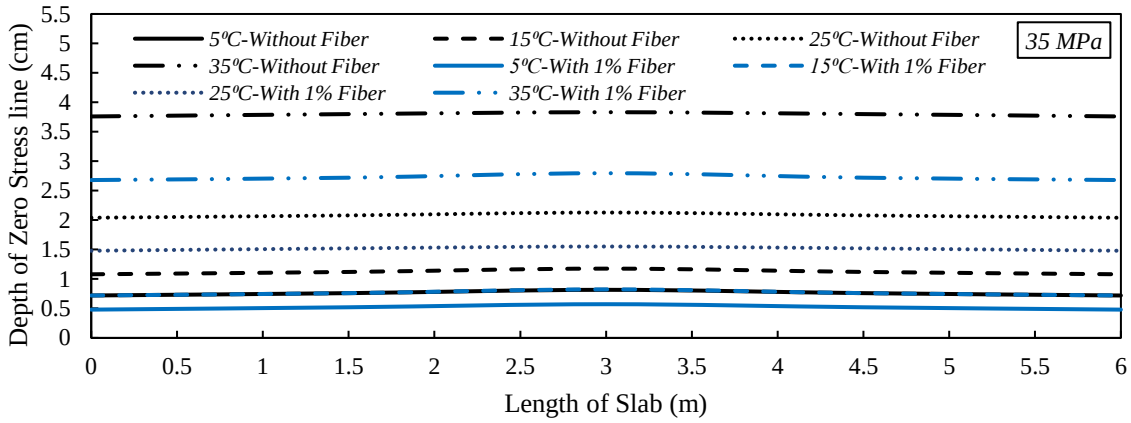

(c)

Figure 6.12: Advanced Zero-Stress line for 10 cm thickness slab, 6m length, and 35 MPa concrete compressive strength with various widths a) 3m, b) 4.5m, and c) 6m

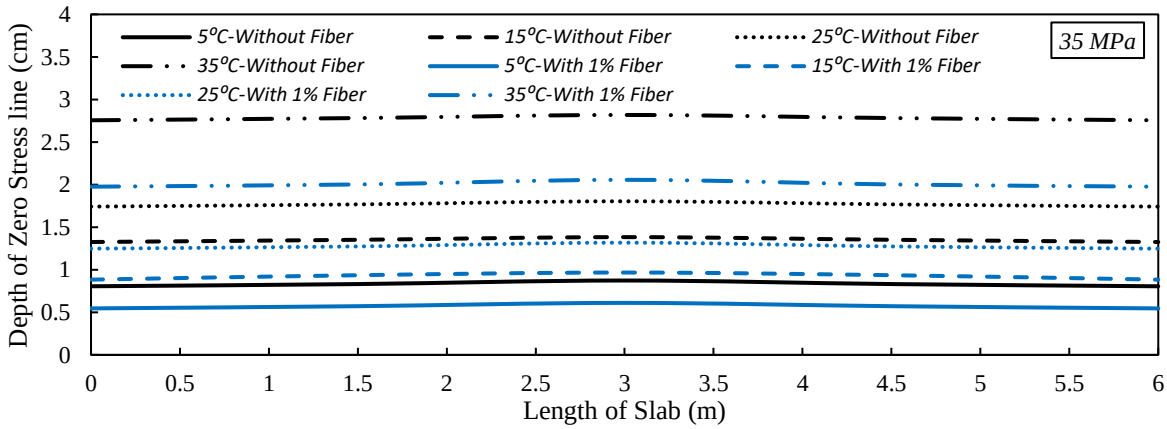

(a)

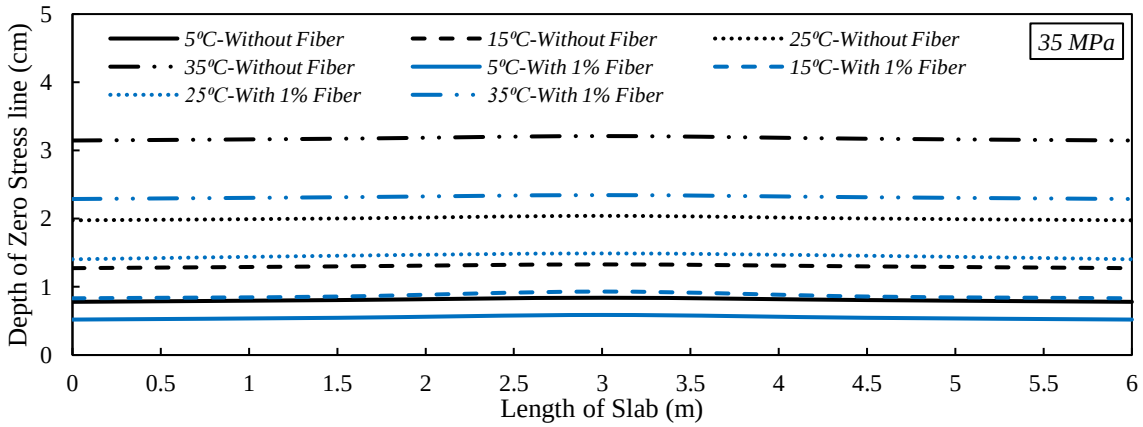

(b)

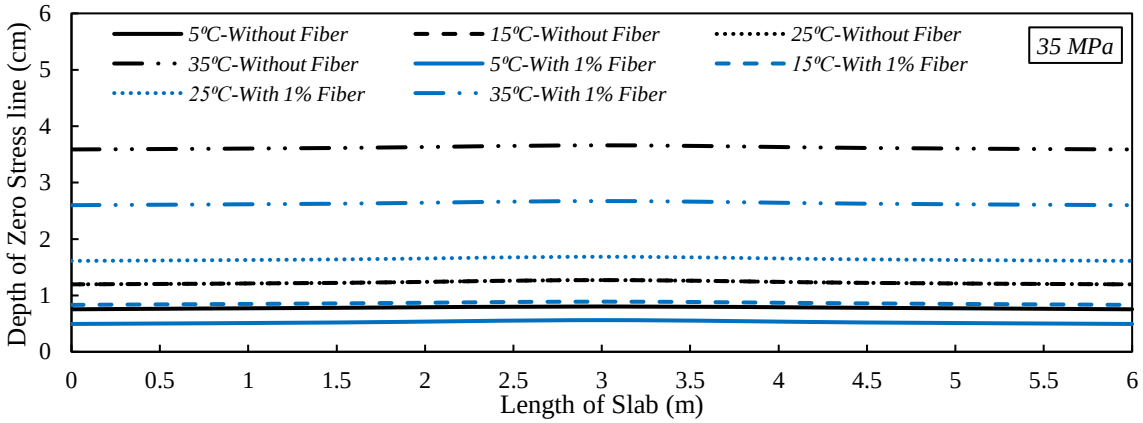

(c)

Figure 6.13: Advanced Zero-Stress line for 30 cm thickness slab, 6m length, and 35 MPa concrete compressive strength with various widths a) 3m, b) 4.5m, and c) 6m

As a consequence, it is advised to use shorter-width slabs when building airport runways because larger slabs are more susceptible to temperature variations. The results for 45MPa concrete slabs with 6m length and different widths, 3m, 4.5m, and 6m, and 10 cm and 30 cm thickness, are shown in Figures 6.14 and 6.15, respectively. Finally, the compressive strength of slabs rose to 45MPa. In those slabs, the simultaneous application of high concrete compressive strength and fiber incorporation greatly improved the cracking behavior of stiff concrete slabs with 6m length and reduced the number of cracks that formed through the thickness, especially for slabs with lower widths. Raising the thickness also significantly reduced the depth of cracks; however, as the slab width increased, the depth of the fissures increased. The results demonstrated that slabs broader than 4.5m were more negatively impacted by thermal gradient than slabs narrower than that, which may be linked to the varying out-of-plane and post-buckling capacities of stiff concrete slabs of various widths.

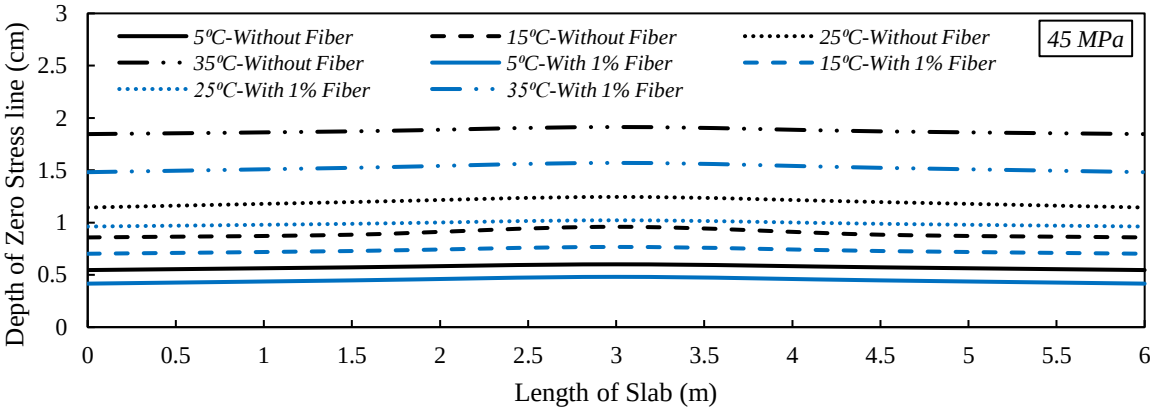

(a)

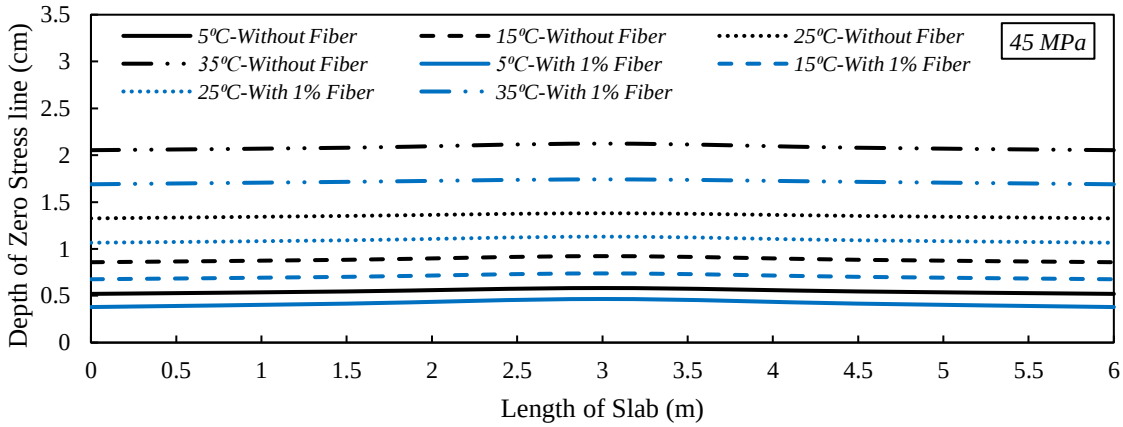

(b)

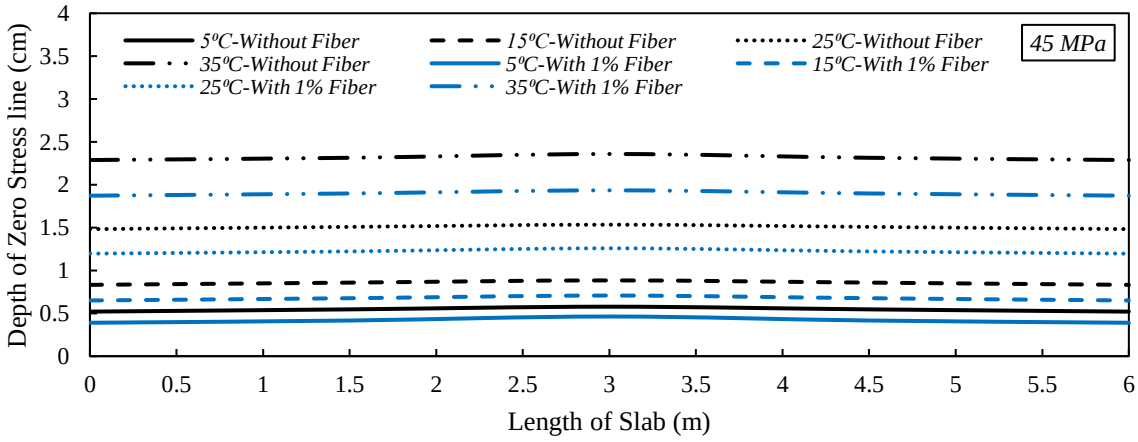

(c)

Figure 6.14: Advanced Zero-Stress line for 10 cm thickness slab, 6m length, and 45 MPa concrete compressive strength with various widths a) 3m, b) 4.5m, and c) 6m

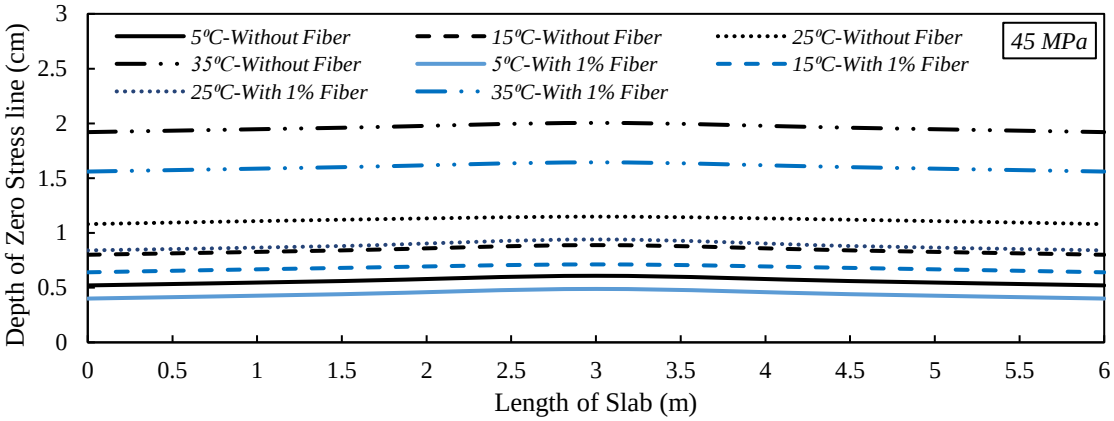

(a)

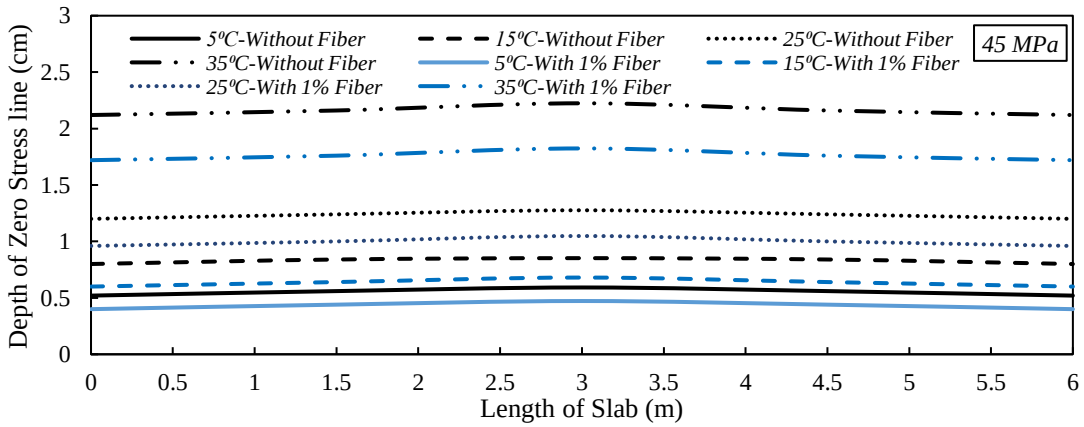

(b)

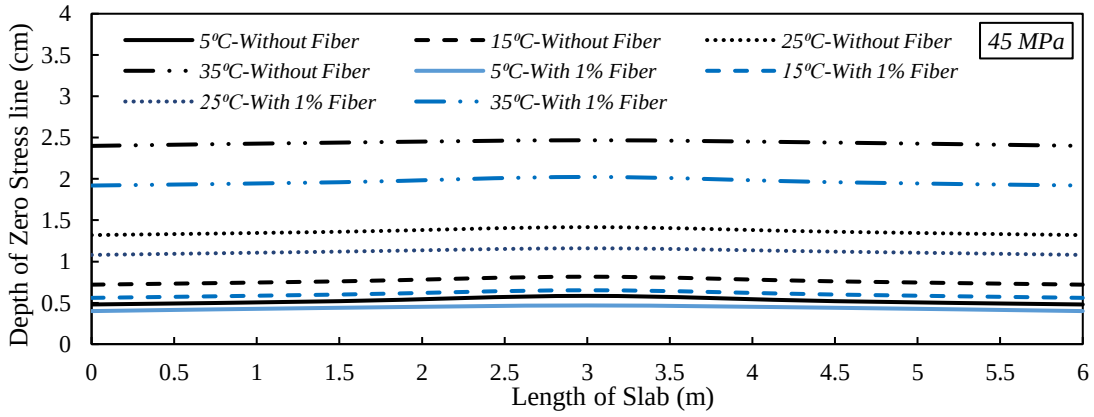

(c)

Figure 6.15: Advanced Zero-Stress line for 30 cm thickness slab, 6m length, and 45 MPa concrete compressive strength with various widths a) 3m, b) 4.5m, and c) 6m

At this step, the longitudinal length of the slab was further increased and the depth of the zero-stress line for slabs width 7.5m length with various compressive strengths and widths are illustrated

in Figures 6.16 to 6.21. Regarding these results, The behavior of concrete slabs with a length of 7.5 m is different from the behavior of slabs with a shorter length. This could be attributed to out-of-plane deformation and bost-buckling behaviors of 7.5m length slabs. So, it is recommended to analyze 7.5m length slabs as membrane shell elements while slabs with shorter lengths are suggested to evaluate as plate elements. So, with an increase in width of 7.5m length slabs, the depth of the zero-stress line was slightly increased, however, in comparison with shorter length slabs (4.5m and 6m), the possible cracks depth was slightly lower. Also, increasing the thermal gradient results in greater crack length while fiber incorporation restricted their depth and enhanced the thermal behavior of slabs in terms of cracking behavior and crack depth. This could be related to the bridging character of fibers which leads to increasing the tensile strength of rigid concrete airfield runways. Conversely, the zero-stress line depth raised in slabs by 7.5m as the thickness increased. So, for longer slab lengths, it is recommended to limit the thickness of airfield runways just in terms of thermal behavior control. Although reducing the thickness of the slab causes higher deformations and more surface cracks in the slabs when the airfield runways open to traffic.

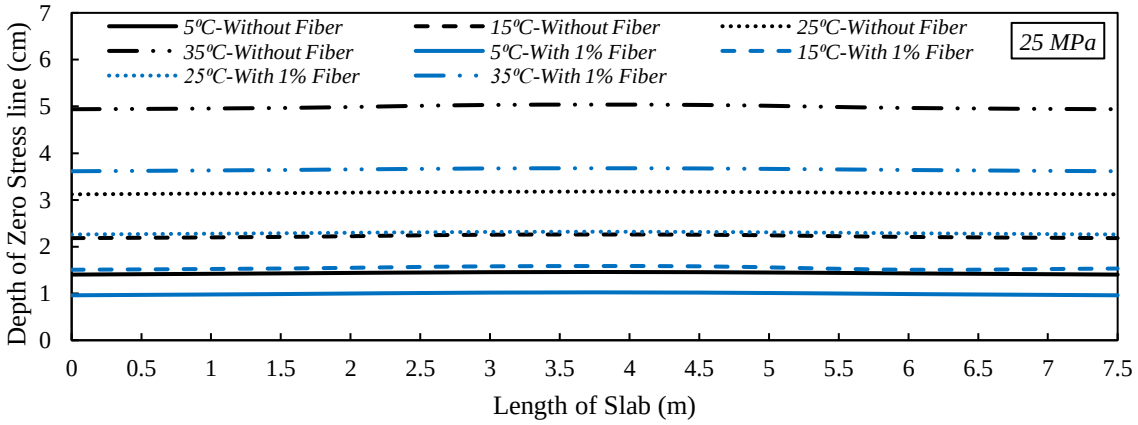

(a)

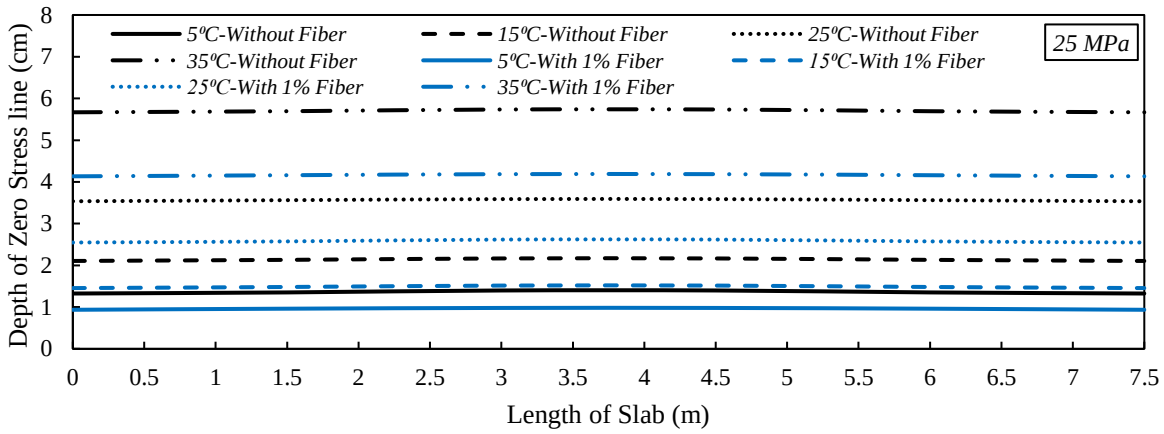

(b)

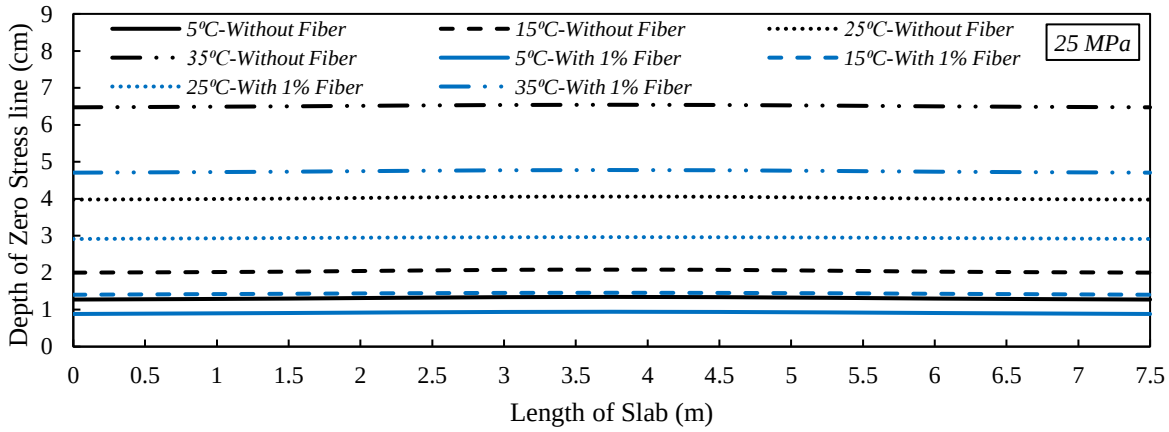

(c)

Figure 6.16: Advanced Zero-Stress line for 10 cm thickness slab, 7.5m length, and 25 MPa concrete compressive strength with various widths a) 3m, b) 4.5m, and c) 6m

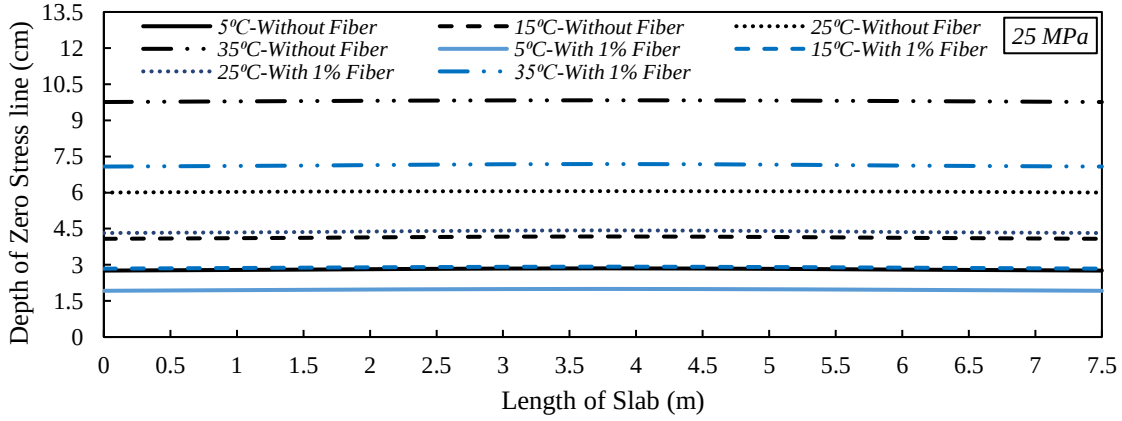

(a)

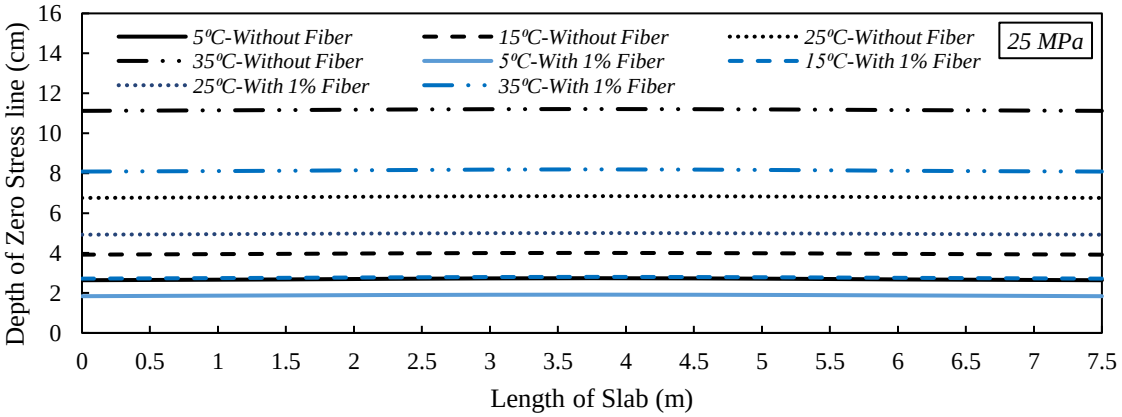

(b)

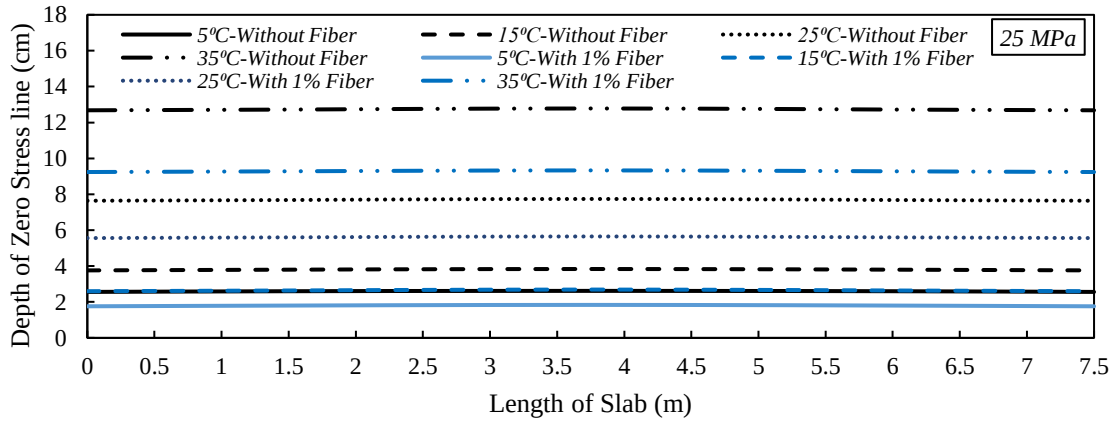

(c)

Figure 6.17: Advanced Zero-Stress line for 30 cm thickness slab, 7.5m length, and 25 MPa concrete compressive strength with various widths a) 3m, b) 4.5m, and c) 6m

In addition to the slabs' length effects, the compressive strength of slabs increased to 35MPa, and the obtained results are presented in Figures 6.18 and 6.19 for slabs with 7.5m length considering various widths. Regarding these results, by increasing the compressive strength of concrete, the depth of the zero-stress line and the length of cracks over the thickness decreased. Also, the depth of the zero-stress line was marginally raised with a rise in the width of 7.5m length slabs. Incorporating fibers reduced the length of cracks and improved the thermal behavior of slabs in terms of fracture behavior and cracks depth, whereas raising the thermal gradient results in longer cracks. This might be connected to fibers' ability to bridge gaps, which increases the tensile

strength of stiff concrete pathways. In contrast, as the thickness grew in slabs, the zero-stress line depth increased by 7.5m which could be related to switching the behavior of rigid concrete slabs from membrane shell element to plate element with higher out-of-plane deformation as a result of increasing the lateral stiffness of slabs. Additionally, the effect of higher strength for concrete mix is taken into account, 45MPa, and the obtained results for 7.5m length slabs with 10cm and 30cm thickness are represented in Figures, 6.20 and 6.21, respectively.

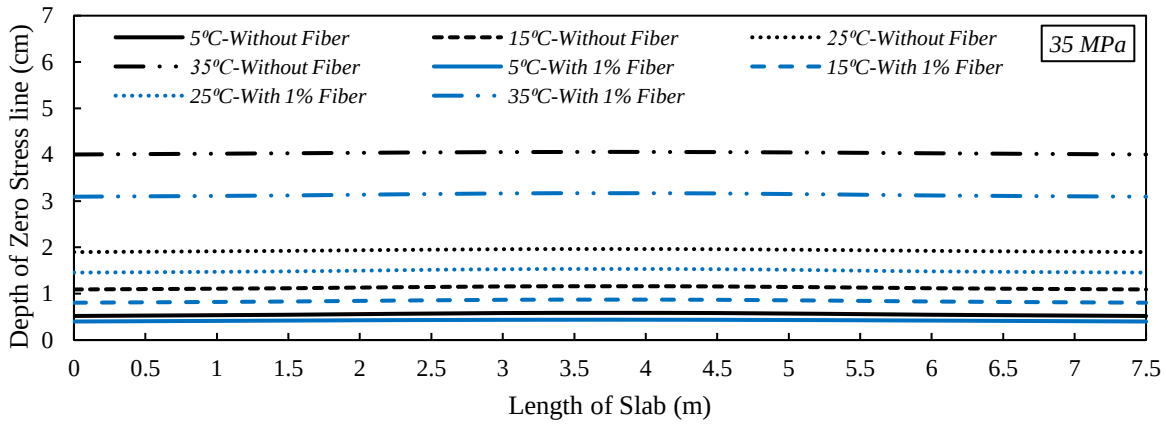

(a)

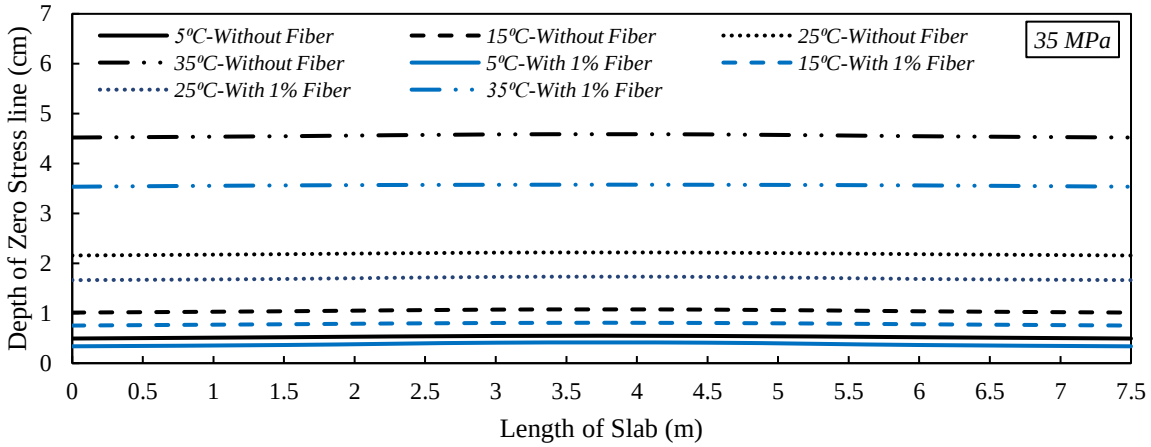

(b)

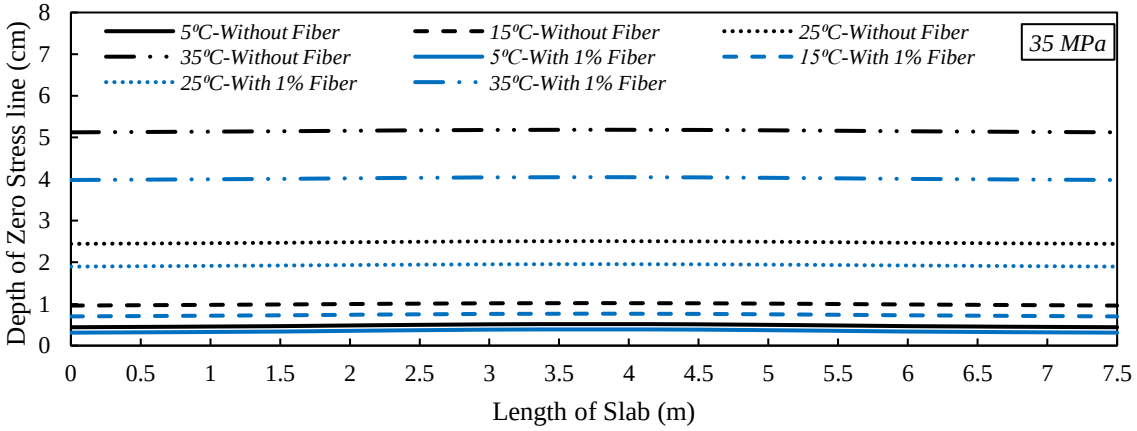

(c)

Figure 6.18: Advanced Zero-Stress line for 10 cm thickness slab, 7.5m length, and 35 MPa concrete compressive strength with various widths a) 3m, b) 4.5m, and c) 6m

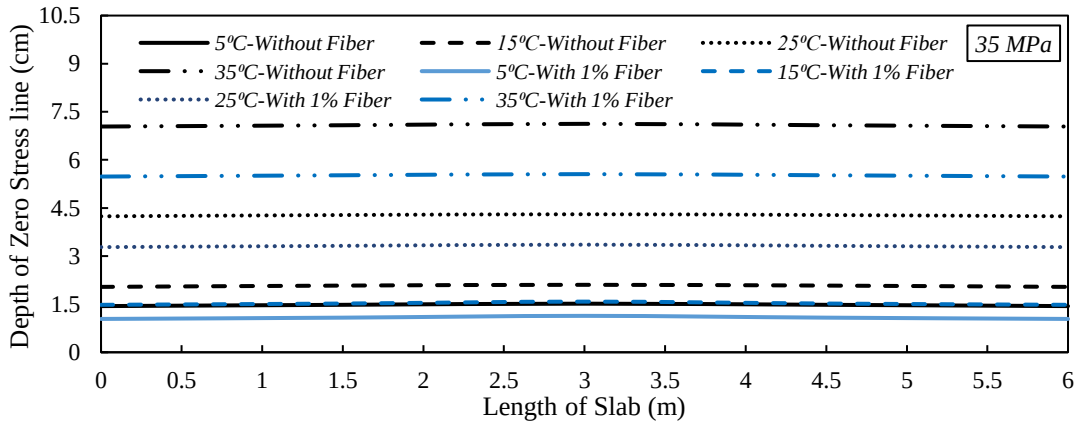

(a)

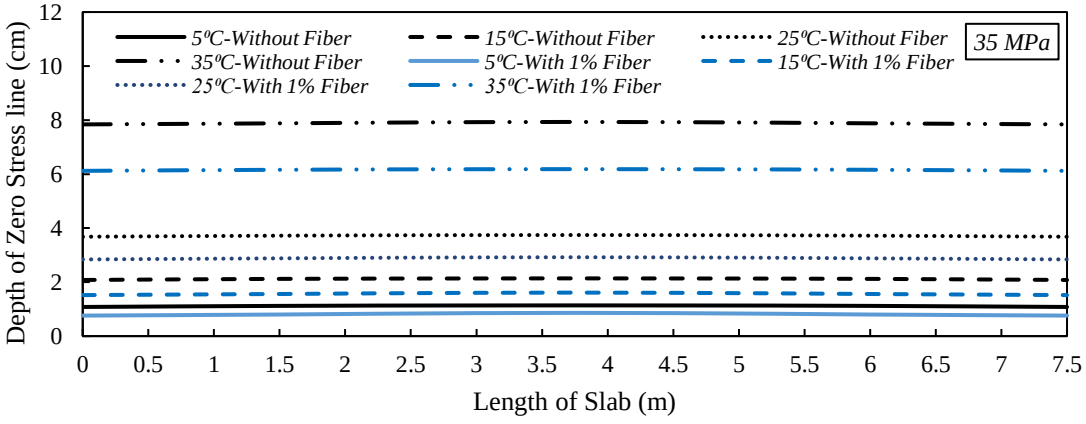

(b)

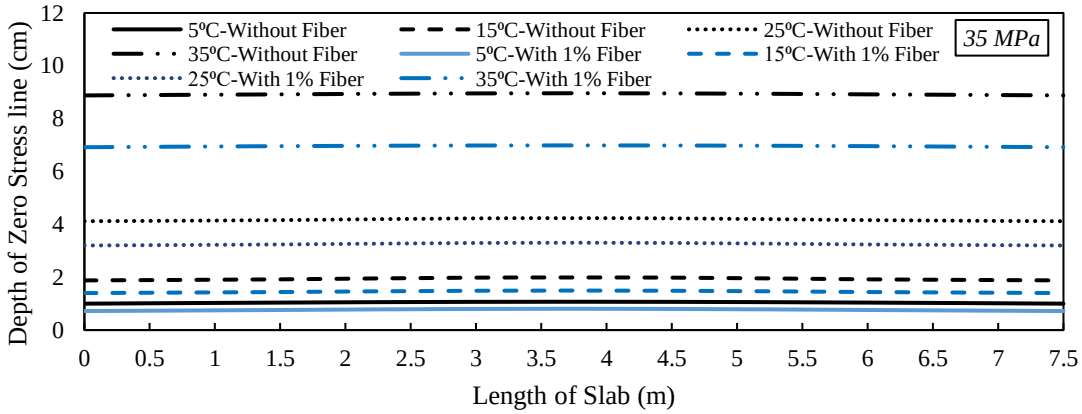

(c)

Figure 6.19: Advanced Zero-Stress line for 30 cm thickness slab, 7.5m length, and 35 MPa concrete compressive strength with various widths a) 3m, b) 4.5m, and c) 6m

According to Figures 6.20 and 6.21, increasing the compressive strength, 45MP, in slabs with 10cm thickness led to an increase in the depth of cracks through the thickness, however, the zero-stress line depth declined when the thickness of slabs increased to 30cm. Additionally, a rise in the width of 7.5m length slabs resulted in a slight increase in the depth of the zero-stress line. Raising the thermal gradient causes longer cracks, whereas incorporating fibers decreased the length of cracks and enhanced the thermal behavior of slabs in terms of fracture behavior and crack depth. The capacity of fibers to span spaces, which raises the tensile strength of rigid concrete paths, may be related to this.

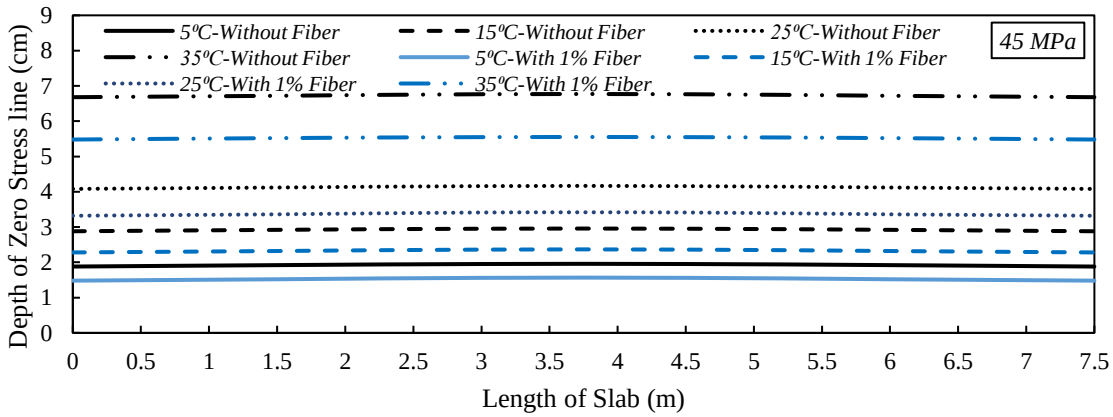

(a)

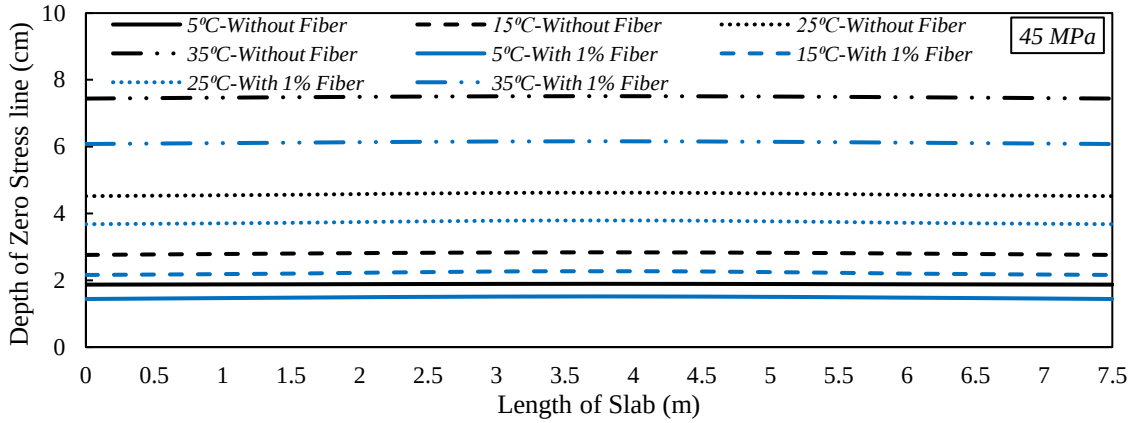

(b)

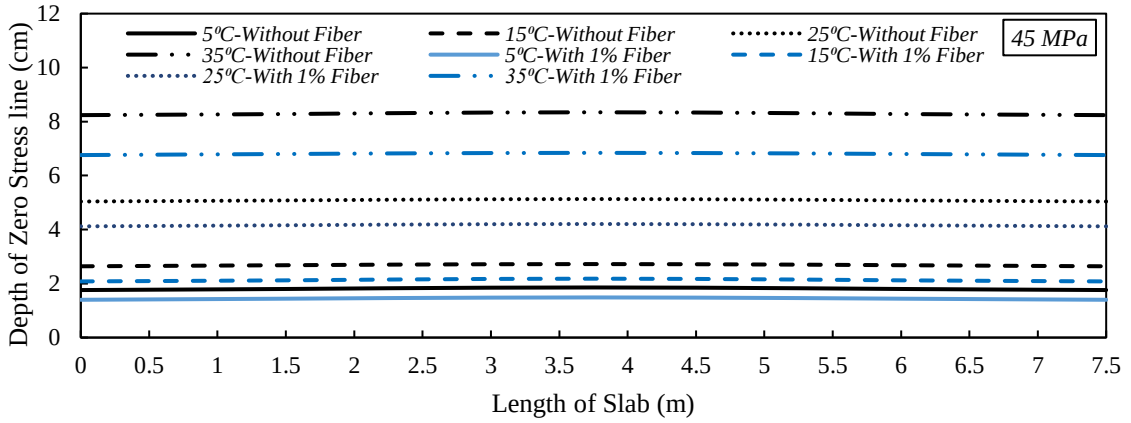

(c)

Figure 6.20: Advanced Zero-Stress line for 10 cm thickness slab, 7.5m length, and 45 MPa concrete compressive strength with various widths a) 3m, b) 4.5m, and c) 6m

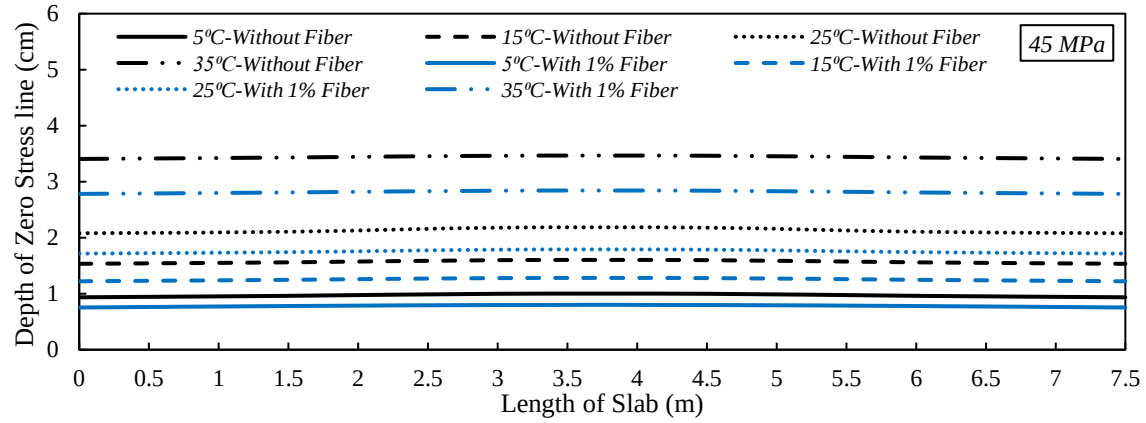

(a)

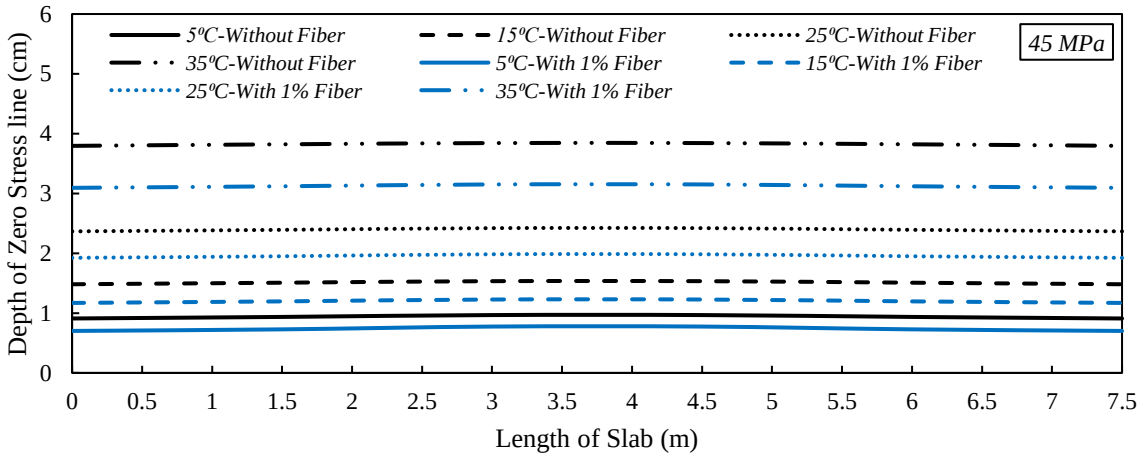

(b)

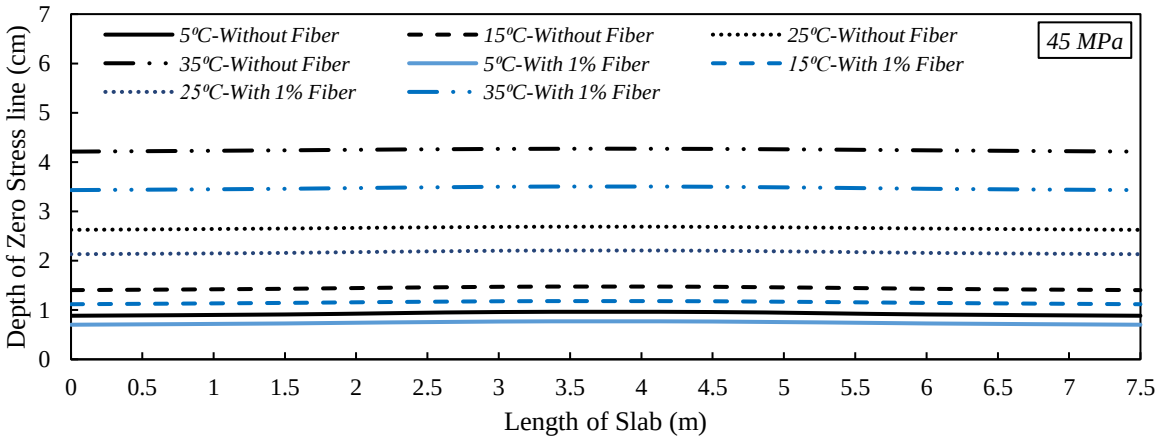

(c)

Figure 6.21: Advanced Zero-Stress line for 30 cm thickness slab, 7.5m length, and 45 MPa concrete compressive strength with various widths a) 3m, b) 4.5m, and c) 6m

6.5. SUMMARY & CONNECTION WITH THE SUBSEQUENT CHAPTER

With the use of the previous chapters results, this chapter offered a new concept to predict the influence of various variables: material properties, geometric characteristics, and PF incorporation on the maximum cracks depth through slab thickness. The result helps to get a beneficial insight into the maintenance period associated with crack propagation and slab performance. For this aim, ready-to-use software, ABAQUS, has been employed. Conversely, the influence of various variables on the performance of slabs in terms of cracking and strength should be beneficial for

companies to develop their designing software and tools. To achieve this aim, a finite element method formulation plays a crucial role in using the coding software, MATLAB. Therefore, using the obtained results from previous and current chapters about the influence of various variables on the curling cracks' depth and slab resistance, a finite element method formulation is developed in the next chapter for both plain and fiber-reinforced concrete slabs to measure the curling performance in terms of deformation and stress. Therefore, deformation and stress associated with the curling and out-of-plane behavior are measured in the next Chapter. Figure 6.22 provides a connection with the subsequent chapter overview.

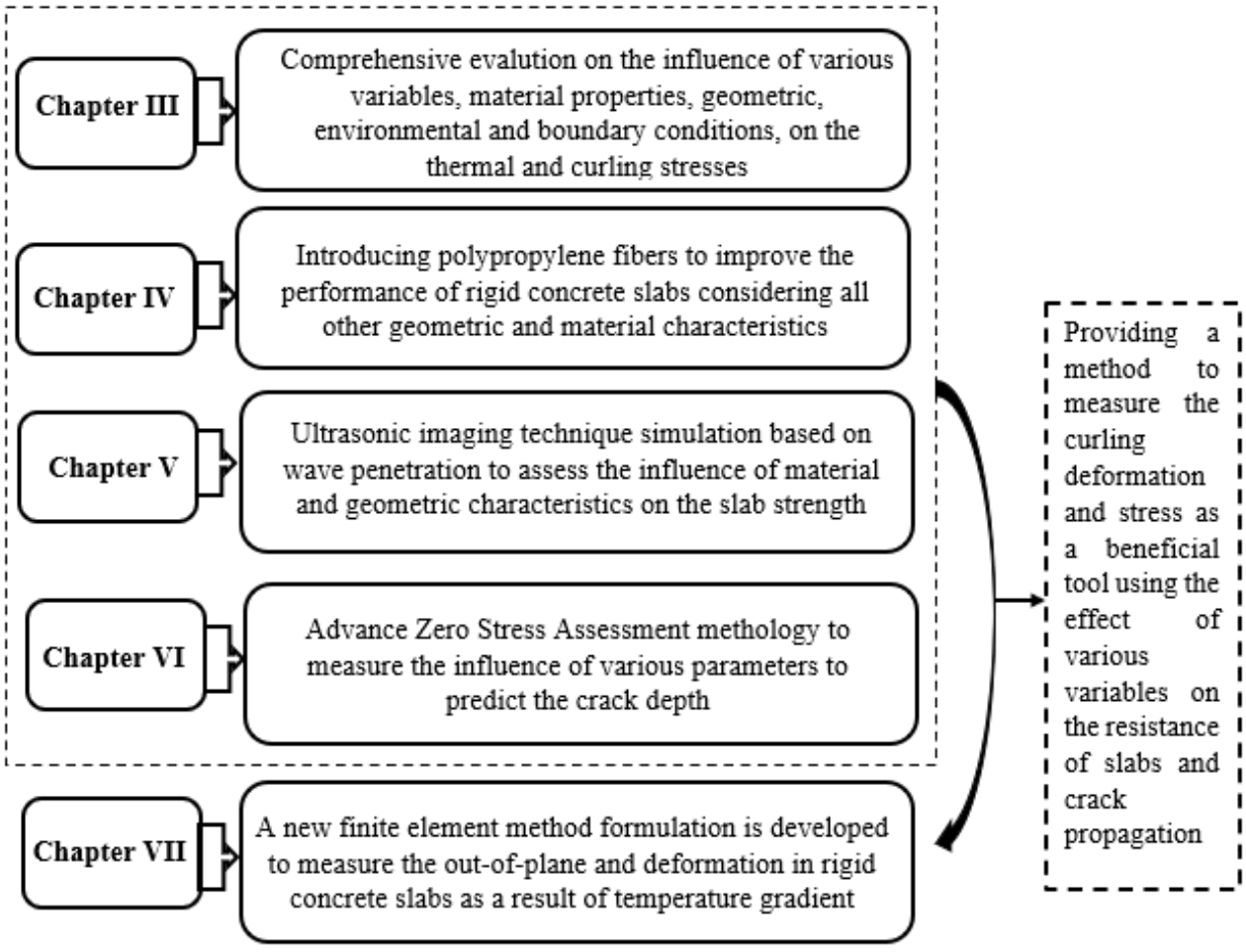

Figure 6.22: Overview of the connection between previous Chapters and Chapter VII

CHAPTER VII

FINITE ELEMENT METHOD FORMULATION

7.1. INTRODUCTION

This chapter intends to present a new finite element method formulation for measuring the curling and lateral buckling deformation in rigid concrete slabs due to thermal gradient and curling stress considering the effect of wide-range main variables. The preceding section of this chapter is followed by MATLAB coding to identify the stress distribution and bending deformation for slabs constructed on the base layer with various stiffness. The results of this task might be used by many companies to develop their designing tools, and DOTs could utilize it to construct robust concrete slabs that better account for the curling stress and bending out-of-plane deformation in rigid concrete slabs.

7.1.1. Organization of the Chapter

This chapter could be categorized into four three sections. Subsequent to the introductory section, Section 2 provides information associated with finite element method formulation, boundary conditions, the out-of-plan deformation in rigid concrete slabs, loading circumstances as well as thermal distribution effects, and basic assumptions. cracking in rigid concrete slabs over time due to shrinkage and stress distributions. Then, the major results of this chapter are presented and discussed to show the effect of PF, geometric characteristics, and material properties on lateral deformation and buckling in rigid concrete slabs using a finite element method formulation. Finally, a summary of this section will be presented so that its connection with the subsequent section and also the significance of the subsequent section can be clearly shown.

7.1.2. Basic concept about the thermal deformation of rigid concrete slabs

The buckling of continuously reinforced concrete pavements subjected to thermal loading has received widespread interest with the increasing number of prolonged heatwaves being experienced and associated with global warming (Bradford, 2013a; Bradford, 2013b). Pavement buckling can clearly lead to loss of life, and it may incur significant financial losses. Several researchers have studied the bucking behavior of pavements. Kerr and Dallis (1985) established the blowup mechanism for concrete pavements based on the assumption that they are caused by thermal lift-off buckling of the pavement, in which the concept of a safe temperature was defined. Kerr and Shade (1984) contributed to a better understanding of the mechanics of pavement buckling and a determination of the essential parameters by extending the bilinear approximation of the resistance between the pavement and the base to a hyperbolic tangent function. Another case of a pavement model, viz. a long continuously reinforced concrete pavement adjoining a rigid structure, was analyzed by Kerr (1994). More recently, Croll (1997) discussed the mechanics involved in the upheaval buckling of pavements and described the analysis for buckling in two separate models: one being a one-dimensional beam and the other a two-dimensional plate. In this and other research, however, the temperature increase was assumed to be homogeneous, while field tests show that large temperature gradients can develop, as the temperature of the top layer is usually much higher than that of the bottom layer when the pavement is exposed to heatwaves (Deen et al. 1982; Yang and Bradford 2015). This temperature gradient may play a significant role in the buckling of pavements.

The effects of a temperature gradient on structural buckling have been investigated by many researchers. Pi and Bradford (2002) presented a systematic treatment of classical buckling analysis for the thermoelastic lateral-torsional buckling and for the in-plane thermoelastic flexural

buckling of a fixed beam of doubly symmetric open thin-walled cross section that is subjected to a linear temperature gradient field over its cross-section. It was found that the fixed beam may bifurcate from its primary equilibrium state to a buckled equilibrium configuration with an increase in the temperature gradient and the average temperature. Subsequently, Pi and Bradford (2002) conducted a non-linear thermal buckling analysis of circular shallow pin-ended arches that are subjected to a linear temperature gradient field in the plane of curvature of the arch.

The bending action produced by the curvature change and the axial compressive action produced by the restrained axial expansion caused by a temperature gradient was shown to potentially cause the arch to buckle suddenly in the plane of its curvature. It has also been found that temperature plays an important role in the buckling of beams at elevated temperatures Tarr et al. 1999; Jeong et al. 2014; Karimi Pour and Noroozinejad Farsangi, 2023b) and the buckling of functionally graded plates (Pi and Bradford, 2010; Karimi Pour and Noroozinejad Farsangi, 2023a). Therefore, it is also necessary for completeness to incorporate the effects of a temperature gradient on the upheaval buckling of continuously reinforced concrete pavements. A concrete pavement may be regarded as a beam on an elastic foundation, and most of the previous work on this topic considered a beam attached to a foundation, for which the beam will not separate from the foundation in the post-buckling stage (Yang and Bradford, 2015; Wang, 2010). Yang and Bradford (2015) showed that symmetric buckling localization can take place on a beam attached to a foundation with softening, and Yang and Bradford (2015) found later that both symmetric buckling and antisymmetric buckling may give rise to a post-buckling localization, which explains the localized lateral buckles observed in railway tracks (Croll 1997) and pipelines (Croll, 1998; Taylor and Tran, 1996; Xu and Lin, 2017). It is generally accepted that temperature gradient does

not need to be considered in the analysis of railway tracks and pipelines, as steel possesses excellent thermal conductivity (Kerr and Dallis, 1985).

In deference to a beam attached to a foundation, a blowup of the pavement will lead to the separation between the pavement and the base. Similar to that of railway tracks and pipelines, the non-linear equilibrium path of the pavement subjected to thermal loading can be divided into three branches: a stable branch, an unstable branch, and a restabilizing branch, from which two important temperatures can be obtained, these being the critical temperature and the safe temperature (Trahair and Bradford, 2008). The critical temperature is sensitive to imperfection, and usually, the safe temperature is taken as the buckling criterion for pavements. Yang and Bradford (2015) found that the stiffness of the foundation had no obvious effect on the safe temperature. Therefore, when the safe temperature of pavement is required, the foundation can be assumed to be rigid, which is consistent with the basic assumptions adopted in previous investigations (Croll, 2005a; Croll, 2005b; Hetenyi, 1974; Pi and Bradford, 2002; Rezaiee-Pajand and Karimi Pour, 2022a). The model of a pavement that does not incorporate the effects of the temperature gradient has been verified against finite element analysis (Yang and Bradford 2017), the purpose of this paper is to quantify the effects of a temperature gradient on the thermal-induced buckling of concrete pavements. The investigation proposes an analytical closed-form solution for thermal upheaval buckling of pavements, with the temperature gradient being embedded in the formulation.

The principle of stationary total potential is invoked to develop the non-linear equations of equilibrium for the post-buckling response of the pavement, and these equations are solved analytically by considering both the lift-off region and the adjoining sliding region (Rezaiee-Pajand and Karimi Pour, 2020). Two types of pavements are analyzed in this investigation, one is

a continuous pavement with a joint and the other is a continuous pavement adjoining a rigid structure. The buckling and post-buckling responses of the pavement with different parameters are analyzed by considering the temperature gradient, and the variables involved in this investigation are the pavement thickness, pavement base, and the effective weight

7.2. ASSUMPTION AND FORMULATION

The basic formulation has been utilized as presented by Yang and Bradford (2018) and then developed for PF-reinforced slabs. The pavement is depicted in Figure 7.1, as a beam on a foundation Ker (1994), with the beam, restrained translationally and with a rotating spring at its left end since the width of the pavement is often considerably less than the length. The pavement on the right is the adjacent region, which is resisted by the pavement base friction, and the raised section of the pavement is referred to as the lift-off area, with a length of l.

The pin joints, where movement is compatible with the findings of Ker and Dallis (1985), are believed to sustain the weight of the lift-off zone of the pavement. A concentrated frictional force will result from this response force at the pin joint. Due to the foundation's typically very high stiffness and the foundation's minimal compression under the weight of the pavement, finite element analysis demonstrates that the vertical stiffness of the foundation has no appreciable impact on the thermally induced buckling performance of the slabs Yang and Bradford (2017a).

The axial and vertical displacements of the pavement are designated as u and v, respectively, and the origin of the coordinate system is situated in the center of the joint. This geometrical arrangement matches Ker's postulate exactly (Ker 1994). The axial resistance of the base of the adjacent pavement may be a significant factor in the thermal buckling of the pavement. Typically, it is considered that solely frictional factors are responsible for the pavement base's resistance. According to studies conducted recently by Yang and Bradford (2017b), the resistance

of the pavement base includes contributions from both cohesive and frictional effects. The relationship between the axial displacement of the slab and the resistance of the base may be expressed as follows (Yang and Bradford, 2018).

$$f(u) = f_0 \tanh(\mu x) \tag{7.1}$$

Where f indicates the axial resistance, f_0 denotes the ultimate resistance, and μ is the parameter that outlines the curvature shape. Additionally, the value of f_0 could be determined as:

$$f_0 = ab + ap\xi \tag{7.2}$$

In which, p, b, a, and ξ denote the contact stress between the pavement and the base, cohesive parameter, slab's width and length, and the coefficient of friction, correspondingly. Noting that $bp = -W$ is negative in the coordinate system, where W is the weight of the pavement per unit length. Therefore:

$$f_0 = ab - W\xi \tag{7.3}$$

The value of b and ξ could be determined as per Yang and Bradford (2017b). With appropriate precision, the strain at the cross-centroid section (ε_m) and the pavement's bending curvature κ may be represented as:

$$\varepsilon_m = u' + \frac{1}{2}v'^2 \tag{7.4}$$

$$\kappa = v'' \tag{7.5}$$

where v and $()' = \frac{d()}{dx}$ is the pavement's vertical displacement (Yang and Bradford, 2018).

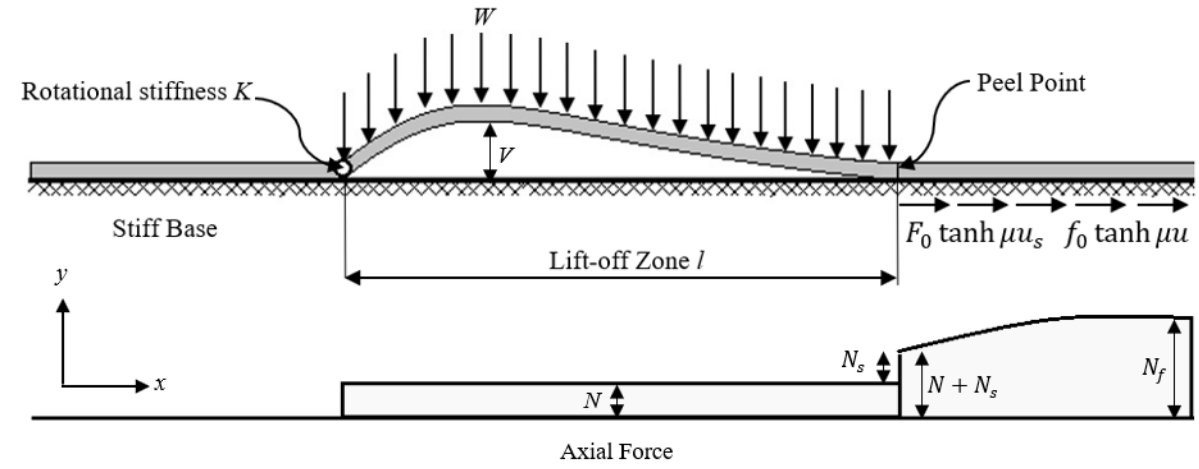

(a)

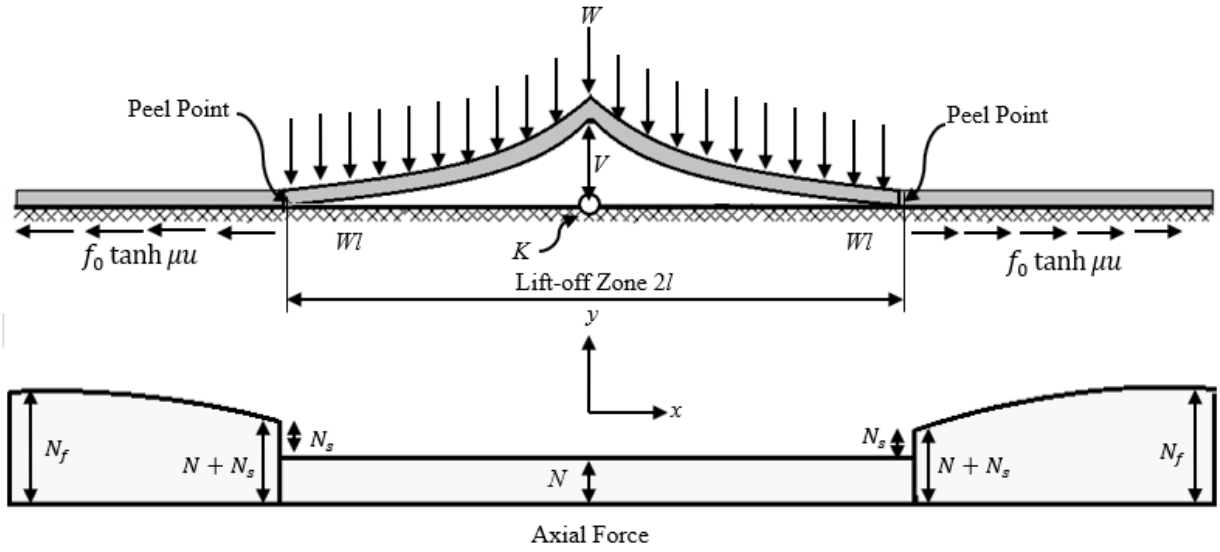

(b)

Figure 7.1: Buckling in rigid concrete slabs a) rigid base and b) weakened base

The whole potential of the pavement, comprising its elastic bending, axial compression, deformation of the longitudinal resistance at its base, and variation in gravitational potential, may be expressed mathematically as

$$\prod = \int_0^{\infty} \frac{1}{2} EIk^2 dx + \int_0^{\infty} \frac{1}{2} EA(\varepsilon_m - \varepsilon_T)^2 dx + \frac{1}{2} K[v'(0)]^2 + \int_l^{\infty} \int_0^u f_0 tan\mu\xi \, dudx - \int_0^{u_p} Wl\xi \tanh \mu\xi \, du - \int_0^l Wv dx \tag{7.6}$$

where K is the end restraint's rotational stiffness. $\varepsilon_m = \alpha T$ is the thermal strain in which α denotes the coefficient of thermal expansion. Additionally, E, A, I and u_p indicate the modulus of elasticity, slab's cross-sectional area, pavement's second moment of cross-sectional area, and axial displacement at the point of peeling, correspondingly. The constraint conditions for the adjoining region are clear:

$$v(x) = 0,\ v'(x) = 0,\ v''(x) = 0,\ l < x < \infty \tag{7.7}$$

The governing equilibrium equations are found by dividing the pavement into the lift-off region and the adjoining region (using the Euler-Lagrange formulation of variational calculus for $\delta\prod$=0 (Yang and Bradford, 2018).

$$EIv_i^{iv} - [AE(\varepsilon_m - \varepsilon_T)V']' = q \quad when\ 0 < x < l \tag{7.8}$$

as well as for the buckling area

$$v_a = 0 \quad \text{when} \quad l < x \tag{7.9}$$

in the vertical direction for the adjoining area, and as

$$[AE(\varepsilon_m - \varepsilon_T)]' = 0 \quad when\ 0 < x < l \tag{7.10}$$

as well as for the buckling area

$$AEu_a'' - f_0 \tanh(\mu\xi_a) = 0 \quad when\ l < x \tag{7.11}$$

for the adjoining area along the longitudinal axis. Equations (7.8) to (7.11) are identical in general form to those given by Ker (1994), Bradford (2013), and others for the equilibrium of arches under thermal effects. Additionally, at the peel point ($x = l$):

$$V(l) = 0,\ V'(l) = 0,\ V''(l) = 0 \tag{7.12}$$

in the upward direction, and

$$u_1(l) = u_a(l),\ EA[u_a'(l - u_1'(l)] = -Wl\xi tanh\ [\mu\xi(l)] \tag{7.13}$$

where the regularity criteria are and $u(l) = u_a(l) = u_1(l)$

$$u_a(l_a) = 0,\ u_a'(l_a) = 0, \quad l_a \to \infty \tag{7.14}$$

Also, the origin's boundary conditions are

$$EIV''(0) - KV'(0) = 0,\ u_1(0) = 0,\ v_1(0) = 0 \tag{7.15}$$

because a hard framework restrains the pavement, and

$$EIv''(0) - 2Kv'(0) = 0,\ u_1(0) = 0,\ \ [EA(\varepsilon_m - \alpha T)v_1' - EIv_1'']_{x=\infty} = 0 \tag{7.16}$$

Equation (7.8) may be reduced as follows since Equation (7.10) shows that the compressive force in the pavement in the lift-off zone $N = EA(\varepsilon_m - \alpha T)$ is constant, and so Equation (7.8) can be simplified as

$$V^{in} + \Phi^2 V'' = \widetilde{W}, \quad 0 < x < l \tag{7.17}$$

in which

$$\Phi = N/EI \tag{7.18}$$

$$\widetilde{W} = W/\mathrm{EI} \tag{7.19}$$

In general, Equation (7.17) is the same as that for an arch or the in-plane buckling of a beam-column. The first boundary condition in Equation (7.15) can be reduced as follows by introducing the dimensionless stiffness $k = K/EI$ (Yang and Bradford, 2018).

$$V''(0) - kV'(0) = 0 \ at\ x = 0 \tag{7.20}$$

and the first of Equation (7.16) can be found as

$$V''(0) - 2kV'(0) = 0 \ at\ x = 0 \tag{7.21}$$

The general solution of Equation (7.17) is

$$V = X_1 \cos \Phi x + X_2 \sin \Phi x + X_3 x + X_4 + \frac{\widetilde{W}}{2\Phi^2} x^2 \tag{7.22}$$

where the boundary conditions may be used to derive the constants X_1 to X_4. The linear homogeneous equations for X_1 to X_4 are obtained by applying the boundary conditions provided by the first and third of Equation (7.15) and the first two of Equation (7.12).

$$\begin{bmatrix} -\Phi^2 & -k\Phi & -k & 0 \\ 1 & 0 & 0 & 1 \\ \cos\Phi l & \sin\Phi l & l & 0 \\ -\Phi\sin\Phi l & -\Phi\cos\Phi l & -1 & 0 \end{bmatrix} \begin{bmatrix} X_1 \\ X_2 \\ X_3 \\ X_4 \end{bmatrix} = \begin{bmatrix} \widetilde{W}/\Phi^2 \\ 0 \\ \widetilde{W}l^2/2\Phi^2 \\ \widetilde{W}l/\Phi^2 \end{bmatrix} \tag{7.23}$$

It allows for the determination of X_1 to X_4 for the pavement confined by a rigid base as

$$X_1 = \frac{\widetilde{W}}{\Phi^4} \frac{\tilde{k}\varphi^2 - \tilde{k}\varphi sis\varphi + \varphi\cos\varphi - \sin\varphi}{\tilde{k}(\varphi\sin\varphi + 2\cos\varphi - 2\tilde{k}) - \varphi\cos\varphi - sin\varphi} \tag{7.24}$$

$$X_2 = \frac{\widetilde{W}}{2\Phi^4} \frac{\tilde{k}(\varphi^2\sin\varphi + 2\varphi cos\varphi - 2\varphi) - \varphi^2 + 2(\varphi\sin\varphi + \cos\varphi - 1)}{\tilde{k}(\varphi\sin\varphi + 2\cos\varphi - 2) + \varphi\cos\varphi - sin\varphi} \tag{7.25}$$

$$X_3 = \frac{\widetilde{W}}{2\Phi^4} \frac{\tilde{k}(\varphi^2 + 2\varphi cos\varphi - 2\varphi) + \varphi^2\cos\varphi - 2(\varphi\sin\varphi + 1 - \cos\varphi)}{\tilde{k}(\varphi\sin\varphi + 2\cos\varphi - 2) + \varphi\cos\varphi - sin\varphi} \tag{7.26}$$

$$X_4 = \frac{\widetilde{W}}{2\Phi^4} \frac{\tilde{k}(\varphi^2\cos\varphi - 2\varphi sin\varphi + \varphi^2) + 2(\varphi\cos\varphi - \sin\varphi)}{\tilde{k}(\varphi\sin\varphi + 2\cos\varphi - 2) + \varphi\cos\varphi - sin\varphi} \tag{7.27}$$

Where,

$$\varphi = \Phi l \tag{7.28}$$

The linear homogeneous algebraic equations for X_1 to X_4 are obtained by applying the boundary conditions provided by the first and third terms of Equation (7.16) and the first two terms of Equation (7.12).

$$\begin{bmatrix} -\Phi^2 & -2k\Phi & -2k & 0 \\ 0 & 0 & \Phi^2 & 0 \\ \cos\Phi l & \sin\Phi l & l & 1 \\ -\Phi\sin\Phi l & -\Phi\cos\Phi l & -1 & 0 \end{bmatrix} \begin{bmatrix} X_1 \\ X_2 \\ X_3 \\ X_4 \end{bmatrix} = \begin{bmatrix} \widetilde{W}/\Phi^2 \\ 0 \\ \widetilde{W}l^2/2\Phi^2 \\ \widetilde{W}l/\Phi^2 \end{bmatrix} \tag{7.29}$$

from which

$$X_1 = \frac{\widetilde{W}}{\Phi^3}\frac{2kl + \cos\Phi l}{\Phi\cos\Phi l + 2ksin\Phi l} \tag{7.30}$$

$$X_2 = \frac{\widetilde{W}}{\Phi^3}\frac{-\Phi l + \sin\Phi l}{\Phi\cos\Phi l + 2ksin\Phi l} \tag{7.31}$$

$$X_3 = 0 \tag{7.32}$$

$$X_4 = \frac{\widetilde{W}}{\Phi^3}\frac{\Phi l^2 + \cos\Phi l + 2k\Phi l^2 sin\Phi l + 4klcos\Phi l - 2\Phi lsin\Phi l + 2}{\Phi\cos\Phi l + 2ksin\Phi l} \tag{7.33}$$

The characteristic equation for the lift-off length l of a slab confined by a rigid structure is then produced by applying the third matching condition of Equation (7.12) and is denoted by

$$\tilde{k}\varphi^2\cos\varphi - \varphi^2\sin\varphi + \tilde{k}\varphi^2 - 4\tilde{k}\varphi\sin\varphi - 2\varphi\cos\varphi - 4\tilde{k}\cos\varphi + 2\varphi + 4\tilde{k} = 0 \tag{7.34}$$

Also, the characteristic equation for the lift-off length of a slab weakened by a joint as a result of implementing the third matching condition provided in Equation (7.12)

$$2k\Phi l\cos\Phi l - \Phi^2 l\sin\Phi l + \Phi - \Phi\cos\Phi l - 2ksin\Phi l = 0 \tag{7.35}$$

The first of Equations (7.10), (7.4), and (7.5) provide the term $u_1'(x)$.

$$u_1'(x) = \alpha T - \frac{N}{EA} - \frac{1}{2}V^2(x) \tag{7.36}$$

while the second matching condition in Equation (7.13) results in an axial displacement at the peel point as a result of

$$u_p = \left(\alpha T - \frac{N}{EA}\right)l - \int_0^l \frac{1}{2}V'^2(x)dx \tag{7.37}$$

The second term in Equation (7.37) may be derived from Equation (7.22) by designating $\tilde{k} = k/\Phi$.

$$\int_0^l \frac{1}{2} V'^2(x)dx = \frac{\widetilde{W}^2 l^2}{48\varphi^7}\frac{\beta_1}{\beta_2} \tag{7.38}$$

because a rigid base restrains the pavement, and because

$$\int_0^l \frac{1}{2} V'^2(x)dx = \beta \widetilde{W}^2 l^7 \tag{7.39}$$

for the pavement weakened by a joint, where $\beta_1(\tilde{k},\varphi)$, $\beta_2(\tilde{k},\varphi)$ and $\beta(\tilde{k},\varphi)$, can be achieved by integrating Equation (7.11), and noting the regularity condition that $u_a'(\infty) = 0$, as:

$$u_a'(x) = \sqrt{\frac{2f_0}{\mu EA}\ln[\cosh \mu\xi]} \tag{7.40}$$

7.3. RESULTS AND DISCUSSIONS

7.3.1. Buckling amplitude

The analytical approach suggested in this study can track a rigid concrete airfield runway's post-buckling reaction after thermal stress. The post-buckling route for the straight arrangement approaches infinity because the bifurcation buckling thermal of the rigid concrete slabs is infinite due to the gravitational influences. To start the bending examination in finite element analysis, a flaw should be added. The confirmation of the analytical model presented in this research against finite element analysis is shown in Figure 7.1 and is based on the simulation approach suggested by Yang and Bradford (2017). In the post-buckling phase, it can be seen that the two answers concur well with one another and that the imperfection has no discernible impact on the safe thermal gradient. If external interference results in a change in the equilibrium state from the straight outline to a position on the unstable division by snap-through buckling, the minimum location of the post-buckling equilibrium route determines the safe thermal gradient, overhead

which buckling may occur. The safe thermal gradient is widely agreed to be the location at which slabs exposed to heatwaves begin to buckle. Therefore, the impacts of base stiffness, geometric characteristics of slabs, and effective weight on slab buckling on post-buckling behavior will be examined in this part. The post-buckling reaction is typically shown as the connection between the thermal gradient rise and the center uplift deformation in thermomechanical investigations of slabs. The minimum value of the post-buckling route defines the safe thermal gradient, and it can be seen that the post-buckling route of the rigid concrete airfield runways subjected to thermal gradient is made up of an unstable division (for which the buckling thermal gradient declines with a rise in the liftoff magnitude) and a consequent stabilizing division. The external interference may cause the equilibrium state to switch from the straight configuration to the unstable footpath when the thermal gradient rise is greater than the safe thermal gradient. This will then result in snap-through buckling, which will cause an abrupt surge in the vertical direction as is detected in real projects. Figures 7.2 and 7.3 show the effect of thermal gradient on the post-buckling of slabs with 10 cm thickness, 3 m width, and various lengths (4.5 m, 6m, and 7.5m) constrained by a weakened and rigid base layer, respectively.

According to Figure 7.2, the post-buckling value was increased by raising the temperature. This could be associated with increasing the temperature variation between the top and bottom surfaces of slabs which results in higher stresses and consequently higher bending moment. Additionally, fiber incorporation played a crucial role in reducing the post-buckling performance of rigid concrete airfield runways. Because the briding character of fibers enhances the tensile strength of concrete and reduces the crack spacing. So, higher stress could be transferred through cracks resulting in a post-buckling performance reduction considerably. Additionally, the post-buckling behavior of rigid concrete slabs could be considered linear for a thermal gradient up to

20^{o}C while by a further increase in thermal gradient, the nonlinearity significantly increased. Therefore, it is necessary to consider the nonlinear behavior for concrete slabs as well as the nonlinear thermal gradient through slabs' thickness for temperature variation over 20^{o}C. Also, the post-buckling deformation could be taken into account as almost linear when the compressive strength of concrete is greater than 35 MPa. It could also be observed that the post-buckling behavior decreased by increasing the compressive strength in slabs with 4.5m and 6m lengths. This could be associated with the potential of bending and curve deformation in slabs with shorter lengths. However, in slabs with 7.5m length, with an increase in the compressive strength up to 35MPa, the post-buckling values increased and then decreased when the compressive strength reached to 45MPa. This could be associated with the membrane shell element behavior and plate element behavior in long-length slabs with lower and higher concrete compressive strength, correspondingly. Therefore, the ratio of tensile stress over the tensile strength declined which resulted in a significant reduction in post-buckling behavior.

As can be seen from Figure 7.2c, the post-buckling behavior of slabs with 7.5m length has been changed in comparison with 4.5m and 6m length slabs. This could be associated with the mode of failure and out-of-plane behavior of slabs. When the length of the slabs is increased by 7.5m, the behavior of the slabs is recommended to analyze as a membrane shell element. while for slabs up to 6m in length, the behavior should be taken into account as a plate element. Therefore, by increasing the compressive strength as well as fiber incorporation, the post-buckling increased in slabs with 7.5m length and the maximum values were obtained for slabs with 35MPa concrete compressive strength. Furthermore, according to Figure 7.3, for slabs constrained with a stabilized rigid base layer, the post-buckling behavior was decreased which could be associated with lower deformation of the base layer as well as a higher contact between the base layer and concrete slabs.

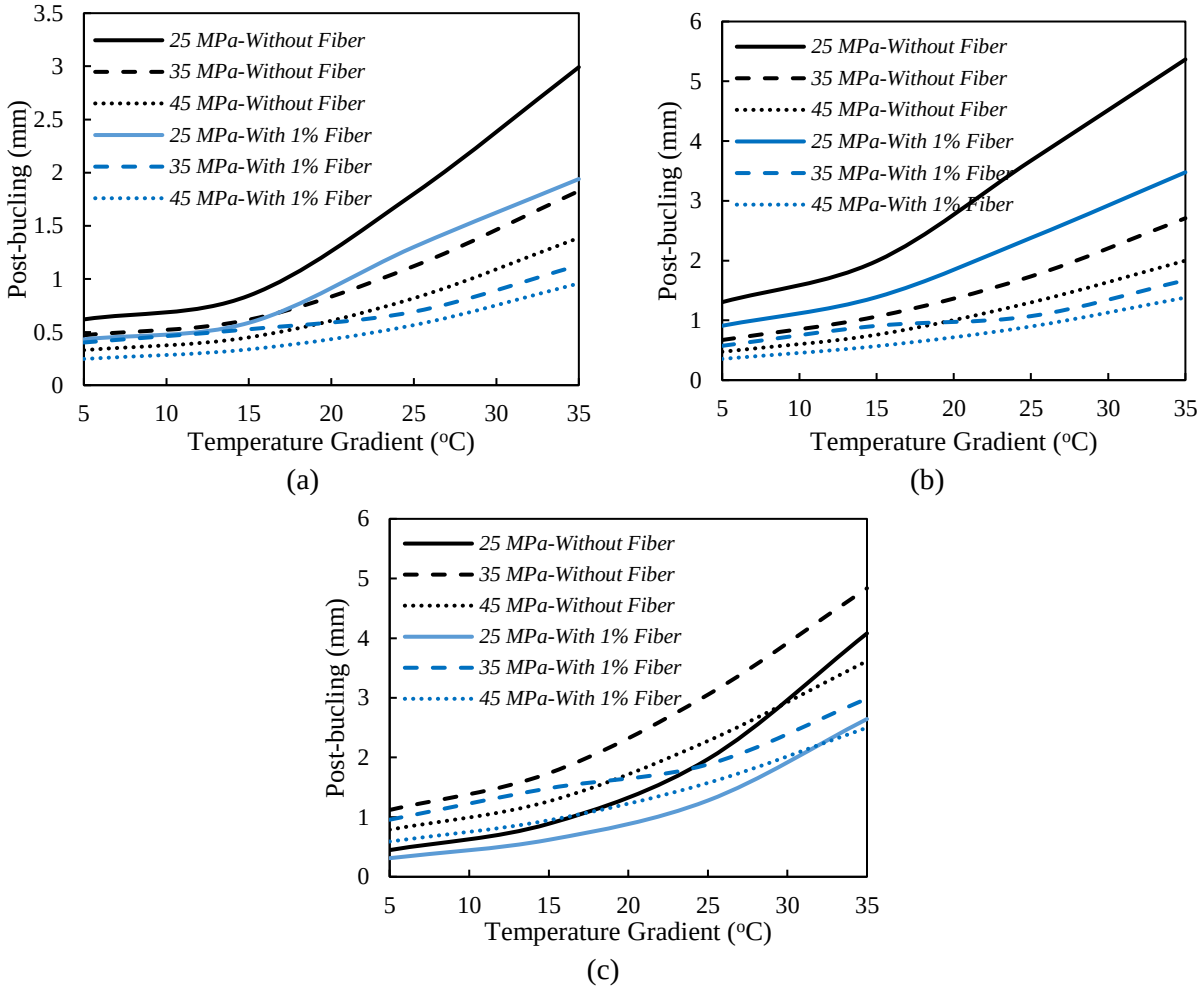

Figure 7.2: Effect of thermal gradient on the post-buckling of slabs with 10 cm thickness on the constrained by a weakened base with 3 m width and a) 4.5m, b) 6m, and c) 7.5 m length

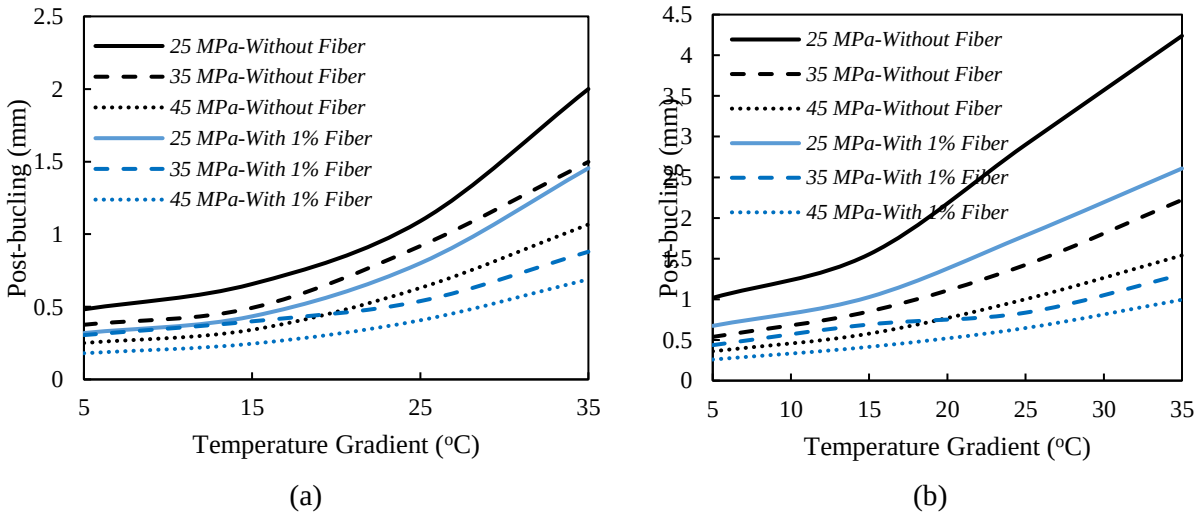

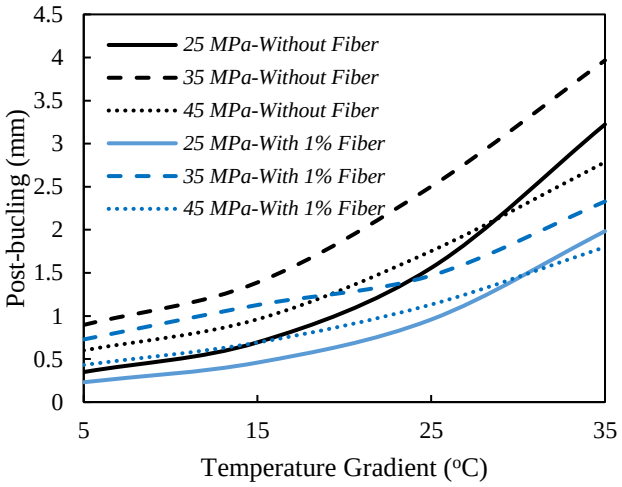

(c)

Figure 7.3: Effect of thermal gradient on the post-buckling of slabs with 10 cm thickness on the constrained by a rigid base with 3 m width and a) 4.5m, b) 6m and 7.5 m length

Moreover, Figures 7.4 and 7.5 provide the results for the post-buckling behavior of slabs with 30 cm thickness constrained by a weakened and rigid base with 3 m width and various lengths: 4.5m, 6m, and 7.5 m. According to these results, increasing the thickness led to reducing the post-buckling behavior of 4.5m and 6m length slabs while the post-buckling value for slabs with 7.5m length increased. This could be associated with the mode of failure and also out-of-plane deformation in long-length slabs which showed the jumping behavior from membrane shell to plate bending element. Additionally, the post-buckling performance of rigid concrete airfield runways was significantly decreased by fiber inclusion. Due to the fact that fibers' bridging properties increase the tensile strength of concrete and decrease cracks propagation. Therefore, greater tension could be transmitted through cracks, significantly reducing post-buckling performance. Furthermore, rigid concrete slabs' post-buckling behavior was linear up to a thermal gradient of 20°C, but as the thermal gradient grew, the nonlinearity considerably increased. For temperature variations over 20°C, it is essential to take into account the nonlinear behavior of concrete slabs as well as the nonlinear thermal gradient through the width of the slabs. Additionally, if the compressive strength

of concrete is higher than 35 MPa, the post-buckling distortion could be considered to be almost straight. Additionally, it was seen that in slabs with 4.5m and 6m in length, the post-buckling behavior was reduced by raising compressive strength. This might be connected to the possibility of bending and curvature deformation in shorter-length slabs. However, in slabs with 7.5m length, the post-buckling values rose as the compressive strength increased up to 35MPa before decreasing as the compressive strength increased up to 45MPa. This may be related to the behavior of the membrane shell and plate elements in lengthy slabs of concrete having proportionally greater and lower compressive strengths. It is advised to evaluate the behavior of the slabs as a membrane shell element when their length is raised by 7.5m. While the behavior should be considered as a plate feature for slabs up to 6m in length. Therefore, post-buckling increased in slabs with 7.5m length as compressive strength and fiber incorporation increased, and the highest values were found for slabs with 35MPa concrete compressive strength. Figure 7.5 also shows that the post-buckling behavior was reduced for slabs restrained by a stabilized stiff base layer, which may be related to both less base layer deformation and increased interaction with the concrete slabs.

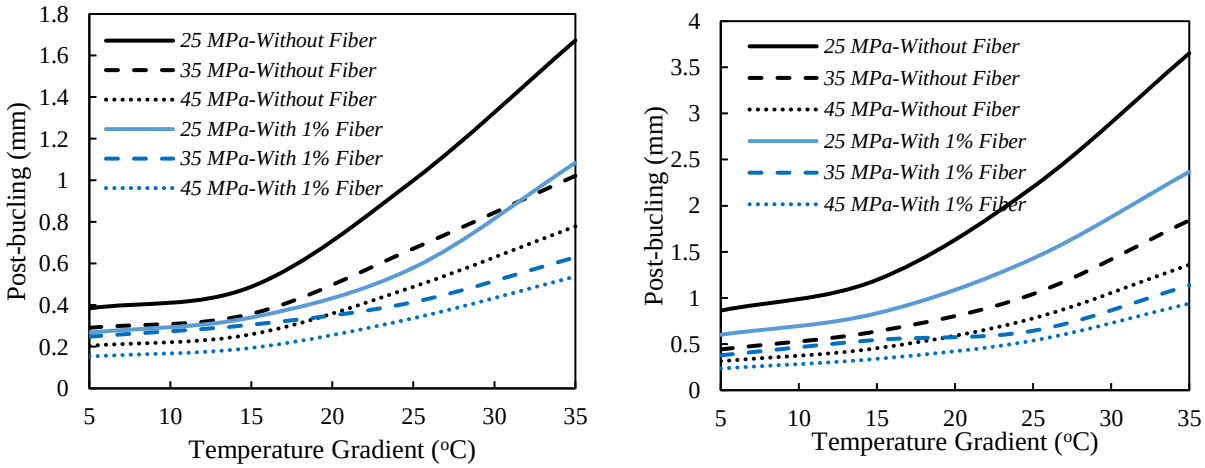

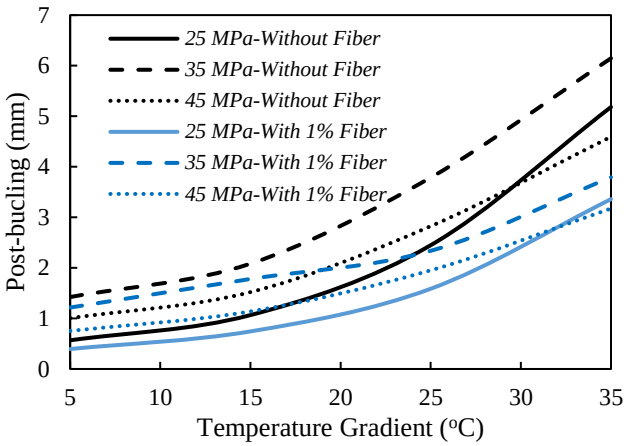

(c)

Figure 7.4: Effect of thermal gradient on the post-buckling of slabs with 30 cm thickness on the constrained by a weakened base with 3 m width and a) 4.5m, b) 6m and 7.5 m length

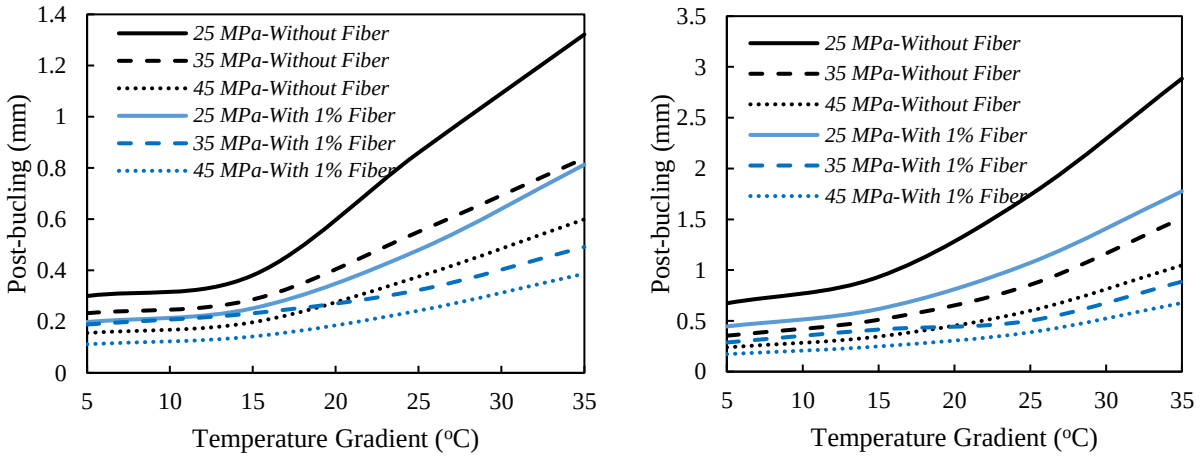

(a) (b)

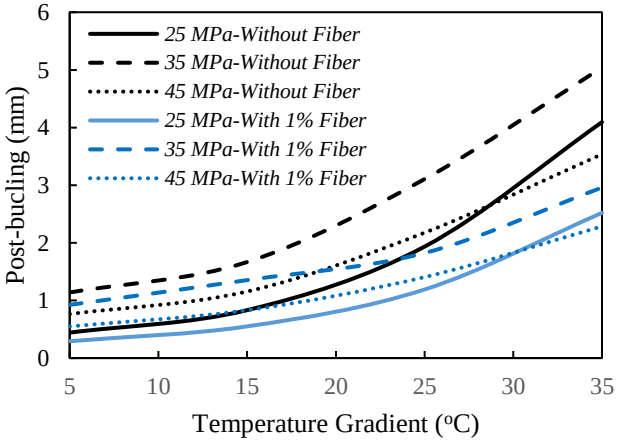

(c)

Figure 7.5: Effect of thermal gradient on the post-buckling of slabs width 30 cm thickness on the constrained by a rigid base with 3 m width and a) 4.5m, b) 6m and 7.5 m length

In this study, the influence of slab width was also taken into account as an important factor affecting the thermal performance of rigid concrete airfield runways. The post-buckling results of slabs with 10 cm thickness constrained by a weakened and rigid base with 4.5 m width and various lengths are provided in Figures 7.6 and 7.7, respectively. Increasing the width of slabs led to a significant increase in post-buckling behavior of 4.5m and 6m length slabs while marginally rose this behavior in slabs with 7.5m length. Additionally, by increasing the temperature, the post-buckling value was raised. This might be related to an increase in the temperature difference between the top and bottom sides of slabs, which causes higher stresses and, as a result, a higher bending moment. Additionally, fiber incorporation was essential in lowering stiff concrete airfield runways' post-buckling performance. As a result of fibers' ability to bridge gaps, concrete's tensile strength is improved, and crack propagation is decreased. As a consequence, greater tension could be transmitted through cracks, significantly reducing the performance after buckling. For a thermal gradient of up to 20^{o}C, the post-buckling behavior of rigid concrete slabs could also be regarded as linear; however, as the thermal gradient grew, the nonlinearity greatly increased. Because of this, it is important to take into account the nonlinear behavior of concrete slabs as well as the nonlinear thermal gradient through the width of the slabs for temperature variations greater than 20°C. When the compressive strength of concrete is higher than 35 MPa, it is also possible to consider the post-buckling displacement as almost linear. Additionally, it was seen that in slabs with lengths of 4.5m and 6m, boosting compressive strength reduced post-buckling behavior. This might be connected to the possibility of bending and curvature deformation in shorter-length slabs. However, in slabs with 7.5m in length, the post-buckling values rose with a rise in compressive strength up to 35MPa before falling when it hit 45MPa. This may be related to the behavior of the membrane shell and plate elements in lengthy slabs of concrete having proportionally greater and

lower compressive strengths. Due to the decrease in the ratio of tensile tension to tensile strength, post-buckling behavior was significantly reduced. The post-buckling behavior of slabs with 7.5m length has altered in contrast to slabs with 4.5m and 6m length, as shown in Figure 7.6c. This might be connected to slab failure modes and slab out-of-plane behavior. The behavior of the slabs should be examined as a membrane shell element when their length is extended by 7.5m. As a plate part, the behavior should be considered for slabs up to 6 meters in length. In addition, Figure 7.7 shows that for slabs restrained by a stabilized stiff base layer, the post-buckling behavior was reduced, which may have been due to less base layer deformation and more interaction between the base layer and concrete slabs. Additionally, according to Figures 7.8 and 7.9, greater thickness decreased the post-buckling behavior of slabs with 4.5m and 6m lengths while raising the post-buckling value for slabs with 7.5m lengths. This may be connected to the mechanism of failure as well as out-of-plane deformation in slabs of lengthy lengths that displayed a jumping behavior from the membrane shell to the plate bending element. Additionally, fiber addition greatly reduced the rigid concrete airport runways' post-buckling performance.

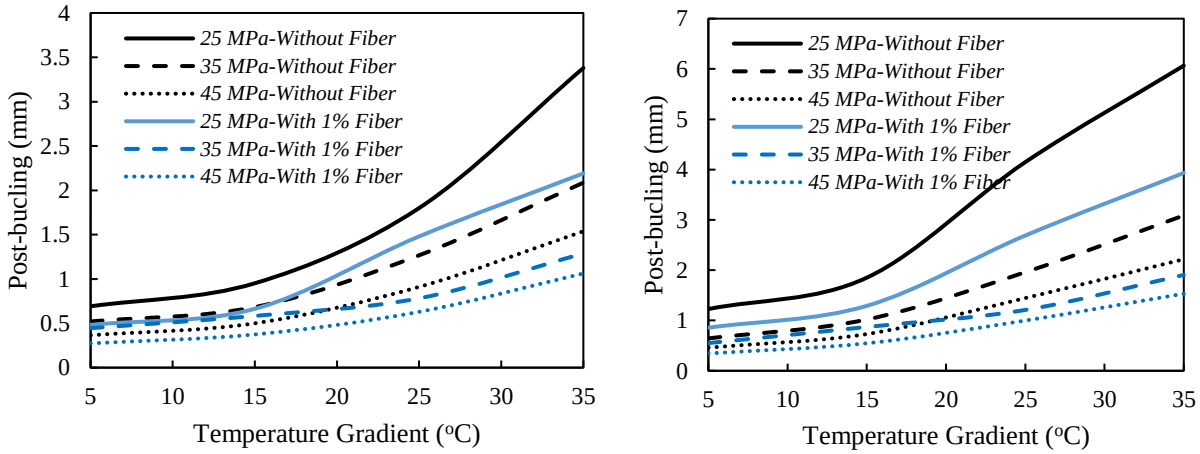

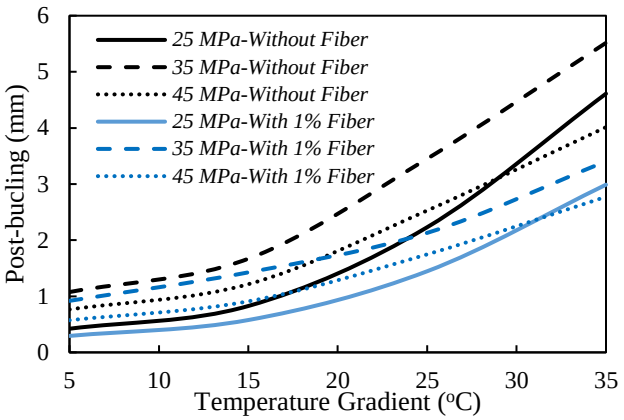

(c)

Figure 7.6: Effect of thermal gradient on the post-buckling of slabs with 10 cm thickness on the constrained by a weakened base with 4.5 m width and a) 4.5m, b) 6m and 7.5 m length

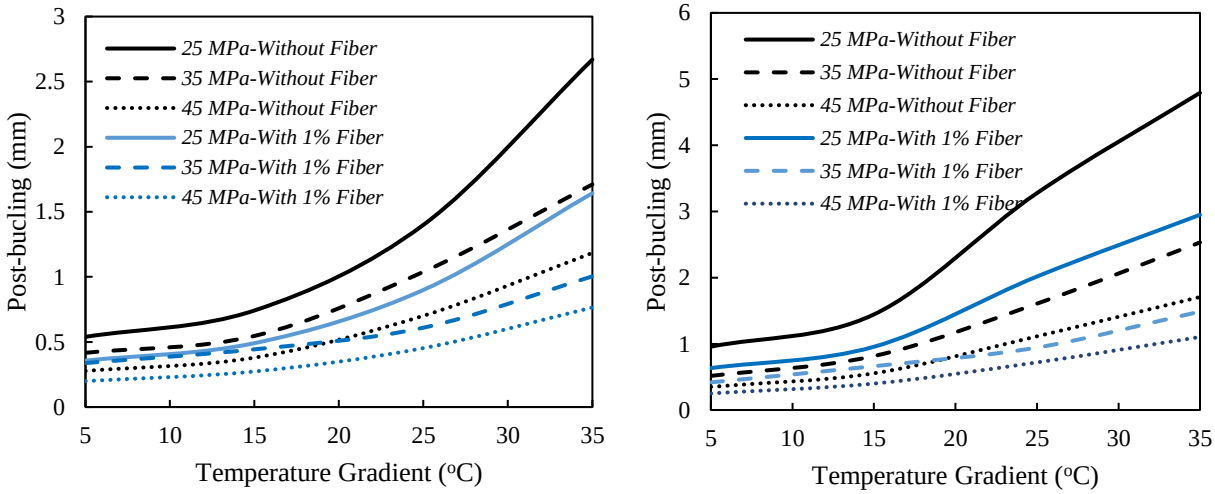

(a) (b)

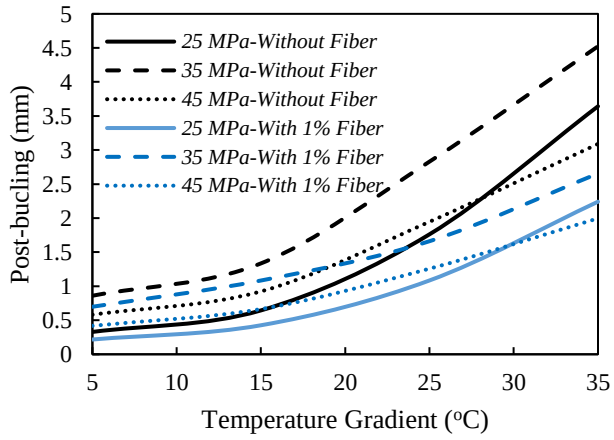

(c)

Figure 7.7: Effect of thermal gradient on the post-buckling of slabs with 10 cm thickness on the constrained by a rigid base with 4.5 m width and a) 4.5m, b) 6m and 7.5 m length

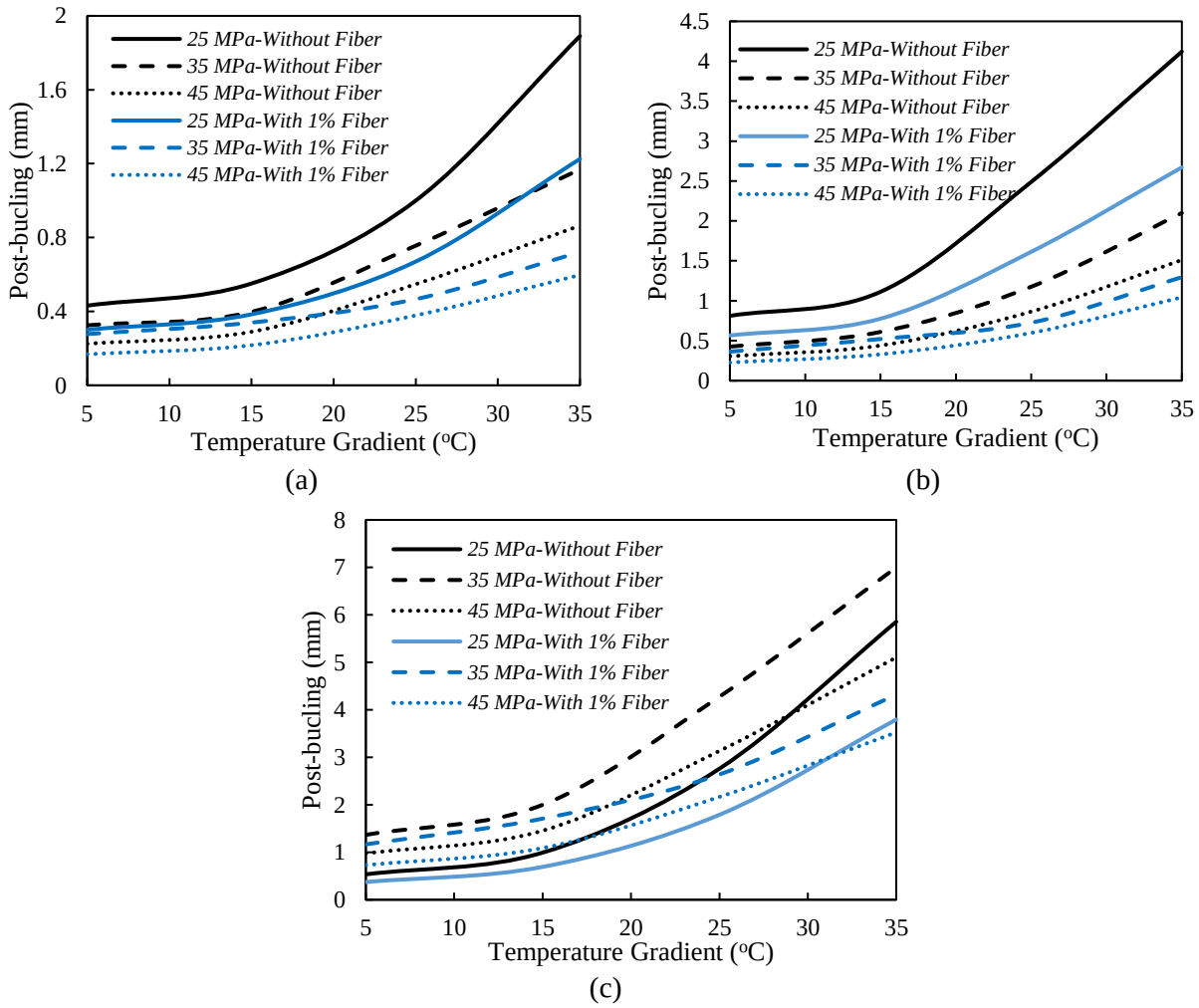

Figure 7.8: Effect of thermal gradient on the post-buckling of slabs with 30 cm thickness on the constrained by a weakened base with 4.5 m width and a) 4.5m, b) 6m and 7.5 m length

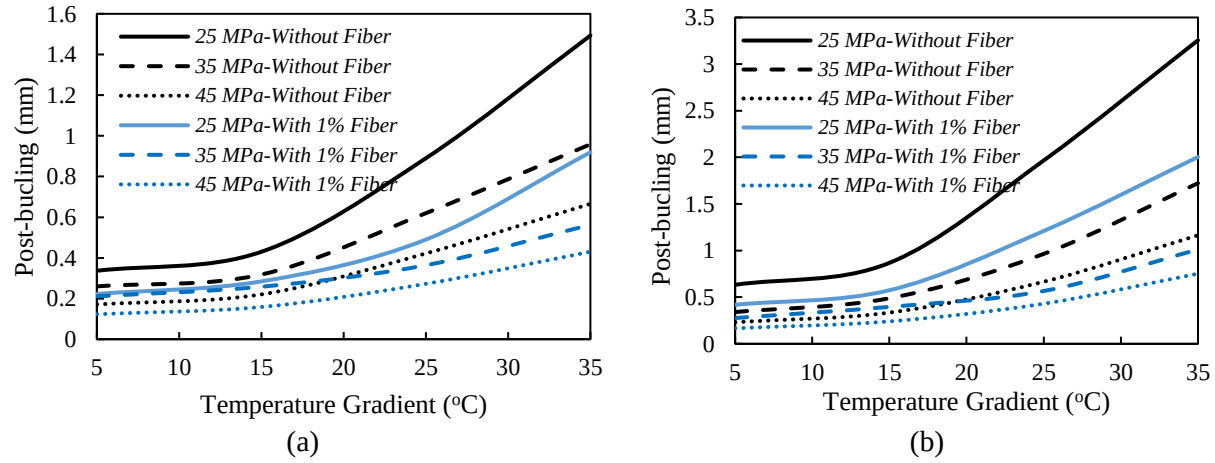

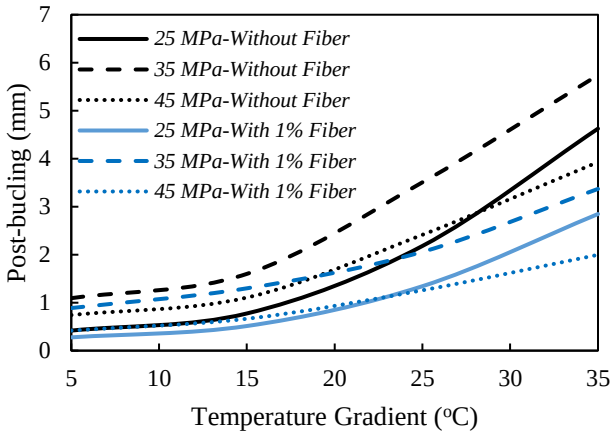

(c)

Figure 7.9: Effect of thermal gradient on the post-buckling of slabs with 30 cm thickness on the constrained by a rigid base with 4.5 m width and a) 4.5m, b) 6m and 7.5 m length

Figures 7.10 to 7.13 provide the post-buckling behavior of rigid concrete slabs with 6m width and various lengths and thicknesses. The post-buckling behavior of slabs with lengths of 4.5m and 6m climbed significantly as slab thickness increased, while slabs with lengths of 7.5m only slightly increased this behavior. Additionally, the post-buckling value was increased by raising the temperature. This could be a result of a rise in the temperature differential between the top and bottom of slabs, which raises stresses and, as a result, the bending moment. Additionally, fiber integration was crucial in reducing the post-buckling performance of concrete airfield runways. Fibers' capacity to fill voids enhances the compressive strength of concrete and lessens crack propagation. The performance after buckling could be greatly reduced as a result of increased strain being transferred through cracks. It is also feasible to consider the post-buckling movement as almost linear when the compressive strength of concrete is greater than 35MPa. Additionally, it was observed that increasing tensile strength decreased post-buckling behavior in slabs with lengths of 4.5m and 6m. The potential for bending and curvature distortion in shorter-length pieces may be related to this. In slabs longer than 7.5 meters, however, the post-buckling values increased as compressive strength increased up to 35 MPa before declining at 45 MPa. This might be connected to how the membrane shell and plate components behave in long concrete slabs with proportionately higher and lower compressive strengths. Post-buckling behavior was greatly diminished as the ratio of tensile strain to tensile

strength decreased. Figure 7.6c illustrates how the post-buckling behavior of slabs with a 7.5m length has changed in comparison to slabs with a 4.5m and 6m length. For slabs up to 6 meters in length, the behavior should be taken into account as a plate component.

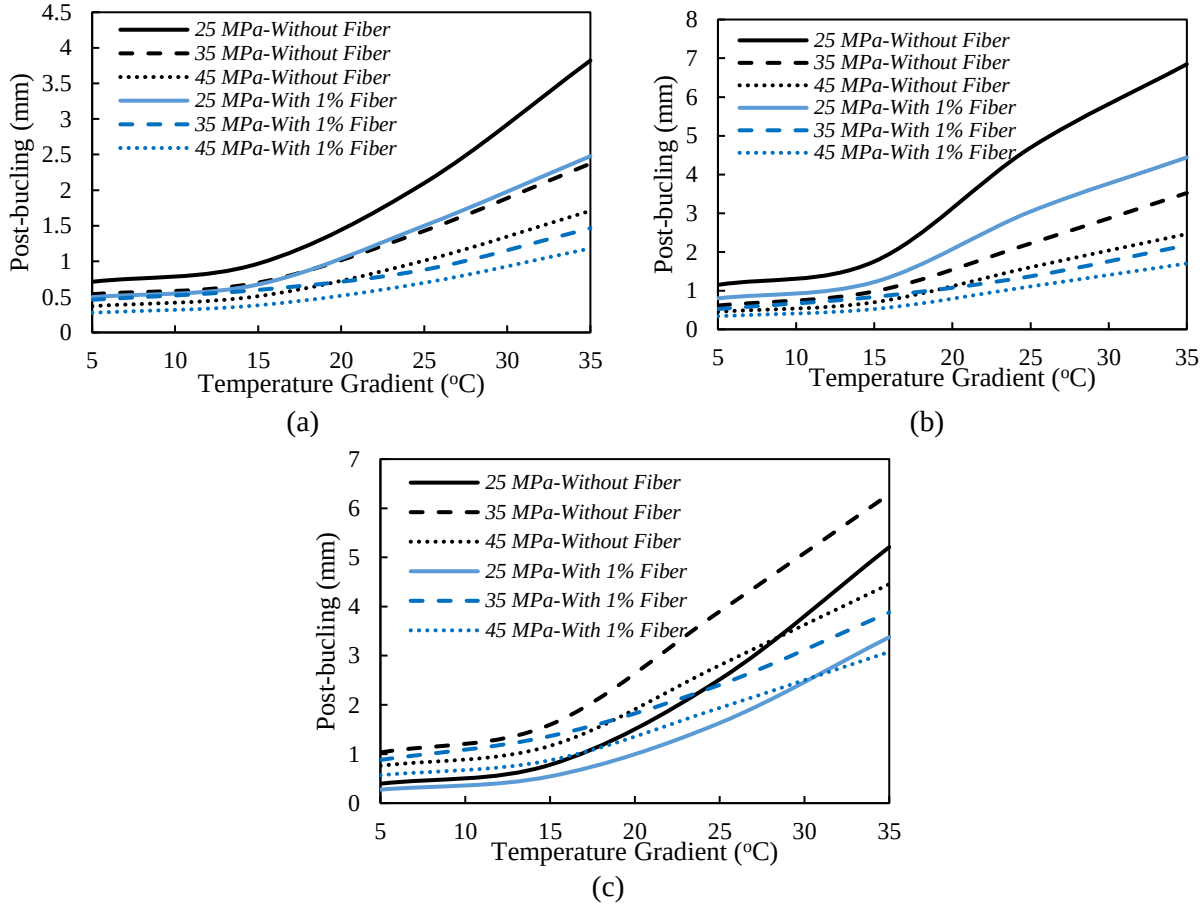

Figure 7.10: Effect of thermal gradient on the post-buckling of slabs with 10 cm thickness on the constrained by a weakened base with 6 m width and a) 4.5m, b) 6m and 7.5 m length

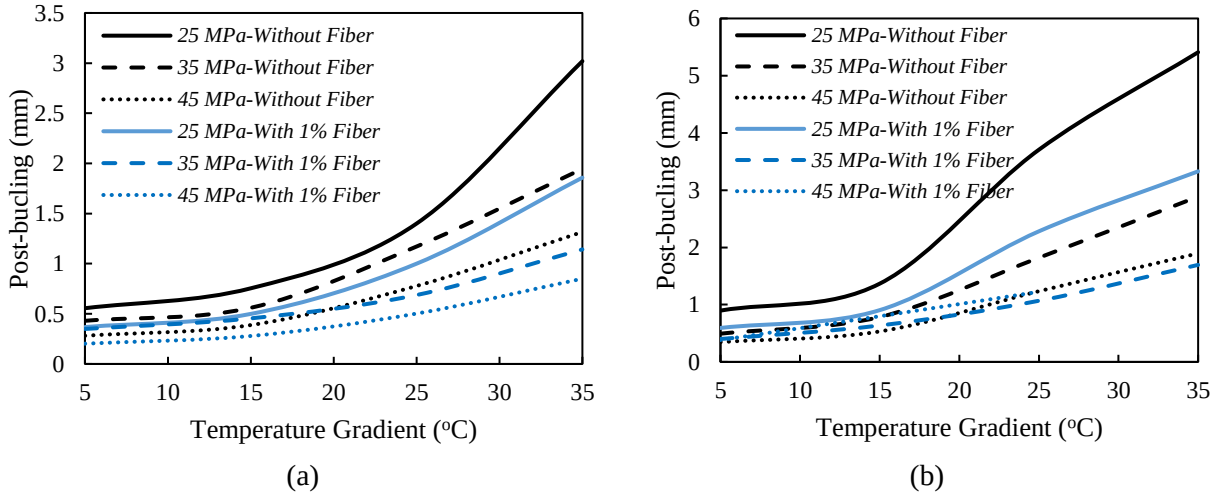

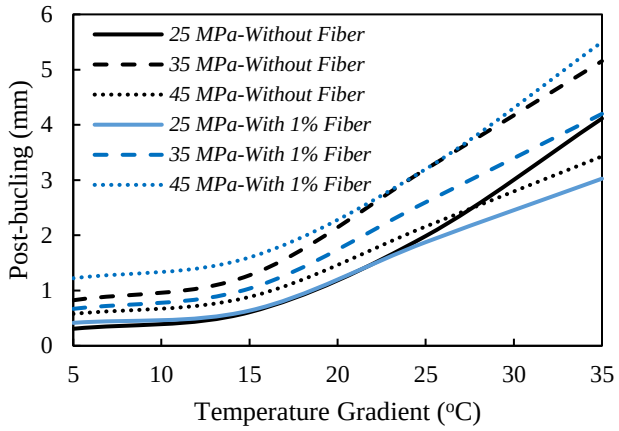

(c)

Figure 7.11: Effect of thermal gradient on the post-buckling of slabs with 10 cm thickness on the constrained by a rigid base with 6 m width and a) 4.5m, b) 6m and 7.5 m length

The findings for the post-buckling behavior of slabs with a 10cm thickness and 3m width that are restrained by a weakened and rigid base come from Figures 7.12 and 7.13 and span lengths of 4.5, 6, and 7.5m. These findings showed that while the post-buckling value for slabs with 7.5m length rose, the post-buckling behavior of slabs with 4.5m and 6m length decreased as thickness was raised. This might be connected to the mechanism of failure as well as the out-of-plane deformation in lengthy slabs that displayed switching behavior from membrane shell to plate bending element. Additionally, fiber addition greatly reduced the post-buckling performance of rigid concrete airfield runways. Due to the fibers' ability to bridge gaps, which increases concrete's tensile strength and reduces crack detachment. As a result, more strain might be transferred through cracks, greatly lowering post-buckling performance. Additionally, the post-buckling behavior of rigid concrete slabs was linear up to a thermal gradient of 20°C, but as the thermal gradient rose, the nonlinearity significantly increased. It is crucial to consider the nonlinear behavior of concrete slabs as well as the nonlinear thermal gradient through the width of the slabs for temperature changes over 20°C. Additionally, the post-buckling deformation may be regarded as almost linear if the concrete's compressive strength is greater than 35 MPa. Additionally, it was observed that

increasing tensile strength decreased post-buckling behavior in slabs with lengths of 4.5m and 6m. The potential for bending and curvature distortion in shorter-length pieces may be related to this. The post-buckling values, however, grew as the compressive strength rose up to 35 MPa in slabs with 7.5 m in length before declining as the compressive strength rose up to 45 MPa. This might be connected to how the membrane shell and plate components behave in long concrete slabs with proportionately higher and lower compressive strengths. When their length is increased by 7.5m, it is recommended to assess the behavior of the slabs as a membrane shell element. However, for slabs up to 6m in length, the behavior should be taken into account as a plate characteristic. As compressive strength and fiber incorporation rose, post-buckling increased in slabs with 7.5m length, and the greatest values were discovered for slabs with 35MPa concrete compressive strength. Additionally, Figure 7.13 demonstrates that for slabs controlled by a stabilized rigid base layer, the post-buckling behavior was decreased, which may be linked to both less base layer deformation and greater contact with the concrete slabs.

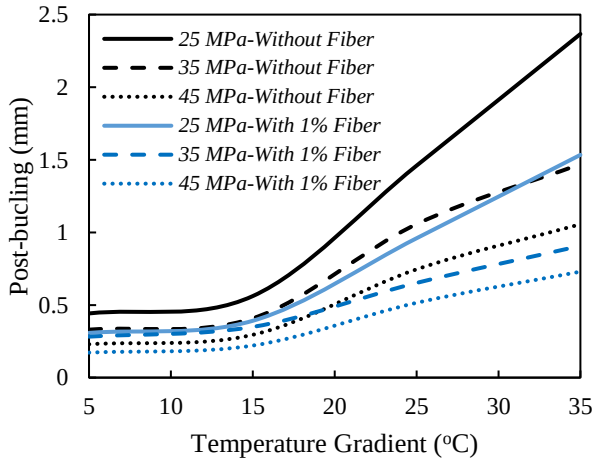

(a)

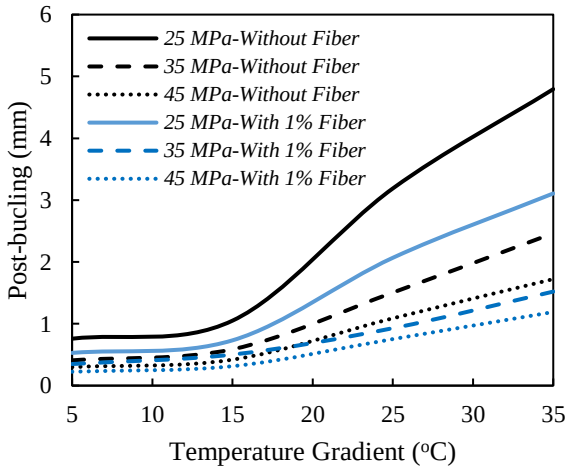

(b)

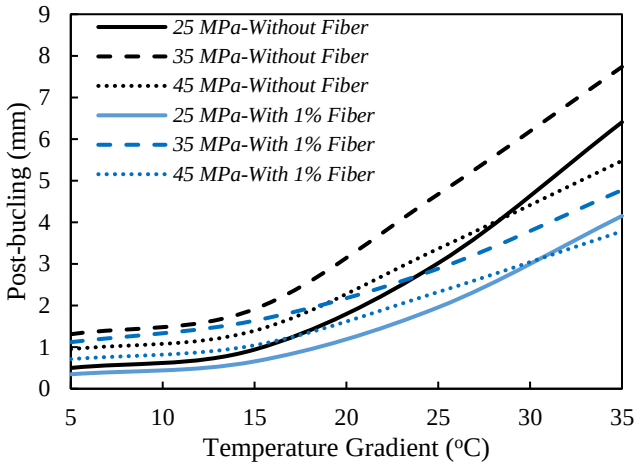

(c)

Figure 7.12: Effect of thermal gradient on the post-buckling of slabs with 30 cm thickness on the constrained by a weakened base with 6 m width and a) 4.5m, b) 6m and 7.5 m length

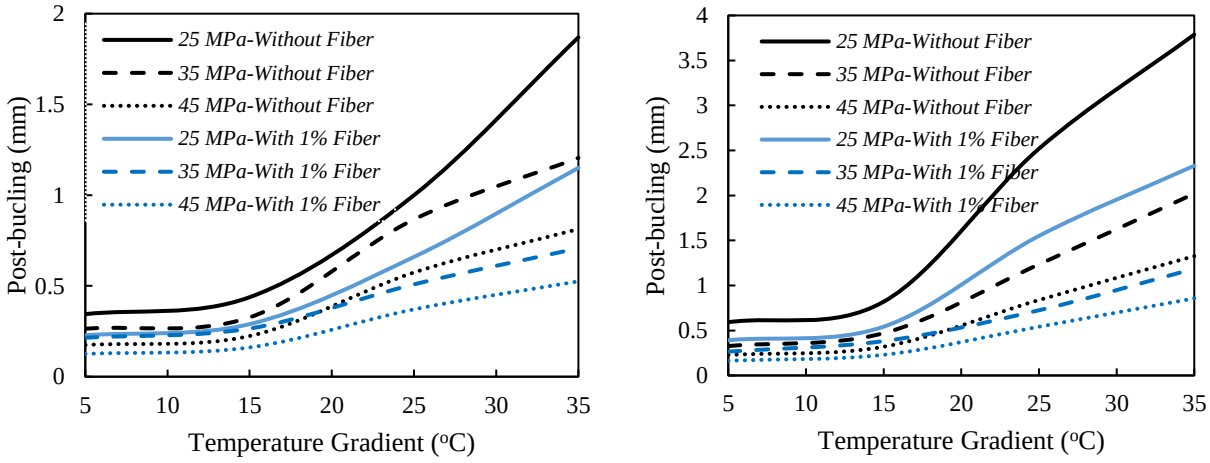

(a) (b)

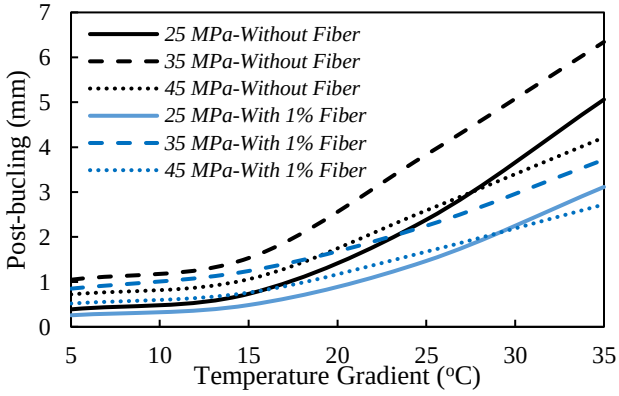

(c)

Figure 7.13: Effect of thermal gradient on the post-buckling of slabs with 30 cm thickness on the constrained by a rigid base with 6 m width and a) 4.5m, b) 6m and 7.5 m length

7.3.2. Axial force

An axial force is one of the most important factors to measure the out-of-plane deformation in rigid concrete slabs due to thermal gradient. Therefore, in this section, the influence of geometric characteristics, thermal gradient, material properties, and post-buckling behavior on the axial force are measured. The effects of thermal gradient on the axial load of slabs with a 10 cm thickness, 3m width, and different lengths (4.5 m, 6 m, and 7.5 m), respectively, are depicted in Figures 7.14 and 7.15. Figure 7.14 shows that increasing the temperature raised the axial load value. This may be related to a rise in the temperature difference between the slabs' top and bottom sides, which raises tensions and, as a result, the bending moment. Additionally, the axial load in rigid concrete airfield runways was significantly decreased by fiber inclusion. Due to the fact that fibers' bridging role increases the tensile strength of concrete and decreases cracks propagation. Therefore, greater tension stress could be transmitted through cracks, significantly reducing axial stress in concrete. Furthermore, rigid concrete slabs' axial load was nonlinear, and the nonlinearity considerably increased with an increase in a thermal gradient. For temperature variations over 20°C, it is essential to take into account the nonlinear behavior of concrete slabs as well as the nonlinear thermal gradient through the width of the slabs.

Additionally, it was seen that in slabs with 4.5m and 6m in slabs, the axial load was reduced by raising compressive strength. This might be connected to the possibility of bending and curvature deformation in shorter-length slabs. However, in slabs with 7.5m in length, the axial load values rose with a rise in compressive strength up to 35MPa before falling when it hit 45MPa. This may be related to the behavior of the membrane shell in lengthy slabs of concrete having lower compressive strength. Figure 7.14c illustrates how the axial of slabs with a 7.5m length has altered in contrast to slabs with a 4.5m and 6m length. This might be related to slab out-of-plane

movement and cracking modes. It is advised to evaluate the behavior of the slabs as a membrane shell element when their length is raised by 7.5m. While the behavior should be considered as a plate feature for slabs up to 6m in length. Therefore, axial increased in slabs with 7.5m length as compressive strength and fiber incorporation increased, and the highest values were found for slabs with 35MPa concrete compressive strength. Figure 7.3 also shows that the axial load was increased for slabs restrained by a stabilized rigid base layer, which may be related to lateral restriction due to the contact between concrete and base layers which results in generating an additional load in rigid concrete slabs.

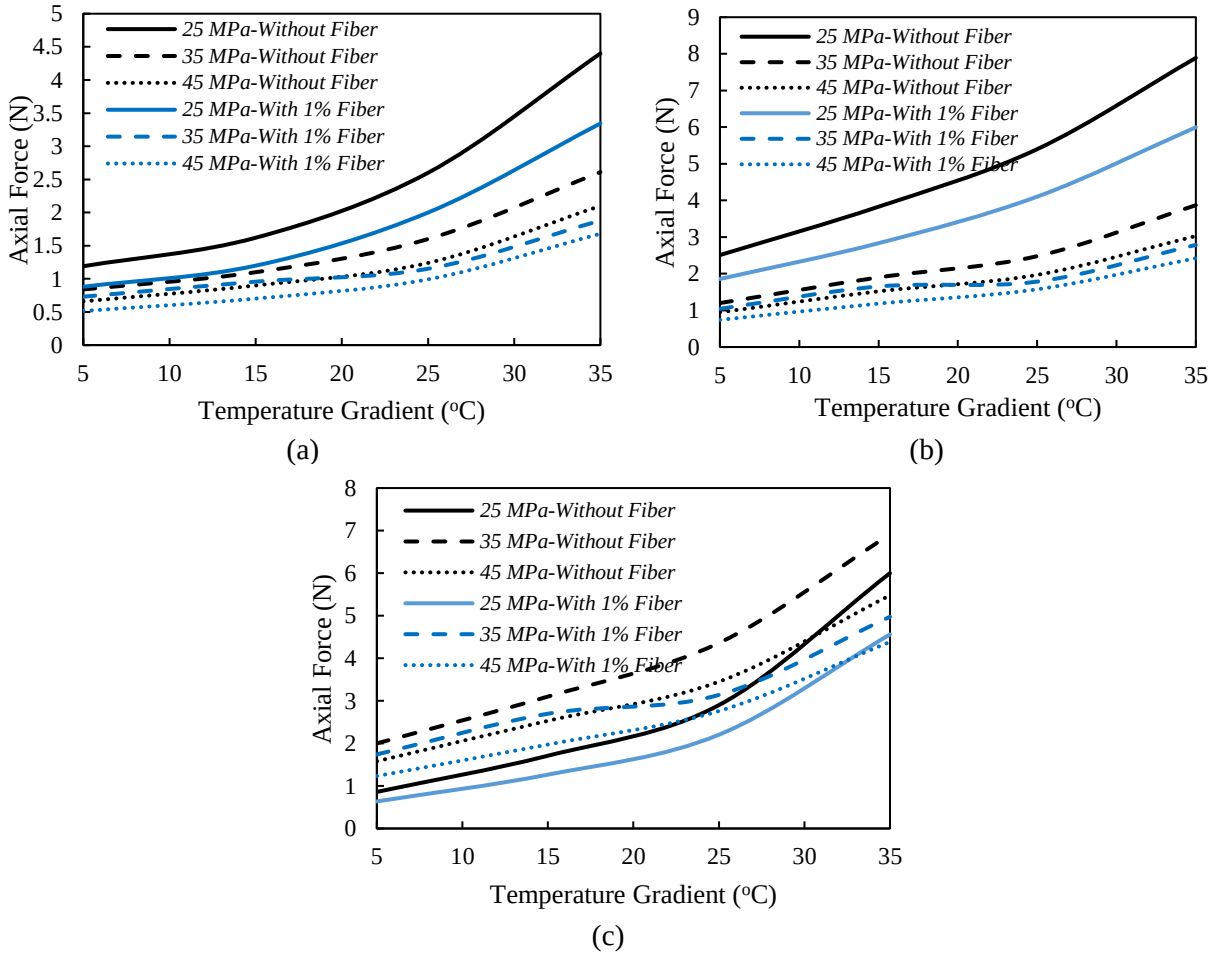

Figure 7.14: Effect of thermal gradient on the axial force of slabs with 10 cm thickness on the constrained by a weakened base with 3 m width and a) 4.5m, b) 6m and 7.5 m length

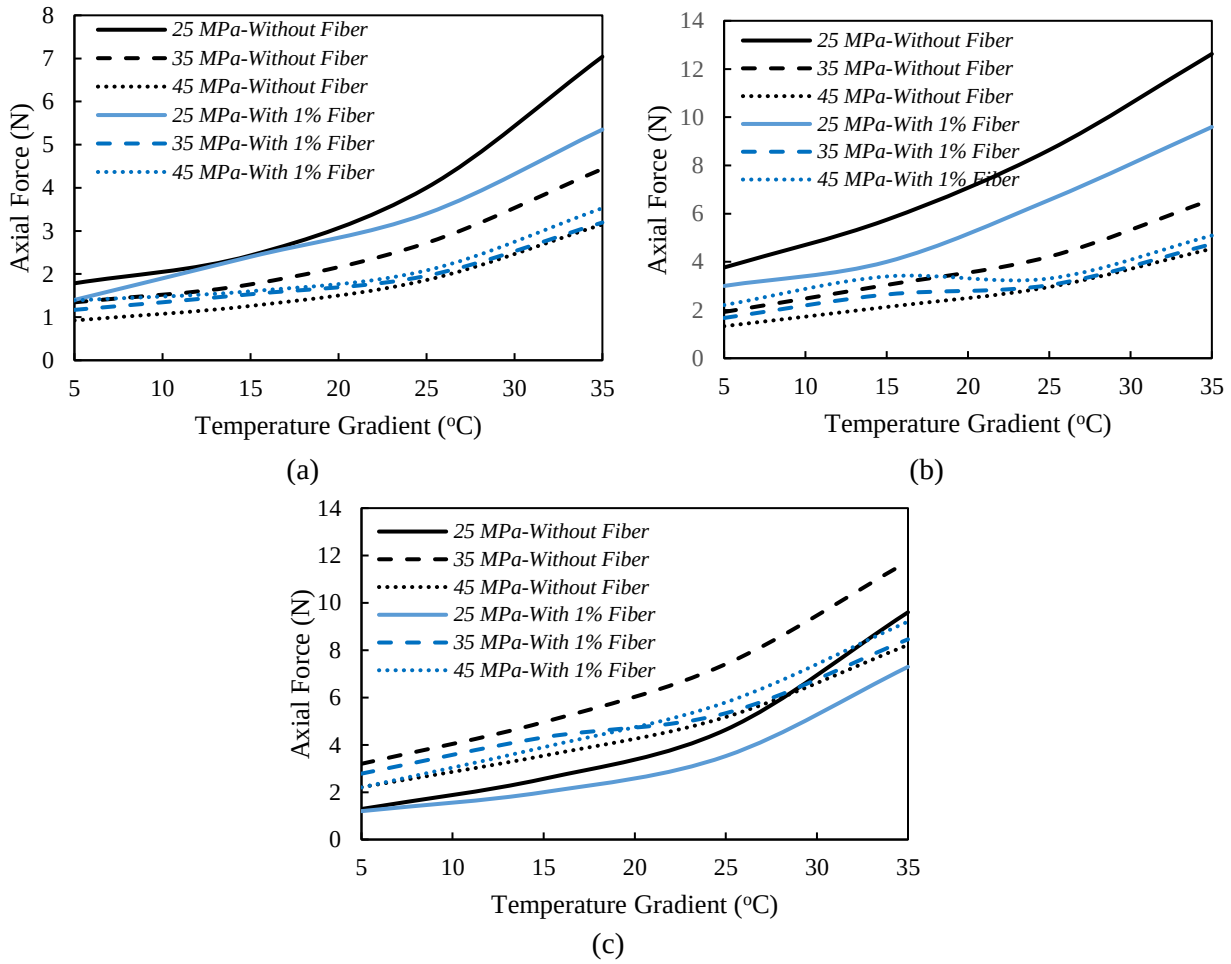

Figure 7.15: Effect of thermal gradient on the axial force of slabs with 10 cm thickness on the constrained by a rigid base with 3 m width and a) 4.5m, b) 6m and 7.5 m length

Additionally, Figures 7.16 and 7.17 show the outcomes for the axial load in slabs with a thickness of 30cm, 3m width, and various lengths that are restrained by a rigid base layer. These findings showed that while the axial value for slabs with 7.5m length rose, the axial load of slabs with 4.5m and 6m length decreased as thickness was raised. This behavior change in the axial load confirms the post-buckling buckling behavior of the slabs that were examined in the previous section. This may be connected to the mechanism of failure as well as the out-of-plane deformation in lengthy slabs that displayed switching behavior from membrane shell to plate bending element. Additionally, fiber addition greatly reduced the axial load value of rigid concrete airfield runways.

Due to the fibers' ability to bridge gaps, which increases concrete's tensile strength and reduces crack spacing. As a result, more strain might be transferred through cracks, greatly lowering axial load value. Additionally, it was observed that increasing compressive strength decreased axial load in slabs with lengths of 4.5m and 6m. When slab length is increased by 7.5m, it is recommended to assess the behavior of the slabs as a membrane shell element. However, for slabs up to 6m in length, the behavior should be taken into account as a plate characteristic. In addition, Figure 7.17 demonstrates that for slabs controlled by a stabilized rigid base layer, the axial was increased, which may be associated with generated extra load as a restriction in the deformation of slabs.

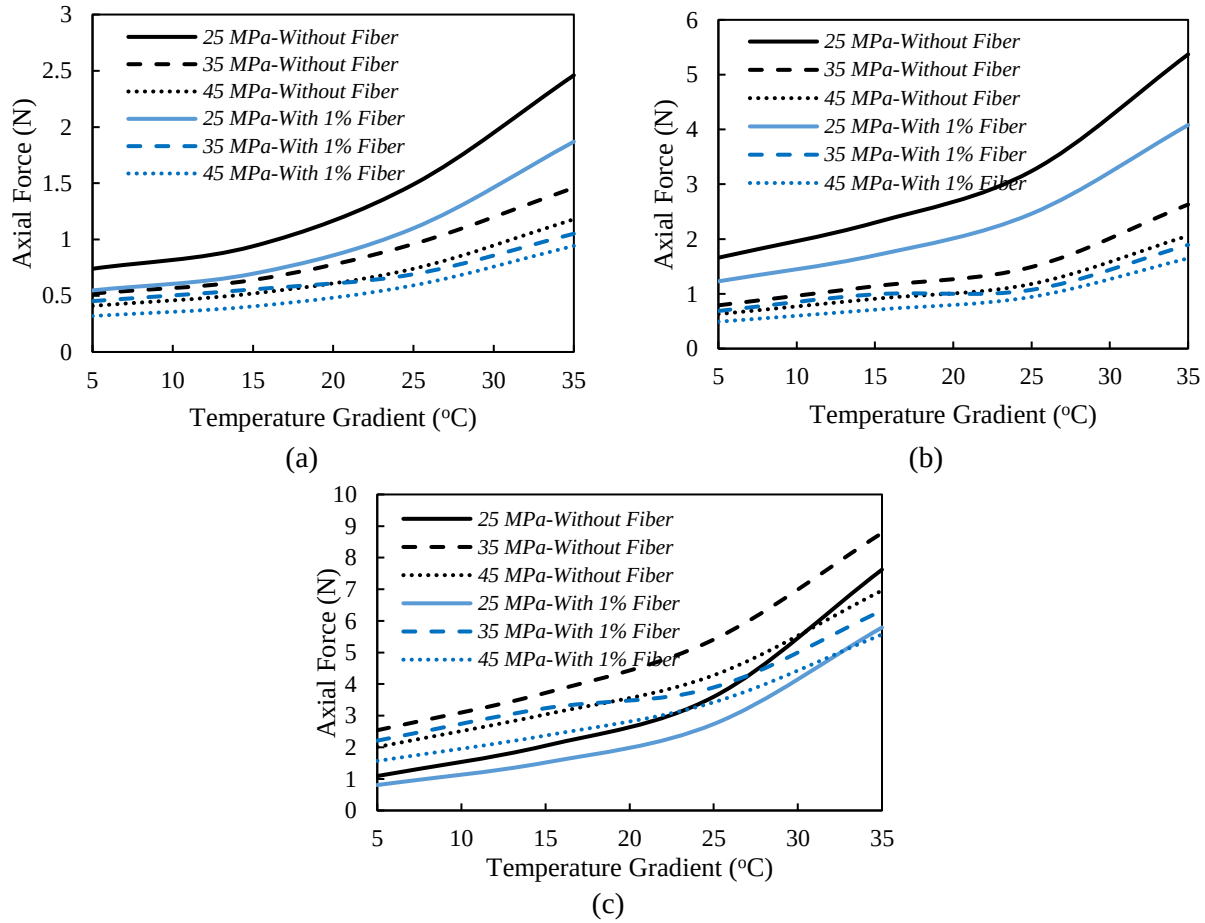

Figure 7.16: Effect of thermal gradient on the axial force of slabs with 30 cm thickness on the constrained by a weakened base with 3 m width and a) 4.5m, b) 6m and 7.5 m length

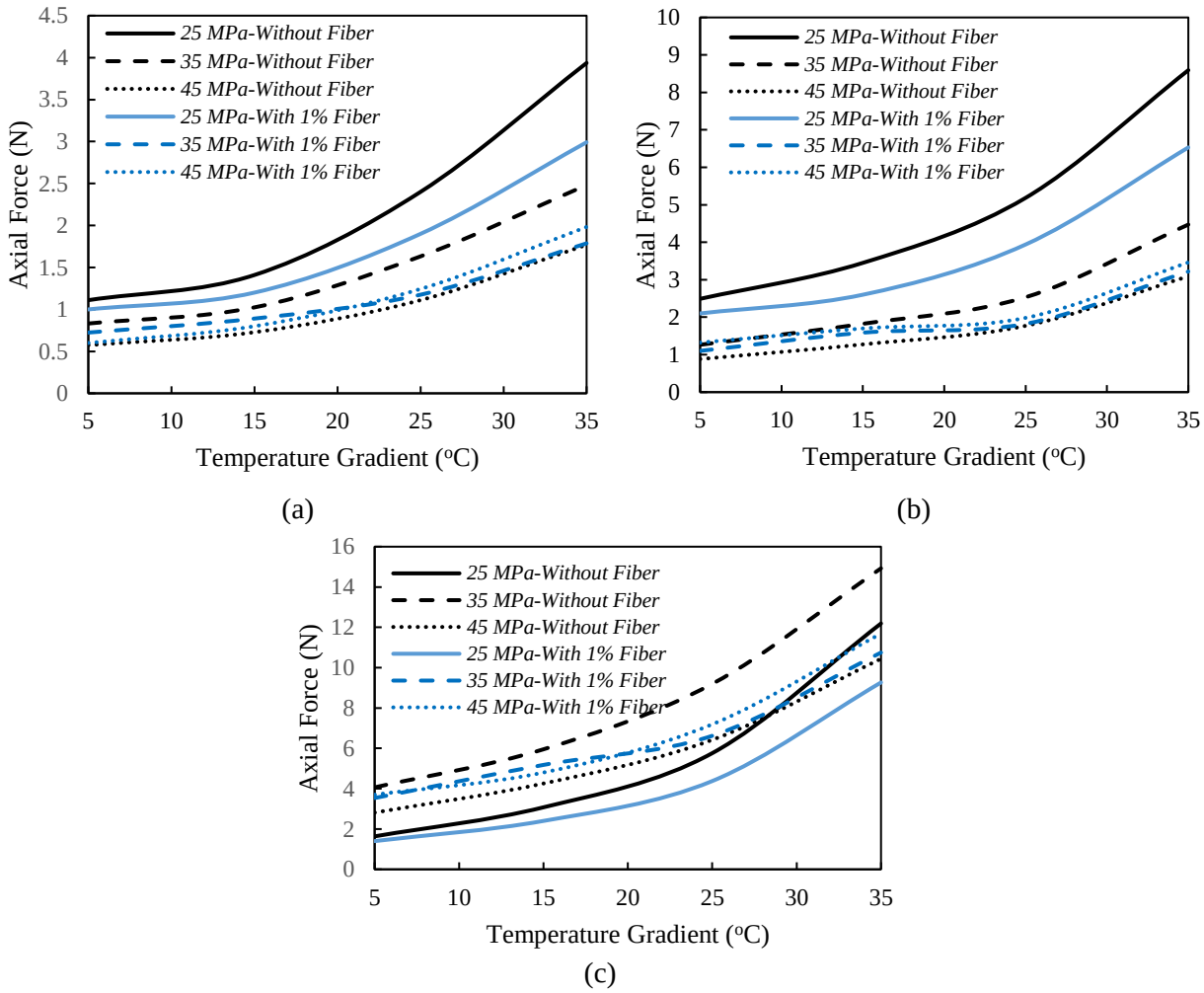

Figure 7.17: Effect of thermal gradient on the axial force of slabs width 30 cm thickness on the constrained by a rigid base with 3 m width and a) 4.5m, b) 6m and 7.5 m length

In this study, an essential factor influencing the thermal performance of rigid concrete airfield runways was also considered to be the effect of slab width. Figures 7.18 and 7.19, respectively, show the axial load outcomes of slabs with a 10cm thickness restrained by a weakened and rigid base layer with a 4.5m width and different lengths. The axial load performance of slabs with lengths of 4.5m and 6m climbed significantly as slab width increased, while slabs with lengths of 7.5m only slightly increased this behavior. Additionally, the axial load value was increased by raising the temperature gradient. This could be a result of a rise in the temperature differential between the top and bottom of slabs, which raises stresses and, as a result, the bending moment.

Additionally, fiber integration was crucial in reducing the post-buckling performance of rigid concrete airfield runways. The performance after buckling could be greatly reduced as a result of increased strain being transferred through cracks which results in improving the axial-load characteristics. Additionally, it was observed that increasing tensile strength decreased axial behavior in slabs with lengths of 4.5m and 6m, and with further width, as well. The potential for bending and curvature distortion in shorter-length pieces may be related to this. Moreover, Figure 7.19 demonstrates that the post-buckling behavior was increased for slabs controlled by a stabilized rigid base layer, possibly as a result of higher load and stress resulting from the contact between the concrete layer and a rigid base layer. Additionally, Figures 7.20 and 7.21 show that while slabs with 7.5m lengths exhibited higher axial load value, slabs with 4.5m and 6m lengths exhibited lower values as thickness increased. This may have something to do with the failure mechanism and the out-of-plane deformation in long slabs that exhibited a shifting behavior from the membrane shell to the plate bending element.

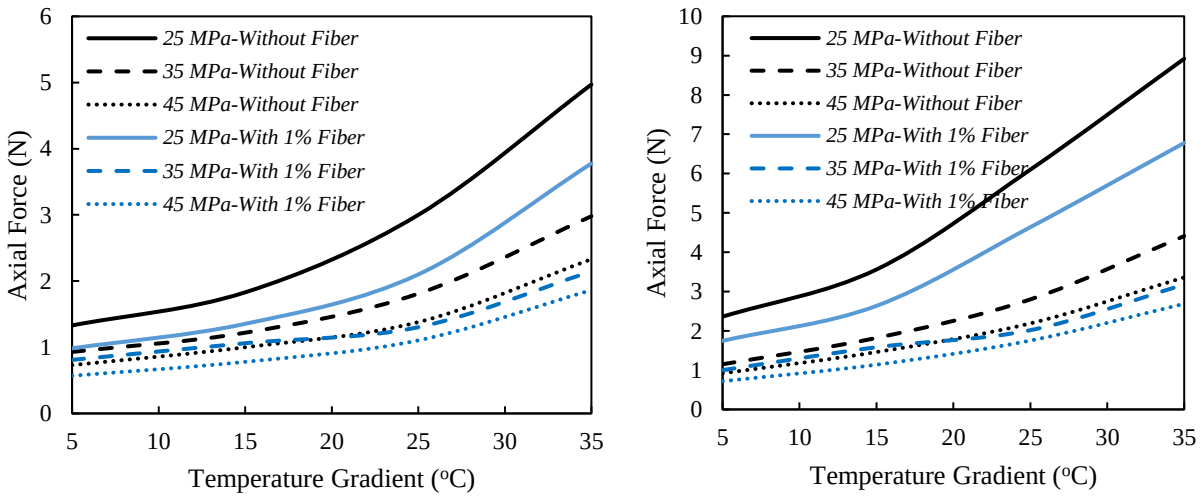

(a) (b)

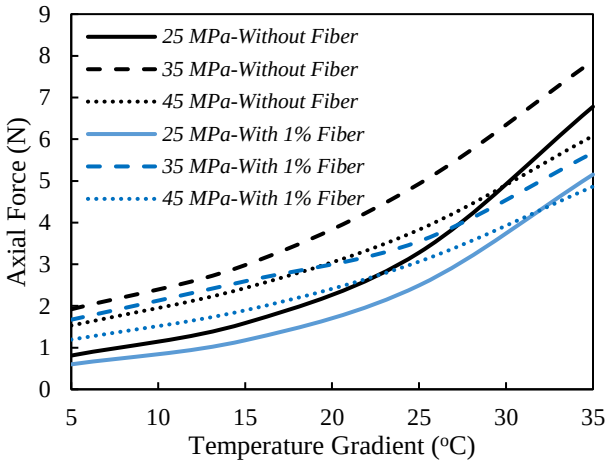

(c)

Figure 7.18: Effect of thermal gradient on the axial force of slabs with 10 cm thickness on the constrained by a weakened base with 4.5 m width and a) 4.5m, b) 6m and 7.5 m length

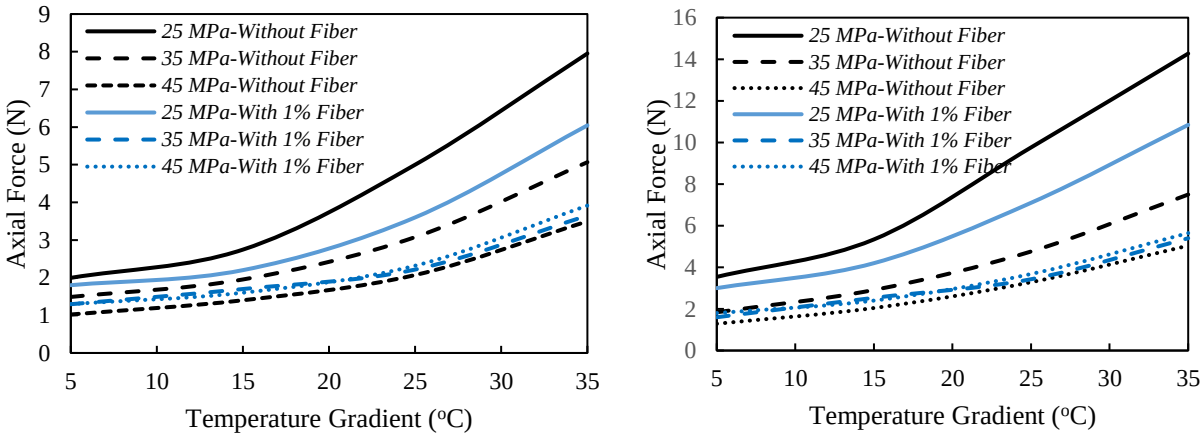

(a) (b)

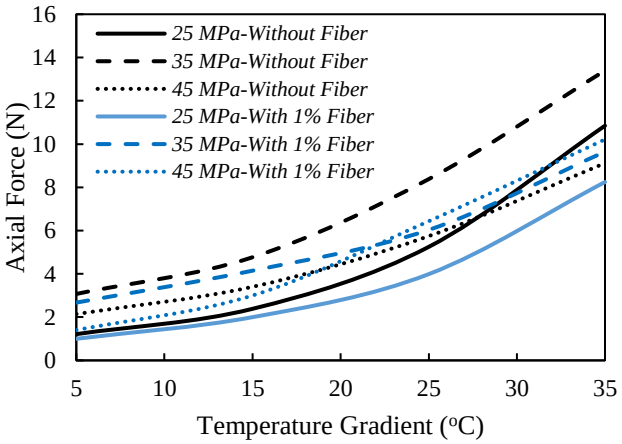

(c)

Figure 7.19: Effect of thermal gradient on the axial force of slabs with 10 cm thickness on the constrained by a rigid base with 4.5 m width and a) 4.5m, b) 6m and 7.5 m length

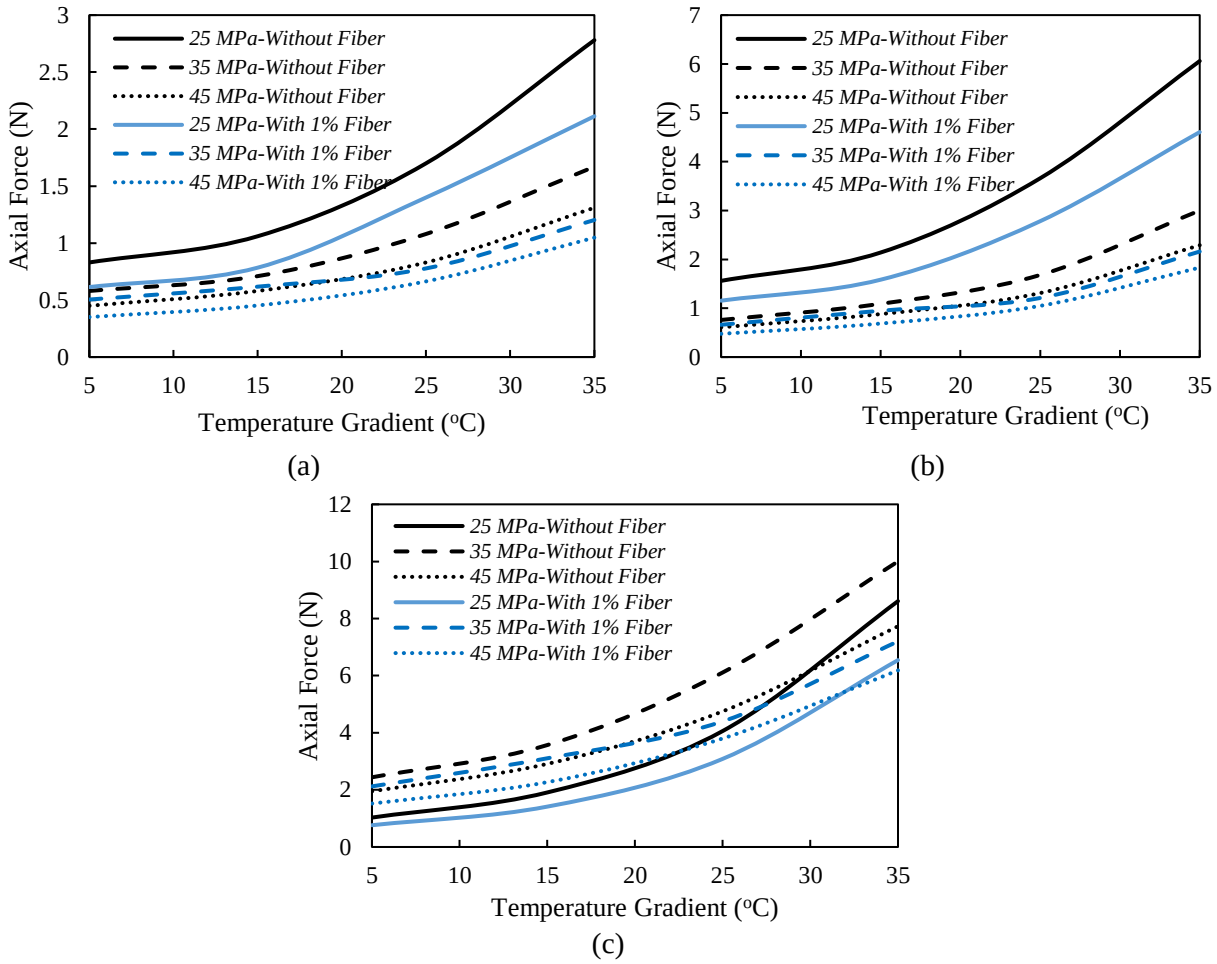

Figure 7.20: Effect of thermal gradient on the axial force of slabs with 30 cm thickness on the constrained by a weakened base with 4.5 m width and a) 4.5m, b) 6m and 7.5 m length

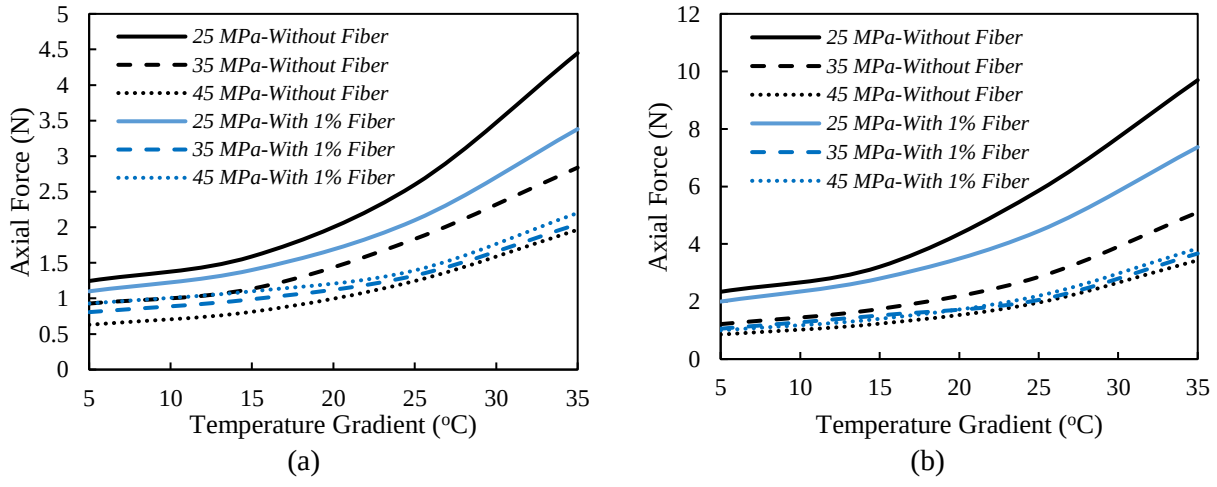

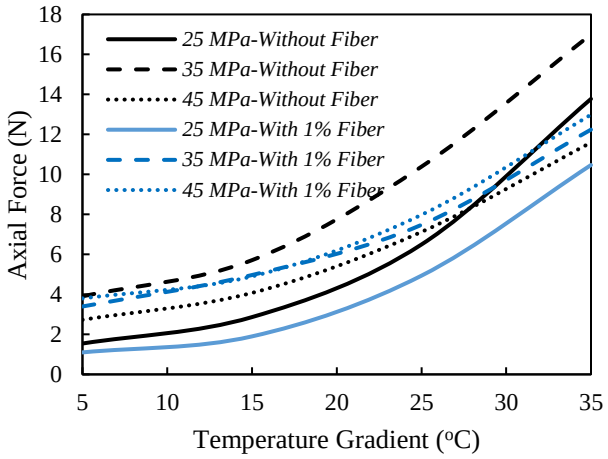

(c)

Figure 7.21: Effect of thermal gradient on the axial force of slabs with 30 cm thickness on the constrained by a rigid base with 4.5 m width and a) 4.5m, b) 6m and 7.5 m length

The axial load results in concrete slabs with a 6m width and a range of lengths and thicknesses are shown in Figures 7.21 to 7.22. In contrast to slabs with lengths of 7.5m, which only marginally increased axial load, slabs with lengths of 4.5m and 6m increased considerably as slab width increased. Raising the temperature also resulted in a rise in the axial load value. The behavior of the membrane shell and plate elements in lengthy concrete slabs with proportionally higher and lower compressive strengths may have something to do with this. As the ratio of tensile strain to tensile strength dropped, the axial load value significantly decreased.

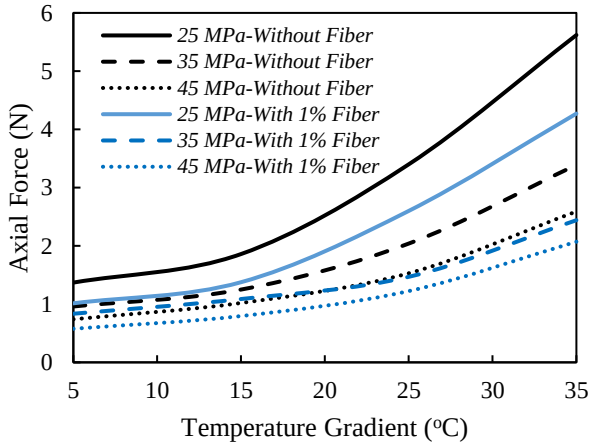

(a)

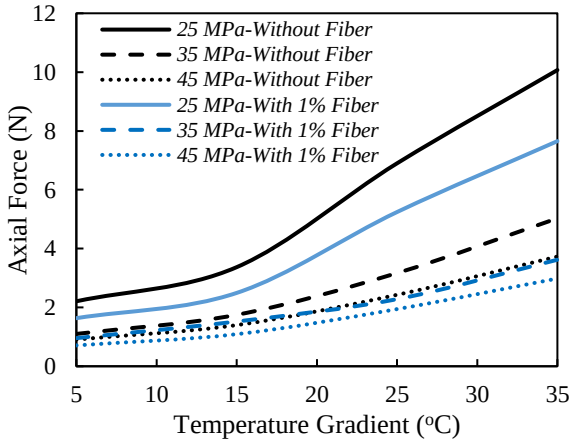

(b)

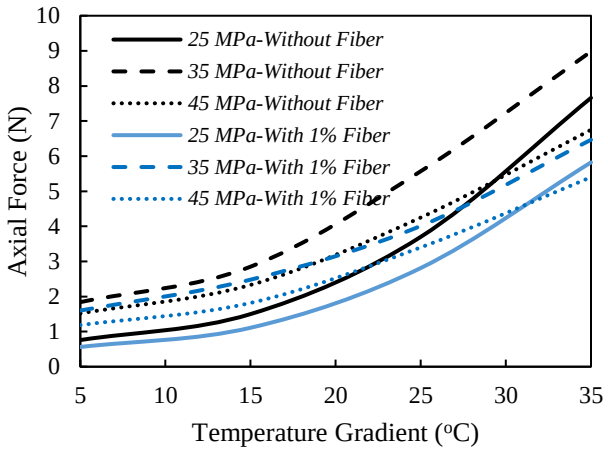

(c)

Figure 7.22: Effect of thermal gradient on the axial force of slabs with 10 cm thickness on the constrained by a weakened base with 6 m width and a) 4.5m, b) 6m and 7.5 m length

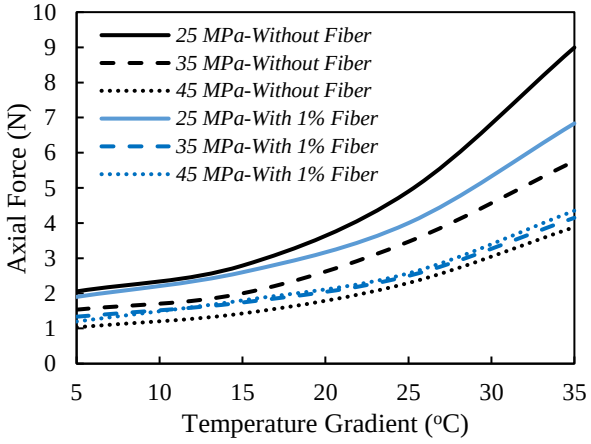

(a)

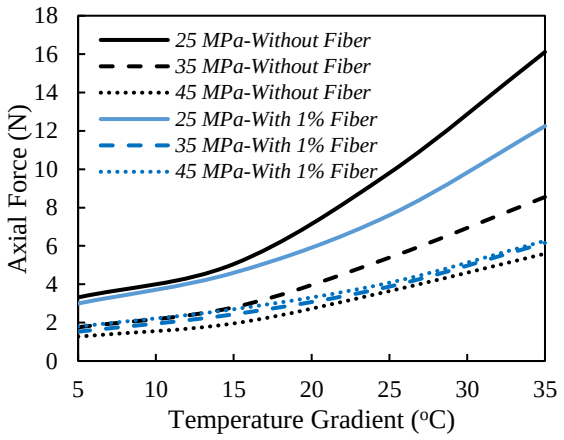

(b)

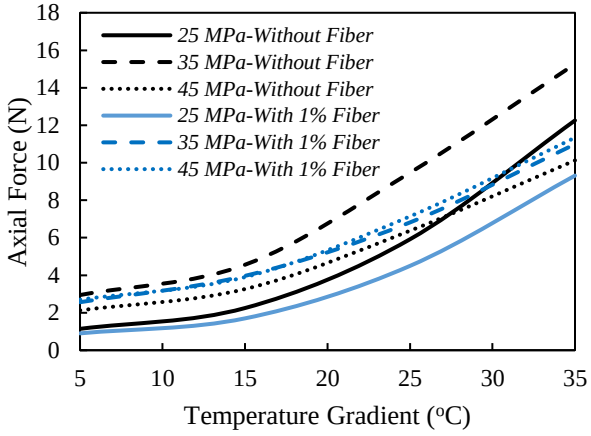

(c)

Figure 7.23: Effect of thermal gradient on the axial force of slabs with 10 cm thickness on the constrained by a rigid base with 6 m width and a) 4.5m, b) 6m and 7.5 m length

Figures 7.24 and 7.25 provide the results for the axial load behavior of slabs with a 10cm thickness and a 6 m width that is held in place by a weak and rigid foundation and length of 4.5, 6, and 7.5 m. The same trend was observed for these samples. These results demonstrated that while the axial value for slabs with 7.5m in length increased, the axial behavior of slabs with 4.5m and 6m in length decreased as thickness increased. Additionally, rigid concrete airfield runways' axial load performance was significantly diminished by fiber addition. Additionally, it was found that slabs with lengths of 4.5m and 6m exhibited less axial load as tensile strength increased. However, in slabs with 7.5m length, the axial load values, however, increased as the compressive strength increased up to 35 MPa before decreasing as the compressive strength increased up to 45 MPa. The performance of rigid slabs should be considered as a plate feature for slabs up to 6m in length. Post-buckling increased in 6m wide slabs with 7.5m length as compressive strength and fiber inclusion grew, with slabs with 35MPa concrete compressive strength showing the highest values.

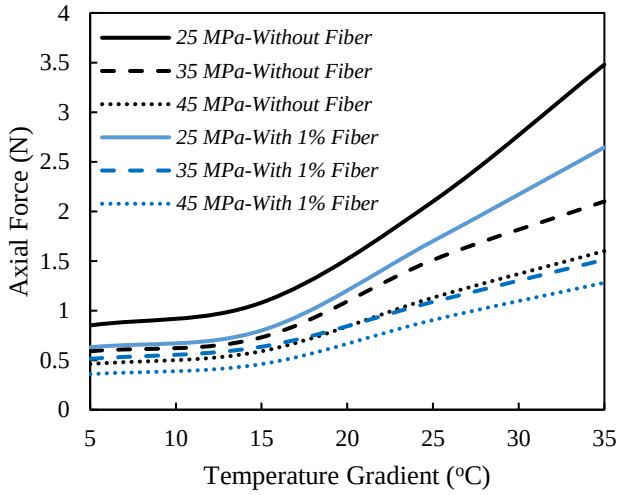

(a)

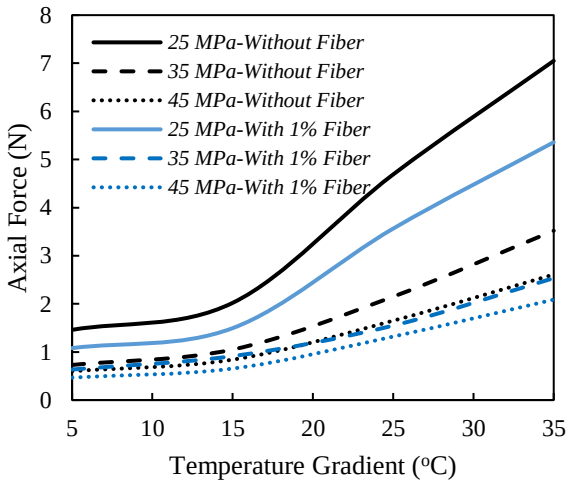

(b)

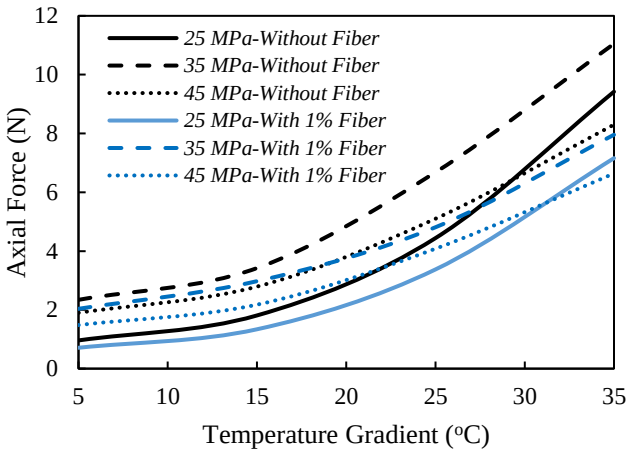

(c)

Figure 7.24: Effect of thermal gradient on the axial force of slabs with 30 cm thickness on the constrained by a weakened base with 6 m width and a) 4.5m, b) 6m and 7.5 m length

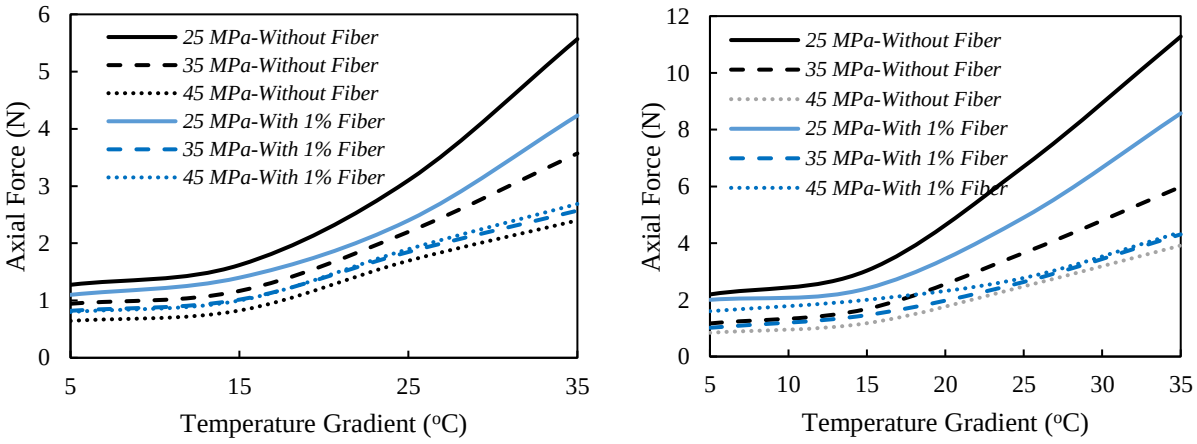

(a) (b)

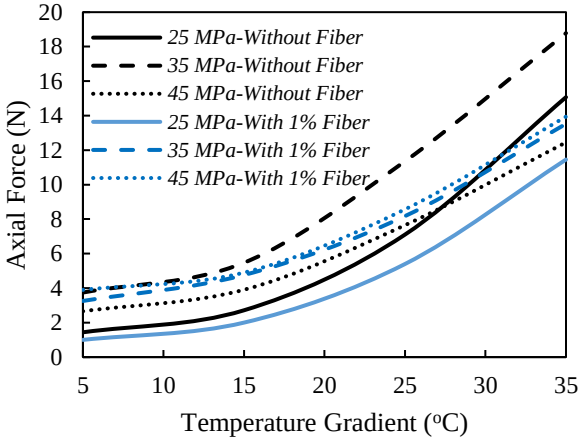

(c)

Figure 7.25: Effect of thermal gradient on the axial force of slabs with 30 cm thickness on the constrained by a rigid base with 6 m width and a) 4.5m, b) 6m and 7.5 m length

7.4. SUMMARY & CONNECTION WITH THE SUBSEQUENT CHAPTER

This chapter offered a new finite element method formulation to measure the influence of thermal gradient on the deformation and stress responses of rigid plain and fiber-reinforced concrete slabs. For this aim, MATLAB coding software was utilized to identify the stress distribution and bending deformation for slabs constructed on the base layer with various stiffness, and the buckling, out-of-plane deformation, and stresses are measured. As a result, the consequences and formulation provided in this Chapter could be employed by companies, agencies, and DOTs to develop their software and designing tools considering all geometric and material characteristics. But the results are complex to use by engineers, particularly the entry-level staff to design rigid concrete slabs for in-field construction in terms of thermal and temperature influences. To achieve this aim, a simple and highly accurate practical formula is required. Therefore, using the results of the previous and the current Chapter, a new practical formula is proposed to measure the thermal and curling stresses in both rigid plain and fiber-reinforced concrete slabs considering all material properties, geometric characteristics, boundary conditions, environmental circumstances, and fiber content. For this aim, a multi-layer genetic programming machine learning approach is utilized. The developed formula in the next Chapter has two main features: 1) simple form to facilitate use by engineers and 2) high accuracy with experimental and numerical results. Figure 7.26 provides a connection with the subsequent chapter overview.

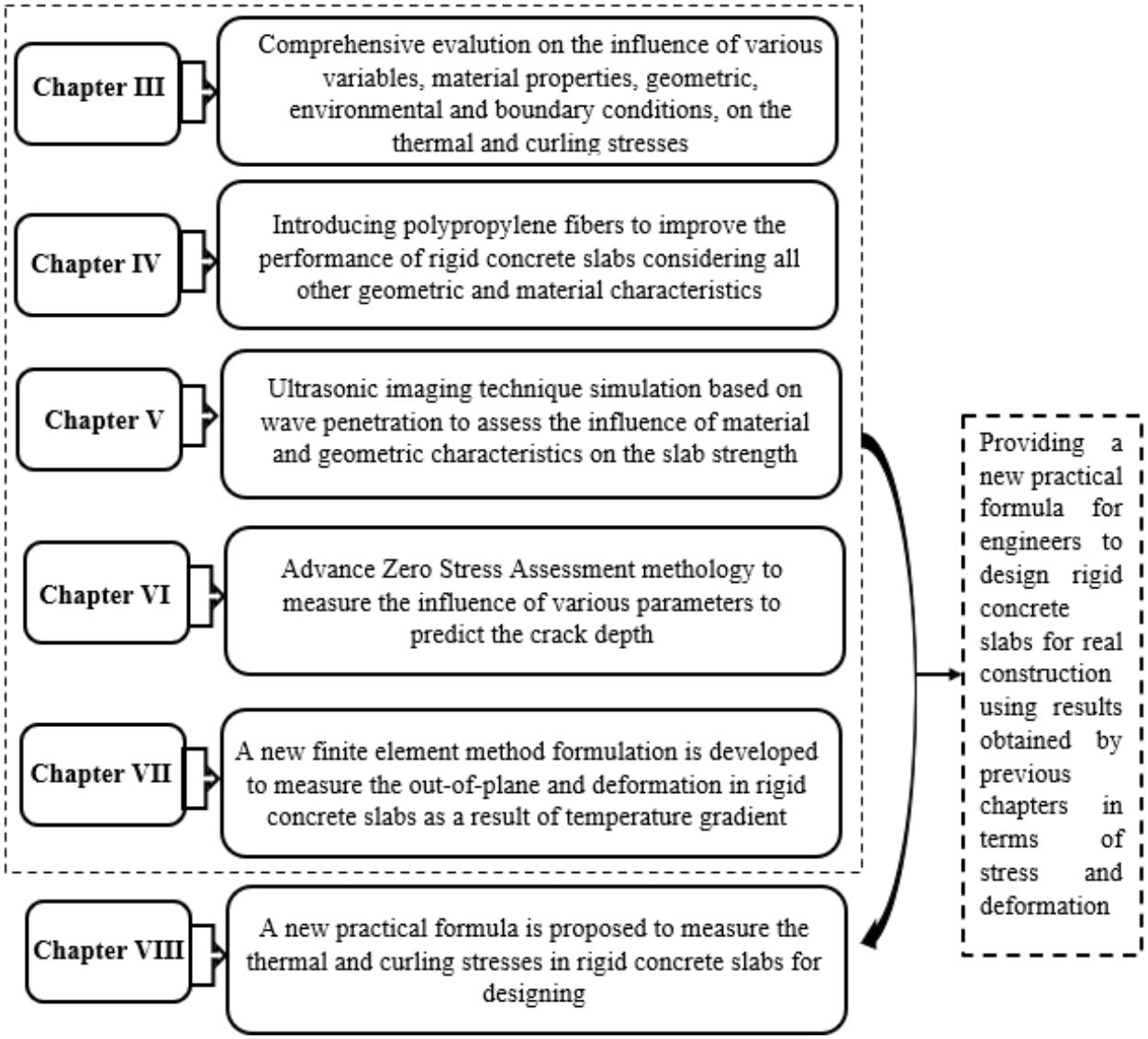

Figure 7.26: Overview of the connection between previous Chapters and Chapter VIII

CHAPTER VIII

NOVEL PRACTICAL FORMULATION

8.1. INTRODUCTION

This chapter aims to provide a practical formula for engineers, agencies, and DOTs to measure the thermal and curling stresses in rigid concrete slabs. The preceding section of this chapter is surveyed by finite element method results collected from previous chapters, in-field results, and also those reported by previous investigations to propose the new formula. For this aim, a multi-layer genetic programming machine learning approach (MLGPML) has been employed. Therefore, the proposed formula will have two main features: high accuracy to predict the curling and thermal stresses, and simple form which gives this opportunity to engineers to calculate stresses easily and fast. The results of this task might be used by many businesses to design the thermal behavior of rigid concrete slabs, and DOTs could use them to construct robust concrete slabs that better account for improving the curling and thermal stresses of rigid concrete slabs.

8.1.1. Organization of the Chapter

This chapter comprises five main sections. Subsequent to the introductory section, Section 2 provides information about the weakness of current models to determine the curling stress in rigid concrete slabs. Section 3 discusses the role of genetic programming and machine learning in developing highly accurate practical formulations. So, the power of the multi-layer genetic programming machine learning approach (MLGPML) will be discussed to propose a new formula in this study considering the influence of various variables. Then, the primary results of this chapter are presented and discussed. Ultimately, a summary of this section will be presented so that its

connection with the subsequent section and also the significance of the subsequent section can be clearly shown.

8.2. EXISTING MODELS TO MEASURE CURLING STRESS IN RIGID CONCRETE SLABS

Measuring curling stress in rigid concrete slabs has become one of the main concerns for engineers. Because cracks happen over the thickness and surface of the slab before the pavement opens to traffic. So, the maintenance costs and service life of slabs could be significantly affected under the influence of temperature gradient and environmental conditions. Therefore, highly accurate robotistic tools could play a crucial role in controlling the thermal performance of rigid concrete slabs. It is worth mentioning that each model should have two main features: 1) highly accurate prediction ability considering all main variables, and 2) simple form which gives the opportunity to engineers to calculate the curling stress shortly and easily (Karimi Pour et al. 2021c; Rezaiee-Pajand et al. 2020). Up to now, various researchers have tried to identify the main variable and incorporate their influence into their proposed models.

In this regard, Nishizawa et al (1990) declared that the thermal gradient, width, and thickness of the slab, and modulus of the subbase are the main variables affecting the curling stress. Considering these parameters, they proposed the following formula to predict the curling stress:

$$\sigma_t = c_0 \Delta t^{c_1} h^{c_2} B^{c_3} k^{c_4} \tag{8.1}$$

In which σ_t, Δt, k, h, and B indicate the ultimate curling stress, thermal gradient, subbase modulus of rupture, thickness, and width of rigid concrete slabs, respectively. Also, c_o, c_1, c_2, c_3 and c_4 are constant coefficients. Equation (8.1) was converted to a linear equation by taking the logarithms of both sides. For this aim, they utilized the calculations from the 192 examples, and multi-regression analysis was employed to derive the constants, c_0 through c_4. As shown in

Equation (8.1), the proposed models were unable to consider the influence of all geometric characteristics such as slab length, location of notch and load transfer devices as well as the boundary condition between slab and base layer and concrete material characteristics such as modulus of rupture, compressive strength, and flexural resistance. Therefore, developing a more accurate model is required.

Recently, Hernandez and Al-Qadi (2019) proposed a closed-form formula to calculate the curling stress in rigid concrete slabs. Based on their assumptions, the slab is built of a material that is linearly elastic and has an elastic modulus (E), Poisson's ratio (ν), and thermal expansion constant (α). The foundation that supports the rigid concrete slab was assumed to be elastic and has a subgrade response modulus of κ that prevents disconnection. The slab is additionally subjected to a linear thermal gradient, with a variation between the top and bottom of the slab of ΔT. Linear elastic springs were considered to limit the vertical displacement and rotation along edges that are perpendicular to the x-axis. The magnitude per unit length of the translational and rotational linear springs are S_a and κ_a, correspondingly, along the edge $y = b/2$. The rotational and translational springs per unit length along the edge $y = -b/2$ are, correspondingly, S_b and κ_b.

The benefit of elastic constraints is that they can capture traditional boundary conditions. For instance, the edges are free and there is no constraint on movement if S_a, κ_a, S_b and κ_b are all zero. On the other hand, if the spring magnitude is very large, the edges are completely constrained and clamped. The edges are pinned if they can rotate freely but cannot move. It can be discovered that for an infinitely long slab subjected to a linear temperature gradient, the bending moment concerning the y-axis is the following (Timoshenko and Krieger 1959; Westergaard 1927), presuming that the slab's cross-section before and after bending are both planes, h is insignificant in comparison to the slab width and length, and vertical strain is negligible.

$$M_y = -\frac{Eh^3}{12(1-v^2)}\left[\frac{d^2w}{dy^2} + \frac{(1+v)}{h}\alpha\Delta T\right] \tag{8.2}$$

The differential equation for the vertical deflection is d^2M_y/dy^2 due to the equilibrium of a differential element in the slab.

$$l^4\frac{d^4w}{dy^4} + w = 0 \tag{8.3}$$

In which $D = Eh^3/12/(1-v^2)$ is the slab's bending stiffness and $l = \sqrt[4]{D/k}$ is the stiffness radius. Westergaard (1927) employed equations (8.2) and (8.3). Along the partially restrained edges of the slab, the shear and bending moments per unit length are

$$V(b/2) = -S_a w(b/2) \tag{8.4}$$

$$V(-b/2) = S_b w(-b/2) \tag{8.5}$$

$$M(b/2) = \kappa_a \theta(b/2) \tag{8.6}$$

$$M(-b/2) = -\kappa_b \theta(-b/2) \tag{8.7}$$

$$\begin{aligned} w(y) = {} & C_1 \cosh\frac{y}{l\sqrt{2}}\cos\frac{y}{l\sqrt{2}} + C_2 \cosh\frac{y}{l\sqrt{2}}\sin\frac{y}{l\sqrt{2}} + C_3 \sinh\frac{y}{l\sqrt{2}}\cos\frac{y}{l\sqrt{2}} \\ & + C_4 \sinh\frac{y}{l\sqrt{2}}\sin\frac{y}{l\sqrt{2}} \end{aligned} \tag{8.8}$$

In which the boundary conditions in Equations (8.4) to (8.8) are replaced with $w(y)$ from Equation (8.8), and C_1, C_2, C_3, and C_4 are constants identified by solving the linear system of Equations (8.7). The answer to the vertical displacement of the slab is

$$w(y) = \frac{1}{\det(A)} \frac{(1+v)\alpha\Delta T}{h} l^2 \left[c_1 \cosh\frac{y}{l\sqrt{2}} \cos\frac{y}{l\sqrt{2}} + c_2 \cosh\frac{y}{l\sqrt{2}} \sin\frac{y}{l\sqrt{2}} + c_3 \sinh\frac{y}{l\sqrt{2}} \cos\frac{y}{l\sqrt{2}} + c_4 \sinh\frac{y}{l\sqrt{2}} \sin\frac{y}{l\sqrt{2}} \right] \quad (8.9)$$

After deflection is calculated, the stresses on top of the slab $\sigma_y = 6M_y/h^2$ and rotation, curvature, bending moment M_y from Equation (8.2), shear force, and deflection $w(y)$ can also be calculated. The y-direction stresses are

$$\sigma_y(y) = -\frac{E\alpha\Delta T}{2(1-v)} [1 - \frac{1}{\det(A)} (c_1 \sin\frac{y}{l\sqrt{2}} \sinh\frac{y}{l\sqrt{2}} - c_2 \cos\frac{y}{l\sqrt{2}} \sinh\frac{y}{l\sqrt{2}} + c_3 \cosh\frac{y}{l\sqrt{2}} \sin\frac{y}{l\sqrt{2}} - c_4 \cos\frac{y}{l\sqrt{2}} \cosh\frac{y}{l\sqrt{2}})] \quad (8.10)$$

In another study, Salehi-Ashtiani (2011) performed a comprehensive study to assess the curling and thermal stresses in rigid concrete slabs. A different simple form formula was presented for measuring curling stress at edges, as presented in Equation (8.11):

$$\sigma_t = \frac{CEe\Delta T}{2} \quad (8.11)$$

Where, σ_t, C, E, e, and ΔT denote the curling stress, constant coefficient counting the geometric characteristics, elastic moduli of concrete slab, thermal coefficient, and temperature gradient, respectively. Additionally, the following formula has been recommended for calculating the interior curling stress.

$$\sigma_t = \frac{Ee\Delta T}{2} \left[\frac{C_1 + vC_2}{1 - v^2} \right] \quad (8.12)$$

In which, C_1, v and C_2 indicate coefficient in direction of calculation, Poisson's ratio, and Coefficient in the direction perpendicular to C_1, correspondingly. It is worth to be mentioned that

C_1 and C_2 is accounting for the geometric characteristics of slabs. As could be found, the proposed model does not take into account the effect of all main material properties and contact circumstances between slab and underlayer as well as the effect of additional materials such as fibers. Therefore, it is necessary to develop a new formula for considering the influence of all main variables. Therefore, the main aim of this Chapter is to provide a highly accurate simple form equation to measure the curling stress in rigid concrete slabs considering the influence of concrete material properties, geometric characteristics, and environmental conditions. For this aim, a Multilayer Genetic Programming Machine Learning Approach (MGPML) has been employed as discussed in the next section.

8.3. GENETIC PROGRAMMING

Numerous applications in a variety of scientific and engineering fields rely on the creation of some kind of mathematic model. There is no exception in the process industries, where applications like an inferential estimate, optimization, process simulation, and process control all rely on precise models to the fullest extent possible. When creating a model, there are two alternative routes that can be taken. Building a mechanistic model based on an understanding of the underlying physical processes is the conventional method. Unfortunately, the system could be incredibly complicated, making it challenging to construct a model from scratch. Additionally, the final model might not be able to achieve the appropriate level of accuracy since some components of the process might be unclear or depend on empirical relationships. As a result, any advantages of using a model of this kind may be outweighed by the development expenses. The alternative is to create a model based on data. The differential and/or algebraic equations that characterize the underlying system are not attempted to be derived using this method. Instead, a model that links the target variable (or output) to other process variables is created using the process data that is currently available.

In some cases, a linear model will suffice to complete this task. However, more sophisticated methodologies are frequently required because of the complexity and non-linearity of calculation processes. Because of the significantly shorter development durations, the resulting models are more cost-effective than mechanistic models. Additionally, since the same set of fundamental tools can typically be used across a greater range of processes, data-based techniques are more adaptable. Figure 8.1 (derived from Söderström and Stoica, 1989) depicts the main flow of the traditional method for developing empirical formulas.

The parameter estimate stage follows the specification of the model structure, demonstrating the sequential nature of this process. Until an appropriate model structure is found, the process must be repeated if the final model does not satisfy the intended performance criteria. Genetic programming (GP) (Koza, 1992) is an evolutionary algorithm that uses the Darwinian idea of natural selection to try and evolve a collection or population of solutions to a problem. The capability of GP to carry out structural optimization is one of its advantages. The approach may simultaneously evolve a model's functional form and numerical parameter values, which is an appealing prospect. As a result, GP has the potential to serve as a tool for automatically creating models. This method has the benefit of requiring fewer assumptions about the eventual shape of the model because the algorithm may develop the model's structure from basic building pieces.

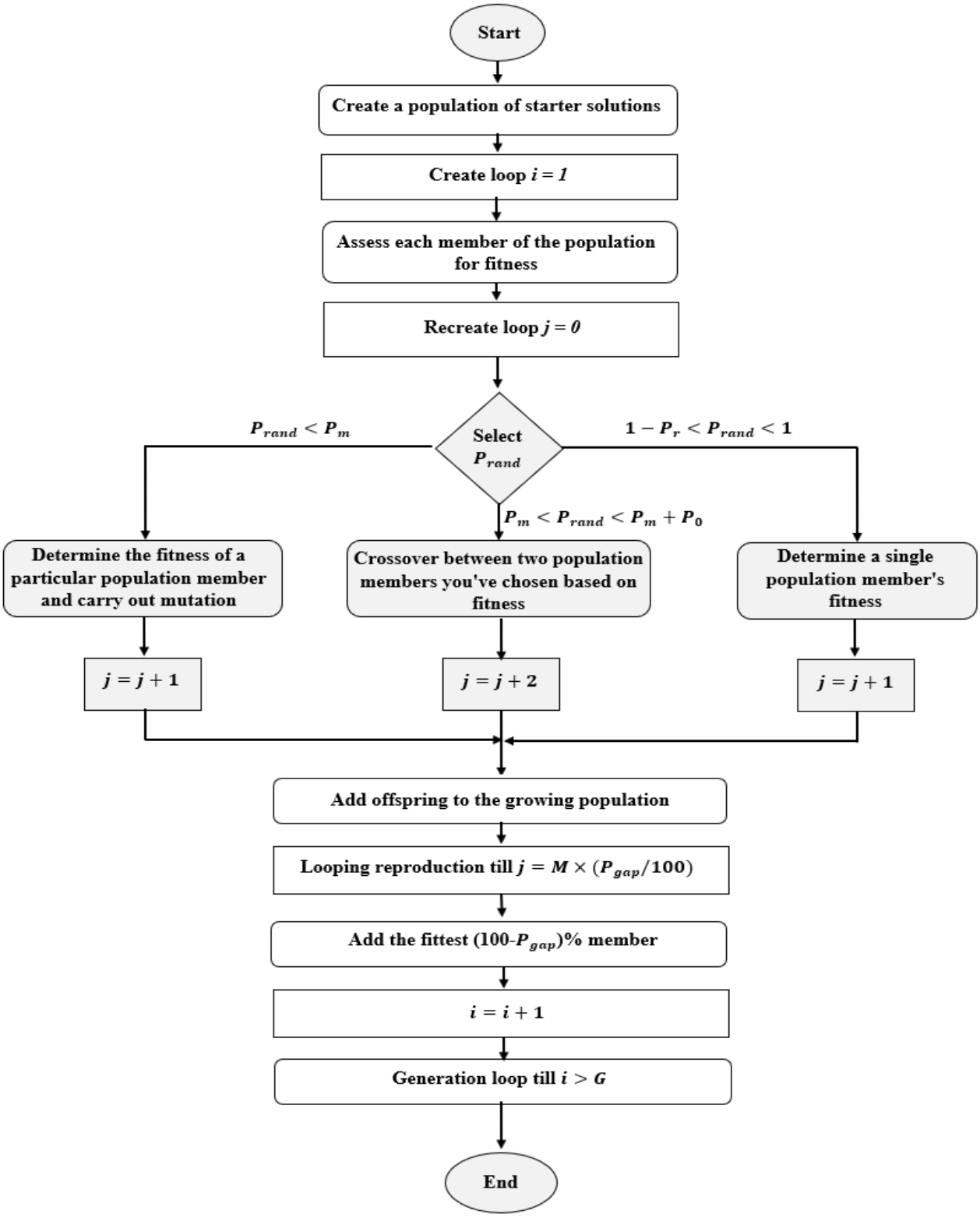

Figure 8.1: Simple GP flow diagram

In Figure 8.1, P_m, P_r and P_o indicate the probability of mutation, reproduction, and crossover, respectively. Model validation is the next phase in the model development process. The model's suitability can be evaluated using a variety of different criteria in this procedure. The fact that the validation criteria are typically used after the model's structure and parameters have been established could be a disadvantage. Multi-objective problem solving is a field of study that has attracted a lot of attention lately. Population-based algorithms, like GP, are well suited to this kind of issue due to their parallel nature. A multi-objective GP method may have the advantage of allowing for the inclusion of new modeling criteria during the evolutionary phase. Due to the ability to handle the three primary steps (see Figure 8.1.) concurrently, this strategy differs from the conventional method. The usage of unseen data, for example, must be done after model creation and cannot be included in this scheme, which is unfortunate. Although more design criteria can be taken into account during the model evolution stage, this approach still has the potential to enhance model performance.

The GP's next responsibility is to assess each member of the population's performance. This is done by employing a "fitness" function, which gives each population member a numerical value. This function will depend on the problem at hand and needs to be carefully selected to give an accurate indication of performance for all potential solutions that might be found as the algorithm is being performed. It is typical, but not required, to choose a function that yields larger values as performance increases to give more "fit" people higher fitness values. Then, using the concepts of survival and reproduction of the fittest, these values are utilized to choose people for breeding. There are other selection techniques that could be used, but they are all consistent with the same fundamental ideas.

- The likelihood of selecting someone who performs at a higher level is increased. It follows that these solutions can be utilized to build even fitter solutions if it is thought that fitter people are more likely to have the genetic material needed to produce a successful solution.
- Probabilistic selection criteria are used. This means that even if the selection process favors fitter people, there is a risk that those with low fitness values could be chosen. As a result, the GP can explore areas of the solution space that a hill-climbing approach would not be able to reach.
- Re-election is allowed. This is advantageous because it promotes the finding of even more effective solutions by allowing fitter population members to be chosen more frequently than fewer fit individuals.

With this method, population members can be represented in a way that is unique to the issue at hand. The population members can be expressed as tree-structured mathematical expressions, for instance, to address a regression problem. Individuals are often encoded as fixed-length character strings in the genetic algorithm (GA), hence complex encoding strategies are necessary to enable its applicability to a larger range of issues.

Koza (1992) was the first to show how GP may be used to solve regression issues. To get the best fit feasible, this process often calls for the specification of a model structure, followed by the optimization of the related numerical parameters. One intriguing aspect of GP is its capacity for structural optimization through the evolution of populations of model expressions with a tree structure. This means that both the model's functional form and its numerical parameters can be optimized using GP. Symbolic regression is the name given to this phenomenon. The function and terminal sets, which contain the building blocks used to create the members of the tree-structured

population, are two of the most crucial components of the GP algorithm. These ideas are covered in more detail below, with a focus on how GP might be used for process modeling. The components or variables that make up the problem's inputs are contained in the terminal set. The terminal set may simply consist of the process input variables for modeling purposes (u_1, u_2, ..., u_n). Determining the proper numerical parameters that fit the selected model structure to the output data is a crucial component of all regression procedures. Including a term that represents a randomly generated real number is one technique to help GP evolve regression constants. According to Koza (1992), these values are ephemeral random constants, and they are denoted by the symbol '" in the terminal set. A new numerical constant is created and added to the model equation if this terminal is chosen during tree generation. The algorithm can build alternative solutions to the problem using the terminal set and the function set, which are made up of a variety of domain-specific functions. Any number of mathematical operations, from the fundamental plus, minus, times, and divide operators to operations like the square root, logarithm, and exponential, may be included in the function set for regression. The inclusion of functions that the engineer believes may aid the algorithm in formulating a solution at this point may incorporate a priori knowledge about the problem. Figure 8.2 shows how the function set's mathematical operators and the process input terminals can be used to create a tree-structured model equation (y represents the expected process output).

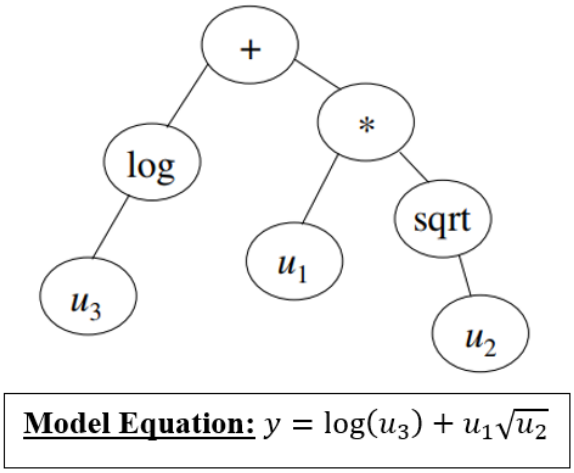

Figure 8.2: Tree to illustrate a mathematical equation

Any feasible combination of the functions and terminals must be able to return values that the functions can accept. This indicates that protected versions of some functions may need to be provided to the algorithm. For example, the absolute value of the input can be used, i.e. $SQRT(x) = \sqrt{|x|}$, to prevent square roots of negative values. More specialized function sets may be needed for different purposes. The function set, for instance, might include functions for conditional expressions and Boolean operations (such as AND, OR, and NOT) (e.g., if-then-else).

8.4. MULTILAYER GENETIC PROGRAMMING MACHINE LEARNING TOOL

The new model was suggested in this research using a multilayer genetic programming machine learning approach (MLGPML). The effectiveness of MLGPML differs from traditional GA techniques in that it determines variable coefficients through optimization. As a result, not only will the connections that are given be quite correct, but their coefficients will also have been chosen carefully. The form of simplification produced by GA is called MLGPML (Cheng 2000; Alavi et al. 2011). While GA delivers linear strings of chromosomes, MLGPML offers alternative strings

of different sizes and forms of nonlinear entities; as a result, MLGPML is a versatile approach to the creation of novel models and the computation of attributes. To put it another way, the illustration's answer is represented by the system of an examined tree with various string widths and shapes. The computer program then sets out on its own to identify the problem's optimal solution (Shi et al. 2011; Aminian et al. 2011; Baykasoglu et al. 2004). The following phases make up the general guidelines of MLGPML for solving a problem through programming:

1) Create individual chromosomes using arbitrary problem selection in the function and terminal grouping technique. As shown in Figure 8.3, these groups randomly choose their members and build models in the form of trees with roots that reach the terminal set.
2) The MLGPML technique then carries out iterative actions to gather the chromosomes with the highest degree of suitability, and it generates new individual chromosomes with three measures—reproduction, alteration, and border.
   - Reproduction: The parts of individuals are copied into the succeeding procedure in a new population without any changes (Alavi et al. 2011).
   - Border: A node is arbitrarily chosen on each program's origin, and the function with each package's terminal set is then switched, creating a new program as depicted in Figure 8.4. Two parental computer-based programs can be seen to have been transformed into two new ones (Koza 1992; Alavi et al. 2011).
   - Alteration: The terminal and function groups' nodes of persons are arbitrarily chosen and replaced with the same parity. This creates novel descendants by randomly choosing sets, and the best generation results in a tree, as shown in Figure 8.5 (Aminian et al. 2011).
   - After confirming its best remedy to the issue, MLGPML then resolves a computer program (Baykasoglu et al. 2004; Ashour et al. 2003; Gandomi and Alavi 2012a).

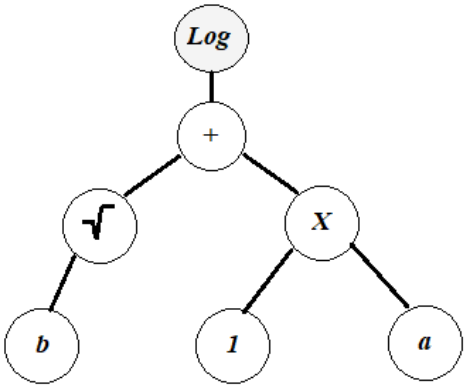

Figure 8.3: Illustration of MLGPML tree

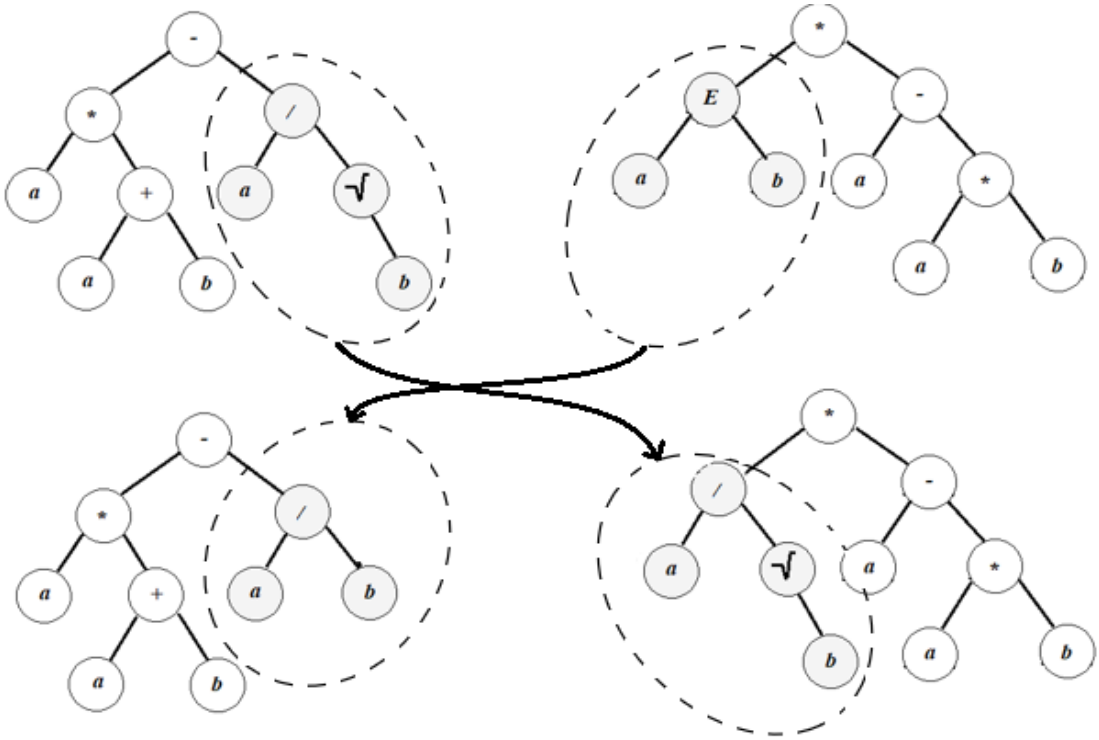

Figure 8.4: Crossover example based on MLGPML

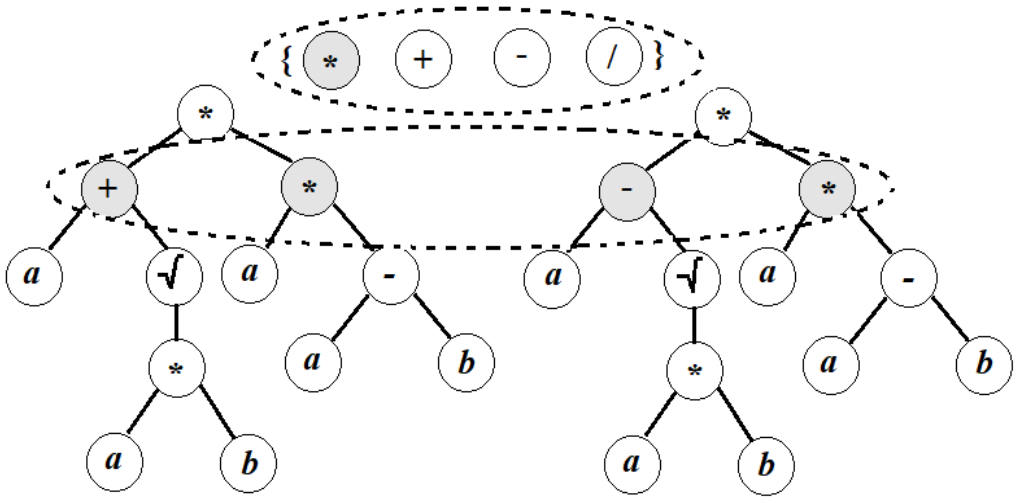

Figure 8.5: Mutation example based on MLGPML

The aptness function, terminal set, control parameters, terminal conditions, and function set are the five parameters that make up the MLGPML model. To characterize its solutions with precise expression, the MLGPML technique develops a population set of arbitrarily named individual chromosomes and then adapts each one into an appearance tree of diverse forms. The aim is then connected to the projected one, and each individual object's aptness score is calculated. If the model provides the best fit, it ends; if not, members are identified using the toothed wheel choice. Previously, this would take the best chromosomes from an individual and pass them on to the next generation. This cycle keeps going until the best chromosome with the highest fitness score is found. Figure 8.6 lists the essential phases that make up the solution's illustration.

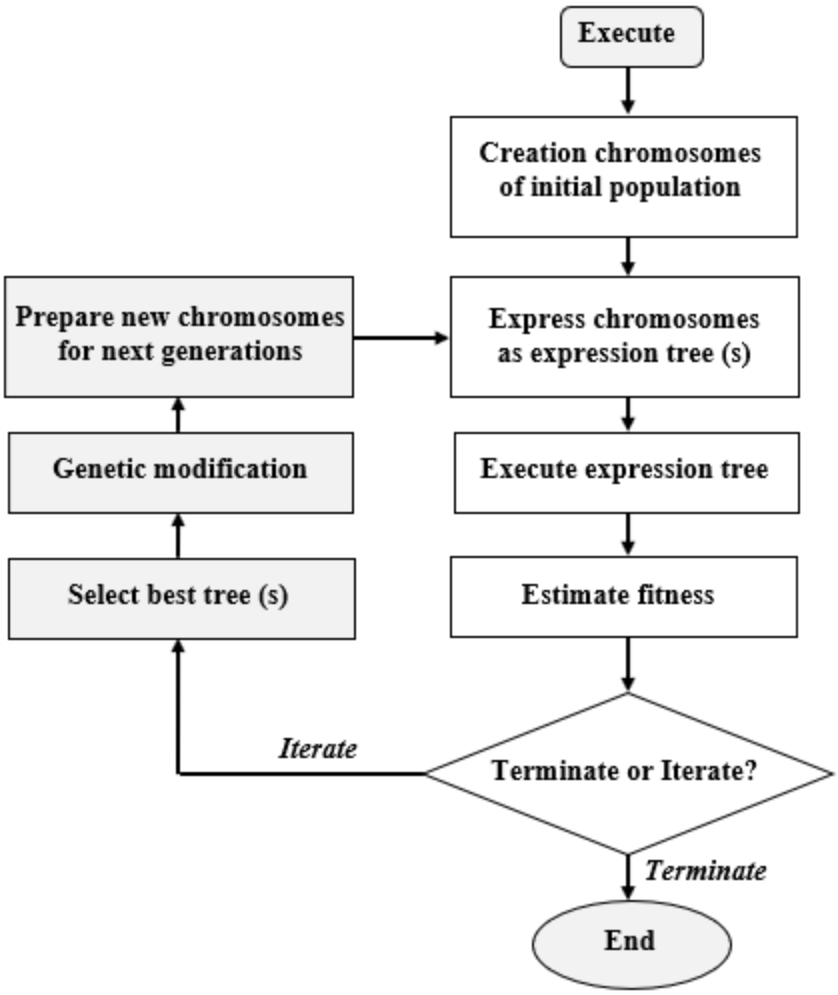

Figure 8.6: Mutation example based on MLGPML

The MLGPML chromosomes (genes) contain a list of symbols with fixed-length variables, a set of functions for the arithmetic operations {+, ×, −, /, sqrt}, and terminal sets for constants such {A, B, C, D, 4}. The individual (chromosomes), function set, and terminal set in the genetic code operator all have a linear relationship. With the specified function and terminal settings, the MLGPML gene is

$$+.x.\sqrt{A}.A.-.+.B.A.C.3.B.C.4 \tag{8.13}$$

In which 3 and 4 are constants while A, B, C, and D are variables. This phrase, according to its definition, is a K phrase that suggests an experimental connection between sets and individuals (Gandomi and Alavi 2012a; Gandomi et al. 2011). The following formulas are used to calculate the coefficient of determination (R^2), mean absolute error (MAE), relative mean-square error (RSE), and relative root-mean-square error (RRMSE), which are all used to evaluate each model's performance:

$$RMSE = \sqrt{\frac{\sum_{i=1}^{n}(ex_i - mo_i)^2}{n}} \tag{8.14}$$

$$MAE = \frac{\sum_{i=1}^{n}|ex_i - mo_i|}{n} \tag{8.15}$$

$$RSE = \frac{\sum_{i=1}^{n}(ex_i - mo_i)^2}{\sum_{i=1}^{n}(\overline{ex_i} - ex_i)^2} \tag{8.16}$$

$$RRMSE = \frac{1}{e}\sqrt{\frac{\sum_{i=1}^{kn}(ex_i - mo_i)^2}{n}} \tag{8.17}$$

$$R = \frac{\sum_{i=1}^{n}(ex_i - \overline{ex_i})(mo_i - \overline{mo_i})}{\sqrt{\sum_{i=1}^{n}(ex_i - \overline{ex_i})^2 \sum_{i=1}^{n}(mo_i - \overline{mo_i})^2}} \tag{8.18}$$

$$\rho = \frac{RRMSE}{1 + R} \tag{8.19}$$

In which ex_i and mo_i are the values of the experiment and the model, respectively, and $\overline{ex_i}$ and $\overline{mo_i}$ are the average values of the findings of the experiment. Additionally, a performance index (ρ) is suggested to quantify model efficacy as a result of both R^2 and RRMSE (Gandomi et al. 2012b). Overfitting of the data is the fundamental problem with machine learning techniques. To assess the correctness of models, the objective function (OBF) is utilized (Gandomi and Roke, 2015; Gandomi and Roke, 2012b)

$$OBF = \left(\frac{n_{Train} - n_{Test}}{n}\right)\rho_{Train} + 2\left(\frac{n_{Test}}{n}\right)\rho_{Test} \quad (8.20)$$

8.5. RESULTS AND DISCUSSIONS

In this section, a new formula is provided to predict the curling stress in rigid concrete slabs using MLGPML considering all geometric characteristics, materials properties, and environmental conditions. This is worth to be mentioned, the developed equation could be employed for both plain and PF-reinforced concrete airfield runways. This equation is presented below:

$$\sigma_t = 2300e\Delta T(1 - P^{0.1})\sqrt{f_c}\left[\frac{\left(\frac{L}{h}\right) + v\left(\frac{W}{h}\right)}{1 - v^{1.8}}\right] \quad (8.21)$$

Where σ_t, e, ΔT, P, f_c, L, W, and h indicate the curling stress, coefficient of thermal expansion, thermal gradient, and fiber content in terms of volume percentage, compressive strength of concrete, length, width, and thickness of slabs, respectively. To identify the accuracy of the proposed formula, a comparison has been performed in the following section with other previous models, and the error between the calculated stress and obtained results by using advanced numerical simulation and field tests are provided for both plain and PF-reinforced concrete slabs

8.5.1. Plain concrete slabs

In this part, the curling stress in plain concrete airfield runways was investigated as an essential property using various equations. The consequences are illustrated in Figure 8.7. The new model as well as those models presented by Nishizawa et al (1990), Hernandez and Al-Qadi (2019), and Salehi-Ashtiani (2011) were employed to calculate the relationship between the calculated outcomes and those results obtained by advanced numerical modeling and field test. As a result,

the coefficients of determination (R^2) for the new model and the model of Nishizawa et al (1990), Hernandez and Al-Qadi (2019) and Salehi-Ashtiani (2011) were 0.9762, 0.6842, 0.9843 and 0.8379, correspondingly. Therefore, to calculate the curling stress in rigid concrete slabs, the model provided by Hernandez and Al-Qadi (2019) had the highest agreement with the numerical and field test findings. The main reason could be associated with the concept of their model Because their model has been established based on highly accurate finite element method formulation. But the disadvantage of their model is complex. Therefore, to use Hernandez's and Al-Qadi's (2019) model, a professional computer and finite element method specialist are necessary which limits the application of their model for fast-in-field calculation by engineers. Conversely, the proposed model in the current research with high accuracy could be utilized as a simple and beneficial technique to predict the curling stress of rigid concrete slabs in the field for designing purposes. While the model developed by Nishizawa et al (1990) exhibited the lowest agreement due to the use of a simple regression technique in their model.

Furthermore, the error values and their distribution for the used models are given in Figure 8.8. Therefore, the close-real curling stress can be predicted using the model provided in this study and by Hernandez and Al-Qadi (2019), as well. This could promote the use of MLGPML going forward to predict engineering phenomena for different designing purposes. Therefore, a straightforward way to predict the behavior of rigid concrete airfield runways may encourage engineers to consider a large number of variables in actual applications.

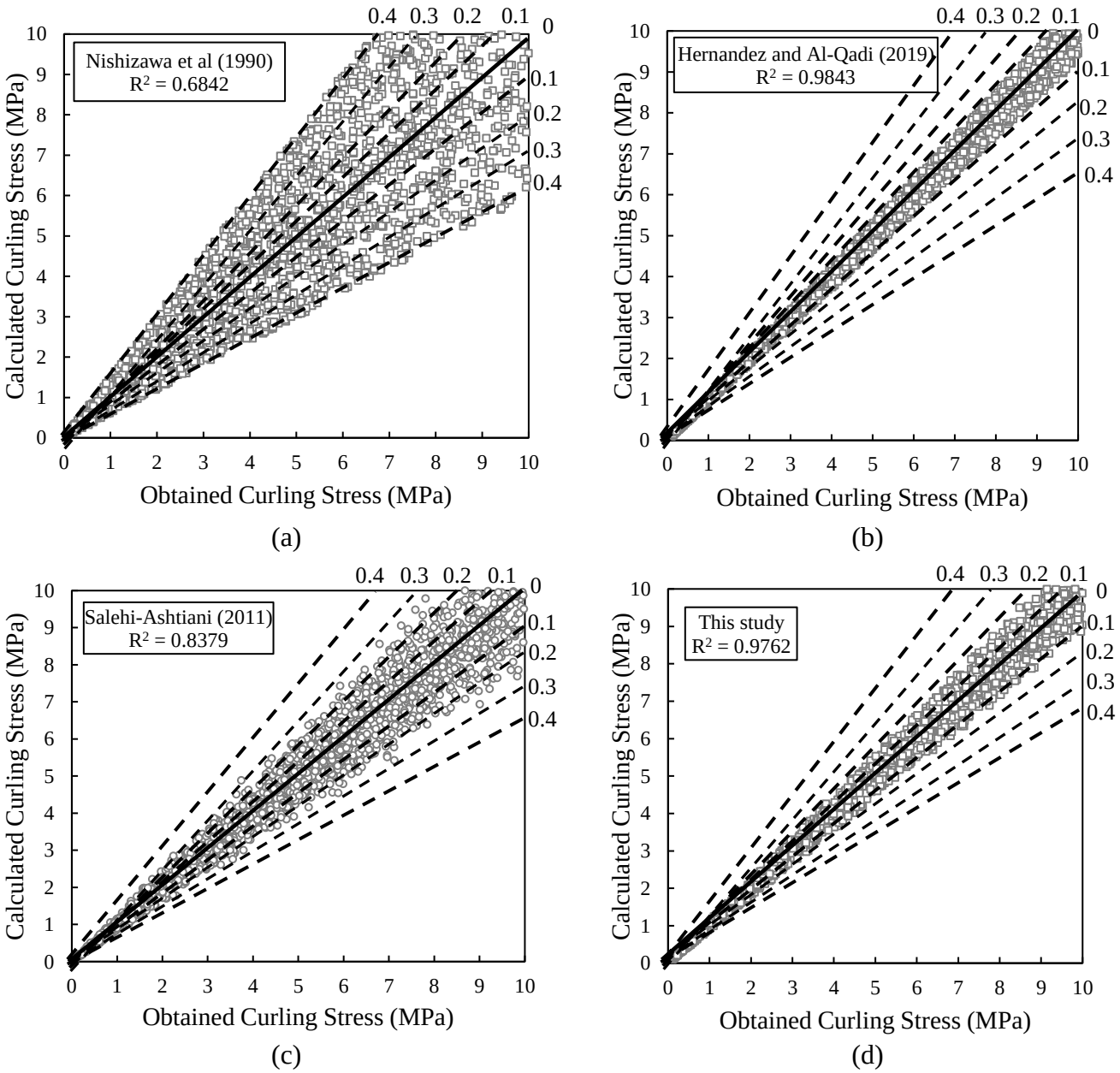

Figure 8.7: Accuracy of curling stress calculation for plain concrete slabs using different models considering all geometric and mechanical characteristics of rigid concrete slabs a) Nishizawa et al (1990), b) Hernandez and Al-Qadi (2019), c) Salehi-Ashtiani (2011) and d) this study

Figure 8.8 displays the spread of the error for the trained and tested values. There, using Hernandez's and Al-Qadi's (2019) model with the highest frequency between 0 and 0.01, the least error was found for the curling stress in plain concrete airfield runways (Figure 8.8b). These

findings demonstrated that Hernandez's and Al-Qadi's (2019) model can offer the most accurate forecast mapping between the input materials and the output curling stress. The model proposed by Nishizawa et al (1990), which was also used in this research, had the highest error distribution, with maximum error frequencies for curling stress calculation ranging from 0.13 and 0.22. Additionally, the new model in this study predicted the curling stress in rigid concrete slabs with a low error of as much as 0.03 which indicates the acceptable accuracy for this model (Figure 8.8d).

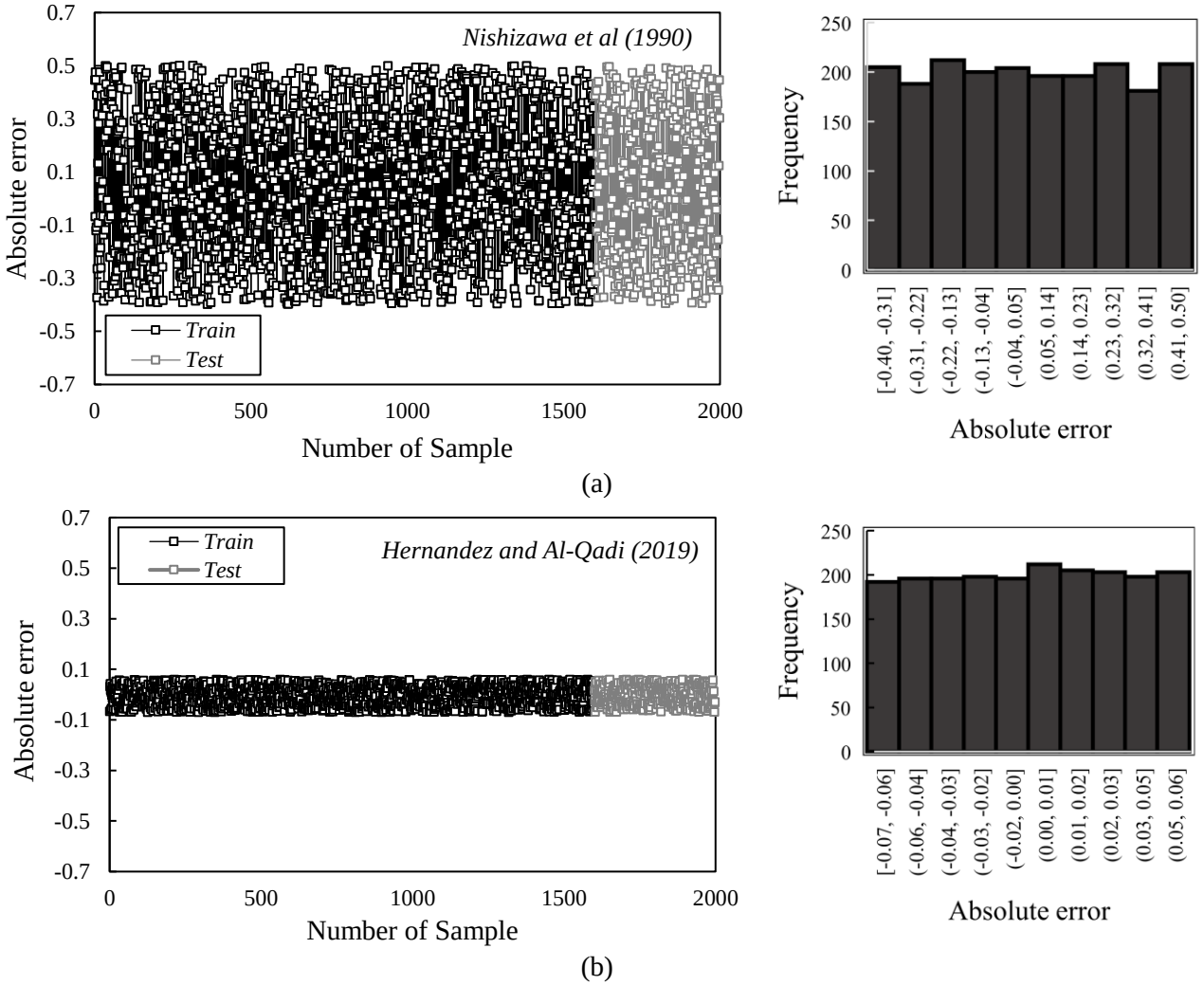

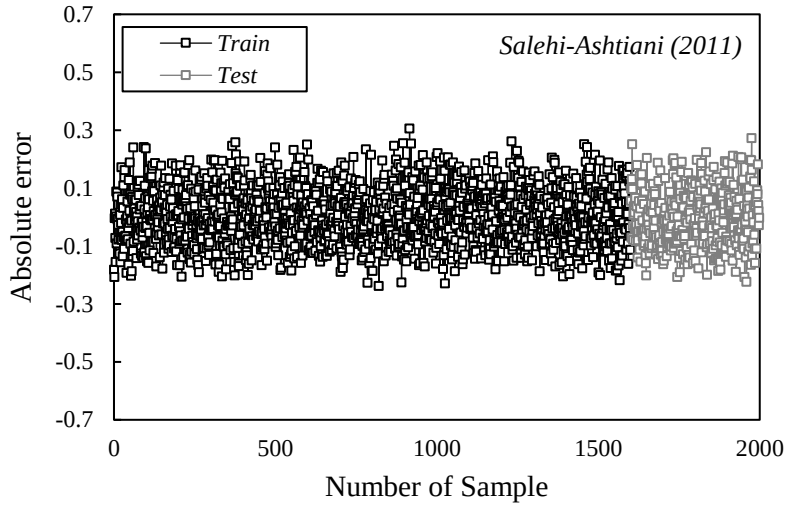

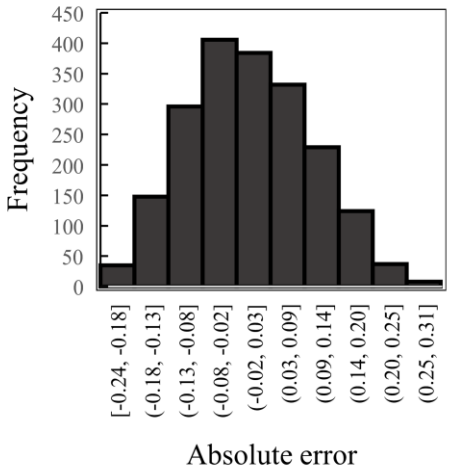

(c)

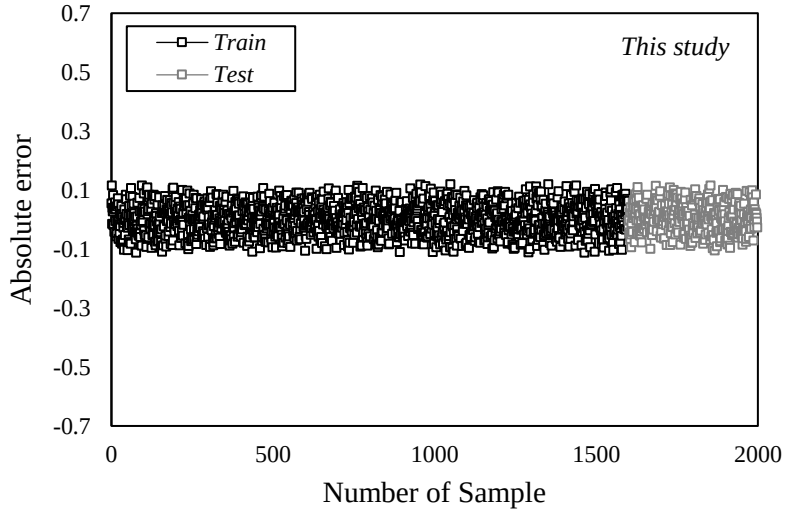

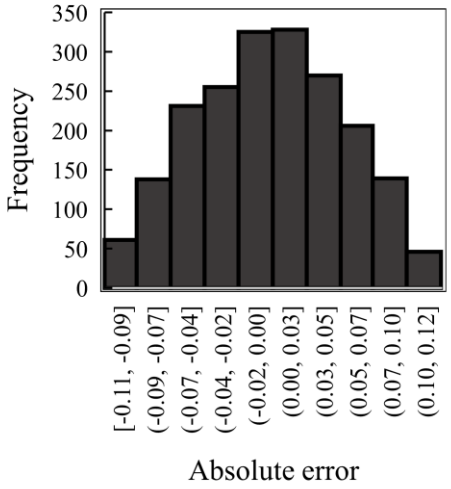

(d)

Figure 8.8: Error distribution and accuracy of different models for curling stress calculation in plain concrete slabs a) Nishizawa et al (1990), b) Hernandez and Al-Qadi (2019), c) Salehi-Ashtiani (2011) and d) this study

8.5.2. Fiber-reinforced concrete

Another significant characteristic that was measured in this area was the curling stress in fiber-reinforced rigid concrete airfield runways. For this aim, The new model as well as those models presented by Nishizawa et al (1990), Hernandez and Al-Qadi (2019), and Salehi-Ashtiani (2011) were used to calculate the correlation among the calculated and numerical and field test results

obtained in terms of curling stress. The consequences are exhibited in Figure 8.9. As a result, the coefficients of determination (R^2) for the new model and the model of Nishizawa et al (1990), Hernandez and Al-Qadi (2019) and Salehi-Ashtiani (2011) were 0.9821, 0.5729, 0.9356 and 0.7943, respectively. Therefore, in order to predict the curling stress in fiber-reinforced concrete airfield runways, the new model developed in the current research had the highest agreement with the numerical and in-field findings. It could be also observed that the accuracy of previous models declined for fiber-reinforced concrete slabs in comparison with the plain concrete samples. This could be attributed to the lack of fiber incorporation influence in previous models. However, the model developed by Hernandez and Al-Qadi (2019) could be also employed as an accurate technique to calculate the curling stress in fiber-incorporated rigid concrete airfield runways while their model is complex. Therefore, based on different material contents, the MLGPML techniques employed in this research could serve as effective tools to generate a simple and highly accurate formula in order to calculate the curling stress in fiber-reinforced concrete slabs. Additionally, Figure 8.10 presents the error values and their spread for the employed models. This could promote the use of MLGPML going forward to predict the engineering phenomena for different designing purposes, particularly when new additional materials such as fibers are utilized for structural response improvement. Therefore, a straightforward way to predict the behavior of fiber incorporation in rigid concrete airfield runways may encourage engineers to consider a large number of variables and additional improvement materials in actual applications.

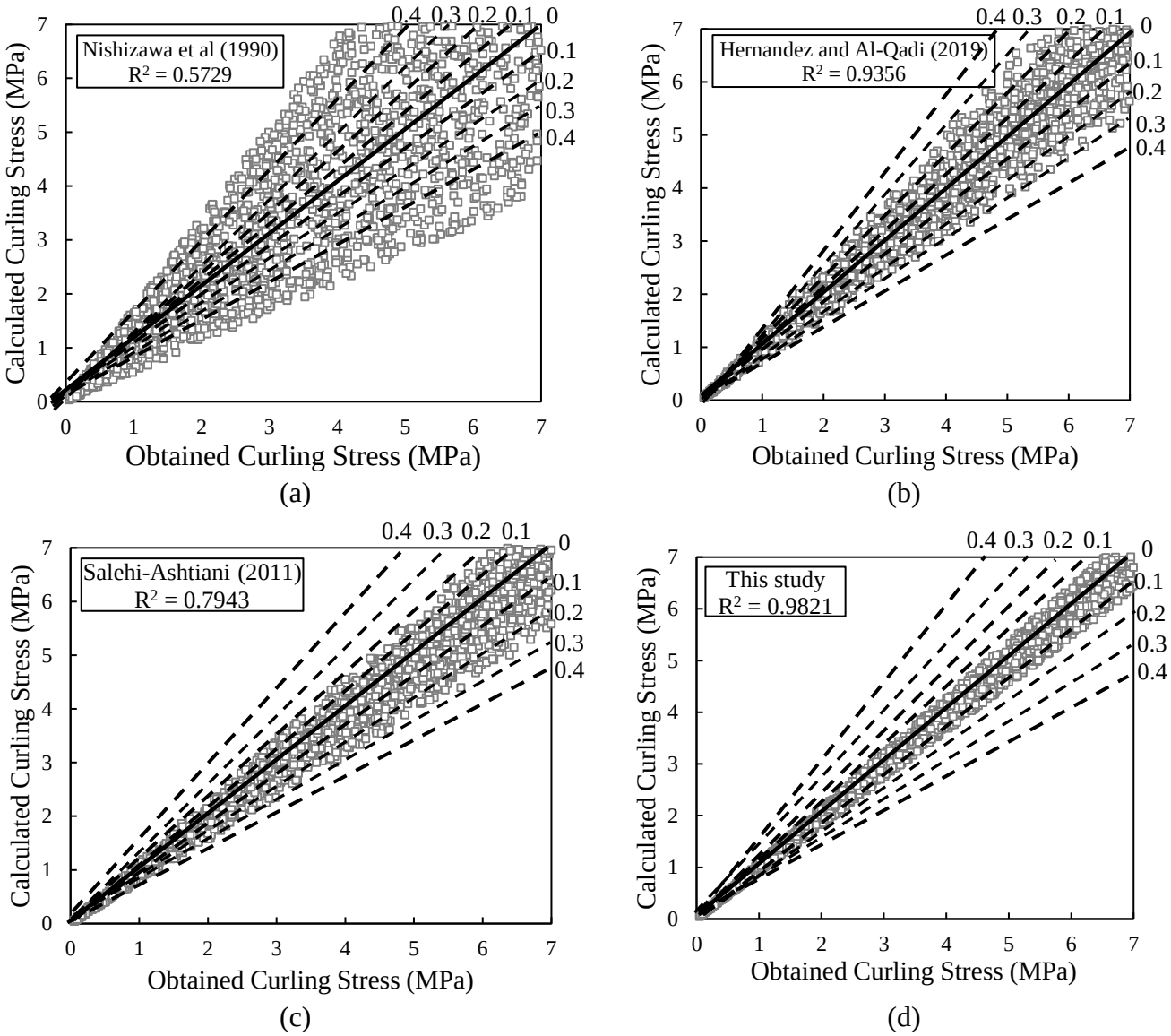

Figure 8.9: Accuracy of curling stress calculation for fiber-reinforced concrete slabs using different models considering all geometric and mechanical characteristics of rigid concrete slabs a) Nishizawa et al (1990), b) Hernandez and Al-Qadi (2019), c) Salehi-Ashtiani (2011) and d) this study

Among all the models utilized to calculate the curling stress in fiber-reinforced rigid concrete slabs, as per Figure 8.10, the proposed equation in this study demonstrated the lowest error distribution with the uppermost frequency spanning from 0.02 to 0.04. In contrast, the model provided by Nishizawa et al (1990) had maximal error distributions with error frequencies between 0.22 and 0.33. Additionally, the complex finite element method formulation of Hernandez and Al-Qadi

(2019) demonstrated high correctness in the inferior limit (calculated values close to the numerical and field test findings) of the curling stress in rigid fiber-incorporated concrete slabs. The calculated curling stress error, which ranged from 0.01 to 0.04, was measured with the highest frequency of 400 for the model provided by Salehi-Ashtiani (2011). Additionally, a maximum frequency of 350 was found using this technique for calculated curling stress in fiber-reinforced concrete slab errors ranging from 0.03 to 0.07 for Hernandez's and Al-Qadi's (2019) formula. Consequently, Figure 8.10 showed a fair degree of agreement between numerical and field test findings and calculated values of curling stress with the use of the new model and Hernandez's and Al-Qadi's (2019) formula.

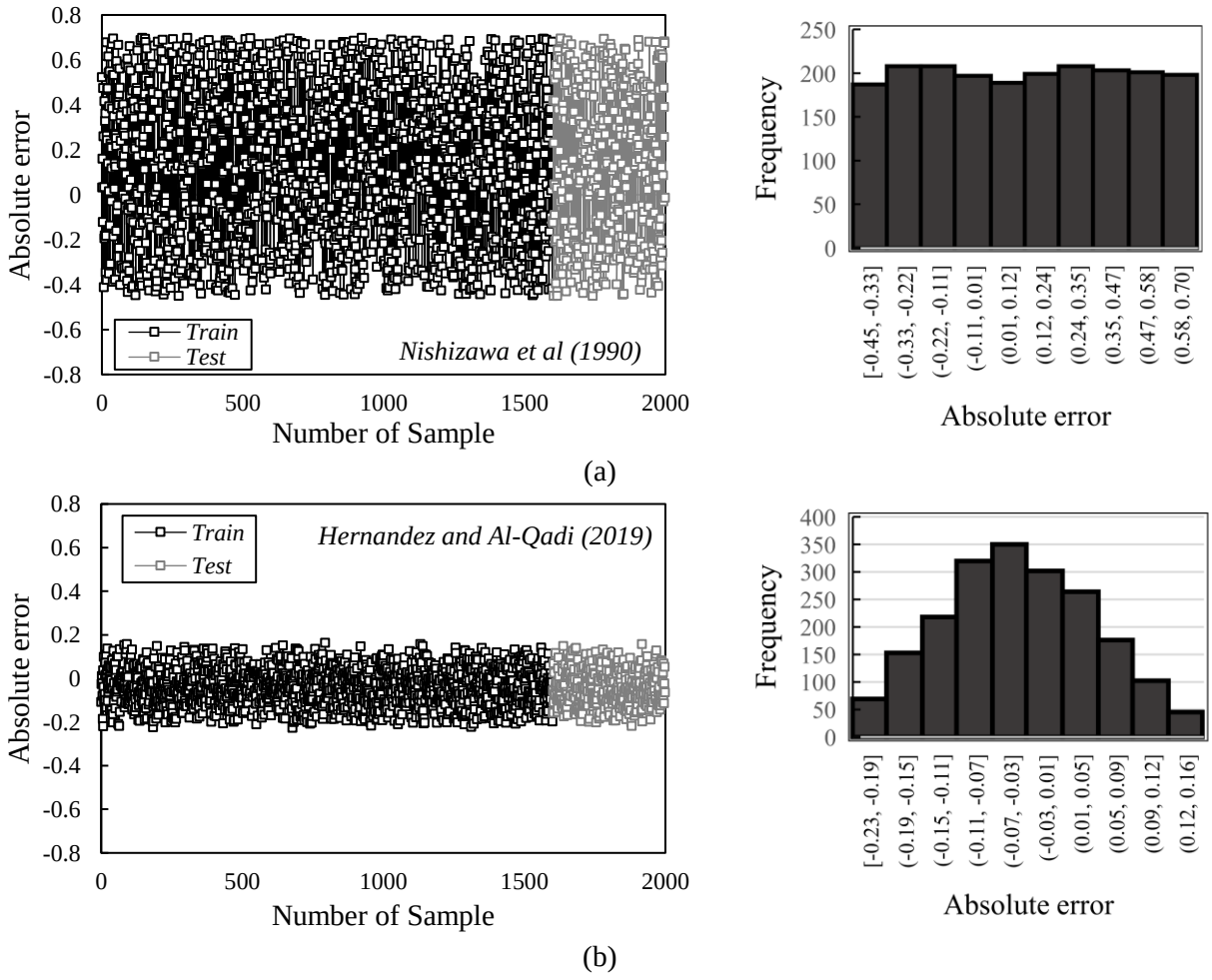

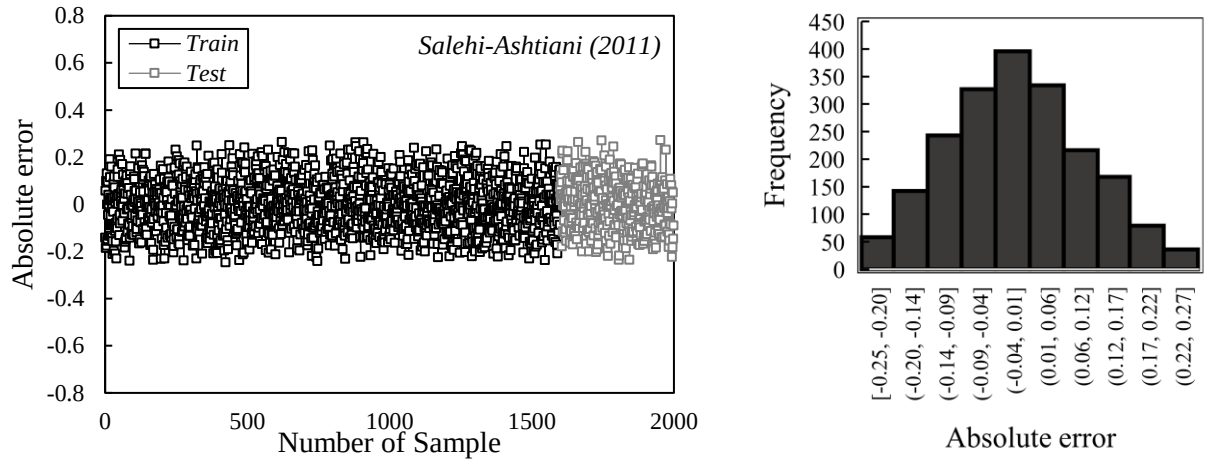

(c)

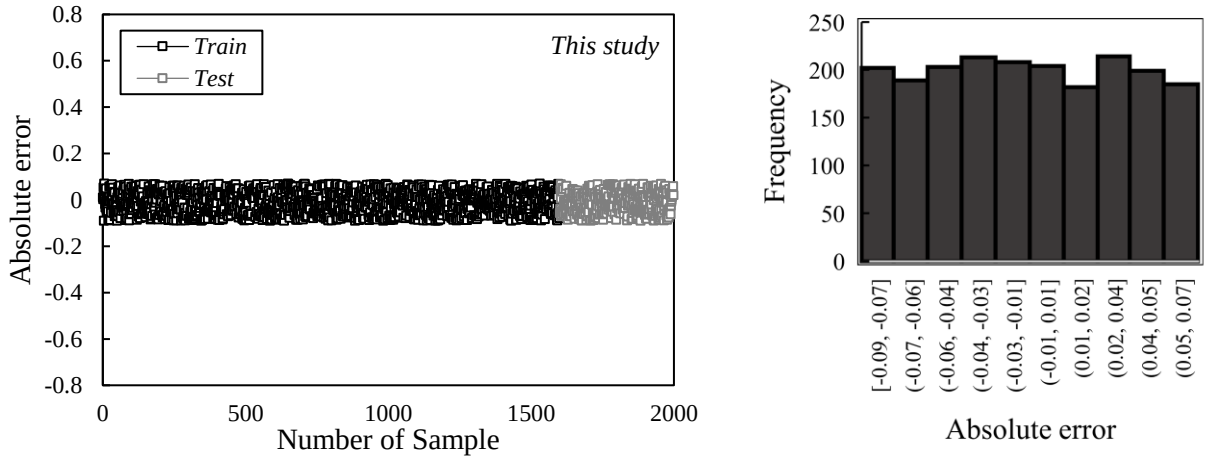

(d)

Figure 8.10: Error distribution and accuracy of different models for curling stress calculation in fiber-reinforced concrete slabs a) Nishizawa et al (1990), b) Hernandez and Al-Qadi (2019), c) Salehi-Ashtiani (2011) and d) this study

As was already stated, various techniques were employed in this study to evaluate the effectiveness of the presented models. The consequences are revealed in Table 8.1. For the plain concrete, There, the model of Hernandez and Al-Qadi (2019) achieved the greatest correctness and lowest error. As a result, their technique yielded the following values for MSE, RMSE, MAE, MAPE, NMSE, and NMAE: 0.5783, 0.6273, 0.3206, 0.8223%, 1.9055%, and 3.0287%, correspondingly. Then, for the MAPE, NMSE, and NMAE, respectively, the new model displayed an adequate prediction with values of 1.5897%, 2.7604%, and 5.6892%. While Nishizawa et al.'s

(1990) model showed the lowest accuracy for MSE, RMSE, MAE, MAPE, NMSE, and NMAE with 1.6982, 2.2834, 1.2167, 3.4896%, 4.7539%, 9.1165%, correspondingly. Conversely, for fiber-reinforced rigid concrete slabs, the value of MSE, RMSE, MAE, MAPE, NMSE, and NMAE were found by around 0.6429, 0.8267, 0.4927, 1.1189%, 2.0876%, 4.2855% for the new model developed in this study in terms of curling stress. Additionally, a small calculation error performance was obtained for Hernandez and Al-Qadi (2019). So, the MAPE was obtained by 1.7692% for their model. Moreover, when Nishizawa et al.'s (1990) model was used, the curling stress for fiber-reinforced concrete slab estimation accuracy was found to be the lowest, resulting in MSE, RMSE, MAE, MAPE, NMSE, and NMAE values that, correspondingly, were achieved by about 2.1529, 2.8937, 2.0981, 4.2867%, 6.1068%, and 11.2852%.

Table 8.1: Results of curling stress calculation for both plain and fiber-reinforced concrete slabs using the common effectiveness assessment techniques

Parameter	Method	R	R^2	MSE	RMSE	MAE	MAPE (%)	NMSE (%)	NMAE (%)
Plain Concrete	Nishizawa et al (1990)	0.8271	0.6842	1.6982	2.2834	1.2167	3.4896	4.7539	9.1165
	Hernandez and Al-Qadi (2019)	0.9921	0.9843	0.5783	0.6273	0.3206	0.8223	1.9055	3.0287
	Salehi-Ashtiani (2011)	0.9153	0.8379	1.0094	1.4863	0.9291	2.1608	3.6879	7.2566
	This study	0.9880	0.9762	0.7631	1.0872	0.6792	1.5897	2.7604	5.6892
Fiber-Reinforced Concrete	Nishizawa et al (1990)	0.7569	0.5729	2.1529	2.8937	2.0981	4.2867	6.1068	11.2852
	Hernandez and Al-Qadi (2019)	0.9672	0.9356	0.9428	1.8567	0.8992	1.7692	2.8827	6.0527
	Salehi-Ashtiani (2011)	0.8912	0.7943	1.3429	2.0876	1.0933	2.9729	4.1219	8.7653
	This study	0.9910	0.9821	0.6429	0.8267	0.4927	1.1189	2.0876	4.2855

Furthermore, the accuracy of all models is provided in Figure 8.11 using the Taylor technique. Regarding Figure 8.11a, only the planned formula in this research and that provided by Hernandez and Al-Qadi (2019) had the highest correlation coefficient of 0.9921 and 0.9880, and the lowest standard deviation by roughly 0.18 and 0.21, showing a high accuracy of the proposed formula to predict the curling stress in plain concrete airfield runways. But the model developed by Salehi-Ashtiani (2011) and Nishizawa et al (1990) respectively with correlation coefficients (R) of 0.9153 and 0.8271 and standard deviations of 0.29 and 0.37 showed a remarkably weak correlation with numerical and field test findings for plain concrete slabs. Additionally, for fiber-incorporated rigid concrete slabs, the new model and also the model presented by Hernandez and Al-Qadi (2019) which have high correlation coefficients and low standard deviations, could be used as suitable tools to forecast the curling stress. Therefore, compared to earlier models, the freshly available formula in this investigation to predict the curling stress in concrete airfield runways could be used for both plain and fiber-reinforced concrete slabs.

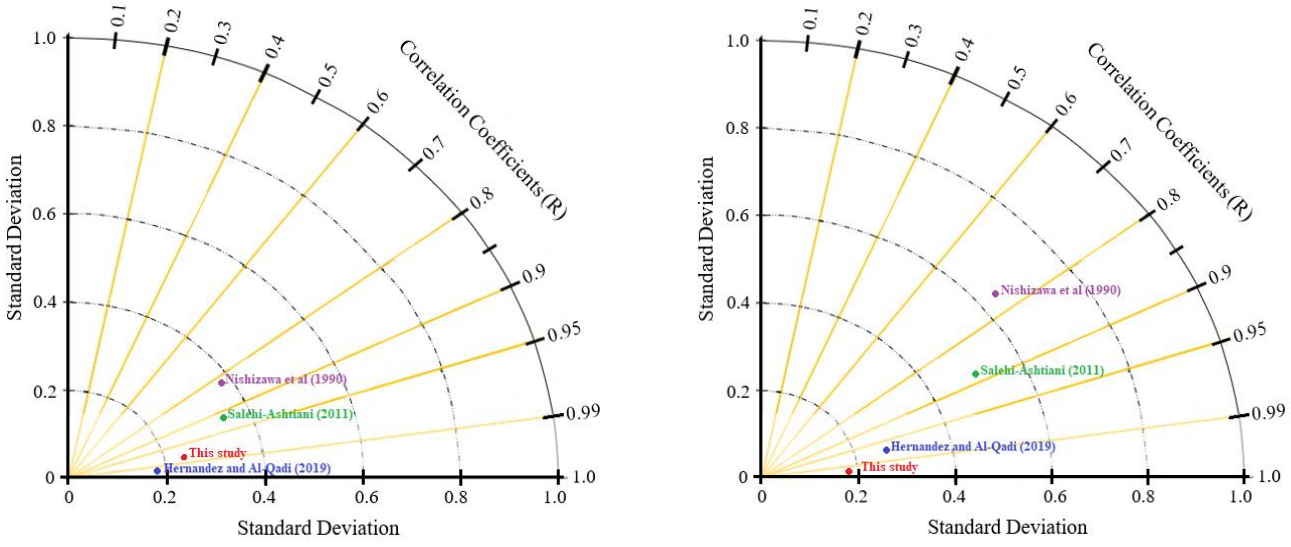

(a) (b)

Figure 8.11: Taylor illustration for the current and prior curling stress calculation models for a) plain concrete and b) fiber-reinforced concrete

8.6. SUMMARY & CONNECTION WITH THE SUBSEQUENT CHAPTER

With the use of previous chapters' results in terms of deformation, cracking, out-of-plane buckling, and cracking in rigid concrete slabs, a practical formula was proposed in this chapter considering all geometric, material, boundary, and environmental characteristics. The model was established using a multi-layer genetic programming machine learning approach. Additionally, the accuracy of the formula was measured using various techniques in comparison with other prior models. Therefore, the developed formula has two main features: 1) simple form to facilitate use by engineers and 2) high accuracy with experimental and numerical results. It is worth to be mentioned that the results presented in previous Chapters and also the generated formula in this Chapter has been established using our team field test results and variables considered in this study. Therefore, a prediction could play a supportive role in measuring the thermal and curling behaviors in rigid concrete slabs for those designed with different geometric, material, boundary, and environmental characteristics. Additionally, pavement management systems forecast the overall pavement performance at the network management level to help with budget provision and management development. Therefore, developing highly accurate prediction models could play an effective role in controlling the performance, maintenance cost, and life cycle of rigid concrete slabs. Therefore, using the results of the previous and the current Chapter, various prediction algorithms are proposed in the next Chapter to measure the thermal and curling stresses in both rigid plain and fiber-reinforced concrete slabs considering all material properties, geometric characteristics, boundary conditions, environmental circumstances, and fibers content. Figure 8.12 provides a connection with the subsequent chapter overview.

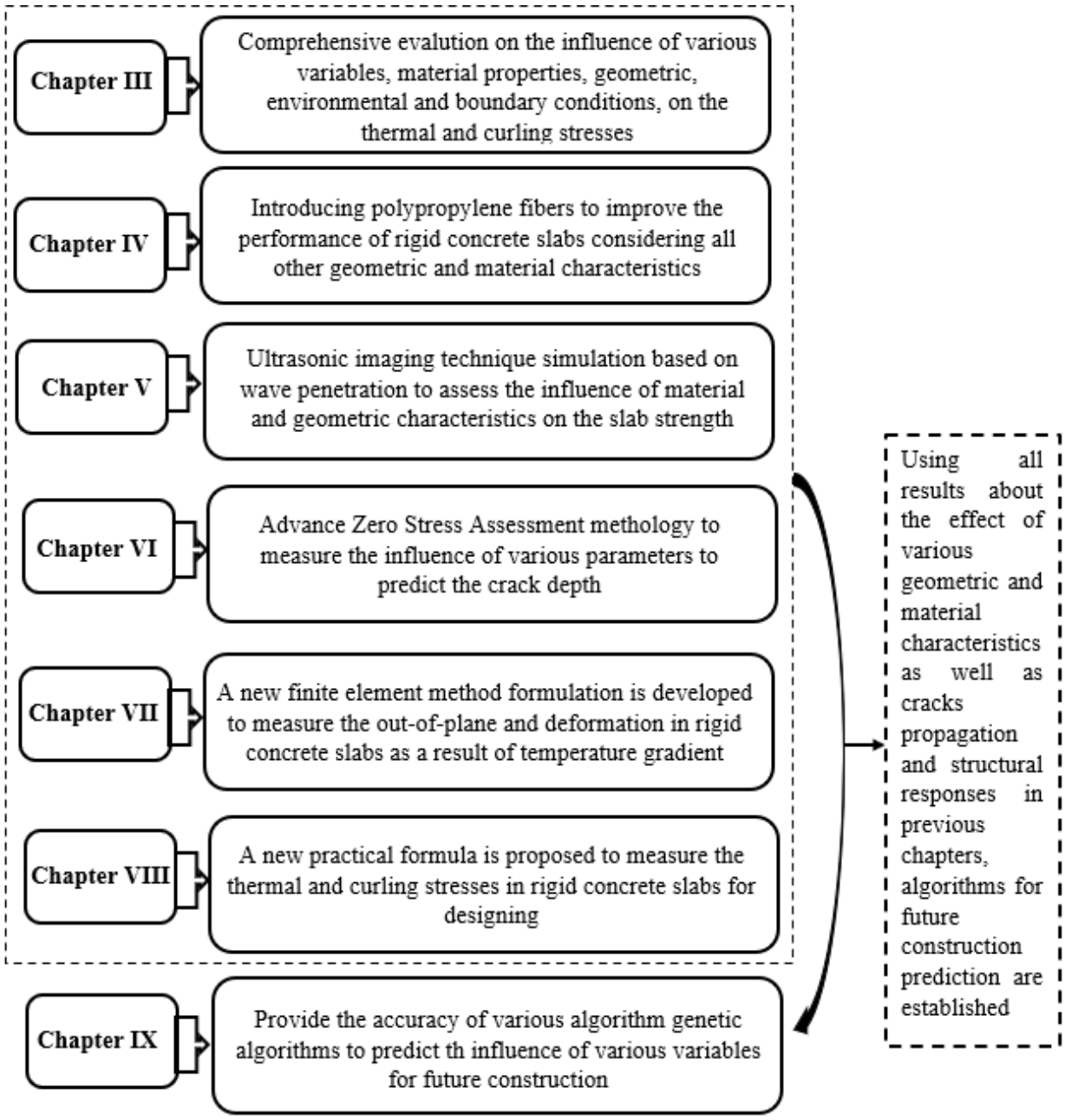

Figure 8.12: Overview of the connection between previous Chapters and Chapter IX

CHAPTER IX

CURLING AND THERMAL BEHAVIORS PREDICTION ALGORITHMS

9.1. INTRODUCTION

This chapter intends to present various prediction frameworks for measuring the curling and thermal behaviors in rigid concrete slabs considering wide-range variables. The preceding section of this chapter is followed by a definition of artificial neural networks and prediction algorithms result collected from previous chapters' results to forecast the stress and deformation responses stress in rigid concrete slabs to assess damages and service life in future constructions considering the effect of PF and nonlinear thermal gradient. The results of this task might be utilized by many businesses to create models, and DOTs could use them to predict the influence of different parameters on the thermal and curling behaviors for future field constructions.

9.1.1. Organization of the Chapter

This chapter consists of four main sections. Subsequent to the introductory section, Section 2 provides information associated with the foundation of various artificial neural network algorithms. Then, in the next section, stress and deformation in rigid concrete slabs associated with thermal gradient through the slab's thickness will be assessed using various prediction techniques. For this aim, the influence of different neurons is also assessed to show the ability of each algorithm. Therefore, the main results of this study are presented and discussed to show the effect of PF, geometric characteristics, and material properties on thermal deformation and stress for future constructions. Ultimately, a summary of this section will be presented so that its connection

with the subsequent section and also the significance of the subsequent section can be clearly shown.

9.2. STATE OF ART

To satisfy statutory, organizational, and public needs, state highway agencies invest millions of dollars each year in maintenance and restoration. An efficient methodology that incorporates project planning, design, construction, maintenance, and rehabilitation is necessary for effective pavement management. In order to maintain the pavement condition at an acceptable level so that it can meet the demands of traffic and the environment for the duration of its service life, pavement management systems (PMS) play a noteworthy character in managing the condition of highway networks professionally based on cost-effective approaches to be applied at a given time. The network and project management levels are the two administrative tiers on which individual PMSs function. A PMS forecasts the overall pavement performance at the network management level to help with budget provision and management development. To ascertain when a certain slab segment would require maintenance or treatment action, project managers will need more precise information and treatment alternatives. Rigid concrete slab discomfort is caused by environmental and traffic-related factors. Researchers and agency decision-makers can create performance prediction algorithms by following the distress over time. Historical information on rigid concrete slab requirements, traffic, structural parameters, and environmental conditions is needed to predict rigid concrete slab performance.

To gather information for more useful prediction models, data can be collected from a single test road or from rigid concrete slabs that are already in use. For small and local authorities, building and maintaining a single test road is however expensive and impracticable. Creating precise rigid concrete slab prediction models enables a pavement management system as a

component of transportation infrastructure asset management that incorporates all modes of mobility. Large transportation assets require tools for coordinating activities in the best possible way. The PMS is "a set of tools or methodologies that assist decision makers in discovering the best approaches for delivering, evaluating, and maintaining rigid concrete slabs in a serviceable state over time," according to the American Association of State Highway and Transportation Officials (AASHTO 2012). The PMS model was developed in the middle of the 1960s as support implements to assist decision-makers in providing necessary highway restoration and maintenance with limited funding (Kirbas, 2010). Planned investment activities include design, construction, maintenance, and regular pavement review (Falls et al., 2001). By analyzing the effects of decisions made at various management levels, a PMS can increase the effectiveness of decisions (George, 2000). Additionally, by adopting a PMS, the potential effects of restricted funds can be lessened by optimizing budget distribution, prioritizing projects through a data-driven process, and utilizing efficient maintenance techniques (TAC, 1999). According to AASHTO (2012), a PMS gives highway agencies the following capabilities:

- Assessing current and future rigid concrete slab conditions.
- Calculating the amount of budget needed to improve rigid concrete slab condition to a specific level.
- Determining pavement preservation and treatment choices based on funding sources.
- Assessing the long-term effects of modifications to material qualities, building techniques, or design processes on the performance of rigid concrete slabs

Understanding the PMS stages, PMS components, and available prediction models are prerequisite for developing a PMS.

9.2.1. Pavement Management Stages

Any pavement management and decision-making system have two administrative levels: network management and project management (Mbwana, 2001). At this stage, a timetable for maintenance activities is prepared as well as prioritized rebuilding and rehabilitation tasks in order to accomplish the agency's goals. Agencies work to strike a balance between the level of precision in data and available resources since gathering particular data about a whole pavement network involves a large expenditure (AASHTO, 2012). Since they want to know the general indices of pavement conditions, riding quality, or safety, directors of state-level transportation agencies or budget directors frequently use the network level (Mbwana, 2001). Conversely, choices at the project stage are focused on specific network segments, necessitating the use of more in-depth data collection techniques such as material testing to assess rigid concrete slab problems. The inputs for project-level analysis are thought to include traffic loads, environmental considerations, material qualities, building and maintenance activities, and available financing (Dillon, 2003). These thorough data are used to forecast pavement performance and create the best repair plans. Table 9.1 compares the various criteria between the project and network levels.

Table 9.1: Variations between PMS network and project stages (AASHTO, 2012)

Decision Stage	Decision Makers	Sort of Decisions	Asset Types Considered	Degree of Feature	Scope of Decision
Network	Asset manager Pavement management engineer District engineer	Treatment recommendations for a multi-year plan Funding needed to achieve performance targets Consequences of different investment strategies	Range of resources at a location	Average	Average

Project	Design Engineer Construction engineer Materials engineer Operations Engineer	Maintenance activities for current funding year Pavement rehabilitation thickness design Material type selection Life cycle costing	Specific resources in a location	Large	Dedicated

Depending on the information and resources readily available, PMS components change. According to AASHTO (2012), pavement management systems perform the following tasks:

- Inventorying the resources for paving, including all data on network pavements.
- Making informed decisions requires the use of models to examine and forecast the performance of future rigid concrete slabs.
- Storing all relevant data regarding slab networks for use as input in creating standards or reports that other agencies may use to enhance their PMS.

A PMS must at the very least include inventories of the physical slab features, the conditions of the rigid concrete slabs, traffic data, performance analysis, and investment strategies for deciding which projects to prioritize for maintenance or rehabilitation work on state highways and the federal highway system (Cottrel et al., 1996). Data on pavement state should be gathered by modern PMSs, and the data should then be analyzed to create plans for maintenance and rehabilitation (Vines-Cavanaugh et al., 2016). Regarding the following tasks, performance prediction models are crucial in rigid concrete slab management systems:

- Forecasting the state of the rigid concrete slab.
- Determining the best time to take maintenance and repair measures for slabs.
- Identifying the pavement network's most cost-effective treatment plan.

- Predicting the amount of money needed to achieve agency goals; and
- Evaluating the effects of various pavement investment plans (AASHTO, 2012).

The federal law known as the Moving Ahead for Progress in the 21st Century Act (MAP-21), which was introduced in July 2012, also mandates modeling rigid concrete slab performance. Each state is obligatory by MAP-21 to have a risk-based benefit organization plan and performance goals for safety, bettering the state of the infrastructure, reducing traffic, ensuring system dependability, promoting efficient movement and economic vitality, environmental sustainability, and project delivery (Corley-Lay, 2014). MAP-21's infrastructure conditions standards mandate that highway pavement quality be evaluated. In order to determine a fundamental relationship between them and identify aspects affecting the rigid concrete slab performance, the conventional structure of a performance model involves relating a slab's performance indicator to explanatory variables. Long-term historical data of in-service rigid concrete slabs, including all factors that significantly affect response variables, an appropriate model form that takes into account interaction and nonlinearity, and criteria to assess the model's accuracy are the four requirements of a reliable performance prediction model (Darter, 1980). In pavement management, a variety of rigid concrete slab performance models are utilized, including expert or knowledge-based, deterministic, probabilistic, and artificial neural network (ANN) models (Wolters and Zimmerman, 2010).

9.2.2. Deterministic Schemes

A single dependent value is expected by deterministic models from one or more independent variables (e.g., concrete age, traffic volume, environment, and material characteristics. Three subcategories of deterministic models, which mostly rely on regression analysis, can be distinguished: practical, mechanistic, and experimental-mechanistic models (Li et al. 1996).

Practical models, which are frequently employed in investigations of rigid concrete slab performance, need a ton of data for the model. They calculate the pavement's sensitivity to changes in some input factors. S-shaped curves, polynomials, and logistic growth patterns are examples of empirical models. Silva et al. (2000) noted several benefits and drawbacks of utilizing empirical models, including the following:

- *Advantages of using empirical models:*
  - The performance of the rigid concrete slabs can be predicted using a straightforward mathematical technique.
  - It is simple to explain the links between the predicted and actual coefficients.
  - Future analytical findings can be used to update practical models.
- *Disadvantages of using empirical models:*
  - To build a good regression pattern, accurate data is necessary, and outliers may reduce accuracy.
  - Model performance precision may be impacted by data on maintenance or rehabilitation activities.
  - The performance model must incorporate each significant variable.

The relationship between traffic volume and dynamic slab reactions is determined using mechanistic models (i.e., stress, strain, and deflection). Mechanistic models' key input variables that affect rigid concrete slab performance require significant laboratory testing data or exact measurements (Mills et. al., 2012). When predicting slab performance, pavement engineers typically don't employ primary response parameters since they deal with distress data that is more easily accessible and pavement attributes (Haas et al., 1994). They have so been unable to correctly

forecast rigid concrete slab performance. Additionally, pure mechanistic models aren't thought of as prediction models (Shahin, 2005).

9.2.3. Expert techniques

When historical data are unavailable, data are missing, or a new design is created, expert models can be employed. Expert models are based on the mutual expertise and knowledge of agency engineers who are acquainted with pavement deterioration trends (Wolters and Zimmerman, 2010). According to Hicks and Groeger (2011), numerous organizations have employed expert engineers when projecting rigid concrete slab performance in some states. For instance, the New Hampshire DOT predicts ride, cracking, and rutting indices based on expert information, the Massachusetts DOT employs expert knowledge to anticipate cracking, raveling, ride, and rutting performance, and the Connecticut DOT established their performance curve based on expert panels.

9.2.4. Probabilistic Patterns

When predicting a wide range of values for dependent variables, such as the likelihood that the state of a certain pavement will change to another condition, probabilistic models are utilized. These simulations are employed to account for the unpredictability of material characteristics, ambient factors, and traffic volume that can lead to less precise simulations. The typical varieties of probabilistic models, according to Golroo and Tighe (2012), are semi-Markov models, survivor curves, Bayesian regression, and Markov models. Eq. (9.1) illustrates an initial probability matrix and a transition probability matrix for the fundamental Markov chain model.

$$P_i = P_0(P)^i \tag{9.1}$$

In which, P_i, P_0, P and i indicate probability provision of i_{th} duty cycle, vector of preliminary, conversion matrix probability, and duty cycle, respectively. Also, P could be determined using the next formula:

$$P = \begin{bmatrix} P_{11} & P_{12} & P_{13} & P_{14} & \dots & P_{1n} \\ 0 & P_{22} & P_{23} & P_{24} & \dots & P_{2n} \\ 0 & 0 & P_{33} & P_{34} & \dots & P_{3n} \\ 0 & 0 & 0 & P_{44} & \dots & P_{4n} \\ \vdots & \vdots & \vdots & \vdots & \vdots & \vdots \\ 0 & 0 & 0 & 0 & 0 & P_{(n-1)n} \\ 0 & 0 & 0 & 0 & 0 & 1 \end{bmatrix} \quad (9.2)$$

The main advantage of utilizing probabilistic models is that they require fewer data for model creation than deterministic models do (Jack and Chou, 2001). The advantages of applying probabilistic models for forecasting rigid concrete slab performance, according to Golroo and Tighe (2012), could be presented below:

- Probabilistic techniques can represent uncertainty in a rigid concrete slab performance prediction scheme when used in conjunction with other techniques.
- The probabilistic method mixes field observations and expert opinion, making it more realistic than the deterministic techniques.
- In circumstances when the database is lacking, inaccurate, or of low quality, expert information can be added.

9.2.5. Artificial Neural Network (ANN) Models

Rigid concrete slab performance modeling has been used in numerous studies that include parameters affecting slabs behavior, but most of the models have encountered difficulties dealing with a high number of input variables, the lack of some variables, and correlations between the variables (Kargah-Ostadi and Stoffels, 2015). ANN models have become popular in recent years

as a way to imitate the biological nervous systems seen in the human brain. There are billions of neuron cells in the biological nervous system, and each one takes input from other neurons, which means that input uses a transfer function, and then sends its own output to the layer below (Mehta et al., 2008). Instead of relying on the inherent correlations between variables, ANN models compute the relative importance of variables and develop prediction models using data. A computational mechanism that has the ability to obtain, represent, and compute a mapping from one multivariate space of information to another, given a set of data that represents that mapping, is known as an ANN (Rafiq et. al., 2001). Because they can connect neurons between layers to process enormous amounts of data, ANN approaches are capable of solving complicated issues (Basheer and Hajmeer, 2000).

Engineers frequently deal with imperfect or noisy data; hence ANN models may be the best models for identifying significant associations from data patterns to address a specific issue (Rafiq et al. 2001; Karimi Pour et al. 2021d; Rezaiee-Pajand et al. 2021; Rezaiee-Pajand et al. 2020). According to Zhang et al. (1998), ANN techniques can expect nonlinear connections between variables just as well as conventional models, which are typically utilized to do so. Because they are precise and practical, ANN models have been widely applied with good results in various fields of civil engineering (Karlaftis and Vlahogianni, 2011). According to Adeli (2001), who reviewed the literature on neural network models from 1989 to 2000 with an emphasis on structural engineering, construction engineering, and management, ANN models are effective for simulating complicated issues. In contrast to regression models, more recent investigations have demonstrated the robustness of ANN algorithms. In the case of forecasting freeway speeds, for instance, a comparison between ANN and autoregressive time series models revealed that neural networks offer more precise forecasts than traditional statistical methods (Vlahogianni and

Karlaftis, 2013). For modeling two crucial trip-related outcomes related to travel mode and departure time, Golshani et al. (2017) examined the predictive ability of conventional statistical techniques versus ANNs. Based on their findings, ANNs performed better while requiring a simpler and quicker deployment method.

Additionally, multivariable regression models and ANN were utilized to forecast the stress intensity components that cause rigid concrete slab cracking, with the findings demonstrating that ANN has a predictive accuracy advantage over multivariable regression models (Wu et. al., 2014). Felker et al. (2014) found that statistical analysis produced an R^2 of 0.73 whereas ANN models produced an R^2 of 0.90 for forecasting roughness for jointed rigid concrete slabs. The ANN technique also demonstrated efficacy in forecasting IRI values utilizing complicated input variables in a study by Kargah Ostad et al. (2010). Additionally, the cracking index for Florida's highways has been predicted using ANN models, which were found to be more accurate than an autoregressive model (Lou et. al., 2001). In order to determine the relationship between cement fraction, metal amount, and traffic volume on rough wear of concrete, Gencel et al. (2011) developed ANN and linear regression models. The ANN models were superior to linear regression models in predicting the abrasive wear of concrete. As a result, according to Basheer and Hajmeer (2000), ANN schemes may address a wide range of problems from a variety of areas, including:

- Pattern set: ANN models, unlike conventional statistics models, do not rely on the linearity assumption and can deal with unspecified input patterns using controlled learning.
- Clustering: By identifying similarities and variations between inputs, ANN algorithms can employ unsupervised learning to group together similar trends.
- Modeling: Utilizing a multilinear ANN algorithm, input and output data are trained to determine their connection.

- Optimization: By maximizing or minimizing an objective function while taking into account several restrictions, ANN algorithms were more effective at handling optimization challenges. Additionally, Attoh-Okine (1994) noted two advantages of ANN algorithms over more conventional statistical prediction techniques: ANN models can handle unforeseen inputs and generalize conclusions, and they can tackle complicated problems because of their extensive parallelism and robust interconnection.

According to the literature, ANN rigid concrete slab performance models have been effective modeling techniques used by researchers to forecast slab performance at least since the 1990s. Though, the majority of the research that has been done so far on predicting rigid concrete slab performance at the project management level has concentrated on a particular pavement type. A paucity of data has prevented many models from including all the aspects that can affect rigid concrete slabs including environmental conditions, material properties, and geometric characteristics as well as boundary conditions, and numerous earlier research failed to quantify the influence of input factors like weather on ANN model predictions. Figure 9.1 summarized all various techniques including their advantages and disadvantages, as discussed above.

9.3. DESCRIPTION OF THE NEURAL NETWORKS UTILIZED IN THE CURRENT RESEARCH

Five distinct machine learning models—MLP, RBF, SVR, ANFIS, and DNN—were employed in this research to forecast the thermal and curling characteristics of rigid concrete slabs for future constructions considering all important variables including the environmental circumstances, material properties, geometric features, and boundary conditions. Below is a description of these models. The model is evaluated using 5-fold cross-validation. The data is separated into five groups using this methodology. Model evaluation is done in five steps. Four groups are utilized

for each step's model training, and one group is used for each step's model testing. In these algorithms, the models are often tested using all of the data at once. Figure 9.1 summarized the steps carried out in this chapter.

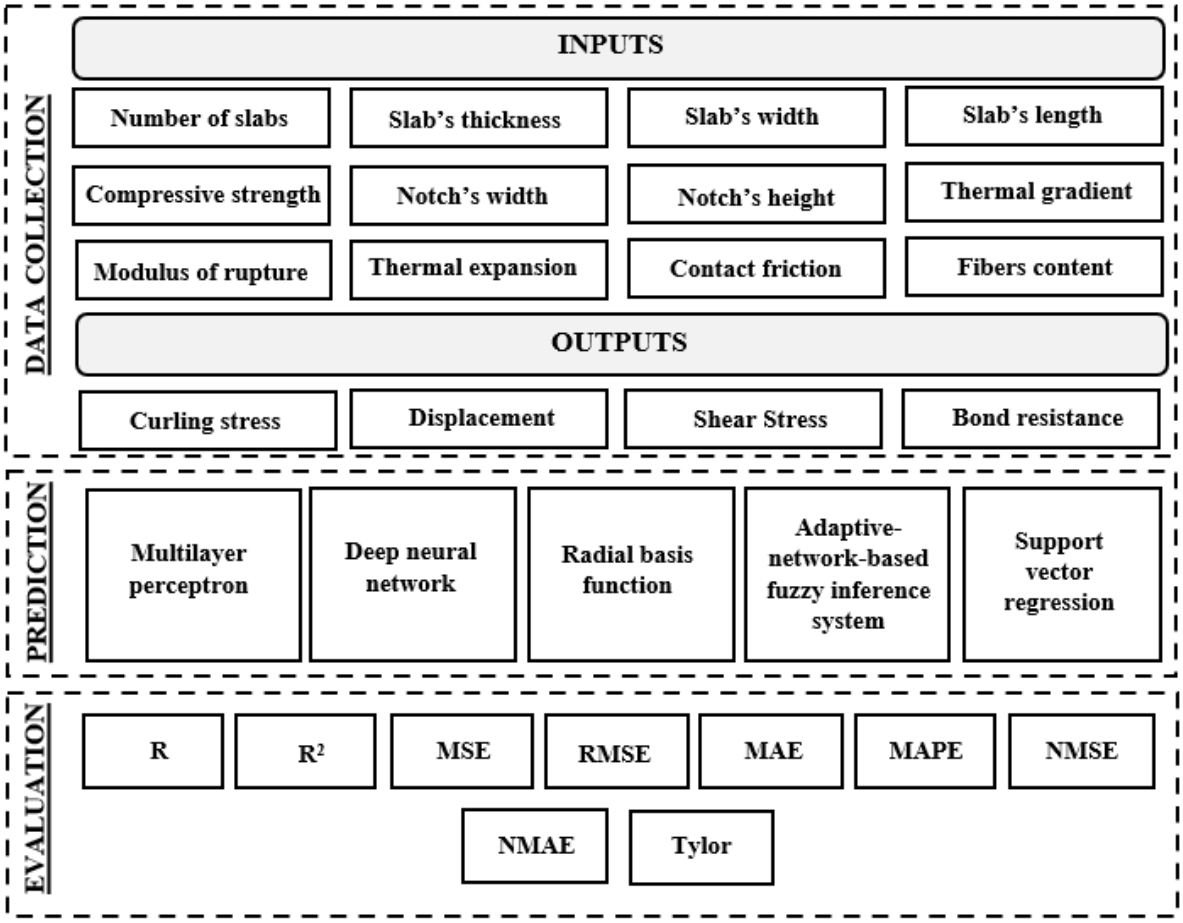

Figure 9.1: Detailed flowchart of the actions taken through this chapter

9.3.1. Multilayer perceptron (MLP)

One class of ANNs called MLP imitates biological neural networks, such as the human brain, to process prediction (Arena et al. 1998). The structure of the approach is made up of several neurons with internal connections that cooperate to find solutions to issues. MLP learns by transferring the information or rules underlying the data to the network structure through the analysis of experimental and numerical data. In essence, an intelligent system's capacity for learning is its most crucial quality (Huang, 2007; Kang et al. 2007). In engineering sciences, MLPs are employed

for a variety of tasks including modeling, pattern recognition, organization, estimation, and optimization. This method is appropriate for modeling engineering problems since these networks may produce a mapping between input and output data with tolerable inaccuracy. In Figure 9.2, the MLP network is displayed. The input, hidden, and output layers of this approach are shown in this figure as three layers. Additionally, each layer has a number of neurons. In addition, Figure 9.3 depicts the anatomy of each neuron. Each neuron's output is calculated by multiplying its inputs by the corresponding weights attached to it. The neuron bias is then increased by the results that were obtained. Finally, using the following equation (Arena et al. 1998), the transfer function *(f)*, which can be either linear or non-linear, is employed to monitor the neuron output.

$$f_i = f\left(b + \sum_{j-1}^{m} x_j w_j\right) \tag{9.3}$$

In which, for each neuron, x_j and w_j represent the input and associated weight, respectively. Additionally, *m* and *b* stand for the respective input neuron and bias numbers (Arena et al. 1998; Huang, 2007; Kang et al. 2007) [33–35]. Therefore, the flowchart for the MLP network is provided in Figure 9.4.

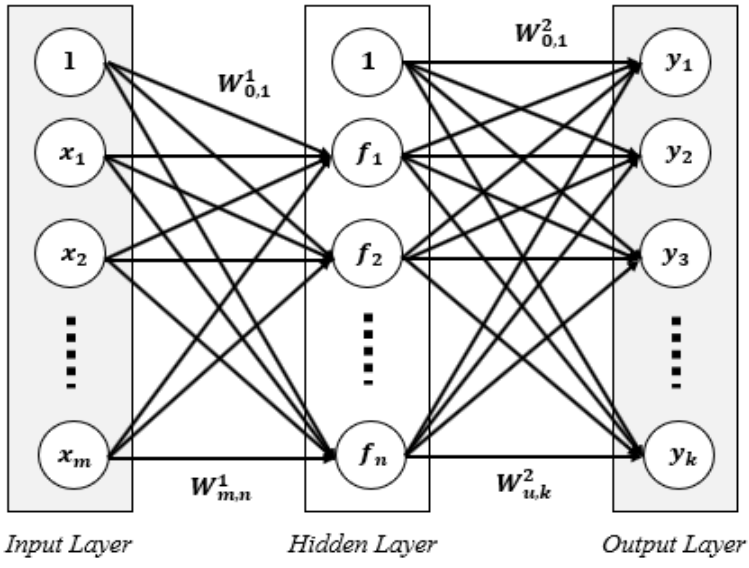

Figure 9.2: General design of the MLP algorithm

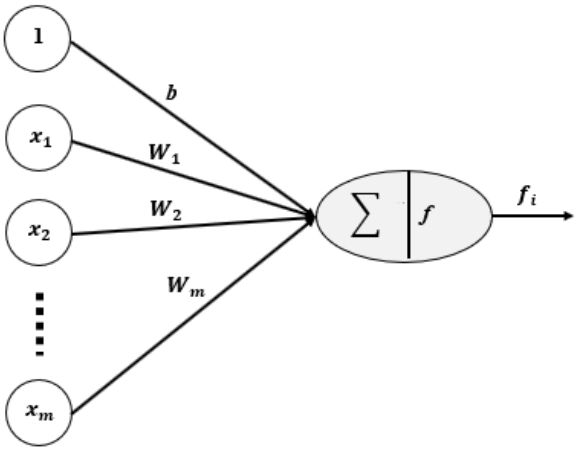

Figure 9.3: Structure of MLP algorithm with one neuron.

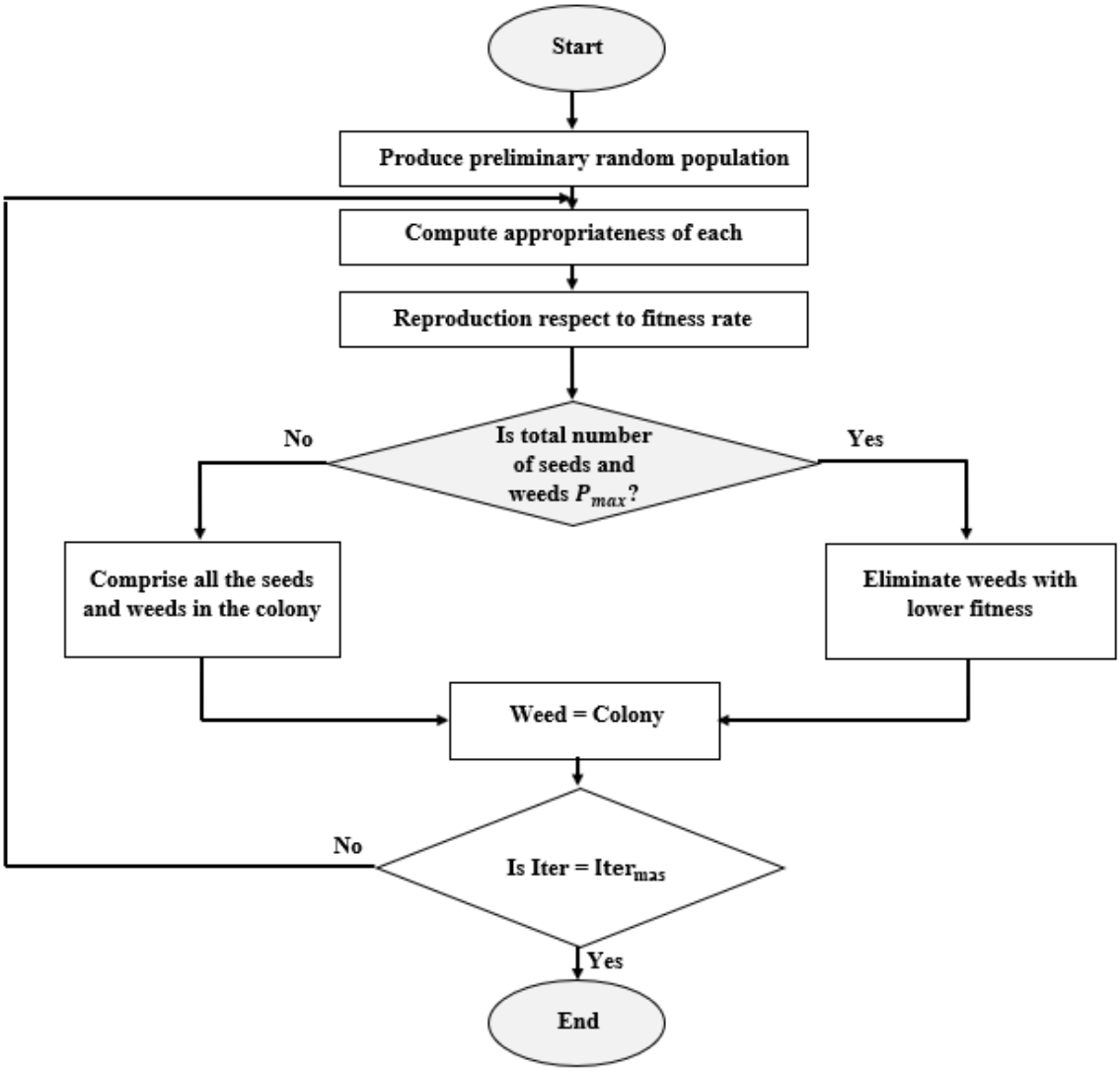

Figure 9.4: Flowchart for MLP network to predict the thermal and curling responses

9.3.2. Deep neural network (DNN)

Deep learning systems are used extensively throughout a wide range of industries, from automatic driving to medical equipment. Dealing with a deep network implies working with a sizable neural network. This phrase describes how many hidden layers there are in neural networks. Most ANNs and machine learning algorithms require the relevant model features to be extracted using various approaches. However, the right features are automatically extracted in the deep learning system thanks to a procedure (Antonio and Pal, 2017). The scale of the deep learning algorithm with the data is another difference. Many algorithms converge with a small number of data, and adding more data does not affect the model's performance (Ball et al. 2020a; Ball et al. 2020b; Ball et al. 2019a; Ball et al. 2019b).

Another benefit of the DNN is that the model's performance can keep getting better by adding more data, especially for complex systems (Antonio and Pal, 2017). One of the biggest problems with this network is the lack of a precise theory to choose the kind of layers, the number of layers, the number of neurons in each layer, and the architecture of the network as a whole. Even though in many instances, stochastic methods that are inspired by nature aid in defining the model agriculture. The fact that this network frequently works well for issues with a lot of data is another disadvantage. The MLP network, which has an input layer, a number of hidden layers, and an output layer, is extended by this algorithm. It delivers excellent accuracy on complex data because of the number of layers and connections between them. To choose the best network performance, various models have been tested experimentally and using methods like varying the number of layers and neurons and picking the right transfer functions (Hasannezhad et al. 2021). The Dense function has been used in this research is depicted in Figure 9.5.

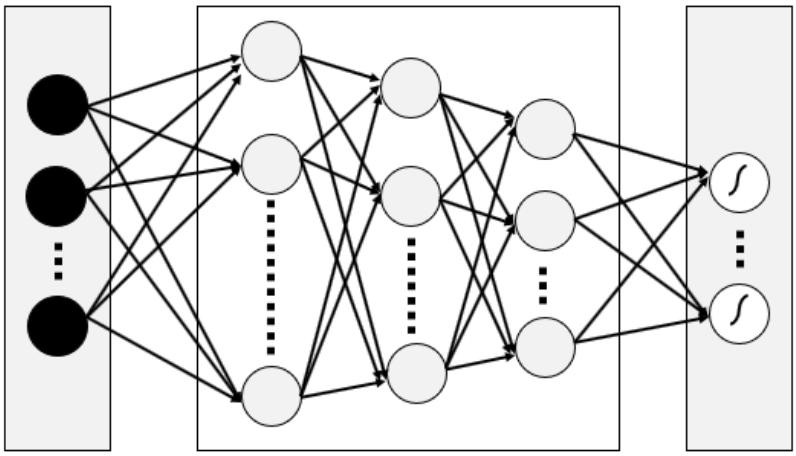

Figure 9.5: DNN algorithm with three hidden layers

The first layer serves as the input layer where input values are received. Following numerous studies, the following three layers—designated as hidden layers—were chosen for the various number of neurons, respectively (Hasannezhad et al. 2021; Yang et al. 2021). One of the transfer functions frequently utilized for various regression issues is this straightforward nonlinear function. Additionally, the output layer, which makes up the network's final layer, uses the Sigmoid function in its neurons as a transfer function. The batch size and the epoch value are two additional options that were selected after conducting numerous trials. The network weights are updated and the adaptive learning rate for each parameter is calculated using the Adam optimizer. A DNN model was developed using Tensor Flow, a library designed for high-performance numerical calculations, as the backend to forecast the thermal and curling critical responses of rigid concrete slabs considering the influence of PF, environmental condition, material properties, and geometric characteristics as well as the boundary conditions. It should be mentioned that Python3 libraries as well as a sequential API model have been created and tested with Keras, a deep-learning framework (Yang et al. 2021). Therefore, the flowchart for the MLP network is provided in Figure 9.6.

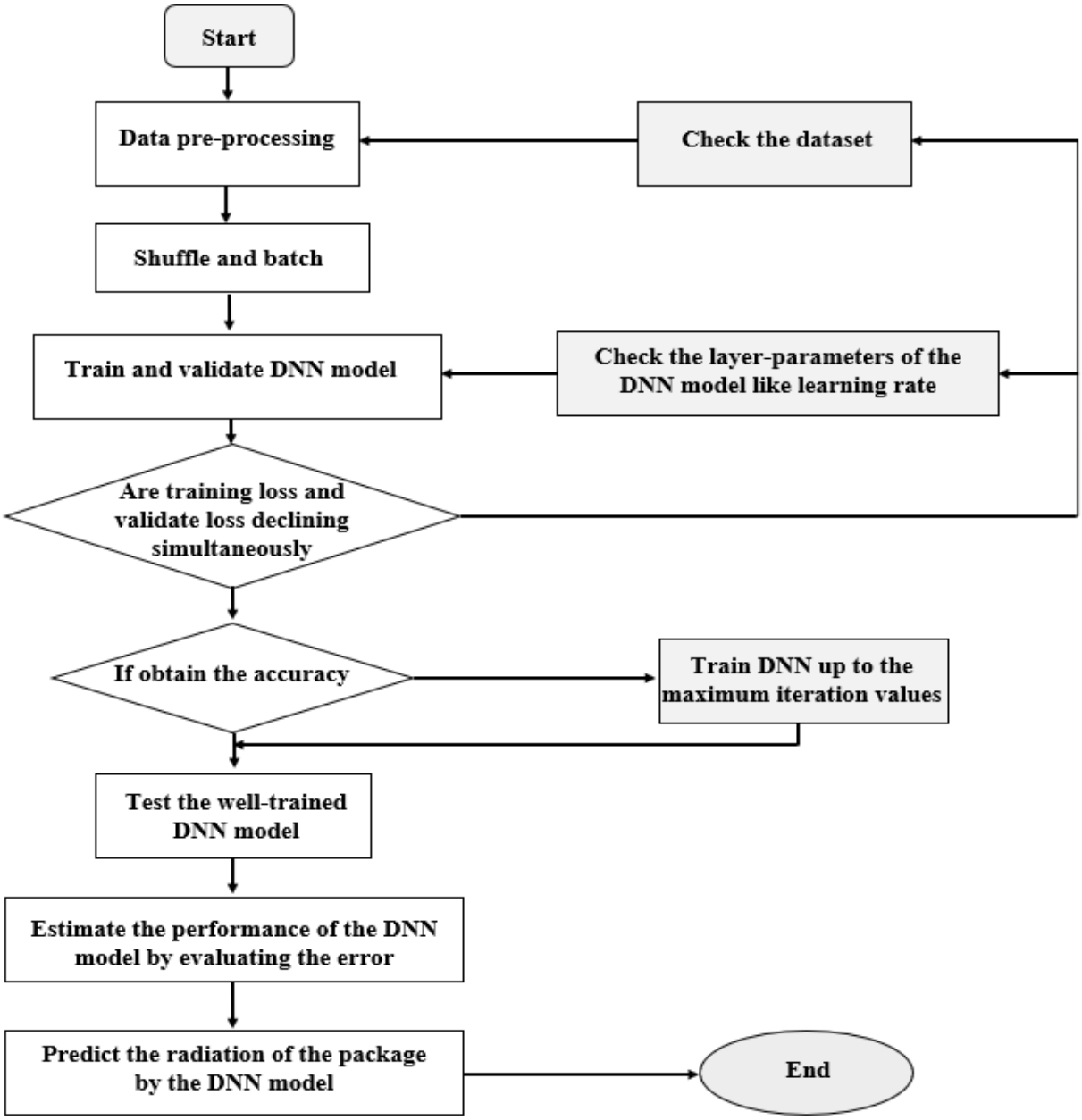

Figure 9.6: Flowchart for DNN algorithm to predict the thermal and curling responses

9.3.3. Radial basis function (RBF)

Through a small training dataset, RBF has been routinely utilized to estimate nonparametric multidimensional functions. If sufficient neurons are chosen for the hidden layer, this approach with just one hidden layer may predict any continuous operation with any level of accuracy. In order to transform nonlinear patterns into linear separable patterns, the hidden layer provides a

nonlinear adaption between the input and output regions with generally large dimensions. A weighted sum of the linearized patterns is also generated by the output layer, which is suitable for function estimation. To produce the neuron i's output following input vector X, Equation (9.4) is utilized (Liu, 2013; Iurlaro et al. 2014):

$$F_i(X) = \sum_{j=1}^{P} w_j \varphi\left(\left\|X - U_j\right\|\right) \tag{9.4}$$

In which, P denotes the number of neurons in the hidden layer; w_j indicates the weight among neurons in the hidden layer and output neuron, and U_j is the center of neuron j in the hidden layer. The Gaussian function is usually used in the RBF network to improve the performance of the network as below (Liu, 2013; Iurlaro et al. 2014):

$$\varphi\left(\left\|X - U_j\right\|\right) = e^{\frac{\|X - U_j\|}{\sigma_j}} \tag{9.5}$$

In which, σ_j is the hidden layer's *j-th* neuron kernel parameter. It should be mentioned that RBF has two functional modes for training and testing, just like other ANNs. In order to reduce the mean error between the outputs in a training set and the real values, the adjustable network parameters U_j and σ_j are modified during the training mode. Additionally, the trained network is imported with the new input vectors in the testing mode to produce the desired outputs. Figure 9.7 illustrates the structures of the RBF algorithm. Therefore, the flowchart for the MLP network is provided in Figure 9.8.

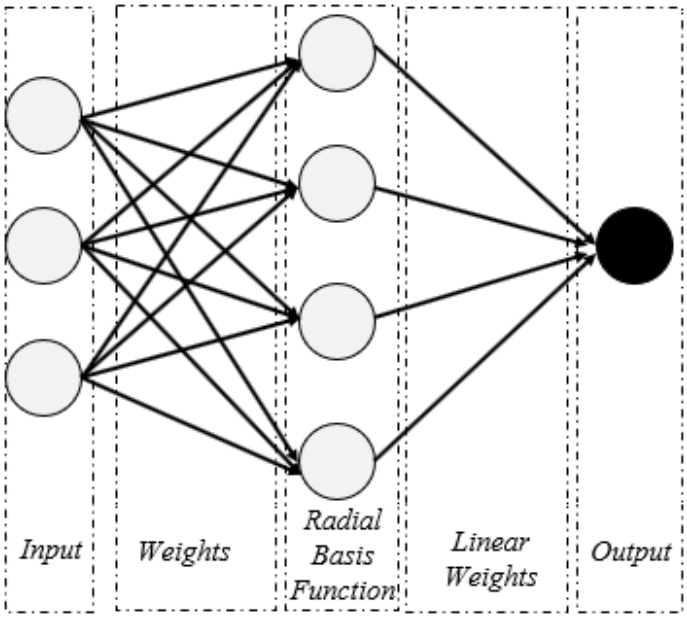

Figure 9.7: Diagram of RBF structure

9.1.1. Adaptive-network-based fuzzy inference system (ANFIS)

Fuzzy rules and the adaptive network were combined to create this model. In other terms, Takagi-Sugeno Fuzzy Inference System (FIS) is ANN-based (Roger et al. 1997). The only restriction on node functions in this architecture is that they must be somewhat derivable. Takagi-Sugeno rules are regarded as fuzzy rules. The ANFIS approach divides data processing across multiple layers, as seen in Figure 9.9. In this diagram, the fuzzy rule's antecedent component takes into account the variables X and Y. The fuzzy rule is an x and y linear arrangement with a fixed value (Roger et al. 1997). As a result, the first layer has movable nodes with maximum and minimum values of one and zero, respectively, based on bell-shaped or Gaussian functions. Therefore, at the Fuzzification layer, input qualities are added up to the input membership functions (MF). Additionally, the input MFs create a series of if-then rules in the Rule layer (layer 2).

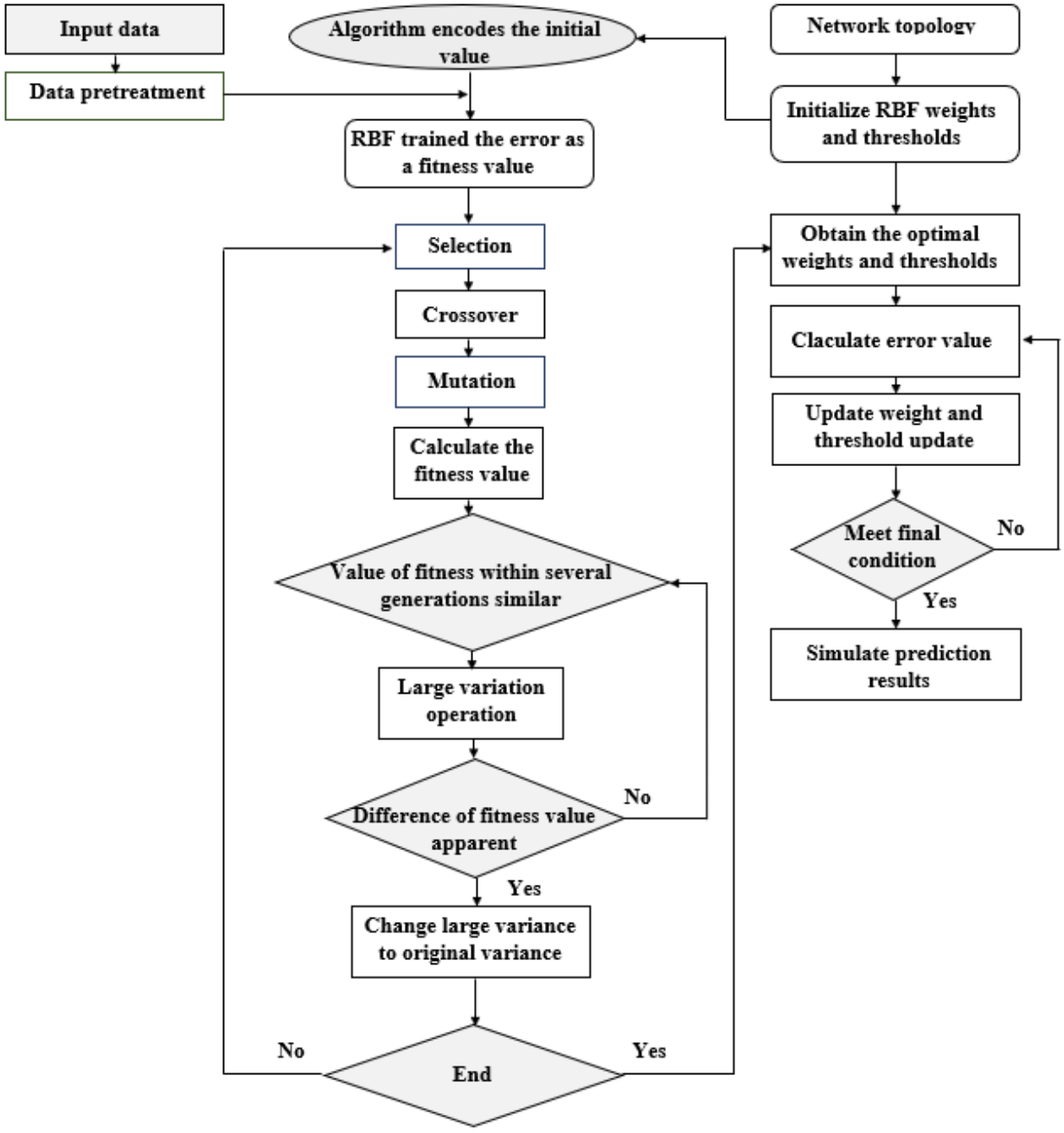

Figure 9.8: Flowchart for RBF algorithm to predict the thermal and curling responses

Fixed nodes that both receive and produce input signals make up this layer. Each node controls the firing power of each rule. A group of the if-then rules' output characteristics are achieved in layer three. In this case, the normalized firing strength—a ratio of each node's firing strength to

the total firing strength—is determined for each node of the preceding layer. For this aim, Eq. (9.6) was employed to assess the stabilized firing strength (Roger et al. 1997; Güler and Übeyli, 2005):

$$\overline{W_i} = \frac{W_i}{\sum_j W_j} \tag{9.6}$$

Next, in layer 4, the output features are converted to output MFs. Each node executes the following operation on the inputs' first-order polynomial and normalized firing strength (Roger et al. 1997; Güler and Übeyli, 2005):

$$\overline{W_i}F_i = \overline{W_i}(P_iX + Q_iY + R_i) \tag{9.7}$$

In which, P_i, Q_i, and R_i are the first-order polynomial equation's constants. Last but not least, layer 5 generates a single value output by adding together all inputs and MF outputs using Eq. (9.8)

$$F = \sum_i \overline{W_i} F_i \tag{9.8}$$

Therefore, the flowchart for the ANFIS network is provided in Figure 9.10.

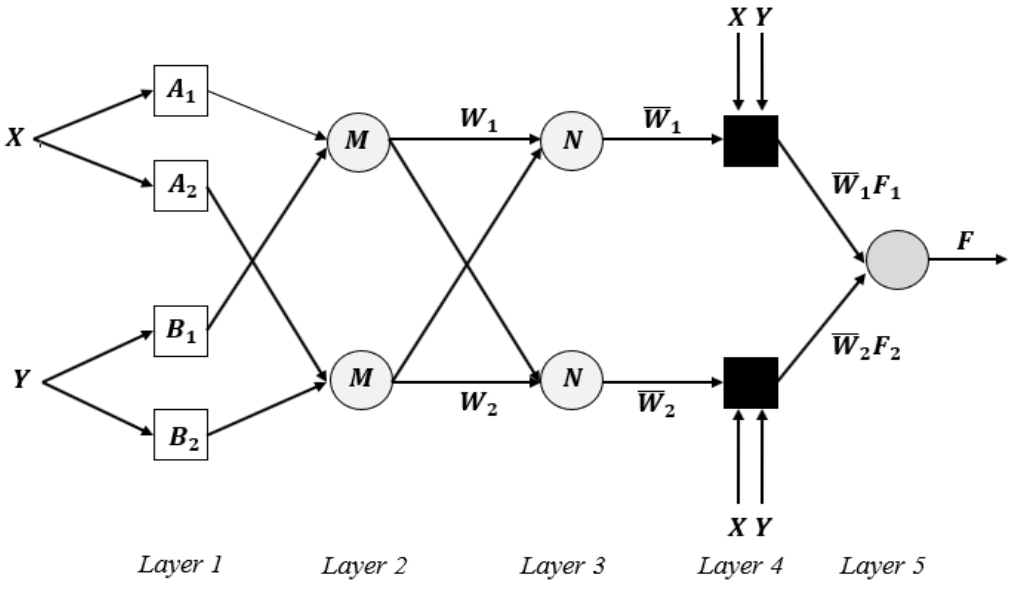

Figure 9.9: Diagram of ANFIS structure

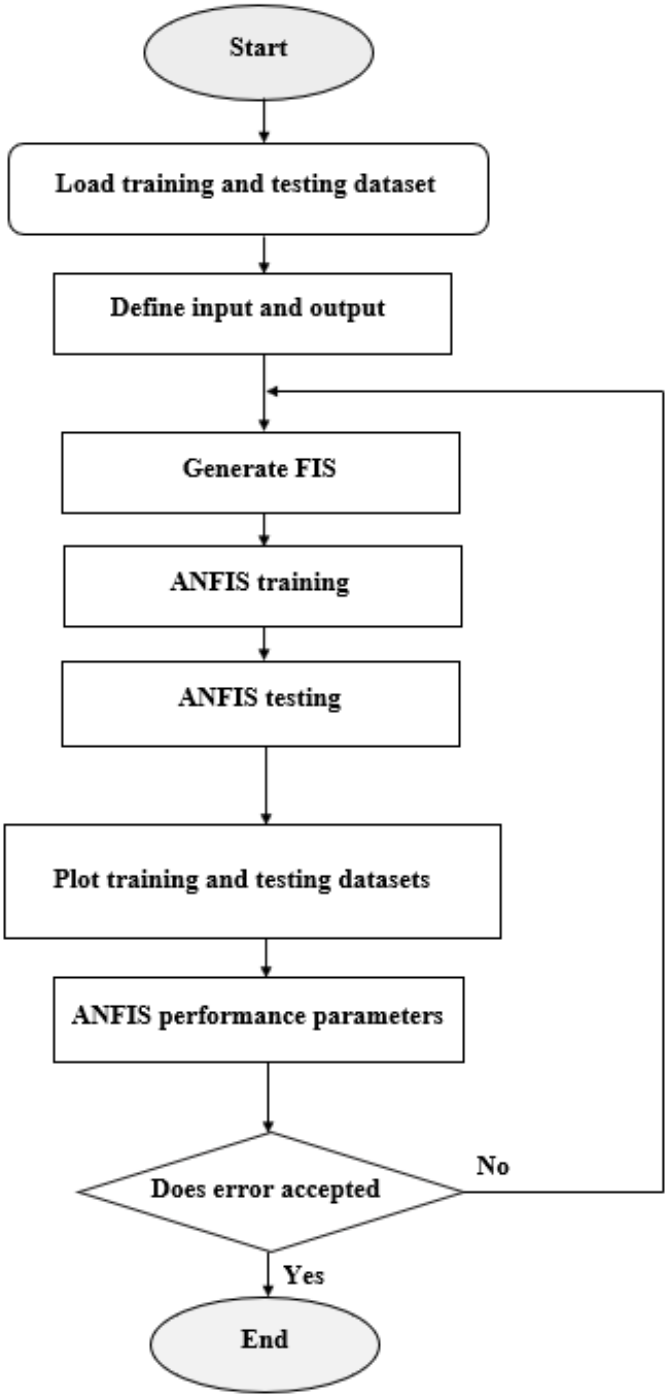

Figure 9.10: Flowchart for ANFIS algorithm to predict the thermal and curling responses

9.1.1. Support vector regression (SVR)

Support Vector Machine (SVM) was first employed for classification before being used for regression. The linear function $f(x) =< w, x > +b$ represents the regression issue in SVM. With the help of the input vectors (x), this function may estimate the output value (y) for a set of l samples, such as $\{(x_1, y_1), \dots, (x_i, y_i) \epsilon R^N, y \epsilon R\}$. Additionally, the regression problem, where the smallest error can be disregarded, is resolved using the Vapnik loss function. Thus, the next definition of the loss function is given (John and Cristianini, 2000):

$$L_\varepsilon(y) = \begin{cases} |f(x) - y|_\varepsilon = 0 & if\ |f(x) - y| < \varepsilon \\ |f(x) - y| = \varepsilon & otherwise \end{cases} \tag{9.9}$$

Where ε indicates the acceptable inaccuracy in the failure function. Furthermore, the ideal regression function is achieved by resolving the following optimization equation (John and Cristianini, 2000; Hwang et al. 2006):

$$minimize\ \varphi(w, \xi, \xi^*) = \frac{1}{2}|w|^2 + c\sum(\xi_i^* - \xi_i) \tag{9.10}$$

$$y_i - f(x_i) \leq \varepsilon + \xi_i \tag{9.11}$$

$$Subject\ to\ \ f(x_i) - y_i \leq \varepsilon + \xi_i^* \tag{9.12}$$

$$\xi_i, \xi_i^{\ *} \geq 0 \tag{9.13}$$

In which ξ_i and $\xi_i^{\ *}$ are slack variables. Also, c is one of the control indicators of function φ. To solve this optimization problem, the Lagrange concept is utilized as presented below (John and Cristianini, 2000; Hwang et al. 2006; Oliveira, 2006):

$$L(a^*, a) = -\varepsilon \sum_{i=1}^{l} (a_i^* + a_i) + \sum_{i=1}^{l} y_i (a_i^* + a_i) - \frac{1}{2} \sum_{i=1}^{l} \sum_{j=1}^{l} (a_i^* + a_i)(a_j^* + a_j)(x_i x_j) \quad (9.14)$$

The values of a and a^* are then found by maximizing Eq. (9.14) while taking into account the next restrictions (Hwang et al. 2006; Oliveira, 2006):

$$\sum a_i^* = \sum a_i \quad (9.15)$$

$$0 \leq a_i^*, a_i \leq c \qquad for\ i = 1, 2, \ldots \quad (9.16)$$

It should be highlighted by using Quadratic Programming (QP) techniques, the optimization problem can be resolved. Data with non-zero Lagrange coefficients are referred to as support vectors in that context. Prediction errors for this data are more than ±ε. The support vectors do not, therefore, fit inside the interval. Eq. (9.17) is also used to achieve the appropriate answer control directories using Lagrange constants and support vectors (John and Cristianini, 2000; Hwang et al. 2006; Oliveira, 2006):

$$w_0 = \sum_{support\ vector} (a_i^* - a_i) x_i \quad (9.17)$$

$$b_0 = -\frac{1}{2} w_0 [x_r + x_s] \quad (9.18)$$

$$f(x) = \sum_{support\ vector} (a_i^* - a_i)(x_i - x) + b_0 \quad (9.19)$$

Where there are two support vectors, x_r and x_s. Additionally, the user defines the *c* and ε indices to build the SVR. Therefore, the next formulas are used to achieve the best function control

indices in the nonlinear regression simulation (John and Cristianini, 2000; Hwang et al. 2006; Oliveira, 2006):

$$w_0 x = \sum_{support\ vector} (a_i^* - a_i) K(x_i - x) \tag{9.20}$$

$$b_0 = -\frac{1}{2} \sum_{support\ vector} (a_i^* - a_i)[K(x_i - x) + K(x_i - x)] \tag{9.21}$$

In which, where K indicates the kernel. In the current research, the RBF kernel function was employed as below (John and Cristianini, 2000; Hwang et al. 2006; Oliveira, 2006):

$$K(x, x_i) = \exp\left(-\frac{1}{\sigma^2}(x - x_i)^2\right) \tag{9.22}$$

In which, σ denotes the kernel factor of RBF. Therefore, the flowchart for the SVR network is provided in Figure 9.11.

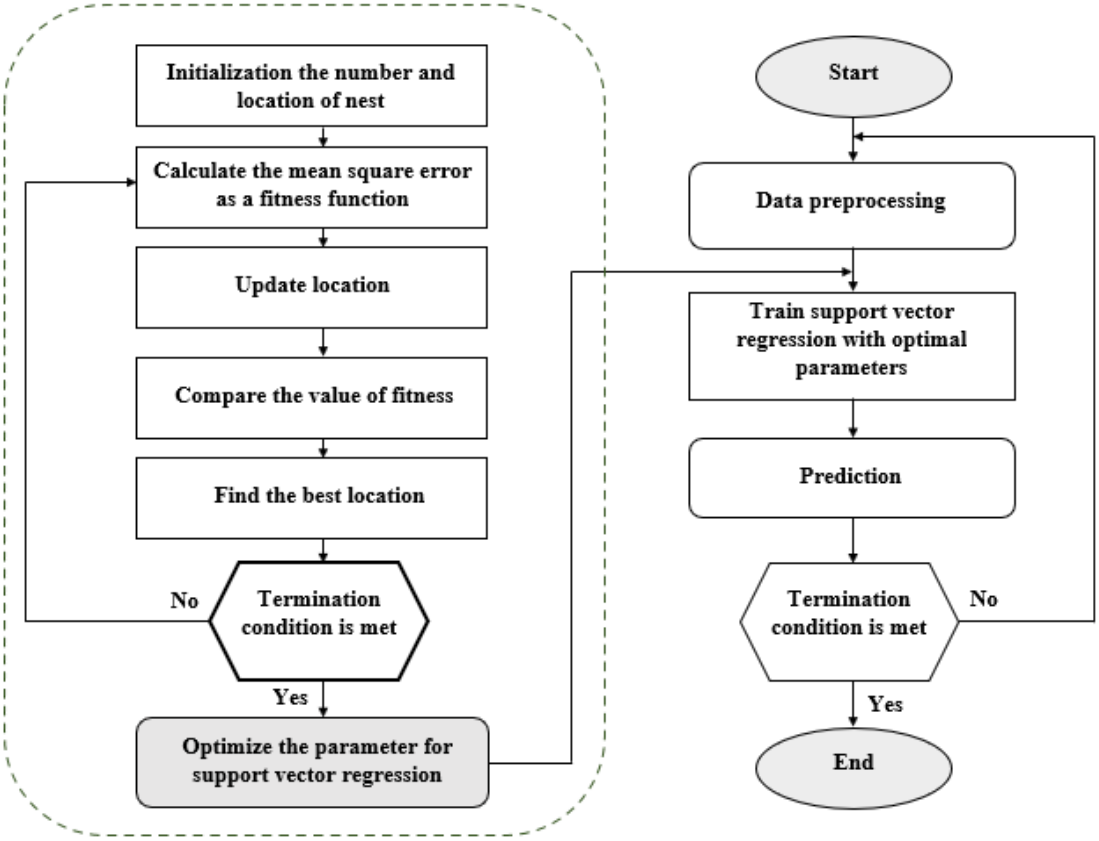

Figure 9.11: Flowchart for SVR algorithm to predict the thermal and curling responses

9.2. RESULTS AND DISCUSSIONS

9.2.1. Out-of-plane deformation

Engineers frequently take into account the Out of plane deformation of rigid concrete slabs when building new structures. As a result, as shown in Figure 9.12, the correlation between the numerical and field test results and those obtained using machine learning algorithms is examined in this section. Figure 9.12a shows that there is good agreement between projected out-of-plane deformation and numerical results when DNN has been employed. Because of this, rather than conducting in-field tests based on the composition of the materials, the machine learning methods used in this research could be used as effective tools to predict the out-of-plane deformation of rigid concrete airfield runways. In this comparison, DNN, ANFIS, RBF, MLP, and SVR have the

best accuracy in predicting out-of-plane deformation for both plain and fiber-incorporated rigid concrete slabs, with coefficients of determination (R2) of 0.9761, 0.9543, 0.9432, 0.9018, and 0.8842, correspondingly. As a result, only 5% of the predicted values in the DNN model had a significant error between all of the out-of-plane deformation output values that were used. For ANFIS, RBF, MLP, and SVR, the percentage of high error predicted values was 9%, 21%, 26%, and 31%, correspondingly. These findings demonstrated how effective the suggested algorithms—in particular, DNN—are at predicting the out-of-plane deformation of concrete slabs under the influence of thermal gradient. Additionally, Figure 9.13 presents the error values and their spread for the employed ANNs. As can be observed, machine learning methods, particularly DNN, can accurately forecast the actual results observed, which is adequate for practical use. This could promote the use of ANNs in the future to forecast the observed rigid concrete airfield runways made of various materials and also under the influence of different stresses.

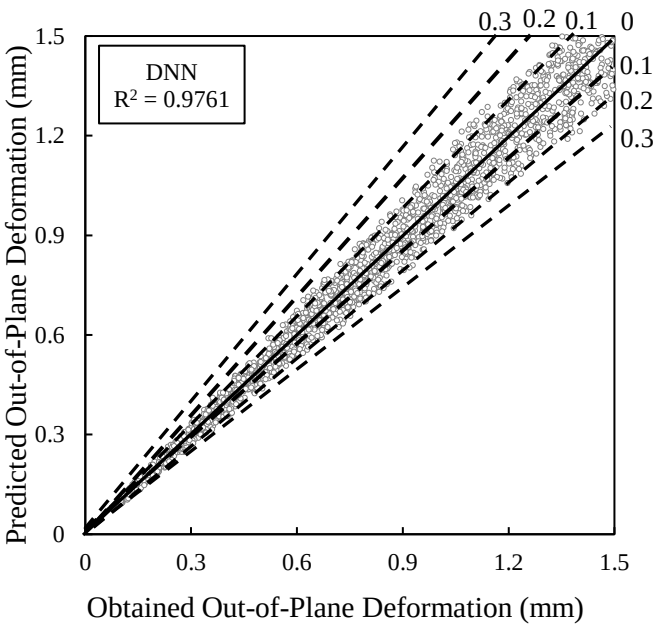

(a)

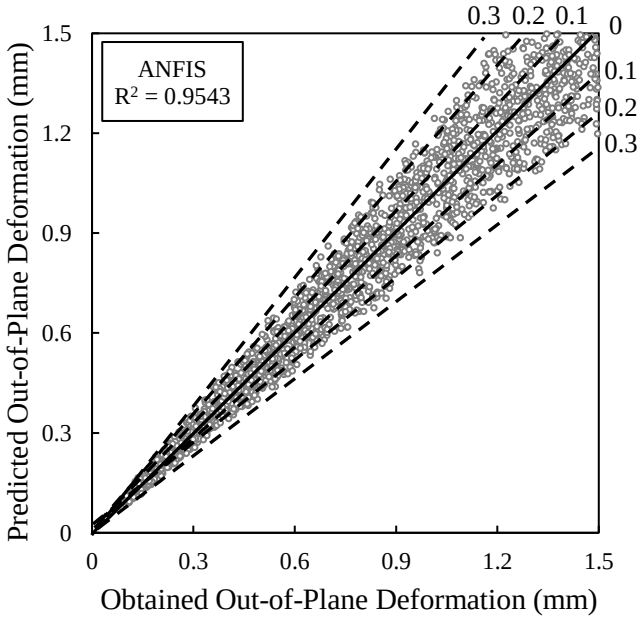

(b)

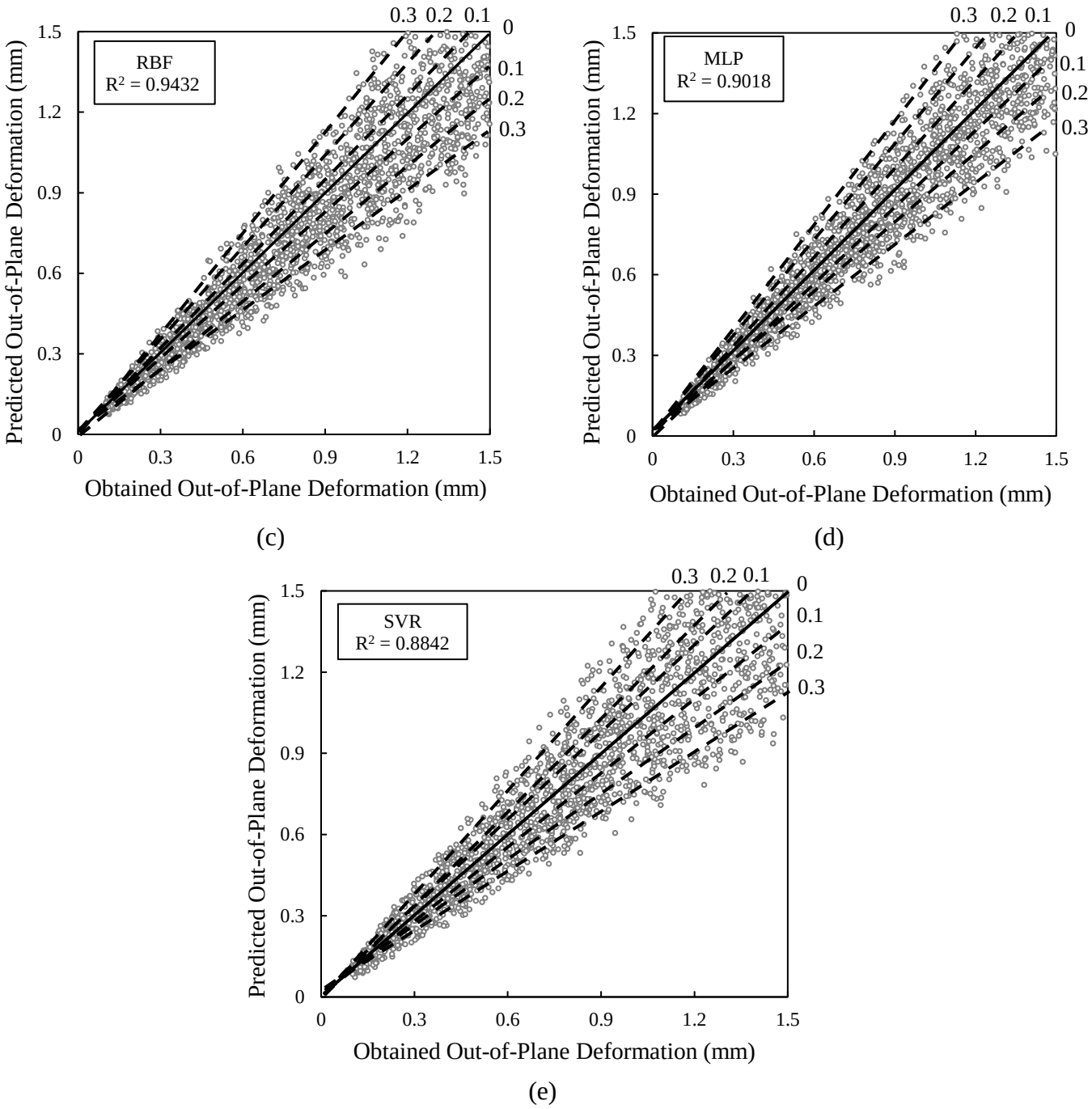

Figure 9.12: Out-of-plane deformation prediction for both plain and fiber-reinforced concrete slabs using various algorithms a) DNN, b) ANFIS, c) RBF, d) MLP, and e) SVR

Figure 9.13 displays the spread of the error for the both trained and tested parts. There, using the DNN algorithm with the uppermost frequency between 0 and 0.03, the least error was found for the curling stress of rigid concrete airfield runways (Figure 9.13a). These findings demonstrated that the DNN can offer the most accurate forecast mapping between the input and the output curling stress values. The MLP and SVR algorithms, which were utilized in this research, had the highest error distribution, with supreme error frequencies for curling stress prediction ranging from -0.04 -0.04 and 0.04-0.11, correspondingly. Additionally, the ANFIS algorithm predicted the curling stress of rigid concrete slabs with an upper limit that was accurate but the lower limit had a few high errors. Additionally, RBF demonstrated a good ability to forecast the curling stress with a supreme error frequency of 0-0.09. As a consequence, the low-range error distributions shown in Figure 9.13c also show how effective the suggested RBF algorithm is. Therefore, it is worth to be mentioned that the main benefit of the DNN technique is its inherent ability to suggest a structured and short model that is more simple in terms of interpretation as compared to other ANN models.

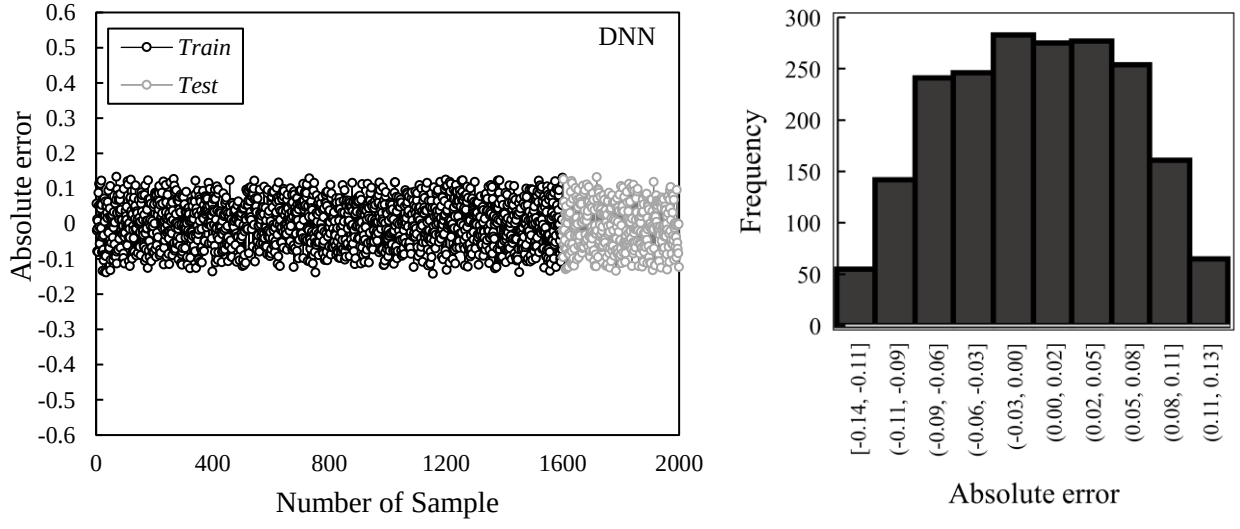

(a)

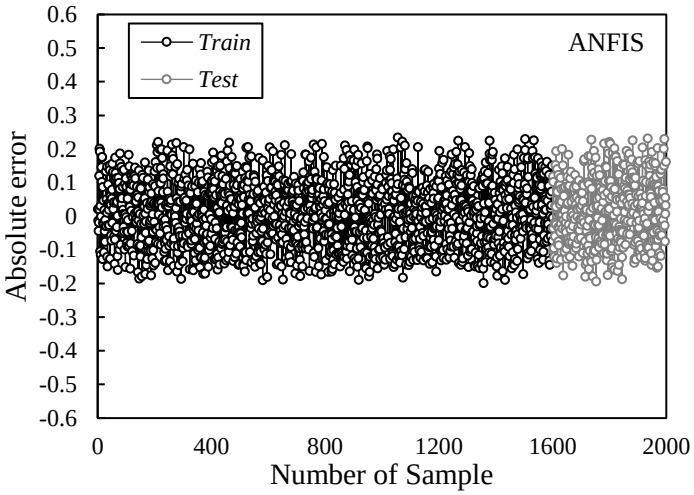
Train
Test
ANFIS
Absolute error
Number of Sample

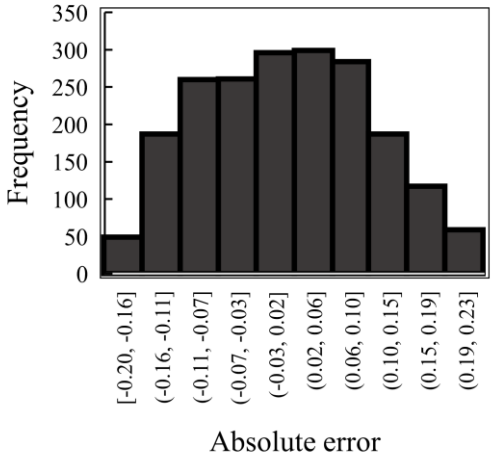
Frequency
[-0.20, -0.16]
(-0.16, -0.11]
(-0.11, -0.07]
(-0.07, -0.03]
(-0.03, 0.02]
(0.02, 0.06]
(0.06, 0.10]
(0.10, 0.15]
(0.15, 0.19]
(0.19, 0.23]
Absolute error

(b)

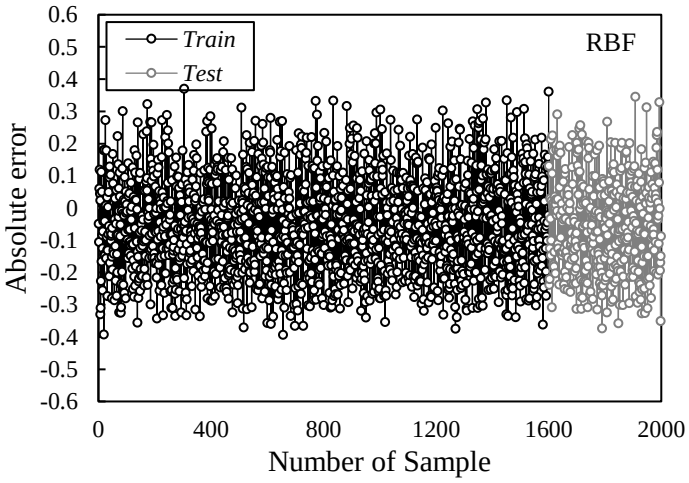
Train
Test
RBF
Absolute error
Number of Sample

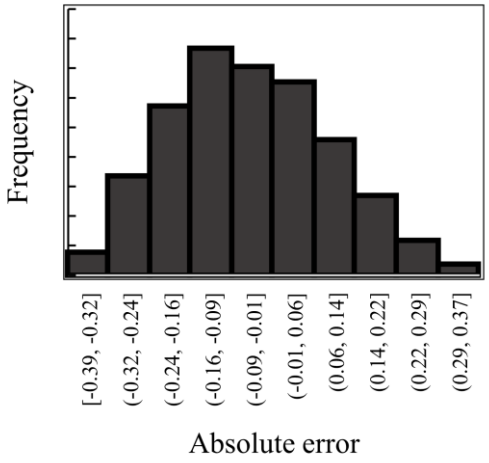
Frequency
[-0.39, -0.32]
(-0.32, -0.24]
(-0.24, -0.16]
(-0.16, -0.09]
(-0.09, -0.01]
(-0.01, 0.06]
(0.06, 0.14]
(0.14, 0.22]
(0.22, 0.29]
(0.29, 0.37]
Absolute error

(c)

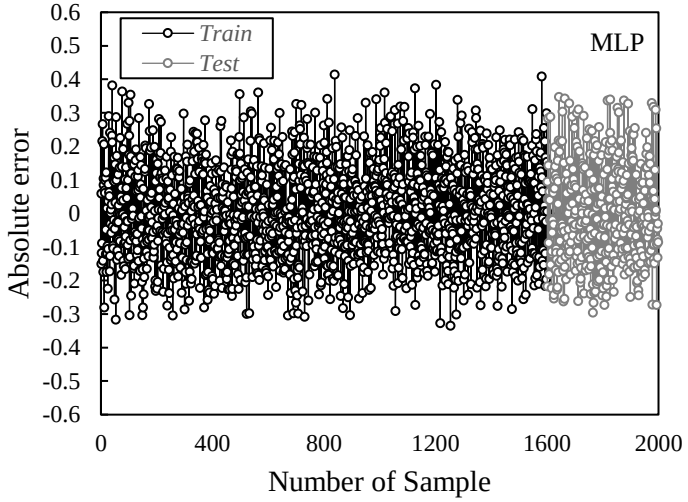
Train
Test
MLP
Absolute error
Number of Sample

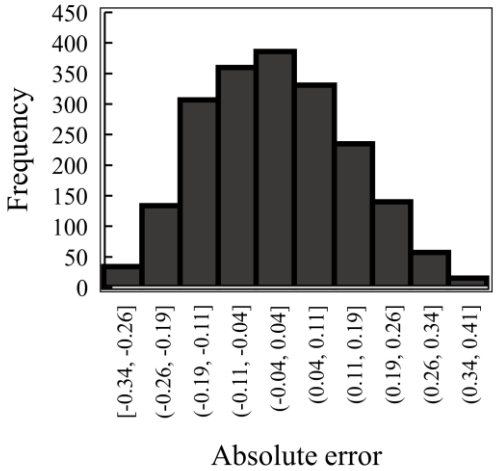
Frequency
[-0.34, -0.26]
(-0.26, -0.19]
(-0.19, -0.11]
(-0.11, -0.04]
(-0.04, 0.04]
(0.04, 0.11]
(0.11, 0.19]
(0.19, 0.26]
(0.26, 0.34]
(0.34, 0.41]
Absolute error

(d)

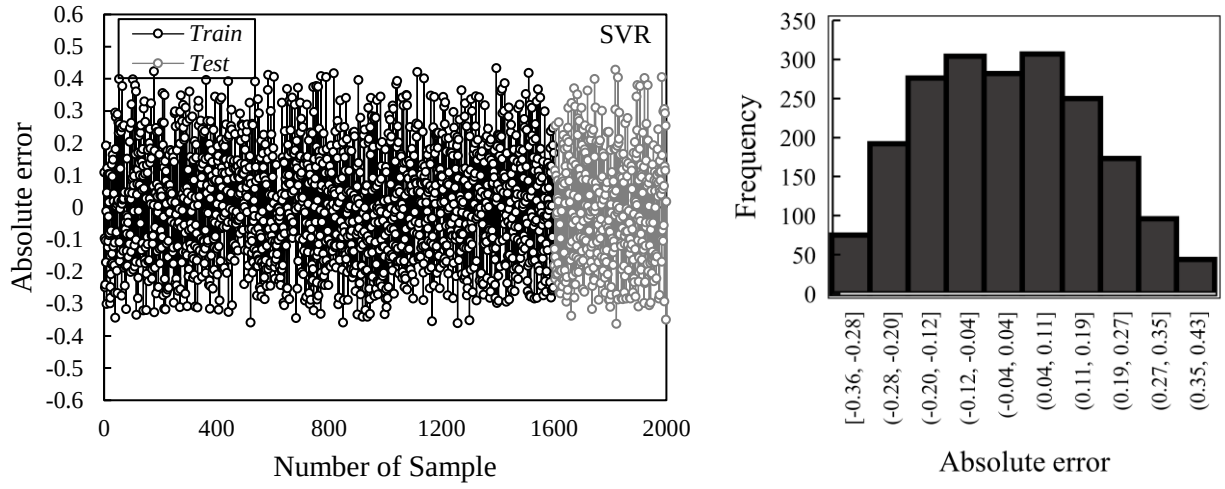

(e)

Figure 9.13: Error distribution and accuracy of various algorithms in terms of out-of-plane prediction for a) DNN, b) ANFIS, c) RBF, d) MLP, and e) SVR

9.2.2. Tensile stress

Another crucial factor to consider when thermal gradient affects the structural performance of rigid concrete airfield runways is tensile stress. As a result, in this part, the numerical and in-filed test findings and predicted values for tensile stress were compared. Figure 9.14 presents the obtained findings. The perfect fit in this figure is represented by a diagonal stripe that indicates the greatest level of method suitability and correctness and occurs when the correlation coefficient (R) is equal to 1. Similar to out-of-plane deformation, the DNN algorithm demonstrated the best tensile stress prediction ability, with an R^2 coefficient of 0.9814 (Figure 9.14a). As a result, ANFIS, RBF, and MLP with coefficients of determination (R^2) of 0.9587, 0.9509, and 0.9127 demonstrated the best prediction potential, while SVR had a greater error distribution than other suggested algorithms. Figure 9.15 presents the error distribution and their frequency to demonstrate the techniques' accuracy.

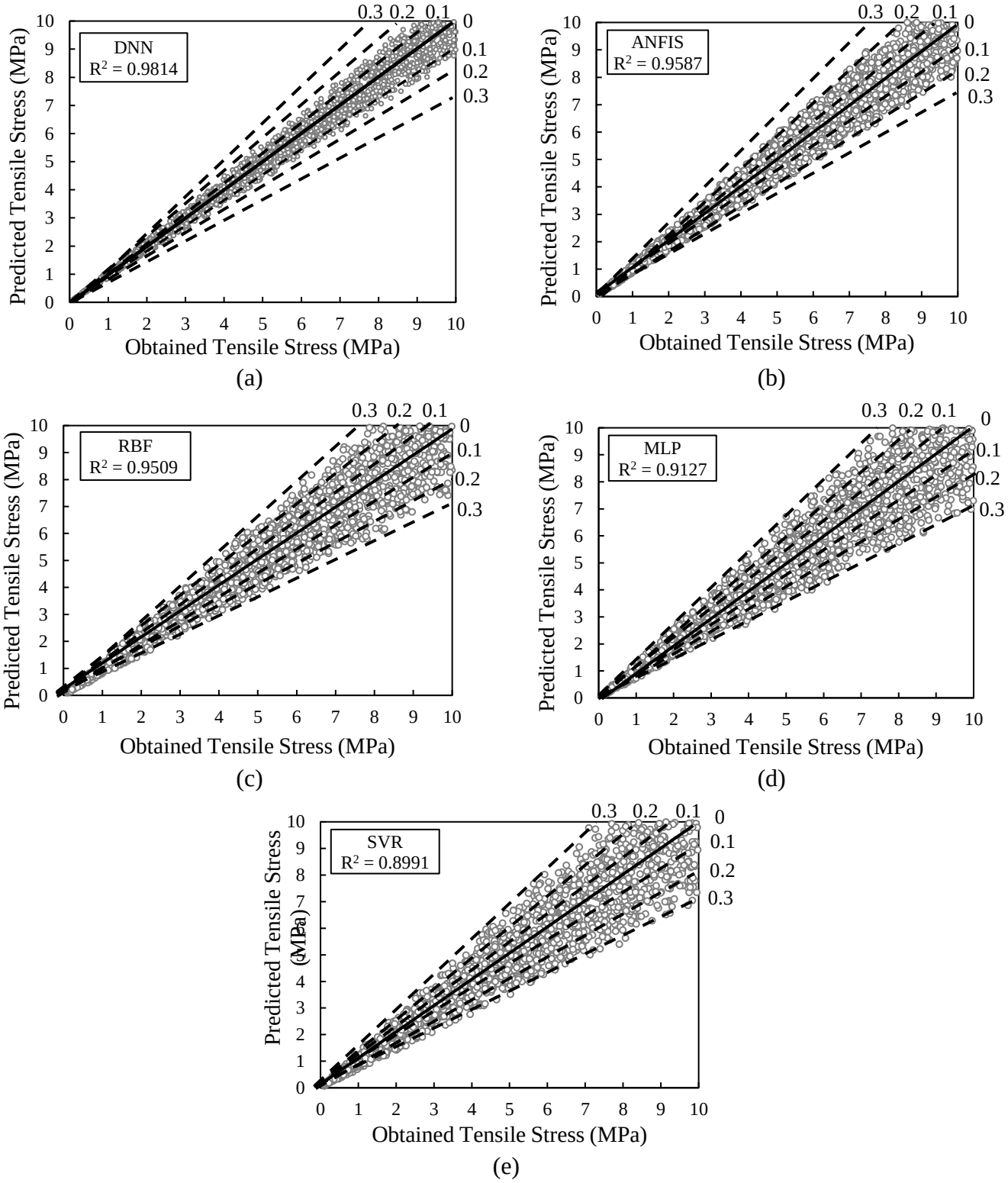

Figure 9.14: Tensile stress prediction for both plain and fiber-reinforced concrete slabs using various algorithms a) DNN, b) ANFIS, c) RBF, d) MLP, and e) SVR

Among all the ANNs used to predict the tensile stress of rigid concrete slabs under the effect of thermal gradient as shown in Figure 9.15, DNN demonstrated the lowest error distribution with the highest frequency spanning from -0.05 to 0.03. In contrast, MLP and SVR had maximal error distributions with error frequencies between -0.01 and 0.3. When predicting the tensile stress in rigid concrete slabs due to thermal gradient, the ANFIS technique demonstrated good correctness, but there were a few high errors in the upper limit. The highest frequency of 250 for the ANFIS algorithm was found for projected tensile stress errors varying from 0 to 0.04. Additionally, a maximum frequency of 270 was found in the RBF algorithm for predicted tensile stress errors ranging from -0.09 to 0.07. As a result, it can be concluded that DNN performs better than other models and have the greatest accuracy and robustness. The DNN method outperforms ANN models and has smaller absolute percentage error ranges when predicting the tensile stress of both plain and fiber-incorporated rigid concrete slabs exposed to a thermal gradient.

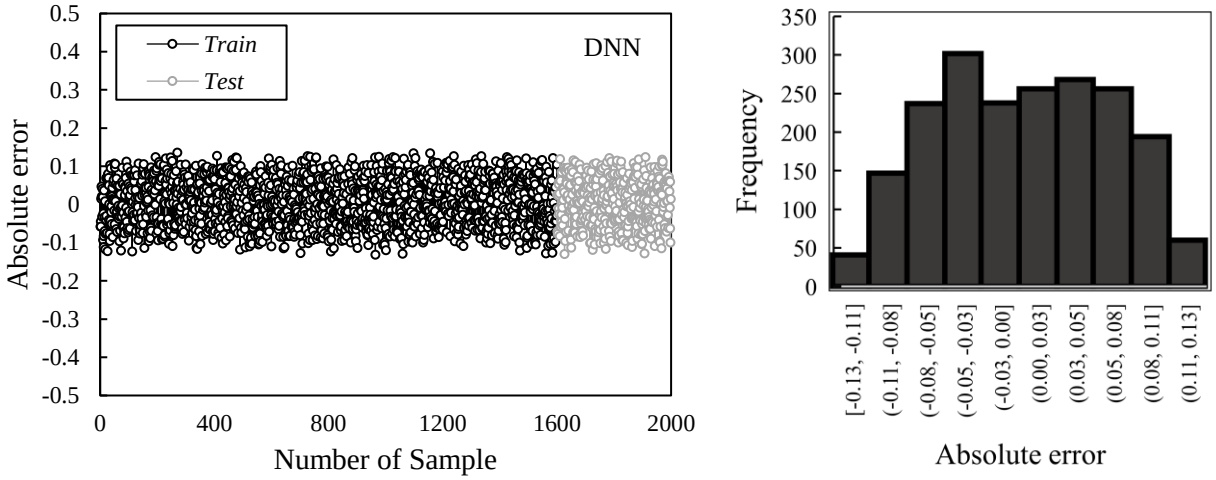

(a)

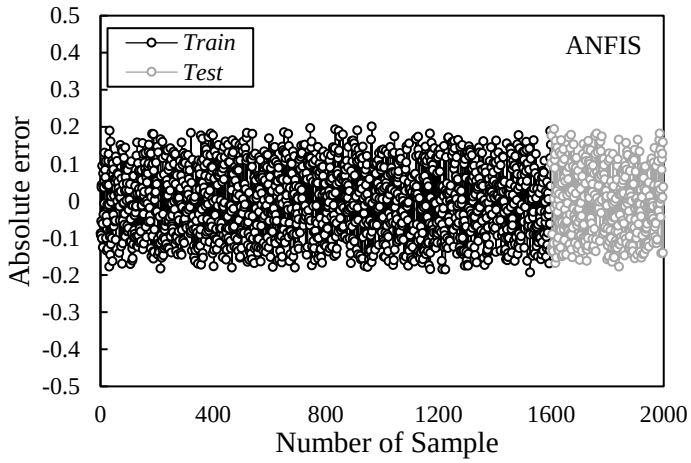
Train
Test
ANFIS
Absolute error
Number of Sample
0.5
0.4
0.3
0.2
0.1
0
-0.1
-0.2
-0.3
-0.4
-0.5
0
400
800
1200
1600
2000

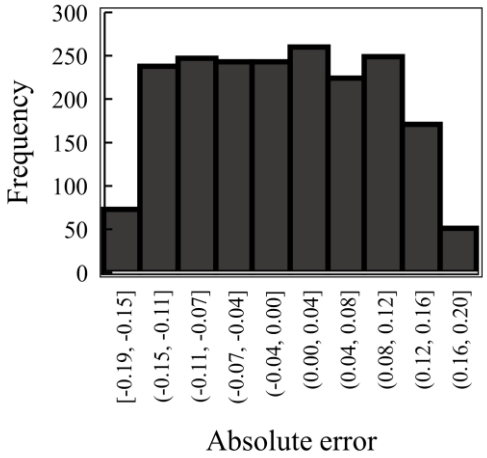
Frequency
Absolute error
300
250
200
150
100
50
0
[-0.19, -0.15]
(-0.15, -0.11]
(-0.11, -0.07]
(-0.07, -0.04]
(-0.04, 0.00]
(0.00, 0.04]
(0.04, 0.08]
(0.08, 0.12]
(0.12, 0.16]
(0.16, 0.20]

(b)

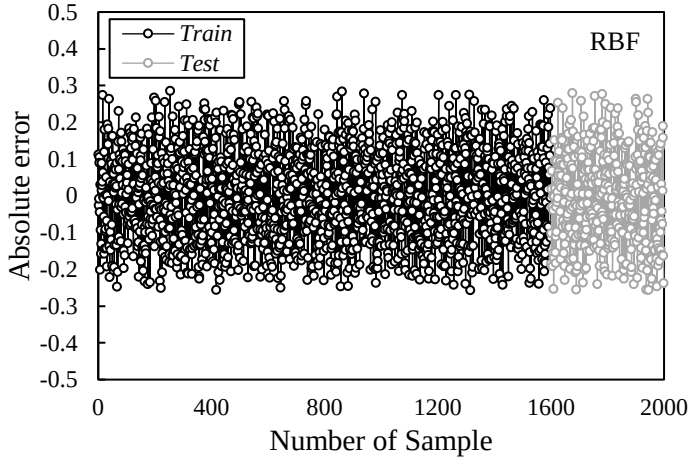
Train
Test
RBF
Absolute error
Number of Sample
0.5
0.4
0.3
0.2
0.1
0
-0.1
-0.2
-0.3
-0.4
-0.5
0
400
800
1200
1600
2000

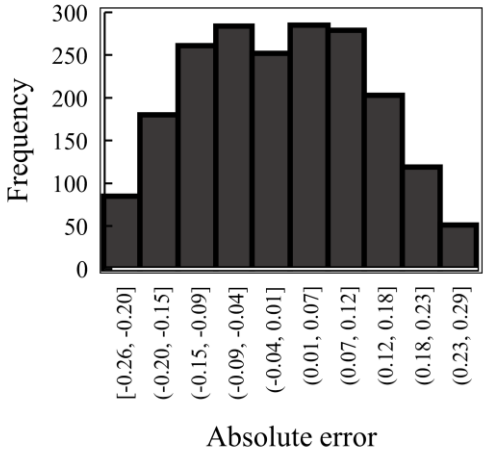
Frequency
Absolute error
300
250
200
150
100
50
0
[-0.26, -0.20]
(-0.20, -0.15]
(-0.15, -0.09]
(-0.09, -0.04]
(-0.04, 0.01]
(0.01, 0.07]
(0.07, 0.12]
(0.12, 0.18]
(0.18, 0.23]
(0.23, 0.29]

(c)

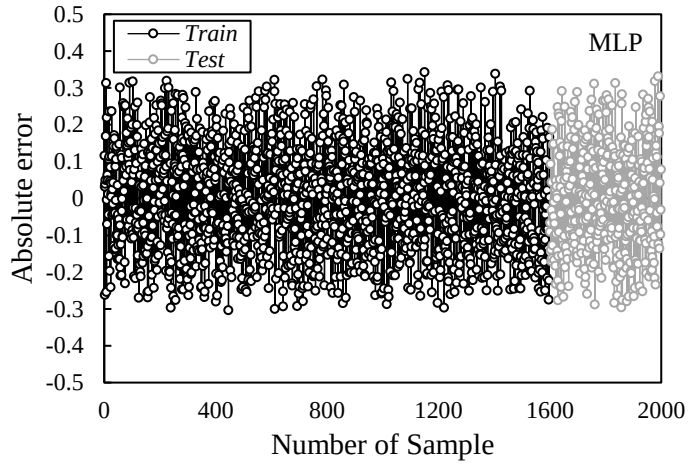
Train
Test
MLP
Absolute error
Number of Sample
0.5
0.4
0.3
0.2
0.1
0
-0.1
-0.2
-0.3
-0.4
-0.5
0
400
800
1200
1600
2000

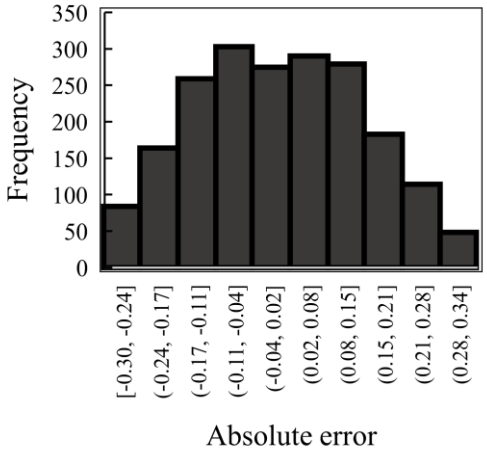
Frequency
Absolute error
350
300
250
200
150
100
50
0
[-0.30, -0.24]
(-0.24, -0.17]
(-0.17, -0.11]
(-0.11, -0.04]
(-0.04, 0.02]
(0.02, 0.08]
(0.08, 0.15]
(0.15, 0.21]
(0.21, 0.28]
(0.28, 0.34]

(d)

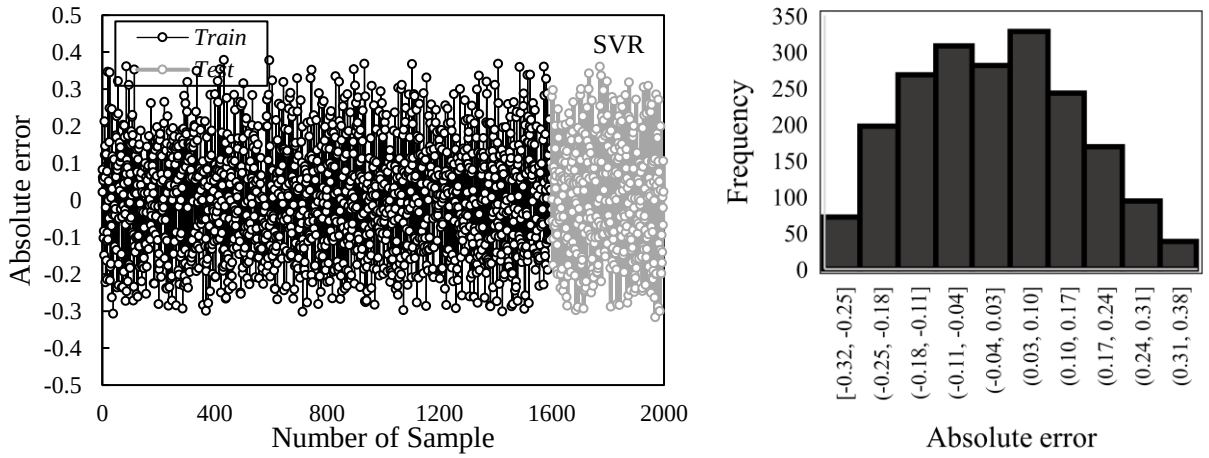

(e)

Figure 9.15: Error distribution and accuracy of various algorithms in terms of tensile stress prediction for a) DNN, b) ANFIS, c) RBF, d) MLP, and e) SVR

9.2.3. Shear stress under the saw-cutting region

Another significant characteristic that was measured in this area was the shear stress under the saw-cutting region. For this purpose, RBF, MLP, SVR, ANFIS, and DNN were employed to calculate the correlation between the predicted, numerical, and field tests. The outcomes are displayed in Figure 9.16. As a result, the coefficients of determination for DNN, ANFIS, and RBF were 0.9828, 0.9613, and 0.9584, correspondingly. Therefore, in order to shear stress under the saw-cutting region for both plain and fiber-reinforced concrete slabs, the SVR had the lowest agreement with the benchmark findings. Thus, the machine learning techniques utilized in this research could serve as effective tools to predict the shear stress under the saw-cutting region due to thermal gradient and environmental conditions. In this study, DNN, ANFIS, RBF, MLP, and SVR demonstrated good precision and efficiency in predicting the shear stress under the saw cutting region, with coefficients of determination (R^2) of 0.9828, 0.9613, 0.9584, 0.9279, and 0.9091, correspondingly. These findings demonstrated that the suggested algorithms—in particular, DNN—are very effective at predicting the shear stress under the saw-cutting region in rigid concrete airfield runways. Additionally, Figure 9.17 presents the error values and their spread for the employed ANNs. Therefore, the almost shear stress under the saw-cutting region can be

predicted using machine learning methods, particularly DNN, with sufficient precision for practical use. This could promote the use of ANNs going forward to predict the structural performance and various behaviors of airfield runways.

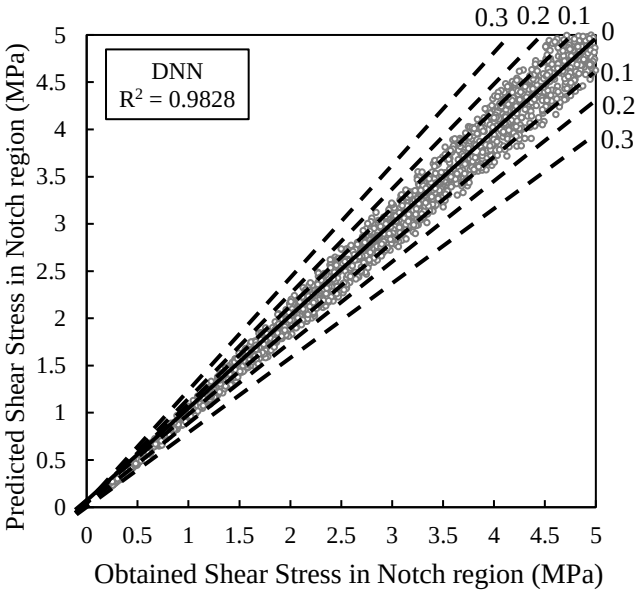

(a)

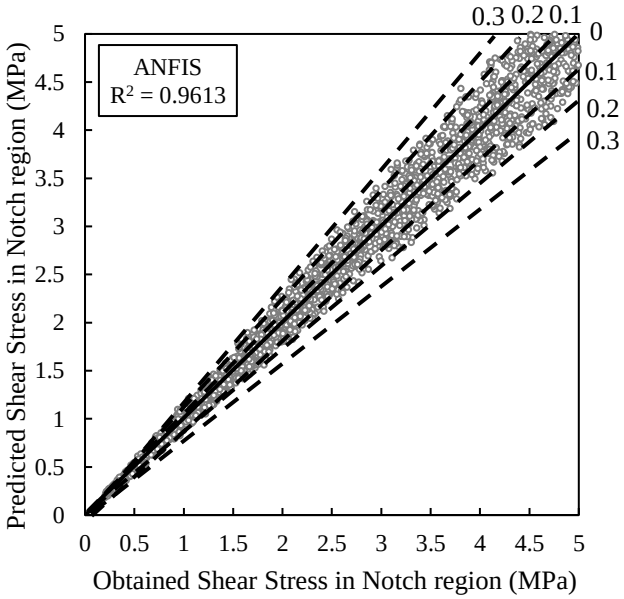

(b)

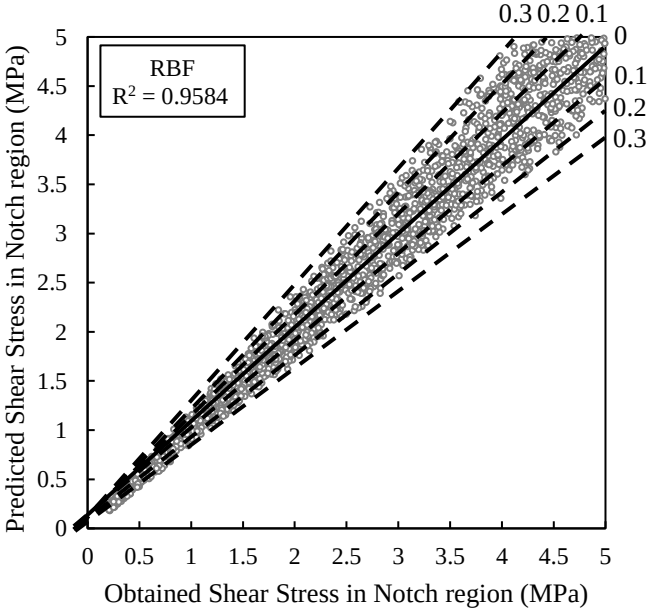

(c)

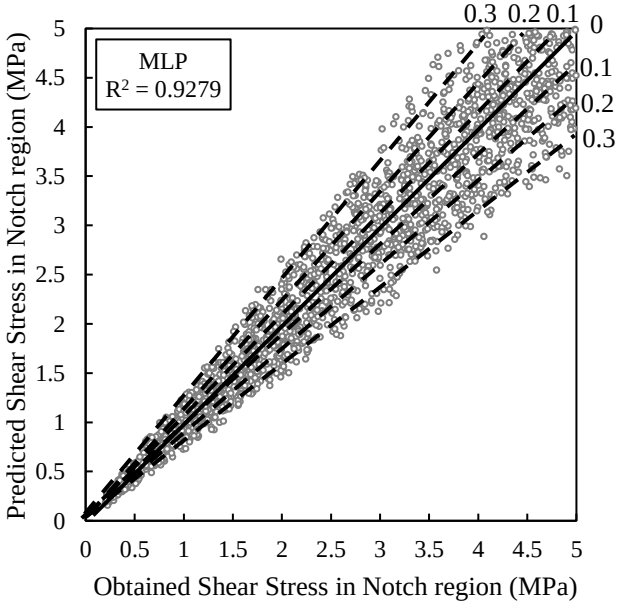

(d)

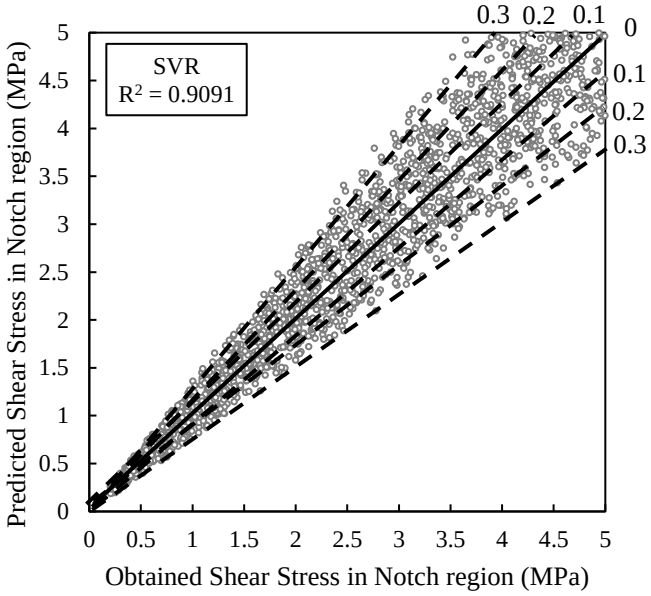

(e)

Figure 9.16: Shear stress prediction for both plain and fiber-reinforced concrete slabs using various algorithms a) DNN, b) ANFIS, c) RBF, d) MLP, and e) SVR

As seen in Figure 9.17, the obtained errors with MLP and SVR in the test phase did not significantly vary from one another, whereas the obtained error for SVR in the test phase was greater than other techniques. Therefore, the maximum errors varied from 0-0.09 and 0-0.13 for MLP and SVR, correspondingly which demonstrates the weak efficiency of these algorithms in predicting the shear stress under the saw-cutting region. In terms of predicting shear stress under the saw-cutting region, DNN performed well prediction performance with the lowest errors spanning from 0 to 0.02. Therefore, DNN, ANFIS, and RBF displayed the best prediction results. As a result, it can be concluded that DNN models performed better performance than other models and have the greatest accuracy and robustness. The DNN method outperforms ANN models and has smaller absolute percentage error ranges for predicting the shear stress under the saw-cutting region for both plain and fiber-reinforced rigid concrete airfield runways.

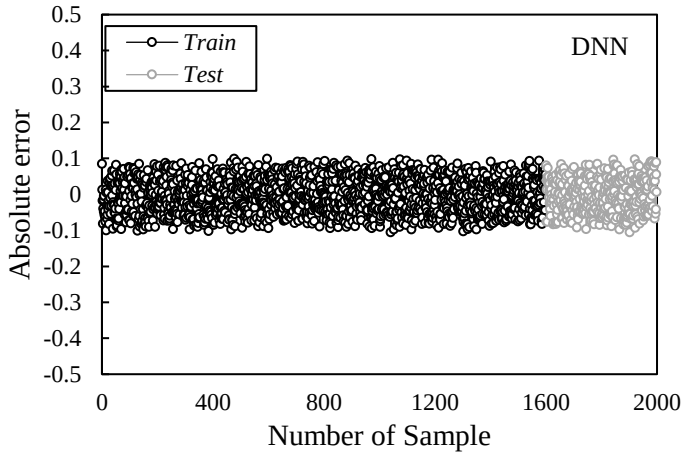
Train
Test
DNN
Absolute error
Number of Sample
0.5
0.4
0.3
0.2
0.1
0
-0.1
-0.2
-0.3
-0.4
-0.5
0
400
800
1200
1600
2000

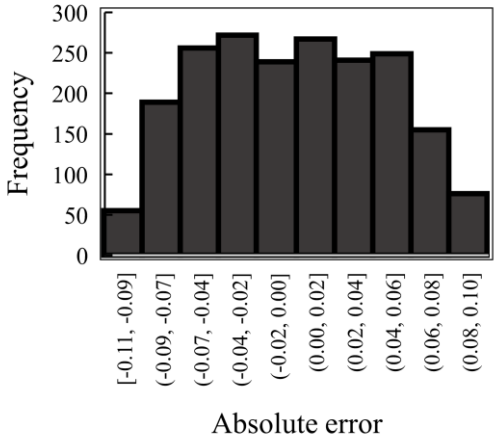
Frequency
Absolute error
300
250
200
150
100
50
0
[-0.11, -0.09]
(-0.09, -0.07]
(-0.07, -0.04]
(-0.04, -0.02]
(-0.02, 0.00]
(0.00, 0.02]
(0.02, 0.04]
(0.04, 0.06]
(0.06, 0.08]
(0.08, 0.10]

(a)

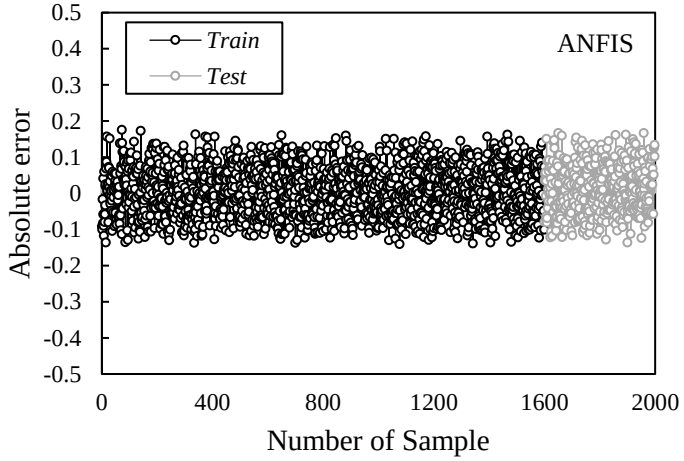
Train
Test
ANFIS
Absolute error
Number of Sample
0.5
0.4
0.3
0.2
0.1
0
-0.1
-0.2
-0.3
-0.4
-0.5
0
400
800
1200
1600
2000

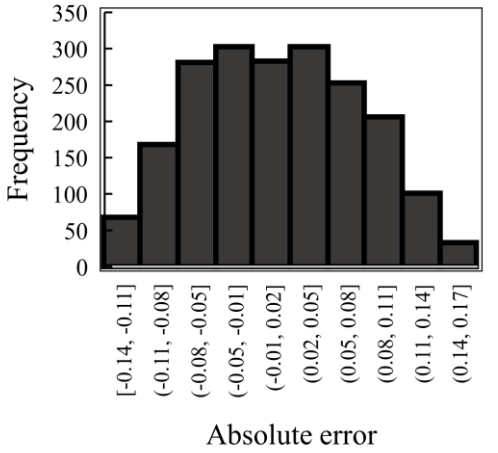
Frequency
Absolute error
350
300
250
200
150
100
50
0
[-0.14, -0.11]
(-0.11, -0.08]
(-0.08, -0.05]
(-0.05, -0.01]
(-0.01, 0.02]
(0.02, 0.05]
(0.05, 0.08]
(0.08, 0.11]
(0.11, 0.14]
(0.14, 0.17]

(b)

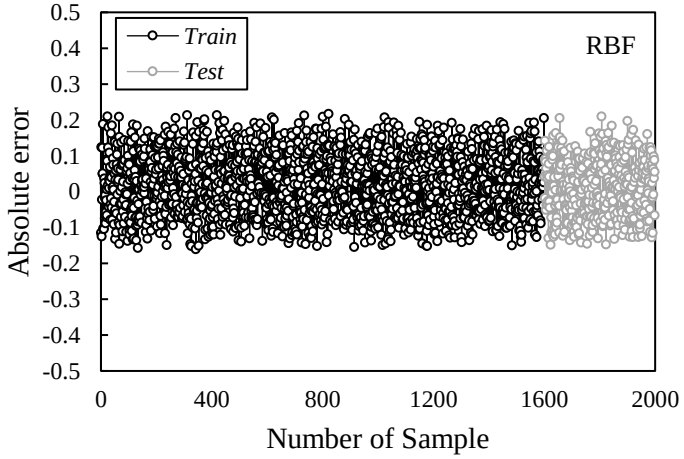
Train
Test
RBF
Absolute error
Number of Sample
0.5
0.4
0.3
0.2
0.1
0
-0.1
-0.2
-0.3
-0.4
-0.5
0
400
800
1200
1600
2000

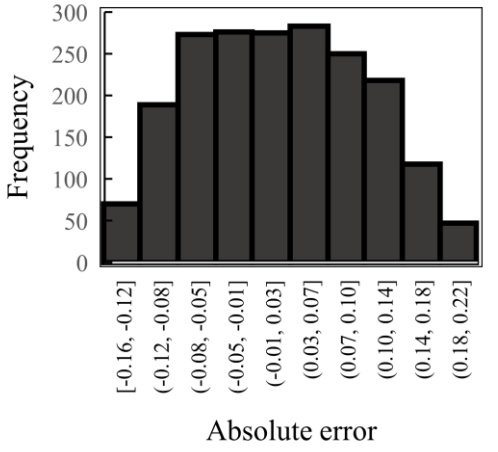
Frequency
Absolute error
300
250
200
150
100
50
0
[-0.16, -0.12]
(-0.12, -0.08]
(-0.08, -0.05]
(-0.05, -0.01]
(-0.01, 0.03]
(0.03, 0.07]
(0.07, 0.10]
(0.10, 0.14]
(0.14, 0.18]
(0.18, 0.22]

(c)

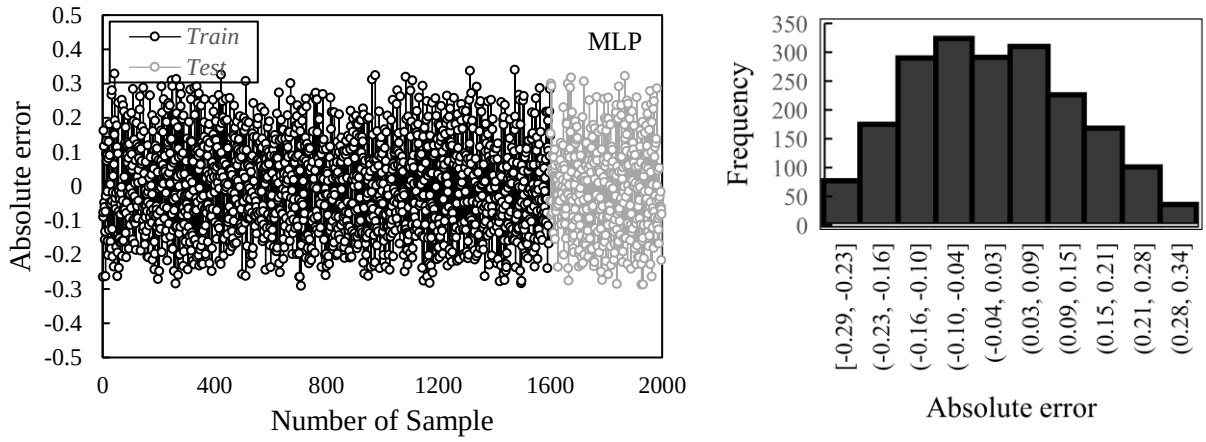

(d)

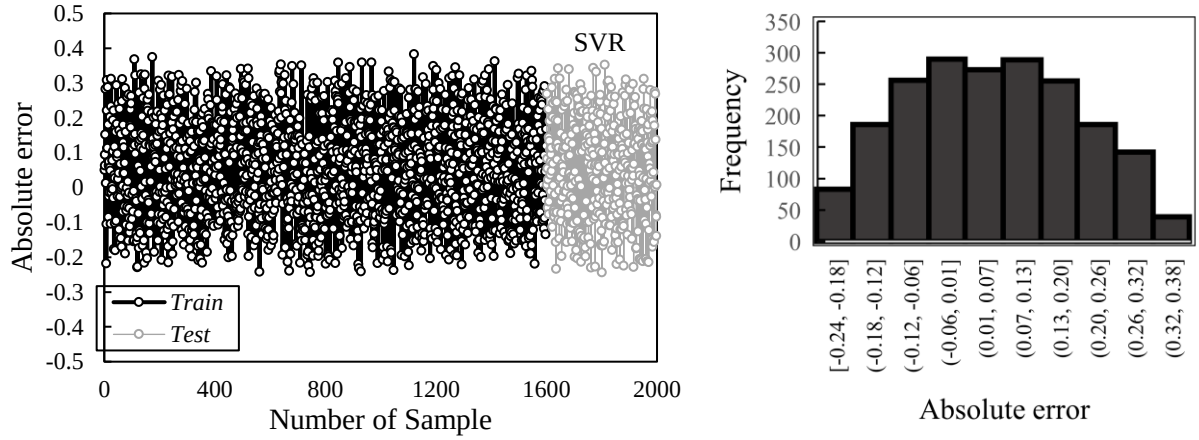

(e)

Figure 9.17: Error distribution and accuracy of various algorithms in terms of shear stress in the notch region prediction for a) DNN, b) ANFIS, c) RBF, d) MLP, and e) SVR

9.2.4. Bond resistance of dowel bars

Another significant characteristic that was measured in this study was the bond resistance of dowel bars. The outcomes are displayed in Figure 9.18. Regarding the achieved results, the coefficients of determination (R^2) in terms of the bond resistance of dowel bars prediction for DNN, ANFIS, RBF, MLP, and SVR were 0.9801, 0.9647, 0.9417, 0.9180, and 0.8872, correspondingly. Therefore, to predict the bond resistance of dowel bars in rigid concrete airfield runways, the SVR had the lowest agreement with the benchmark results. In this study, DNN, ANFIS, and RBF demonstrated good precision and efficiency in predicting the bond resistance of dowel bars. These findings demonstrated that the suggested algorithms—in particular, DNN—are very effective at

predicting the bond resistance of dowel bars in rigid concrete airfield runways. Additionally, Figure 9.19 presents the error values and their spread for the employed ANNs. Therefore, the nearly physical bond resistance of dowel bars can be prophesied using machine learning methods, particularly DNN, with sufficient precision for applied practice.

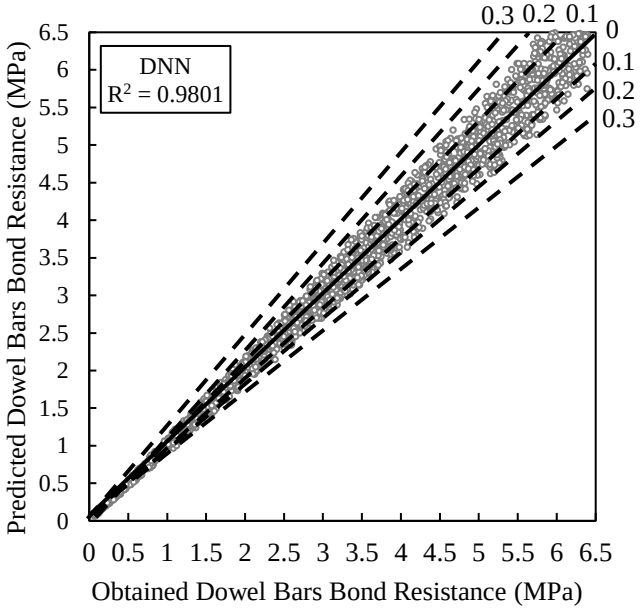

(a)

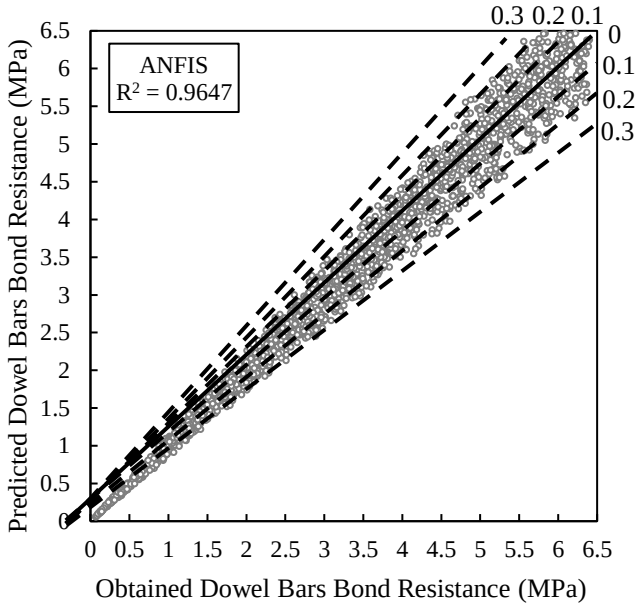

(b)

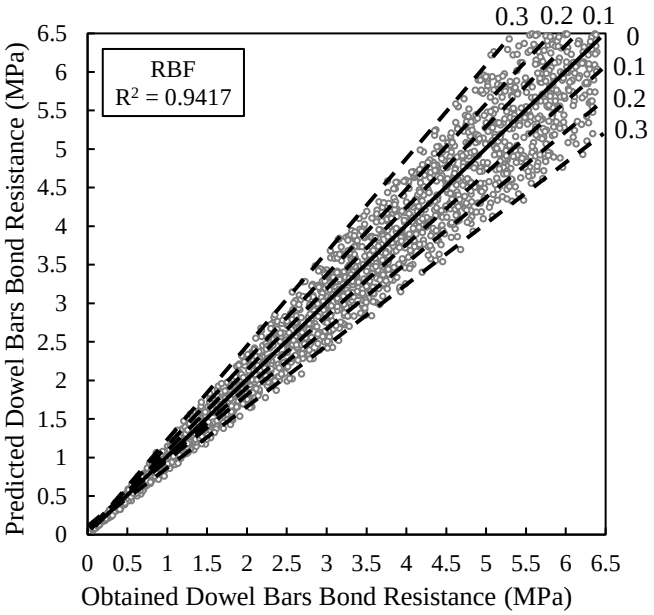

(c)

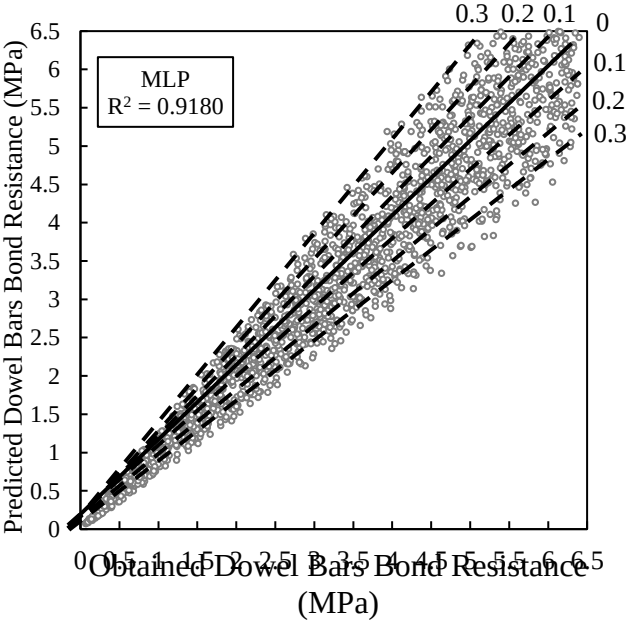

(d)

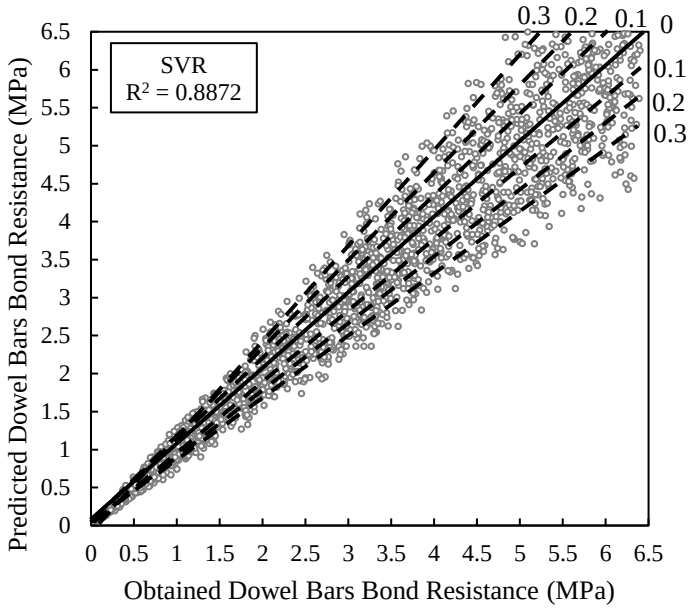

(e)

Figure 9.18: Dowel bars bond resistance prediction for both plain and fiber-reinforced concrete slabs using various algorithms a) DNN, b) ANFIS, c) RBF, d) MLP, and e) SVR

As seen in Figure 9.19, the obtained errors with MLP and SVR in the test phase did not significantly vary from one another, whereas the obtained error for ANFIS in the training phase was greater than that of DNN. Consequently, the highest errors for MLP and SVR were -0.04-0.02 demonstrating the effectiveness of these algorithms in predicting the dowel bars' bond resistance. The DNN, ANFIS, and RBF, therefore, displayed the best results in terms of dowel bars bond resistance prediction. Alternatively, DNN and ANFIS had the lowest error distribution, with error frequencies spanning from 0 to 0.04 and 0 to 0.03, respectively. The findings, which take into account the effectiveness of the DNN and ANFIS approaches, are shown in Figures 9.19a and b to illustrate the frequency of error values in less than 0.2 intervals. As a result, it can be concluded that ANN models, particularly DNN, perform a good prediction performance in terms of dowel bars bond resistance prediction with an acceptable greatest accuracy and robustness. The DNN method outperforms ANN models and has smaller absolute percentage error ranges for predicting

the dowel bars bond resistance in both plain and fiber-reinforced concrete airfield runways under the influence of thermal gradient and environmental temperature.

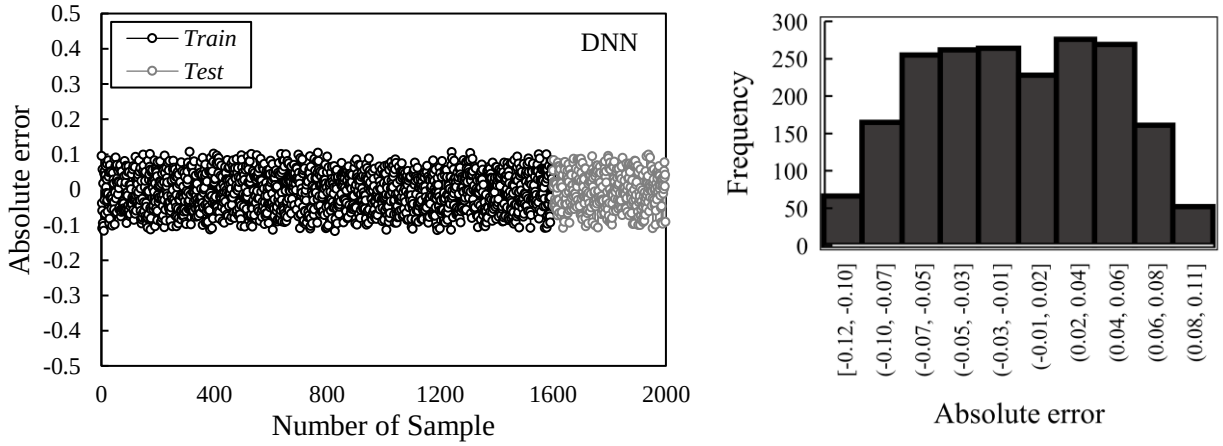

(a)

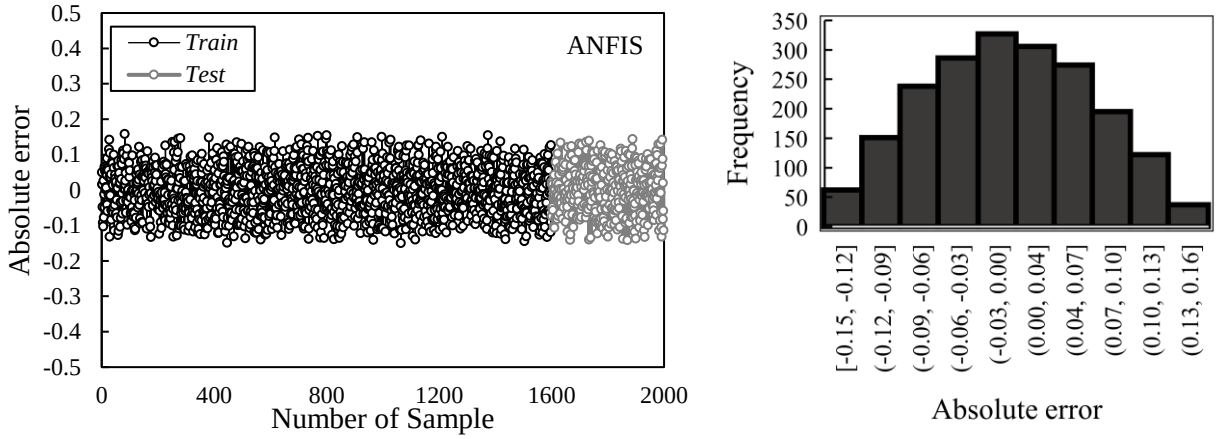

(b)

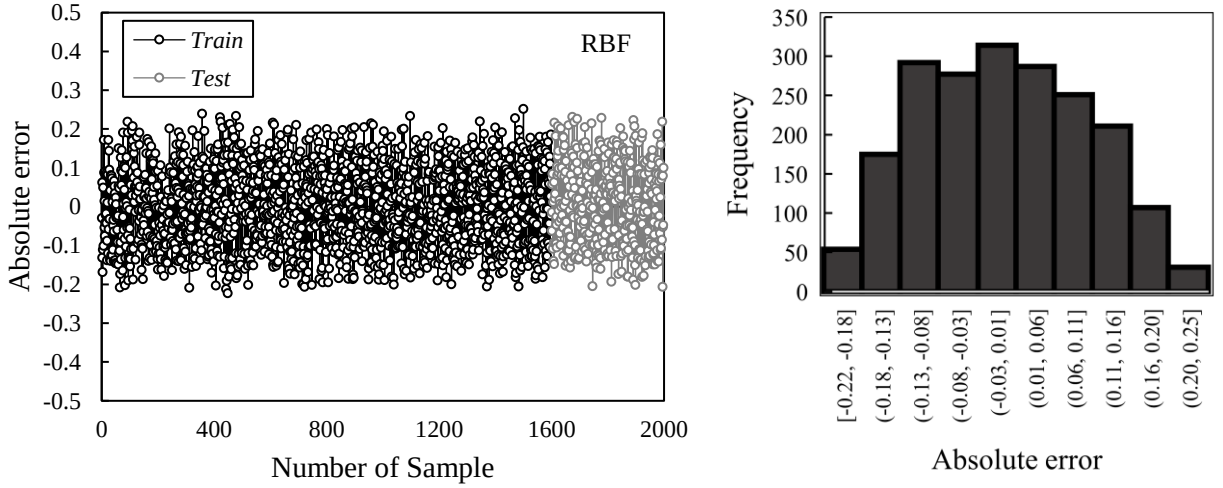

(c)

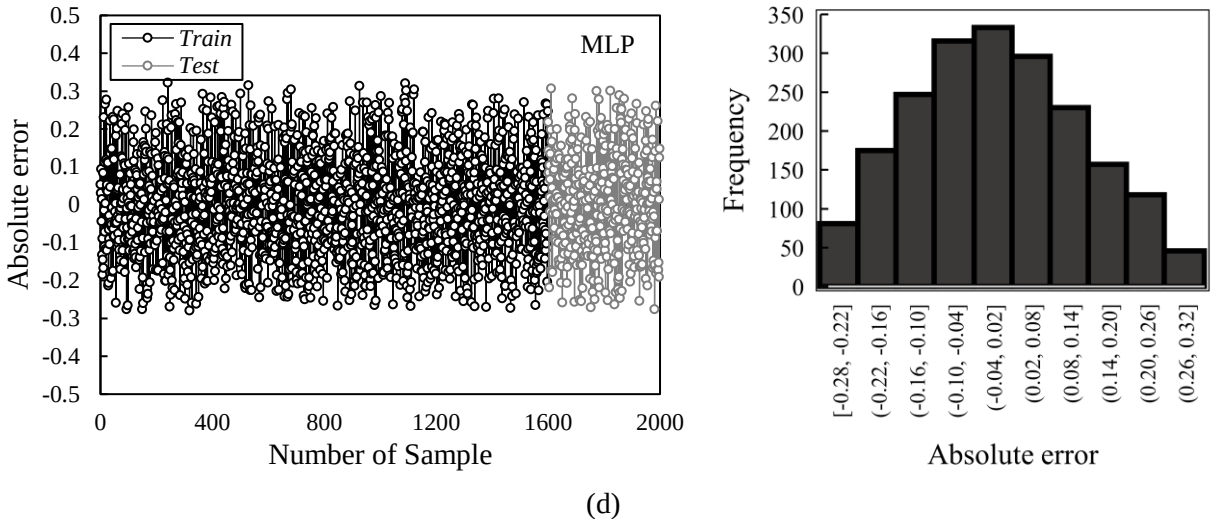

(d)

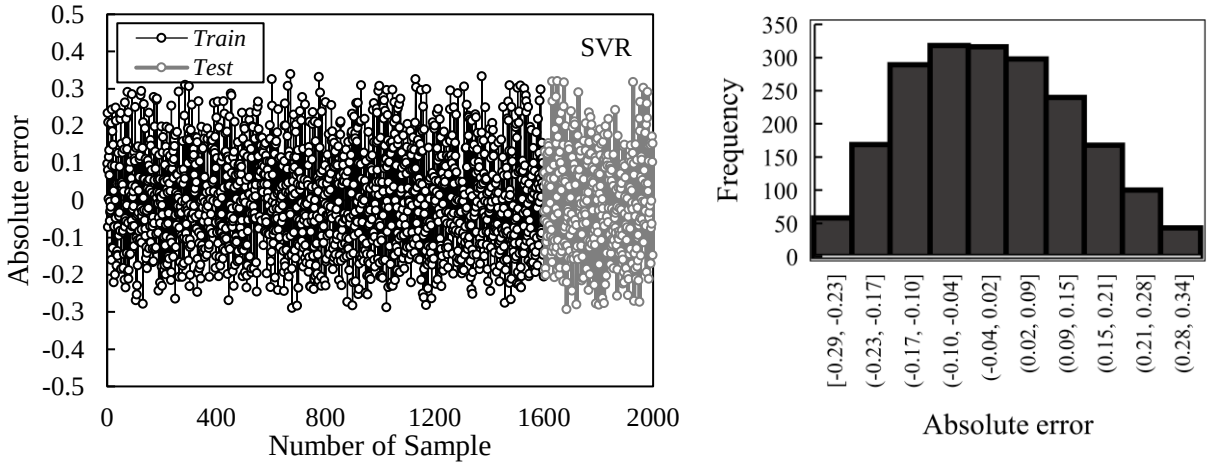

(e)

Figure 9.19: Error distribution and accuracy of various algorithms in terms of dowel bars bond resistance prediction for a) DNN, b) ANFIS, c) RBF, d) MLP, and e) SVR

As was already stated, various techniques were employed in this study to evaluate the effectiveness of the presented algorithms. The results are shown in Table 9.2. There, DNN achieved the greatest accuracy and lowest error. As a result, the DNN technique yielded the following values of MSE, RMSE, MAE, MAPE, NMSE, and NMAE: 0.7329, 0.8427, 0.5941, 1.3729%, 1.9948%, 5.2876%, respectively, in terms of out-of-plane deformation. Then, in terms of tensile stress prediction for the MAPE, NMSE, and NMAE, respectively, the ANFIS displayed an adequate prediction with values of 1.3484%, 1.9592%, and 5.1934%. While the SVR algorithm

showed the lowest accuracy for MSE, RMSE, MAE, MAPE, NMSE, and NMAE with 1.8204, 2.0931, 0.5472, 1.2646%, 1.8374%, and 4.8705%, correspondingly. Similar to this, DNN effectively predicted the shear stress in the notch region. Thus, for DNN in terms of shear stress in notch region forecast, the values of MSE, RMSE, MAE, MAPE, NMSE, and NMAE were achieved by approximately 0.6824, 0.7846, 0.5981, 1.3823%, 2.0085% and 5.3239%, correspondingly. Similar results were obtained for the forecast of the dowel bars bond resistance prediction by DNN, ANFIS, and RBF with MAPE values of 1.3785%, 1.3569%, and 1.3245%, respectively. Additionally, when SVR was used, the modulus of elasticity estimation accuracy was found to be the lowest, resulting in MSE, RMSE, MAE, MAPE, NMSE, and NMAE values that, respectively, were achieved by about 1.8637, 2.1429, 0.5399, 1.2478%, 1.8131%, and 4.8061%.

Table 9.2: Results of curling behavior prediction for both plain and fiber-reinforced concrete slabs using the common effectiveness assessment techniques

Parameter	Method	R	R^2	MSE	RMSE	MAE	MAPE (%)	NMSE (%)	NMAE (%)
Out-of-Plane Deformation	DNN	0.9880	0.9761	0.7329	0.8427	0.5941	1.3729	1.9948	5.2876
	ANFIS	0.9769	0.9543	0.9288	1.0679	0.5808	1.3422	1.9502	5.1695
	RBF	0.9712	0.9432	1.2234	1.4067	0.5742	1.3266	1.9275	5.1094
	MLP	0.9496	0.9018	1.7922	2.0607	0.5488	1.2684	1.8429	4.8851
	SVR	0.9403	0.8842	1.9246	2.2129	0.5381	1.2436	1.807	4.7898
Tensile Stress	DNN	0.9907	0.9814	0.7247	0.8333	0.5973	1.3803	2.0056	5.3163
	ANFIS	0.9791	0.9587	0.9146	1.0516	0.5835	1.3484	1.9592	5.1934
	RBF	0.9751	0.9509	1.1784	1.3549	0.5787	1.3374	1.9433	5.1511
	MLP	0.9554	0.9127	1.6004	1.8401	0.5555	1.2837	1.8652	4.9442
	SVR	0.9482	0.8991	1.8204	2.0931	0.5472	1.2646	1.8374	4.8705
Shear Stress in Notch Region	DNN	0.9914	0.9828	0.6824	0.7846	0.5981	1.3823	2.0085	5.3239
	ANFIS	0.9805	0.9613	0.9019	1.0371	0.585	1.3521	1.9645	5.2075
	RBF	0.9790	0.9584	1.1185	1.2861	0.5833	1.3489	1.9586	5.1917
	MLP	0.9633	0.9279	1.5387	1.7692	0.5647	1.3051	1.8963	5.0265
	SVR	0.9535	0.9091	1.6480	1.8949	0.5533	1.2786	1.8578	4.9247
Dowel Bars Bond Resistance	DNN	0.9900	0.9801	0.7308	0.8403	0.5965	1.3785	2.0029	5.3093
	ANFIS	0.9822	0.9647	0.8227	0.9459	0.5871	1.3569	1.9715	5.2259
	RBF	0.9704	0.9417	1.4259	1.6395	0.5731	1.3245	1.9245	5.1013
	MLP	0.9581	0.9180	1.5846	1.8222	0.5587	1.2912	1.8759	4.9729
	SVR	0.9419	0.8872	1.8637	2.1429	0.5399	1.2478	1.8131	4.8061

Regarding Figure 9.20, the DNN algorithm in this research had the highest correlation coefficient (0.99) and the lowest standard deviation of roughly 0.04, showing high accuracy to predict the out-of-plane deformation, tensile stress, shear stress in notch region and dowel bars bond resistance for both plain and fiber-reinforced concrete airfield runways. The presented results of DNN and ANFIS algorithms with high correlation coefficients and low standard deviation could be used as appropriate tools to predict the thermal characteristics of both plain and fiber-incorporated rigid concrete airfield runways. In contrast, the MLP and SVR models had lower prediction performance, with R-values of 0.9496 and 0.9403 and standard deviations of 0.26 and 0.31 in terms of out-of-plane prediction performance, respectively. In addition, compared to all ANN models, DNN could be employed as a useful technique to predict the out-of-plane deformation, tensile stress, shear stress, and dowel bars bond resistance with correlation coefficient (R) and standard deviation of 0.9880, 0.9907, 0.9914 and 0.9900, respectively.

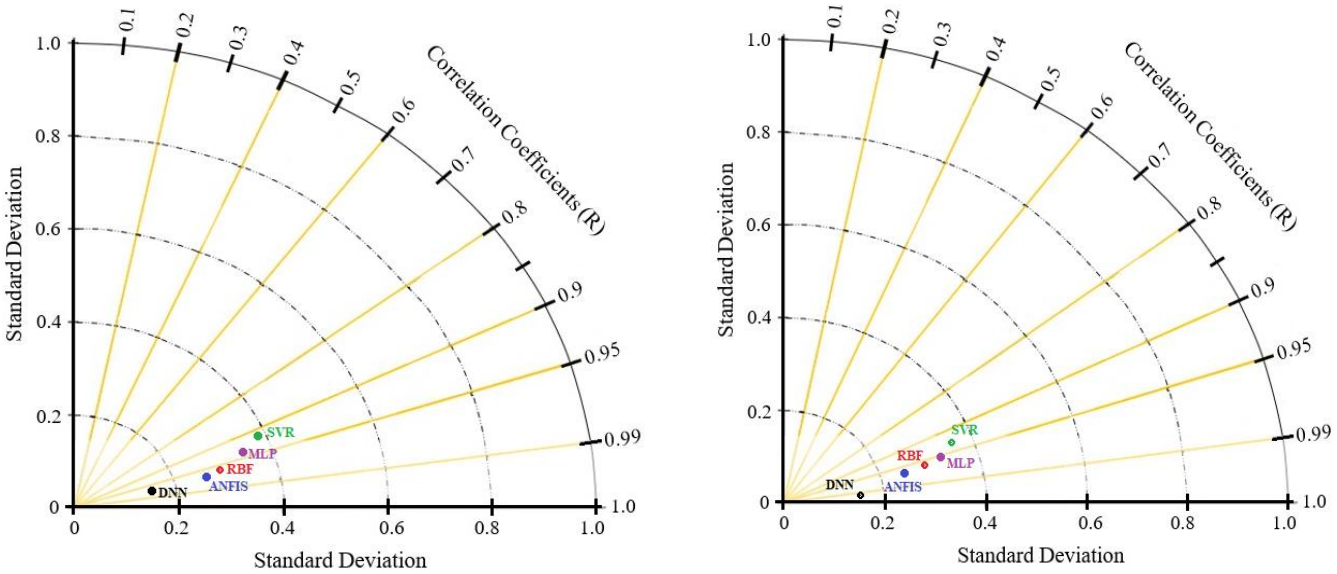

(a) (b)

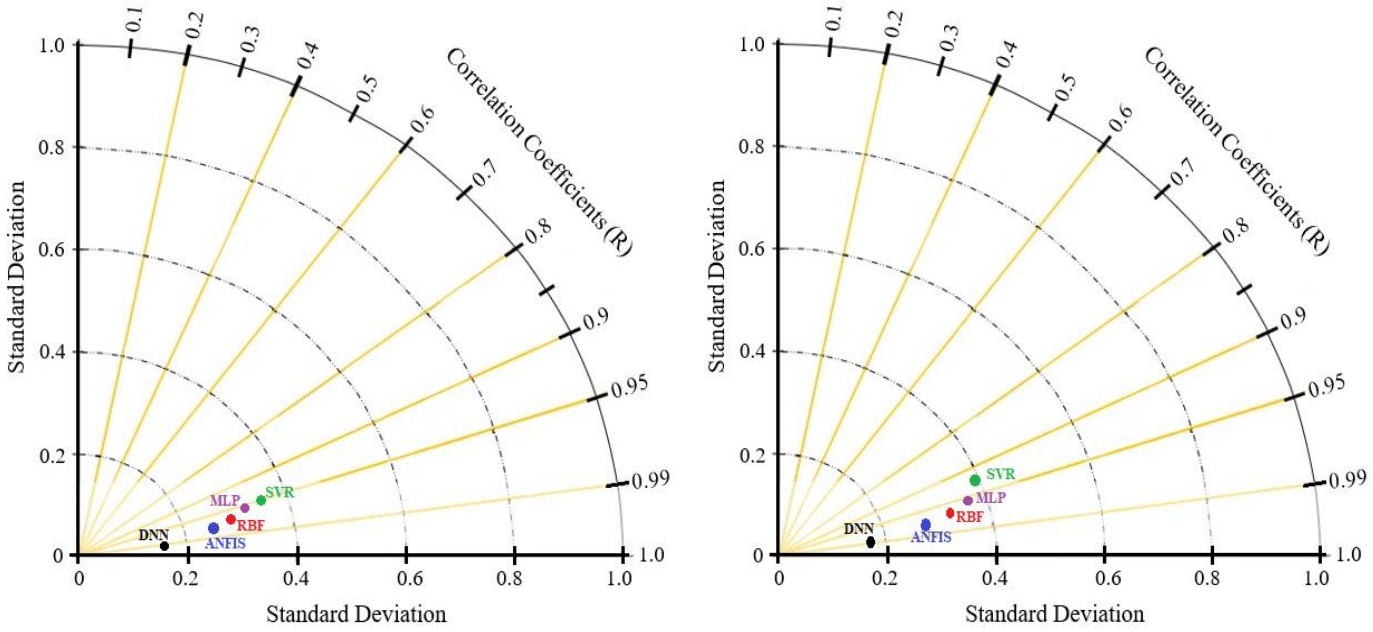

(c) (d)

Figure 9.20: out-of-plane deformation, b) tensile stress, c) shear stress in notch region, and d) dowel bars bond resistance

9.3. SUMMARY & CONNECTION WITH THE SUBSEQUENT CHAPTER

In this chapter, various prediction algorithms are developed to predict the thermal and curling behaviors of rigid concrete slabs based on previous Chapters' results. The accuracy of models was also measured to show their robustness. Five distinct machine learning models—MLP, RBF, SVR, ANFIS, and DNN—were employed. For this aim, PYTHON coding software was utilized to predict the stress and deformation of rigid concrete slabs. As a result, the consequences and formulation provided in this Chapter could be employed by companies, agencies, and DOTs to predict their future airfield runways' performance considering all geometric and material characteristics. However, it is not possible to make accurate opinions and engineering judgments in engineering sciences. Therefore, risk analysis plays an effective role in considering the probability of failure. This issue makes it possible to always consider a safety margin in the construction, which increases the reliability of the structures. For this aim, the results of previous

Chapters as well as other previous theoretical models have been taken into account, and the probability of failure is assessed using the Rackwitz-Fiessler method in the next Chapter. The results of this task might be used by many businesses to develop their designing software, and DOTs could use them to construct robust concrete slabs that better account for improving the curling and thermal stresses of rigid concrete slabs. Figure 9.21 provides a connection with the subsequent chapter overview.

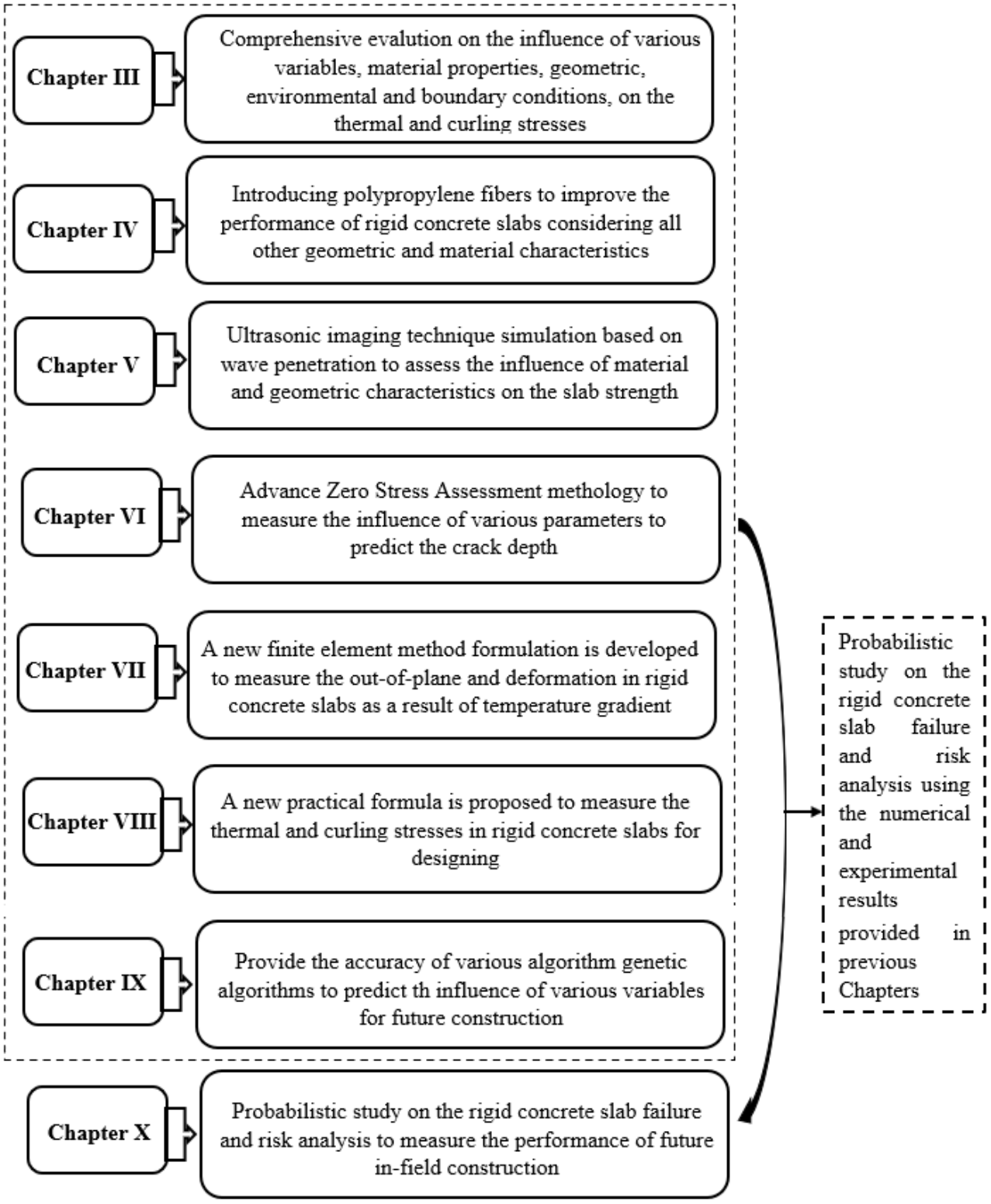

Figure 9.21: Overview of the connection between previous Chapters and Chapter X

CHAPTER X

PROBABILISTIC STUDY ON THE RIGID CONCRETE SLAB FAILURE AND RISK ANALYSIS

10.1. INTRODUCTION

This chapter's main goal is to present a risk analysis and life cycle for rigid concrete slabs considering a wide range of effective variables. The preceding section of this chapter is followed by probabilistic techniques using the experimental and numerical results of current research collected from previous chapters to identify the effect of materials properties, geometric characteristics, environmental conditions as well as boundary conditions on the possible failure of rigid concrete slabs for better future construction. The results of this task might be used by many businesses to develop their designing software, and DOTs could use them to construct robust concrete slabs that better account for improving the curling and thermal stresses of rigid concrete slabs.

10.1.1. Organization of the Chapter

This chapter consists of five main sections. Subsequent to the introductory section, Section 2 provides information associated with risk analysis and life cycle techniques that could be utilized to identify the performance of slabs due to thermal and curling stresses. Section 3 discusses the probabilistic and risk analysis methods. These techniques could be utilized as beneficial tools to predict the failure probability in future cast rigid concrete slabs. Then, the main results of this study are presented and discussed to show the various variables that affect failure in rigid concrete

runways. Ultimately, a summary of this section will be presented to highlight the importance of doing probabilistic study and risk analysis in civil engineering constructions.

10.2. RELIABILITY ANALYSIS FOR COMPLEX SYSTEMS

One of the most important steps of design, according to most systems engineering techniques, is integration. Integration is necessary even in the initial phases of design. The system is viewed as a whole at these earlier design stages; therefore, the performance analysis's scope is the broadest. But because technical knowledge and analytical tools are typically produced along highly specialized disciplinary lines (e.g., thermal), many theoretical design techniques require a major integration of various disciplinary studies. The ensuing interdisciplinary analysis uses a "bottom-up" methodology but is used in practically all design phases. Additionally, integration along different system architectures follows the same fundamental procedure as the integration of discipline design or analysis tools. Risk analysis and reliability are beneficial techniques being used for aerospace and civil system design. In the literature, many formulations for systems performance evaluation have been created (Sobieszczanski-Sobieski et al, 2000). The kind of interdisciplinary analytical formulation used has a big impact on the amount of processing needed for probabilistic evaluation and risk analysis. The computing cost of wrapping one iterative process (optimization) around another is a particular problem for complex systems. Iterative convergence loops are required in this situation to ensure transdisciplinary viability (i.e., consistency of disciplinary responses throughout the system). The complex systems convergence loops are nested inside the loops for probabilistic analysis and/or risk analysis in a traditional or fully-integrated way. For the majority of high-quality studies, the resulting computing effort is unacceptable. Therefore, employing techniques that take use of a dispersed formulation of complex system analysis, this work investigates alternatives to the fully-integrated approach. In the literature,

distributed formulations for dependability analysis have previously been put out (Du and Chen, 2002).

10.2.1. Complex system analysis

Complex systems analysis comprises integrating individual analyses, which share input and output data. Integrating independent studies that share input and output data is known as multidisciplinary analysis. The simultaneous resolution of all disciplinary analyses is necessary for a "feasible" complex system. Interdisciplinary coupling for analyses carried out in each order might take either a feedforward or feedback form. The output of an earlier analysis feeds "forward" as the input of a later analysis in a feed-forward connection. When a linked analysis is required before the analysis that will determine its input, feedback will occur. Iteration is necessary for systems with feedback coupling to maintain consistency of responses, necessitating several "runs" of a single set of studies. Therefore, a sample of a two-discipline complex system is provided in Figure 10.1.

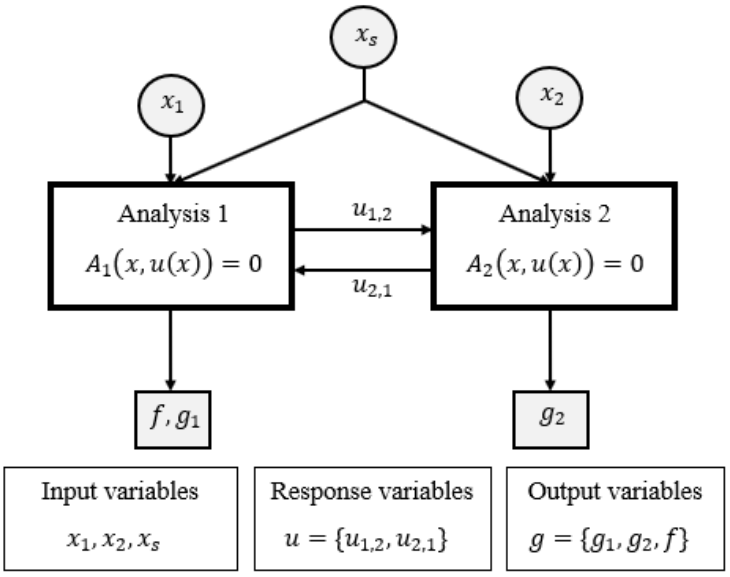

Figure 10.1: Sample of a two-discipline complex system

Coupled behavior in a two-discipline complex system is seen in Figure 10.1. Here, the local input variables for analyses 1 and 2 are denoted by x_1 and x_2, respectively, whereas the common input variables for both analyses are denoted by x_s. Response factors (variables $u_{1,2}$ and $u_{2,1}$) link the two studies (defined such that $u_{i,j}$ is an output of analysis i and an input to analysis j). The three output variables of the system are f, g_1, and g_2. In the context of probabilistic evaluation and risk analysis, f may stand in for a system objective, while g_1, and g_2 might stand in for reliability analysis limit states. Therefore, it is possible to determine the multidisciplinary feasibility by concurrently solving a series of non-linear equations that reflect disciplinary analyses, as provided in Equation (10.1).

$$A_i\big(x, u(x)\big) = 0 \quad and\ i = \text{ number of disciplines in the system} \tag{10.1}$$

It can be observed that a feedback condition requires an unknown variable (either $u_{1,2}$ or $u_{2,1}$) regardless of whether an analysis is conducted initially. Fixed-point iteration is frequently used to solve systems with feedback coupling. The studies from which they are produced are utilized to update the initial set of assumed values for the unknown variables in this procedure. With the new values, the analyses are run once more, and the procedure is repeated until convergence is achieved. The starting point affects the efficiency of fixed-point iteration, and many systems will display a diverging pattern at some starting points.

10.2.2. Implications for Reliability Analysis

The goal of a complex system reliability evaluation is to forecast how a sophisticated, designed system will behave. This measure of performance uncertainty characterizes the reliability of the system, and these predictions are produced with a certain amount of uncertainty. Using fixed-point iteration for interdisciplinary analysis inside probabilistic analysis algorithms may not be effective

for connected systems. Figure 10.2 illustrates this impact. Obtaining gradient data, which is often necessary for the more effective analytical approximation approaches, is another challenge. The fixed-point iteration procedure for convergence would have to be performed for each variable if a finite difference technique is employed.

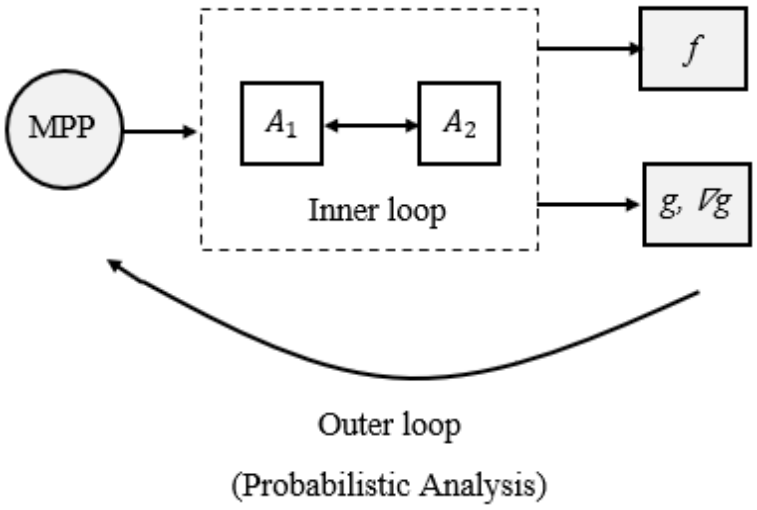

Figure 10.2: Statistical evaluation of systems using feedback

To further prevent needless fixed-point iterations, one may choose less strict convergence criteria, although this might add "noise" that can interfere with finite difference estimates for the gradient. As a result, in such circumstances, probabilistic analysis algorithms that only treat the system analysis as a black box may even fail to converge. Mahadevan and Gantt (2005) demonstrated that a conventional probabilistic strategy did not converge for many starting points and needed over 10,000 function evaluations for those starting locations that did lead to convergence.

10.3. RISK ANALYSIS AND UNCERTAINTY ASSESSMENT IN RIGID CONCRETE SLABS DESIGN

It is common knowledge that there is uncertainty practically in pavement designs. As seen in Figure 10.3, it is practical to break down uncertainty in a rigid concrete slab as per its life cycle. Most inputs have variances, which can be divided into three categories: traffic, climate, and materials. Modeling simplification and compute truncation are the causes of design uncertainty. The way that machines work and the construction process both introduce variation. Finally, through model calibration, the variability in performance evaluation is transferred back to the design model. To improve the pavement design process, uncertainty needs to be properly examined and measured.

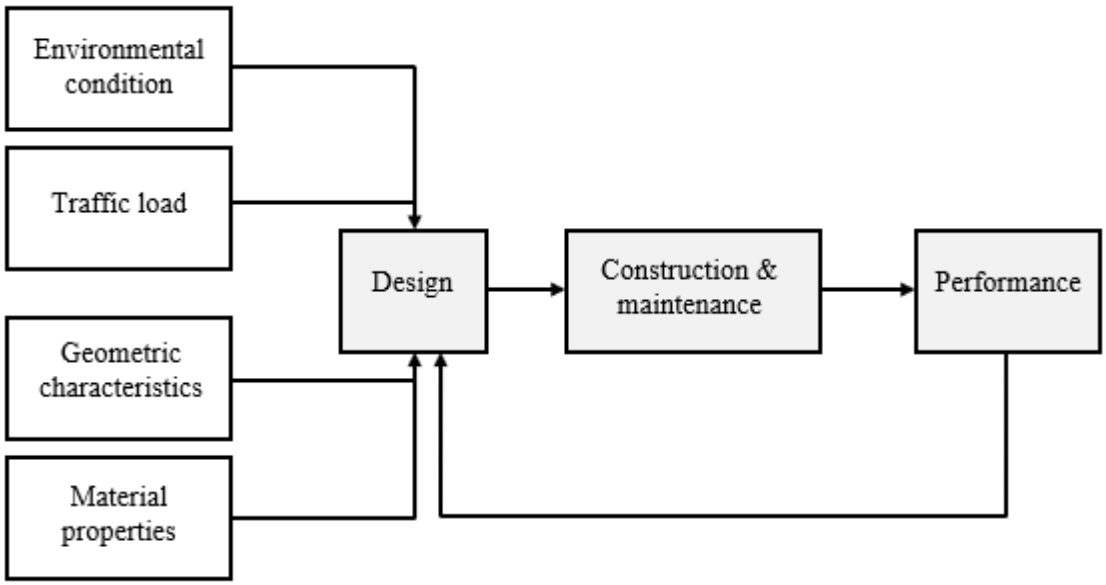

Figure 10.3: Uncertainty in a slab's life-cycle

10.3.1. Terminology

First, a closer examination of a few keywords is warranted. The Merriam-Webster dictionary and Von Quintus et al. served as the foundation for the definitions below (16):

- Accurateness: A prediction's accuracy refers to how well it matches the observed or "real" value. Accuracy and bias are both included in the definition of accurateness.
- Bias: An phenomenon that prevents forecasts from accurately reproducing "real world" observations by systematically distorting them, as opposed to a random mistake, which may distort sometimes but balances out on average. A "biased" prediction model considerably overpredicts or underpredicts observed discomfort or roughness.
- Precision: Precision is the capacity of a model to repeatedly produce estimates that have a strong correlation with the measured data. Regardless of whether they are continuously higher or lower, they have a significant correlation with observed values.
- Risk: Someone or something that produces or implies a hazard is said to be at risk.
- Reliability: The consistency with which an experiment, test, or measurement process produces the same findings after several tries are known as reliability.
- Uncertainty: Uncertainty is a term that describes the character or state of uncertainty including design, construction, upkeep, traffic, the environment, and materials performance
- Variation: noun, the degree or range of variation in anything.
- Variance: noun, change in something as a square of standard deviation (in statistics).
- Variability: variability is a term that refers to the condition or quality of being variable.

10.3.2. Uncertainty Taxonomy

Huang (1993) divided the causes of uncertainty for pavement design into three categories: variation resulting from design parameters, poor fit of the design equation, and unexplained variance. The uncertainty has four components, according to Von Quintus (2009), namely measurement error, input error, model error, and pure error. The sources of variability in this study were broken down into the four categories listed below.

10.3.2.1. Reducible uncertainty of tests and construction

Reducible uncertainty of tests and construction covers the statistical fluctuation connected to the quantity of samples used for the material characterization tests and the evaluation of rigid concrete slab performance. Due to the restricted number of samples from quarries that are used for sieve analysis, for instance, aggregates blended from several quarries range from the intended gradation. At this part, level 3 includes data from catalogues or common values, which introduces more uncertainty into the design process than level 1 inputs, which need site-specific testing. The concrete mixture plant has quality variances as well. Since it has long been argued that bad construction is to blame for poor runways, the building process is usually brought up when discussing slab quality and performance.

10.3.2.2. Reducible uncertainty of simplification and assumptions

If more time and budget are required, it may be able to decrease this kind of uncertainty by increasing the sample size. Equipment advancement also helps to lessen some ambiguity. For instance, pavement cores can be drilled to measure layer thickness. The use of Ground Penetrating Radar (GPR), which can deliver a continuous profile of the pavement structure, increases the accuracy of layer thickness. The same holds true for buildings. Construction-related uncertainty will be reduced through the use of modern machinery and tools, such as intelligent compaction and material transport trucks.

10.3.2.3. Reducible uncertainty of materials

Pavement design guides are a skewed representation of reality due to the system's complexity and/or the impossibility of employing current technology. In other words, even if we know how to accomplish it, a flawless model cannot be created at this time. For example, uneven tire pressure

on a slab has been commonly employed in pavement design, despite uneven distribution. Additionally, even though the majority of a material's characteristics are nonlinear, a linear elastic model was incorporated into the present design guide, and complicated finite element analysis may be used to do nonlinear analysis as discussed in Chapter III. Moreover, the assumptions of homogenous layers and complete contact between layers were viewed as a condensed version of reality. It is anticipated that as computer technology advances and an original era of computing emerges, the uncertainty brought on by these oversimplifications and presumptions will diminish. Material uncertainty cannot be reduced. Materials' characteristics and behaviors, as well as the runway system as a whole, have intrinsic irregularities. Rigid concrete runway constructions are exceptional in that a design segment is built across a considerable distance.

10.3.2.4. Reducible uncertainty of knowledge and experiences

As a result, a probabilistic design is necessary to enhance the deterministic design. Unknown uncertainty brought on by ignorance. This indicates, however, that a straightforward question—why certain slab portions function better than others—had not been adequately understood. The paving system is intricate. For example, a clear correlation between surface roughness and the dynamic effect of tires on skin has yet to be established. On the mechanism of top-down cracking due to curling and thermal stresses, there is still disagreement. Another difficulty is figuring out how to translate micro-level anguish into macro-level harm. All these flaws should be taken into account for a probability-based design.

10.3.3. Risk analysis

According to Webster's dictionary, a risk is someone, something, or both that indicates or causes a danger. According to this viewpoint, hazards that might threaten a good rigid concrete slab design

include ambiguity and variance in runway design. A risk analysis of the rigid concrete slab design process is to be done in this chapter. A crucial public asset, the rigid concrete slab has to be carefully planned, built, and maintained. The task of creating more effective and affordable pavements has propelled pavement engineering ahead. The Federal Highway Administration (FHWA) reports that the proportion of pavements with high ride quality has increased significantly over time, from around 39% in 1997 to nearly 57% in 2010. However, there are fresh difficulties to be overcome. First off, cost growth is a significant issue for state highway agencies (SHAs), particularly during a recession.

According to research done by Flyvbjerg et al. (2002), the anticipated costs of the 258 projects were understated for around 90% of them, and the real costs were, on average, 30% higher. There is a negative impact on subsequent programs and a loss of trust in the agency's capacity to effectively spend taxpayer money if an SHA fails to execute certain projects and programs within set budgets (Molenaar et al. 2008). Second, life-cycle cost analysis is becoming increasingly significant. The need for a balance between initial construction and ongoing maintenance costs has been recognized. If not, rigid concrete slabs might anticipate early failure, decreased serviceability, and higher maintenance costs. Nevertheless, predicting is dubious. Novel methods are thus required to take uncertainty into account and raise the dependability of pavement design. Third, the mechanistic-empirical technique is replacing the empirical method in pavement design. The American Association of State Highway and Transportation Officials (AASHTO) has approved the new Mechanistic-Empirical Pavement Design Reference (MEPDG), making it the official design guide is known as DARWin-ME. The MEPDG contains many more inputs than the outdated AASHTO (1993) Guide, including traffic, climate, and materials. Besides, MEPDG is not an empirical equation but a full design and modeling program. There is a requirement to carry

out a risk analysis on pavement design using MEPDG due to the nature of uncertainty in design inputs as well as the complexity of the new technology. Risk is often a measurement of the possible loss brought on by human or natural events. Engineering solutions may now be built using risk analysis to reduce risk. Risk assessment, management, and communication are the three main components of risk analysis. Three questions are addressed by risk assessment:

- What can probably go wrong?
- How likely is it?
- What are the consequences?

The goal of risk management is to identify the major threats and implement preventative measures (Modarres, 2006). Risk analysis has mostly been used up until this point in cost analysis, performance-related requirements, and transportation safety. Rackwitz-Fiessler simulations were performed to calculate the risk variables for work zone safety using risk analysis (Elias and Herbsman, 2000). The length and duration of closures for highway rebuilding and rehabilitation projects were optimized by the author using the model. Life cycle cost analysis was given a risk analysis technique to account for the uncertainty involved (Walls and Smith, 1998). Risk management was utilized by the California Department of Transportation to reduce negative effects on the project's scope, cost, and schedule and to optimize the chances to achieve the project's goals at lower costs and greater quality (Caltrans, 2007).

Risk analysis methodology was added to pavement performance models and maintenance models, on which a contract pricing model was constructed, to take into account the uncertainty in performance-related specifications (Damnjanovic and Zhang, 2008). NCHRP sponsored a study to introduce risk analysis tools and management methods to control transportation project costs to address the issue of project cost escalation (Molenaar et al. 2008). The guidebook's risk analysis

methodologies were modified to meet the requirements of developing highway projects. Risk identification, assessment, mitigation, allocation, and monitoring were the five phases that made up the framework. Planning, programming, and designing were the three project phases to which these five steps were then applied. Engineers were curious about what the most important factors were after the initial release of MEPDG. Many researchers have undertaken sensitivity analysis, mostly utilizing the One-factor-At-a-Time (OAT) technique. Subgrade stiffness and traffic were consistently significant in the cracking and rutting model's sensitivity analysis, it was discovered (MEPDG, 2009). Kim (2005) investigated the impact on several distress models using two actual pavement sections from Iowa. It was discovered that the majority of the projected performance indicators were typically impacted by the concrete grade, volumetric characteristics, climate, and stiffness of the base layer.

Axle load spectra were crucial for MEPDG prediction, according to Tran and Hall (2007). Additionally, this discovery was made in North Carolina (2010). The study also discovered that vehicle class distributions and monthly adjustment variables had a big impact. However, it was shown that standard WSDOT pavement designs were only moderately responsive to the axle load spectrum (Li et al. 2009). Eleven design and material factors that were evaluated as part of MEPDG in Michigan (Buch et al. 2008) were shown to have a substantial impact on performance. These include the parameters of the concrete mixtures, the base, subbase, and subgrade moduli, as well as the base and subbase thickness. It was discovered that the most important factor determining transverse cracking was the concrete grade. According to a focused study on the Poisson's ratio, the MEPDG predictions were clearly influenced by the material Poisson's ratio (Maher and Bennert, 2008). Alligator cracking, overall rutting, and longitudinal cracking all reduced as Poisson's ratio rose. However, it was determined that Poisson's ratio of unbound materials was not

important. NCHRP supported projects 1-47 to conduct a systematic investigation of the relationship and take into account the combined effects of variations in two or more input parameters (also known as global sensitivity analysis) in light of the OAT method's limitations (Schwartz et al. 2011). The metric used to describe how sensitive a variable was to the expected performance was called the normalized sensitivity index (NSI). The importance of the NSI increased with its absolute value. Positive or negative refers to the influence's direction (plus means the same direction).

In conclusion, the author was unable to locate any literature that directly applied the risk analysis approach to rigid concrete slab design, particularly under the effect of thermal and curling stresses. The MEPDG program was used for all sensitivity analyses to identify the critical factors that significantly impacted MEPDG predictions. One drawback of this approach was that the MEPDG software's limitations may be taken to represent the reality of the actual mechanism. For instance, the NCHRP1-47 experiment discovered that neither the subgrade detail nor the level of the groundwater table had a substantial impact on the performance of the pavement. One should be aware that this conclusion was based on, and solely applicable to, the study's software. It might not be the real connection. The study simply demonstrated that further work was required to include materials characteristics, environmental concrete as well as boundary conditions in future design tools.

10.3.4. Risk identification

The first step in lowering the risk and raising the dependability of a system is to thoroughly comprehend its design and parts. Rackwitz-Fiessler is a potent technique for assessing risk (Haimes, 1998). The aim of rigid concrete slab design is to create a pavement that is affordable and can offer a smooth, secure road surface for traffic. When seen as a system, a slab design is

made up of several parts, including design engineers, material testing specialists, design software, traffic forecast, climate change, construction, and maintenance after the road is finished. The system is also subject to several limitations, including site conditions, material availability, financial limitations, design timelines, building capabilities, etc. As indicated in Figures 10.4-10.10: diverse persons, temporal, components, and cost allocation affect the risk analysis and reliability assessment of rigid concrete slabs using the Rackwitz-Fiessler technique. The six perspectives affecting the performance of rigid concrete slabs are depicted in Figure 10.4. Figure 10.5 shows rigid concrete slabs from the perspectives of many researchers. For instance, end users might be interested in:

i. How long it takes to build a runway

ii. How smooth it is

iii. Whether noise from the runway affects drivers and residents nearby

iv. Whether the runway requires maintenance or not

v. How much more or fewer fuel users must pay due to different runway conditions

vi. Whether the road is safe to use, and

vii. Whether it is appropriate for use in all types of weather.

Other categories received the same evaluation. The study is shown in Figure 10.6 from a temporal viewpoint or the lifetime circle of a pavement. For instance, the following topics are important to consider when building:

(1) When is the best time for rigid concrete runway paving

(2) What are the economical restrictions,

(3) How many resources, including personnel, engineers, technicians, and equipment, are available for this project,

(4) The location, price, and material accessibility

(5) What is the required least level of quality and how may a greater level of quality be attained

(6) The security of the construction workers and nearby road users, and

(7) How the environment may affect the construction procedure

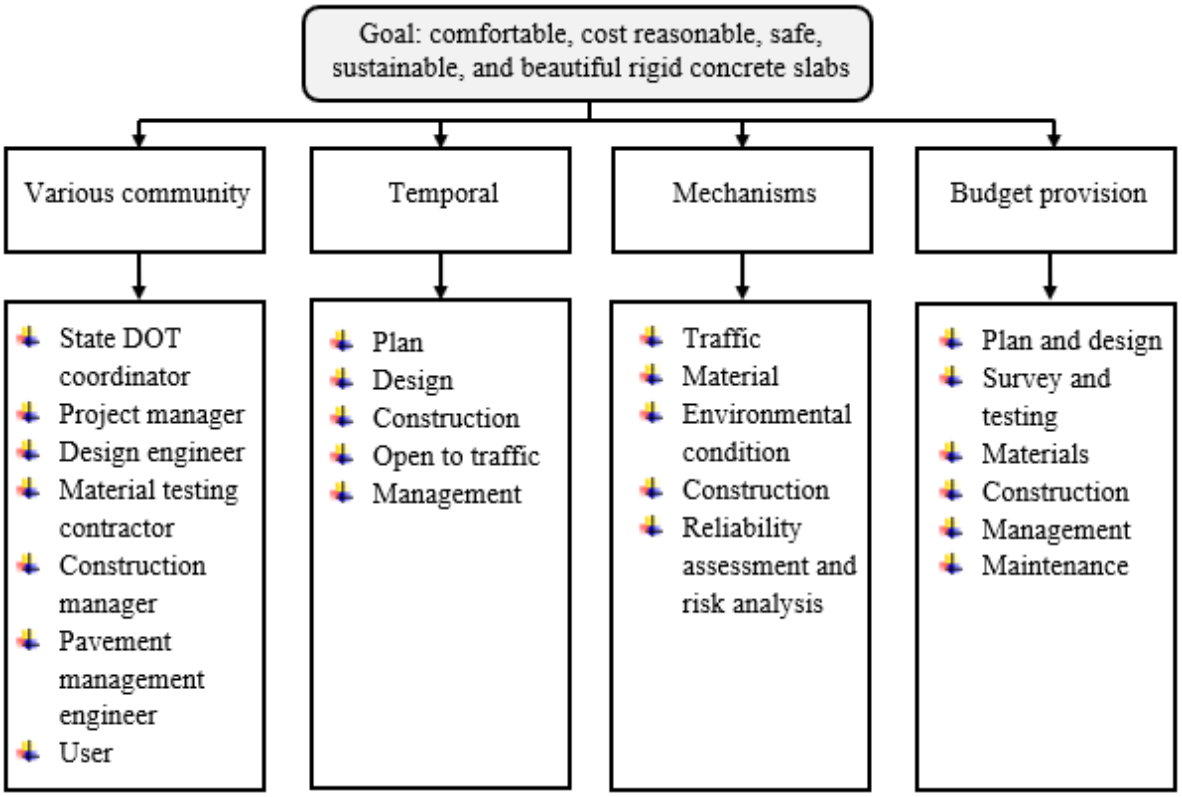

Figure 10.4: Outlooks to examine rigid concrete runways

Any procedure might include risks, which can prevent the goal from being achieved.

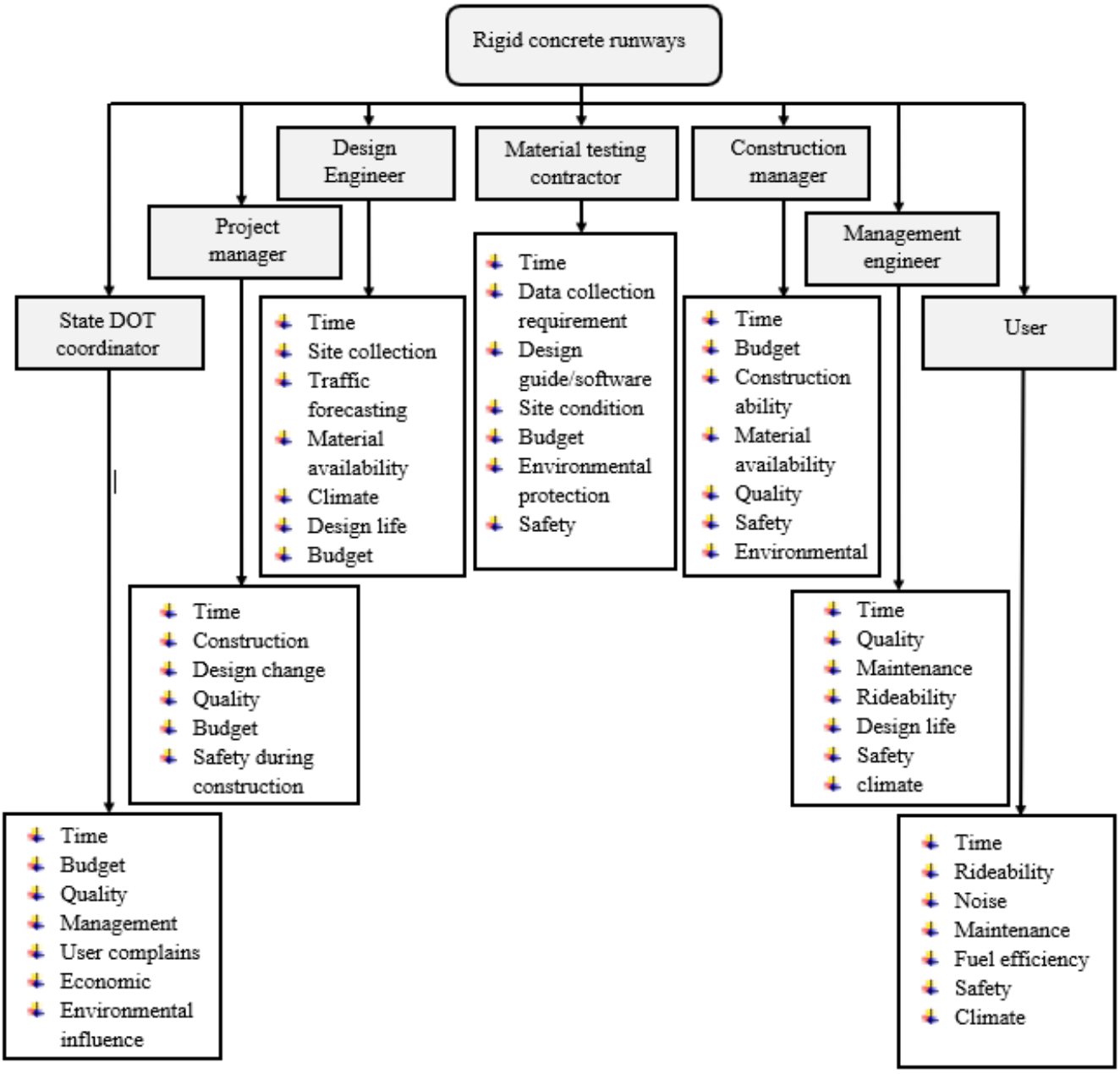

Figure 10.5: Rigid concrete runways in view of various parts

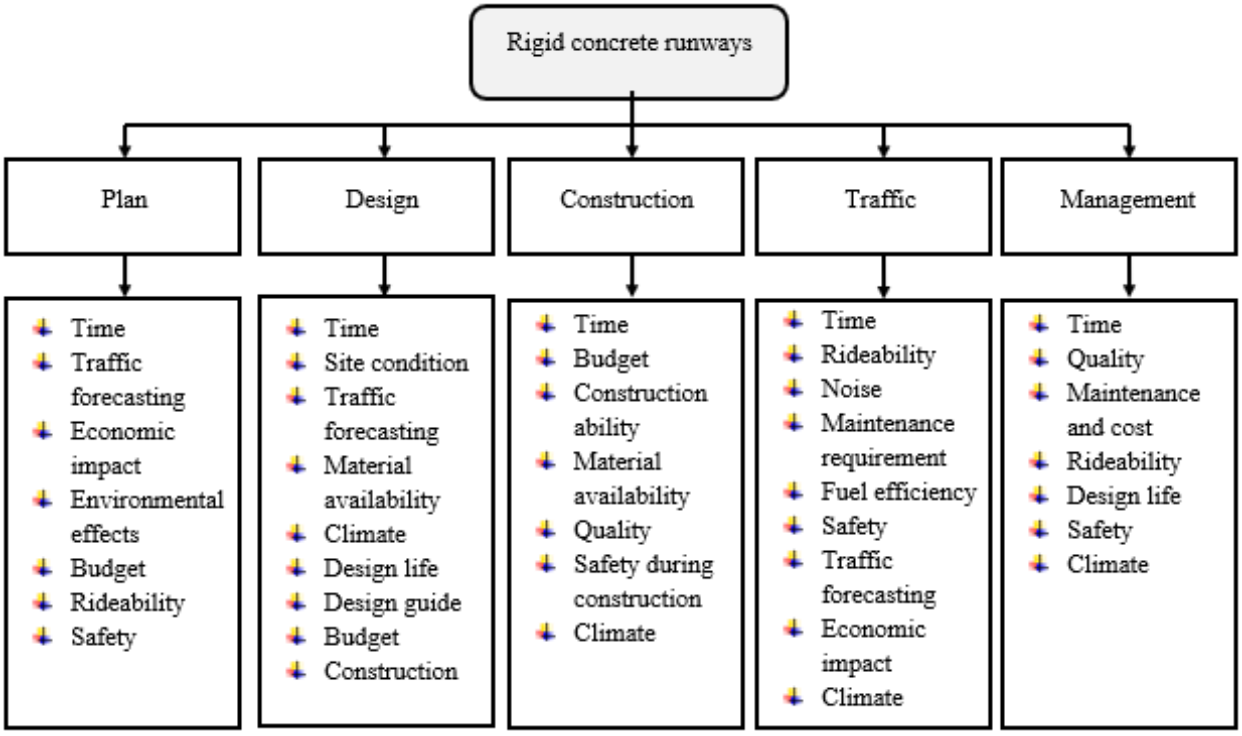

Figure 10.6: Rigid concrete runway design in Temporal view

Using climate as an example, uncertainties may arise in the following areas:

i. Using one advert to signify a miles-long project, where local circumstances may vary

ii. The actual temperature gradient is typically simplified using the mean temperature

iii. The variance between the project and the network-level rainfall statistics

iv. The number and degree of freeze/thaw cycles

v. Material characteristics differ under various weather circumstances

The rigid concrete runway is broken down in Figure 10.7 based on how the funding is distributed among various tasks, from planning to maintenance. For instance, maintenance takes into account the use of resources, personnel, materials, traffic management, and environmental protection. Specific rigid concrete runway designs employing MEPDG and future mechanistic empirical techniques are shown in Figures 10.8 and 10.9. Figure 10.9 has more thorough elements than Figure 10.8 does, which is how the two vary from one another. Due to the assumption that all components might be probabilistic and therefore carry some risk, Figure 10.9 shows most of the key parameters in the MEPDG program.

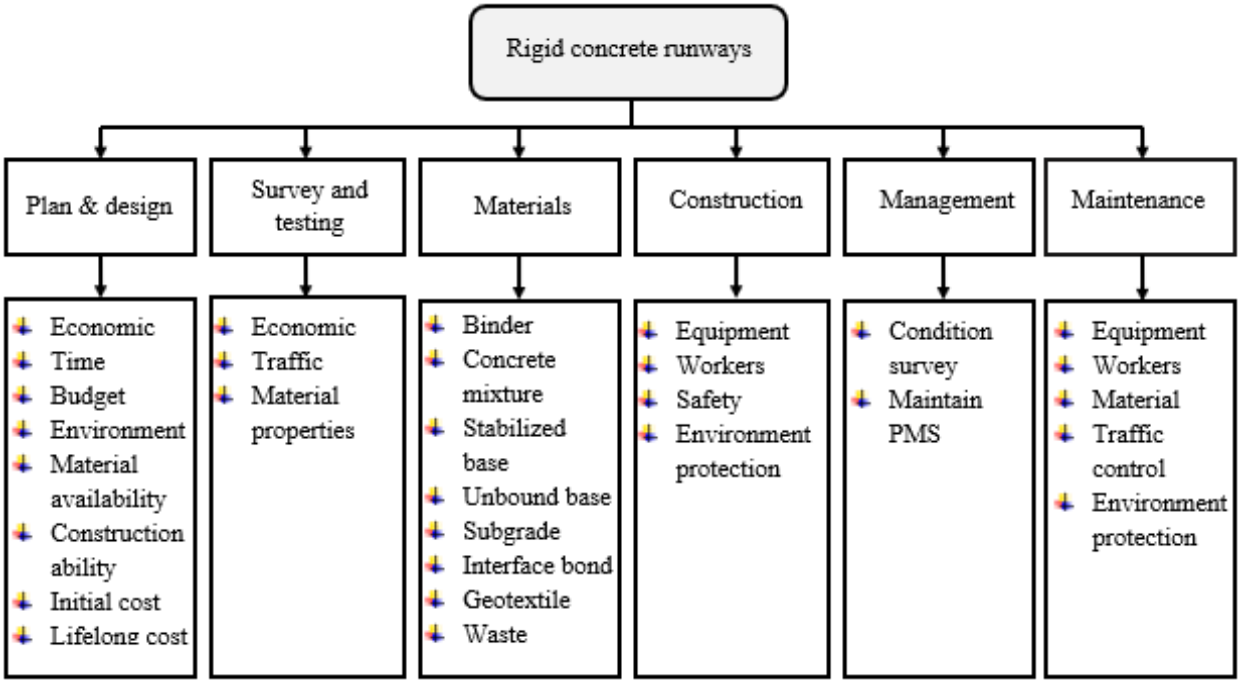

Figure 10.7: Rigid concrete runway design in cost allocation view

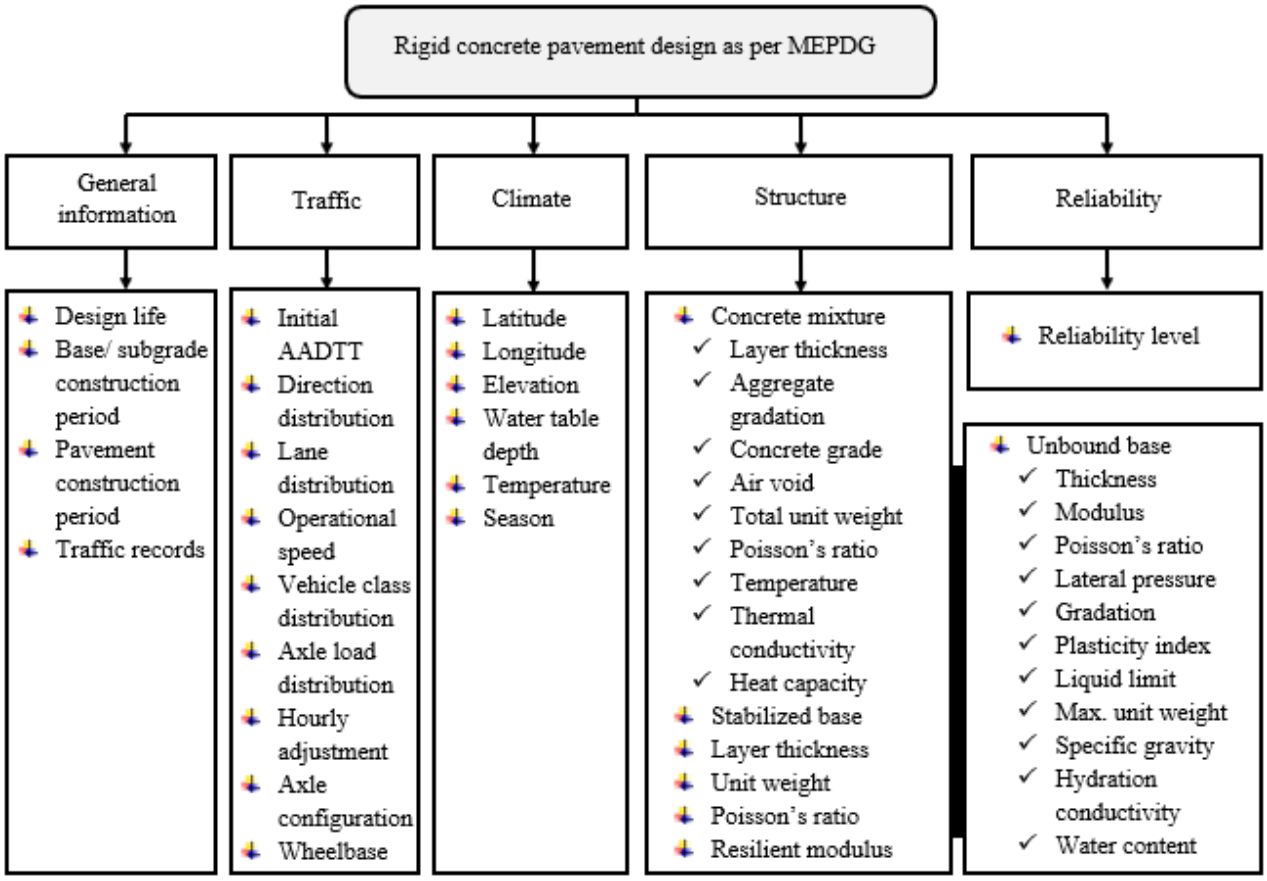

Figure 10.8: Rigid concrete pavement design as per MEPDG

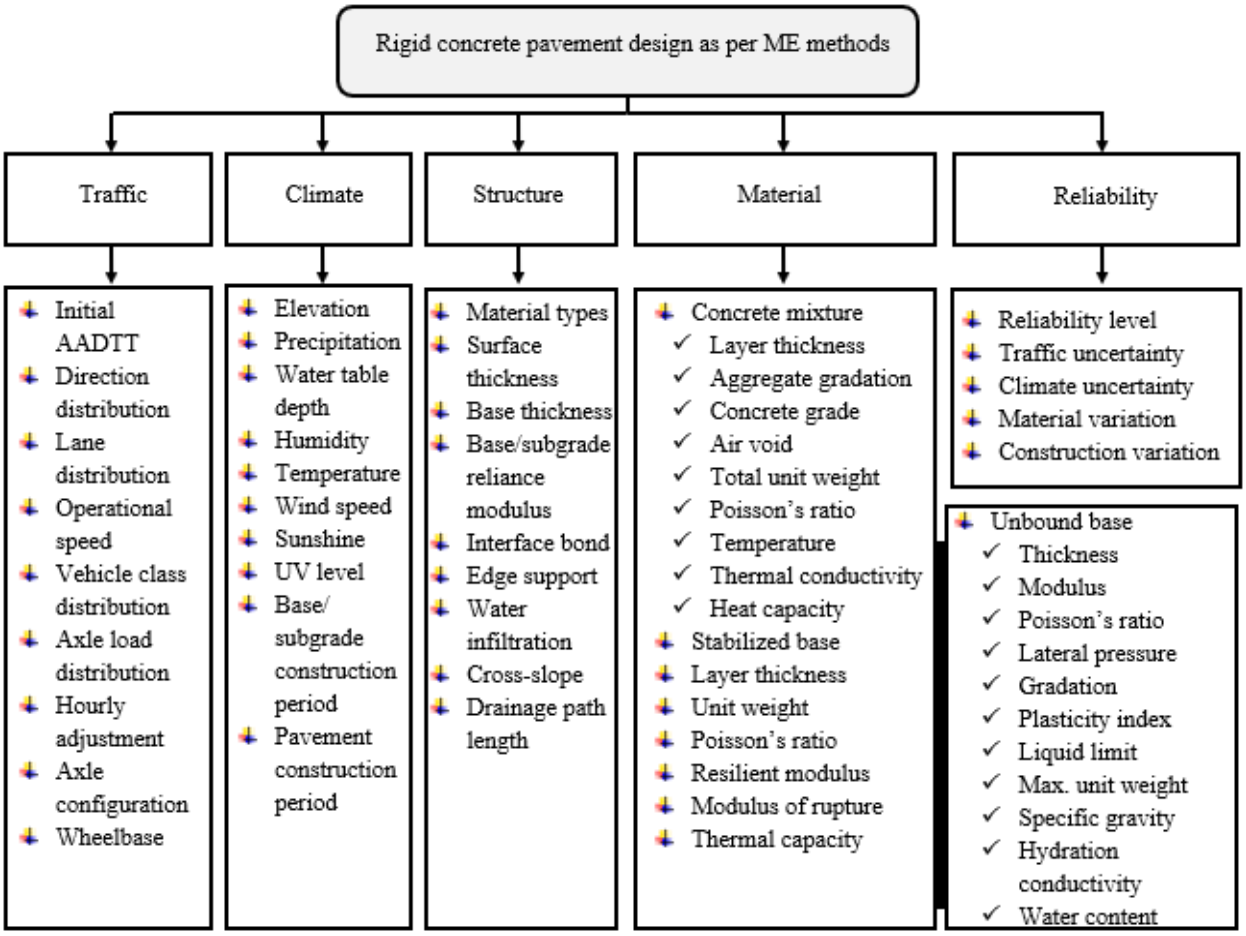

Figure 10.9: Rigid concrete pavement design as per ME methods

10.4. PROBABILISTIC STUDY ON RIGID CONCRETE SLABS FAILURE USING RACHQITZ-FIESSLER METHOD

One of the important shortcomings in previous studies is the lack of investigation into the possibility of failure and cracking in rigid concrete slabs under different climatic conditions. Because it is not possible to comment on the occurrence of a phenomenon with high determination. As a result, the probabilistic study can give a broad view of the properties of the influence of various parameters on the curling and thermal behaviors of the slabs for engineers and DOTs. Therefore, non-mechanistic analysis mistakes have the potential to endanger the accuracy of transportation facility damage quantification and their life analyses. An anomaly persistent that

has been noted in the literature is the failure to consider all geometric variables and the simultaneous effect of ambient temperature. According to the author's past experience, curling and thermal stress have a significant impact on stress distribution patterns. As a result, mitigating the influence of environmental temperature in a highly accurate evaluation of the service life and damage failure of rigid concrete slabs could be significantly beneficial.

As a result, chapter, the effect of different parameters and temperature gradients on the probability of failure and cracking of rigid concrete slabs will be probabilistically investigated using the Rackwitz-Fiesler Reliability Method. A probabilistic study is used based on random variables and their participation in the occurrence of a phenomenon. The Rackwitz-Fiessler procedure is employed to compute the reliability index of the curling stress equation with similar parameters as the Beta method with the main difference being the inclusion of the distributions of each of the random variables. The basic procedure of the Rackwitz-Fiessler method utilized in this study is shown in Figure 10.10.

As seen in Figure 10.11, Rackwitz and Fiessler (1978) proposed a rough mapping that, at a given place, corresponds to the values of the original and equivalent normal distribution functions as well as their relative densities. The following distributional parameters are produced by these two equivalent normal conditions.

$$\mu_{Z_i}^{(k)} = \left(x_i^{(k)} - \sigma_{Z_i}^{(k)} \Phi^{-1}\left[F_{X_i}\left(x_i^{(k)}\right)\right]\right) \tag{10.2}$$

$$\sigma_{Z_i}^{(k)} = \frac{\phi\left\{\Phi^{-1}\left[F_{X_i}\left(x_i^{(k)}\right)\right]\right\}}{fX_i\left(x_i^{(k)}\right)} \tag{10.3}$$

where $\mu_{Z_i}^{(k)}$ and $\sigma_{Z_i}^{(k)}$ are the mean and standard deviation of the equivalent normal variable Z_i, respectively; $x_i^{(k)}$ is the *i*th component of the *k*th iteration point $x^{(k)}$; $F_{X_i}(.)$ and $fX_i(.)$ are the

distribution function and the density function of the original variable X_i, respectively; $\Phi(.)$ and $\phi(.)$ are the standard normal distribution function and density function, correspondingly.

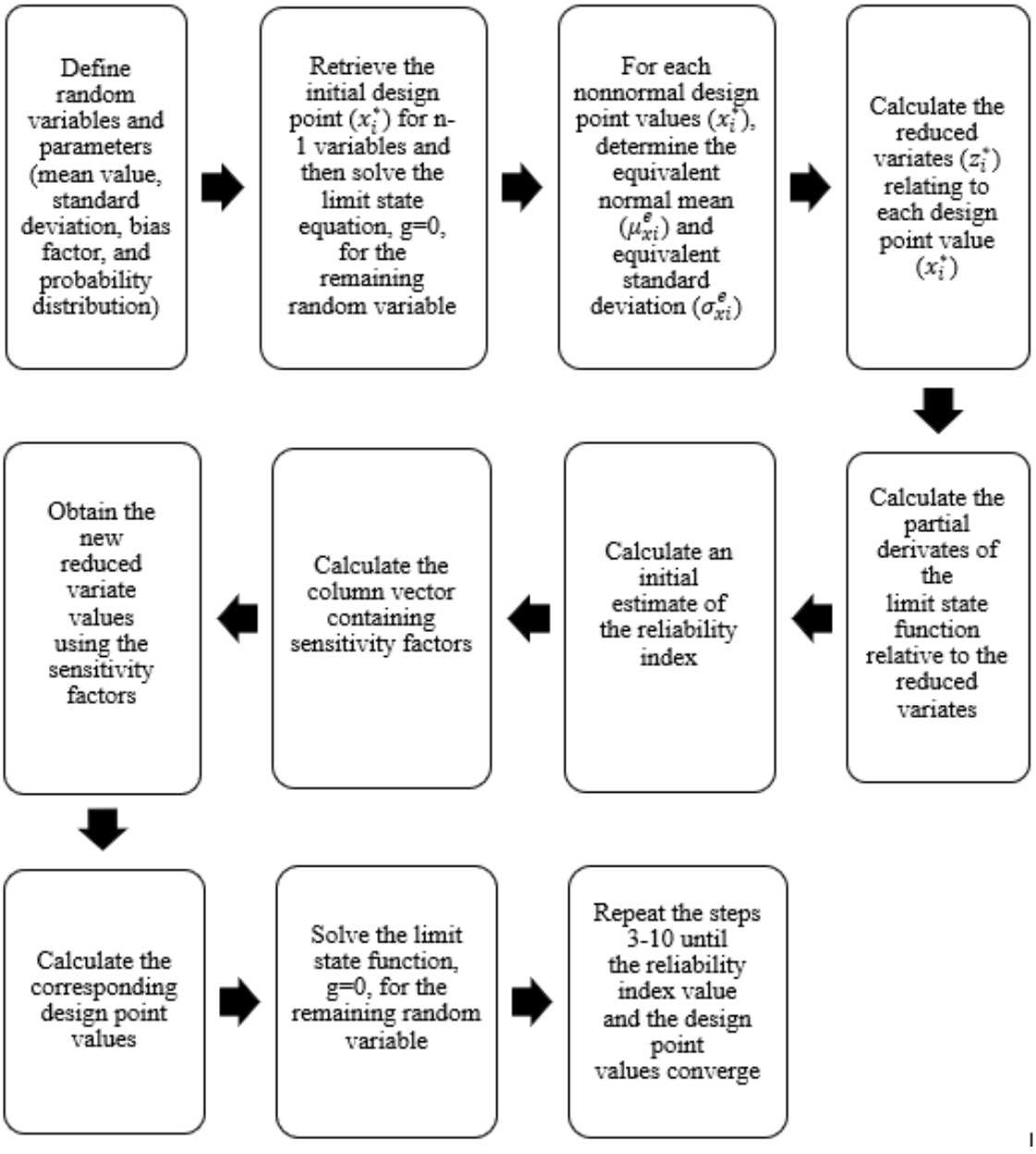

Figure 10.10: Rackwitz-Fiessler procedure

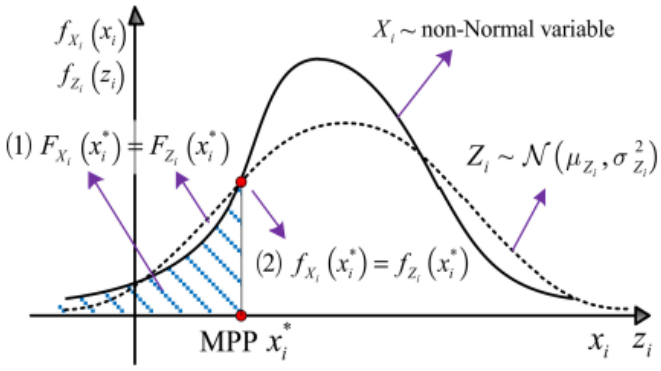

Figure 10.11: Equivalent normal conditions of non-normal variable

When used in the reliability algorithm, the obtained equivalent Normal vector Z at the kth iteration has to be further transformed into the standard Normal vector Y by the standardization transformation and then transformed into the independent standard Normal vector U by the orthogonal transformation. Here, let $\mu_Z^{(k)} = \left[\mu_{Z1}^{(k)}, \mu_{Z2}^{(k)}, \ldots, \mu_{Zn}^{(k)}\right]^T$ and $D_k = diag(\sigma_{Z_i}^{(k)})$, the forward and backward processes of the Rackwitz-Fiessler method are summarized as follows:

- **Forward process of Rackwitz-Fiessler (RF) method at the *k*th iteration:**

$$T_1^{RF}: D_X \to equivalent\ R^n, x^{(k)} \to z^{(k)} = x^{(k)} \quad (from\ X\ to\ Z) \tag{10.4}$$

$$T_2^{RF}: R^n \to R^n, z^{(k)} \to y^{(k)} = (D_k)^{-1}(z^{(k)} - \mu_z^{(k)}) \quad (from\ Z\ to\ Y) \tag{10.5}$$

$$T_3^{RF}: R^n \to R^n, y^{(k)} \to u^{(k)} = L^{-1}y^{(k)} \quad (from\ Y\ to\ U) \tag{10.6}$$

- **Backward process of Rackwitz-Fiessler (RF) method at the *k*th iteration:**

$$T_1^{-1\,RF}: R^n \to R^n, u^{(k+1)} \to y^{(k+1)} = Lu^{(k+1)} \quad (from\ U\ to\ Y) \tag{10.7}$$

$$T_2^{-1\,RF}: R^n \to R^n, y^{(k+1)} \to z^{(k+1)} = D_k y^{(k+1)} + \mu_z^{(k)} \quad (from\ Y\ to\ Z) \tag{10.8}$$

$$T_3^{-1\,RF}: R^n \to R^n, z^{(k+1)} \to x^{(k+1)} = z^{(k+1)} \quad (from\ Z\ to\ X) \tag{10.9}$$

where L is the Cholesky factor of the Pearson correlation matrix R_Y of vector Y, i.e., $R_Y = LL^T$. Also, there are four random spaces in the Rackwitz-Fiessler method, i.e., the X, Z, Y, and U spaces.

10.5. RESULTS AND DISCUSSIONS

In this section, the influence of material properties, geometric characteristics, and environmental conditions on the probability of safety is assessed using the Rackwitz-Fiessler technique. For this aim, the influence of variables was taken into account one by one and simultaneously to identify the importance and influence of different parameters. Figures 10.12 to 10.14 provides the influence of geometric characteristics and thermal gradient on the probability of failure of slabs with 25 MPa concrete compressive strength and various PF incorporation fractions. According to Figure 10.12, in 25 MPa compressive strength concrete slabs, increasing the slabs' width led to raising the probability of failure. However, for slabs with up to 6m length, increasing the thickness decreased the probability of failure while for slabs with 7.5m length, increasing the slab's thickness significantly increased the probability of failure. Additionally, increasing the thermal gradient played a crucial role in increasing the probability of failure and generally cracking in rigid concrete airfield runways. However, increasing the slab's thickness had a negative influence on the probability of failure when the length of the slab was considered 7.5m. Also, it could be observed that the probability of failure increased with a surge in slabs' length for up to 6m and then declined when the length was further increased to 7.5m. The negative influence of increasing thickness for a 7.5m slab's length could be associated with the modes of failure and the potential of curve deformation which results in out-of-plane deformation.

Furthermore, fiber incorporation played an effective role in reducing the probability of failure when 0.5% fibers were utilized. However, the positive influence of increasing the thickness declined when the fibers fraction increased as the slope of changes has been considerably altered (Figure 10.13). The main reason for this behavior could be associated with reducing the positive influence of fibers when the thickness of slabs increases. The same trend was observed when 1.0%

fibers were employed as demonstrated in Figure 10.14. However, there is no significant difference between the influence of 0.5% and 1.0% fiber incorporation in terms of the probability of failure. So, to consider the construction and material cost, the fiber incorporation fraction could be limited to 0.5% when a low strength compressive strength is considered for construction (in this study 25MPa).

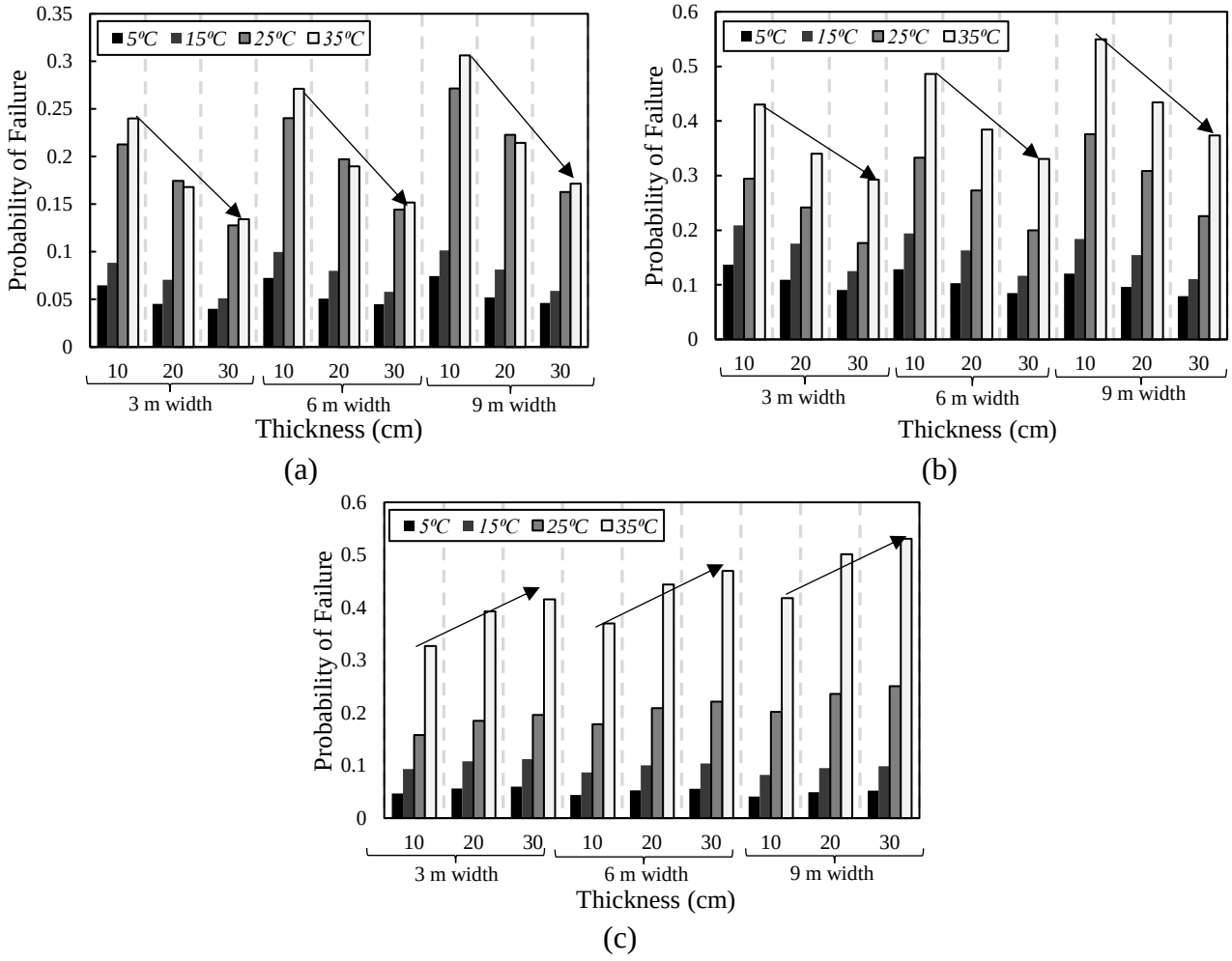

Figure 10.12: Influence of thermal gradient and geometric characteristics on the probability of failure in plain concrete slabs with 25 MPa compressive strength and various lengths a) 4.5m, b) 6m, and c) 7.5m

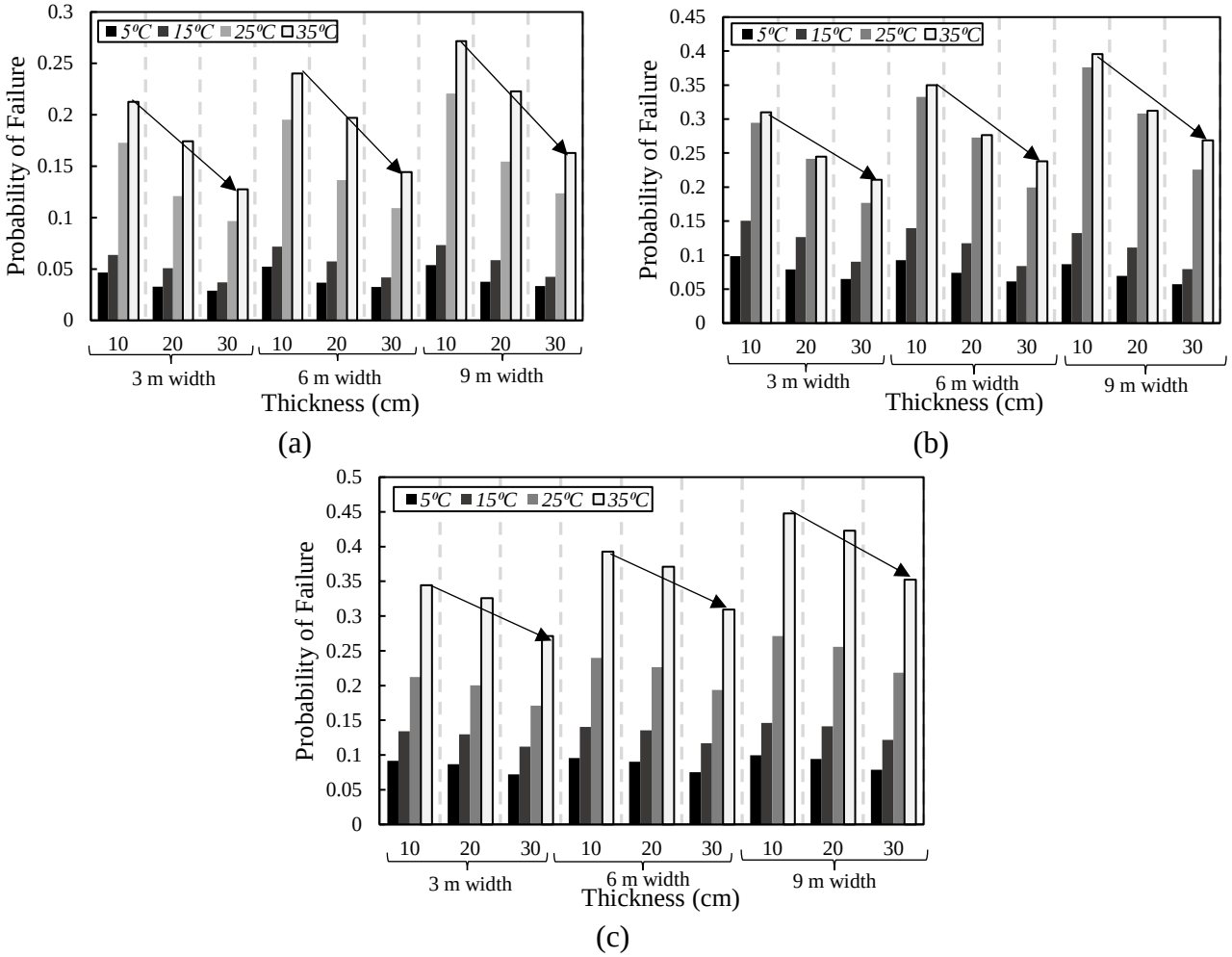

Figure 10.13: Influence of thermal gradient and geometric characteristics on the probability of failure in 0.5% fiber-reinforced concrete slabs 25 MPa compressive strength and with various lengths a) 4.5m, b) 6m and c) 7.5m

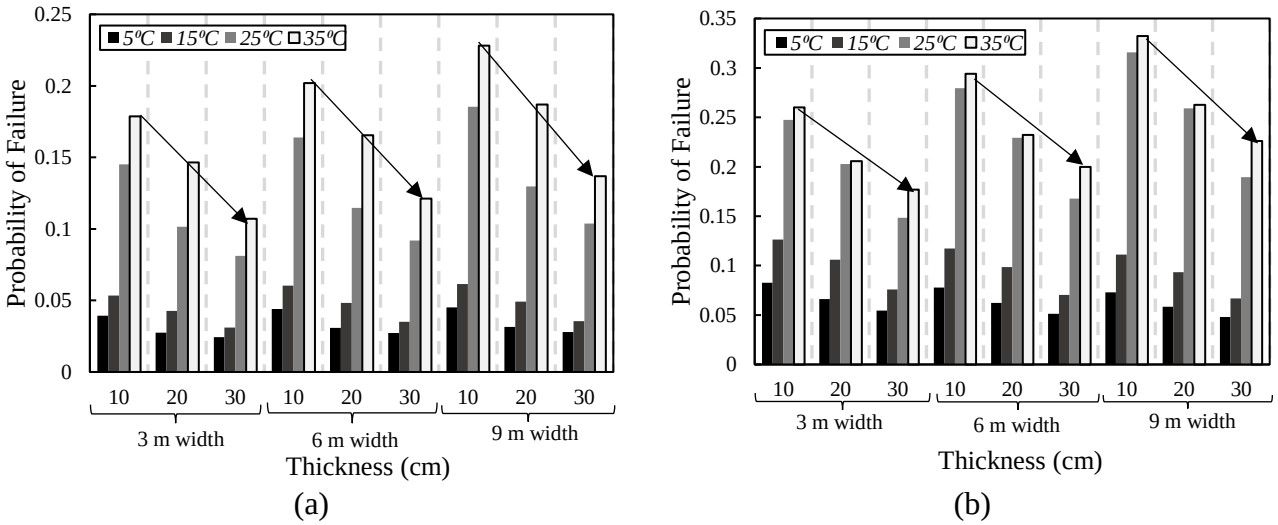

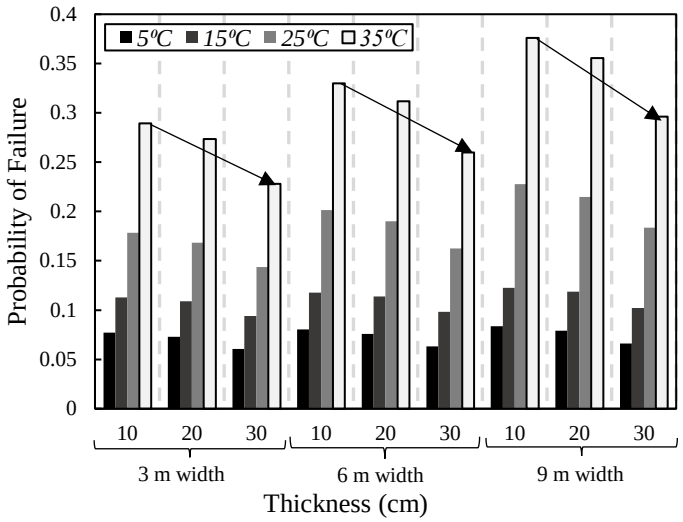

(c)

Figure 10.14: Influence of thermal gradient and geometric characteristics on the probability of failure in 1.0% fiber-reinforced concrete slabs with 25 MPa compressive strength and with various lengths a) 4.5m, b) 6m and c) 7.5m

To measure the influence of compressive strength as well as geometric characteristics, the compressive strength of concrete was increased and the probability of failure was measured. The results for 35 MPa concrete compressive strength having various fiber incorporation are illustrated in Figures 10.15 to 10.17. Regarding Figure 10.15, the probability of failure in plain concrete declined for slabs with up to 6m length when the compressive strength increased to 35MPa while for 7.5m length slabs, increasing the compressive strength had an inverse influence and the probability of failure increased. This could be associated with the mode of failure and out-of-plane deformation for the case when 7.5m slabs were used. Additionally, increasing the slab's thickness had a negative influence on the probability of failure when the length of the slab was considered 7.5m. Also, it could be observed that the probability of failure increased with a surge in the slabs' length. For 0.5% fiber-incorporated concrete slabs, Figure 10.16, the probability of failure decreased when the compressive strength increased from 25MPa to 35MPa This could be associated with the full curve deformation of slabs which led to increasing the vertical cracks over

the slabs' thickness. Moreover, the positive influence of increasing the thickness declined when the fibers fraction increased as the slope of changes has been considerably altered. The main reason for this behavior could be associated with dropping the optimistic effect of fibers when the thickness of slabs rises. As per Figure 10.17, the almost same trend was observed when 1.0% PF were incorporated. However, increasing the length of slabs resulted in raising the probability of failure.

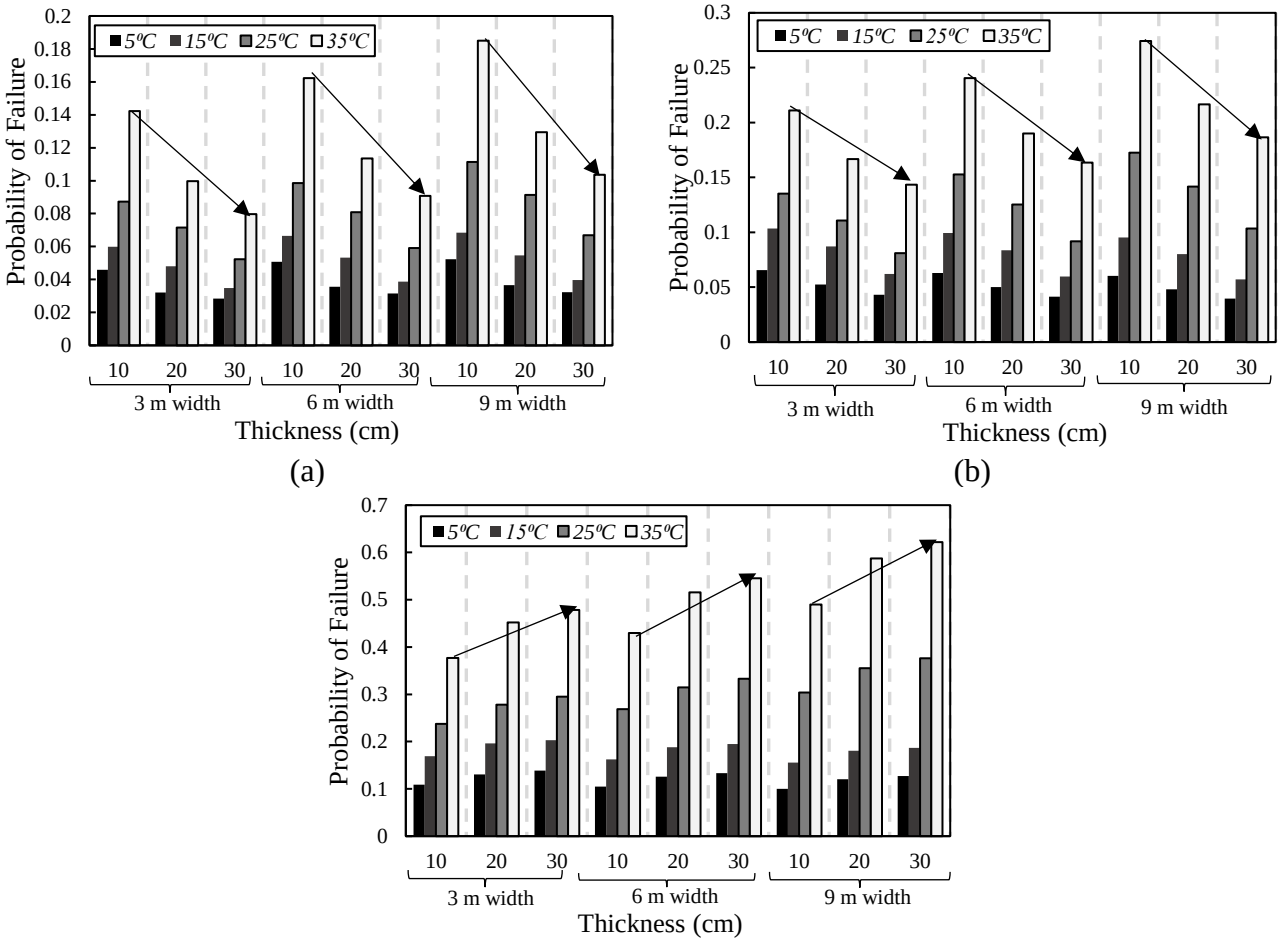

Figure 10.15: Influence of thermal gradient and geometric characteristics on the probability of failure in plain concrete slabs with 35 MPa compressive strength and various lengths a) 4.5m, b) 6m, and c) 7.5m

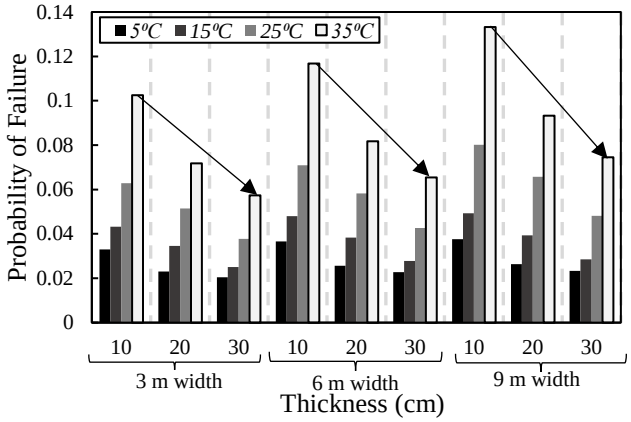

(a)

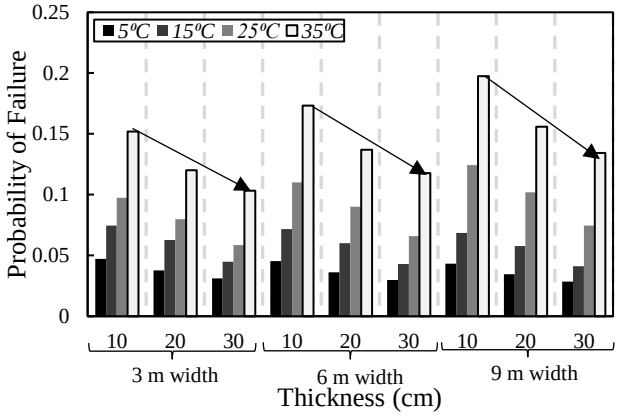

(b)

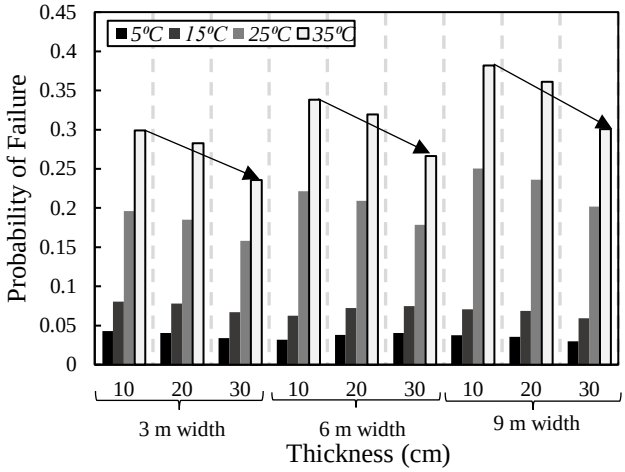

(c)

Figure 10.16: Influence of thermal gradient and geometric characteristics on the probability of failure in 0.5% fiber-reinforced concrete slabs 35 MPa compressive strength and with various lengths a) 4.5m, b) 6m and c) 7.5m

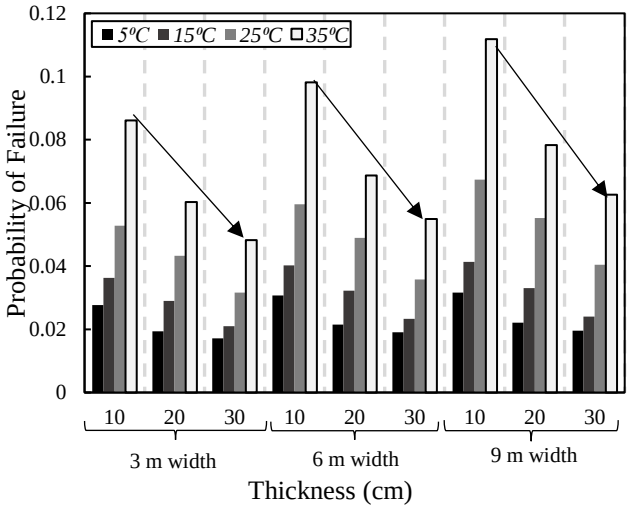

(a)

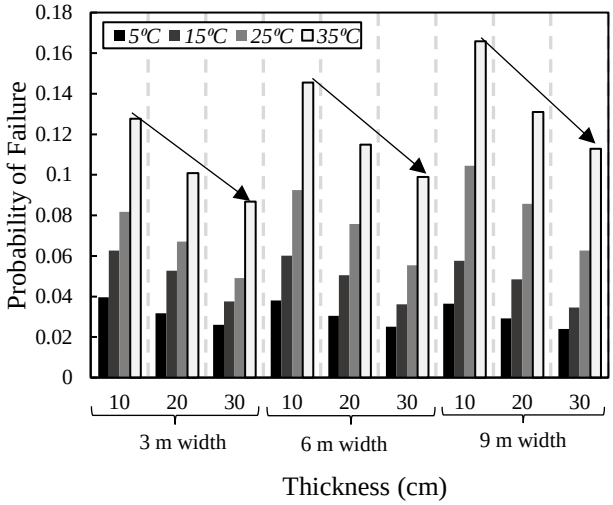

(b)

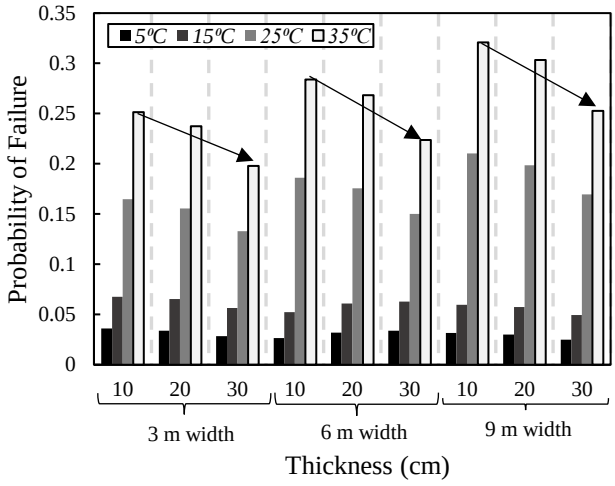

(c)

Figure 10.17: Influence of thermal gradient and geometric characteristics on the probability of failure in 1.0% fiber-reinforced concrete slabs with 35 MPa compressive strength and with various lengths a) 4.5m, b) 6m and c) 7.5m

Figures 10.18 to 10.20 provides the probability of failure for rigid concrete slabs with 45MPa concrete compressive strength considering the influence of geometric characteristics and thermal gradient. Regarding Figure 10.18, for plain concrete slabs, increasing the compressive strength of concrete from 35MPa to 45MPa led to reducing the probability of failure, however, the positive influence is lower than the case when the compressive strength was increased from 25MPa to 35MPa. Additionally, increasing the width of slabs increased the probability of failure while failure decreased in slabs with up to 6m length when the thickness increased. Conversely, increasing the thickness in slabs with 7.5m length resulted in raising the probability of failure due to increasing the potential of out-of-plane deformation and curve-shaped failure. Moreover, fiber incorporation could be taken into account as a beneficial tool in reducing the probability of failure which could be associated with increasing the service life of airfield runways and decreasing the maintenance cost of construction. Therefore, Figure 10.19 shows that the probability of failure decreased for concrete slabs with 0.5% fiber incorporation as the compressive strength rose from 35 MPa to 45 MPa. This may be related to the complete curve deformation of the slabs, which increased the

vertical cracks throughout the thickness of the slabs. Additionally, as the slope of changes was significantly altered, the beneficial effect of growing thickness was diminished as the fiber fraction rose. The primary cause of this behavior may be due to fibers' loss of their upbeat impact as slab thickness increases. Figure 10.20 shows that when 1.0% PF were added, nearly the same pattern was seen. But as slab length was increased, the likelihood of failing also increased.

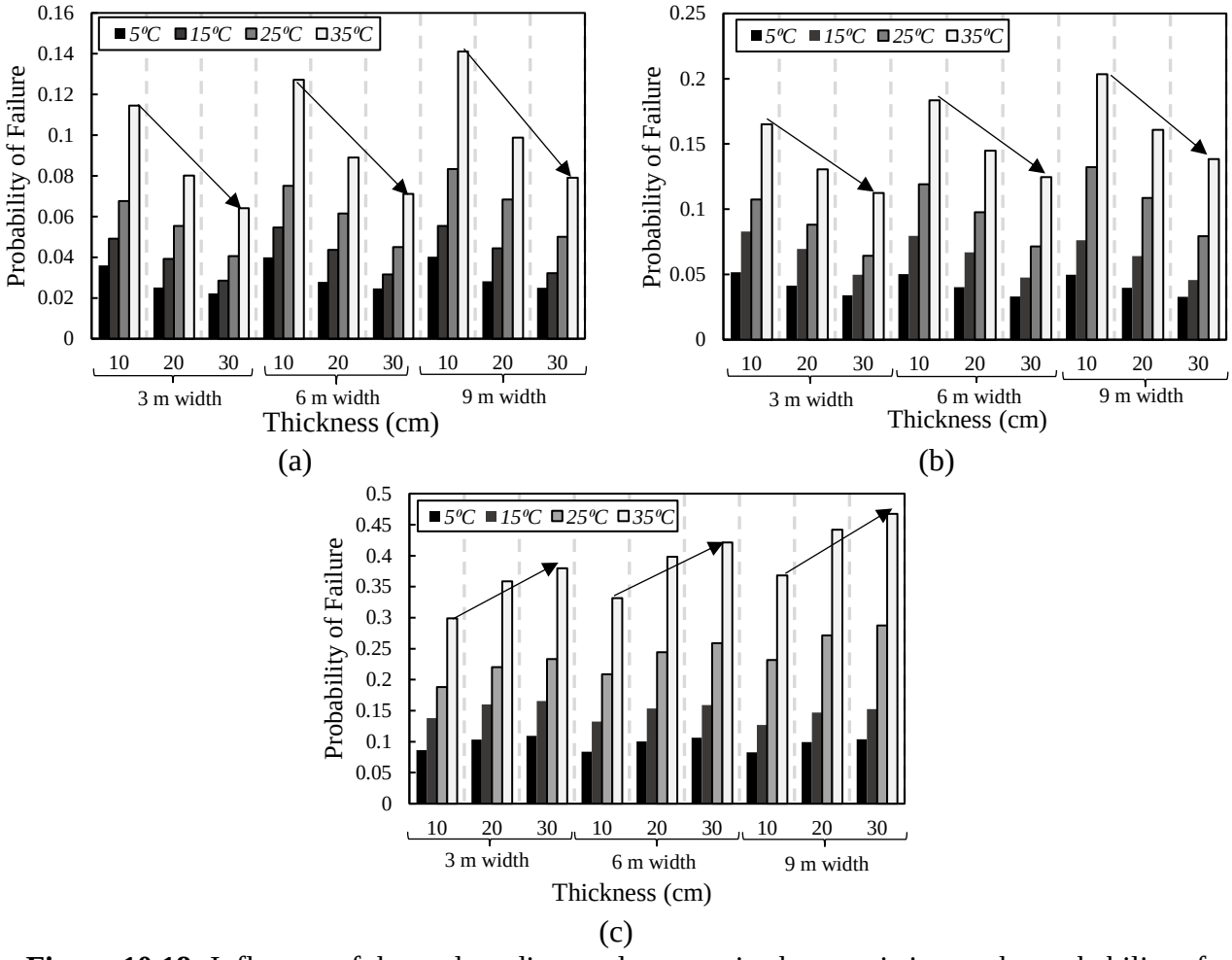

Figure 10.18: Influence of thermal gradient and geometric characteristics on the probability of failure in plain concrete slabs with 45 MPa compressive strength and various lengths a) 4.5m, b) 6m, and c) 7.5m

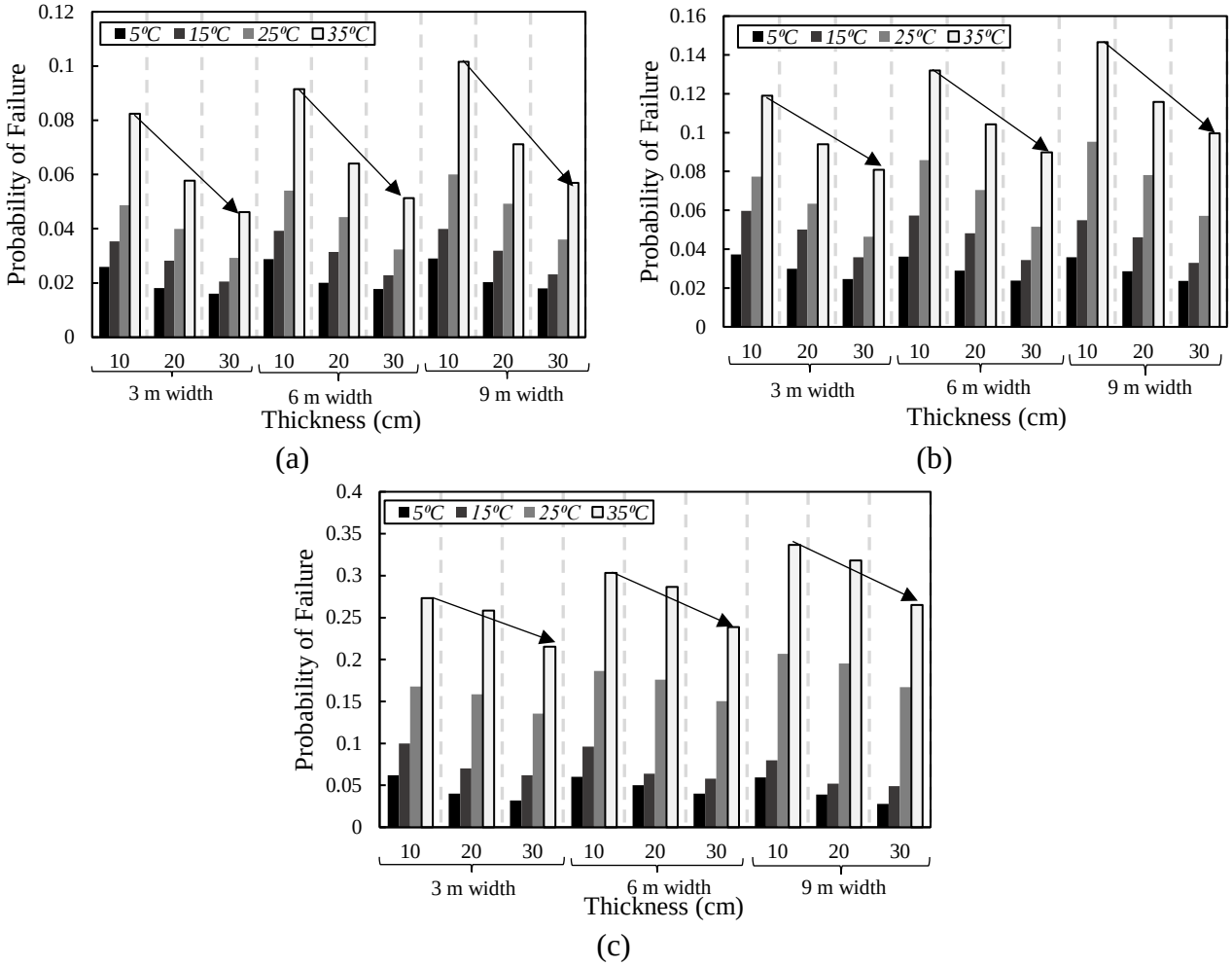

Figure 10.19: Influence of thermal gradient and geometric characteristics on the probability of failure in 0.5% fiber-reinforced concrete slabs 45 MPa compressive strength and with various lengths a) 4.5m, b) 6m and c) 7.5m

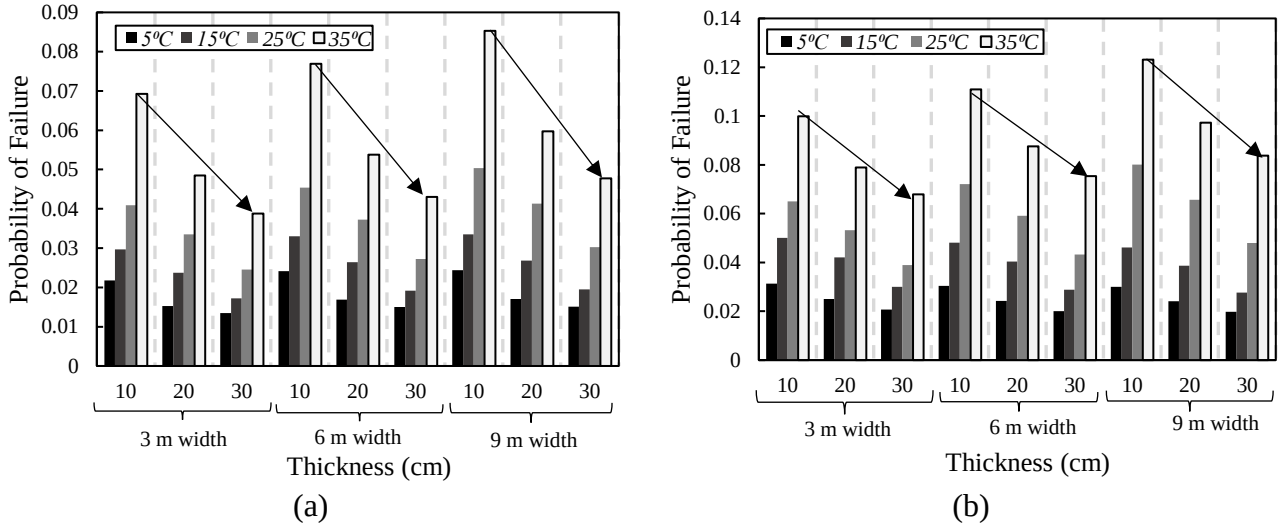

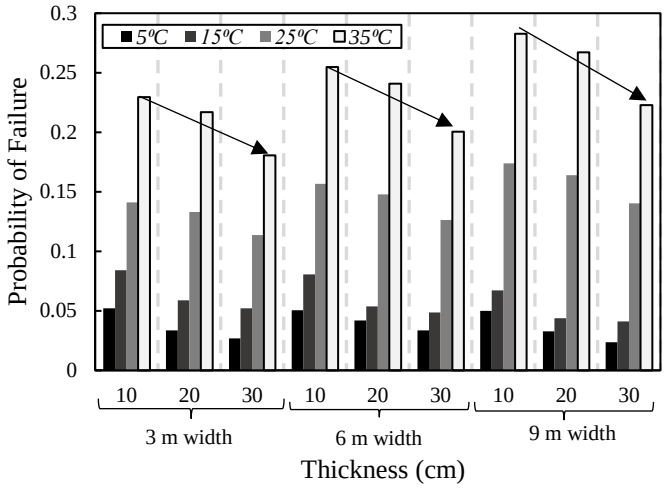

(c)

Figure 10.20: Influence of thermal gradient and geometric characteristics on the probability of failure in 1.0% fiber-reinforced concrete slabs with 35 MPa compressive strength and with various lengths a) 4.5m, b) 6m and c) 7.5m

According to the obtained results, fiber incorporation could be considered as an excellent technique for reducing the probability of failure as well as maintenance costs. To have a better understanding of the positive influence of PF, the reduction in the probability of failure as a result of fiber incorporation for concrete with various compressive strengths is measured, as provided in Figure 10.21. According to this figure, the influence of fibers on reducing the probability of failure was greater for concrete slabs with lower compressive strength, 25MPa in this study. This could be associated with the potential of cracking in lower concrete compressive strength which highlights the performance of fibers in controling the cracks' width and their propagation. Additionally, increasing the thermal gradient led to reducing the positive performance of fiber incorporation in falling the probability of failure. In real construction, this could be associated with reducing the bond resistance between fibers and concrete matrix when temperature increases and also melting the fibers under the influence of high temperature. Also, the probability of failure was further declined with an increase in fiber fraction. However, the difference between the reduction in the probability of failure of slabs with 0.5% and 1.0% fiber incorporation fraction is up to 10%.

Therefore, the percentage of fiber incorporation could be limited to 0.5% in order to consider the construction cost, particularly when the concrete casting volume is large.

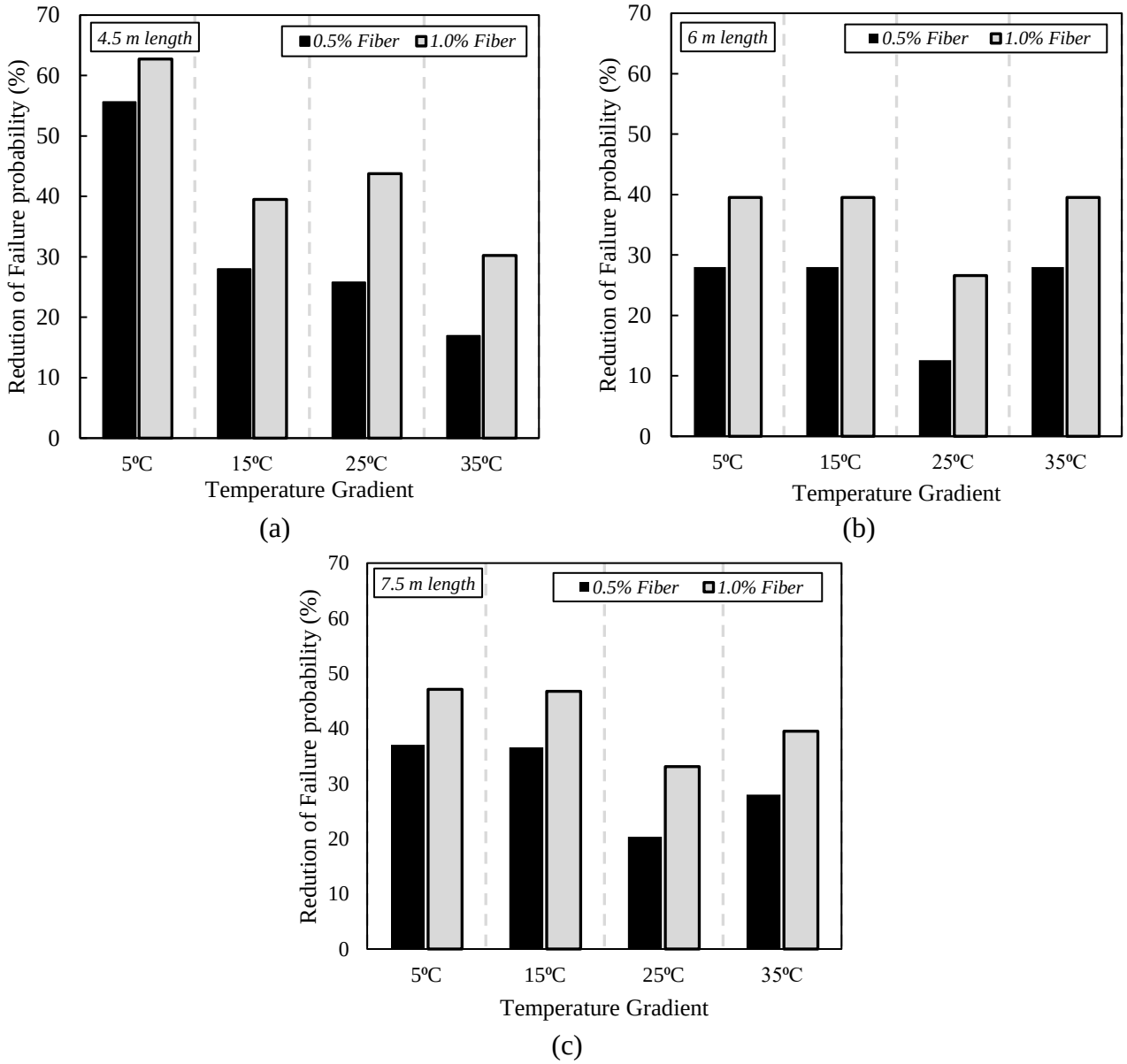

Figure 10.21: Influence of fibers incorporation on reducing the probability of failure for slabs with various lengths a) 4.5m, b) 6m, and c) 7.5m

CHAPTER XI

CONCLUSIONS AND RECOMMENDATIONS

This chapter summarizes the extensive efforts made in this study to characterize the influence of curling and thermal stresses on the structural responses of plain and fiber-reinforced rigid concrete airfield runways. The primary goal of this study was to mechanistically identify the role of geometric characteristics and material properties as well as the boundary conditions in the damages and structural impacts imparted on rigid concrete slabs under the influence of thermal gradient. The proposed analysis protocol consisted of multiple categories, including the analysis of stresses, deformation, cracking, and their propagation, and flexural and buried utility risk assessment. The secondary goal of the research was to incorporate polypropylene fibers (PF) to mitigate the negative influence of thermal gradient and temperature distribution through runways using finite element method software, ABAQUS considering the complex nature of thermal gradient. To achieve research objectives, initially, the research team developed a comprehensive database of temperature distribution and gradient in demanding runways of an airport in El Paso, Texas, based on the calibrated filed data. Sets of data were collected at various times to analyze the environmental conditions in this study. The collected data sets were then utilized to develop numerical analysis to identify the influence of various geometric and material characteristics. For this aim, a total of 8213 numerical models have been carried out to consider the effect of slab dimensions, modulus of rupture, compressive strength, and thermal expansion coefficient of concrete on the structural responses of rigid concrete slabs.

Then, the author utilized the ultrasonic imaging evaluation numerically to simulate the non-destructive test using wave propagation over the thickness and surface of rigid concrete slabs. Ultrasonic imaging is a powerful nondestructive evaluation technology for examining the condition of concrete structures through focused images obtained with the Synthetic Aperture Focusing Technique. The numerical simulation models account for the fiber incorporation, slab thickness, mechanical properties, and the boundary condition between the concrete slab and base layers, to realistically simulate the non-destructive wave propagation to identify the strength of rigid concrete airfield runways. Therefore, the results of this evaluation provide a comprehensive opportunity to measure the influence of material properties and geometric characteristics on the strength of rigid concrete slabs using wave propagation. Formerly, by using the field-derived databases and the devised analysis, an all-encompassing protocol was established for developing a theoretical concept named “advanced zero-stress assessment” to measure the depth of cracks through the slab’s thickness considering the effect of various material properties and geometric characteristics. This impression provides a comprehensive overview of the cracking in rigid slabs due to the bending curvature under the influence of curling stress.

A series of parametric analyses were then conducted to develop a finite element method formulation understanding curling stress in rigid concrete slabs considering all effective variables. The relevant information on curling and thermal stresses considering material properties and geometric characteristics was incorporated into a finite element modeling for developing a formulation to measure the curling-buckling behavior in rigid slabs under thermal stresses. The developed finite element method provides an inclusive evaluation to consider the effect of boundary conditions and fiber incorporation as well as the effect of base stiffness on the curvature, deformation, and buckling in rigid concrete slabs exposed to the temperature gradient. The

proposed approach aimed to bridge the existing gap in the literature for stress and deformation in plain and fiber-reinforced concrete slabs under the effect of environmental conditions.

Another noteworthy finding of this study was providing a highly accurate practical formula using a multi-layer genetic programming machine learning approach to determine the curling stress in rigid concrete airfield runways. Previously proposed equations showed a low accuracy and the lack of some main parameters' consideration. As a result, providing a new highly accurate formula including all effective geometric and material variables is necessary. This proposed theory's findings will undoubtedly be put to use by many firms to develop models, and DOTs and concrete pavement designing standards may use them to build sturdy concrete slabs that better take into consideration the curling and thermal stresses. Additionally, a methodologically sound and robust protocol was developed using various artificial neural networks for the mechanistic characterization prediction of the curling and thermal stress impacts on transportation infrastructure. The devised multilevel prediction approach consists of the following analysis procedures: quantification of cracking, (2) pavement curling and thermal resistances, the potential of buckling resistance, and deformation.

Ultimately, findings were also employed for risk analysis for slab reliability measurement. The synthesized contour maps can be further instrumental for pavement design and analysis Divisions in state DOTs during rigid concrete airfield runways evaluation process in having a mechanistic means for the approval (or rejection) of seasonal circumstances, considering the geometric characteristics, material properties, and boundary conditions. These reliability analysis methods will be used to verify how the structure would perform under loading and analyze the reliability index of determinate and indeterminate rigid concrete slabs and their failure probability under the effect of temperature considering a wide range of variables. The best practice

recommendations presented in this study can also guide highway agencies in adopting proper strategies to preserve the existing transportation networks in airports and highways. This can potentially protect state assets by reducing or eliminating reconstruction costs associated with premature failure of transportation facilities subjected to thermal gradient and temperature variations.

The following sections provide noteworthy observations and a summary of major findings pertaining to thermal and curling behaviors of plain and fiber-reinforced rigid concrete airfield runways considering the impact of material properties, geometric characteristics, boundary circumstances, and environmental conditions. The conclusions are accompanied by suggestions for feature work and research potential in the area of analysis and design of rigid concrete airfield runways subjected to thermal gradient and temperature variations.

11.1. CONCLUSIONS

The following gives an overview of the study's main conclusions:

- This study provided a comprehensive evaluation of the influence of various variables including material properties, geometric characteristics, environmental circumstances, and boundary conditions, on the thermal and curling stresses of rigid concrete airfield runways. The results of this study provide a comprehensive decision-making strategy for in-field construction and rigid concrete airfield runways design.
- Therefore, with an increase in the length of slabs, the maximum tensile stress increased and the nonlinearity behavior was considerably amplified when the length of slabs was greater than 6m, particularly under the influence of a high thermal gradient. Therefore, it is necessary to consider the nonlinear mechanical behavior of concrete materials as well as nonlinear thermal

gradient distribution over the thickness of the slab when the temperature variation is high and long-length slabs are constructed. This could be concluded that in long-length slabs (greater than 6m in this study), the maximum tensile stress due to curling stress increased with a simultaneous rise in thickness and compressive strength up to 35MPa, particularly under the influence of a 35^{o}C thermal gradient.

- The maximum tensile stress in all slabs with various lengths and thicknesses was decreased when the compressive strength of concrete was greater than 35MPa. Additionally, in high-strength concrete slabs, the plate element behavior was observed in slabs with various lengths and thicknesses. Additionally, with a raise in thermal gradient, higher maximum tensile stress due to curling and a higher flexural moment happened. However, increasing the thickness of slabs led to a considerable reduction in tensile stress as a result of improving the lateral and out-of-plane deformation, predominantly in slabs with shorter lengths, up to 6m.
- The simultaneous increase in compressive strength of concrete and thickness of slabs could be considered for a substantial improvement in lateral out-of-plane deformation and generally the thermal and curling behaviors of rigid concrete airfield runways. The curve-shaped lateral deformation could be observed in slabs with 6m length. However, with an increase in slab length, the lateral deformation value was slightly increased due to increasing the bending moment and reduction in lateral stiffness of slabs. With a rise in concrete's compressive strength, which may be related to raising the lateral resistance, the greatest lateral deformation was reduced. It should be mentioned that the 6m long slabs' overall lateral motion could be regarded as a bending plate element similar to 4.5m long rigid concrete slabs. The lateral out-of-plane deformation and generally the thermal and curling behaviors of rigid concrete airfield

runways could thus be improved in short-length slabs due to the simultaneous increase in concrete's compressive strength and slab thickness.

- The out-of-plane behavior of long slabs is different from short slabs. Therefore, the behavior of short slabs should be considered as bending plates and long slabs as membrane shells. With the increase in the length of the slab from 6m to 7.5m, the lateral deformation of the slab and the overall shape of its failure have changed, and the shape of the curve has changed to the deformation of our peak point. Also, increasing the compressive strength of concrete in a slab with a thickness of 10cm causes an increase in lateral deformation and, as a result, intensification of thermal stresses and an increase in cracks along the thickness of the slab. This change of state in the lateral behavior of the slabs can be considered as a transition state from the plate bending behavior to the membrane shell state. Also, the increase in thermal gradient has increased the lateral deformation in slabs with a length of 7.5m, although the amount of changes in long slabs is less than in slabs with a shorter length.
- Generally, increasing the thermal gradient led to increasing the maximum tensile stress. In 25MPa concrete compressive strength, with an increase in thickness of slabs with 7.5m length, the tensile stress increased while in shorter slabs, this response declined. Additionally, in 4.5m long slabs exposed to up to $15^{o}C$ thermal gradient, increasing the slab width increased the tensile stress while for 6m and 7.5m long slabs, the maximum tensile stress declined.
- The presented advanced finite element method simulation in this study could be utilized to model the mechanical characteristics of fiber-reinforced concrete materials as well as the structural responses of fiber-incorporated concrete structures, and rigid concrete airfield runways in this study.
- Fibers incorporation, polypropylene fibers in this study, could be taken into consideration as a useful technique to enhance the structural performance of rigid concrete airfield runways.

Because not only does the fiber incorporation improves the thermal behaviors of the rigid concrete airfield as well as crack width control but also could improve the structural responses of airfield runways under the influence of traffic load.

- Fiber incorporation improved the thermal behavior of slabs and the out-of-plane deformation decreased when fiber was utilized in concrete. The bridging function of PF keeps particles together in the matrix and decreases the distance between cracks. The flexural strength was improved by increasing the compressive and splitting tensile strengths of concrete because the top and bottom cross-sectional sections of concrete slabs experience compressive and tensile strains when they are subjected to a flexural load. Therefore, the curling behavior of rigid concrete slabs is enhanced and the fiber incorporation could be considered as an operative way to enhance the curling performance of rigid concrete airfield runways. Additionally, the improvement influence of fiber on reducing the lateral deformation of slabs is more prominent when the thickness was increased. This could be associated with the higher incorporation volume of fiber when the thickness increased and generally, the volume of used concrete increased.
- Ultrasonic imaging test using a synthetic aperture focusing technique is one of the beneficial tools to identify the influence of material properties, geometric characteristics, and the stiffness of underneath soil layers on the resistance of the concrete airfield runways and its structural responses. In this regard, advanced numerical simulation using ABAQUS proposed in this study could be utilized to model the non-destructive test in order to predict the strength of rigid concrete airfield runways numerically.
- The maximum received frequency by ultrasonic imaging test was increased when the compressive strength of the concrete increased. So, it could be concluded that by increasing

the compressive strength more energy dissipated and the maximum amplitude of frequency amplified. Increasing the thickness of slabs led to increasing the peak frequency which indicates the improvement in the strength and structural responses of rigid concrete slabs. It is worth to be mentioned that by increasing the thickness of slabs, the fluctuation in received frequency was smoother which indicated higher continuity and uniformity in the real airfield runways constructions. Additionally, fiber incorporation led to a sharper fluctuation in frequency-time responses of slabs, and the peak of received frequency was increased when fiber was incorporated and the value was further amplified by increasing the fiber incorporation fraction which indicates more energy dissipation as a result of increasing the strength of slabs.

- The thickness of the slabs was an important factor in increasing their strength. Therefore, more energy was dissipated and consequently, the peak frequency was increased when the thickness of the slabs increased. Therefore, in slabs with 30 cm thickness, adding 0.5% and 1.0% PF led to increasing the maximum frequency by 40% and 47% when the compressive strength of concrete was also increased from 25MPa to 45MPa, which indicates the improvement in the structural performance of rigid concrete airfield runways.
- The maximum received stress increased as the concrete's compressive strength rose. Therefore, it could be inferred that as compressive strength increased, more energy was lost and the highest stress amplitude was amplified. Additionally, raising slab thickness increased to stress's peak, indicating that rigid concrete slabs' strength and structural responses have significantly improved. For fiber-reinforced airfield runways, nearly the same results were obtained as with conventional concrete slabs. However, fiber integration caused slabs' stress-time reactions to fluctuating more sharply, as a result of the airfield runways’ structural performance improvement.

- In the field, the Synthetic Aperture Focusing Technique based on ultrasonic imaging only provides engineers with the frequency performance and received responses by the receiver sensor. However, the obtained frequency results give a prediction about the possible micro-cracks and the inside structure of rigid concrete airfield runways. The disadvantage of using this apparatus is the lack of slab resistance and strength prediction. According to obtained results, increasing the compressive strength of concrete slabs resulted in increasing the stress values which indicates an improvement in the strength and structural performance of concrete slabs. Also, by increasing the compressive strength of concrete slabs considering various thicknesses of slabs, the stress value rose with almost the same slope and relationship. Therefore, the proposed relationship in this study helps engineers to predict the compressive strength of rigid concrete airfield runways using the received frequency from the ultrasonic imaging non-destructive test.
- The reflected frequency from the harder base layer using Synthetic Aperture Focusing Technique was superior to those samples with lower base layer stiffness which indicates better performance of the pavement. Also, by incorporating the fiber, the maximum received frequency increased. So, using the fiber and harder base layer simultaneously played a crucial role in improving the structural performance of rigid concrete airfield runways, particularly when the runways open to traffic.
- The advanced zero-stress assessment technique proposed in this study could be utilized as an acceptable tool to predict the possible length of cracks through the slab's thickness due to thermal gradient. Generally, fiber incorporation significantly decreased the depth of the zero-stress line which indicates fewer cracks in depth. This could be attributed to the bridging character of fibers in reducing the cracks width. Therefore, the width of cracks declined and

more cracks propagated through the thickness. Also, with an increase in thermal gradient, the zero-stress line depth increased with indicates to increase in the dept of propagated cracks. In 4.5m length slabs, a rise in slabs' width led to increasing the depth of cracks as well as their width due to increasing the curvature in rigid concrete airfield runways under the effect of the thermal gradient. Increasing the compressive strength in slabs with 4.5m length led to reducing the depth of possible cracks and by raising the compressive strength to 35MPa, the crack depth was further decreased.

- Increasing the thickness of slabs could be considered an effective factor in reducing the depth of cracks as the ratio of bending-tensile stress over the bending-tensile resistance of concrete declined. Also, increasing the thickness played an effective role in reducing the cracks depth, however, by increasing the width of the slabs, the cracks' depth was increased. As it could be observed from the presented results, the negative influence of thermal gradient on slabs with 7.5m width was more obvious than those slabs with shorter width which could be associated with the difference in out-of-plane and post-buckling performance of shorter width rigid concrete slabs. As a result, slabs with a longer width are more sensitive to temperature changes and it is recommended to use shorter width slabs in the airfield runways construction.
- The simultaneous use of high concrete compressive strength and fiber incorporation significantly enhanced the cracking behavior of rigid concrete slabs with 4.5m length and fewer cracks developed through the thickness, particularly for shorter-width slabs. Additionally, increasing the length of slabs to 6m led to increasing the depth of the zero-stress line and more cracks depth in comparison with 4.5m length slabs. Therefore, the depth of the zero-stress line considerably dropped with the inclusion of fibers, indicating fewer cracking. This may be ascribed to the fibers' ability to bridge gaps, narrowing cracks.

- Increasing compressive strength reduced the potential depth of cracks. The negative influence of thermal gradient on slabs with a 6m width was more obvious than those slabs with shorter width which could be associated with the difference in out-of-plane and post-buckling performance of shorter-width rigid concrete slabs. The findings showed that the negative impact of thermal gradient on slabs wider than 6m was more pronounced than on narrow slabs. As a consequence, it is advised to use shorter-width slabs because larger slabs are more susceptible to temperature variations.
- The behavior of concrete slabs with a length of 7.5 m is different from the behavior of slabs with a shorter length. This could be attributed to out-of-plane deformation and post-buckling behaviors of 7.5m length slabs. So, it is recommended to analyze 7.5m length slabs as membrane shell elements while slabs with shorter lengths are suggested to evaluate as plate elements. So, with an increase in width of 7.5m length slabs, the depth of the zero-stress line was slightly increased, however, in comparison with shorter length slabs (4.5m and 6m), the possible cracks depth was slightly lower. So, for longer slab lengths, it is recommended to limit the thickness of airfield runways just in terms of thermal behavior control. Although reducing the thickness of the slab causes higher deformations and more surface cracks in the slabs when the airfield runways open to traffic.
- The post-buckling behavior of concrete airfield runways was increased by raising the temperature. This could be associated with increasing the temperature variation between the top and bottom surfaces of slabs which results in higher stresses and consequently higher bending moment. However, fiber incorporation played a crucial role in reducing the post-buckling performance of rigid concrete airfield runways. Because the briding character of fibers enhances the tensile strength of concrete and reduces the crack spacing. So, higher stress

could be transferred through cracks resulting in a post-buckling performance reduction considerably.

- The post-buckling behavior of rigid concrete slabs could be considered linear for a thermal gradient up to 20^{o}C while by a further increase in thermal gradient, the nonlinearity significantly increased. Therefore, it is necessary to consider the nonlinear behavior for concrete slabs as well as the nonlinear thermal gradient through slabs' thickness for temperature variation over 20^{o}C. Also, the post-buckling deformation could be taken into account as almost linear when the compressive strength of concrete is greater than 35 MPa. It could also be observed that the post-buckling behavior decreased by increasing the compressive strength in slabs with 4.5m and 6m lengths. This could be associated with the potential of bending and curve deformation in slabs with shorter lengths. However, in slabs with 7.5m length, with an increase in the compressive strength up to 35MPa, the post-buckling values increased and then decreased when the compressive strength reached to 45MPa. This could be associated with the membrane shell element behavior and plate element behavior in long-length slabs with lower and higher concrete compressive strength, correspondingly. Therefore, the ratio of tensile stress over the tensile strength declined which resulted in a significant reduction in post-buckling behavior.
- For slabs constrained with a stabilized rigid base layer, the post-buckling behavior was decreased which could be associated with lower deformation of the base layer as well as a higher contact between the base layer and concrete slabs. Increasing the thickness led to reducing the post-buckling behavior of 4.5m and 6m length slabs while the post-buckling value for slabs with 7.5m length increased. This could be associated with the mode of failure and

also out-of-plane deformation in long-length slabs which showed the jumping behavior from membrane shell to plate bending element.

- The axial load was increased for slabs restrained by a stabilized rigid base layer, which may be related to lateral restriction due to the contact between concrete and base layers which results in generating an additional load in rigid concrete slabs. Additionally, an increase in the length of slabs restrained by a stabilized rigid base layer increased the axial load due to increasing the contact surface between the rigid concrete layer and base layer.
- Multilayer Genetic Programming Machine Learning Approach (MGPML) is a highly accurate and beneficial tool to develop highly accurate relationships and formulas for engineering problems
- To calculate the curling stress in rigid plain concrete slabs, the model provided by Hernandez and Al-Qadi (2019) had the highest agreement with the numerical and field test findings. The main reason could be associated with the concept of their model. Because their model has been established based on highly accurate finite element method formulation. But the disadvantage of their model is complex. Therefore, to use Hernandez's and Al-Qadi's (2019) model, a professional computer and finite element method specialist are necessary which limits the application of their model for fast-in-field calculation by engineers. Conversely, the proposed model in the current research with high accuracy could be utilized as a simple and beneficial technique to predict the curling stress of rigid plain concrete slabs in the field for designing purposes. Therefore, the close-real curling stress can be predicted using the model provided in this study and by Hernandez and Al-Qadi (2019), as well. This could promote the use of MLGPML going forward to predict engineering phenomena for different designing purposes.

Therefore, a straightforward way to predict the behavior of rigid concrete airfield runways may encourage engineers to consider a large number of variables in actual applications.

- To predict the curling stress in fiber-reinforced concrete airfield runways, the new model developed in the current research had the highest agreement with the numerical and in-field findings. It could be also observed that the accuracy of previous models declined for fiber-reinforced concrete slabs in comparison with the plain concrete samples. This could be attributed to the lack of fiber incorporation influence in previous models. However, the model developed by Hernandez and Al-Qadi (2019) could be also employed as an accurate technique to calculate the curling stress in fiber-incorporated rigid concrete airfield runways while their model is complex.
- Artificial intelligence is one of the strong tools for real-world phenomena prediction. The results of this study showed that there is good agreement between projected responses: out-of-plane deformation, tensile stress, shear stress, and bond-slip resistance in dowel bars, and numerical results when DNN has been employed. Because of this, rather than conducting in-field tests based on the composition of the materials, the machine learning methods used in this research could be used as effective tools to predict the structural responses of both plain and fiber-incorporated rigid concrete airfield runways.
- The probability of failure increased with a surge in slabs' length for up to 6m and then declined when the length was further increased to 7.5m. The negative influence of increasing thickness for a 7.5m slab's length could be associated with the modes of failure and the potential of curve deformation which results in out-of-plane buckling.
- Fiber incorporation played an effective role in reducing the probability of failure when 0.5% fibers were utilized. However, the positive influence of increasing the thickness declined when

the fibers fraction increased as the slope of changes has been considerably altered. The same trend was observed when 1.0% of fibers were employed. So, to consider the construction and material cost, the fiber incorporation fraction could be limited to 0.5% when a low strength compressive strength is considered for construction (in this study 25MPa). Therefore, fiber incorporation could be considered as an excellent technique for reducing the probability of failure as well as maintenance costs. The influence of fibers on reducing the probability of failure was greater for concrete slabs with lower compressive strength, 25MPa in this study. This could be associated with the potential of cracking in lower concrete compressive strength which highlights the performance of fibers in controling the cracks' width and their propagation.

- For plain concrete slabs, increasing the compressive strength of concrete from 35MPa to 45MPa led to reducing the probability of failure. Additionally, increasing the width of slabs increased the probability of failure while failure decreased in slabs with up to 6m length when the thickness increased. Conversely, increasing the thickness in slabs with 7.5m length resulted in raising the probability of failure due to increasing the potential of out-of-plane deformation and curve-shaped failure.

11.2. RECOMMENDATIONS FOR FUTURE WORK

The following topics are listed by the author as possible study areas to be taken into account for upcoming studies on the analysis and design of rigid concrete airfield runways subjected to a thermal gradient:

- The simultaneous influence of airplane load during landing and taking off and thermal gradient should be assessed. According to the presented results, the curling stress and deformation were dropped when the length of the slabs increased by 7.5 m and the thickness of the slabs decreased, as well. However, the reduction in the slab's thickness significantly decreases the structural performance of concrete runways during the traffic period.
- The influence of base layer soil characteristics could be measured. In this regard, the influence of soil variables such as anisotropy, stabilization, and also fiber-stabilized base layer could be analyzed to identify the best pavement design method for airfield runways.
- In the current study, jointed plain and fiber-reinforced concrete slabs strengthened with steel dowel bars in the saw-cutting region were investigated. Therefore, it is highly recommended to measure the influence of various variables as well as fiber incorporation on the thermal performance of other types of rigid concrete pavements.

REFERENCES

AASHTO. (2012). Pavement management guide. 2012. *(2nd ed.). AASHTO*.

ABAQUS/Standard User's Manual (2015). *Michael Smith. United States*.

Adeli, H. (2001). Neural networks in civil engineering: 1989–2000. *Computer-Aided Civil and Infrastructure Engineering*, 16(2): 126-142.

Aitcin, P. C., Mehta, P. K. (1990). Effect of coarse aggregate characteristics on mechanical properties of high-strength concrete. *Materials Journal*, 87(2): 103–107.

Al-Nasra, M., Wang, L. R. (1994). Parametric study of slab-on-grade problems due to initial warping and point loads. *ACI Structural Journal*, 91(2): 198–210.

Al-Qadi, N. S. A, Mustapha, K. N. B., Qahir. N. S. (2011). Effect of polypropylene fibres on fresh and hardened properties of self-compacting concrete at elevated temperatures. *Australian Journal of Basic and Applied Sciences*. 5(10): 378-384.

Al-Rousan, R. Z. (2018). Failure Analysis of Polypropylene Fiber Reinforced Concrete Two-Way Slabs Subjected to Static and Impact Load Induced by Free Falling Mass. *Latin American Journal of Solids and Structures*, 2018, 15(1), e05.

Altoubat, S. (2010). Early age creep and shrinkage of concrete with Shrinkage Reducing Admixtures (SRA). *Jordan Journal of Civil Engineering*, 4(3): 281–291.

Alavi, A. H., Ameri, M., Gandomi, A. H., Mirzahosseini, M. R. (2011). Formulation of flow number of asphalt mixes using a hybrid computational method. *Construction and Building Materials.* 25(3): 1338–1355.

Aminian, P., Javid, M. R., Asghari, A., Gandomi, A. H., Esmaeili, M. A. (2011). A robust predictive model for base shear of steel frame structures using a hybrid genetic programming and simulated annealing method. *Neural Computing and Applications*. 20(8): 1321–1332.

Andersland, O. B., Ladanyi, B. (1994). An Introduction to Frozen Ground Engineering. *New York: Chapman & Hall*. 352.

Antonio, G., Pal, S. (2017). Deep learning with Keras. *Packt Publishing Ltd*.

ARA, Inc. (2004). Guide for Mechanistic-Empirical Design of New and Rehabilitated Pavement Structures. Draft Final Report, NCHRP Project 1-37A. *Transportation Research Board, National Research Council, Washington, DC.*

Arena, P., Fortuna, L., Muscato, G. (1998). Neural networks in multidimensional domains: fundamentals and new trends in modeling and control. Edited by Maria Gabriella Xibilia. London: Springer. 234.

Asbahan, R. E. (2009). Effects of the built-in construction gradient and environmental conditions on jointed plain concrete pavements. *Ph.D. dissertation, University of Pittsburgh, PA.*

Ashour, A. F., Alvarez, L. F., Toropov, V. V. (2003). Empirical modeling of shear strength of RC deep beams by genetic programming. *Computers & Structures*. 81(5): 331–338.

Attoh-Okine, N. (1994). Predicting roughness progression in flexible pavements using artificial neural networks. *Transportation Research Board Conference Proceedings*. 1(1).

Baykasoglu, A., Dereli, T., Tanis¸ S. (2004). Prediction of cement strength using soft computing techniques. *Cement and Concrete Research*. 34. 2083–2090.

Ball, A. K., Das, R., Roy, S. S., Kishu, D. R., Murmu, N. C. (2019a). Experimentation modeling and optimization of electrohydrodynamic inkjet microfabrication approach: a Taguchi regression analysis, *Sadhana*, 44:167.

Ball, A. K., Das, R., Roy, S. S., Kisku, D. R., Murmu, N. C. (2019b). A New Approach to Quantify the Uniformity Grade of the Electrohydrodynamic Inkjet Printed Features and Optimization of Process Parameters Using Nature-Inspired Algorithms. *International Journal of Precision Engineering and Manufacturing*. 21(3).

Ball, A. K., Roy, S. S., Kisku, D. R., Murmu, N. C., dos Santos Coelho, L. (2020). Optimization of drop ejection frequency in EHD inkjet printing system using an improved Firefly Algorithm. *Applied Soft Computing*. 94: 106438.

Ball, A. K., Das, R., Roy, S. S., Kisku, D. R., Murmu, N. C. (2020a). Modeling of EHD inkjet printing performance using soft computing-based approaches. Soft Computing. 24: 571–589.

Basheer, I. A., Hajmeer. M. (2000). Artificial neural networks: Fundamentals, computing, design, and application. *Journal of Microbiological Methods*. 43(1): 3-31.

Babaei, K., Purvis, R. L. (1995). Prevention of Cracks in Concrete Bridge Decks: Report on Laboratory Investigation of Concrete Shrinkage. *Report PA-FHWA-95-004+89-01. Pennsylvania Department of Transportation*, Harrisburg, PA.

Badr, A., Ashour, A. F., Platten. A. (2006). Statistical variations in impact resistance of polypropylene fiber-reinforced concrete. *International Journal of Impact Engineering*. 32:

1907–1920.

Bentz, D. P. (2000). A computer model to predict the surface temperature and time-of wetness of concrete pavements and bridge decks. *National Institute of Standards and Technology, NISTIR* 6551.

Bissonnette, B., Attiogbe, E. K., Miltenberger, M. A., Fortin, C. (2007). Drying shrinkage, curling, and joint opening of slabs-on-ground. *ACI Materials Journal*, 104(3): 259–267.

Bradbury, R. D. (1938). Reinforced Concrete Pavements. *Wire Reinforcement Institute*, Washington, DC.

Breitenbücher, R. (1990). Investigation of thermal cracking with the cracking frame. Materials and Structures. 23: 172–177.

Bradford, M. A. (2013a). Computational modeling of thermally-induced concrete pavement upheaval buckling. *In: International conference on civil, structural, and environmental engineering computing*. Cagliari, Italy. 93: 1–18.

Bradford, M. A. (2013b). Structural modeling of pavement upheaval buckling. *In: 26th Biennial Conference on the Concrete Institute of Australia. Gold Coast*, Australia. 218: 1–9.

Buch, N., Chatti, K., Haider, S. W., Manik, A. (2008). Evaluation of the 1-37A Design Process for New and Rehabilitated JPCP and HMA Pavements. *Michigan Department of Transportation*, Lansing, MI.

Caltrans. (2007). Project Risk Management Handbook: Threats and Opportunities. *Office of Statewide Project Management Improvement*, Sacramento, CA.

Castillo, C., Durrani, A. J. (1990). Effect of transient high temperature on high-strength concrete. *ACI Materials Journal*. 87(1): 47-53.

Cement Concrete & Aggregates Australia. (2002). *Drying Shrinkage of Cement and Concrete*.

Ceylan, H. (2007). Impact of Curling, Warping, and Other Early-Age Behavior on Concrete Pavement Smoothness: Early, Frequent, and Detailed (EFD) Study: FHWA Report. *Federal Highway Administration*, Washington, D.C.

Cheng, R. (2000). Genetic Algorithms and Engineering Design. *Wiley*, *Hoboken*, NJ, USA.

Choubane, B., Tia, M. (1992). Nonlinear temperature gradient effect on maximum warping stresses in rigid pavements. *Transportation Research Record: Journal of the Transportation Research Board*, 1370: 14–24.

Choubane, B., Tia, M. (1995). Analysis and verification of thermal-gradient effects on concrete pavement. *ASCE Journal of Transportation Engineering*, 121(1): 75–81.

Channakeshava, C., Barzegar, F., Voyiadjis, G. Z. (1993). Nonlinear FE analysis of plain concrete pavements with dowelled joints. *ASCE Journal of Transportation Engineering*, 119(5): 763–781.

Chung, Y. (2012). Thermal stress analysis of jointed plain concrete pavements containing fly ash and slag. *Ph.D. dissertation, Louisiana State University, LA.*

Chung, Y., Shin, A. H. C. (2015). Local calibration of EICM using measured temperature gradients and numerical analysis. *International Journal of Pavement Research and Technology.* 8(4): 259–266.

Childs, L. D., Kapernick, J. W. (1958). Tests of Concrete pavements on gravel subbases. *ASCE Journal of Highway Division*, 84, 3.

Chen, J., Kou, S. C., Poon, C. S. (2012). Hydration and properties of nano-TiO_2 blended cement composites. *Cement and Concrete Composites*. 34 (5): 642–649.

Chung, Y., Shin, H. C. (2009). Characteristics of coefficient of thermal expansion of PCC pavement. *Transportation Research Record 2009 Annual meeting CD-ROM; Washington D.C.: National Academy Council*.1-18.

Cottrel, W., Lee, H.. Nepstad, J., Crandall. M. (1996). Efforts toward developing a regional pavement management system in Utah. *Transportation Research Record: Journal of the Transportation Research Board*. 1524. 48-57.

Corley-Lay, J. (2014). Pavement performance measures: How states see good, fair, and poor. *Transportation Research Record: Journal of the Transportation Research Board*. 2431. 1-5.

Croll, J. G. (1997). A simplified model of upheaval thermal buckling of subsea pipelines. *Thin-Walled Structures*. 29(1): 59–78.

Croll, J. G. A. (1998). A simplified analysis of imperfect thermally buckled subsea pipelines. *International Journal of Offshore and Polar Engineering*. 8(4): 283–91.

Croll, J. G. A. (2005a). Some comments on the mechanics of thermal buckling. *Structural Engineering*. 83(8): 27–33.

Croll, J. G. (2005b). Thermal buckling of pavement slabs. *In: Proceedings of the ICETransport*. 158(2): 115–26.

Cumming, I. G., Wong, F. H. (2017). Digital signal processing of synthetic aperture radar data: algorithms and implementation. Norwood, MA: *Artech House; Hansen RE. Introduction to synthetic aperture sonar. In: Sonar systems. InTech*; 3–28.

Damnjanovic, I., Zhang, Z. (2008). Risk-Based Model for Valuation of Performance-Specified Pavement Maintenance Contracts. *Journal of Construction Engineering and Management*. 492-500.

Davids, W. G. (2001). 3D finite element study on load transfer at dowelled joints in flat and curled rigid pavements. *ASCE International Journal of Geomechanics*, 1(3): 309–323.

Darter, M. (1980). Requirements for reliable predictive pavement models. *Transportation Research Record: Journal of the Transportation Research Board*. 766. 25-31.

Deen, R. C., Azevedo, W. V., Rahal, A. S., Havens, J. H. (1980). Cracking in concrete pavements. *Transportation Engineering*. 106(2): 155–69.

Dere, Y., Asgari, A., Sotelino, E. D., Archer, G. C. (2006). Failure prediction of skewed jointed plain concrete pavements using 3D FE analysis. *Engineering Failure Analysis*, 13(6): 898–913.

De La Haza, O., Samokrutov, A. A., Samokrutov, P. A. (2014). Assessment of concrete structures using the Mira and EyeCon ultrasonic shear wave devices and the SAFT-C image reconstruction technique. *Construction and Building Materials.* 1276–91.

Dillon, B. (2003). State of the art and practice of site pavement management systems: recommendations for Union Pacific's site pavement management system. *Masters's Thesis, College of Engineering and Technology,* Brigham Young University, Provo, UT.

Duan, P., Yan, C., Luo, W., Zhou, W. (2016). Effects of adding nano- TiO_2 on compressive strength, drying shrinkage, and carbonation and microstructure of fluidized bed fly ash-based geopolymer concrete. *Construction and Building Materials*. 106: 115–125.

Du, X., Chen, W. (2002). Sequential Optimization and Reliability Assessment Method for Efficient Probabilistic Design. *Engineering Conference*. Montreal. Canada.

Eisenmann, J., Leykauf, G. (1990). Effect of paving temperatures on pavement performance. *2nd International Workshop on Theoretical Design of Concrete Pavements*, Spain.

Eidan, J., Rasoolan, I., Rezaeian, A., Poorveis, D. (2019). Residual mechanical properties of polypropylene fiber-reinforced concrete after heating. *Construction and Building Materials*. 198: 195-206.

Elias, A. M., Herbsman, Z. J. (2000). Risk Analysis Techniques for Safety Evaluation of Highway Work Zones. *In Transportation Research Record: Journal of Transportation Research Board*, 1715: 10-17.

Fang, Q., Zhang, J. (2013). Three-dimensional modeling of steel fiber reinforced concrete material under intense dynamic loading. *Construction and Building Materials*. 44: 118-132.

Falls, L., Haas, R., McNeil, S., Tighe. S. (2001). Asset management and pavement management: Using common elements to maximize overall benefits. *Transportation Research Record: Journal of the Transportation Research Board*. 1769. 1-9.

Felicetti, R., Gambarova, P. G., Rosati, G. P., Corsi, F., Giannuzzi, G. (1996). Residual mechanical properties of HSC subjected to high-temperature cycles. *4th International Symposium on Utilization of High-Strength/High-Performance Concrete, Paris, France*. 579-588.

Felker, V., Najjar, Y. M., Hossain. M. (2004). Modeling the roughness progression on Kansas Portland cement concrete (PCC) pavements. *Kansas Department of Transportation*.

Flyvbjerg, B., Holm, M. S., Buhl, S. (2002). Underestimating costs in public works projects: Error or lie? *Journal of the American Planning Association*. 279-295.

Freeseman, K., Khazanovich, L., Nojavan, A., Schultz, A., Chao, S. (2016). Nondestructive monitoring of subsurface damage progression in concrete columns damaged by earthquake loading. *Engineering Structures*.114: 148–57.

Ghalehnovi, M., Karimipour, A., de Brito, J. nd Chaboki, H. R. (2020). Crack Width and Propagation in Recycled Coarse Aggregate Concrete Beams Reinforced with Steel Fibres. *Applied Sciences*, 10

Ghalehnovi, G., Karimipour, A., Anvari, A. and de Brito, J. (2021). Flexural strength enhancement of recycled aggregate concrete beams with steel fiber-reinforced concrete jacket. *Engineering Structures*, 240, 112325

Ganesh, A. C., Muthukannan, M. (2020). Development of high-performance sustainable optimized fiber-reinforced geopolymer concrete and prediction of compressive Strength. *Journal of Cleaner Production*. 7: 124543.

Gandomi A. H., Roke, D. A. (2015). Assessment of artificial neural network and genetic programming as predictive tools. *Advances in Engineering Software*. 88, 63–72.

Gandomi, A. H., Babanajad, S. K., Alavi, A. H., Farnam, Y. (2012a) Novel approach to strength

modeling of concrete under triaxial compression. *Journal of Materials in Civil Engineering*, 24(9): 1132–1143.

Gandomi A. H., Alavi, A. H. (2012b). A new multi-gene genetic programming approach to nonlinear system modeling. Part I: materials and structural engineering problems. *Neural Computing and Applications*. 21(1): 171–187.

Gandomi, A. H., Alavi, A. H., Mirzahosseini, M. R., Nejad, F. M. (2011). Nonlinear genetic-based models for prediction of flow number of asphalt mixtures. *Journal of Materials in Civil Engineering*. 23(3): 248–263.

George, K. P. (2000). MDOT pavement management System: Prediction models and feedback system. *Mississippi Department of Transportation*.

Gencel, O., Kocabas, F., Gok, M. S., Koksal. F. (2021). Comparison of artificial neural networks and general linear model approach for the analysis of abrasive wear of concrete. *Construction and Building Materials*. 25(8): 3486-3494.

Ge, Z. (2005). Predicting temperature and strength development of field concrete. *Iowa State University*. 215

Goering, D. J., Kumar, P. (1996). Winter-time convection in open-graded embankments. *Cold Regions Science and Technology*, 24(1): 57-74.

Golroo, A., Tighe. S. (2012). Development of previous concrete pavement performance models using expert opinion. *Journal of Transportation Engineering*. 138(5). 634-648

Golshani, N., Shabanpour, R., Mahmoudifard, S., Derriblr, S., Mohammadian. A. (2017). Comparison of artificial neural networks and statistical copula-based joint models 17-01202.

Güler, İ., Übeyli, E. D. (2005). Adaptive neuro-fuzzy inference system for classification of EEG signals using wavelet coefficients. *Journal of Neuroscience Methods*. 148: 113-121.

Gencel, O., Saleem Kazmi, S. M., Munir, M. J., Kaplan, G., Yavuz Bayraktar, O. and Karimi Pour, A. (2021). Influence of bottom ash and polypropylene fibres on the physicomechanical, durability and thermal performance of foam concrete: An experimental investigation. *Construction and Building Materials*, 306, 124887.

Haas, R., Hudson, W. R., Zaniewaski, J. (1994). Modern pavement management. *Malabar, FL*: Krieger.

Hasannezhad, M., Yu. H., Zhu, W. P., Champagne, B. (2021). PACDNN: A phase-aware

composite deep neural network for speech enhancement. *Speech Communication*, 58: 658-669.

Hansen, W., Wei, Y., Smiley, D. L., Peng, Y., Jensen, E. A. (2006). Effects of paving conditions on built-in curling and pavement performance. *International Journal of Pavement Engineering*, 7(4): 291–296.

Hansen, W., Wei, Y. (2008). PCC Pavement Acceptance Criteria for New Construction When Built-In Curling Exists. Research Report RC-1481. *Michigan Department of Transportation, Lansing, MI*.

Hansen, W., Wei, Y., Schlangen, E. (2008). Moisture warping in jointed plain concrete pavements. *9th International Conference on Concrete Pavements*, San Francisco, CA.

Hansen, W., Wei, Y., Smiley, D. L. Peng, Y., Jensen, E. A. (2006). Effects of paving conditions on built-in curling and pavement performance. *International Journal of Pavement Engineering*. 291–296.

Harik, I. E., Jianping, P. Southgate, H., Allen, D. (1994). Temperature effects on rigid pavements. *ASCE Journal of Transportation Engineering*, 120 (1): 127–143.

Haimes, Y. Y. (1998). Risk Modeling, Assessment, and Management. *John Wiley & Sons, Inc*., New York.

Hetenyi, M. (1974). Beams on elastic foundation. *Ann Arbor: the University of Michigan Press*.

Hernandez, J., Al-Qadi, I. L. (2019). A closed-form solution for curling responses in rigid pavements. *Civil and Environmental Engineering Faculty Research and Publications*, Marquette University.

Hicks, R. G., Groeger, J. (2011). Pavement management practices in state highway agencies: Newington, Connecticut peer exchange results. *Federal Highway Administration*. FHWA-HIF-11-036.

Hiller, J. E. Roesler, J. R. (2006). Alternative Failure Modes for Long-Life Jointed Plain Concrete Pavements, *Proceedings of the International Conference on Long-Life Concrete Pavements*, Chicago, IL.

Hoegh, K., Khazanovich, L., Maser, K., Tran, N. (2012). Evaluation of an ultrasonic technique for detecting delamination in asphalt pavements. *Transportation Research Record: Journal of the Transportation Research Board*. 2306:105–10.

Hudson, W. R., Flanagan, P. R. (1987). An examination of environmental versus load effects on

pavements. *Transportation Research Record: Journal of the Transportation Research Board,* 1121: 34–39.

Huang, J., Zhang, Y., Tian, Y., Xiao, H., Shi, J., Shen, J., Zhang, N. (2020). Research on the Dynamic Mechanical Properties and Constitutive Models of Steel Fiber Reinforced Concrete and Polypropylene Fiber Reinforced Concrete. *Advances in Civil Engineering*. 17. 9174692.

Huang, Y. H. (2004). Pavement analysis and design. *Upper Saddle River, NJ*: Pearson Education, Inc.

Huang, C. J. (2007). Clustered defect detection of high-quality chips using self-supervised multilayer perceptron. *Expert Systems with Applications*. 33: 996-1003.

Huang, Y. H. (1993). Pavement Analysis and Design. Prentice Hall, *Upper Saddle River*, NJ.

Hveem, F. N. (1949). A Report of an Investigation to Determine Causes for Displacement and Faulting at the Joints in Portland Cement Concrete Pavements on California Highways. *California Division of Highways, Sacramento, CA*.

Hwang, C., Hong, D. H., K. H. (2006). Seok, Support vector interval regression machine for crisp input and output data. *Fuzzy Sets and Systems*. 157: 1114-1125.

Islam, G. M. S., Gupta, S. D. (2016). Evaluating plastic shrinkage and permeability of polypropylene fiber reinforced concrete. International Journal of Sustainable Built Environment. 5: 345-354.

Iurlaro, L., Gherlone, M., Sciuva, M. D. (2014). Energy-based approach for shape parameter selection in radial basis functions collocation method. *Composite Structures*. 107: 70-78.

Jack, J., Chou, Y. (2001). Pavement performance analysis applying probabilistic deterioration methods. *Transportation Research Record: Journal of the Transportation Research Board*. 1769: 20-27.

Janssen, D. J., Snyder, N. B. (2000). Temperature-moment concept for evaluating pavement temperature data. *ASCE Journal of Infrastructure Systems*. 6(2): 81–83.

Jeong, J. H., Zollinger, D. G. (2005). Environmental effects on the behavior of jointed plain concrete. *ASCE Journal of Transportation Engineering*, 131(2): 140–148.

Jeong, J. H., Park, J. Y., Lim, J. S., Kim, S. H. (2014). Testing and modeling of friction characteristics between the concrete slab and subbase layers. *Road Materials and Pavement Design*. 15(1): 114–30.

Jiji, L. M. (2009). Heat Convection (Second Edition). *Berlin Heidelberg*: Springer.

Johnson, A. M., Smith, B. C., Hong Johnson, W., Gibson. L. W. (2010). Evaluating the Effect of Slab Curling on IRI for South Carolina Concrete Pavements. *South Carolina Department of Transportation Research Report FHWA-SC-10-04. SCDOT Office of Materials and Research*, Columbia, SC.

Joshaghani, A., Balapour, M., Mashhadian, M., Ozbakkaloglu, T. (2020). Effects of nanoTiO_2, nano-Al_2O_3, and nano-Fe_2O_3 on rheology, mechanical and durability properties of self-consolidating concrete (SCC): An experimental study, *Construction and Building Materials*. 245: 118444.

John, T. S., Cristianini, N. (2000). An introduction to support vector machines and other kernel-based learning methods. *Cambridge University Press*. 204: 258-267.

Karimipour, A., Mohebbi Najm Abad, J. and Fasihihour, N. (2021d). Predicting the load-carrying capacity of GFRP-reinforced concrete columns using ANN and evolutionary strategy. *Composite Structures*, 275, 114470.

Karamihas, S. M. Senn, K. (2012). Curl and Warp Analysis of the LTPP SPS-2 Site in Arizona. Research Report No. FHWA-HRT-12-068. *Federal Highway Administration, Turner-Fairbank Highway Research Center. McLean*, VA.

Kapila, D., Falkowsky, J., Plawsky, J. L. (1997). Thermal effects during the curling of concrete pavement. *ACI Materials Journal*, 94(2): 119-127.

Kaw, K. K. (2006). Mechanics of composite Material. *Second Edition Tayler & Francis Group*. The Academic Division of T&F Information Plc.

Kargah-Ostadi, N., Stoffels. S. M. (2015). Framework for development and comprehensive comparison of empirical pavement performance models. *Journal of Transportation Engineering*. 141(8), 0000779.

Karlaftis, M. G., Vlahogianni. E. I. (2011). Statistical methods versus neural networks in transportation research: Differences, similarities and some insights. *Transportation Research Part C*. 19(3): 387-399.

Kargah-Ostadi, N., Stoffels, S., Tabatabaee. N. (2010). Network-level pavement roughness prediction model for rehabilitation recommendations. *Transportation Research Board: Journal of the Transportation Research Board*. 2155: 124-133.

Kang, S., Park, S., Kim, K. W., Woo, S. I., Park, S. (2007). High-throughput screening of ferroelectric materials for non-volatile random-access memory using multilayer perceptrons. *Applied Surface Science*. 254: 725-733.

Kerr, A. D., Dallis, J. W. A. (1985). Blowup of concrete pavements. *Journal of Transportation Engineering, Part B: Pavements*. 111(1):33–53

Kerr, A. D. (1994). Blowup of a concrete pavement adjoining a rigid structure. *International Journal of Non-Linear Mechanics*. 29(3): 387–96.

Karimi Pour, A. and Noroozinejad Farsangi, E. (2023a). Representing Capabilities of Novel Semi-Analytical Triangular Plate Elements. *The Journal of Strain Analysis for Engineering Design*.

Karimi Pour, A. and Noroozinejad Farsangi, E. (2023b). Airy Stress Function for Proposed Thermoelastic Triangular Elements. *Journal of Engineering Mathematics*.

Kerr, A. D., Shade, P. J. (1984). Analysis of concrete pavement blowups. *Acta Mechanica*. 52 (3–4): 201–24.

Karimipour, A., Ghalehnovi, M. and de Brito, J. (2021c). New Model for the Lap-Splice Length of Tensile Reinforcement in Concrete Elements. *Journal of Structural Engineering*, 147 (12)

Kim, S., Ceylan, H., Gopalakrishnan, K. (2007). Initial smoothness of concrete pavements under environmental loads. *Magazine of Concrete Research,* 59(8): 599–609.

Kim, S., Ceylan, H., Gopalakrishnan, K. (2008). Smoothness variations of early-age jointed plain concrete pavements. *Canadian Journal of Civil Engineering*, 35(12): 1388–1398.

Kim, S., Ceylan, H., Heitzman, M. (2005). Sensitivity Study of Design Input Parameters for Two Flexible Pavement Systems Using the Mechanistic-Empirical Pavement Design Guide. *Proceedings of the 2005 Mid-Continent Transportation Research Symposium*. Ames, Iowa: Iowa State University.

Kim, K. H., Jeon, S. E., Kim, J. K., Yang, S. (2003). An experimental study on thermal conductivity of concrete. *Cement and Concrete Research,* 33(3): 363-371.

Karimipour, A., Ghalehnovi, M., Golmohammadi, M. and de Brito, J. (2021b). Experimental Investigation on the Shear Behaviour of Stud-Bolt Connectors of Steel-Concrete-Steel Fibre-Reinforced Recycled Aggregates Sandwich Panels. *Materials*, 14 (18), 5185.

Karimipour, A., Ghalehnovi, M., Edalati, M. and de Brito, J. (2021a). Properties of Fibre-Reinforced High-Strength Concrete with Nano-Silica and Silica Fume. *Applied Science*, 11,

9696.

Kinsler, L. E., Frey, A. R., Coppers, A. B., Sanders, J. V. (1999). Fundamentals of acoustics. fourth ed. John Wiley and Sons Inc.

Khan, M. I. (2002). Factors affecting the thermal properties of concrete and applicability of its prediction models. *Building and Environment*, 37(6): 607-614.

Khazanovich, L., Hoegh, K. (2016). Quantitative ultrasonic evaluation of concrete structures using one-sided access. *In: Proceedings of 42nd annual review of progress in quantitative nondestructive evaluation*, 020007: 1–16.

Karimi Pour, A. (2022). Experimental and numerical evaluation of steel fibres RC patterns influences on the seismic behaviour of the exterior concrete beam-column connections. *Engineering Structures*, 263, 114358

Kirbas, U., Gursoy. M. (2010). Developing the basics of the pavement management system in the Besiktas district and evaluation of the selected sections. *Scientific Research and Essays*. 5(8): 806-812.

Karimi Pour, A., de Brito, J., Ghalehnvoi, M., and Gencel, O. (2022c). Torsional behaviour of rectangular high-performance fiber-reinforced concrete beams. *Structures*, 35, 511-519

Koza, J. R. (1992). Genetic Programming: On the Programming of Computers by Means of Natural Selection. *MIT Press, Cambridge, MA*, USA.

Krause, M., Mielentz, F., Milman, B., Müller, W., Schmitz, V., Wiggenhauser, H. (2001). Ultrasonic imaging of concrete members using an array system. *NDT E Int*. 34(6): 403–8.

Karimi Pour, A., Mohajeri, Z. and Noroozinejad Farsangi, E. (2022b). Impact of Polypropylene Fibers on the Mechanical and Durability Characteristics of Rubber Tire Fine Aggregate Concrete. *Materials*

Kuo, C., Hall, K., Darter, M. (1996). Three-dimensional finite element model for analysis of concrete pavement support. *Transportation Research Record: Journal of the Transportation Research Board*. 1505: 119–127.

Kuo, C. M. (1998). Effective temperature differential in concrete pavements. *ASCE Journal of Transportation Engineering*, 124(2): 112–116.

Karimi Pour, A., Shirkhani, A., Zeng, J. J., Zhuge, Y. and Noroozinejad Farsangi, E. (2023a). Experimental investigation of GFRP-RC beams with Polypropylene fibers and waste granite

recycled aggregate. *Structures.*

Karimi Pour, A., Shirkhani, A., Serkan KIRGIZ, M. and Noroozinejad Farsangi, E. (2023b). Influence of Fiber Type on the Performance of Reinforced Concrete Beams Made of Waste Aggregates: Experimental, Numerical and Cost Analyses. *Practice Periodical on Structural Design and Construction*. ASCE.

Langenberg, K., Bergerm M., Kreutter, T., Mayer, K., Schmitz, V. (1986). Synthetic aperture focusing technique signal processing. *NDT Int*. 19(3):177–89.

Lederle, R. E., Lothschutz, R. W., Hiller, J. E. (2011). Field Evaluation of Built-In Curling Levels in Rigid Pavements. *Report MN/RC 2011-16. Minnesota Department of Transportation*, St. Paul, MN.

Leonards, G. A., Harr, M. E. (1959). Analysis of concrete slabs on the ground. *ASCE Journal of the Soil Mechanics and Foundations Division*, 85(3): 35–58.

Lederle, R. E., Lothschutz, R. W., Hiller, J. E. (2011). Field Evaluation of Built-In Curling Levels in Rigid Pavements. *Minnesota Department of Transportation Research Report MN/RC 2011-16*, Michigan Technological University. Houghton, MI.

Levinson, R., Akbari, H. (2002). Effects of composition and exposure on the solar reflectance of Portland cement concrete. *Cement and Concrete Research*. 32(11): 1679-1698.

Lim, S., Tayabji, S. D. (2005). Analytical technique to mitigate early-age longitudinal cracking in jointed concrete pavements. *8th International Conference on Concrete Pavements*, Colorado Springs, CO.

Liang, R. Y., Niu, Y. Z. (1998). Temperature and curling stress in concrete pavements: analytical solutions. *ASCE Journal of Transportation Engineering*, 124(1): 91–100.

Liu, J. (2013). Radial Basis Function (RBF) neural network control for mechanical systems: design, Analysis and Matlab simulation. *Springer Science & Business Media*.

Li, N., Xie, W. C., Haas, R. (1996). Reliability-based processing of Markov chains for modelling pavement network deterioration. *Transportation Research Record: Journal of the Transportation Board*. 1524: 203-213.

Li, J., Pierce, L. M., Hallenbeck, M. E., Uhlmeyer, J. (2009). Sensitivity of Axle Load Spectra in the Mechanistic–Empirical Pavement Design Guide for Washington State. *In Transportation Research Record: Journal of the Transportation Research Board*. 2093. 50–56.

Lou, Z., Gunaratne, M., Lu, J. J., Dietrich, B. (2001). Application of neural network model to forecast short-term pavement crack condition: Florida case study. *Journal of Infrastructure Systems*. 7(4): 166-171.

Marar, K., Eren. A. (2001). Relationship between impact energy and compression toughness energy of high-strength fibre-reinforced concrete. *Materials Letters*. 47: 297-304.

Masad, E., Taha, R., Muhunthan, B. (1996). Finite-Element Analysis of Temperature Effects on Plain-Jointed Concrete Pavements. *Journal of Transportation Engineering*, 122(5): 388-398.

Mahboub, K. C., Liu, Y., Allen, D. L. (2004). Evaluation of temperature responses in concrete pavement. *ASCE Journal of Transportation Engineering*, 130(3): 395–401.

Mackiewicz, P. (2014). Thermal stress analysis of jointed plane in concrete pavements. *Applied Thermal Engineering*. 73 (1): 1167–1174.

Mackiewicz, P., Szydło, A. (2020). Thermal Stress Analysis in Concrete Pavements. *Journal of Transportation Engineering, Part B: Pavements*. 146(3): 06020002.

Martinez, O., Parrilla, M., Izquierdo, M. A. G., Ullate, L. G. (1999). Application of digital signal processing techniques to synthetic aperture focusing technique images. *Sensor Actuator*. 76: 448–56.

Mahadevan, S., Rebba, R. (2005). Validation of Reliability Computational Models using Bayes Networks. *Journal of Reliability Engineering and System Safety*, 87 (2): 223-232.

Maher, A., Bennert, T. (2008). Evaluation of Poisson's Ratio for Use in the Mechanistic-Empirical Pavement Design Guide (MEPDG). *New Jersey Department of Transportation*, Trenton, NJ.

McCracken, J. K. (2008). Seasonal analysis of the response of jointed plain concrete pavements to FWD and truck loads. *Thesis, University of Pittsburgh, PA.*

McCracken, J. K., Asbahan, R. E., Vandenbossche. J. M. (2008). Smart Pavement: Response Characteristics of a Jointed Plain Concrete Pavement to Applied and Environmental Loads – Phase II Final Report. *Report FHWA-PA-2008-007-22021-2B- 013. University of Pittsburgh*, Pittsburgh, PA.

McCullough, B. F., Rasmussen, R. O. (1999). Fast track paving, Concrete temperature control and traffic opening criteria for bonded concrete overlays. *U.S. Department of Transportation.*

Mehta, A., Mehta, H., Manjunath, T. C., Ardil, C. (2008). A multi-layer artificial neural network architecture design for load forecasting in power systems. *International Journal of Applied*

Mathematics and Computer Sciences. 4(4): 227-240

Metin, H. (2006). The effects of high temperature on compressive and flexural strengths of ordinary and high-performance concrete. *Fire Safety Journal*. 41: 155-163.

MEPDG. (2004). Guide for Mechanistic-Empirical Design of New and Rehabilitated Pavement Structures. *In: NCHRP. Champaign, IL*. 1-49.

Merritt, D. K., Chang, G. K., Torres, H. N. Mohanraj, K., Rasmussen, R. O. (2015). Evaluating the Effects of Concrete Pavement Curling and Warping on Ride Quality. *Report CDOT-2015-07. Colorado Department of Transportation*, Denver, CO.

Mills, L., Attoh-Okine, N., McNeil, S. (2012). Developing pavement performance models for Delaware. *Transportation Research Record: Journal of the Transportation Research Board*. 2304: 97-103.

Moradikhou, A. B., Esparham, A., Avanaki, M. J. (2020). Physical & mechanical properties of fibre reinforced metakaolin-based geopolymer concrete, *Construction and Building Materials*. 251: 118965.

Modarres, M. (2006). Risk Analysis in Engineering: Techniques, Tools, and Trends. *Taylor & Francis Group*, Boca Raton, FL.

Molenaar, K., Anderson, S., Schexnayder, C. (2008). NCHRP Report 658: Guidebook on Risk Analysis Tools and Management Practices to Control Transportation Project Costs. *Transportation Research Board*, Washington D.C.

Müller, P., Novák, J., Holan, J. (2019). Destructive and non-destructive experimental investigation of polypropylene fibre reinforced concrete subjected to high temperature. *Journal of Building Engineering*. 26: 100906.

Muller, W., Kreutter, T., Thumser, D., Schmitz, V. (1991). Ultrasonic turbine shaft inspection using the synthetic aperture focusing technique (SAFT). *Nuclear Engineering and Design*. 130(1): 339–46.

Naskar, S., Kumar, A. (2016). Chakraborty Effect of nanomaterials in geopolymer concrete Perspectives in science, *Applied Science*. 8: 273–275.

Nantung, T. E. (2011). High-Performance Concrete Pavement in Indiana. Report FHWA/IN/JTRP-2011/20. *Indiana Department of Transportation, Division of Research and Development*, West Lafayette, IN.

Nassiri, S. (2011). Establishing permanent curl/warp temperature gradient in jointed plain concrete pavements. *Ph.D. dissertation, University of Pittsburgh*, PA.

Nam J. H. (2005). Early-age behavior of CRCP and its implications for long-term performance. Ph.D. Dissertation, *The University of Texas at Austin, Texas*, USA.

Nishizawa, T., Fukda, T., Matsuno, S., Himeno, K. (1990). Curling stress equation for the transverse joint edge of a concrete pavement slab based on finite-element method analysis. *Transportation Research Record*. 1525.

Oliveira, A. L. I. (2006). Estimation of software project effort with support vector regression. *Neurocomputing*. 69: 1749-1753.

Pi, Y. L., Bradford, M. A., Uy, B. (2002). In-plane stability of arches. *International Journal of Solids and Structures*. 39(1): 105–25

Pi, Y. L., Bradford, M. A. (2010). Nonlinear in-plane elastic buckling of shallow circular arches under uniform radial and thermal loading. *International Journal of Mechanical Sciences*. 52(1): 75–88.

Popovics, J. S., Roesler, J. R., Bittner, J., Amirkhanian, A. N., Brand, A. S., Gupta, P., Flowers, K. (2017). Ultrasonic imaging for concrete infrastructure condition assessment and quality assurance. *Research Report No. FHWA-ICT-17–1007. Illinois Department of Transportation.*

Proceq. Pundit 250 Array Application Booklet. (2017).

Rao, S., Roesler, J. R. (2005a). Characterizing effective built-in curling from concrete pavement field measurements. *ASCE Journal of Transportation Engineering*, 131 (4): 320–327.

Rao, S., Roesler, J. R. (2005b). Characterization of Effective Built-in Curling and Concrete Pavement Cracking on the Palmdale Test Sections. *University of Illinois at Urbana Champaign*, Urbana, IL.

Rezaiee-Pajand, M. and Karimi Pour, A. (2020). Analytical Scheme for Solid Stress Analysis. *International Journal of Applied Mechanics*, 12 (6), 2050071.

Rezaiee-Pajand, M. and Karimi Pour, A. (2022). Easy function for solving linear elasticity problem. *Structural Engineering and Mechanics* 81 (3), 335-348.

Rao, C., Barenberg, E. J., Snyder. M. B. (2001). Effects of temperature and moisture on the response of jointed concrete pavements. *7th International Conference on Concrete Pavements*, Orlando, FL.

Rashidian-Dezfouli, H., Rangaraju, P. R., Kothala, V. S. K. (2018). Influence of selected parameters on compressive strength of geopolymer produced from ground glass fibre, *Construction and Building Materials*. 162. 393–405.

Rattanasak, U., Pankhet, K., Chindaprasirt, P. (2010). Effect of chemical admixtures on the properties of high calcium fly ash geopolymer. *International Journal of Minerals, Metallurgy and Materials*. 18: 364–369.

Rackwitz, R., Fiessler, B. (1978). Structural reliability under combined random load sequences. *Computers & Structures*. 9(5): 489–494.

Rafiq, M. Y., Bugmann, G., Easterbrook, D. J. (2001). Neural Network Design for Engineering Applications. *Computers & Structures*. 79(17): 1541-1552.

Rivero-Vallejo, F., McCullough, B. F. (1976). Drying shrinkage and temperature drop stress in jointed reinforced concrete pavement. *Report CFHR 3-8-75-177-1. Texas State Department of Highways and Public Transportation,* Austin, TX.

Rohsenow, W. M., Hartnett, J. P., Cho, Y. I. (1998). Handbook of Heat Transfer. *New York: McGraw-Hill*. 1501.

Roger, J. J. S., Sun, C. T., Mizutani, E. (1997). Neuro-fuzzy and soft computing a computational approach to learning and machine intelligence. *IEEE Transactions on automatic control*. 42: 1482-1484.

Ruiz, J. M. (2001). Concrete temperature modeling and strength prediction using maturity concepts in the FHWA HIPERPAV software. *Proceeding of the 7th International Conference on Concrete Pavements, International Society for Concrete Pavements*, Orlando, FL, 97-111.

Rezaiee-Pajand, M., Rezaiee-Pajand, A. and Karimi Pour, A. (2022). A Particle Swarm Optimization algorithm to suggest formulas for the behaviour of the recycled materials reinforced concrete beams. *International Journal of Optimization in Civil Engineering*, 10 (3), 451-479.

Rezaiee-Pajand, M., Karimi Pour, A. and Attari, M. (2020). A precise splice length model for reinforced concrete structures. *Proceedings of the Institution of Civil Engineers - Structures and Buildings*.

Rezaiee-Pajand, M., Mohebi Najm Abad, J. and Karimi Pour, A. (2021). Propose new implement models to determine the compressive, tensile and flexural strengths of recycled coarse aggregate

concrete via Imperialist Competitive Algorithm. *Journal of Building Engineering*, 40, 102337

Sastry, G. K., Sahitya, P., Ravitheja, A. (2021). Influence of nano TiO_2 on strength and durability properties of geopolymer concrete. *Materials Today: Proceedings*. 12: 102568.

Sanchez, F., Sobolev, K. (2010). Nanotechnology in concrete- A review. *Construction and Building Materials*. 24, (11): 2060–2071.

Sayyady, F., Stone, J. R., Taylor, K. L., Jadoun, F. M., Kim, Y. R. (2010). Clustering Analysis to Characterize Mechanistic–Empirical Pavement Design Guide Traffic Data in North Carolina. *In Transportation Research Record: Journal of the Transportation Research Board*. 2160. 118–127.

Sutcu, M., Gencel, O., Erdogmus, E., Kizinievic, O., Kizinievic, V. and Karimi Pour, A. (2022). Low cost and eco-friendly building materials derived from wastes: Combined effects of bottom ash and water treatment sludge. *Construction and Building Materials*, 324, 126669

Salehi-Ashtini, R. (2011). Stresses in Rigid Pavements: Chapter 3. *University of Texas at El Paso*, Texas. The USA.

Schmitt, T. R., Darwin, D. (1999). Effect of material properties on cracking in bridge decks. *ASCE Journal of Bridge Engineering*, 4(1): 8–13.

Schickert, M., Krause, M., Muller, W. (2003). Ultrasonic imaging of concrete elements using reconstruction by synthetic aperture focusing technique. *Journal of Materials in Civil Engineering*. 153: 235–46.

Schindler, A. K., Dossey, T., McCullough, B. F. (2002). Temperature Control During Construction to Improve the Long-Term Performance of Portland Cement Concrete Pavements. *Center for Transportation Research, Austin*, United States, 2002.

Schindler, A. K., Folliard, K. J. (2005). The heat of hydration models for cementitious materials, *ACI Materials Journal*. 102–M04.

Schwartz, C. W., Li, R., Kim, S. H., Ceylan, H. (2011). NCHRP 1-47 Final Report: Sensitivity Evaluation of MEPDG Performance Prediction. *Transportation Research Board*, Washington. 2011.

Shahin, M. Y. (2005). Pavement management for airports, roads, and parking lots. *New York: Springer*. 501.

Shi, M., Lin, Q., Zhang, Q., Zhao, H. (2011). Hybrid genetic Tabu search simulated annealing

algorithm and its application in vehicle routing problems with time windows. *Proceedings of the 2nd International Conference on Artificial Intelligence, Management Science and Electronic Commerce (AIMSEC)*, Dengleng, China, 4022–4025.

Siddique, Z., Hossain, M. (2005). Finite element analysis of PCCP curling and roughness. *8th International Conference on Concrete Pavements*, Colorado Springs, CO.

Siddique, Z., Hossain, M., Devore, J. J. (2004). Investigation of the Effect of Curling on As-Constructed Smoothness and Ride Quality of KDOT Portland Cement Concrete (PCC) Pavements. *Kansas Department of Transportation Research Report, Kansas State University*. Manhattan, KS.

Silva, F., Van Dam, T., Bulleit, W., Ylitalo. R. (2000). Proposed pavement performance models for local government agencies in Michigan. *Transportation Research Record: Journal of the Transportation Research Board*. 1699: 81-86.

Skjelvareid, M. H., Olofsson, T., Birkelund, Y., Larsen, Y. (2011). Synthetic aperture focusing of ultrasonic data from multi-layered media using an Omega-K algorithm, 58; 2011. p. 1037–48. 5.

Smiley, D., Hansen, W. (2007). Investigation of Early Cracking on Selected JPCP Projects. *Report RC-1501. Michigan Department of Transportation*, Lansing, MI.

Sok, T., Kim, Y. K., Lee, S. W. (2020). A numerical approach to predict the zero-stress temperature in concrete pavements. *Construction and Building Materials*. 262. 120076.

Söderström, T., Stoica, P. G. (1989). System Identification. *Englewood Cliffs, NJ, Prentice-Hall International*.

Sobieszczanski-Sobieski, J., Emiley, M. S., Agte, J., S., Sandusky, R. R. (2000). Advancement of Bi-level Integrated System Synthesis (BLISS). *Proceedings of the 38th AIAA Aerospace Sciences Meeting and Exhibit*. Reno. AIAA Paper.

Szydlo, A. (1995). Statistical identification of parameters of airport pavements. *Wrocław, Poland: Scientific Papers of the Institute of Civil Engineering*, Technical Univ. of Wroclaw.

Taylor, P., Wang, X. (2014). Concrete Pavement Mixture Design and Analysis (MDA): Factors Influencing Drying Shrinkage. *National Concrete Pavement Technology Center*, Ames, IA.

Taylor, N., Tran, V. (1996). Experimental and theoretical studies in subsea pipeline buckling. *Marine Structures*. 9(2): 211–57.

Tang, R., Etzion, Y., Meir, I. A. (2004). Estimates of clear night sky emissivity in the Negev Highlands, Israel. *Energy Conversion and Management*, 45(11-12): 1831-1843.

Tarr, S., Okamoto, P., Sheehan, M., Packard, R. (1999). Bond interaction between concrete pavement and lean concrete base. *Transportation Research Record*. 1668: 9–16.

TAC. (1999). Highway asset management systems. Transportation Association of Canda Mbwana. A framework for developing stochastic multi-objective pavement management systems. *In First Road Transportation Technology Transfer Conference in Africa.* 350-363.

Teller, L. W., Sutherland, E. C. (1935). The structural design of concrete pavements, part 2: Observed effects of variations in temperature and moisture on the size, shape, and stress resistance of concrete pavement slabs. *Public Roads*, 16(9): 169–197.

Thomlinson, J. (1940a). Temperature variations and consequence stress produced by daily and seasonal temperature cycles in concrete slabs. *Concrete Constructional Engineering*, 36(6): 298–307.

Thomlinson, J. (1940b). Temperature variations and consequence stress produced by daily and seasonal temperature cycles in concrete slabs. *Concrete Constructional Engineering*, 36(7): 352–360.

Timoshenko, S. P., Woinowsky-Krieger, S. (1959). Theory of plates and shells. *New York: McGraw-Hill*.

Tran, N., Hall, K. D. (2007). Development and influence of statewide axle load spectra and flexible pavement performance. *In Transportation Research Record: Journal of the Transportation Research Board*. 2037. 106-114.

Trahair, N. S., Bradford, M. A., Nethercot, D., Gardner, L. (2008). The behaviour and design of steel structures to EC3. *Abingdon, UK*: Taylor and Francis.

Vandenbossche, J. M., Mu, F., Gutierrez, J. J., Sherwood. J. (2010). An evaluation of the built-in temperature difference input parameter in the jointed plain concrete pavement cracking model of the Mechanistic–Empirical Pavement Design Guide. *International Journal of Pavement Engineering*, 12(3): 215–228.

Vandenbossche, J. M. (2003). Interpreting Falling Weight Deflectometer Results for Curled and Warped Portland Cement Concrete Pavements. The *University of Minnesota*, St. Paul, MN.

Van Breugel, K. (1991). Simulation of hydration and formation of structure in hardening cement-

based materials. Ph.D. thesis, *Delft Univ. of Technology, Delft*, the Netherlands.

Vines-Cavanaugh, D., Shamsabadi, S., Zhao, Y., Huang, G., Wadia-Fascetti, S., Schirner, G., Briken, R., Wang, M. (2016). City-wide application of affordable and rapid streets can pavement-management system. *Journal of Infrastructure Systems*. 23(2).

Vlahogianni, E. I., Karlaftis, M. G. (2013). Testing and comparing neural network and statistical approaches for predicting transportation time series. *Transportation Research Record: Journal of the Transportation Research Board*. 2399: 9-22.

Von Quintus, H. L., Darter, M., Mallela, J. (2009). Recommended Practice for Local Calibration of the ME Pavement Design Guide. *Applied Research Associates, Inc.- Transportation Sector*. Round Rock, Texas, 2009.

Walls, J., Smith, M. R. (1998). Life-Cycle Cost Analysis in Pavement Design -Interim Technical Bulletin. *Federal Highway Administration*, Washington, D.C.

Wang, C. Y. (2010). Buckling of a weakened infinite beam on an elastic foundation. *Journal of Engineering Mechanics*. 136(4): 534–7.

Wells, S. A. (2005). Early age response of jointed plain concrete pavements to environmental loads. *Thesis, University of Pittsburgh, PA.*

Westergaard, H. M. (1926). Analysis of stress in concrete pavements due to variations of temperature. *Highway Research Board Proceedings*, 6: 201-215.

Westergaard, H. M. (1927). Analysis of stress in concrete pavements caused by variations of temperature. *Public Roads*, 8(3): 54–60.

White, J., Hurlebaus, S., Shokouhi, P., Wimsatt, A. (2014). Use of ultrasonic tomography to detect structural impairment in tunnel linings. *Transportation Research Record: Journal of the Transportation Research Board*. 2407: 20–31.

Wilson, M. L., Kosmatka, S. H. (2011). Design and Control of Concrete Mixtures. *15th Edition. Portland Cement Association*, Skokie, IL.

Wolters, A., Zimmerman, K. (2010). Research of Current Practices in Pavement Performance Modeling. No. FHWA-PA-2010-007-080307.

Wu, Z., Shi, C., He, W., Wu, L. (2016). Effects of steel fibre content and shape on mechanical properties of ultra-high-performance concrete. *Construction and Building Materials*. 103: 8–14.

Wu, H., Chen, J., Yang, K., Hu, X. (2016). Ultrasonic array imaging of multi-layer structures using

full matrix capture and extended phase shift migration. *Measurement Science and Technology*. 27: 1–8.

Wu, Z., Zhou, F., Hu, S. (2014). Prediction of stress intensity factors in pavement cracking with neural networks based on semi-analytical FEA. *Expert Systems with Applications*. 41(4): 1021-1030.

Xu, L., Li, B., Ding, X., Chi, Y., Li, C., Huang, B., Shi, Y. (2018). Experimental Investigation on Damage Behavior of Polypropylene Fiber Reinforced Concrete under Compression. *International Journal of Concrete Structures and Materials*. 12: 68.

Xu, L., Lin, M. (2017). On the critical axial forces of upheaval buckling for imperfect submarine pipelines. *Engineering Structures*. 147: 692–704.

Yang, H., Wang, S., Xia, X. (2021). Identification of enhancers and their strength using RKPK features and deep neural networks. *Analytical Biochemistry*. 630: 114318.

Yang, L. Y., Jia, Z. J., Zhang, Y. M., Dai, J. G. (2015). Effects of nano-TiO_2 on strength, shrinkage and microstructure of alkali-activated slag pastes. *Cement and Concrete Composites*. 57: 1–7.

Yang, C., Qin, K., Li, Y. (2006). Real-time ultrasonic imaging for multi-layered objects with synthetic aperture focusing technique. *In: Proceedings of instrumentation and measurement technology conference*.

Yang, G., Bradford, M. A. (2015). Thermoelastic buckling and post-buckling of weakened columns. *Structures*. 1: 12–9.

Yang, G., Bradford, M. A. (2018). Thermal-induced upheaval buckling of continuously-reinforced semi-infinite concrete pavements. *Engineering Structures*. 168: 865–876

Yang, G., Bradford, M. A. (2017a). Postbuckling snaking of the axially loaded infinite beam on a nonlinear foundation with restabilizing effects. *Journal of Engineering Mechanics*. 04017019

Yang, G., Bradford, M. A. (2017b). Refined modelling for thermal-induced upheaval buckling of continuously reinforced concrete pavements. *Engineering Structures*. 150: 256–70.

Yahaghi, J., Muda, Z. C., Beddu, S. B. (2016). Impact resistance of shells concrete reinforced with polypropylene fibre. *Construction and Building Materials*. 123: 394–403.

Yeon, J. H., Choi, S., Won, M. C. (2013). Evaluation of zero-stress temperature prediction of model for Portland cement concrete pavements. *Construction and Building Materials*. 492–500.

Yeon, J. H. (2011). Zero-stress temperature and its implications for long-term performance of

continuously reinforced concrete pavements. Ph.D. Dissertation, *The University of Texas at Austin, Texas*, USA.

Yinghong, Q. (2011). Numerical study on the curling and warping of hardened rigid pavement slabs. *Ph.D. dissertation, Michigan Technological University, MI.*

Yoo, D. Y., Shin, W., Chun, B., Banthia, N. (2020). Assessment of steel fibre corrosion in self-healed ultra-high-performance fibre-reinforced concrete and its effect on tensile performance. *Cement and Concrete Research*. 133: 106091.

Yoder, E. J., Witczak, M. W. (1975). Principles of Pavement Design. *2nd Edition. John Wiley & Sons, NY.*

Ytterberg, R. F. (1987). Shrinkage and curling of slabs on grade, Part II: Warping and curling. *Concrete International*, 9(5): 54–61.

Yu, H. T., Khazanovich, L., Darter, M. I. (2004). Consideration of JPCP curling and warping in the 2002 design guide. *83rd Annual Meeting of the Transportation Research Board*, Washington, DC.

Yu, H. T., Khazanovich, L. (2001). Effects of construction curling on concrete pavement behavior. *7th International Conference on Concrete Pavements*, Orlando, FL.

Yu, H. T., Khazanovich, L., Darter, M. I., Ardani, A. (1998). Analysis of concrete pavement responses to temperature and wheel loads measured from instrumented slabs. Transportation Research Record. *Transportation Research Board*, Washington, D.C. 94-101.

Zaghloul, S., White, T., Kuczek, T. (1994). Evaluation of heavy load damage effect on concrete pavements using three-dimensional, nonlinear dynamic analysis. *Transportation Research Record: Journal of the Transportation Research Board*. 1449: 123–133.

Zhang, J., Fwa, T. F., Tan, K. H., Shi, X. P. (2003). Model for nonlinear thermal effect on pavement warping stresses. *ASCE Journal of Transportation Engineering*, 129(6): 695–702.

Zhang, G., Patuwo, B. E., Hu, M. Y. (1998). Forecasting with artificial neural networks: The state of the art. *International Journal of Forecasting*. 14(1): 35-62.

CURRICULUM VITA

Arash Karimi Pour (AKP) completed graduate work at the Ferdowsi University of Mashhad (FUM) in Structural Engineering in 2017. Besides completing his master's studies, he began working as a project manager and structural engineer at the most well-known engineering consulting firms to gain practical skills. In August 2019, he joined the doctoral program in Civil Engineering at the University of Texas at El Paso (UTEP). Obtaining a GPA of 3.91/4, he worked as a Research Associate at the Center for Transportation Infrastructure Systems (CTIS) from August 2019 to August 2020. During his Ph.D. studies, he has being actively involved in a number of research projects funded by TxDOT and NASA emphasizing transportation infrastructures such as Roadways and Highway Pavements as well as Granular Mechanics of Mars Regolith Simulant. He has contributed to several scholarly publications; including book chapters, project technical reports, conference proceedings, and journal articles published by ELSEVIEW, ASCE, Springer, Taylor & Francis, Wiley, MPDI, and Techno-Press. He is an active peer reviewer for several prestigious journals such as ASCE, ELSEVIER, Springer, and MPDI. His research interests include different areas such as Finite Element Methods, Retrofitting Reinforced Concrete Members and New Concrete Technologies, Eco-Friendly and Sustainable Concrete Materials, Seismic Assessment of Structures and Dynamic Analysis, Transportation Soils and Pavement Design, Retaining walls, Characterization of geomaterials, Large Data Analytics, Fibers-Reinforced Materials, Artificial Intelligence, Geotechnical Earthquake Analysis, Soil Stabilization, Risk/Reliability Analysis of Infrastructure Systems and Steel and Reinforced Concrete Structures Design.

Email: akarimipour@miners.utep.edu